Transactions of the ASME®

Journal of Heat Transfer

Published Quarterly by The American Society of Mechanical Engineers

VOLUME 119 • NUMBER 3 • AUGUST 1997

Transactions of the ASME, Journal of Heat Transfer (ISSN 0022-1481) is published quarterly (Feb., May, Aug., Nov.) for $220.00 per year by The American Society of Mechanical Engineers, 345 East 47th Street, New York, NY 10017. Periodicals postage paid at New York, NY and additional mailing offices. POSTMASTER: Send address changes to Transactions of the ASME, Journal of Heat Transfer, c/o THE AMERICAN SOCIETY OF MECHANICAL ENGINEERS, 22 Law Drive, Box 2300, Fairfield, NJ 07007-2300. **CHANGES OF ADDRESS** must be received at Society headquarters seven weeks before they are to be effective. Please send old label and new address. **PRICES:** To members, $40.00, annually: to nonmembers, $220.00. Add $30.00 for postage to countries outside the United States and Canada.

TECHNICAL PAPERS

(Contents continued on Outside Back Cover)

(Contents continued)

Phase Change and Multiphase Heat Transfer

Heat Exchangers

Heat Transfer in Manufacturing

Heat Transfer Enhancement

Applications of Heat Transfer

TECHNICAL NOTES

(Contents continued on Inside Back Cover)

(Contents continued)

ANNOUNCEMENTS

Thermal Conductivity Measurements in Printed Wiring Boards

J. E. Graebner
jeg@bell-labs.com

Lucent Technologies,
Bell Laboratories,
600 Mountain Avenue,
PO Box 636,
Murray Hill, NJ 07974-0636

K. Azar
Lucent Technologies Inc.,
Bell Laboratories,
North Andover, MA 01845

The effective thermal conductivity κ of multilayer printed wiring boards (PWBs) has been measured for heat flowing in a direction either parallel ($\kappa_\parallel$) or perpendicular ($\kappa_\perp$) to the plane of the board. The conductivity of the glass/epoxy insulating material from which the boards are manufactured is anisotropic ($\kappa_\parallel^{ge} \approx 3 \times \kappa_\perp^{ge}$) and nearly three orders of magnitude smaller than the conductivity of copper. This large difference between glass/epoxy and copper produces extremely high anisotropy in PWBs that contain continuous layers of copper. For such boards, values of the board-averaged conductivity in the two directions can differ by a factor of ~100 or more. The value of $\kappa_\parallel$ is found to depend on the ratio of the total thickness of continuous layers of copper to the total thickness of glass/epoxy, while it depends hardly at all on the amount of copper circuitry visible on the surface.

Introduction

Multilayer printed wiring boards (PWBs) are currently in wide use because of the three-dimensional connectivity of circuitry that is allowed by buried conductors and the electromagnetic shielding that is provided by continuous layers of copper molded into the board. Careful thermal design is important if high-power-density devices are mounted on the board (Azar and Yuan, 1993), but so far there has been only limited experimental data available for the thermal conductivity of such boards (Sarvar et al., 1990; Vanlaer and Lasance, 1994). The literature on calculated thermal conductivities of PWBs is much more extensive (see, for example, Agarwal et al., 1991; Ellison, 1996; Lemczyk et al., 1992; Robinson and Mravic, 1996; and Stefani et al., 1993). Here we report thermal conductivity measurements of a variety of PWB samples which differ in the amount and type of circuitry, the number and thickness of buried copper layers, and the direction of heat flow. We find low conductivity in the glass/epoxy insulating material with a relatively small (factor of 3) anisotropy. The average conductivity of the glass/epoxy is nearly three orders of magnitude below that of copper, so that the in-plane board-averaged conductivity $\kappa_\parallel$ can be a factor of 100 higher than the perpendicular board-averaged conductivity $\kappa_\perp$. Simple expressions are given for $\kappa_\parallel$ and $\kappa_\perp$ depending on the fractional thickness that is comprised of copper in continuous layers (Azar and Graebner, 1996; Graebner, 1995).

Experimental Details

Fifteen thermal conductivity samples, labelled PC1 to PC16 and typically of dimensions 1 cm × 3 cm (Table I), were cut from six circuit boards (A through F in Table I) which were selected as being very typical of multilayer boards currently used in the production of electronic equipment. The FR-4 glass/epoxy insulating material incorporates glass fibers running in perpendicular directions in the plane of the board. The boards differed in the nominal number N of copper layers available, with N taking values from 1 to 8. (N as defined here includes copper layers on either or both surfaces of the board; e.g., board F with $N = 8$ has six buried layers and circuitry on each surface.) The samples were cut from locations selected for the number N_c of continuous layers of Cu (ground or power planes), the presence of partial layers (circuitry), or the number of vias, etc., as summarized in Columns 4 and 9 of Table I.

The measurement of thermal conductivity in materials with very low conductivity, such as glass/epoxy, requires special precautions because the heat flowing through the sample can be comparable to or less than the heat lost from the surface of the sample to the environment by radiation or convection (Carslaw and Jaeger, 1959; Maglic et al., 1984). To minimize such loss, most of the measurements reported here were performed with the sample located in a vacuum chamber and covered with thermal radiation reflecting material (multiple layers of 0.0025 cm thick aluminized Mylar, known as superinsulation). Even with such precautions, surface loss is important enough that disregarding it can cause the measured conductivity to be too large by a factor of 2 or 3. The techniques to detect and correct for surface loss are different for the $\kappa_\perp$ and $\kappa_\parallel$ cases and are discussed separately.

To make accurate measurements of $\kappa_\parallel$ for samples of intermediate conductivity (i.e., samples with at least one layer of continuous copper), a simple heated-bar technique with many thermocouples is used (Fig. 1). The thermocouples are thin enough that conduction through them to thermal ground is a negligible fraction (0.01 percent) of the conduction through the sample. To improve thermal contact with the embedded Cu layers, a line of approximately ten holes (0.060 cm diameter) is drilled across the sample at either end and Cu wire (0.025-cm. diameter) is threaded through the holes which are then filled with alumina-filled epoxy. With power $\dot{Q}$ applied at the free end of a uniform sample, the measured temperature profile is expected to be a straight line in the absence of surface heat loss. The upwardly curving profile in Fig. 1 can be least-squares fitted by the solution to the one-dimensional diffusion equation with surface loss (Carslaw and Jaeger, 1959, pp. 139–140). The solution $T(x)$ describes the temperature profile along a sample of length L with its ends at temperatures T_1 and T_2 and with an outward heat flux at the surface given by $h\Delta T$, where h is the surface heat loss coefficient. The assumed linear dependence of radiative heat loss on ΔT is adequate at room temperature with $\Delta T < 10°C$ (cf. Carslaw and Jaeger, 1959, p. 21). With this approximation, the solution is

$$T(x) = \frac{T_1 \sinh \mu(L - x) + T_2 \sinh \mu x}{\sinh \mu L}. \qquad (1)$$

μ is a measure of the importance of surface loss relative to bulk conduction,

Contributed by the Heat Transfer Division for publication in the JOURNAL OF HEAT TRANSFER. Manuscript received by the Heat Transfer Division April 15, 1996; revision received April 11, 1997; Keywords: Conduction; Measurement Techniques; Thermal Packaging. Associate Technical Editor: A. S. Lavine.

Table 1 Summary of characteristics of the PWBs labelled A through F from which samples PC1 through PC16 were cut. N is the nominal number of Cu layers in a board, and N_c is the number of continuous layers of Cu in the part of the board from which the sample was cut. The width W, length L, and thickness Z of the samples are given in centimeters, with uncertainties of 0.007, 0.007, and 0.002 cm, respectively. An asterisk after an entry for Z indicates that the sample is only the center section of the board, after removing all copper layers. The total thickness Z_{Cu} of continuous copper is given in microns, with an uncertainty in the thickness of each layer of 3 microns. Circuitry refers to the copper lines, vias, and pads visible on either or both surfaces. The board-averaged parallel ($\kappa_\parallel$) or perpendicular ($\kappa_\perp$) conductivity of each sample is given in units of $Wm^{-1}\,K^{-1}$. The uncertainties in $\kappa_\parallel$ and $\kappa_\perp$ are 5–10 percent.

Board	N	Sample	N_c	W	L	Z	Z_{Cu}	Circuitry	$K_\perp$	$K_\parallel$
A	1	PC11	1	1.70	3.6	0.150	1 × 32	none		9.0
B	2	PC14	0	1.00	1.00	0.156	0	none	0.33	
"	"	PC5	0	2.18	3.6	0.156	0	none		0.81
C	4	PC1	2	1.00	1.00	0.166	2 × 66	none	0.32	
"	"	PC15	0	1.04	2.7	0.067*	0	none		0.76
"	"	PC3	"	0.48	2.0	0.170	2 × 68	none		35.7
"	"	PC4	"	0.63	5.0	0.168	"	none		28.9
D	6	PC12	1	1.05	3.0	0.149	1 × 32	little		8.1
E	6	PC2	4	1.00	1.00	0.168	4 × 66	none	0.36	
"	"	PC16	0	1.07	3.2	0.0376*	0	none		1.05
F	8	PC6	2	2.46	4.1	0.147	2 × 34	none		15.9
"	"	PC7	"	1.68	4.5	0.143	"	many vias		14.6
"	"	PC8	"	2.6	4.7	0.146	"	surface mounts		14.5
"	"	PC9	"	2.06	5.1	0.146	"	surface mounts		14.4
"	"	PC10	"	2.02	5.8	0.146	"	much		18.0

$$\mu = (Ph/A\kappa)^{1/2}. \tag{2}$$

The quantity μ^{-1}, sometimes called the thermal healing length, is the length of sample for which the conductance along the sample is equal to the conductance out through the surface. P is the perimeter around sample cross section A, and the plane of A is perpendicular to the direction of heat flow. Equation 1 can be fitted to the data (Fig. 1) and the conductivity can be calculated from the fitting parameters μ, T_1, and T_2 as follows:

$$\kappa_\parallel = \frac{\dot{Q} \sinh \mu L}{\mu A (T_2 \cosh \mu L - T_1)}. \tag{3}$$

The overall uncertainty in the value of $\kappa_\parallel$ is 5–10 percent, judging by the residuals of the fit in Fig. 1. This uncertainty is dominated not by errors in the measurement of temperature or position (which are smaller than the size of the symbols in Fig. 1) but by real variations in conductivity along the sample due to the local configuration of the copper circuitry. The effective thermal conductivity depends on how small a region is studied. The fit in Fig. 1 clearly gives a conductivity averaged over a few centimeters. If one examined the thermal gradient on a submillimeter scale, one would expect to find regions of significantly lower or higher local conductivity.

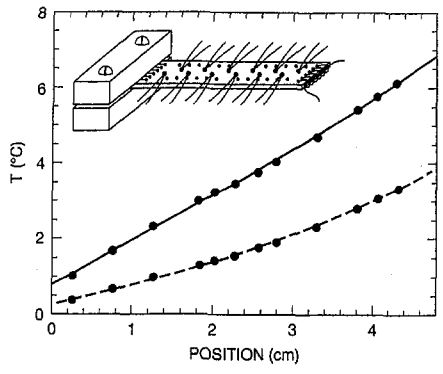

Fig. 1 Data for $\kappa_\parallel$ of sample PC9 in air (lower) and in vacuum with radiation insulation (upper). Twelve type-E thermocouples (0.005 cm diameter) and an electrical heater are glued to the sample. The thermocouples measure the temperature relative to that of a large copper block at room temperature. The uncertainties in temperature and position are smaller than the size of the symbols. The lines are fits of Eq. 1 to the data. (After Azar and Graebner, 1996)

To make accurate measurements of $\kappa_\parallel$ for lower-conductivity samples (without any copper layers), we use a two-heater, three-thermometer technique (Fig. 2), which provides an even more sensitive test for the presence of surface heat loss (Graebner et al., 1994). A bar of the material is clamped to thermal ground at one end and equipped with two electrical heaters, one (H1) at the free end, and one (H2) near thermal ground. Three thermocouples are located along the center line, away from the heaters. Power is first applied to heater H2, and the temperature profile is recorded after thermal equilibrium is attained (which can take an hour or more). If the profile is flat, then surface loss is not important compared to conduction through the sample. If, as is more generally the case for low-conductivity materials, a gradient exists, with the free end cooler than the H2 end (Fig. 3), this indicates heat flowing along the sample from H2 to replace heat lost through the surface. The shape of the temperature profile can be least-squares fitted with the solution (Carslaw and Jaeger, 1959) to the one-dimensional steady-state heat flow equation which takes into account heat loss from the surface; for the case of a long bar heated near the fixed end

$$T(x) = T_2 \frac{\cosh \mu(L - x)}{\cosh \mu L} \tag{4}$$

where T_2 is the temperature at H2. The three thermocouple temperatures are sufficient to perform a least-squares fit with Eq. (4) to determine T_2 and the important quantity μ.

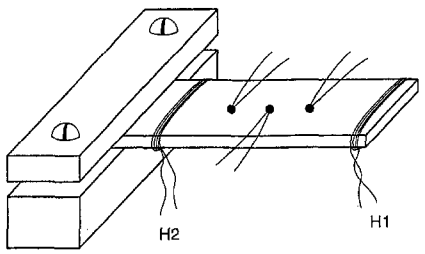

Fig. 2 Configuration of a sample for measurement of $\kappa_\parallel$ using the two-heater, heated-bar method. The three thermocouples measure the temperature distribution when the sample is heated by either heater, H1 or H2. The thermocouples are type E, 0.005 cm diameter, with special limits of error, and the heaters are wound with 0.0025 cm diameter Manganin wire.

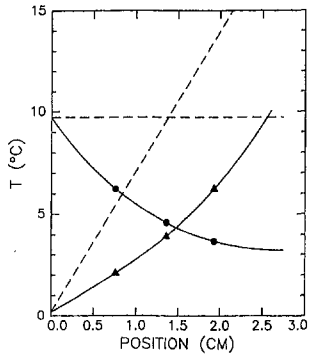

Fig. 3 Data for measuring $\kappa_\parallel$ of a sample of particularly low conductivity, PC15, with the two-heater method. The circles are data taken with H2 energized (Fig. 2), and the triangles are with 3.90 mW produced in H1. The circles are fit with Eq. 4 to determine the surface heat loss parameter $\mu = 0.645$ cm^{-1}. This value of μ is then used as a constant in the fitting of Eq. 1 to the triangles to determine $\kappa_\parallel$ (Eq. 3). The dashed lines are the predictions of Eqs. 1 and 4 if surface heat loss did not exist ($\mu = 0$). The uncertainties in temperature and position are smaller than the size of the symbols.

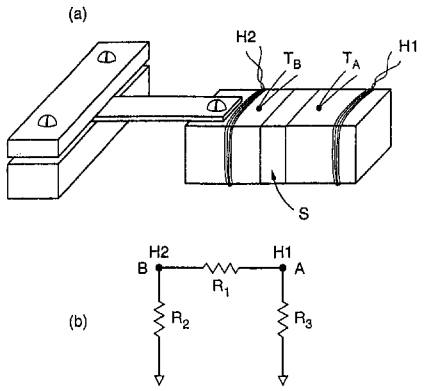

Fig. 4 (*a*) Schematic illustration of a sample *S* glued between two copper blocks for measurement of $\kappa_\perp$ with the two-heater technique. One copper block is attached to thermal ground through a copper foil. Thermocouples T_A and T_B measure the temperatures generated by heaters H1 or H2. The apparatus is located in a vacuum chamber to avoid convective loss. (*b*) Electrical analog of the thermal arrangement in (*a*). R_1 and R_2 are the thermal resistances of the sample and the copper foil, respectively, while R_3 represents the thermal leakage path due to radiation. H1 or H2 can be used to inject electrical current at points A or B, respectively.

Following the determination of μ, H2 is switched off and H1 switched on to generate heat flow $\dot{Q}$ into the free end of the rod. The temperature profile generated by $\dot{Q}$ flowing toward thermal ground is a straight line if $\mu = 0$ and concave upward if $\mu > 0$. The data can again be fitted with Eq. 1 but now with μ fixed at the previously determined value and with only T_1 and T_2 adjusted for a best fit. Finally, $\kappa_\parallel$ is calculated from μ, T_1, and T_2 using Eq. 3. Figure 3 shows typical data and the results of fitting Eqs. 4 and 1 to the data. Equation (3) is incorrect if part of $\dot{Q}$ generated in the heater is lost by radiation from the free end of the sample (past the heater). Using the values of $\mu = 0.645$ cm^{-1} and $\Delta T = 10$°C (Fig. 3), we calculate such loss to be only ~2 percent of the heat dissipated in heater H1, and we ignore it. The precision of the measurement in this case of a uniform glass/epoxy sample without copper is not determined by inhomogeneities in the sample as in Fig. 1, but rather by the precision and bias contributions to the uncertainties in temperature and position, which are smaller than the size of the symbols in Fig. 3. The latter, combined with the above uncertainty due to radiative loss, produces ~5 percent uncertainty for $\kappa_\parallel$.

To make accurate measurements of $\kappa_\perp$ in the presence of surface losses, we use a modification of the two-heater technique. The sample (approximately 1.0 cm × 1.0 cm × 0.15 cm) is attached with thin layers of Ag-filled epoxy to the 1.0 × 1.0 cm^2 polished faces of two blocks of copper (Fig. 4*a*). Each block is equipped with a heater and thermocouple, and one block is connected to thermal ground through a copper foil, the thickness and width of which are chosen to provide a conductance close to that expected for the sample. The electrical analog consisting of three resistors R_1–R_3 connected as shown in Fig. 4*b* is useful in analyzing the experiment to extract a value for the sample resistance R_1 and thus $\kappa_\perp$. R_2 represents the thermal resistance of the copper foil, and R_3 is any finite resistance from H1 to thermal ground by way of surface heat loss. By applying heat only at point B (with heater H2), the ratio $C_{31} = R_3/R_1$ is determined: $C_{31} = T_A^{H2}/(T_B^{H2} - T_A^{H2})$. Similarly, by applying heat $\dot{Q}^{H1}$ at point A (with heater H1), the ratio $C_{21} = R_2/R_1 = T_B^{H1}/(T_A^{H1} - T_B^{H1})$ is determined. Furthermore, by calculating the heat current flowing from H1 through R_1 and R_2, one can show that $R_1 = (T_A^{H1} - T_B^{H1})(1 + C_{21} + C_{31})/(\dot{Q}^{H1}C_{31})$. The perpendicular conductivity can be calculated by including the sample dimensions: $\kappa_\perp = Z/R_1A$, where Z is the thickness and A is the area perpendicular to the heat flow. With typical values of R_1, C_{21}, and C_{31}, the combined uncertainty in $\kappa_\perp$ is 5 percent.

The above analysis for $\kappa_\perp$ determines an overall, board-averaged perpendicular conductivity. It is insensitive to details within the board or at the interfaces with the copper blocks, and it would be seriously in error if there were any significant thermal contact resistance at interfaces. For this reason, two of the samples, PC1 and PC2, were examined by high-resolution infrared imaging of the side of the sample while heat was flowing from one block to the other, as reported elsewhere in greater detail (Azar and Graebner, 1996). The imaging system was calibrated against temperature without a gradient present. The response of each pixel was calibrated individually to take into account differences in emissivity of the Cu and the glass/epoxy. A temperature profile with heat flowing from one copper block to the other is shown for sample PC2 in Fig. 5.

One might expect that radiative/convective loss at the glass/epoxy outer surface might lower the temperature of the surface

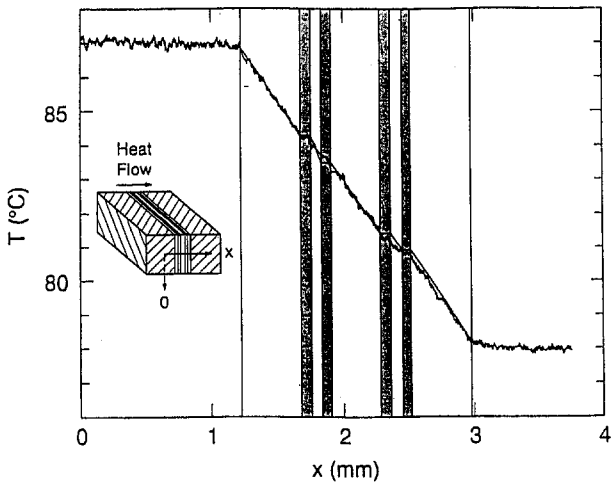

Fig. 5 Temperature profile obtained by infrared imaging of sample PC2 with four embedded Cu layers, the positions of which are indicated by the shaded regions. The solid lines through the data represent a simple model of thermal resistances in series. The absence of temperature discontinuities at the interfaces indicates very good thermal contact at the interfaces. The uncertainty in position is ~30 μm. The precision contribution to the uncertainty in temperature is 0.1°C, while the bias contribution is considerably larger (~2°C), as determined with a thermocouple. (After Azar and Graebner, 1996)

below that at the sample center. However, the absence of upward curvature of the temperature versus position across any of the glass/epoxy surfaces in Fig. 5 indicates that heat loss at the surface is not an important effect.

It is clear that the thermal gradient in Fig. 5 occurs in the glass/epoxy and not at any of the interfaces. The results of such infrared data are very important for judging the thermal quality of the interfaces and providing assurance that the values of $\kappa_\perp$ obtained by the two-heater technique described above are not limited by spurious interface resistance caused by cracks or defective joints. In fact, the interfacial thermal resistance is negligible compared with the resistance of the glass/epoxy layers. However, the infrared thermometry technique requires somewhat elevated temperatures for good sensitivity and, because the sample could not be placed in a vacuum or shielded to prevent radiative and/or convective loss (especially from the bulky heater itself), the amount of heat flowing through the sample, and thus the value obtained for $\kappa_\perp$, is quite uncertain ($\sim \pm 20$ percent). Therefore, the more reliable values of $\kappa_\perp$ obtained with the two-heater approach are reported in Table I.

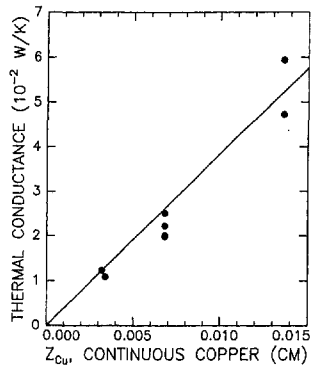

Fig. 6 Total non-(glass/epoxy) conductance ($\kappa_\parallel Z - \kappa_\parallel^{ge} Z_{ge}$) versus the total thickness Z_{Cu} of copper in continuous layers. The combined precision and bias contribution to the uncertainty in Z_{Cu} is less than the size of the symbols. The scatter in the thermal conductivity is dominated by the real sample-to-sample variations and illustrates the ~10–15 percent uncertainty caused by differences in the configuration of circuitry, vias, and noncontinuous buried layers of copper. The line is drawn with a slope of 385 $Wm^{-1} K^{-1}$.

Results

The results for $\kappa_\parallel$ or $\kappa_\perp$ of the 15 samples are summarized in Table I. We discuss first the data for $\kappa_\perp$, i.e., samples PC1, PC2, and PC14. Ignoring interfacial thermal resistance, as discussed above, the perpendicular conductivity of the glass/epoxy, $\kappa_\perp^{ge}$, can be deduced by first writing down the thermal resistance of resistors in series:

$$\frac{Z}{\kappa_\perp} = \frac{Z_{Cu}}{\kappa_{Cu}} + \frac{Z_{ge}}{\kappa_\perp^{ge}}, \tag{5}$$

where $\kappa_\perp$ is the measured conductivity averaged over the full thickness Z of the sample, κ_{Cu} is the conductivity of copper, and Z_{Cu} and Z_{ge} are the total thicknesses of all continuous layers of copper or glass/epoxy, respectively, in the particular sample. Equation (5) can be written as

$$\kappa_\perp^{ge} = \frac{\kappa_\perp (Z - Z_{Cu})}{Z\left[1 - \left(\frac{\kappa_\perp Z_{Cu}}{\kappa_{Cu} Z}\right)\right]} \approx \kappa_\perp \left(1 - \frac{Z_{Cu}}{Z}\right). \tag{6}$$

The approximation in Eq. (6) is good to better than 0.1 percent for the values typically encountered with the present boards. Using the $\kappa_\perp$, Z, and Z_{Cu} data (Table I) in Eq. (6) for samples P14, P1, and P2 yields values of $\kappa_\perp^{ge} = 0.33$, 0.29, and 0.31 $Wm^{-1} K^{-1}$, respectively, or an average value $\kappa_\perp^{ge} = 0.31 \pm 0.02$ $Wm^{-1} K^{-1}$ which is ~1200 times smaller than κ_{Cu}.

The parallel conductivity $\kappa_\parallel^{ge}$ of the glass/epoxy can be deduced from those $\kappa_\parallel$ samples for which no copper layers are present, i.e., samples PC5, PC15, and PC16. The latter two samples consist of only the centermost glass/epoxy layer, the copper and other layers having been physically removed. The average value for the three samples is $\kappa_\parallel^{ge} = 0.87 \pm 0.1$ $Wm^{-1} K^{-1}$, or ~500 times smaller than κ_{Cu}. Comparing the two directions, we find an anisotropy $\kappa_\parallel^{ge}/\kappa_\perp^{ge} = 2.8 \pm 0.3$ for the glass/epoxy. A value of this magnitude is not unexpected, as the glass fibers, which may have a thermal conductivity of 1–1.5 $Wm^{-1} K^{-1}$, or 3 to 5 times that of typical epoxy, lie predominantly parallel to the plane of a board. A quantitative estimate of the theoretical anisotropy would require the conductivities of the constituents and their relative volume fractions, as well as the detailed geometry of the woven glass fibers (Agarwal et al., 1991).

The present results for $\kappa_\parallel^{ge}$ and $\kappa_\perp^{ge}$ may be compared with previous results on FR4 epoxy/glass laminate boards without any copper present (Sarvar et al., 1990): $\kappa_\perp^{ge} = 0.343$ $Wm^{-1} K^{-1}$ and $\kappa_\parallel^{ge} = 1.059$ $Wm^{-1} K^{-1}$, yielding an anisotropy of 3.1. These values are within 15 percent of the present results. Such agreement is considered satisfactory, in view of the different measuring techniques and possible differences in PWB. Similar anisotropy is also suggested by detailed calculations (Agarwal et al., 1991). However, these values for $\kappa_\parallel^{ge}$ are both approximately three times the value of $\kappa_\parallel^{ge} = 0.32$ $Wm^{-1} K^{-1}$ obtained for a copper-free FR4 PWB in another investigation (Vanlaer and Lasance, 1994).

In the present study, the most accurate value for κ_{Cu} is obtained from sample PC11 with only one continuous Cu layer and no circuitry. To separate the contributions of the copper and the glass/epoxy, we write the overall conductance for layers of thermal conductors in parallel as

$$Z\kappa_\parallel = Z_{ge}\kappa_\parallel^{ge} + Z_{Cu}\kappa_{Cu}. \tag{7}$$

Assuming $\overline{\kappa_\parallel^{ge}} = 0.87$ $Wm^{-1} K^{-1}$, we use Eq. (7) with the measured thicknesses and $\kappa_\parallel$ to deduce $\kappa_{Cu} = 385 \pm 15$ $Wm^{-1} K^{-1}$, which is an acceptable value for copper.

Table I lists the results of measurements on many boards which differ in the number of continuous copper layers and in the amount of surface copper circuitry. Because of the enormous difference in conductivity between copper and glass/epoxy, one would expect that any continuous layers of copper in or on a board would dominate the in-plane conductivity $\kappa_\parallel$. A test of this hypothesis is provided by plotting the non-(glass/epoxy) conductance $\kappa_\parallel Z - \kappa_\parallel^{ge} Z_{ge}$ versus the total thickness Z_{Cu} of continuous copper present in a sample (Fig. 6). The straight line is drawn with a slope of $\kappa_{Cu} = 385$ $Wm^{-1} K^{-1}$, which is expected if the hypothesis is correct. Reasonably good agreement is observed. The deviations, mostly falling below the line, can be accounted for qualitatively by observing that the "continuous" copper layers in those samples are in fact partially interrupted to allow for electrical vias through the board. Thus, Fig. 6 indicates that the parallel conductivity is dominated by conduction along the copper layers. Depending on the number of continuous Cu layers present, the copper carries between 90 and 99 percent of the heat for in-plane heat flow.

For perpendicular heat flow, the various layers appear as thermal resistors in series; the highest-resistance (lowest-conductance) material therefore dominates $\kappa_\perp$. Thus, $\kappa_\perp$ is limited to small values by $\kappa_\perp^{ge}$, and the presence of Cu layers affects $\kappa_\perp$ only by a geometric factor close to unity. (The actual number of interfaces is not important, as the interfacial resistance is negligible compared with the glass/epoxy resistance, Fig. 5.) The resulting overall anisotropy can be very high. Board C, for example, shows an anisotropy $\kappa_\parallel/\kappa_\perp \approx 100$ (Table I).

The in-plane conductivity of printed wiring boards is sometimes estimated by observing the amount of circuitry on the

surface. Examination of $\kappa_\parallel$ in Table I as a function of surface coverage indicates that such a rule of thumb is useless for these multilayer boards. Sample PC3, for example, with no surface circuitry (but with two thick buried layers of continuous copper) has a conductivity that is more than twice the conductivity of samples PC7–PC10 with much circuitry (and two thinner buried layers). It has been shown (Azar and Graebner, 1996) that breaks or discontinuities in the otherwise continuous Cu layers can reduce the local conductivity by as much as a factor of 10. Thus, only truly continuous layers of copper are important for determining the board-averaged $\kappa_\parallel$.

The present findings can be summarized in numerical versions of Eqs. (5) and (7):

$$\kappa_\perp[\mathrm{Wm}^{-1}\,K^{-1}] = [3.23(1 - (Z_{Cu}/Z)) + 0.0026(Z_{Cu}/Z)]^{-1}, \quad (8)$$

and

$$\kappa_\parallel[\mathrm{Wm}^{-1}\,\mathrm{K}^{-1}] = 385\,\frac{Z_{Cu}}{Z} + 0.87. \quad (9)$$

These expressions represent the present data for κ_{Cu}, $\kappa_\perp^{ge}$, and $\kappa_\parallel^{ge}$, superceding slightly different expressions given earlier in a preliminary report (Graebner, 1995). The uncertainties in $\kappa_\perp$ or $\kappa_\parallel$ calculated from Eqs. (8) or (9) are estimated to be 5–10 percent if all the copper layers present are fully continuous. Larger deviations, 10–15 percent, can be expected for boards with surface circuitry, vias, or noncontinuous buried layers of copper, as illustrated in Fig. 6.

Equations (8) and (9) can be used to obtain accurate board-averaged values for $\kappa_\perp$ and $\kappa_\parallel$ under the assumption of one-dimensional heat flow (either perpendicular or parallel to the plane of the board). In the case of $\kappa_\parallel$, however, establishing heat flow that is equally distributed among all the continuous Cu layers is not easy because of the huge thermal resistance of the glass/epoxy layers (low $\kappa_\perp$). For example, a hot device mounted on one surface of the board will be quite isolated thermally from buried layers of Cu unless it is connected to them through a Cu-plated via. Once the heat is conveyed to all layers of continuous copper that are present, Eq. (9) can be used to calculate accurately the in-plane spreading.

Summary

Measurements of many different samples of multilayer printed wiring boards give thermal conductivity values which depend on the internal structure of the boards and on the direction of heat flow. The conductivity of continuous layers of copper is the same large value as for bulk copper. The conductivity of the glass/epoxy is approximately three orders of magnitude smaller and is anisotropic within the glass/epoxy: $\kappa_\parallel^{ge} \approx 3 \times \kappa_\perp^{ge}$. The values of $\kappa_\parallel^{ge}$ and $\kappa_\perp^{ge}$ are in reasonable agreement with previous data. This anisotropy can be understood qualitatively as the result of the glass fibers lying in the plane of the board and having 3–5 times higher intrinsic conductivity than a typical epoxy. The enormous difference in conductivity between copper and glass/epoxy causes an anisotropy in thermal conductivity of 100 or more if a board has continuous layers of copper on the surface or embedded within the board. The presence of such layers dominates the in-plane conductivity and minimizes the contribution of surface circuitry to the conductivity. To a good approximation, if continuous layers of Cu are present, one can ignore the presence of Cu layers (including circuitry) that are not continuous sheets.

The samples used here were intentionally cut with dimensions of several centimeters in order to average over any particular pattern of vias or surface circuitry on the scale of millimeters or smaller. Fine-scale variations of the local conductivity must certainly exist, especially near copper parts. The problem of calculating such local conductivity variations on a fine scale is a good candidate for numerical modeling, using the present data for κ_{Cu}, $\kappa_\perp^{ge}$, and $\kappa_\parallel^{ge}$, and the observed absence of any significant interfacial thermal resistance.

References

Agarwal, R. K., Dasgupta, A., Pecht, M., and Barker, D., 1991, "Prediction of PWB/PCB Thermal Conductivity," *Int. J. for Hybrid Microelectronics,* Vol. 14, pp. 83–95.

Azar, K., and Graebner, J. E., 1996, "Experimental Determination of Thermal Conductivity of Printed Wiring Boards," *Proceedings of the IEEE Semiconductor Thermal Measurement and Management Symposium,* (SEMI-THERM), Austin, TX, March 5–7, pp. 169–182.

Azar, K., and Yuan, T. D., 1993, "Effect of Board Conductivity and Air Velocity on Heat Transfer from an Electronic Component," *Proceedings of the Winter Conference of the ASME,* New Orleans, LA.

Carslaw, H. S., and Jaeger, J. C., 1959, *Conduction of Heat in Solids,* 2nd ed. Clarendon, Oxford, p. 21.

Ellison, G. N., 1996, "Thermal Analysis of Circuit Boards and Microelectronic Components Using an Analytical Solution to the Heat Conduction Equation," *Proceedings of the IEEE Semiconductor Thermal Measurement and Management Symposium,* (SEMI-THERM), Austin, TX, March 5–7, pp. 144–150.

Graebner, J. E., 1995, "Thermal Conductivity of Printed Wiring Boards," *Electronics Cooling,* Vol. 1, p. 27.

Graebner, J. E., Reiss, M. E., Seibles, L., Hartnett, T. M., Miller, R. P., and Robinson, C. J., 1994, "Phonon Scattering in Chemical-Vapor-Deposited Diamond," *Phys. Rev. B,* Vol. 50, pp. 3702–3713.

Lemczyk, T. F., Mack, B. L., Culham, J. R., and Yovanovich, M. M., 1992, "PCB Trace Thermal Analysis and Effective Conductivity," ASME JOURNAL OF ELECTRONIC PACKAGING, Vol. 114, pp. 413–419.

Maglic, K. D., Cezairliyan, A., and Peletsky, V. E., 1984, eds., *Compendium of Thermophysical Property Measurement Methods, Vol. 1,* Plenum Publishing Corp., New York.

Robinson, P., and Mravic, B., 1996, "Use of a One-dimensional Heat Flow Model to Calculate Circuit Board Thermal Resistance for use in the MQUAD Package Thermal Model," *Proceedings of the IEEE Semiconductor Thermal Measurement and Management Symposium,* (SEMI-THERM), Austin, TX, March 5–7, pp. 191–200.

Sarvar, F., Poole, N. J., and Witting, P. A., 1990, "PCB Glass-Fibre Laminates: Thermal Conductivity Measurements and Their Effect on Simulation," *Journal of Electronic Materials,* Vol. 19, pp. 1345–1350.

Stefani, G. G., Goel, N. S., and Jenks, D. B., 1993, "An Efficient Numerical Technique for Thermal Characterization of Printed Wiring Boards," ASME JOURNAL OF ELECTRONIC PACKAGING, Vol. 115, pp. 366–371.

Vanlaer, H. J. L., and Lasance, C. J. M., 1994, "An Experimental Method to Determine the Effective Thermal Conductivity of Printed Circuit Boards," in: *Thermal Management of Electronic Systems,* C. J. Hoogendoorn, R. A. W. M., Henkes, and C. J. M. Lasance, eds., *Proceedings of EUROTHERM Seminar 29,* Delft, The Netherlands, pp. 201–210.

Solving an Inverse Heat Conduction Problem by a "Method of Lines"

L. Eldén
Department of Mathematics,
Linköping University,
S-581 83 Linköping,
Sweden

We consider a Cauchy problem for the heat equation in the quarter plane, where data are given at x = *1 and a solution is sought in the interval* 0 < x < *1. This inverse heat conduction problem is a model of a situation where one wants to determine the surface temperature given measurements inside a heat-conducting body. The problem is ill-posed in the sense that the solution (if it exists) does not depend continuously on the data. In an earlier paper we showed that replacement of the time derivative by a difference stabilizes the problem. In this paper we investigate the use of time differencing combined with a "method of lines" for solving numerically the initial value problem in the space variable. We discuss the numerical stability of this procedure, and we show that, in most cases, a usual explicit (e.g., Runge-Kutta) method can be used efficiently and stably. Numerical examples are given. The approach of this paper is proposed as an alternative way of implementing space-marching methods for the sideways heat equation.*

1 Introduction

There are several important ill-posed problems for parabolic equations. A classical example is the backward heat equation, where, given data at a time $t = t_1$, we want to recover the initial value at $t = 0$. A related problem, which has rather different properties, is the following: given data at $x = 1$, we want to compute the solution for $0 \le x \le 1$. More precisely, we have

$$\begin{cases} T_{xx} = T_t, & x \ge 0, \quad t \ge 0, \\ T(x, 0) = 0, & x \ge 0, \\ T(1, t) = g_m(t), & t \ge 0, \end{cases} \tag{1.1}$$

where g_m is a given function. Note that we are considering the quarter plane problem, so that although we seek to recover T only for $0 \le x < 1$, the problem specification includes the heat equation for $x > 1$ together with boundedness of the solution T at infinity. Since we can obtain T for $x > 1$, by solving a well-posed quarter plane problem, also $T_x(1, \cdot)$ is determined. Thus (1.1) is a Cauchy problem with appropriate Cauchy data (T, T_x) given on the line $x = 1$.

The problem (1.1) is often referred to as the Inverse Heat Conduction Problem (IHCP) (Beck et al., 1985). We will refer to it as the sideways heat equation, in order to distinguish it from other inverse problems for parabolic equations.

The sideways heat equation often occurs in engineering applications where one wants to determine the surface temperature from measurements inside a heat-conducting body. We illustrate this in Figure 1. Applications and numerical algorithms are described in Beck et al. (1985). For recent surveys of numerical procedures, see also Beck and Blackwell (1988), Murio (1993), and Eldén (1988).

The problem of solving the sideways heat equation is ill-posed: if the solution exists, then it does not depend continuously on the data g_m. It has been shown (see, e.g., Eldén (1995)) that the problem can be made well-posed by replacing the time derivative by finite differences. In Section 2 we briefly discuss the nature of the ill-posedness, and the stabilizing properties of time differencing.

The main part of this paper is a discussion of the numerical solution of the stabilized problem where the time derivative is approximated by a central difference. It is shown in Section 3 that this problem can be considered as a "Method of Lines" (analogous to what can be used for the standard problem for a parabolic equation, where the space derivatives have been approximated by finite differences or finite elements). Thus, here we solve an initial value problem for a system of ordinary differential equations (ODE) in the space variable. The stability properties of the numerical solution of the ODE are discussed, and we show that for practical problems a standard Runge-Kutta method can often be used.

Some numerical examples are given in Section 4. The experiments indicate that this method works well for problems with small measurement errors, but is somewhat less useful when the errors are comparatively large[1]. However, the purpose of this paper is only partly to discuss the method as such. Additionally, in Section 5 we argue that the results of Eldén (1995b) and the present paper provide a general framework for analyzing and implementing space-marching methods for the numerical solution of the sideways heat equation.

Throughout, we discuss only the model problem (1.1). One important feature of the "method of lines" is that it can rather easily be modified to deal with problems with nonconstant coefficients and nonlinear problems that are of particular importance in applications.

2 Ill-Posedness and Stabilization

The ill-posedness of (1.1) can be seen by solving the problem using Fourier transforms[2]. Let

$$\hat{g}_m(s) = \frac{1}{\sqrt{2\pi}} \int_{-\infty}^{\infty} gm(t) e^{-jst} dt, \quad -\infty < s < \infty,$$

Contributed by the Heat Transfer Division for publication in the JOURNAL OF HEAT TRANSFER. Manuscript received by the Heat Transfer Division February 19, 1996; revision received February 21, 1997; Keyword: Numerical Methods. Associate Technical Editor: T. Tong.

[1] In the literature it has been shown that the sensitivity to data perturbations of space-marching schemes can be reduced by an initial filtering of the data (Carasso, 1982; Carasso, 1992). Such initial filtering can easily be applied also here.

[2] In Eldén (1995a) we study the ill-posedness of (1.1) in the case, when we only have data for the interval $0 \le t \le 1$. In particular it is shown that it is impossible to reconstruct the solution for t close to 1, cf. also Eldén (1988).

where $j = \sqrt{-1}$, be the Fourier transform of the data function. Then, formally, we can write the solution of (1.1) as

$$T(x, t) = \frac{1}{2\pi} \int_{-\infty}^{\infty} e^{jst} e^{\theta(s)(1-x)} \hat{g}_m(s) ds, \qquad (2.1)$$

where

$$\theta(s) = \begin{cases} (1+j)\sigma, & s \geq 0, \\ (1-j)\sigma, & s < 0, \end{cases} \quad \text{and} \quad \sigma = \sigma(s) := \sqrt{|s|/2},$$

is the principal value of $\sqrt{js}$. Since the real part of $\theta(s)$ is nonnegative and goes to infinity as $|s|$ tends to infinity, (2.1) defines an unbounded operator: if we try to solve (1.1) numerically, the ill-posedness will manifest itself in the blow-up of high frequency perturbations in the data. However, if we impose an a priori bound on the solution at $x = 0$,

$$\|T(0, \cdot)\| \leq M, \qquad (2.2)$$

and, in addition, allow for some imprecision in the matching of the data, and instead consider the problem,

$$\begin{cases} T_{xx} = T_t & x \geq 0, \quad t \geq 0, \\ T(x, 0) = 0, & x \geq 0, \\ \|T(0, \cdot)\| \leq M, & \\ \|T(1, \cdot) - g_m(\cdot)\| \leq \epsilon, & \end{cases} \qquad (2.3)$$

then we have stability in the following sense: any two solutions of (2.3), T_1 and T_2, satisfy (Carasso, 1982; Levine, 1983)

$$\|T_1(x, \cdot) - T_2(x, \cdot)\| \leq 2M^{1-x}\epsilon^x, \quad 0 \leq x \leq 1. \qquad (2.4)$$

For this reason, we refer to (2.3) as the stabilized problem. Further stability results are given in Knabler and Vessella (1987), Engl and Manselli (1989), and Carasso (1994). Approximate methods for the solution of (2.3), with optimal error estimates are presented in Carasso (1982) and Seidman and Eldén (1990).

One important family of methods for the numerical solution of the sideways heat equation are the so-called space-marching schemes, i.e., difference schemes, where both time and space derivatives are replaced by differences. Such schemes are useful since they can easily be adapted to treat nonlinear problems that often occur in applications. Many finite difference discretizations for the sideways heat equation are considered in Beck et al. (1985), and several are analyzed and compared in Carasso (1992, 1993). The stability aspects of finite difference schemes in connection with mollification are considered in a series of papers by Murio (1989), Guo et al. (1990), and Murio and Guo (1990). In these papers successful computations with finite difference schemes are reported.

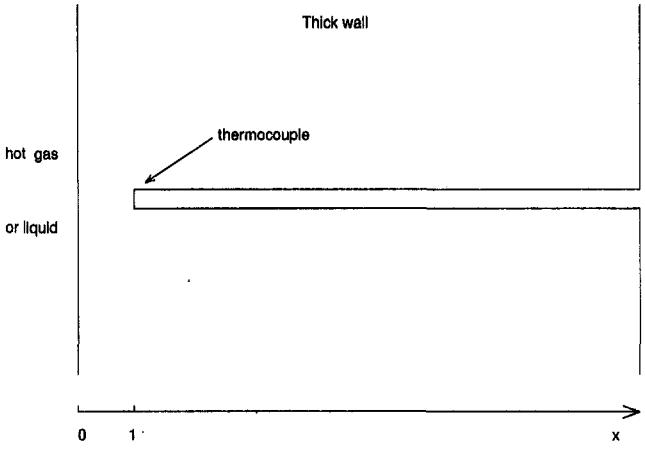

Fig. 1 Determination of surface temperature from interior measurements

In Eldén (1995b) we investigated the stabilizing properties of time differences for (1.1); i.e., we replaced only the time derivative by a difference and studied differential-difference equations, of the type

$$T_{xx}(x, t) = \frac{1}{2\Delta t}(T(x, t + \Delta t) - T(x, t - \Delta t)), \qquad (2.5)$$

where Δt is a step length in time. We showed that the time discretization prevents high frequencies from blowing up and that the difference approximation of the derivative should have a substantial forward component in order that the differential-difference equation (2.5) approximate the heat equation well. A recipe for choosing the step length Δt was given,

$$\Delta t = \frac{1}{2(\log (M/\epsilon))^2}, \qquad (2.6)$$

as well as an error estimate, showing logarithmic continuity for small error levels ϵ. Thus, the conclusion of Eldén (1995b) is that the problem of solving the differential-difference equation (2.5) for $0 < x \leq 1$, with appropriate initial values at $x = 1$, is well-posed.

We conclude this section with a remark concerning the parameters M and ϵ. Since we are dealing with an ill-posed problem, we must supply some extra, a priori information about the solution in order to make the problem well-posed, and study the rate of convergence of the approximate solution to the exact, when the error goes to zero. Also, the analysis gives a recipe for choosing the step length in the time discretization depending on M and ϵ. Of course, in a practical application it may be difficult to obtain values for these parameters; in such situations it is often necessary to experiment with different values and judge the quality of the computed solution from other a priori information about the solution that may be available.

3 Analysis of the "Method of Lines"

In this section, we discuss the numerical solution of the initial value problem

$$U_{xx} = BU, \quad U(1) = G_m, \quad U_x(1) = H, \qquad (3.1)$$

where U is a vector of unknowns approximating the solution T at discrete, equidistant points in the time interval (0, 1),

$$U = U(x) = \begin{pmatrix} U_1(x) \\ U_2(x) \\ \vdots \\ U_n(x) \end{pmatrix} \approx \begin{pmatrix} T(x, t_1) \\ T(x, t_2) \\ \vdots \\ T(x, t_n) \end{pmatrix},$$

$$t_i = i\Delta t, \quad \Delta t = 1/n,$$

where n is some natural number. The matrix B represents the difference approximation of the time derivative. We assume that Δt has been chosen according to (2.6). Then, the matrix B is tridiagonal.

$$B = \frac{1}{2\Delta t} \begin{pmatrix} 0 & 1 & & & & \\ -1 & 0 & 1 & & & \\ & -1 & 0 & 1 & & \\ & & \ddots & \ddots & \ddots & \\ & & & -1 & 0 & 1 \\ & & & & -1 & 0 \end{pmatrix}. \qquad (3.2)$$

In the construction of the matrix B it is necessary to make an assumption concerning the behavior of the solution for $t > 1$. This is equivalent to prescribing numerical boundary values. For simplicity of presentation we have here assumed that the unknown function T is zero for $t > 1$ (with this choice we can

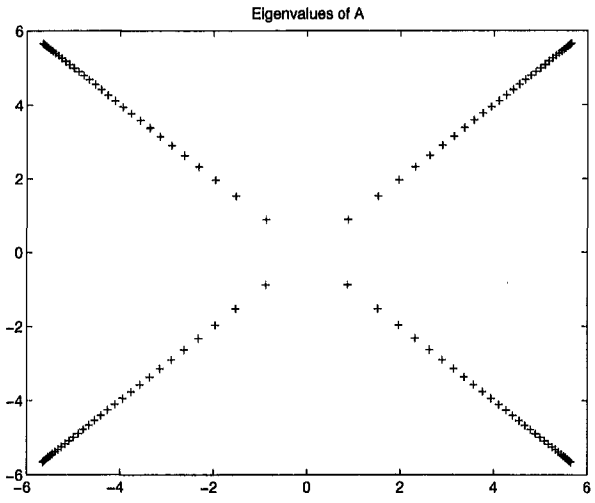

Fig. 2 Eigenvalues (in the complex plane) of the matrix A for $\Delta t = 1/04$

compute analytically the eigenvalues of A). This is, of course, not realistic, and in Section 3.3 we will discuss other choices of numerical boundary values.

We assume that the initial value for U_x has been obtained by solving the (well posed) quarter plane problem (1.1) for $x \geq 1$. We want to compute numerically the solution of the initial value problem (3.1) for $0 \leq x \leq 1$.

Since finite difference approximations in time and space are used for applied computations (Beck et al., 1985), in this paper, we will consider the practical aspects of such methods. Thus we are here less interested in asymptotic error estimates and continuity results, and instead, assuming a certain quality of the data (ϵ in (2.3)), we will discuss the numerical solution of the initial value problem (3.1), in particular the step lengths required for stability and good accuracy.

The initial value problem in the space variable (3.1) for a system of ordinary differential equations (ODE's) can be considered as a "method of lines," in analogy to what is often used for solving initial value problems in the time variable for parabolic equations.

In the rest of this section we will analyze the properties of the initial value problem (3.1), and discuss which methods for the numerical solution of an ODE are suitable, from the point of view of stability. In order to make it easier to phrase the discussion in ODE terms, we here reformulate the equation so that we exchange x for $1 - x$, which means that instead we integrate from 0 to 1. At the same time, we rewrite (3.1) as a first-order system,

$$V_x = AV, \quad A = \begin{pmatrix} 0 & -I \\ -B & 0 \end{pmatrix}, \quad V(0) = \begin{pmatrix} G_m \\ H \end{pmatrix}. \quad (3.3)$$

3.1 Stability Properties. The behavior of the solution of a linear, first order ODE depends on the eigenvalues of the matrix of coefficients. It can be seen[3] that the eigenvalues of A are

$$\frac{\pm 1 \pm j}{\sqrt{2}} \sqrt{|\eta_k|}, \quad \eta_k = \frac{1}{\Delta t} \cos \frac{k\pi}{n+1}, \quad k = 1, \ldots, n, \quad (3.4)$$

where $j\eta_k$ are the eigenvalues of B. In Fig. 2 we illustrate the eigenvalues of A for $\Delta t = \frac{1}{64}$.

[3] B is skewsymmetric, and can be diagonalized by a unitary matrix. Expressions for the eigenvalues are given, e.g., in (Smith, 1978, 115). After diagonalizing B the rows and columns of A can be reordered so that simple 4×4 eigenvalue problems are obtained.

By a transformation of variables, the solution of (3.3) can be uncoupled into components of the type $e^{\lambda x}$, where λ is an eigenvalue of A. The eigenvalues in the left half plane correspond to the components of the solution that decrease when we solve the problem. In the quarter plane framework, they are associated with solutions of the heat equation that grow as x tends to infinity. Since we assumed that the solution is bounded at infinity, these components should not be present in the data. Nevertheless, due to measurement errors and rounding off in the arithmetic, they will inevitably be present in the numerical solution, and when we solve (3.3) numerically we want the corresponding components of the numerical method to decay.

On the other hand, the eigenvalues in the right half plane correspond to the components of the solution that grow as we solve the initial value problem (3.3). These correspond to the wanted solution. Furthermore, we expect that the eigenvalues close to the origin represent most of the information in the solution (cf. the discussion of step size control in Section 3.2).

We will now discuss the numerical solution of (3.3) where we compute a sequence of approximations

$$V_{m+1} = F(V_m, \Delta x), \quad (3.5)$$

where V_m is an approximation of $V(x_m)$, Δx is a step length, and the method is defined by some function F. From the above discussion we see that the numerical method for solving (3.3) should give a decaying solution for the left half plane components, and we require it to give a good approximation for the right half plane solution, at least for those eigenvalues that are not far from the origin. The first requirement is fulfilled by so called A-stable methods (see, e.g., Gear, 1971; Harier and Wanner, 1991); such methods are implicit, which means that in each step of (3.5) we have to solve a linear system of equations to get V_{m+1}. Later in this section we will show that implicit methods can be used efficiently for our problem (3.3). However, first we will show that in many cases it is sufficient to use an explicit method.

For definiteness, we will consider one of the most widely used classes of explicit methods, namely fourth-order Runge-Kutta methods (for a recent extensive treatment of R-K methods, see Hairer et al., 1993). For any component of the solution of a linear ordinary differential equation, $e^{\lambda x}$, with $\mathrm{Re}(\lambda) < 0$, an explicit fourth order R-K method with step length in space Δx, gives a decaying solution if $z = \Delta x \lambda$ is inside the stability region

$$\left| 1 + z + \frac{z^2}{2!} + \frac{z^3}{3!} + \frac{z^4}{4!} \right| < 1.$$

In Fig. 3 we illustrate this stability region together with the eigenvalues of the matrix $\Delta x A$ for $\Delta t = \frac{1}{128}$ and $\Delta x = \frac{1}{6}$.

Given a linear initial value problem (3.3), it is always possible to choose the step length Δx short enough so that $\Delta x \lambda$, where λ has negative real part, is inside the stability region. It is now necessary to answer the question whether this will lead to very short step lengths in interesting cases.

Since both the eigenvalue distribution and the stability region are symmetric around the real axis, it is only necessary to consider the quarter plane where the real part is negative and the imaginary part is positive. The eigenvalue of largest modulus here is approximately (see (3.4))

$$\frac{1}{\sqrt{2\Delta t}} (-1 + j).$$

It is a relatively simple computation to show that the stability region crosses the real line $-\mathrm{Re}(z) = \mathrm{Im}(z)$ at $(-1.91, 1.91)$, approximately. Thus we get the criterion for stability

$$\frac{\Delta x}{\sqrt{\Delta t}} < 1.91\sqrt{2} \approx 2.7. \quad (3.6)$$

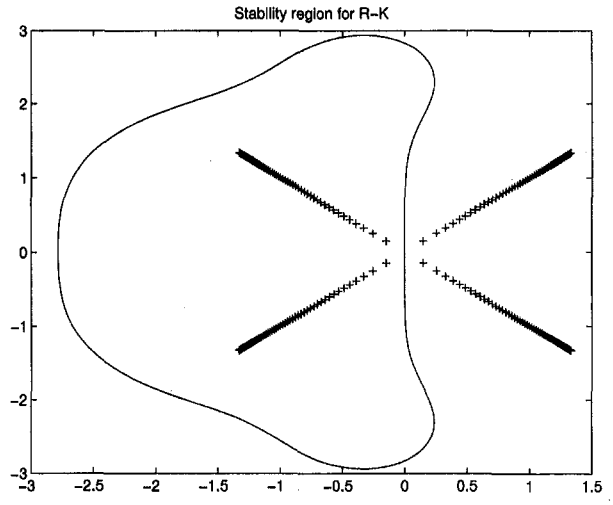

Fig. 3 Stability region in the complex plane for an explicit fourth order Runge-Kutta method. For $\Delta x = \frac{1}{6}$ and $\Delta t = \frac{1}{128}$, the eigenvalues of $\Delta x A$ with negative real part are all well inside the region of stability.

This is a rather mild condition; for instance, with $\Delta t = \frac{1}{256}$, we need $\Delta x < 0.16$ for stability.

The essence of the stability result of Eldén (1995b) is that the larger the noise-to-signal ratio ϵ/M, the longer step length in time Δt we should use in order to stabilize the problem (the relation between Δt and ϵ/M is given in (2.6)). Thus, $\Delta t = \frac{1}{256}$ corresponds to a noise-to-signal ratio $\epsilon/M \approx 1.2 \cdot 10^{-5}$, which would be quite small in an actual application. In Fig. 4 we have plotted the maximal step length in space according to the stability criterion (3.6), as a function of the step length in time, Δt, and, using the recipe (2.6) for choosing Δt, as a function of the noise-to-signal ratio ϵ/M. We see that this stability criterion will not impose restrictions on the numerical solution in the form of prohibitively small steps in space.

We can now draw the following conclusion: if the noise-to-signal ratio is not very small, an explicit method for integrating (3.3) is sufficient for ensuring stability for the unwanted components with negative real parts.

Finally, for completeness, we show that it is easy to use an implicit method in the cases when the noise-to-signal ratio is so low that one uses such a small value of the step length Δt that the stability of an explicit method is not enough. If an implicit method is used for the numerical solution of (3.3), then in each step we must solve a linear system of equations. For definiteness, assume that we use the trapezoidal method, that is A-stable (see, e.g., Dahlquist and Björck, 1974, chap. 8). Then in each step we must solve a system for V_{m+1},

$$\left(I - \frac{\Delta x}{2} A\right) V_{m+1} = \left(I + \frac{\Delta x}{2} A\right) V_m,$$

or,

$$\begin{pmatrix} I & \frac{\Delta x}{2} I \\ \frac{\Delta x}{2} B & I \end{pmatrix} \begin{pmatrix} U_{m+1} \\ W_{m+1} \end{pmatrix} = F_1(U_m, W_m, \Delta x),$$

$$V_m = \begin{pmatrix} U_m \\ W_m \end{pmatrix},$$

with the obvious definition of the function F_1. By taking the Schur complement (Golub and Loan, 1989, 103), we see that this linear system is equivalent to

$$\begin{pmatrix} I & \frac{\Delta x}{2} I \\ 0 & I - \frac{(\Delta x)^2}{4} B \end{pmatrix} \begin{pmatrix} U_{m+1} \\ W_{m+1} \end{pmatrix} = F_2(U_m, W_m, \Delta x).$$

The matrix $I - ((\Delta x)^2/4)B$ is tridiagonal and well-conditioned (see the appendix). Therefore, the extra work using an implicit method is minor compared to an explicit method.

3.2 Step Size Control. In the numerical solution of an ODE, the step length is also determined by the required accuracy of the numerical solution. Here we will show that reasonable accuracy can be obtained without resorting to very small step lengths Δx. The discussion will be made in terms of a fourth-order R-K method, but the essence of it also carries over to other methods.

In principle, we could apply estimates for the global error of a R-K method (Hairer, 1993, Theorem II.3.4), and obtain,

$$\|E(x)\| \leq C \frac{(\Delta x)^4 e^{Lx}}{L}, \tag{3.7}$$

where $E(x)$ is the global error in the numerical solution at x, C is some constant, and L is a Lipschitz constant for the right hand side of the differential equation. Since our system (3.3) is linear we have

$$L = \|A\|_2,$$

and here we see that $\|A\|_2 = \|B\|_2 \approx 1/\Delta t$. Therefore, the global error estimate (3.7) will have a huge factor $\exp(Lx)/L$, and is useless in practice. It would be realistic only if the dominant part of the solution of (3.3) could be expressed mainly in terms of components corresponding to the eigenvalues of largest modulus of A. However, if the solution of (3.3) is smooth, then we can expect that it can be represented well by components corresponding to the eigenvalues of A of smallest modulus.

A R-K method with automatic step size control, see (Hairer, 1993, Chapter II.5), estimates the local error in each step and chooses the step length Δx so that the error per unit step does not exceed a given tolerance. Usually, such a R-K method is based on a combination of two methods of different order where the higher order method is used to estimate the local error. By

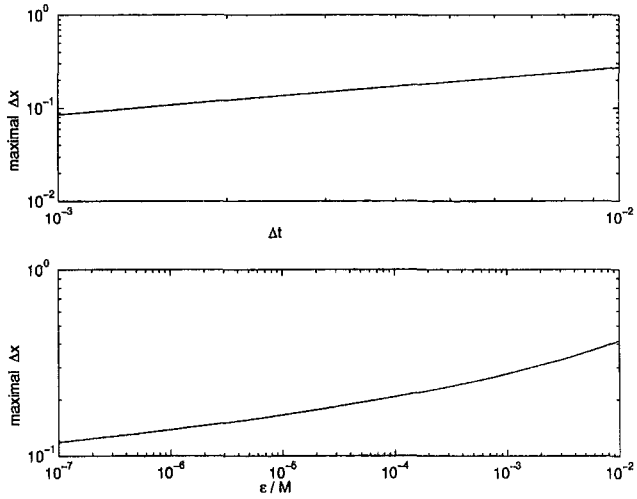

Fig. 4 The maximal step length in space Δx for stability of left half plane eigenvalues as a function of Δt (upper graph) and ϵ/M (lower graph)

a careful choice of the coefficients of the two methods, one can get the error estimate at marginal extra work.

If the solution of (3.3) would contain large components corresponding to eigenvalues of large modulus, then a R-K method with automatic step size control would automatically choose small steps. Similarly, if the main part of the solution is represented in terms of eigenvalues of small modulus, such a method will allow relatively large steps.

General convergence results for R-K methods as the maximal step size goes to zero are given in Hairer (1993), Theorem 3.4.

We will demonstrate in Section 4 that an explicit R-K method with automatic step size control works well in the numerical solution of (3.3).

3.3 Numerical Boundary Values at $t = 1$. In the construction of the matrix B at the beginning of Section 3, we temporarily made the assumption that the solution of (1.1) is equal to zero for $t > 1$. This is, of course, highly unphysical; a discontinuous drop of the temperature in the interior of the heat-conducting body just cannot happen. Also, it is inconsistent with the mathematical model since the solution of a heat equation is differentiable in both the space and time variables (Cannon, 1984).

On the other hand, we have data only for $0 \le t \le 1$, and due to certain properties of the heat equation (essentially causality, and a time delay before the information from the boundary at $x = 0$ is diffused through the medium to the position $x = 1$, see, e.g., Eldén, 1988; Eldén, 1995a), we cannot hope to compute any reliable estimate of the solution $T(x, t)$ of (1.1) for t close to 1. Therefore, it is reasonable to assume that the solution extends smoothly across the boundary at $t = 1$.

The ith row of the matrix B represents an approximation of a time derivative of the solution at $t = t_i = i\Delta t$. For the present discussion we suppress the dependence of T of the space variable, and define

$$D_j = \frac{T_{j+1} - T_{j-1}}{2\Delta t},$$

where, as before, Δt is the step length in time. The last row of B represents the time derivative at $t = t_n = 1$. If we assume that this derivative, call it D_n^*, is a linear extrapolation of D_{n-1} and D_{n-2}, then we get

$$D_n^* = D_{n-1} + (D_{n-1} - D_{n-2})$$
$$= \frac{1}{2\Delta t}(1 \quad -2 \quad -1 \quad 2)\begin{pmatrix} T_{n-3} \\ T_{n-2} \\ T_{n-1} \\ T_n \end{pmatrix}.$$

Thus, with this representation of the time derivative at $t = 1$, the four bottom right elements of the modified derivative matrix, called $\bar{B}$, are

$$\frac{1}{2\Delta t}(1 \quad -2 \quad -1 \quad 2).$$

Rows 1 to $n - 1$ in $\bar{B}$ are identical to those in B.

In Fig. 5 we have plotted the eigenvalues of both the matrix A (3.3) and

$$\bar{A} = \begin{pmatrix} 0 & -I \\ -\bar{B} & 0 \end{pmatrix},$$

for $\Delta t = \frac{1}{64}$. We see that while the eigenvalues of largest modulus of the two matrices are quite close, the eigenvalues of small modulus differ a great deal. The analyses of the preceding subsections are valid also for this case, except that $\bar{B}$ can no longer be diagonalized by a unitary transformation, but by a similarity transformation, and there are no explicit expressions for the eigenvalues. Another difference is that $\|\bar{A}\|_2$ is almost twice as large as $\|A\|_2$, but this is of no consequence in the conclusions of the preceding subsections.

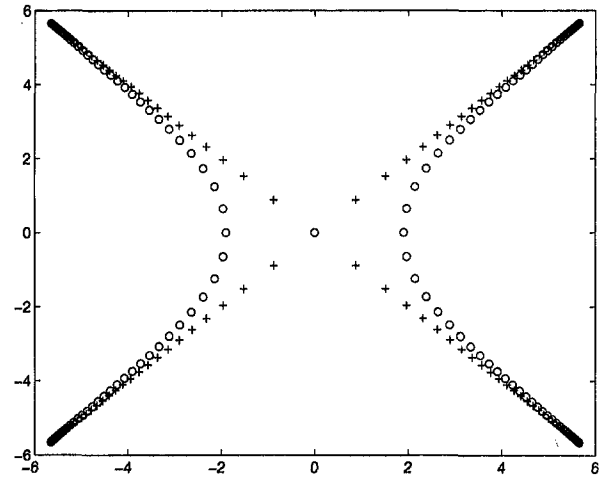

Fig. 5 Eigenvalues (complex) of the matrices A (+) and A (o), for $\Delta t = \frac{1}{64}$

We have observed that choosing $\bar{B}$ instead of B gives a solution that is slightly smoother for t close to 1.

4 Numerical Examples

In this section we will present some numerical experiments that illustrate the practical application of the "method of lines" approach. The tests are not to be considered as comprehensive, but rather they are intended to demonstrate the usefulness of the approach. We solved the sideways heat equation in the quarter plane using Matlab in IEEE double precision with unit round off $2.2 \cdot 10^{-16}$. The time derivative was discretized by a modified central difference approximation $\bar{B}$ (Section (3.3)), and a Runge-Kutta-Fehlberg method (Matlab, 1992, 351) was used where the basic method has order 4 and the embedded method for estimation of the local error has order 5.

A solution $T(0, t) = f(t)$, $0 \le t \le 1$, was selected, and the data function $T(1, t) = g(t)$ as well as $T_x(1, t) = g^{(1)}(t)$ were computed using an (discretized) integral equation formulation of the quarter plane problem, see Eldén (1995a). Then a normally distributed perturbation was added to each data function, giving g_m and $g_m^{(1)}$. These were used as initial values for the solution using the R-K method.

In all our test runs we used the value 10^{-4} for the requested accuracy in the R-K method. We tried smaller values but did not find any visible differences in the results that could be caused by using a too loose accuracy requirement.

In order to determine a suitable value of the step size in time, we first computed

$$\frac{\|g - g_m\|_2}{\|f\|_2} \approx \frac{\epsilon}{M},$$

and then used (2.6) to compute an approximate step length $\overline{\Delta t}$. Then we put $\bar{n} = \lceil 1/\overline{\Delta t} \rceil$.

We first chose the perturbation to be normally distributed with variance $\nu = 10^{-4}$. Typically, for such a perturbation we get a computed value of $\bar{n}$ around 120. In Fig. 6 we have illustrated the results obtained for this value of the step length. It is seen from Fig. 6 that the solution is not very well approximated and oscillates too much. We observed that, in general, the recipe (2.6) gives a too small step length in time, and that choosing the number of intervals $\bar{n}$ 20–25 percent smaller gave much better accuracy. In Fig. 7 we show the results obtained using $\bar{n} = 92$. We also tested the method for a larger value of

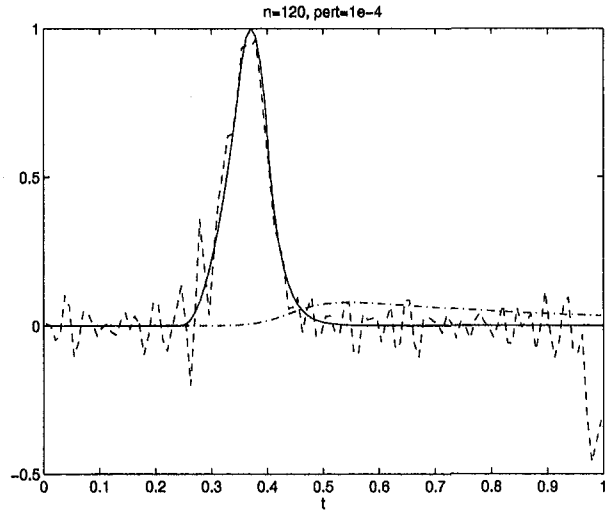

Fig. 6 Numerical solution of the sideways heat equation using $\bar{n} = 120$. The perturbation of the data had variance $\nu = 10^{-4}$. The solid line illustrates the exact solution, the dashed dotted line represents the data function g. The approximate solution is dashed. The R-K method took 12 steps, and the longest step was $\Delta x_{\max} = 0.145$, which gives a quotient $\Delta x_{\max}/\sqrt{\Delta t} = 1.59$.

the variance of the perturbation, $\nu = 10^{-3}$. The results are shown in Fig. 8.

In none of the tests was the quotient $\Delta x_{\max}/\sqrt{\Delta t}$ anywhere close to the stability bound (3.6).

5 Concluding Remarks

There are several methods for solving the sideways heat equation that stabilize the problem by adding a term in the equation (Weber, 1981; Eldén, 1988; Murio and Guo, 1990). The method discussed in the present paper has the advantage that it does not modify the equation, it only approximates it.

The numerical experiments indicate that the proposed method works well for problems with small measurement errors. For problems with higher error levels, the results are less encouraging. Often space-marching schemes are combined with initial filtering of the data, which reduces the sensitivity to perturbations in the data (Carasso, 1982; Guo and Murio, 1991). Such initial filtering can easily be used here also. More work is needed

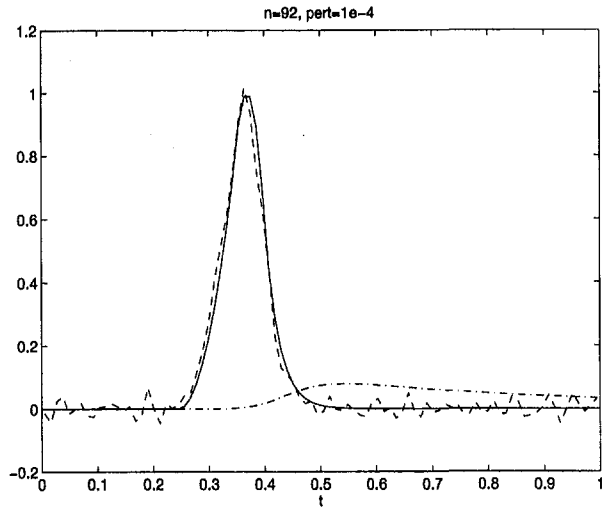

Fig. 7 Numerical solution for perturbation $\nu = 10^{-4}$ using $\bar{n} = 92$. The R-K method took 10 steps, the longest step was $\Delta x_{\max} = 0.148$, and $\Delta x_{\max}/\sqrt{\Delta t} = 1.42$.

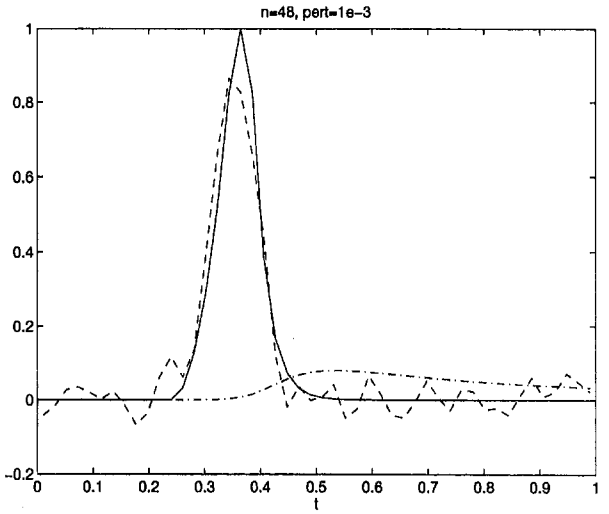

Fig. 8 Numerical solution for perturbation $\nu = 10^{-3}$ using $\bar{n} = 48$. The R-K method took 9 steps, the longest step was $\Delta x_{\max} = 0.159$, and $\Delta x_{\max}/\sqrt{\Delta t} = 1.10$.

to make the present approach an algorithm to be used for practical problems. Also, comparisons to other methods should be made, and more tests should be performed.

However, a discussion of this particular method is not the only purpose of the present paper. We also suggest our approach as an alternative way of dealing with space-marching for the sideways heat equation.

In the literature, numerous space-marching schemes are proposed for the solution of the sideways heat equation, see, e.g., (Beck et al., 1985, Section 6.10; Carasso, 1982, 1992, 1993; Murio, 1989; Guo et al., 1990; Murio and Guo, 1990). A space-marching scheme is a discretization of the differential equation in time and space, which allows for numerical solution by starting from the data at $x = 1$ and marching to the left to compute the solution $T(x, t)$ for $0 \le x < 1$. These schemes are, essentially, adaptations to the sideways heat equation of similar schemes for well-posed problems for partial differential equations.

One major advantage of space-marching schemes is that they can easily be adapted to deal with different geometries, two-space dimensions, nonlinearities, etc. (Beck et al., 1985; Guo and Murio, 1991; Carasso, 1992). They can also be used in connection with filtering procedures, such as mollification (Guo et al., 1990; Guo and Murio, 1991). However, one drawback is that they are not easy to analyze, compare, and classify as applied to this particular problem.

In the previous paper (Eldén, 1995b), we showed that when (only) the time derivative in the heat equation is replaced by a difference, then the initial value problem for the resulting differential-difference equation is well-posed and can be treated as a standard system of ordinary differential equations (a "method of lines"). In the present paper we have demonstrated that in most practical situations this initial value problem can be solved by an explicit method, e.g., a Runge-Kutta method. Note also that modern implementations of such ODE solvers have automatic step size and numerical error control.

By treating the discretizations in time and space separately, we are able to perform also the analyses of the ill-posedness of the problem and of the numerical properties of space-marching separately, thereby avoiding some of the difficulties inherent in the analyses of previously proposed space-marching schemes. This approach can also be combined with prefiltering of the data, and with other ways of discretizing the time derivative, e.g., by wavelets (Regińska and Eldén, 1996). Thus, we propose that the techniques and methods described here and in Eldén (1995b) constitute a convenient and powerful framework for analyzing and implementing space-marching methods for the sideways heat equation.

Acknowledgment

Comments and suggestions from referees have been very helpful for improving the presentation.

References

Beck, J. V., and Blackwell, B., 1988, "Inverse problems," *Handbook of Numerical Heat Transfer,* W. J. Minkowycz et al., eds., chap. 19, pp. 787–834, John Wiley & Sons, New York.

Beck, J. V., Blackwell, B., and Clair, S. R., 1985, *Inverse Heat Conduction, Ill-Posed Problems,* Wiley, New York.

Cannon, J. R., 1984, *The One-Dimensional Heat Equation,* Addison-Wesley, Reading, MA.

Carasso, A. S., 1982, "Determining Surface Temperatures From Interior Observations," *SIAM J. Appl. Math.,* Vol. 42, pp. 558–574.

Carasso, A. S., 1992, "Space Marching Difference Schemes in the Nonlinear Inverse Heat Conduction Problem," *Inverse Problems,* Vol. 8, pp. 25–43.

Carasso, A. S., 1993, "Slowly Divergent Space Marching Schemes in the Inverse Heat Conduction Problem," *Numerical Heat Transfer,* part B, Vol. 23, pp. 111–126.

Carasso, A. S., 1994, "Overcoming Hölder Continuity in Ill-Posed Continuation Problems," *SIAM J. Numer. Anal.,* Vol. 31, pp. 1535–1557.

Dahlquist G., and Björck, Å., 1974, *Numerical Methods,* Prentice-Hall, Englewodd Cliffs, N.J.

Eldén, L., 1988, "Hyperbolic Approximations for a Cauchy Problem for the Heat Equation," *Inverse Problems,* Vol. 4, pp. 59–70.

Eldén, L., 1995, "Numerical Solution of the Sideways Heat Equation," *Inverse Problems in Diffusion Processes,* H. Engl and W. Rundell, eds., SIAM, PA, pp. 130–150.

Eldén, L., 1995, "Numerical Solution of the Sideways Heat Equation by Difference Approximation in Time," *Inverse Problems,* Vol. 11, pp. 913–923.

Engl, H. W., and Manselli, P., 1989, "Stability Estimates and Regularization for an Inverse Heat Conduction Problem in Semi-Infinite and Finite Time Intervals," *Numer. Funct. Anal. Optimiz.,* Vol. 10, pp. 517–540.

Gear, C. W., 1971, *Numerical Initial Value Problems in Ordinary Differential Equations,* Prentice-Hall, Englewood Cliffs, N.J.

Golub, G. H., and Van Loan, C. F., 1989, *Matrix Computations,* 2nd ed., Johns Hopkins Press, Baltimore, MD.

Guo, L., and Murio, D., 1991, "A Mollified Space-Marching Finite-Difference Algorithm for the Two-Dimensional Inverse Heat Conduction Problem With Slab Symmetry," *Inverse Problems,* Vol. 7, pp. 247–259.

Guo, L., Murio, D. A., and Roth, C., 1990, "A Mollified Space Marching Finite Differences Algorithm for the Inverse Heat Conduction Problem With Slab Symmetry," *Computers Math. Applic.,* Vol. 19, pp. 75–89.

Hairer, E., Nørsett, S. P., and Wanner, G., 1993, *Solving Ordinary Differential Equations I,* 2nd ed., Springer, Berlin.

Hairer, E., and Wanner, G., 1991, *Solving Ordinary Differential Equations II,* Springer, Berlin.

Knabner, P., and Vessella, S., 1987, "Stability Estimates for Ill-Posed Cauchy Problems for Parabolic Equations," *Inverse and Ill-Posed Problems,* Academic Press H. W. Engl and C. W. Groetsch, eds., St. Wolfgang, Austria, pp. 351–368.

Levine, H. A., 1983, "Continuous Data Dependence, Regularization, and a Three Lines Theorem for the Heat Equation With Data in a Space Like Direction," *Ann. Mat. Pura Appl. (IV),* Vol. CXXXIV, pp. 267–286.

Matlab, 1992, *Reference Guide,* Mathworks Inc., Natick Mass.

Murio, D. A., 1989, "The Mollification Method and the Numerical Solution of the Inverse Heat Conduction Problem by Finite Differences," *Computers Math. Applic.,* Vol. 10, pp. 1385–1396.

Murio, D. A., 1993, *The Mollification Method and the Numerical Solution of Ill-Posed Problems,* John Wiley & Sons, New York.

Murio, D. A., and Guo, L., 1990, "A Stable Space Marching Finite Differences Algorithm for the Inverse Heat Conduction Problem With no Initial Filtering Procedure," *Computers Math. Applic.,* Vol. 19, No. 10, pp. 35–50.

Regińska, T., and Eldén, L., 1996, "Numerical Solution of the Sideways Heat Equation by Meyer Wavelets," Technical Report Report LiTH-MAT-R-96, Department of Mathematics, Linköping University, in press.

Seidman, T., and Eldén, L., 1990, "An Optimal Filtering Method for the Sideways Heat Equation," *Inverse Probl.,* Vol. 6, pp. 681–696.

Smith, G. D., 1978, *Numerical Solution of Partial Differential Equations,* 2nd ed., Oxford University Press, Oxford.

Weber, C. F., 1981, "Analysis and Solution of the Ill-Posed Inverse Heat Conduction Problem," *Int. J. Heat Mass Transfer,* Vol. 24, pp. 1783–1792.

A APPENDIX

A.1 Condition Number of $I - [(\Delta x)^2/4]B$.

For simplicity assume that n is even. First, since B is skew-symmetric, its Schur decomposition (Golub and Van Loan, 1989) is $B = QDQ^T$, where Q is orthogonal, and D has the quasi-diagonal form

$$D = \begin{pmatrix} D_1 & & & \\ & D_2 & & \\ & & \ddots & \\ & & & D_{n/2} \end{pmatrix},$$

where

$$D_j = \frac{1}{\Delta t} \begin{pmatrix} 0 & \cos \dfrac{j\pi}{\bar{n}+1} \\ -\cos \dfrac{j\pi}{\bar{n}+1} & 0 \end{pmatrix}.$$

The condition number of $I - (\Delta x)^2/4B$ is equal to $\kappa := (\lambda_{\max}/\lambda_{\min})^{1/2}$, where $\lambda_{\max}$ and $\lambda_{\min}$ are the smallest and largest eigenvalues of

$$C := (I - (\Delta x)^2/4B)^T(I - (\Delta x)^2/4B),$$

respectively. Now, since B is skew-symmetric,

$$C = I - \frac{(\Delta x)^2}{4}(B + B^T) + \frac{(\Delta x)^4}{16} B^T B = I + \frac{(\Delta x)^4}{16} B^T B.$$

The eigenvalues of C are the same as those of

$$\bar{C} = I + \frac{(\Delta x)^4}{16} D^T D = \begin{pmatrix} I + \dfrac{(\Delta x)^4}{16} D_1^T D_1 & & & \\ & I + \dfrac{(\Delta x)^4}{16} D_2^T D_2 & & \\ & & \ddots & \\ & & & I + \dfrac{(\Delta x)^4}{16} D_{n/2}^T D_{n/2} \end{pmatrix}.$$

Since

$$D_j^T D_j = \frac{1}{(\Delta t)^2} \begin{pmatrix} \cos^2 \dfrac{j\pi}{n+1} & 0 \\ 0 & \cos^2 \dfrac{j\pi}{n+1} \end{pmatrix},$$

we see that

$$\lambda_{\max} \approx 1 + \frac{(\Delta x)^4}{16(\Delta t)^2}, \quad \lambda_{\min} \approx 1.$$

Thus, κ is normally quite small. For instance, with $\Delta t = 10^{-3}$ (which corresponds to an extremely low noise level, $\epsilon/M \approx 10^{-10}$), and $\Delta x = 0.1$ we have $\kappa \approx 2.7$.

Turbulent Transport Measurements in a Heated Boundary Layer: Combined Effects of Free-Stream Turbulence and Removal of Concave Curvature

M. D. Kestoras
Assistant Professor.
Cyprus International Institute of Management,
21 Akademias Avenue,
PO Box 378, Aglandjia,
CY-2151 Nicosia, Cyprus
mkestor@ciim.ciim.ac.cy

T. W. Simon
Professor.
ASME Fellow.
Department of Mechanical Engineering,
University of Minnesota,
111 Church Street, S. E.,
Minneapolis, MN 55455

Turbulence measurements for both momentum and heat transport are taken in a boundary layer over a flat recovery wall downstream of a concave wall (R = 0.97 m). The boundary layer appears turbulent from the beginning of the upstream concave wall and grows over the flat test wall downstream of the curved wall with negligible streamwise acceleration. The strength of curvature at the bend exit, $\delta_{99.5}$/R, is 0.04. The free-stream turbulence intensity (FSTI) is ~8 percent at the beginning of the curve and is nearly uniform at ~4.5 percent throughout the recovery wall. Comparisons are made with data taken in an earlier study, in the same test facility, but with a low FSTI (~0.6 percent). Results show that on the recovery wall, elevated FSTI enhances turbulent transport quantities such as $-\overline{u}\overline{v}$ and $\overline{v}\overline{t}$ in most of the outer part of the boundary layer, but near-wall values of $\overline{v}\overline{t}$ remain unaffected. This is in contrast to near-wall $\overline{v}\overline{t}$ values within the curve which decrease when FSTI is increased. At the bend exit, decreases of $-\overline{u}\overline{v}$ and $\overline{v}\overline{t}$ due to removal of curvature become more profound when FSTI is elevated, compared to low-FSTI behavior. Measurements in the core of the flow indicate that the high levels of cross transport of momentum over the upstream concave wall cease when curvature is removed. Other results show that turbulent Prandtl numbers over the recovery wall are reduced to ~0.9 when FSTI is elevated, consistent with the rise in Stanton numbers over the recovery wall.

Introduction

This paper provides information about turbulent transport useful to designers and turbulence modelers for flows with curvature including those over turbine airfoils. The concave and flat recovery walls of the test section represent, respectively, simulations of the upstream and downstream parts of the pressure side of a gas turbine blade. In this study, the high free-stream turbulence intensity (FSTI) of real turbine blades (~15–30 percent, Mayle, 1991) is approached by elevating FSTI over the test section to ~8 percent.

Discussions on the effects of the introduction and removal of curvature on fluid mechanics and heat transfer are given in Kestoras and Simon (1992; 1993a, b). Concave curvature has destabilizing effects on the boundary layer, promoting turbulence activity and enhancing momentum and heat transfer. Furthermore, concave curvature effects a fundamental change in the structure of the boundary layer (Barlow and Johnston, 1988). Large eddies, under the action of centrifugal forces, enlarge and migrate toward the wall. Simultaneously, smaller-scale eddies move away from the wall.

Regarding the effects of free-stream turbulence intensity, it is well known that both level and scale of turbulence, as well as momentum thickness Reynolds number, are important (Hancock and Bradshaw, 1983, 1989; Blair, 1983). Blair documented the rise of skin friction coefficient and Stanton number with increasing FSTI and noted that over a flat wall the logarithmic regions of the velocity and temperature profiles remain unaffected by FSTI level. Kestoras and Simon (1993b) reported that the inner part of the logarithmic region of the velocity profile over a concave wall also remains unaffected by FSTI level.

Measurements on a concave wall upstream of the flat recovery wall of the present study showed that $\sqrt{\overline{v^2}}$, $\overline{v}\overline{t}$, $-\overline{u}\overline{v}$, $\overline{u}\overline{t}$, and l_m increase in the outer region of the boundary layer with FSTI level, Kestoras and Simon (1994). In contrast, $\sqrt{\overline{v^2}}$ and $\overline{v}\overline{t}$ near the concave wall are reduced with increases in FSTI. They attributed this to the absence of the Görtler vortices[1] which were present in the low-FSTI case (Kestoras and Simon, 1992). Mixing lengths over the concave wall in the high-FSTI case increase linearly with distance from the wall whereas near-wall ($y/\delta_{99.5} < 0.2$) distributions remain as on a flat wall under low-FSTI conditions ($l_m = \kappa \cdot y$). Turbulent Prandtl numbers rise from 0.9 to 1.3 with the introduction of the concave curvature under high-FSTI conditions but return to ~0.9 by the end of the curve.

Kestoras and Simon (1993a), in reporting time-averaged measurements taken over the flat recovery wall, noted that turbulent eddies seem to lift off the recovery wall while the viscous sublayer thickens, relative to those on the upstream concave wall. A resulting "stabilized" region (a nearly eddy-transport-free region adjacent to the wall) remained, as indicated by mean

Contributed by the Heat Transfer Division for publication in the JOURNAL OF HEAT TRANSFER. Manuscript received by the Heat Transfer Division November 8, 1995; revision received April 3, 1997; Keywords: Transient & Unsteady Heat Transfer; Turbines; Turbulence. Associate Technical Editor: M. S. Sohal.

[1] No spanwise traces appeared on a liquid crystal sheet covering the test wall. Also, spanwise profiles of streamwise velocity were uniform in the high-FSTI case.

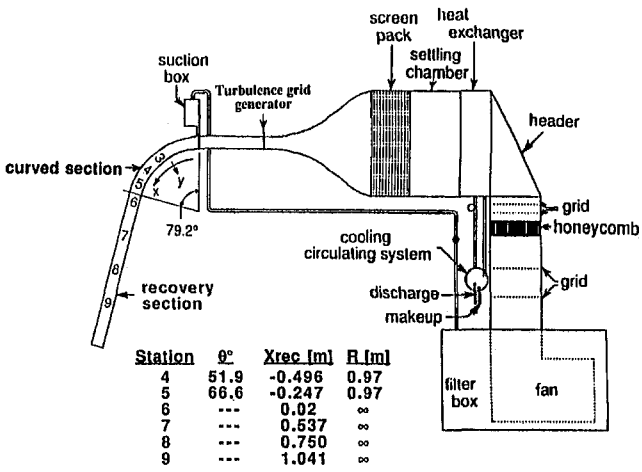

Station	θ°	Xrec [m]	R [m]
4	51.9	-0.496	0.97
5	66.6	-0.247	0.97
6	---	0.02	∞
7	---	0.537	∞
8	---	0.750	∞
9	---	1.041	∞

Fig. 1 Schematic diagram of the test facility

velocity profiles, as FSTI was elevated. Eddies seem to penetrate the outer part of this layer, and are thus coupled with sharp velocity and temperature gradients in that region, resulting in increased skin friction coefficients and Stanton numbers. Similarly, mean velocity gradients in this stabilized layer remain unaffected by enhancing the turbulence level.

In the present study, turbulence quantities are measured. Measurements of turbulent shear stresses and turbulent heat fluxes provide new information and support the conclusions obtained from the mean-field measurements. Moreover, these measurements provide the data base against which turbulence models can be compared and improved. To the best of the authors' knowledge, this is the first time that removal of concave curvature is documented by turbulence quantity measurements, including heat transport.

Test Facility and Instrumentation

The facility is an open-circuit blown-type wind tunnel (Fig. 1). Details of the flow delivery section are given by Wang and Simon (1989). Measurements are taken at a nominal velocity of 17.2 m/s, uniform to within 3 percent across the face of the nozzle. The free-stream temperature of the flow is uniform to within 0.1°C.

A free-stream turbulence intensity of ~8 percent at the inlet of the test channel is achieved using an insert section downstream of the contraction nozzle (Fig. 1). This insert (Kim et al., 1992), consists of a bi-plane grid of 4.2 cm OD PVC pipes on 10.8 cm centers. Downstream of the grid, there is a 96.5 cm long development region. The grid is similar to that used by O'Brien and vanFossen (1985) although the opportunity to blow jets through the grid is not utilized in this study. Free-stream turbulence intensity decays to 4.5 percent by the bend exit and remains essentially uniform at 4.5 percent throughout the recovery wall. A power spectral density (PSD) function taken at the nozzle exit shows that 20 percent of the turbulence energy in the free-stream resides at frequencies below 25 Hz. The function is flat below 25 Hz. The free-stream integral length scale determined by fitting the spectrum of the streamwise velocity fluctuations is 3.7 cm (see details in Hinze, 1975). A rotating slant wire (Russ, 1989) used to measure all three components of velocity showed that $u \sim 1.06\ v$ and $u \sim w$. The turbulence was, thus, quite isotropic.

The test channel was rectangular, 68 cm wide, 11 cm deep, and 283 cm long. The concave wall, which preceded the flat recovery wall of the present study, was 138 cm long and had a radius of curvature of 97 cm. The recovery wall was 145 cm long. The test walls were designed to provide smooth, uniformly heated surfaces. Their construction details were similar. For example, the recovery wall consisted of a layer of fiberglass insulation (10 cm), a sheet of Plexiglas® [2] (1.7 cm), an electrical resistance heater (1.6 mm), a thin spacer (0.6 mm), a stainless sheet (0.1 mm), and, adjacent to the flow, a layer of liquid crystal (0.21 mm).

The outer wall of the test channel was adjusted to obtain negligible streamwise acceleration; static pressure coefficients based upon static pressures taken at a radial distance of 2 cm from the concave wall, Cp_c, were kept to within 0.03 for the entire test length. Static pressures were measured using an array of static pressure taps on an end wall. Over the concave wall, the taps were distributed both in the streamwise and radial directions. Over the recovery wall, the taps were distributed only in the streamwise direction.

Data acquisition and processing was controlled by a Hewlett-Packard series 200, model 16 personal computer. Reynolds stresses were measured using cross wires (TSI 1243 boundary layer "X" probe) of which the prongs were bent at 90 deg to the probe holder to minimize flow interference (the hot wires lead the probe holder in meeting the flow). A constant temperature, four-channel bridge (TSI-IFA-100) was used to power the hot wires. Simultaneous digitization of the hot wires was performed using two Norland (now Hi-Techniques) Prowler digital storage oscilloscopes. For statistical quantities, the sampling rate was 100 Hz. Sampling time was at least 40 seconds. Calibrations of the cross wires were in the wind tunnel core flow over the upstream part of the flat recovery wall (Fig. 1). They were performed against a total pressure tube after first aligning both the cross-wire and the tube with the flow. When the cross-wire was aligned, the product of the voltages of the two wires reached a maximum (Kim, 1986). The Champagne et al. (1967) correction for tangential cooling was applied to Reynolds stress measurements. Hot-wire uncertainty comes from precision and bias error. Such uncertainties, which arise during calibration and measurement, are larger at smaller velocities. They result from items such as changes in fluid properties between calibration and measurement, near-wall effects, and sensor drift. A standard propagation, as detailed by Kline and McClintock (1953), of uncertainty contributions, which we assign for these various effects, yields a combined uncertainty of 7 percent for single-wire measurements, and 10 percent for two-

[2] Plexiglas is a registered trademark of Rohm Haas Company.

Nomenclature

c_p = specific heat capacity at constant pressure
C_{pc} = static pressure coefficient, $C_{pc} = (P - P_{ref})/(0.5\rho U_{cw}^2)$
l_m = mixing length for momentum
Pr_t = turbulent Prandtl number
$\sqrt{\overline{u^2}}$ = root-mean-square fluctuation of streamwise velocity
FSTI = free-stream turbulence intensity
U_∞ = free-stream velocity
U_{cw} = core velocity extrapolated to wall (same as U_{pw} for low FSTI cases)
$\overline{ut}$ = streamwise turbulent heat flux
$-\overline{uv}$ = turbulent shear stress
$\overline{uv^2}$ = wall-normal transport of turbulent shear stress
$\sqrt{\overline{v^2}}$ = root-mean-square fluctuation of wall-normal velocity
$\overline{vt}$ = wall-normal turbulent heat flux
x = streamwise distance
y = normal distance from the test surface

Greek Symbols

$\delta_{99.5}$ = boundary layer thickness
κ = Kármán constant
ρ = density

wire measurements. Due to the large sample sizes and long sampling time associated with the hot-wire calibration and measurement, stochastic errors associated with sampling size and time fall well below the deterministic errors and are negligible in comparison. Comparisons of mean velocity and turbulence intensity to data in fully developed turbulent boundary layer flows are used to corroborate these uncertainty values. Our uncertainties are consistent with previous experience with such measurements, with uncertainties reported in the literature, and with Yavuzkurt (1984). All uncertainties are expressed with 95 percent confidence; they represent single-sample uncertainties. Data from profiles and other multiple measurements within a similar portion of the flow allow discussion of effects based on mean values that have a lower pooled-sample uncertainty than this single-sample uncertainty value.

Turbulent heat fluxes are measured using a specially designed and manufactured triple-wire probe (Kim and Simon, 1988). The probe supports two constant temperature, 2.5 μm diameter platinum-plated tungsten wires (0.5 mm long) in an X-configuration for measuring the U and ν-components of the flow. The third wire, 1 μm in diameter, is made of platinum. (It is a flanking sensor, held in the same orientation as the hot wire which is in the middle of the probe.) The separation between the wires is 0.35 mm. The measuring volume is 0.09 mm^3, not allowing accurate measurements to be taken within a distance of 200 μm from the wall. This platinum-plated tungsten wire is operated in the constant-current mode as a resistance temperature sensor. Compensation is performed digitally following the procedure outlined by Hishida and Nagano (1978). A low-noise circuit was built to amplify the cold-wire signal and to provide its time derivative. The time derivative is needed to determine the compensation constant of the cold wire. The current supplied to the cold wire is switched from a high value (up to 6.7 mA) to a lower operating value (1 mA). Thus, a square-wave test is performed to determine the time constant required for digital processing. The hot wires of the three-wire probe are calibrated using the cross-wire probe calibration techniques discussed above. The temperature-resistance calibration of the cold wire is a two-point calibration found by using a 0.1°C resolution mercury-in-glass thermometer.

Two Norland Prowler digital oscilloscopes are operated in the master-slave configuration to simultaneously digitize the four traces required: two hot-wire signals, the cold-wire signal, and the cold-wire signal time derivative. The uncertainty in turbulent heat flux measurements is nominally 10 percent of the wall heat flux.

Heat transfer experiments are conducted with the test walls uniformly heated to, nominally, 193 W/m^2, within 5 percent nonuniformity. Wall surface heat flux is determined by measuring the energy supplied by the heater, accounting for radiation heat losses and back heat losses. The emissivity of the liquid crystal covering the test wall (needed to determine the radiation heat losses) is experimentally measured (Kim, 1990). The back heat loss is determined by measuring the temperature across the fiberglass insulation at the back of the test wall.

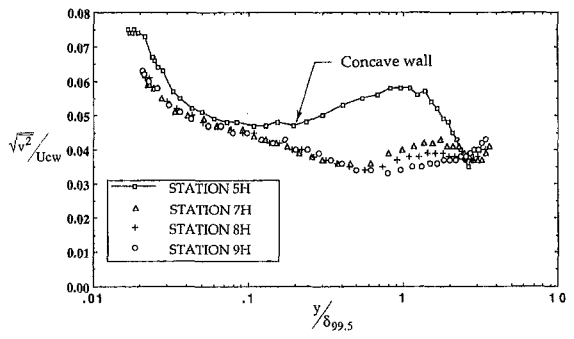

Fig. 2 Profiles of cross-stream velocity fluctuations over the recovery wall (stations 7H–9H) under high-FSTI (~8 percent) conditions. Station 5H—concave wall (high FSTI).

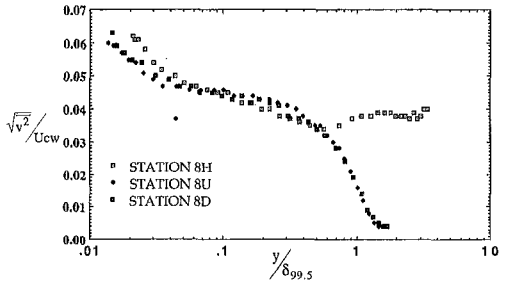

Fig. 3 Effect of elevated FSTI (~8 percent) on profiles of cross-stream velocity fluctuations over the recovery wall. Station 8H—high FSTI (~8 percent); Station 8D and 8U refer, respectively, to the downwash and upwash regions of the Görtler vortices in the low-FSTI (~0.6 percent) case.

Data are plotted against the distance from the wall, nondimensionalized with $\delta_{99.5}$—the thickness of the boundary layer. This thickness is determined using the local inviscid velocity distribution: $\delta_{99.5}$ is the distance from the wall where the measured velocity equals 99.5 percent of the local inviscid velocity. The local inviscid velocity profile is obtained by least-square fitting the core flow velocities and extrapolating toward the wall. It is also used to determine its value at the wall, U_{cw}, (corresponding to U_{pw} in potential flows, the equivalent wall value used in the low-FSTI cases).

Results

Cross-Stream Velocity Fluctuations. The effect of the removal of concave curvature on $\sqrt{\overline{\nu^2}}$ values under high-FSTI conditions is abrupt and dramatic (Fig. 2); values of $\sqrt{\overline{\nu^2}}$ at station 7H (first station on the recovery wall, "H" indicates a high FSTI ~ 8 percent) drop almost 30 percent from concave-wall values (station 5H, $y/\delta_{99.5} \approx 0.5$). A similar but slightly smaller percentage drop (~28 percent) in values of $\sqrt{\overline{\nu^2}}$) after the removal of curvature was also observed in the low-FSTI case (Kestoras, 1993).

A large reduction in $\sqrt{\overline{\nu^2}}$ occurs, also, outside of the boundary layer at the bend exit under high-FSTI conditions (Fig. 2). In fact, the magnitude of the drop in the core of the flow over the recovery wall is comparable to the drop in values within the boundary layer. This drop shows the far-reaching effects of the wall on free-stream turbulence (Thomas and Hancock (1977) reported such an effect of free-stream turbulence on a flat wall).

After the bend exit, the low core-flow values persist throughout the recovery wall (Fig. 2). In contrast, as shown by Kestoras and Simon (1992), at the bend exit, core-flow values of $\sqrt{\overline{u^2}}$ in the high-FSTI case do not show so large a drop. This difference in the behavior of $\sqrt{\overline{u^2}}$ and $\sqrt{\overline{\nu^2}}$ may indicate a reorientation of the vortices at the bend exit. Further study is required however.

In the high-FSTI case, $\sqrt{\overline{\nu^2}}$ profiles for $y/\delta_{99.5} < 0.4$ over the recovery wall assume a near-asymptotic shape while values in the region $y/\delta_{99.5} > 0.4$ slowly continue to drop. This asymptotic behavior was also observed in the low-FSTI case, but in that case, such self-similar behavior was present throughout the boundary layer (Kestoras, 1993). It is plausible that the difference is associated with decay of free-stream turbulence.

The effects of free-stream turbulence on $\sqrt{\overline{\nu^2}}$ values on the recovery wall are exemplified in Fig. 3 (only station 8 is shown). The symbols "U" and "D" refer, respectively, to the upwash and downwash regions of the Görtler vortices present in the low-FSTI case. No longitudinal vortices are detected in

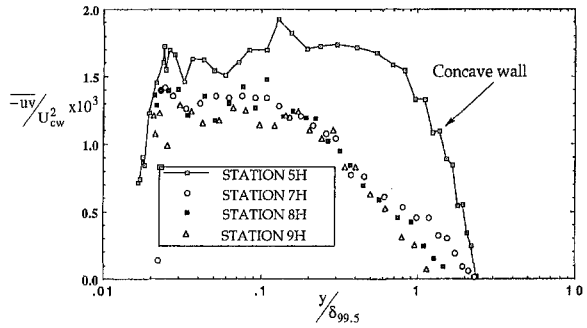

Fig. 4 Streamwise evolution of turbulent shear stresses over the recovery wall (stations 7H–9H) under high-FSTI (~8 percent) conditions. Station 5H—concave wall.

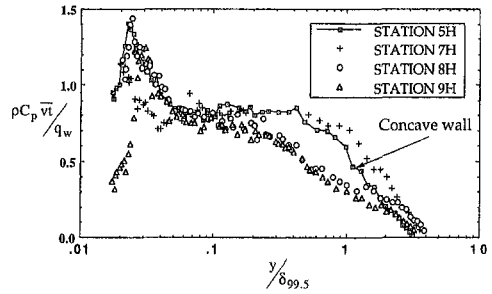

Fig. 6 Streamwise evolution of cross-stream turbulent heat fluxes over the recovery wall (Station 7H–9H) under high-FSTI (~8 percent) conditions. Station 5H—concave wall.

the high-FSTI case. In the outer half of the boundary layer $\sqrt{\overline{v^2}}$ is increased with free-stream turbulence. However, in the inner half of the boundary layer, values are as in the low-FSTI case. This is significant since, over the concave wall, near-wall $\sqrt{\overline{v^2}}$ values in the high-FSTI case were lower than $\sqrt{\overline{v^2}}$ values in the low-FSTI case. This reduction of $\sqrt{\overline{v^2}}$ values with the increase in FSTI was attributed to the disappearance of the Görtler vortices in the high-FSTI case (Kestoras and Simon, 1994). Following this reasoning, it is suggested that over the recovery wall the agreement in $\sqrt{\overline{v^2}}$ values in the two FSTI cases may be a result of the lifting of the Görtler vortices in the low-FSTI case (Kestoras and Simon, 1992; Kestoras, 1993). Therefore, the near-wall region over the recovery wall is not under the influence of the Görtler vortices either in the low-FSTI case (vortices lift off) or in the high-FSTI case (vortices not present).

Turbulent Shear Stresses. The effects on turbulent shear stresses of removal of concave curvature under high-FSTI conditions are shown in Fig. 4. On the recovery wall, turbulent shear-stress values, like $\sqrt{\overline{v^2}}$ values, exhibit an abrupt and dramatic drop (~64 percent at $y/\delta_{99.5} \approx 0.5$) from the concave-wall values. A similar, but smaller drop in shear stress values was observed in the low-FSTI case (~62 percent at $y/\delta_{99.5} \approx 0.5$; Kestoras, 1993).

Throughout the recovery wall, turbulent shear stress profiles exhibit a near-asymptotic behavior in the innermost 60 percent of the boundary layer (Fig. 4). Beyond this, values of $-\overline{uv}$ show a slow, continuous decline with streamwise distance. In contrast, under low-FSTI conditions asymptotic behavior in $-\overline{uv}$ profiles was exhibited over the same recovery length throughout the boundary layer.

Comparisons of $-\overline{uv}$ values in the high and low-FSTI case are exemplified in Fig. 5. Increased levels of FSTI increase $-\overline{uv}$ throughout the boundary layer. This increase reduces with streamwise distance.

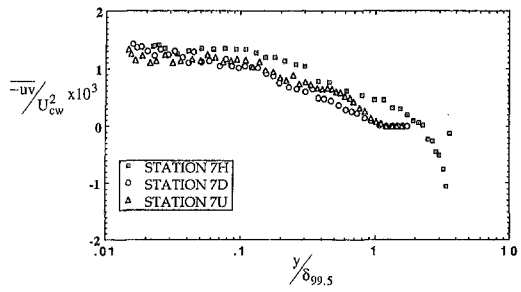

Fig. 5 Effect of elevated FSTI on turbulent shear stresses over the recovery wall. Station 7H—high FSTI (~8 percent); station 7D and 7U refer, respectively, to the downwash and upwash regions of the Görtler vortices in the low-FSTI (~0.6 percent) case.

Turbulent shear stress measurements (Kestoras and Simon, 1994) taken in the core of the flow over the upstream concave wall display cross-transport of momentum by boundary work, as described by Eckert (1987). According to Eckert, this cross transport of momentum takes place when (1) the flow path-lines are curved and (2) the flow is unsteady. Since the flow is turbulent, it is unsteady and the stream tubes wiggle, folding and unfolding. They, therefore, perform work against the static pressure forces. Both conditions for cross transport of momentum in the core are met in a turbulent flow over a concave wall. Over the recovery wall, however, the flow path-lines are no longer curved. Consequently, cross transport of momentum in the core of the flow ceases. As a result, in the high-FSTI case, turbulent shear stress values outside of the boundary layer over the recovery wall are reduced 75 percent (Fig. 4). Large-scale eddies, which are enlarged and amplified by concave curvature, also seem to contribute to the increased values of $-\overline{uv}$ in the core of the flow, as will be discussed with the $\overline{vt}$ data. Such large-scale eddies appear to be the primary contributors to enhanced $\overline{vt}$ values in the core of the flow over both the concave and recovery walls since cross transport by boundary work cannot enhance $-\overline{vt}$. This appears to be a plausible explanation of why $-\overline{uv}$ values in the core at the bend exit are reduced much more than are $\overline{vt}$ values; the large-scale eddies that contribute to both $-\overline{uv}$ and $\overline{vt}$ decay slowly, but the cross transport mechanism that contributes only to $-\overline{uv}$ is removed abruptly as the flow straightens.

Cross-Stream Turbulent Heat Flux. After the bend exit (e.g., station 7H in Fig. 6), turbulent heat flux values in the high-FSTI case exhibit a sudden drop from the concave-wall values (station 5H); at $y/\delta_{99.5} = 0.5$, they drop by more than 40 percent. A similar drop was observed under very low FSTI conditions (Kestoras, 1993).

In the inner half of the boundary layer over the recovery wall (stations 7H, 8H, 9H), $\overline{vt}$ profiles assume a near-asymptotic shape (Fig. 6), similar to that observed in the low-FSTI case. However, in the low-FSTI case, asymptotic behavior is exhibited throughout the boundary layer over the recovery wall. Again, high free-stream turbulence appears to prevent sustained asymptotic behavior in the outer part of the boundary layer.

Outside of the momentum boundary layer, under high-FSTI conditions, turbulent heat flux values downstream of the bend (e.g., station 7H in Fig. 6) are slowly reduced with streamwise distance throughout the recovery section (stations 7H, 8H, 9H at $y/\delta_{99.5} \approx 1.5$ for instance). This appears to be caused mainly by the decay of large-scale eddies within and outside of the momentum boundary layer. As the eddies weaken, their ability to transfer hot fluid outside of the momentum boundary layer to the core (still within the thermal boundary layer) is reduced. Apparently, this decay is slow, as revealed by the slow evolution of $\overline{vt}$.

The effect of FSTI on $\overline{vt}$ over the recovery wall is shown in Fig. 7. High FSTI enhances turbulent heat flux in most of the

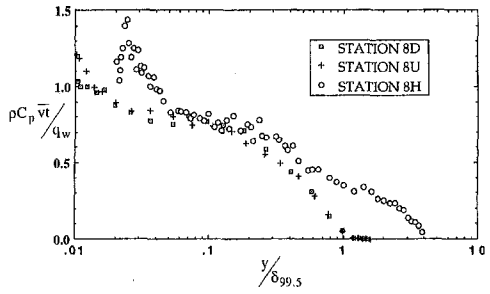

Fig. 7 Effect of FSTI on cross-stream turbulent heat fluxes on the recovery wall. Station 8H—high FSTI (~8 percent); station 8D and 8U refer, respectively, to the Downwash and Upwash regions of the Görtler vortices in the low-FSTI (~0.6 percent) case.

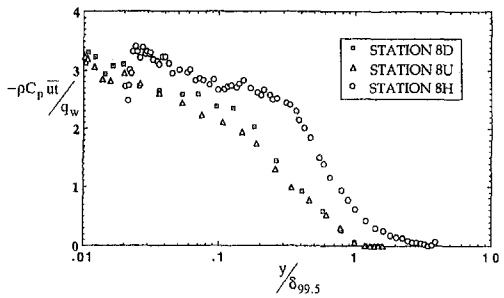

Fig. 9 Effect of FSTI on streamwise turbulent heat fluxes on the recovery wall. Station 8H—high FSTI (~8 percent); station 8D and 8U refer, respectively, to the downwash and upwash regions of the Görtler vortices in the low-FSTI (~0.6 percent) case.

boundary layer. Near the surface, $y/\delta_{99.5} < 0.1$, $\overline{vt}$ values are at low-FSTI-case levels. In contrast, over the concave wall, $\overline{vt}$ values in the region $y/\delta_{99.5} < 0.1$ in the high-FSTI case were lower than $\overline{vt}$ values in the low-FSTI case (Kestoras and Simon, 1993b). The agreement in $\overline{vt}$ values near the recovery wall between the high and low-FSTI-case values may be related to the lifting of the Görtler-like vortices off the recovery wall, as previously suggested.

Streamwise Turbulent Heat Flux. On the recovery wall (station 7H of Fig. 8) streamwise turbulent heat flux values, $-\overline{ut}$, (mean amount of heat transport by turbulence in the streamwise direction) under high-FSTI conditions rise immediately by more than 20 percent above concave-wall values (station 5H in Fig. 8 is the last station on the concave wall). In contrast, cross-stream turbulent heat flux, $\overline{vt}$, values drop at the bend exit below concave-wall values (Fig. 6). Streamwise turbulent heat flux profiles show little evolution with streamwise distance over the recovery wall (stations 7H, 8H, 9H in Fig. 8).

The effects of free-stream turbulence on $-\overline{ut}$ values on the recovery wall are profound (e.g., profiles at station 8, Fig. 9), with increased $-\overline{ut}$ values observed throughout the boundary layer and within the core of the flow. At $y/\delta_{99.5} \sim 0.4$, $-\overline{ut}$ values are more than double the low-FSTI-case value. This rise becomes larger with streamwise distance (not shown).

Mixing Length of Momentum. Over the recovery wall, in the high-FSTI case, mixing length values calculated using $l_m = \sqrt{-\overline{uv}/(\partial U/\partial y|\partial U/\partial y|)}$, in the outer part of the boundary layer ($y/\delta_{99.5} > 0.1$, station 7H, Fig. 10), drop below concave-wall values (station 5H). Mixing length profiles on the recovery wall (stations 7H–9H), appear to follow a two-layer model; the inner layer has a slope of nearly half the traditional slope while the outer layer has a much steeper slope, similar to that of the curved flow. The inner-layer profile shows little evolution over the recovery wall. The extent of the inner layer increases with streamwise distance over the recovery wall however. By the end of the recovery wall, the inner layer has consumed much of the boundary layer (station 8H and 9H in Fig. 10). Overall, the effect of removal of curvature on l_m is opposite to the effect of the introduction of concave curvature (Kestoras and Simon, 1994); while the concave wall increases the extent of the outer layer, at the expense of the inner layer, the recovery wall decreases the extent of the outer layer, in favor of the inner layer.

The slope of 0.28 for the inner layer over the recovery wall when FSTI is elevated is lower than the slope $\kappa = 0.41$ (Kármán constant) observed over the upstream concave wall (Kestoras and Simon, 1994) or over a flat wall. The lower slope may be an indication that the effective eddies have moved away from the recovery wall. A similar conclusion was reached in the low-FSTI case (Kestoras, 1993). In fact, the slope of the inner layer of the l_m distribution remains virtually unaffected by the increase in FSTI (Fig. 11).

The effect of free-stream turbulence on values of l_m over the recovery wall is exemplified in Fig. 11. Mixing length profiles in the high and low-FSTI cases collapse on one another in the region $y/\delta_{99.5} < 0.2$. The extent of the region where mixing length values of the two FSTI cases agree, increases from $y/\delta_{99.5} < 0.2$ upstream on the recovery wall (station 7H, not shown) to $y/\delta_{99.5} < 0.27$ (station 9H, not shown) at the end of the recovery wall. In the outer part of the boundary layer ($y/\delta_{99.5} > 0.2$), mixing length profiles in the high-FSTI case continue to grow (Fig. 10) while those in the low-FSTI case are slow to change.

Turbulent Prandtl Number. Turbulent Prandtl numbers on the recovery wall, in the high-FSTI case, were calculated using

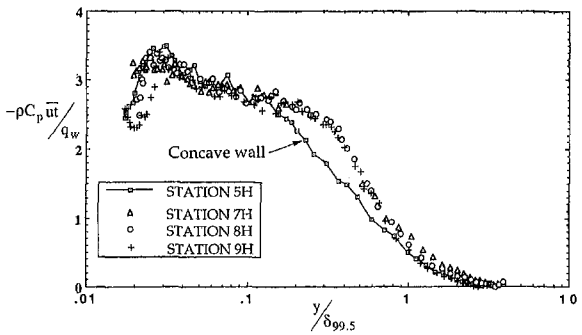

Fig. 8 Streamwise turbulent heat fluxes over the recovery wall (station 7H–9H) under high-FSTI (~8 percent) conditions. Station 5H—concave wall.

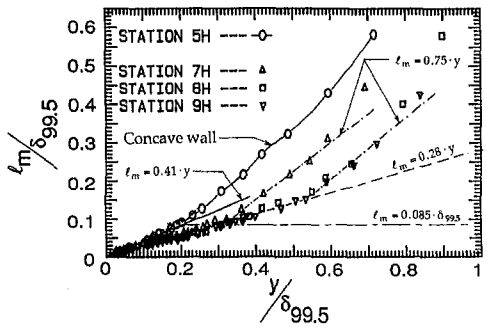

Fig. 10 Streamwise evolution of mixing length of momentum over the recovery wall (station 7H–9H) under high-FSTI (~8 percent) conditions. Station 5H—concave wall.

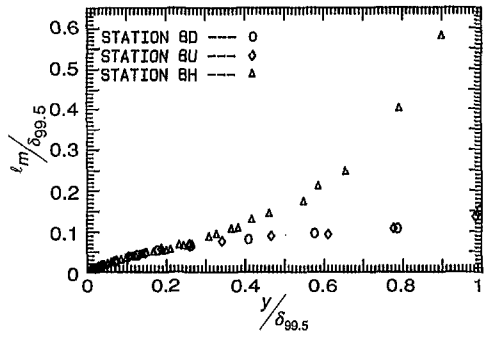

Fig. 11 Effect of FSTI on mixing length of momentum on the recovery wall. Station 8H—high FSTI (~8 percent); station 8D and 8U refer, respectively, to the downwash and upwash regions of the Görtler vortices in the low-FSTI (~0.6 percent) case.

$$\mathrm{Pr}_t = \left(\frac{-\overline{uv}}{\partial U/\partial y}\right) \Big/ \left(\frac{\overline{vt}}{\partial T/\partial y}\right).$$

Though the single-sample uncertainty in Pr_t is 20–25 percent in the inner half of the boundary layer, general levels, based upon several values, can be stated with lower uncertainty (about 10 percent) for a pooled sample of four). It can be said that removal of concave curvature does not cause a major change in Pr_t. Values are within the 0.9–1.0 range throughout the recovery wall (not shown)—the range of values of Pr_t on a flat wall under low free-stream turbulence.

The effects of free-stream turbulence on the recovery wall values are shown in Fig. 12. Apparently, this effect is weak since values of the two cases of different FSTI remain around 0.9–1.0. It appears that in the high-FSTI case (station 8H), Pr_t values may be somewhat lower than values under low-FSTI conditions (stations 8D and 8U) however.

Cross-Stream Transport of Turbulent Shear Stress. On the recovery wall, in the high-FSTI case, values of $\overline{uv^2}$ (stations 7H, 8H and 9H in Fig. 13) drop abruptly from concave wall values (station 5H). At the location of maximum values, $y/\delta_{99.5} \sim 0.4$, $\overline{uv^2}$ values are reduced to half the values of $\overline{uv^2}$ at the last station on the concave wall (station 5H). Keeping in mind that the large scales contribute mostly to $\overline{uv^2}$, this implies that the large-scale eddies created over the concave wall reduce in size. Throughout the recovery wall, profiles of $\overline{uv^2}$ appear to assume a near-asymptotic shape (Fig. 13). Values of $\overline{uv^2}$ are higher than $\overline{uv^2}$ values in the low-FSTI case (not shown). Only the region $0.05 < y/\delta_{99.5} < 0.3$ exhibits a mild streamwise

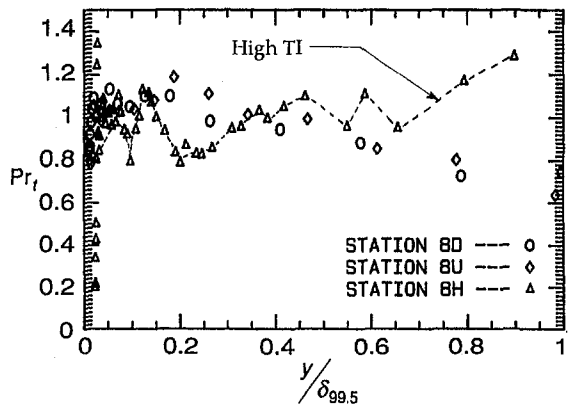

Fig. 12 Effect of FSTI on turbulent Prandtl Number on the Recovery Wall. Station 8H—High FSTI (~8 percent); station 8D and 8U refer, respectively, to the downwash and upwash regions of the Görtler vortices in the low-FSTI (~0.6 percent) case.

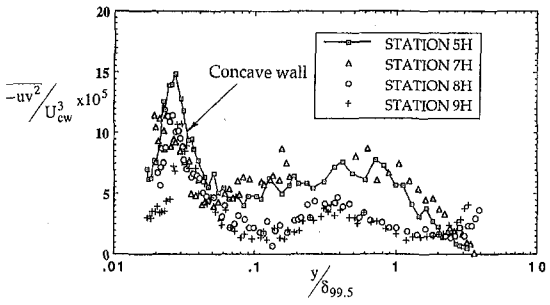

Fig. 13 Streamwise evolution of cross-stream transport of turbulent shear stresses over the recovery wall (station 7H–9H) under high-FSTI (~8 percent) conditions. Station 5H—concave wall.

evolution. In this region, values of $\overline{uv^2}$ decrease with streamwise distance.

Free-stream turbulence increases $\overline{uv^2}$ values on the recovery wall throughout the boundary layer (low-FSTI values not shown). At the location of peak values, $y/\delta_{99.5} \sim 0.4$, $\overline{uv^2}$ in the high-FSTI case are nearly three times the values in the low-FSTI case. The shapes of the low-FSTI $\overline{uv^2}$ profiles remain essentially unchanged when FSTI is elevated.

Implications on Turbulence Modeling. The results show that a two-dimensional code would suffice in modeling the turbulent boundary layer over a concave surface and on a downstream flat wall under high free-stream turbulence intensity conditions (FSTI ~ 8 percent) because of the absence of longitudinal vortices.

Mixing length distributions indicate that care should be exercised when modeling the flow adjacent to a recovery wall however. The turbulence activity is lower and eddy scales associated with transport are smaller, in the boundary layer over a flat recovery wall (downstream of a concave wall) under high FSTI (~8 percent), than in a standard flat-wall turbulent boundary layer. The extent of this near-wall region appears to be variable with streamwise distance.

Conclusions

Turbulence quantities such as $-\overline{uv}$ and $\overline{vt}$ are substantially affected by the combined effects of the removal of concave curvature (R = 0.97 m) and the elevation of free-stream turbulence (from ~0.6 percent to ~8 percent). As with low-FSTI flows, $-\overline{uv}$ and $\overline{vt}$ values drop at the bend exit. However, this drop is more pronounced with increased levels of FSTI. Concave curvature and elevated FSTI result in large-scale eddies, which appear to decay very slowly downstream, on a recovery wall. Nearly asymptotic behavior observed in $-\overline{uv}$ and $\overline{vt}$ in the low-FSTI case (Kestoras, 1993) is not sustained in the outer part of the boundary layer when FSTI is elevated. In detail, the following observations are made:

1 At the bend exit, turbulence quantities such as $\sqrt{\overline{v^2}}$, $-\overline{uv}$, $\overline{vt}$, $-\overline{ut}$, and l_m immediately drop. Elevated FSTI leads to a more dramatic drop than with the low-FSTI case.
2 On the recovery wall, under high-FSTI conditions, mixing length profiles follow a two-layer model. In the inner layer, mixing lengths exhibit a lower slope than the traditional slope which comes from low-FSTI flow over a flat wall, and, in the outer layer, a higher slope is found. This lower slope of the mixing length distribution in the inner layer seems to indicate that the effective eddies move away from the recovery wall. The thickness of this inner layer increases with streamwise distance on the recovery wall.
3 On the recovery wall, in the high-FSTI case, Pr_t values are around 0.9. This appears to be a slight reduction over low-FSTI case values of Pr_t.

Acknowledgments

This work was supported by the Air Force Office of Scientific Research under the grant number AF/AFOSR-91-0322. The project manager was Maj. Daniel Fant.

References

Barlow, S. R., and Johnston, J. P., 1988, "Structure of a Turbulent Boundary Layer on a Concave Surface," *J. Fluid Mech.,* Vol. 191, pp. 137–176.

Blair, M. F., 1983, "Influence of Free-Stream Turbulence on Turbulent Boundary Layer Heat Transfer and Mean Profile Development: Part II—Analysis of Results," ASME JOURNAL OF HEAT TRANSFER, Vol. 105, pp. 41–47.

Champagne, F. H., Sleicher, C. A., and Wehrmann, O. H., 1967, "Turbulence Measurements with Inclined Hot-Wires: Parts 1 and 2," *J. Fluid Mech.,* Vol. 28, pp. 153–182.

Eckert, E. R. G., 1987, "Cross Transport of Energy in Fluid Streams," *Wärme- und Stoffübertragung,* Vol. 21, pp. 73–81.

Hancock, P. E., and Bradshaw, P., 1983, "The Effect of Free-Stream Turbulence on Turbulent Boundary Layer Flow and Heat Transfer," *ASME Journal of Fluids Engineering,* Vol. 105, pp. 284–289.

Hancock, P. E., and Bradshaw, P., 1989, "Turbulence Structure of a Boundary Layer Beneath a Turbulent Free-Stream," *J. Fluid Mech.,* Vol. 205, pp. 45–76.

Hinze, J. O., 1975, *Turbulence,* McGraw-Hill Book Co., Inc., New York.

Hishida, H., and Nagano, Y., 1978, "Simultaneous Measurements of Velocity and Temperature in Nonisothermal Flows," ASME JOURNAL OF HEAT TRANSFER, Vol. 100, No. 2, pp. 340–345.

Kestoras, M. D., 1993, "Heat Transfer and Fluid Mechanics Measurements in Turbulent Boundary Layers: Effect of Free-Stream Turbulence Intensity on the Introduction and Removal of Concave Curvature," Ph.D. thesis, Dept. of Mech. Engr., Univ. of Minnesota, Minneapolis, MN.

Kestoras, M. D., and Simon, T. W., 1992, "Hydrodynamic and Thermal Measurements in a Turbulent Boundary Layer Recovering from Concave Curvature," ASME *Journal of Turbomachinery,* Vol. 114, No. 4, pp. 891–898.

Kestoras, M. D., Simon, T. W., 1993a, "Effects of Free-Stream Turbulence Intensity on a Boundary Layer Recovering from Concave Curvature Effects," ASME *Journal of Turbomachinery,* Vol. 117, No. 2, pp. 240–247.

Kestoras, M. D., Simon, T. W., 1993b, "Combined Effects of Concave Curvature and High Free-Stream Turbulence Intensity on Boundary Layer Heat and Momentum Transport," ASME Paper No. 93-WA/HT-56, 1993 ASME Winter Annual Meeting, New Orleans, LA.

Kestoras, M. D., Simon, T. W., 1994, "Turbulence Measurements in a Heated Concave Boundary Layer under High Free-Stream Turbulence Conditions," ASME *Journal of Turbomachinery,* Vol. 118, No. 1, pp. 172–180.

Kim, J., 1986, "The Development of a Turbulent Heat Flux Probe and its Use in a Two-Dimensional Boundary Layer over a Convex Surface," MSME thesis, Dept. of Mech. Engr., Univ. of Minnesota, Minneapolis, MN.

Kim, J., 1990, "Free-Stream Turbulence and Concave Curvature Effects on Heated, Transitional Boundary Layers," Ph.D. thesis, Dept. of Mech. Engr., Univ. of Minnesota, Minneapolis, MN.

Kim, J., and Simon, T. W., 1988, "Measurements of the Turbulent Transport of Heat and Momentum in Convexly Curved Boundary Layers: Effects of Curvature, Recovery and Free-Stream Turbulence," ASME *Journal of Turbomachinery,* Vol. 110, No. 1, pp. 80–87.

Kim, J., Simon, T. W., and Russ, S. G., 1992, "Free-Stream Turbulence and Concave Curvature Effects on Heated, Transitional Boundary Layers," ASME JOURNAL OF HEAT TRANSFER, Vol. 114, pp. 338–347.

Kline, S. J., and McClintock, F. A., 1953, "Describing Uncertainties in Single-Sample Experiments," *Mechanical Eng.,* ASME, January, pp. 3–8.

Mayle, R. E., 1991, "The Role of Laminar-Turbulent Transition in Gas Turbine Engines," ASME Paper No. 91-GT-261, Int'l. Gas Turbine and Aeroengine Congress and Exposition, Orlando, FL.

O'Brien, J. E., and vanFossen, G. J., 1985, "The Influence of Jet Grid Turbulence on Heat Transfer From the Stagnation Region of a Cylinder in Cross Flow," presented at the National Heat Transfer Conference, Denver, Colorado, August 4–7.

Russ, S. G., 1989, "The Generation and Measurement of Turbulent Flow Fields," MSME thesis, Dept. of Mech. Engr., Univ. of Minnesota, Minneapolis, MN.

Thomas, N. H., and Hancock, P. E., 1977, "Grid Turbulence Near a Moving Wall," *J. Fluid Mech.,* Vol. 82, pp. 481–496.

Wang, T., and Simon, T. W., 1989, "Development of a Special Purpose Test Surface Guided by Uncertainty Analysis," *AIAA J. Thermophysics,* Vol. 3, No. 1, pp. 19–26.

Yavuzkurt, S., 1984, "A Guide to Uncertainty Analysis of Hot-Wire Data," *J. Fluids Engineering,* June, Vol. 106, pp. 181–186.

Boundary Layer Transition Under High Free-Stream Turbulence and Strong Acceleration Conditions: Part 1—Mean Flow Results

R. J. Volino
Department of Mechanical Engineering,
United States Naval Academy,
Annapolis, MD
volino@nadn.navy.mil

T. W. Simon
Heat Transfer Laboratory,
Department of Mechanical Engineering,
University of Minnesota,
Minneapolis, MN

Measurements from heated boundary layers along a concave-curved test wall subject to high (initially 8 percent) free-stream turbulence intensity and strong ($K = (\nu/U_\infty^2)\, dU_\infty/dx$) as high as 9×10^{-6}) acceleration are presented and discussed. Conditions for the experiments were chosen to roughly simulate those present on the downstream half of the pressure side of a gas turbine airfoil. Mean velocity and temperature profiles as well as skin friction and heat transfer coefficients are presented. The transition zone is of extended length in spite of the high free-stream turbulence level. Transitional values of skin friction coefficients and Stanton numbers drop below flat-plate, low-free-stream-turbulence, turbulent flow correlations, but remain well above laminar flow values. The mean velocity and temperature profiles exhibit clear changes in shape as the flow passes through transition. To the authors' knowledge, this is the first detailed documentation of a high-free-stream-turbulence boundary layer flow in such a strong acceleration field.

Introduction

Boundary layer transition is generally accepted to be an important phenomenon experienced by the flow through the core of gas turbine engines. Mayle (1991) stated that a substantial fraction of the boundary layer on both sides of a gas turbine airfoil may be transitional. This statement was based on the strong acceleration rates present in engine flows, which, under simpler flow conditions, are known to delay transition or cause relaminarization. The ability to understand and predict transition in turbine environments is potentially very important since airfoil heat transfer rates and drag coefficients may increase several fold when a boundary layer undergoes transition. Current turbulence and transition models are often poor predictors of transition under turbine airfoil conditions (Mayle 1991). Models can be tuned to match a particular set of conditions, but they are not robust. Designers, however, are dependent on such models. To improve modeling, a better understanding of boundary layer transition under the complex conditions present in gas turbine environments is needed. This understanding is provided by experiments which capture at least some of the important effects of the gas turbine flow, but are simple enough to be interpreted.

The literature contains much on transition, but only a small fraction is directly applicable to gas turbine environments. Most early transition work focused on low free-stream turbulence intensity (FSTI) environments. Under very low disturbance conditions (FSTI $\ll$ 1 percent), boundary layers undergo Tollmien-Schlichting (TS) transition. Such transition is characterized by an early stage of growth of small disturbances which is amenable to linear stability analysis. Some elements of TS transition may be observed in flows with FSTI as high as 2 percent (Sohn and Reshotko, 1991), but the TS mechanism appears to be overwhelmed by other effects at higher turbulence levels. In gas turbines, FSTI of 3 percent to over 20 percent are possible. Mayle (1991) states that recent measurements in turbine and compressor rigs show approach flow turbulence levels of 5 to 10 percent, except in the wakes of upstream blades and vanes, where values as high as 15 to 20 percent are found. If free-stream fluctuation levels remain approximately constant (i.e., frozen turbulence) through a blade passage, FSTI levels of 10 to 20 percent between wakes and 30 to 40 percent in wakes are possible at the regions of maximum acceleration on the pressure side of the airfoils (where the free-stream velocity is significantly lower than at the blade row inlet). More recent experiments in a two-stage, rotating rig were with approach flow unsteadiness levels of 2–3 percent between wakes and 4–5 percent within wakes (Halstead et al., 1997). These fluctuation levels could result in FSTI values of ~5 percent and ~9 percent on the pressure surface between and within wakes, respectively. Transition under high FSTI conditions is termed "bypass transition" (Morkovin, 1978) because TS transition appears to be "bypassed" by strong, nonlinear processes. There may be some relationship between bypass and TS transition, but in general, the results obtained under low FSTI conditions are not directly applicable to high FSTI flows.

A few studies have been conducted in high FSTI flows. A review of recent work is provided by Volino and Simon (1995a). In the absence of a stabilizing, favorable pressure gradient, transition occurs very early at elevated FSTI and the boundary layer can be treated as fully turbulent. Sohn and Reshotko (1991), for example, found that above 3 percent FSTI, transition was so immediate that their first station was in the very last stages of transition. Kim et al. (1992, 1994) similarly documented profiles of velocity, temperature, and turbulence quantities through transition at 0.3 percent and 1.5 percent FSTI on a flat wall, but at 8 percent FSTI were able to capture only the end of transition.

Favorable pressure gradients are stabilizing and have the potential to delay transition and extend transition even at high FSTI. Documentation of the effect of pressure gradient on turbulent and transitional boundary layers is rather complete, except at elevated FSTI. Blair (1992) documented transition in flat

Contributed by the Heat Transfer Division for publication in the JOURNAL OF HEAT TRANSFER. Manuscript received by the Heat Transfer Division September 14, 1995; revision received April 7, 1997; Keywords: Flow Transition; Forced Convection; Turbulence. Associate Technical Editor: S. Ramadhyani.

plate boundary layers subject to favorable pressure gradients and FSTI values to 5 percent. For flows with acceleration parameter, $K = (\nu/U_\infty^2)(dU_\infty/dx)$, values of 0.2×10^{-6} and 0.75×10^{-6}, both acceleration rates affected the boundary layer; the stronger acceleration extended transition even at 5 percent FSTI. Zhou and Wang (1993) considered various acceleration rates and FSTI values to about 6 percent. Rued and Wittig (1986) considered flat plate boundary layers subject to various favorable pressure gradients with K as high as 6×10^{-6} and FSTI up to 11 percent. Their measurements suggest that for FSTI > 5 percent, acceleration at $K = 2 \times 10^{-6}$ is not strong enough to influence transition, but that acceleration with $K > 5 \times 10^{-6}$ can extend the transition zone, even at 11 percent FSTI. Acceleration rates in gas turbines can exceed $K = 20 \times 10^{-6}$, thus high-FSTI transition is expected to be important to gas turbine design.

Another factor which may influence transition is surface curvature. Convex curvature on the suction side of turbine airfoils is stabilizing and tends to extend transition. Concave curvature on the pressure side of airfoils is destabilizing and has the opposite effect. A few studies have considered the effects of curvature on transition at low to moderate FSTI (e.g., Wang and Simon, 1987; Kim et al., 1992), but there does not appear to be any documentation of curvature effects on transition at high FSTI.

In this study, the combined effects of high FSTI (~8 percent with inlet free-stream integral length scales of 2 cm and 4 cm based on u' and v' fluctuations, respectively), strong acceleration (K as high as 9×10^{-6}), and concave curvature are considered. Focus is on detailed measurements of mean velocities and temperature. An earlier paper (Volino and Simon, 1994) documented spectral measurements from this flow, and Part 2 of this work (the following paper) documents turbulence statistics including eddy momentum and heat transport terms.

Experiments

Facility. All experiments were conducted in an open-return, blown-type wind tunnel (Fig. 1). Details are available in Kim and Simon (1991). Air is drawn in through a filter, a heat exchanger, a screen pack, and a nozzle. The nozzle has a 10.6:1 contraction ratio and a 68.6 cm × 11.4 cm exit area. The 6:1 aspect ratio at the exit was chosen to minimize secondary flows at the centerline of the curved test section. At the exit of the nozzle is a bi-planar turbulence generating grid, discussed by

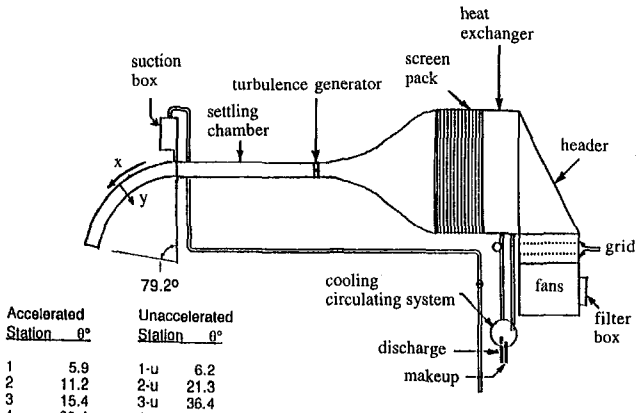

Fig. 1 Schematic of the test facility

Kim et al. (1992). It is constructed of 4.2 cm OD cylinders and has 60 percent blockage. Downstream of the grid is a 96.5 cm long rectangular development section of the nozzle exit dimensions. The flow exits the development section with nominally 8 percent FSTI. Further details of the free-stream turbulence are provided below and more detail can be found in Russ and Simon (1991). The mean velocity at the end of the development section is uniform to within 3 percent and the turbulence intensity to within 6 percent of the mean value. The flow temperature is uniform and constant to 0.1°C.

Downstream of the development section, the flow enters the test section, a curved channel. The test wall, 68.6 cm wide × 138 cm long, has a constant radius of curvature of 97 cm. It contains an electrical resistance heater which provides a uniform heat flux. Between the heater and the flow are an 0.8 mm thick sheet of Lexan® and a sheet of liquid crystal. The liquid crystal, which forms the surface on which the boundary layer grows, is used for visualization of the surface temperature. The back side of the test wall is insulated with 10 cm of fiberglass insulation which reduces back heat losses to 1.5 percent of the heat flux supplied by the heater. At the leading edge of the test wall is a suction slot used to bleed off the boundary layer which grows in the development section. The

Nomenclature

$C_f = (\tau_w/(\rho U_\infty^2/2))$, skin friction coefficient
c = specific heat
FSTI = free-stream turbulence intensity
H = shape factor
$K = (\nu/U_\infty^2)(dU_\infty/dx)$, acceleration parameter
q = heat flux
R = radius of curvature of the test wall
Re_x = Reynolds number based on distance from leading edge
Re_{Δ_2} = enthalpy thickness Reynolds number
Re_θ = momentum thickness Reynolds number
St = $q/\rho c U_\infty (T_w - T_\infty)$, Stanton number
T = local mean temperature
T_w = wall temperature
T_∞ = free-stream temperature
$t^+ = (T - T_w)\rho c u_\tau/q$, local temperature in wall coordinates
U = local streamwise velocity
U_c = core velocity
U_{cw} = core velocity extrapolated to the wall
U_{cw_o} = core velocity at entrance to the test section
U_∞ = free-stream velocity
$u^+ = (U/u_\tau)$, local velocity in wall coordinates
u' = fluctuation component of streamwise velocity
$u_\tau = \sqrt{\tau_w/\rho}$, friction velocity
v' = fluctuation component of cross-stream velocity
x = streamwise coordinate
y = coordinate normal to the wall
$y^+ = yu_\tau/\nu$, distance from wall in wall coordinates
$\delta_{99.5}$ = momentum boundary layer thickness
δ^* = displacement thickness
ν = kinematic viscosity
ρ = density
θ = momentum thickness
τ_w = wall shear stress
overbar = time averaged

outer wall of the test section is a flexible Lexan sheet which can be positioned to produce any desired streamwise velocity distribution. Ten access holes distributed in the streamwise direction along the centerline of the outer wall are used for velocity and temperature profile measurements. For the accelerated flow case discussed below, measurements were taken along the first 82 cm of the test section, downstream of which the boundary layers begin to merge.

Instrumentation. Velocity measurements were made using a boundary layer type hot-wire probe (TSI model 1218-T1.5) and a constant-temperature, hot-wire bridge (TSI model IFA-100). The uncertainty in mean velocity is 3–5 percent, except in the very near-wall region ($y^+ < 5$) where conduction effects between the hot-wire and the test wall are significant and near-wall corrections (Wills, 1962) are applied. At each position in the velocity profiles, data were acquired for 40 seconds at a 100 Hz sampling rate. The hot wire signal was low-pass filtered at 5 kHz. Velocity measurements were made in isothermal flow. Kim et al. (1994) showed that at FSTI > 1.5 percent, wall heating at the levels considered here does not affect transition.

Temperature measurements were made with a traversing thermocouple probe constructed following the design of Blackwell and Moffat (1975). The uncertainty in the mean temperature is 3–5 percent of the total wall-to-free-stream temperature difference. At each point in the temperature profiles, five thermocouple readings were taken over a 5 s period.

Both the hot-wire and thermocouple probes were moved for profile measurements with a motorized traversing assembly capable of a minimum step size of 5 μm. All data acquisition and probe traversing were controlled with a 386 computer through an IEEE interface bus.

Data Processing. Most of the data processing used in this study is based on standard techniques, but a few items require mentioning. The free-stream velocity is not uniform, nor does it follow a potential flow solution due to the curvature of the test channel and the high free-stream turbulence level. The curvature and high FSTI cause cross transport of momentum, as described by Eckert (1987). Although this prevents the core velocity distribution from following a potential flow or free-vortex solution, the velocity profile in the core of the channel is, to a close approximation, linear. Using the technique of Kestoras and Simon (1993), a line, $U_c(y)$, fit to the core velocity measurements, is extrapolated to the test wall to give the reference velocity U_{cw}. The boundary layer thickness, $\delta_{99.5}$, is taken as the point where the data, $\bar{U}(y)$, and the line $0.995U_c(y)$ cross. The reference velocity, U_{cw}, is fairly insensitive to the fitting of the core velocities and has an uncertainty of 3–5 percent. The boundary layer thickness, $\delta_{99.5}$, in contrast, is quite sensitive to the choice of which points are fit and has an uncertainty of 20 percent. Momentum thickness, with an uncertainty of 10 percent, is an integral quantity and is less sensitive to the choice of fitting.

Local wall temperatures, T_w, and local wall heat fluxes, q, were determined from the near wall temperature profiles using the technique of Qiu et al. (1995). The uncertainty in T_w and q are 3 percent and 5 percent, respectively. The uncertainty in local Stanton numbers is 7 percent.

Skin friction coefficients were determined using a technique whereby τ_w was adjusted until the u^+ versus y^+ data fit profiles computed using near-wall similarity, as described by Volino and Simon (1997). Briefly, the computed profiles were determined through analytical solution of the boundary layer momentum equations with a mixing length closure model. The derivation is similar to that used to develop the unaccelerated flow law of the wall, but with convection and pressure gradient terms included. The uncertainty in C_f is 7–8 percent.

Table 1 Flow parameters for accelerated—Stations 1 thru 10—and unaccelerated—Stations 1-*u* thru 5-*u*—cases

Station	x [m]	$Re_x \times 10^{-5}$	$K \times 10^6$	$\theta/R \times 10^3$	FSTI [%]
1	0.0993	0.39	5.56	0.655	5.3
2	0.1895	0.87	4.03	0.425	4.2
3	0.2607	1.37	3.13	0.430	3.5
4	0.3449	2.11	2.29	0.345	2.9
5	0.4231	2.92	1.80	0.358	2.6
6	0.5033	3.76	1.53	0.415	2.2
7	0.5805	4.71	1.30	0.486	2.1
8	0.6587	5.72	1.13	0.501	2.0
9	0.7353	6.79	1.01	0.547	1.8
10	0.8165	8.26	0.84	0.563	1.6
1-u	0.105	1.12	0	0.356	7.2
2-u	0.362	3.87	0	1.01	6.2
3-u	0.616	6.65	0	1.43	5.7
4-u	0.875	9.44	0	1.67	5.2
5-u	1.133	12.05	0	1.80	4.6

Cases Considered. Three cases were conducted in two-dimensional boundary layers on the same test wall and with 8 percent FSTI at the inlet to the test section:

Case	$K \times 10^6$	dU_∞/dx (l/s)	U_{cw_0} (m/s)	FSTI (percent)	$\theta/R \times 10^3$
1	0.75	3.0–8.3	8.0	8–3.0	0–1.2
2	4.6–0.4	28.0	9.8	8–1.4	0–0.6
3	9.1–0.8	13.7	4.9	8–1.6	0–0.6

Stable streamwise vortices, reported in low-FSTI flow by Kim et al. (1992), were not observed. Variable-K, Cases 2 and 3, were chosen because it is impossible to maintain a constant and large value of K over an appreciable distance, except in low Reynolds number flows. The K and Reynolds number ranges for Case 3 simulate those present on the downstream half of the pressure side of a gas turbine blade.

Results

Acceleration with $K = 0.75 \times 10^{-6}$ was strong enough to influence the turbulent boundary layer, but had little effect in delaying transition, which occurred near the leading edge, as in unaccelerated flow at this FSTI. Blair (1992) saw that acceleration at $K = 0.75 \times 10^{-6}$ was sufficient to influence transition on a flat plate at 5 percent FSTI. Rued and Wittig (1986) reported that moderate acceleration such as this was insufficient to delay transition at FSTI above 7 percent. The current results confirm this and illustrate a difference between 5 percent and 8 percent FSTI. The second and third cases had qualitatively different behavior than the first case and similar behavior to one another; both exhibited an extended region of transitional flow. The effects of acceleration were most pronounced in the third case, due to the higher K-levels and lower Reynolds numbers. Details of all three cases are available in Volino and Simon (1995b). Presently, attention is focused only on the third case. Comparison data are taken from an unaccelerated, 8 percent FSTI, concave wall, turbulent boundary layer case, which is a repeat of measurements of the same case presented by Kim et al. (1992). Important parameters from the accelerated flow and comparison cases are presented in Table 1.

Acceleration Profile. The acceleration parameter K in the accelerated flow experiment decreased monotonically from a maximum of 9.1×10^{-6} at the leading edge to 0.8×10^{-6} at the last measurement station. For comparison, the maximum-K value on the pressure side of a CF6 high-pressure turbine blade

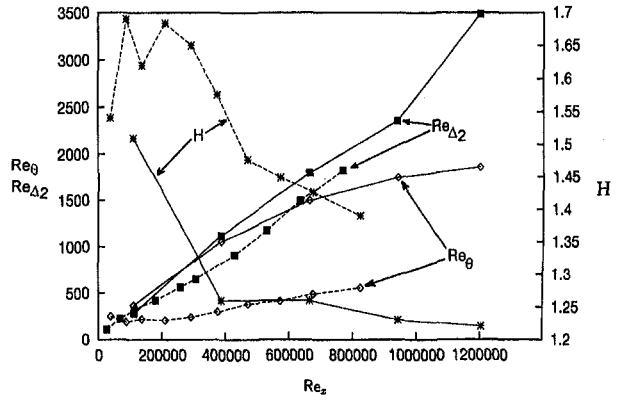

Fig. 2 Re_θ, Re_{Δ_2}, and H versus Re_x for unaccelerated—and accelerated----boundary layers

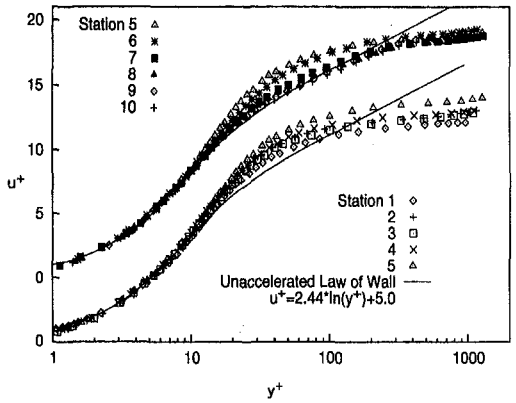

Fig. 3 Mean velocity profiles in wall coordinates for accelerated flow case

at altitude conditions is estimated to be 8×10^{-6}. On a more modern turbine blade, K values of over 20×10^{-6} are estimated. The Reynolds number range for the experiment is comparable to those of both the CF6 and more modern turbine blades.

Free-Stream Turbulence Intensity. The free-stream turbulence intensity in this experiment decreased rapidly from a maximum of about 8 percent at the leading edge to 1.6 percent at the last measurement station. The literature would indicate that this is representative of gas turbine flows. Values of FSTI are calculated as

$$\sqrt{\frac{u'^2 + 2v'^2}{3}} \Big/ U_{cw}$$

where u' and v' were measured with a cross-wire probe. Measurements of all three components of the turbulence in this facility are reported for unaccelerated flow by Russ and Simon (1991). The rapid drop in FSTI is partially due to decay of u'^2 (v'^2 remains nearly uniform) but is mainly due to the increase in U_{cw} resulting from the acceleration. Spectral measurements of the free-stream turbulence in this case are presented by Volino and Simon (1994).

Boundary Layer Growth. Acceleration has a strong effect on the growth of the momentum boundary layer and a lesser effect on the thermal boundary layer growth. This is shown in Fig. 2. In the unaccelerated boundary layer, Re_θ and Re_{Δ_2} are comparable in magnitude. In the accelerated flow, momentum boundary layer growth is suppressed. The value of Re_θ remains nearly constant for the first five measurement stations, rising thereafter. The beginning of the rise in Re_θ corresponds to a dropping of K below about 2×10^{-6}. Transition correlations, such as that given by Abu-Ghannam and Shaw (1980), when extrapolated to high FSTI, would predict that the boundary layer at the upstream stations in this flow should be in the beginning of the transition process. Mayle (1991) presents a transition correlation (Mayle's Eq. 9), and states that transition cannot begin unless $K < 3 \times 10^{-6}$. For the high FSTI case under consideration, Mayle's correlation predicts the start of transition downstream of Station 3. This agrees with what is seen in the flow. Spectral measurements for this case presented by Volino and Simon (1994) indicate that the boundary layer is badly disturbed due to the influence of the high free-stream turbulence but that near-wall turbulence production is suppressed below fully turbulent values until downstream of Station 5. Spectra of the turbulent shear stress show significant turbulent transport at the upstream stations but at levels much lower than observed downstream. A significant rise in the shear stress does not occur until downstream of Station 5. Shear-stress profiles in Part 2 of this work similarly show a rise downstream of Station 4. Based on the spectra, the conclusion is drawn that the boundary layer is not laminar but that it does not begin to look fully turbulent until the downstream stations. Rued and Wittig (1986) also described their strongly accelerated, high FSTI boundary layer as disturbed by the free-stream turbulence but still nonturbulent.

The value of Re_{Δ_2} is much less affected by acceleration than is Re_θ, leading to a large mismatch between Re_θ and Re_{Δ_2}, as expected for accelerated boundary layers.

Shown in Fig. 2 is the shape factor, $H = \delta^*/\theta$. In the unaccelerated flow, H is nearly constant at a turbulent value of about 1.25. In the accelerated case, H is relatively high ($\sim$1.6) at the upstream stations, dropping to more turbulent-like values after Re_θ begins to rise. It should be noted that at no point is H near the laminar, low-disturbance value, which for this case should be about 2.2. The upstream boundary layer is neither a developed, fully turbulent boundary layer, nor is it laminar. In low-FSTI flows, boundary layers relaminarize at $K > 3 \times 10^{-6}$ (Jones and Launder, 1972) and at the acceleration rates of this case, they would be laminar.

Strength of Curvature. The maximum strength of curvature, θ/R, is 0.6×10^{-3} for the accelerated flow experiment and 1.8×10^{-3} for the comparison case. The ratio $\delta_{99.5}/\theta$ is approximately 20 for both cases, so $\delta_{99.5}/R$ is about 1 percent for the accelerated case and 3 percent for the unaccelerated. Acceleration, by suppressing the boundary layer growth, effectively reduces the importance of curvature. The maximum strength of curvature, θ/R, for the pressure sides of the CF6 airfoil and a more modern airfoil are estimated to be 2×10^{-3} and 4×10^{-3}, respectively. The strength of curvature for the unaccelerated flow experiment is comparable to that of the CF6 blade and significantly below that of the more modern blade. With acceleration, the strength of curvature is low compared to either blade.

Mean Velocity Profiles. Figure 3 shows mean velocity profiles plotted in wall coordinates for the accelerated flow case. Over the first five stations, the profiles rise to higher u^+ values while keeping approximately the same shape. There is considerable deviation from the unaccelerated flow law of the wall, and the profiles appear somewhat laminar-like. At Station 6, the profile shape begins to change to one that is more turbulent-like. This trend is more obvious at Station 7, and by Stations 9 and 10 the profiles are almost in agreement with the unaccelerated flow law of the wall. The change in profile shape at Station 6 is consistent with the beginning of the rise in Re_θ and the drop in the shape factor, H (Fig. 2). The profiles exhibit no wake region. The absence of a wake is consistent with previous observations in high FSTI turbulent

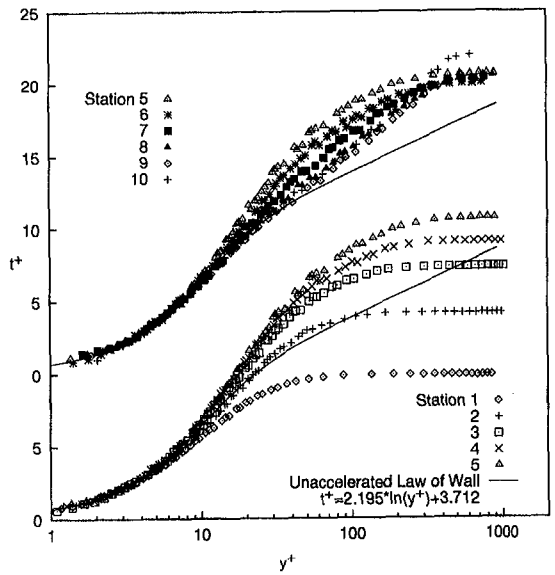

Fig. 4 Mean temperature profiles in wall coordinates for accelerated flow case

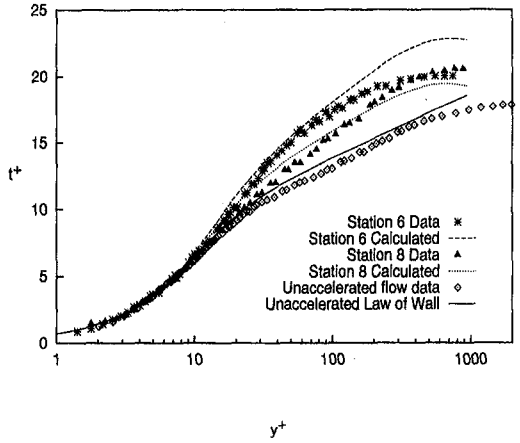

Fig. 5 Comparison of mean temperature profile data to computed profiles for accelerated and unaccelerated flows

flow and indicates considerable turbulent mixing in the outer part of the boundary layer. Kim et al. (1992) presented profiles for the unaccelerated flow comparison case which agree with the unaccelerated flow law of the wall and also exhibit no wake. The Abu-Ghannam and Shaw (1980) transition correlation would predict the end of transition at the 8th or 9th measurement station. The agreement of the mean velocity profiles with the unaccelerated law of the wall supports this prediction. Profiles of turbulence quantities, presented in Part 2, appear to reach asymptotic values at Stations 9 and 10, also suggesting fully turbulent flow at these locations.

Mean Temperature Profiles. Figure 4 shows temperature profiles from the accelerated boundary layer plotted in wall coordinates. The trends are similar to those observed in the velocity profiles in Fig. 3. The profiles rise in t^+ through the first five stations, with a laminar-like shape. At Station 6 the trend is reversed, and the profiles begin to collapse onto a turbulent-like shape. At the downstream stations a wake emerges, which is contrary to velocity profile development. The wake in the temperature profiles may be due to the thickness of the thermal boundary layer relative to the momentum boundary layer, a product of acceleration's suppression of the momentum boundary layer growth. High-FSTI, combined with concave curvature, results in high levels of turbulent mixing in the outer part of the momentum boundary layer, suppressing the wake. The presence of the thermal wake suggests that surface heat transfer should be relatively low compared to skin friction, as shown below.

At the downstream stations (Fig. 4), the temperature profiles do not agree with the unaccelerated flow law of the wall, although there is reasonable agreement between the velocity profiles and the law of the wall (Fig. 3). Acceleration tends to stabilize the boundary layer and reduce turbulence, causing a rise in both the velocity and temperature profiles when plotted in wall coordinates. The favorable pressure gradient also has a direct effect on the velocity profile, causing it to drop, somewhat negating the rise caused by the reduction in turbulence. The pressure gradient has no similar effect on the temperature profiles, so the temperature profiles remain high relative to those in unaccelerated flow. A more detailed explanation of these effects is given in Volino and Simon (1997).

Temperature profiles agree with profiles calculated according to Volino and Simon (1997). The calculated profiles were determined from analytical solution of the boundary layer momentum and energy equations with a mixing length closure model. The derivation is similar to that used to develop the unaccelerated flow thermal law of the wall, but with convection and pressure gradient terms included. Figure 5 shows the temperature profile data at Stations 6 and 8 along with the calculated profiles for the conditions present at these stations. Also shown is a typical profile from the unaccelerated flow case and the unaccelerated flow law of the wall. The matches between the experimental data and the calculated profiles are good. Some difference should be expected since the calculated profiles account for the effect of acceleration, but do not include curvature or free-stream turbulence effects. The calculated profiles do not attempt to capture the wake, so no agreement at high y^+ should be expected.

Skin Friction Coefficients. Figure 6 shows skin friction coefficients C_f plotted verses Re_θ for the accelerated flow experiment. Also shown are correlations for low-FSTI, unaccelerated laminar flow (Blasius solution) and fully turbulent flow on a flat plate (Schlichting, 1979). Values in parentheses are local FSTI levels. At the upstream stations, C_f drops while Re_θ remains nearly constant. The flow appears to be relaminarizing in some sense, although C_f values always remain much closer to the turbulent correlation than laminar. Once the flow proceeds toward fully turbulent behavior (Figs. 3 and 4), C_f rises above the turbulent correlation. Acceleration, high FSTI, and concave curvature all tend to produce a rise in C_f at a given

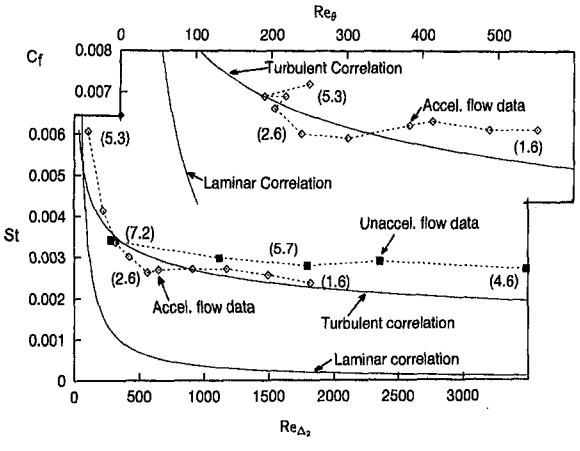

Fig. 6 Skin friction coefficient versus Re_θ and Stanton number versus Re_{Δ_2}. Local FSTI given parenthetically (in percent)

Re_θ. The trend observed here is, therefore, expected. The extent to which each effect is separately responsible for the rise in C_f cannot be determined. The effects interact with one another; for example, acceleration was shown above to reduce FSTI and the strength of curvature. Comparisons to cases in unaccelerated flow are difficult since unaccelerated boundary layers tend to have much higher Re_θ values. It would be useful to compare these data to data from accelerated, high-FSTI boundary layers on flat plates or surfaces with stronger curvature, but such data do not exist.

Stanton Numbers. Figure 6 also shows Stanton number, St, plotted verses enthalpy thickness Reynolds number, Re_{Δ_2}, for the accelerated flow case and the unaccelerated comparison case. Also shown are flat plate, low-FSTI unaccelerated flow correlations for laminar and fully turbulent flow (Kays and Crawford, 1993). The unaccelerated flow data show no sign of transition and are significantly higher than the flat-wall correlation. The combined effects of FSTI and concave curvature raise the Stanton numbers by as much as 40 percent above the flat wall correlation. The rise in Stanton number is large, but not unexpected. Simonich and Moffat (1982) reported a significant (~20 percent) rise in Stanton numbers above flat plate values in a low-FSTI, unaccelerated concave wall boundary layer with strength of curvature comparable to the unaccelerated case presented here. Simonich and Bradshaw (1978) reported a 5 percent increase in Stanton number for every 1 percent increase in FSTI in boundary layers on flat plates. This is roughly consistent with the data of Blair (1983); they considered FSTI up to 7 percent.

In the accelerated flow, the data drop below the flat wall correlation in the transition region and rise to meet the correlation at the downstream stations. The Stanton numbers in the transition region are much closer to the turbulent correlation than to the laminar correlation, as with the skin friction coefficients (Fig. 6). At the downstream stations, the integrated effect of acceleration has kept the curvature effect small and has led to a reduction in FSTI. At the end of the test section, the three effects are apparently weak, with a remaining acceleration effect compensating the remaining enhancement due to FSTI (1.6 percent at this point) and curvature ($\delta_{99.5}/R \approx 1$ percent at this point).

Conclusions

Transition to turbulence has been documented in boundary layers subject to high free-stream turbulence, strong acceleration, and moderate-to-weak concave curvature. In the early stations, the boundary layer is in a highly disturbed state but is not truly turbulent. Transition is delayed and retarded by the strong acceleration. This early transitional boundary layer is one of strong unsteadiness and eddy transport, but with near-wall production suppressed by the acceleration. Much of the boundary layer turbulence energy is apparently taken from the turbulence of the core flow.

Skin friction and heat transfer coefficients in the transition zone drop below turbulent correlations, but never approach laminar values due to the influence of the high free-stream turbulence on the boundary layer. The rises in skin friction coefficients and Stanton numbers during transition are, therefore, less than in a low-FSTI flow. Transition models which predict skin friction and heat transfer by some combination of laminar and fully turbulent values are not accurate in this case.

Free-stream turbulence, acceleration, and concave curvature interact to produce the results presented. The effect of curvature on accelerated flow transition is still unclear. There is an interaction of effects because acceleration affects the streamwise variation of FSTI and curvature strength. To help separate effects, experiments should be conducted for the high-K conditions described here, but on a flat wall and on a wall with stronger curvature.

A more complete explanation of the results presented here requires an examination of turbulence quantities. These are presented in the following paper, and have been used in support of the discussion presented herein.

Acknowledgments

This work was supported by the NASA Lewis Research Center under grant NASA/NAG3-1249. The grant monitor is Fred Simon.

References

Abu-Ghannam, B. J., and Shaw, R., 1980, "Natural Transition of Boundary Layers—The Effects of Turbulence, Pressure Gradient and Flow History," *J. Mechanical Engineering Science,* Vol. 22, No. 5, pp. 213–228.

Blackwell, B. F., and Moffat, R. J., 1975, "Design and Construction of a Low Velocity Boundary Temperature Probe," ASME JOURNAL OF HEAT TRANSFER, Vol. 97, No. 2, pp. 313–315.

Blair, M. F., 1983, "Influence of Free-Stream Turbulence on Turbulent Boundary Layer Heat Transfer and Mean Profile Development: Part 1—Experimental Data," ASME JOURNAL OF HEAT TRANSFER, Vol. 150, pp. 33–40.

Blair, M. F., 1992, "Boundary-Layer Transition in Accelerating Flows With Intense Freestream Turbulence: Part 1—Disturbances Upstream of Transition Onset," ASME JOURNAL OF FLUIDS ENGINEERING, Vol. 114, pp. 313–321.

Eckert, E. R. G., 1987, "Cross Transport of Energy in Fluid Streams," *Wärme- und Stoffübertragung,* Vol. 21, pp. 73–81.

Halstead, D. E., Wisler, D. C., Okiishi, T. H., Walker, G. J., Hodson, H. P., and Shin, H.-W., 1997, "Boundary Layer Development in Axial Compressors and Turbines: Part 3 of 4—LP Turbines," *ASME Journal of Turbomachinery,* Vol. 119, pp. 225–237.

Jones, W. P., and Launder, B. E., 1972, "Some Properties of Sink-Flow Turbulent Boundary Layers," *J. Fluid Mech.,* Vol. 56, pp. 337–351.

Kays, W. M., and Crawford, M. E., 1993, *Convective Heat and Mass Transfer,* McGraw-Hill Book Co. Inc., New York.

Kestoras, M. D., and Simon, T. W., 1993, "Combined Effects of Concave Curvature and High Free-Stream Turbulence Intensity on Boundary Layer Heat and Momentum Transport," ASME paper 93-WA/HT-56.

Kim, J., and Simon, T. W., 1991, "Free-Stream Turbulence and Concave Curvature Effects on Heated Transitional Boundary Layer: Vol. I—Final Report," NASA CR 187150.

Kim, J., Simon, T. W., and Russ, S. G., 1992, "Free-Stream Turbulence and Concave Curvature Effects on Heated, Transitional Boundary Layers," ASME JOURNAL OF HEAT TRANSFER, Vol. 114, pp. 338–347.

Kim, J., Simon, T. W., and Kestoras, M., 1994, "Fluid Mechanics and Heat Transfer Measurements in Transitional Boundary Layers Conditionally Sampled on Intermittency," ASME *Journal of Turbomachinery,* Vol. 116, pp. 405–416.

Mayle, R. E., 1991, "The Role of Laminar-Turbulent Transition in Gas Turbine Engines," ASME *Journal of Turbomachinery,* Vol. 113, pp. 509–537.

Morkovin, M. V., 1978, "Instability, Transition to Turbulence, and Predictability," AGARD-AG-236.

Qiu, S., Simon, T. W., and Volino, R. J., 1995, "Evaluation of Local Wall Temperature, Heat Flux, and Convective Heat Transfer Coefficient from the Near-Wall Temperature Profile," Presented at the 1995 ASME IMECE, *Heat Transfer in Turbulent Flows,* ASME HTD, Vol. 318, pp. 45–52.

Rued, K., and Wittig, S., 1986, "Laminar and Transitional Boundary Layer Structures in Accelerating Flow With Heat Transfer," *ASME Journal of Turbomachinery,* Vol. 108, pp. 116–123.

Russ, S. G., and Simon, T. W., 1991, "On the Rotating, Slanted, Hot-Wire Technique," *Exp. in Fluids,* Vol. 12, pp. 76–80.

Schlichting, H., 1979, *Boundary Layer Theory,* 7th ed., McGraw-Hill Book Co. Inc., New York.

Simonich, J. C., and Bradshaw, P., 1978, "Effect of Free-Stream Turbulence on Heat Transfer through a Turbulent Boundary Layer," ASME JOURNAL OF HEAT TRANSFER, Vol. 100, pp. 671–677.

Simonich, J. C., and Moffat, R. J., 1982, "Local Measurements of Turbulent Boundary Layer Heat Transfer on a Concave Surface Using Liquid Crystals," HMT-35, Thermosciences Division, Department of Mechanical Engineering, Stanford University, CA.

Sohn, K. H., and Reshotko, E., 1991, "Experimental Study of Boundary Layer Transition with Elevated Freestream Turbulence on a Heated Flat Plate," NASA CR 187068.

Volino, R. J., and Simon, T. W., 1994, "Transfer Functions for Turbulence Spectra," *Unsteady Flows in Aeropropulsion,* ASME AD, Vol. 40, pp. 147–155, presented at the 1994 ASME IMECE.

Volino, R. J., and Simon, T. W., 1997, "Velocity and Temperature Profiles in Turbulent Boundary Layer Flows Experiencing Streamwise Pressure Gradients," *ASME Journal of Heat Transfer,* Vol. 119, pp 433–439.

Volino, R. J., and Simon, T. W., 1995a, "Bypass Transition in Boundary Layers Including Curvature and Favorable Pressure Gradient Effects," *ASME Journal of Turbomachinery,* Vol. 117, pp. 166–174.

Volino, R. J., and Simon, T. W., 1995b, "Measurements in Transitional Boundary Layers under High Free-Stream Turbulence and Strong Acceleration Conditions," NASA CR 198413.

Wang, T., and Simon, T. W., 1987, "Heat Transfer and Fluid Mechanics Measurements in a Boundary Layer Undergoing Transition on a Convex-Curved Wall," *ASME Journal of Turbomachinery,* Vol. 109, No. 3, pp. 443–452.

Wills, J. A. B., 1962, "The Correction of Hot-Wire Readings for Proximity to a Solid Boundary," *J. Fluid Mech.,* Vol. 12, pp. 388–396.

Zhou, D., and Wang, T., 1993, "Combined Effects of Elevated Free-Stream Turbulence and Streamwise Acceleration on Flow and Thermal Structures in Transitional Boundary Layers," ASME HTD, Vol. 242, *Gas Turbine Heat Transfer 1993,* D. M. McEligot, ed., pp. 41–52.

Boundary Layer Transition Under High Free-Stream Turbulence and Strong Acceleration Conditions: Part 2—Turbulent Transport Results

R. J. Volino
Department of Mechanical Engineering,
United States Naval Academy,
Annapolis, MD
volino@nadn.navy.mil

T. W. Simon
Heat Transfer Laboratory,
Department of Mechanical Engineering,
University of Minnesota,
Minneapolis, MN

Measurements from heated boundary layers along a concave-curved test wall subject to high (initially 8 percent) free-stream turbulence intensity and strong ($K = \nu/U_\infty^2\, dU_\infty/dx$, as high as 9×10^{-6}) acceleration are presented and discussed. Conditions for the experiments were chosen to simulate those present on the downstream half of the pressure side of a gas turbine airfoil. Turbulence statistics, including the turbulent shear stress, the turbulent heat flux, and the turbulent Prandtl number are presented. The transition zone is of extended length in spite of the high free-stream turbulence level. Turbulence quantities are strongly suppressed below values in unaccelerated turbulent boundary layers. Turbulent transport quantities rise with the intermittency, as the boundary layer proceeds through transition. Octant analysis shows a similar eddy structure in the present flow as was observed in transitional flows under low free-stream turbulence conditions. To the authors' knowledge, this is the first detailed documentation of a high-free-stream-turbulence boundary layer flow in such a strong acceleration field.

Introduction

Boundary layer transition has been studied extensively, but little work has been done to document the nature of transition in flows subject to high (>5 percent) free-stream turbulence intensities (FSTI). Understanding the behavior of high disturbance flows is important, for such flows are found in applications such as gas turbine engines, where FSTI values as high as 20 percent are possible. Mayle (1991) states that recent measurements in turbine and compressor rigs show approach flow turbulence levels of 5 to 10 percent, except in the wakes of upstream blades and vanes, where values as high as 15 to 20 percent are found. These upstream fluctuation levels may result in FSTI of approximately 10 to 20 percent between wakes and 30 to 40 percent in wakes at the regions of maximum acceleration on the pressure side of the turbine airfoils. Mayle (1991) states that the transition zone can cover a substantial fraction of a turbine airfoil surface and that engine designers routinely must calculate through transition. He also points out that current calculations are not always accurate and that there is a need for improvement of transition models. This will require an expanded experimental data base as well as more insight into the physics of high-FSTI transition.

In unaccelerated flow, high free-stream turbulence causes rapid transition to turbulence. For unaccelerated flows with FSTI > 5 percent, transition occurs near the leading edge of a test plate. For example, Kim and Simon (1991) found that in unaccelerated flow on a flat plate at 8 percent FSTI, transition was complete by $\mathrm{Re}_x = 2 \times 10^5$. For calculation of friction and heat transfer this boundary layer could be treated as though it were fully turbulent throughout (Volino and Simon, 1995a). The literature suggests, however, that when strong acceleration is applied concurrently with high free-stream turbulence, extended transition zones are possible. Blair (1992) documented transition in flat plate boundary layers subject to favorable pressure gradients and FSTI values to 5 percent. At 5 percent FSTI, acceleration with a value of the acceleration parameter, K, of 0.75×10^{-6} extended transition noticeably. Rued and Wittig (1986) considered flat-plate boundary layers subject to various favorable pressure gradients, with K as high as 6×10^{-6} and FSTI up to 11 percent. Their measurements suggest that for FSTI > 5 percent, acceleration at $K = 2 \times 10^{-6}$ is not strong enough to influence transition, but that acceleration with $K > 5 \times 10^{-6}$ can extend the transition zone, even at 11 percent FSTI. Acceleration rates in gas turbines can exceed $K = 20 \times 10^{-6}$, thus transition cases with high-FSTI and favorable pressure gradients are expected to be important to gas turbine design. Rued and Wittig's (1986) conclusions were based on surface temperature measurements. Detailed in-flow measurements of turbulent momentum and heat transport are lacking in the literature.

In the present study, measurements from heated boundary layers along a concave-curved test wall subject to high (8 percent) free-stream turbulence intensity and strong acceleration are considered. Of three cases with different acceleration rates investigated (Volino and Simon, 1995b), results from the most strongly accelerated case are presented and discussed in the present paper. In this case, air entered the test section with a free-stream velocity of 5 m/s and the free-stream velocity gradient, dU_∞/dx, was 14 s^{-1} throughout. The value of Re_x at the most downstream station was 8×10^5. The acceleration parameter, K, dropped from 9×10^{-6} at the inlet to the test section to 1×10^{-6} at the last measurement station. For reference, Jones and Launder (1972) suggested that a turbulent boundary layer will laminarize in a low-free-stream-disturbance environment when K is increased to 3×10^{-6}. Conditions (in terms of Re_x and K) for the present experiments roughly simulate those on the downstream half of the pressure side of a gas turbine airfoil. Strong acceleration resulted in a thin momentum boundary layer, and thus a reduced strength of curvature, $\delta_{99.5}/$

Contributed by the Heat Transfer Division for publication in the JOURNAL OF HEAT TRANSFER. Manuscript received by the Heat Transfer Division September 14, 1995; revision received April 7, 1997; Keywords: Flow Transition; Forced Convection; Turbulence. Associate Technical Editor: S. Ramadhyani.

R, to below 1 percent, as documented in Volino and Simon (1997). The FSTI dropped as the free-stream velocity increased, falling from 8 percent at the inlet to the test section, to below 2 percent at the last measurement station.

Mean velocity and temperature profiles from this case were discussed in Volino and Simon (1997). Turbulence spectra from the free-stream and boundary layer were discussed in Volino and Simon (1994a). The mean profiles and spectra indicate that the boundary layer is passing through an extended zone of transition. This transition is considerably different than transition observed under low-FSTI conditions. Under high-FSTI conditions, the early transitional boundary layer is subject to strong buffeting by large-scale, free-stream eddies. In transition, skin friction coefficients and Stanton numbers are always well above laminar values, but are below turbulent flow values that correspond to the local Re_θ values. Spectra taken in the boundary layer show that, although upstream fluctuation levels are high, they are mainly at low frequencies (below 500 Hz). Downstream, higher frequencies are seen (emergence of frequencies in the 500–5000 Hz range). The higher frequencies are associated with a rise in turbulence production in the near-wall region. Also associated with the emergence of higher frequencies is a significant rise in the values of turbulent transport quantities, such as the turbulent shear stress. Low-frequency fluctuations in the boundary layer, induced directly by the free-stream, appear to be less effective in promoting turbulent transport than are the fluctuations which seem to originate in the near-wall region by turbulence production.

In the present paper, turbulence quantities, including profiles of the turbulent shear stress, $-\overline{u'v'}$, the normal component of the turbulent heat flux, $\overline{v't'}$, and the turbulent Prandtl number, Pr_t, are presented. The objective is to support, through detailed turbulence measurements, a physical model for this flow that shows an evolution from a buffeted laminar flow to a fully turbulent flow. It is hoped that the high-FSTI transition will soon be as well understood as transition under low-turbulence, free-stream conditions. This high-FSTI model was partially developed in Volino and Simon (1994a).

Experiments

Facility and Instrumentation. All experiments were conducted in an open-return, blown-type wind tunnel. Details are available in Volino and Simon (1997) and Kim and Simon (1991). The flow enters the test section with nominally 8 percent FSTI. Details of the free-stream turbulence are available in Russ and Simon (1991) and Volino and Simon (1994a). The mean velocity at the end of the development section is uniform to within 3 percent and the turbulence intensity to within 6 percent of the mean value. The flow temperature is uniform and constant to 0.1°C.

The test section is a curved channel. The test wall, 68.6 cm wide × 138 cm long, has a constant radius of concave-curvature of 97 cm. It contains an electrical resistance heater which provides a uniform heat flux. At the leading edge of the test wall is a suction slot, which is used to draw off the boundary layer which grows in the development section. The outer wall of the test section is a flexible Lexan sheet that can be positioned to produce any desired streamwise velocity distribution. Ten access holes distributed in the streamwise direction along the centerline of the outer wall are used for velocity and temperature profile measurements. Station locations were given in Volino and Simon (1997).

Velocity measurements were made using a boundary layer type single-hot-wire probe (TSI model 1218-T1.5), a boundary layer type cross-wire probe (TSI model 1243-T1.5), and a constant-temperature, hot-wire bridge (TSI model IFA-100). The uncertainty in mean streamwise velocity is 3–5 percent. The uncertainties in the rms fluctuating streamwise and normal velocity components, $\overline{u'}$ and $\overline{v'}$, are 5 percent and 10 percent, respectively. The uncertainty in the turbulent shear stress, $-\overline{u'v'}$, is 10 percent.

The output of the hot-wire anemometer was used with an analog circuit (Kim and Simon, 1991) to determine the intermittency, γ—the fraction of time the flow was turbulent at a given location. The circuit determined the first and second time derivatives of the hot-wire signal. When either the first or second derivative were above threshold values the circuit output was at a high voltage, declaring the flow instantaneously turbulent. When both derivatives were below their thresholds the circuit output was at a low voltage, declaring the flow instantaneously laminar. The thresholds were set to distinguish between the two types of flow shown in Fig. 1, a typical near-wall velocity trace. The regions of high amplitude but low frequency fluctuations, while certainly not laminar, are termed "non-turbulent" to distinguish them from the zones of high frequency turbulent fluctuations. The low frequency fluctuations are believed to be induced by the free-stream unsteadiness, and do not exhibit the range of scales usually associated with turbulence. The threshold levels were set manually while the anemometer voltage and circuit output were observed with an oscilloscope. The two zones of the flow are distinct enough so that the threshold did not require adjustment between streamwise stations, even when the flow was accelerated.

Nomenclature

c = specific heat
FSTI = free-stream turbulence intensity
$K = (\nu/U_\infty^2)(dU_\infty/dx)$, acceleration parameter
$\mathrm{Pr}_t = \epsilon_M/\epsilon_H$, turbulent Prandtl number
q = heat flux
R = radius of curvature of test wall
Re_x = Reynolds number based on distance from leading edge
Re_{Δ_2} = enthalpy thickness Reynolds number
Re_θ = momentum thickness Reynolds number
$St = q/(\rho c U_\infty(T_w - T_\infty))$, Stanton number
T = local temperature
t' = fluctuating component of temperature
U = local streamwise velocity
U_{cw} = core velocity extrapolated to the wall (used in place of U_∞ for concave wall boundary layer)
U_∞ = free-stream velocity
u' = streamwise velocity fluctuations
$\overline{u'}$ = rms of u'
$u_\tau = \sqrt{\tau_w/\rho}$, friction velocity
$-\overline{u'v'}$ = turbulent shear stress
V = local cross-stream velocity
v' = cross-stream velocity fluctuations
$\overline{v'}$ = rms of v'
$\overline{v't'}$ = cross-stream component of turbulent heat flux
x = streamwise coordinate
y = coordinate normal to the wall
$y^+ = yu_\tau/\nu$, distance from wall in wall coordinates
γ = intermittency, fraction of time flow is turbulent
$\delta_{99.5}$ = momentum boundary layer thickness
$\epsilon_M = -\overline{u'v'}/(d\bar{U}/dy)$, eddy viscosity
$\epsilon_H = -\overline{v't'}/(d\bar{T}/dy)$, eddy diffusivity of heat
ν = kinematic viscosity
ρ = density
θ = momentum thickness
τ_w = wall shear stress
overbar = time averaged

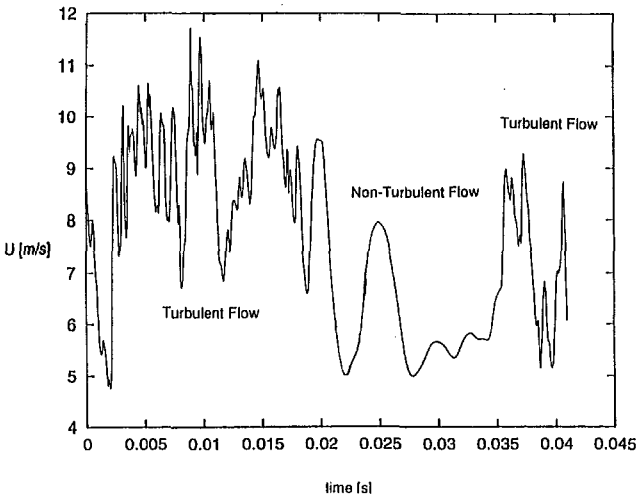

Fig. 1 Velocity time trace showing intermittent flow, Station 7, $Re_x = 5 \times 10^5$, $y^+ = 17$

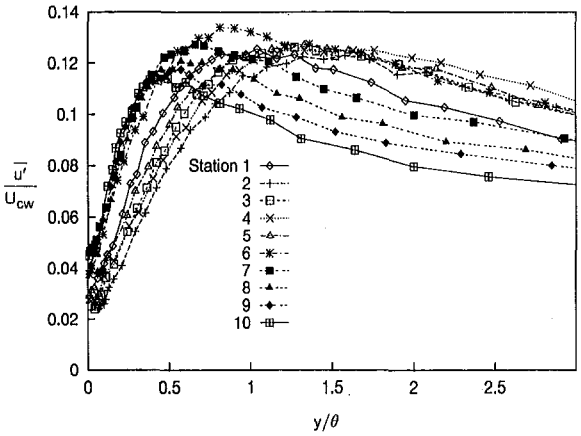

Fig. 2 Near-wall u' profiles in outer coordinates

A three-wire, boundary-layer-type probe (TSI model 1295AM-T1.0) was used to simultaneously measure the instantaneous U and V components of velocity and the instantaneous temperature, T. The probe is described in detail by Kim and Simon (1991). Two of the wires of the probe, arranged in a standard cross-wire arrangement, are used as hot-wires for measuring velocity. The third wire is an uncoated, 1.27 μm diameter platinum wire, used as a cold wire. This wire is parallel and adjacent to one of the hot-wires. The spacing between adjacent wires is 0.35 mm; therefore, overall distance between the outside hot wire and the cold wire is 0.7 mm. The cold wire is run in constant-current mode as a resistance thermometer with a 1 mA current. A compensation scheme employed by Kim and Simon (1991), which was based on a scheme devised by Hishida and Nagano (1978), was used to improve the frequency response of the cold wire to 4 kHz. The uncertainty in the turbulent heat flux, $\overline{v't'}$, measured with the three-wire probe, is 15 percent. The uncertainties in the eddy viscosity, ϵ_M, eddy diffusivity of heat, ϵ_H, and turbulent Prandtl number, Pr_t, are 16 percent, 19 percent, and 25 percent, respectively. The uncertainties in the wall heat flux and wall friction velocity, used to nondimensionalize the data, are 5 percent and 8 percent, respectively.

All probes were moved for profile measurements with a motorized traversing assembly capable of a minimum step size of 5 μm. All data acquisition and probe traversing were controlled with a 386 computer through an IEEE interface bus. At each position in the velocity and temperature profiles, data were acquired for 40 seconds at a 100 Hz sampling rate but with sampling time of less than 1×10^{-5} seconds. The hot wire signals were low-pass filtered at 5 kHz.

Results

Profiles of streamwise fluctuation magnitude, $\overline{u'}$, are shown in Fig. 2, for ten streamwise positions. Data were acquired with the single-hot-wire probe. The peak in $\overline{u'}$ shifts outward between stations 1 and 2, a possible sign of reverse transition. Between stations 2 and 5, the peak $\overline{u'}$ level increases slowly. Between stations 5 and 6, the peak $\overline{u'}$ values rise. As transition proceeds beyond Station 6, the peak in $\overline{u'}$ moves toward the wall and decreases in magnitude. The behavior beyond Station 5 is characteristic of transitional flow and was reported in unaccelerated flow by others, such as Sohn and Reshotko (1991). Some of the shifting of the peak location in the coordinates of Fig. 2 can be tied to the changing boundary layer thickness (Volino and Simon, 1997), which is also related to the transition process. Fluctuation levels are high at all stations, including the upstream stations, in the early part of transition, due to the high FSTI. The $\overline{u'}$ profiles are shown in wall coordinates in Fig. 3. The profiles appear to be similar, with peak values of $\overline{u'}/u_\tau$ between 2 and 2.5 at $y^+ = 17$. The peak level and location are the same as those seen in constant-pressure, fully turbulent boundary layers. The location at $y^+ = 17$ is also characteristic of the peak in near wall turbulence production in turbulent boundary layers. In the outer part of the boundary layer, the accelerated flow case is considerably different than the two comparison cases (Kim and Simon, 1991) of high-FSTI, unaccelerated, fully turbulent boundary layers along either flat or concave walls. The plateau in $\overline{u'}$, seen in the unaccelerated flow (around $y^+ = 100$), is absent at the upstream stations of the accelerated flow and only begins to emerge at downstream stations. Acceleration keeps the boundary layer thin, counteracting the curvature effect and further stabilizing the boundary layer.

Figure 4 shows profiles of the intermittency, γ, which is based on instantaneous u' fluctuations. At the upstream stations, the intermittency is low in spite of the high $\overline{u'}$ fluctuation levels (Fig. 2). This is due to the low frequencies which constitute the unsteadiness. The intermittency remains nearly constant for the first three stations and then begins to rise, reaching a value of near 100 percent (fully turbulent) by Station 8.

Figure 5 shows profiles of $\overline{v'}$ fluctuations. Data were acquired with the cross-wire probe. The minimum at y^+ between 100 and 200, a characteristic of high FSTI flows, separates the region influenced by the large free-stream fluctuations and the near-wall region. The near-wall rise in each $\overline{v'}$ profile indicates significant near-wall turbulence production. The near-wall $\overline{v'}$ levels

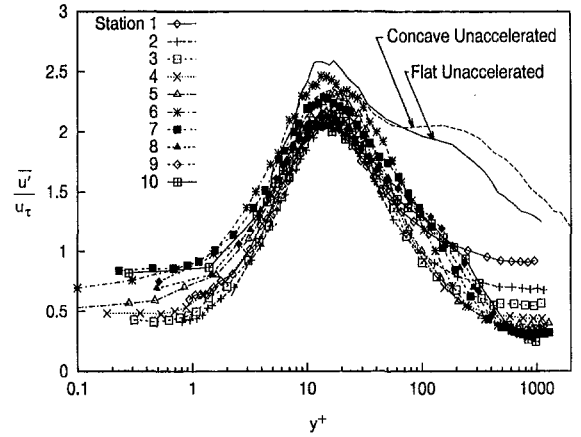

Fig. 3 u' profiles in wall coordinates

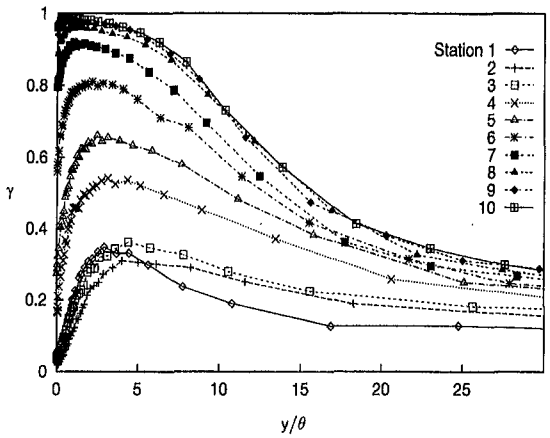

Fig. 4 Intermittency profiles

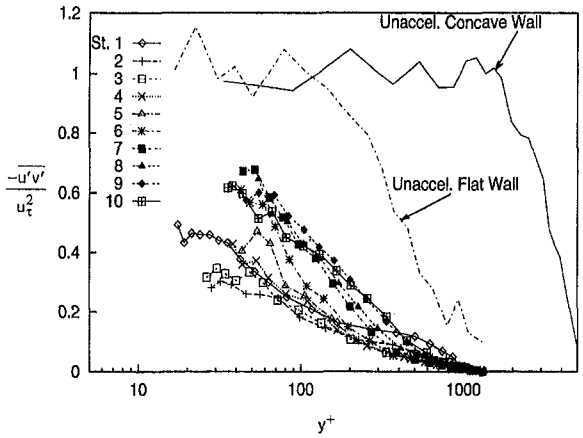

Fig. 6 Turbulent shear stress profiles

are typical of turbulent boundary layers. There is a significant rise in the near-wall $\overline{v'}$ between the upstream and downstream stations, indicating that although there is some turbulence production upstream, it is suppressed by the acceleration early in transition.

Turbulent Transport. Figure 6 shows profiles of the turbulent shear stress plotted in wall coordinates, along with profiles from the unaccelerated cases. Data were acquired with the cross-wire probe. The accelerated flow profiles show a continuous evolution through transition, rising to what appears to be an asymptotic shape by Station 9. At the upstream stations, values are above those for early transitional, low-FSTI flows. Downstream, the profiles extrapolate to about 1 at the wall, as expected. Unaccelerated flow profiles are more full (higher normalized shear stress in the outer part of the boundary layer). Acceleration stabilizes the boundary layer, reducing turbulent transport, particularly in the outer part of the boundary layer. Figure 7 shows profiles of the normal component of the turbulent heat flux, $\overline{v't'}$, plotted in wall coordinates. Results are essentially the same as those given above for the turbulent shear stress.

Profiles of the eddy viscosity, normalized on the kinematic viscosity, are shown in Fig. 8. For unaccelerated, high-FSTI flow, Kim and Simon (1991) reported values of eddy viscosity which are from 10 to 20 times those in Fig. 8 for the same concave wall, and about 3 times those in Fig. 8 for a flat wall. Acceleration is counteracting the strong concave curvature effect and lowering eddy viscosity.

Figure 9 shows profiles of the turbulent Prandtl number. Data were acquired with the three-wire probe. The uncertainties in the quantities used to calculate Pr_t combine to produce considerable scatter in the data. Small mean velocity and temperature gradients cause very high uncertainty at high y^+, and near wall resolution problems result in high uncertainty and generally low Pr_t values at low y^+. At intermediate y^+ between 100 and 500, however, particularly at the downstream stations, most of the Pr_t values lie between 0.9 and 1.3. Values of Pr_t may be slightly elevated above the unaccelerated, flat-wall value of 0.9, but this cannot be stated with certainty, given the uncertainty in the data. The single-sample uncertainty for Pr_t at intermediate y^+ is 25 percent, but uncertainty values that are significantly lower can be applied to levels taken from several nearby values (12 percent for a four-value pool). In Volino and Simon (1997) Stanton numbers are shown to be low, relative to skin friction coefficients in this case, compared to observations in unaccelerated flow. The Pr_t results show that this is not due to any significant difference in eddy diffusivity of heat and momentum. This difference must then come from differences in the thicknesses of the momentum and thermal boundary layers and associated differences in mean-quantity gradients. As expected from documentation in the literature, and as shown in Volino and Simon (1997), acceleration suppresses the growth of the momentum boundary layer but has little effect on the growth of the thermal boundary layer.

Octant Analysis. Volino and Simon (1994b) discussed a technique called octant analysis in which instantaneous turbulence data are segregated into eight categories, based on the

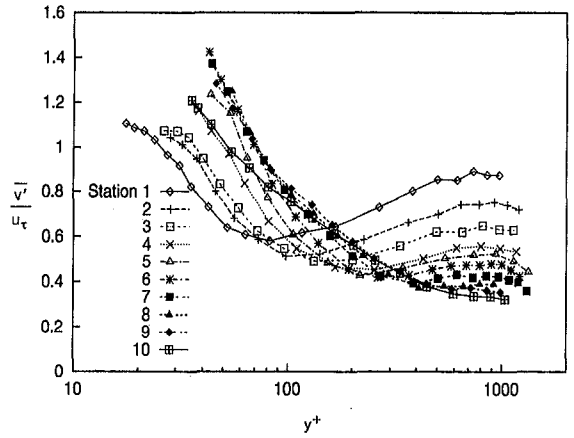

Fig. 5 v' profiles in wall coordinates

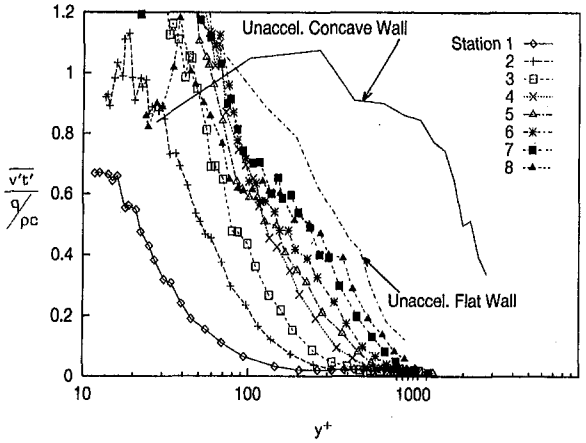

Fig. 7 Normal component of turbulent heat flux profiles

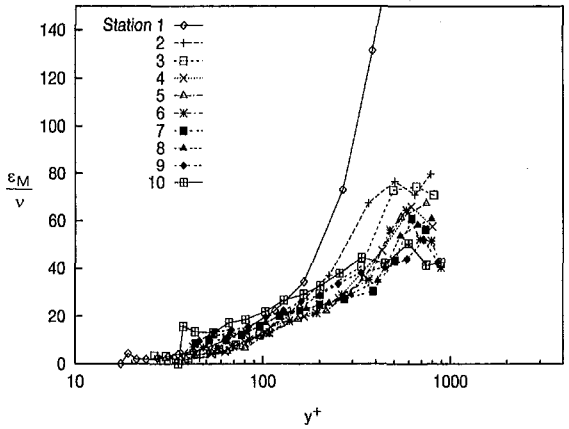

Fig. 8 Eddy viscosity profiles

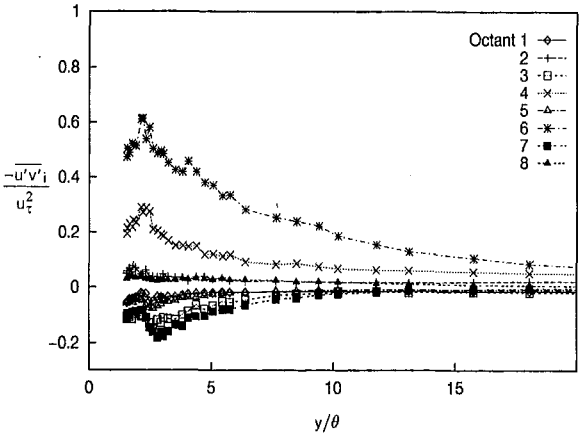

Fig. 10 Octant decomposition of $-\overline{u'v'}$

signs of fluctuating u', v', and t'. The technique is an extension of quadrant analysis (Willmarth and Lu, 1972). Contributions to quantities such as the turbulent shear stress are computed from the data in each octant. Those octants making the largest contribution to the shear stress are then explained in terms of particular eddy motions. Octant decomposition of the turbulent shear stress, applied to mid-transition (Station 4) of the present case, is shown in Fig. 10, and, for the turbulent heat flux, is shown in Fig. 11. Data were acquired with the three-wire probe. The distributions are characteristic of transitional flow. Octant 6 (called the "hot ejection," $u' < 0$, $v' > 0$, and $t' > 0$) dominates, and octant 4 (called the "cold sweep," $u' > 0$, $v' < 0$, and $t' < 0$) and octant 7 (called the "hot wallward interaction," $u' < 0$, $v' < 0$, and $t' > 0$) play a secondary role. Also contributing are octant 3 (called the "cold wallward interaction," $u' < 0$, $v' < 0$, and $t' < 0$) and octant 5 (called the "hot outward interaction," $u' > 0$, $v' > 0$, and $t' > 0$). These two octants appear to be peculiar to accelerated transitional flows and were unimportant in the unaccelerated cases documented by Volino and Simon (1994b). Octants 3 and 5 make negative contributions to the turbulent shear stress but positive contributions to the turbulent heat flux. In agreement with this, a comparison of Figs. 6 and 7 shows that the shear stress is significantly lower than $\overline{v't'}$, compared to unaccelerated flat-wall values. Contributions from octants 3 and 5 are believed to result from the thermal boundary layer being much thicker than the momentum boundary layer. Interestingly, the changes in $-\overline{u'v'}$ and $\overline{v't'}$ do not significantly affect the turbulent Prandtl number (Fig. 9). Changes in the mean velocity and temperature gradients, which also factor into Pr_t, are such that Pr_t remains near 1. In fully turbulent boundary layers, octants 4 and 6 make nearly equal contributions, and all other octants have minimal contributions. The octant results are interpreted to show a lack of small-scale mixing in the transitional flow, relative to that taking place in fully turbulent flow. In particular, the octant 7 contribution is believed to result when fluid from a hot ejection (octant 6) is subsequently caught up in a sweep toward the wall. In fully turbulent boundary layers, octant 7 is not significant, because small-scale eddies tend to disperse fluid from hot ejections quickly, before the octant 7 motion can occur. A more complete description of this hypothesis, along with supporting data is available in Volino and Simon (1994b). All stations show approximately the same octant distributions, indicating that even at the last measurement station, fully turbulent behavior has not yet been achieved. In a comparison case, with higher Reynolds numbers and lower acceleration rates, fully turbulent octant distributions (dominated only by octants 4 and 6) were observed at downstream stations.

Conclusions

The above results show that an extended transition zone is present in the flow in spite of the high free-stream turbulence. In unaccelerated flow at this FSTI, the transition zone would have been very short and would be restricted to near the leading edge of the test wall. The flow has been documented in detail in terms of various turbulence quantities. This is believed to be the first such documentation of a transitional boundary layer under such high free-stream disturbance conditions. Eddy transport of momentum is considerably reduced compared to that of

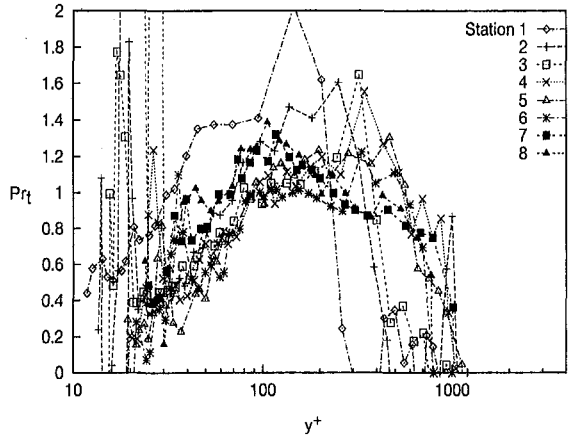

Fig. 9 Turbulent Prandtl number profiles

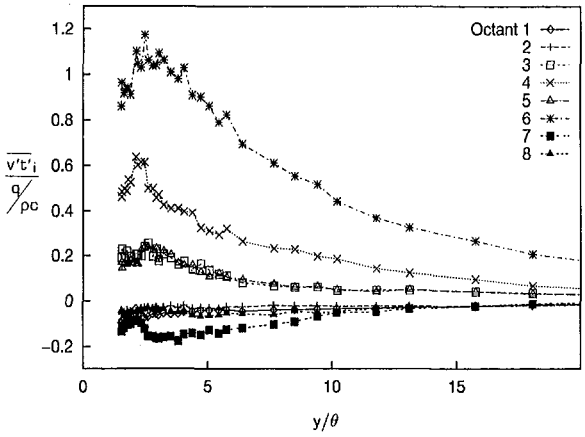

Fig. 11 Octant decomposition of $\overline{v't'}$

unaccelerated flow or compared to the eddy transport of heat in the present case. The diffusivities of heat and momentum are nearly equal for the present case, however, as documented by the nearness of Pr_t to unity, over the entire flow. This suggests that the Reynolds analogy between the transport of heat and momentum holds in both accelerated and unaccelerated transitional boundary layers.

Acknowledgments

This work was supported by the NASA Lewis Research Center under grant NASA/NAG3-1249. The grant monitor is Fred Simon.

References

Blair, M. F., (1992), "Boundary-Layer Transition in Accelerating Flows With Intense Freestream Turbulence: Part 1—Disturbances Upstream of Transition Onset," *ASME Journal of Fluids Engineering,* Vol. 114, pp. 313–321.

Hishida, M., and Nagano, Y., (1978), "Simultaneous Measurements of Velocity and Temperature in Nonisothermal Flows," ASME JOURNAL OF HEAT TRANSFER, Vol. 100, pp. 340–345.

Jones, W. P., and Launder, B. E., (1972), "Some Properties of Sink-Flow Turbulent Boundary Layers," *J. Fluid Mech.,* Vol. 56, pp. 337–351.

Kim, J., and Simon, T. W., (1991), "Free-Stream Turbulence and Concave Curvature Effects on Heated Transitional Boundary Layer: Vol. I—Final Report," NASA CR 187150.

Mayle, R. E., (1991), "The Role of Laminar-Turbulent Transition in Gas Turbine Engines," *ASME Journal of Turbomachinery,* Vol. 113, pp. 509–537.

Rued, K., and Wittig, S., (1986), "Laminar and Transitional Boundary Layer Structures in Accelerating Flow With Heat Transfer," *ASME Journal of Turbomachinery,* Vol. 108, pp. 116–123.

Russ, S. G. and Simon, T. W., (1991), "On the Rotating, Slanted, Hot-Wire Technique," *Exp. in Fluids,* Vol. 12, pp. 76–80.

Sohn, K. H., and Reshotko, E., (1991), "Experimental Study of Boundary Layer Transition with Elevated Freestream Turbulence on a Heated Flat Plate," NASA CR 187068.

Volino, R. J., and Simon, T. W., (1994a) "Transfer Functions for Turbulence Spectra," *Unsteady Flows in Aeropropulsion,* ASME AD-Vol. 40, pp. 147–155.

Volino, R. J., and Simon, T. W., (1994b), "An Application of Octant Analysis to Turbulent and Transitional Flow Data," *ASME Journal of Turbomachinery,* Vol. 116, pp. 752–758.

Volino, R. J., and Simon, T. W., (1995a), "Bypass Transition in Boundary Layers Including Curvature and Favorable Pressure Gradient Effects," *ASME Journal of Turbomachinery,* Vol. 117, pp. 166–174.

Volino, R. J., and Simon, T. W., (1995b), "Measurements in Transitional Boundary Layers under High Free-Stream Turbulence and Strong Acceleration Conditions," NASA CR 198413.

Volino, R. J., and Simon, T. W., (1997), "Boundary Layer Transition Under High Free-Stream Turbulence and Strong Acceleration Conditions: Part 1 — Mean Flow Results," ASME JOURNAL OF HEAT TRANSFER, Vol. 119, pp. 420–426.

Willmarth, W. W., and Lu, S. S., (1972), "Structure of the Reynolds Stress Near the Wall," *J. Fluid Mech.,* Vol. 55, pp. 65–92.

Velocity and Temperature Profiles in Turbulent Boundary Layer Flows Experiencing Streamwise Pressure Gradients

R. J. Volino
Department of Mechanical Engineering,
United States Naval Academy,
Annapolis, MD 21402
volino@nadn.navy.mil

T. W. Simon
Heat Transfer Laboratory,
Department of Mechanical Engineering,
University of Minnesota,
Minneapolis, MN 55455

The standard turbulent law of the wall, devised for zero pressure gradient flows, has been previously shown to be inadequate for accelerating and decelerating turbulent boundary layers. In this paper, formulations for mean velocity profiles from the literature are applied and formulations for the temperature profiles are developed using a mixing length model. These formulations capture the effects of pressure gradients by including the convective and pressure gradient terms in the momentum and energy equations. The profiles which include these terms deviate considerably from the standard law of the wall; the temperature profiles more so than the velocity profiles. The new profiles agree well with experimental data. By looking at the various terms separately, it is shown why the velocity law of the wall is more robust to streamwise pressure gradients than is the thermal law of the wall. The modification to the velocity profile is useful for evaluation of more accurate skin friction coefficients from experimental data by the near-wall fitting technique. The temperature profile modification improves the accuracy with which one may extract turbulent Prandtl numbers from near-wall mean temperature data when they cannot be determined directly.

Introduction

When presented in wall coordinates (u^+ versus y^+), mean velocity profiles from turbulent boundary layers seem to be self-similar in the near-wall region over a wide range of conditions. In the viscous sublayer ($y^+ < 5$), Eq. (1*a*) holds. Outside the viscous sublayer ($30 < y^+ < 150$), in the so called "log region", the standard law of the wall, Eq. (1*b*) holds.

$$u^+ = y^+, \quad u^+ = \frac{1}{\kappa} \ln y^+ + C \qquad (1a,b)$$

The von Kármán constant, κ, and the offset constant, C, are most commonly taken from data as 0.41 and 5.0, respectively. The extent of the log region varies with the flow conditions, extending to higher y^+ as Reynolds number is increased. In the outer, or wake, region of the boundary layer, the self similarity of profiles expressed in wall units breaks down, being influenced by Reynolds number, curvature, pressure gradient, and free-stream turbulence effects.

In the turbulent thermal boundary layer, the mean temperature profile can be expressed as Eq. (2*a*) in the conduction layer, which for a Pr $\approx$ 1 fluid corresponds to the viscous sublayer, and Eq. (2*b*) in the log region.

$$t^+ = \mathrm{Pr} y^+, \quad t^+ = \frac{\mathrm{Pr}_t}{\kappa} \ln y^+ + C_t \qquad (2a,b)$$

The turbulent Prandtl number, Pr_t, is typically taken as 0.9, and C_t is assigned to be 13.2Pr-5.66, based upon experimental data.

The self-similarity of the velocity profile lends considerable utility in the determination of skin friction coefficients. Preston tube and Stanton probe measurements of shear stress, for example, depend on the standard relationship so that, with calibration, they can be employed to measure wall shear stress in terms of measured pressure. Measured velocity distributions may also be used to compute wall shear stress if there is an assurance that the mean velocity profile can be cast in terms of a self similar form. For unaccelerated high-Reynolds-number turbulent boundary layers, this is the "law" given as Eq. (1). If the actual velocity profile were to deviate from Eq. (1) but a technique which depended on Eq. (1) were mistakenly applied, errors in C_f could be expected. Hirt and Thomann (1986) discussed such errors with Preston tube measurements in adverse pressure gradient flows.

The temperature law of the wall expressed by Eq. (2) has utility in the calculation of local Pr_t values from measured wall heat flux, wall temperature, boundary layer mean temperature profile data, and wall shear stress. Numerous instances have been documented where Pr_t deviated from the commonly assumed value of 0.9 (e.g., Kays, 1994; Kim et al., 1992).

The standard law of the wall velocity and temperature distributions were derived for zero-pressure-gradient flows. For such flows they are generally accepted. In the presence of adverse or favorable pressure gradients, however, there remains some controversy over their applicability. Rued (1987), for example, concluded that pressure gradients do have an effect on the wake regions of velocity profiles, and small effects on the viscous sublayer region, but no effect on the log region. He cites several references, including Samuel and Joubert (1974), which support the conclusion that the law of the wall is applicable to flows with streamwise pressure gradients. Galbraith and Head (1975) also concluded that the log-law of Eq. (1*b*) is universal and more fundamental than the standard near-wall mixing length distribution, $l = \kappa y$, upon which the standard law of the wall for velocity was originally derived. To explain discrepancies noted with pressure gradients, they concluded that κ is the variable.

On the other side of the controversy are instances of deviation from the standard profile. Jones and Launder (1972) considered sink flows with constant-K values of 1.5×10^{-6}, 2.5×10^{-6},

Contributed by the Heat Transfer Division for publication in the JOURNAL OF HEAT TRANSFER. Manuscript received by the Heat Transfer Division October 15, 1995; revision received April 7, 1997; Keywords: Forced Convection; Modeling & Scaling; Turbulence. Associate Technical Editor: S. Ramadhyani.

and 3.0×10^{-6}. The velocity profile data fell above the standard log-law at all three accelerations, with the deviation increasing with K. Spalart (1986) performed a direct numerical simulation (DNS) of Jones and Launder's (1972) experiments, finding agreement with their results. He also presented a plot of mixing length, l, versus y, showing that the slope is not a constant (κ is not constant). He went on to suggested that Galbraith and Head (1975) may be correct in stating that the log-law is a more universal relationship than the assumption of a constant κ. The assumption of a universal profile may not be entirely accurate, however, for Spalart's (1986) DNS results showed a displacement and change in slope of the log region as K was changed. McDonald (1969) derived corrections to the mean velocity profile for pressure gradient flows. These corrections have the opposite trend, with acceleration, to that seen in the Jones and Launder (1972) data.

Huffman and Bradshaw (1972) examined the velocity profiles in boundary layers, channels, pipes, annuli, and wall jets to conclude that $\kappa = 0.41$ is a constant, even when there is no log region in the data. Nagano et al. (1992) concluded that the standard log-law does not apply and that $\kappa \approx 0.4$ is unchanging in adverse pressure gradient flows. They stated that "over-fitting" of data to the standard log-law (using the fitting technique in situations where doing so is not justified) is the reason for claims that the standard log-law is universal. With an incorrect choice of C_f, one can always force at least some of the data in a profile to fall along the standard log-law. Nagano et al. warn against the use of wall functions in turbulence models due to these deviations from the standard law of the wall.

Spalart and Watmuff (1993) compared DNS and experimental results for a flow subject to acceleration, followed by deceleration. Skin friction coefficients were obtained from Preston tube measurements. Velocity profiles from the DNS results deviated from the log-law in a manner which was consistent with that described by Jones and Launder (1972). The experimental results showed a better match to the standard log-law. In the laminar sublayer, however, the DNS results showed a good fit to the expected $u^+ = y^+$ line, while the experiments showed deviations from the line for y^+ values as low as 2. Spalart and Watmuff (1993) point out that the Preston tube measurements may have been in error due to these deviations from the standard law of the wall. Differences in C_f between the experiment and DNS of as high as 12 percent were reported. Spalart and Watmuff (1993) state that the DNS results indicate a moderate failure of the law of the wall in flows with pressure gradients. They also state that the body of evidence in support of this statement is small and not conclusive.

Data from the Heat Transfer Laboratory of the University of Minnesota, taken in a favorable pressure gradient flow, suggest that the conclusions of Nagano et al. (1992) are correct—that the standard log-law fails in pressure gradient flows. The log-region tends to be short in such flows due to the immaturity of the boundary layer (low values of Re_θ) as a result of the acceleration. With an appropriate choice of C_f, one can make a "reasonable" fit of most, if not all, of the log-region to the standard profile. When this is done, however, the fit in the sublayer, while still within a possibly acceptable range, is clearly not as close as the fits routinely obtained in zero pressure gradient flows. The behavior in the sublayer is known with more certainty than that in the buffer layer or the log layer. Thus, an alternative was sought which would allow more accurate determination of skin friction coefficients.

There has been much less work in the literature on documentation of pressure gradient effects on the temperature profile. Because no pressure gradient term appears explicitly in the boundary layer energy equation, it is not clear at first glance that a pressure gradient should directly affect the temperature profile. The data which do exist (some of which are presented below) show that the deviations from the standard temperature profile are even stronger than the deviations discussed above for velocity profiles however.

The following paper presents derivations of mean velocity and temperature profiles which can be applied in pressure gradient flows. The velocity law profile is similar to that presented by Huffman and Bradshaw (1972) for accelerated flows. The derivation for the temperature profile is believed to be new. The derived forms are verified by comparisons to experimental data for accelerated and decelerated, turbulent boundary layer flows.

Analysis

The following development of velocity and temperature profiles starts with the boundary layer momentum and energy equations and proceeds in a manner similar to that used in the derivation of the standard law of the wall, but without the deletion of terms which are considered to be relevant in accelerated boundary layer flow. The mixing length model is used for closure of the momentum equation with $\kappa = 0.41$, assumed con-

Nomenclature

A^+ = constant in van Driest damping model
C = constant in standard law of the wall
$C_f = (\tau_o/(\rho U_\infty^2/2))$, skin friction coefficient
C_t = constant in standard thermal law of the wall
c = specific heat
$f_1 = (\nu/(U_\infty C_f/2))(d\sqrt{C_f/2}/dx)$
$f_2 = (\nu t_\infty^{+2}/(U_\infty C_f/2))(d\mathrm{St}/dx)$
$g_1 = 1 + p^+ y^+ + (K/\sqrt{C_f/2} + f_1)\int_0^{y^+} u^{+2} dy^+$
$g_2 = (Kt_\infty^+/\sqrt{C_f/2} + f_2)\int_0^{y^+} u^+ dy^+$
$K = (\nu/U_\infty^2)(dU_\infty/dx)$, acceleration parameter
l = mixing length
P = pressure
$p^+ = (\nu/\rho u_\tau^3)(dP/dx)$, pressure in wall units $= -K(C_f/2)^{-3/2}$
Pr = Prandtl number
Pr_t = turbulent Prandtl number
q = heat flux
Re_x = Reynolds number based on distance from leading edge
Re_{Δ_2} = enthalpy thickness Reynolds number
Re_θ = momentum thickness Reynolds number
St $= q_o/\rho c U_\infty(t_o - t_\infty)$, Stanton number
t = local temperature
$t^+ = (t_o - t)\rho c u_\tau/q_o$, local temperature in wall coordinates
U_∞ = free-stream velocity
u = velocity component in streamwise direction
$u^+ = u/u_\tau$, local velocity in wall coordinates
$u_\tau = \sqrt{\tau_o/\rho}$, friction velocity
v = velocity component normal to wall
x = streamwise coordinate
$x^+ = xu_\tau/\nu$, distance in streamwise direction in wall coordinates
y = coordinate normal to the wall
$y^+ = yu_\tau/\nu$, distance from wall in wall coordinates
α = thermal diffusivity
ϵ_H = eddy diffusivity of heat
ϵ_M = eddy diffusivity of momentum
$\eta = y/\sqrt{\nu x/U_\infty}$, Blasius similarity coordinate
κ = von Kármán constant
ν = kinematic viscosity
ρ = density
τ = shear stress
$\zeta' = u/U_\infty$, dimensionless velocity

Subscripts

o = quantity evaluated at the wall
∞ = quantity evaluated in the free-stream

stant, and with van Driest (1956) damping using the variable A^+ model documented in Kays and Crawford (1993). A more detailed presentation is available in Volino and Simon (1995).

Velocity Profile. We start with the boundary layer momentum equation

$$\rho u \frac{\partial u}{\partial x} + \rho v \frac{\partial u}{\partial y} - \frac{\partial \tau}{\partial y} + \frac{dP}{dx} = 0 \tag{3}$$

and do not make the Couette flow assumption to eliminate the convection terms. Also, the pressure gradient term is kept. In the standard law of the wall development, these terms are dropped. Next, we substitute for the normal velocity, v, using the continuity equation, integrate with respect to y, and rearranged to have

$$\frac{\tau}{\tau_o} = 1 + \frac{y}{\tau_o}\frac{dP}{dx} + \frac{\rho}{\tau_o}\int_0^y \left[u\frac{\partial u}{\partial x} - \frac{\partial u}{\partial y}\int_0^y \frac{\partial u}{\partial x}\, dy \right] dy. \tag{4}$$

For the standard law of the wall, $\tau/\tau_o = 1$. After converting to x-y^+ coordinates, Eq. (4) becomes:

$$\frac{\tau}{\tau_o} = 1 + p^+ y^+ + \left(\frac{K}{\sqrt{C_f/2}} + \frac{\nu}{U_\infty C_f/2}\frac{d\sqrt{C_f/2}}{dx} \right) \int_0^{y^+} u^{+2} dy^+ + \frac{2\nu}{U_\infty \sqrt{C_f/2}} \int_0^{y^+} u^+ \frac{\partial u^+}{\partial x}\, dy^+ - \frac{\nu u^+}{U_\infty \sqrt{C_f/2}} \int_0^{y^+} \frac{\partial u^+}{\partial x}\, dy^+. \tag{5}$$

We seek a formulation which can be used to calculate a local profile based only on local wall and free-stream parameters (i.e., K, C_f, U_∞, and their derivatives). Equation (5), which is still an exact formulation of the boundary layer momentum equation, includes a streamwise dependence on the profile history through the term

$$\left.\frac{\partial u^+}{\partial x}\right|_{y^+}.$$

This prevents an analytical calculation of the profile and forces a numerical solution of the momentum equation—starting at an upstream station where the profile is presumed known and proceeding downstream to the location of interest. Such a calculation may not be accurate, particularly if complications such as boundary layer transition occur between the upstream station and the location of interest. To allow a local, analytical determination of the profile,

$$\left.\frac{\partial u^+}{\partial x}\right|_{y^+}$$

is assumed negligible, reducing Eq. (5) to

$$\frac{\tau}{\tau_o} = 1 + p^+ y^+ + \left(\frac{K}{\sqrt{C_f/2}} + f_1 \right) \int_0^{y^+} u^{+2} dy^+. \tag{6}$$

Figure 1 shows the solution to Eq. (6) for laminar unaccelerated flow along with the Blasius solution and the line $u^+ = y^+$. Note the good agreement between Eq. (6) and the Blasius solution in the inner part of the boundary layer ($\eta < 2$). This shows that $\partial u^+/\partial x$ is not an important term for evaluation of the near-wall profile. For turbulent flow, the assumption that

$$\left.\frac{\partial u^+}{\partial x}\right|_{y^+} = 0$$

is reasonable and consistent with the use of wall coordinates

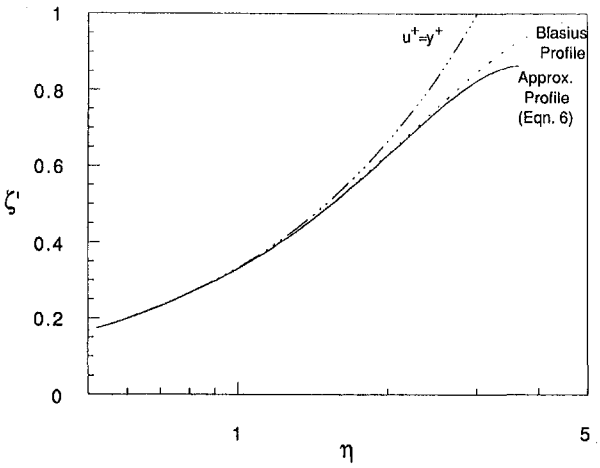

Fig. 1 Velocity profile in laminar unaccelerated flow

for presentation of data in a self similar form. For nonzero streamwise pressure gradient cases,

$$\left.\frac{\partial u^+}{\partial x}\right|_{y^+}$$

is not strictly zero, but is small, even in cases with strong pressure gradients. Although the velocity u and the wall shear stress may vary strongly with x, the normalized quantity u^+ varies slowly with x when y^+ is held fixed.

For turbulent flow, the mixing length model is applied for τ/τ_o as follows:

$$\frac{\tau}{\tau_o} = \frac{(\nu + \epsilon_M)}{u_\tau^2}\frac{du}{dy}, \quad \epsilon_M = l^2\frac{du}{dy}, \quad l = \kappa y(1 - e^{-y^+/A^+}). \tag{7,8,9}$$

The term $(1 - e^{-y^+/A^+})$ is the van Driest (1956) damping term, which provides a continuous transition from the viscous sublayer to the turbulent core flow.

In spite of the controversy discussed above, κ is considered to be a constant (=0.41), and the damping model equilibrium parameter, A^+_{eq}, is assumed to vary with the pressure gradient, as recommended by Kays and Crawford (1993):

$$A^+_{eq} = \frac{25}{1 + ap^+} \text{ where } a = \begin{cases} 20.59 & \text{for } p^+ > 0 \\ 30.18 & \text{for } p^+ < 0 \end{cases}. \tag{10a}$$

The lag model suggested by Kays and Crawford (1993),

$$\frac{dA^+}{dx^+} = \frac{A^+_{eq} - A^+}{4000} \tag{10b}$$

is used to compute A^+ without sudden changes in the sublayer thickness.

Substituting the mixing length into Eq. (7) and converting to wall coordinates,

$$\frac{\tau}{\tau_o} = \left(1 + [\kappa y^+(1 - e^{-y^+/A^+})]^2 \frac{du^+}{dy^+} \right) \frac{du^+}{dy^+}. \tag{11}$$

Equating Eq. (11) and Eq. (6), solving for du^+/dy^+, and integrating, yield

$$u^+ = \int_0^{y^+} \left[\frac{-1 + \sqrt{1 + 4g_1(\kappa y^+(1 - e^{-y^+/A^+}))^2}}{2(\kappa y^+(1 - e^{-y^+/A^+}))^2} \right] dy^+ \tag{12}$$

where $g_1 = 1 + p^+ y^+ + (K/\sqrt{C_f/2} + f_1)\int_0^{y^+} u^{+2} dy^+$. A profile

can be generated with the assignment of K, C_f and f_1. When fitting experimental velocity profile data, the local value of K is known based on the free-stream velocity distribution, and C_f and f_1 are adjusted until the data and calculated profile match in u^+-y^+ coordinates. This is an iterative procedure since f_1, p^+, and A^+ all depend on C_f. To determine f_1, experimental profile data must be fit at two or more stations since f_1 depends on the streamwise derivative of C_f. The dependence of the profile on f_1 is usually weak, so good first estimates of C_f at each streamwise position may found by setting $f_1 = 0$ and fitting the data at each station independently. For further refinement, the initial estimates of C_f may then be used to determine nonzero values of f_1 for inclusion in the calculations.

Temperature Profile. The temperature profile is generated in the same manner. We start with the boundary layer energy equation

$$u\frac{\partial t}{\partial x} + v\frac{\partial t}{\partial y} + \frac{1}{\rho c}\frac{\partial q}{\partial y} = 0. \tag{13}$$

After applying continuity to substitute for v, integrating with respect to y, and transforming to x-y^+ coordinates, we obtain for the case of uniform wall heat flux

$$\frac{q}{q_o} = 1 + \left(\frac{1}{U_\infty^2 \mathrm{St}}\frac{dU_\infty}{dx} + \frac{1}{U_\infty \mathrm{St}^2}\frac{d\mathrm{St}}{dx}\right)\int_0^{y^+} u^+ dy^+ - \frac{\nu}{u_\tau^2}\frac{du_\tau}{dx}\int_0^{y^+} u^+ t^+ dy^+ + \frac{\nu}{u_\tau}\int_0^{y^+} u^+\frac{\partial t^+}{\partial x}dy^+ + \frac{\nu t^+}{u_\tau}\int_0^{y^+}\frac{\partial u^+}{\partial x}dy^+ - \frac{\nu}{u_\tau}\int_0^{y^+} t^+\frac{\partial u^+}{\partial x}dy^+. \tag{14}$$

As with the velocity profile, the terms

$$\left.\frac{\partial u^+}{\partial x}\right|_{y^+}$$

and

$$\left.\frac{\partial t^+}{\partial x}\right|_{y^+}$$

are set to zero, leaving

$$\frac{q}{q_o} = 1 + \left(\frac{Kt_\infty^+}{\sqrt{C_f/2}} + f_2\right)\int_0^{y^+} u^+ dy^+ - \left(\frac{K}{\sqrt{C_f/2}} + f_1\right)\int_0^{y^+} u^+ t^+ dy^+. \tag{15}$$

For computing q/q_o, the mixing length model is used:

$$\frac{q}{q_o} = \frac{\alpha + \epsilon_H}{\nu}\frac{dt^+}{dy^+} = \left(\frac{1}{\mathrm{Pr}} + \frac{\epsilon_H}{\nu}\right)\frac{dt^+}{dy^+}. \tag{16}$$

To eliminate ϵ_H, we use the turbulent Prandtl number, Pr_t, as

$$\frac{\epsilon_M}{\epsilon_H} = \mathrm{Pr}_t,\ \frac{\epsilon_H}{\nu} = \frac{(\kappa y^+[1 - e^{-y^+/A^+}])^2\dfrac{du^+}{dy^+}}{\mathrm{Pr}_t}. \tag{17}$$

Equating (15) and (16), solving for dt^+/dy^+, and integrating gives

$$t^+ = \int_0^{y^+}\left[\frac{1 + g_2 - \left(\dfrac{K}{\sqrt{C_f/2}} + f_1\right)\displaystyle\int_0^{y^+} u^+ t^+ dy^+}{\dfrac{1}{\mathrm{Pr}} + \dfrac{(\kappa y^+[1 - e^{-y^+/A^+}])^2\dfrac{du^+}{dy^+}}{\mathrm{Pr}_t}}\right] dy^+ \tag{18}$$

where $g_2 = (Kt_\infty^+/\sqrt{C_f/2} + f_2)\int_0^{y^+} u^+ dy^+$. With K, C_f, f_1, t_∞^+, f_2, Pr_t, and Eq. (12), Eq. (18) can be integrated numerically. The value of f_2 and t_∞^+ may be determined based on experimental data. The turbulent Prandtl number, Pr_t, can be taken from a correlation such as (Kays and Crawford, 1993)

$$\mathrm{Pr}_t = \frac{1}{\dfrac{1}{2\mathrm{Pr}_{t_\infty}} + C\mathrm{Pe}_t\sqrt{\dfrac{1}{\mathrm{Pr}_{t_\infty}}} - (C\mathrm{Pe}_t)^2\left[1 - \exp\left(-\dfrac{1}{C\mathrm{Pe}_t\sqrt{\mathrm{Pr}_{t_\infty}}}\right)\right]} \tag{19}$$

where $C = 0.2$, $\mathrm{Pe}_t = (\epsilon_M/\nu)\mathrm{Pr}$, and Pr_{t_∞}, the turbulent Prandtl number in the log region of the boundary layer, is either measured, assigned the flat plate value of 0.85, or found by fitting the t^+-y^+ profile to temperature profile data.

For the case of uniform wall temperature (t_o = constant), the derivation is similar, and the final result is

$$t^+ = \int_0^{y^+}\left[\frac{1 + \left(\dfrac{f_2}{t_\infty^+} - f_1\right)\displaystyle\int_0^{y^+} u^+ t^+ dy^+}{\dfrac{1}{\mathrm{Pr}} + \dfrac{[\kappa y^+(1 - e^{-y^+/A^+})]^2\dfrac{du^+}{dy^+}}{\mathrm{Pr}_t}}\right] dy^+. \tag{20}$$

If experimental data, including $\partial t^+/\partial y^+$, from the temperature profile are available, Eq. (18) or (20) can be used to evaluate $\mathrm{Pr}_t(y)$.

Results and Discussion

The following demonstrates the importance of the corrections for pressure gradient and discusses the utility of the profiles developed above. Figures 2 compares velocity and temperature profiles generated for one set of conditions; $K = 2.0 \times 10^{-6}$, $C_f = 6.0 \times 10^{-3}$, $f_1 = -5.0 \times 10^{-6}$, $t_\infty^+ = 20$, and $f_2 = -1.0 \times 10^{-4}$, with various terms in Eqs. (12) and (18) set to zero to demonstrate the importance of each in the evaluation. Included are (*a*) the standard law of the wall (K, f_1, f_2, and p^+ set to zero), (*b*) correction for acceleration using just the A^+ term (K, f_1, f_2, and p^+ set to zero, but $A^+ = 40$, which is consistent with the actual p^+), (*c*) correction with just the p^+ term (K, f_1, and f_2 set to zero and $A^+ = 25$), (*d*) correction with A^+ and p^+ (K, f_1 and f_2 set to zero and $A^+ = 40$), and (*e*) the full correction as given by Eqs. (12) and (18). From the differences in the curves one can see that each part of the correction makes a significant contribution to the total profile. In a favorable pressure gradient the p^+ term causes a drop in u^+ values below those of the standard law of the wall (compare curves *a* and *c* of Fig. 2*a*), and a rise in t^+ values above those of the standard thermal law of the wall (compare curves *a* and *c* of Fig. 2*b*). To explain this, consider a momentum balance on an element of fluid in the boundary layer. If the convection terms in the boundary layer momentum equation (Eq. (3)) were set to zero, the resulting equation would be $dP/dx = \partial\tau/\partial y$. For an accelerating flow, $dP/dx < 0$, τ must therefore decrease with distance from the wall. Since $\tau \propto \partial u/\partial y$, $\partial u/\partial y$ must also decrease with distance from the wall. This results in a drop in u^+ values below those of the standard law of the wall. In turbu-

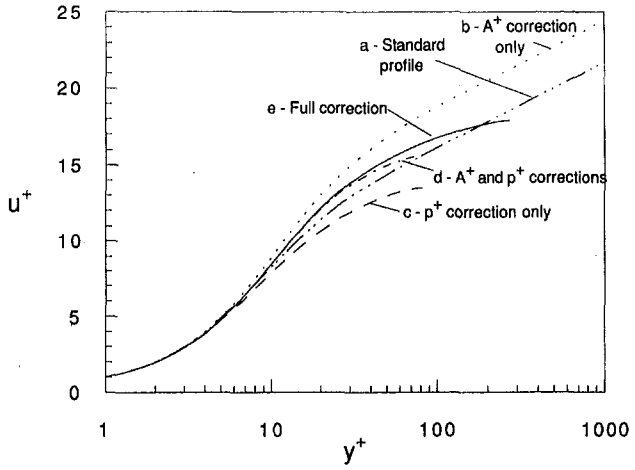

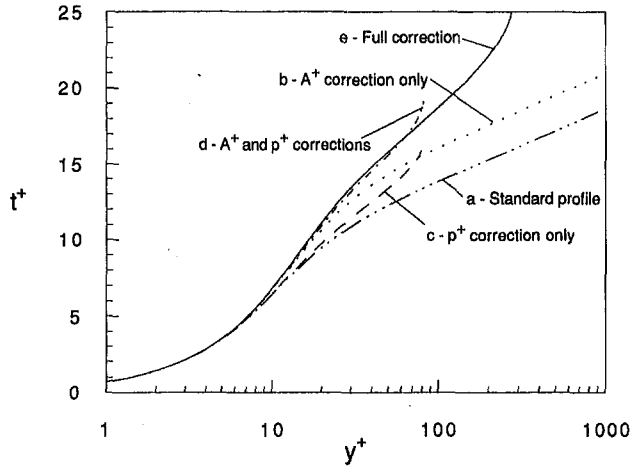

Fig. 2 Velocity and temperature profiles including various correction terms

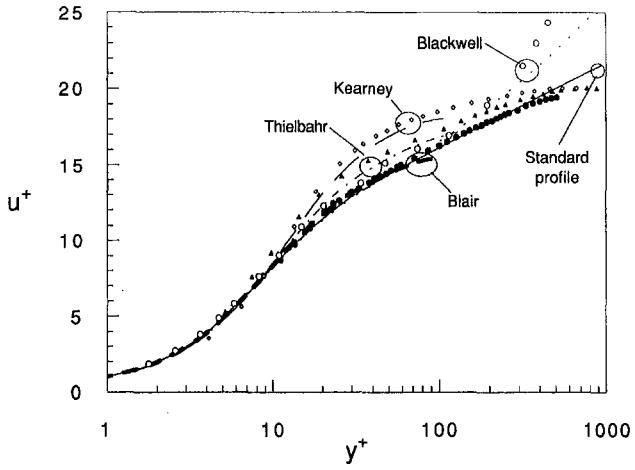

Fig. 3*a* Comparison of experimental and calculated velocity profiles

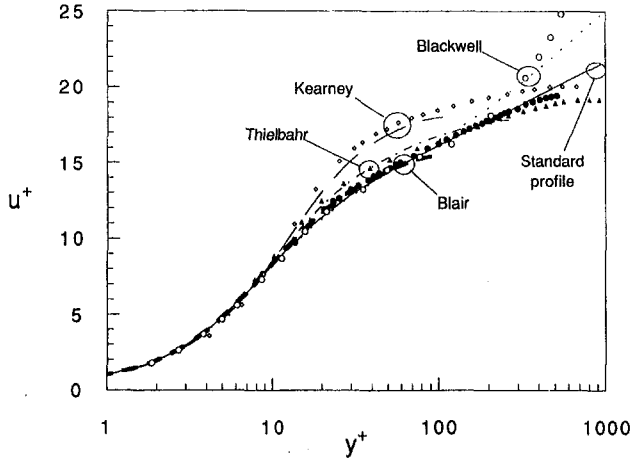

Fig. 3*b* Comparison of experimental and calculated velocity profiles, adjusted C_f

lent flow the p^+ term also has a secondary effect. Since the eddy viscosity is proportional to $\partial u/\partial y$, Eq. (8), ϵ_M must drop in response to the favorable pressure gradient. The eddy viscosity enhances mixing outside of the viscous sublayer, thereby increasing wall shear and reducing $\partial u/\partial y$ and τ outside the sublayer, relative to their values at the wall. In dimensionless variables $\partial u^+/\partial y^+$ drops. In favorable pressure gradients, the reduced eddy viscosity causes a rise in $\partial u^+/\partial y^+$ toward laminar values, somewhat mitigating the drop in $\partial u^+/\partial y^+$ caused by the direct effect of the p^+ term.

The p^+ term has no direct effect on the temperature profile since the pressure gradient does not appear explicitly in the boundary layer energy equation (Eq. (13)). The secondary effect described above is present however. As $\partial u^+/\partial y^+$ drops in a favorable pressure gradient, the eddy diffusivity, ϵ_H, must also fall (Eq. (17)). The result is the rise in t^+ values above the standard thermal law of the wall shown in Fig. 2*b*.

The A^+ term is used to model the thickness of the viscous sublayer. Favorable pressure gradients strain the flow in the streamwise direction, causing a reduction in eddy transport and an increase in sublayer thickness. This is a stabilizing effect. The reduction in eddy transport has the same effect described above with regard to the secondary effect of the p^+ term. When ϵ_M and ϵ_H drop, the velocity and temperature profiles both rise above the standard profiles.

When the A^+ and p^+ effects are combined, they tend to cancel each other in the velocity profile but are additive for the temperature profile. The result is a larger deviation of the temperature profile from the standard profile as a result of acceleration than for the velocity profile. Herein lies the reason for the apparent robustness of the velocity profiles to different accelerations which is not shared by the temperature profiles. Such behavior was noted by Bradshaw and Huang (1994).

The remainder of the corrections in Eqs. (12) and (18) are due to the convection terms in Eq. (3) and (13). The magnitudes and signs of these corrections will depend on local conditions, including, for example, the rates of free-stream acceleration and boundary layer growth. In Eqs. (12) and (18), these effects are expressed in terms of K, f_1, and f_2.

Comparisons to Experimental Data. To evaluate velocity profiles given by Eq. (12), experimental velocity profile data from four studies are plotted in Fig. 3*a* along with calculated profiles corresponding to each. Data were taken from Blair (1981), Blackwell et al. (1972), Thielbahr et al. (1969), and Kearney et al. (1970). All but the first were taken from Kays and Crawford (1993). Pertinent constants from these profiles are given in Table 1. All four studies were done on flat plates with K held constant. Blair's mild acceleration case deviates only slightly from the standard, zero pressure gradient law of

Table 1 Experimental data

Case	$K\times10^6$	$C_f\times10^3$	$f_1\times10^6$	$f_2\times10^4$	t^+_∞	A^+	Re_θ	Re_{Δ_2}
Blair	0.75	4.98	-34.0	-0.065	31.6	30.6	838	2730
Blackwell	-0.31	2.02	-4.43	-1.25	15.2	20.8	4533	2459
Thielbahr	1.67	4.96	-0.88	-1.37	24.9	42.2	747	1880
Kearney	2.68	4.96	-3.88	-7.90	31.3	72.5	550	1345

the wall, and the data match the calculated profile well. The fits of the other three profiles are reasonable, but could stand improvement. Blackwell et al.'s adverse pressure gradient data, and Thielbahr et al.'s favorable pressure gradient data do not match the calculated profile particularly well in the viscous sublayer region (where acceleration effects on the calculated profile are small), indicating that better estimates of C_f than those given with the experimental data might be possible. As shown in Fig. 3*b*, if C_f were increased by approximately 8 percent, to 0.0022 in Blackwell's case and to 0.0053 in Thielbahr's case, the experimental data and the calculated profiles could be brought into good agreement. For the Blackwell et al. and Thielbahr et al. flows, 8 percent is within the experimental uncertainty. Julien et al. (1971), who provided the velocity profiles used in the Thielbahr et al. study, estimate an uncertainty of ±10 percent in C_f in this case. Fitting to Eq. (12) is believed to reduce this uncertainty and improve C_f estimation. Figure 4 shows a force fit of Thielbahr et al.'s velocity data to the standard law of the wall. The required C_f was 0.0061. This is a 15 percent increase above the value estimated above using a fit to Eq. (12) and a 23 percent increase above their published value. The Kearney et al. data could not be brought into quite as good agreement with the calculated profile. Given the relatively strong acceleration parameter in this case, relaminarization effects may have become strong enough to explain the discrepancy between the data and the turbulent flow calculation. Perhaps the flow was stabilized to the point (low momentum thickness Reynolds number) where the mixing length, A^+, and turbulent Prandtl number models are not so accurate.

Temperature Profiles. The measured and calculated temperature profiles are shown in Fig. 5. The unadjusted C_f values given with the data sets and used in Fig. 3*a* were used in the data reduction. Blair's (1981) case was subject to a uniform wall heat flux boundary condition. The other three cases had uniform wall temperature boundary conditions. The matches between calculation and data are reasonable for all four cases and can be improved if the updated C_f values used with Fig. 3*b* are applied (see Volino and Simon, 1995).

Note that the deviations of the temperature profile data from the standard unaccelerated law of the wall values are much larger than those for the velocity profile in all cases. This is particularly apparent in Blair's mild, favorable pressure gradient flow and Blackwell et al.'s adverse pressure gradient flow. In these cases, the deviations of the velocity profile from the unaccelerated law of the wall are small, but the deviations of the temperature profiles are significant and Eqs. (18) and (20) represent major improvements.

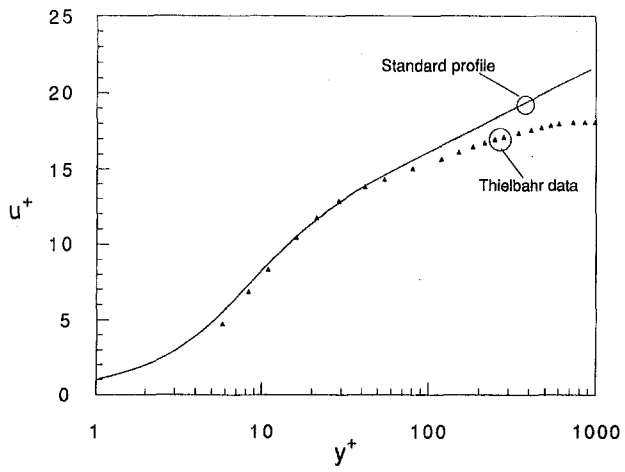

Fig. 4 Force fit of experimental velocity data to standard law of the wall

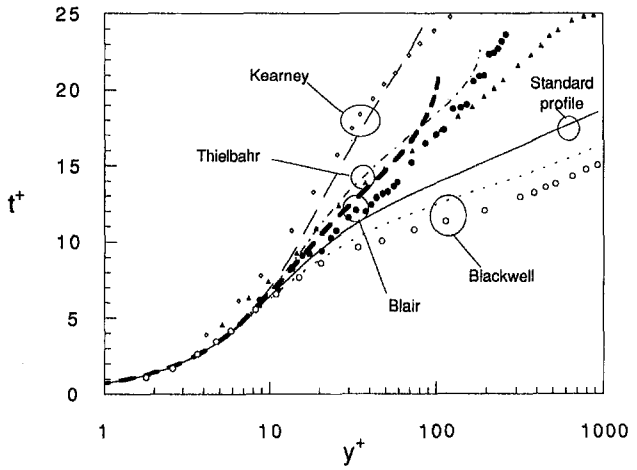

Fig. 5 Comparison of experimental and calculated temperature profiles

Calculation of Pr_t. The temperature profiles presented above were calculated using the turbulent Prandtl number distribution given in Eq. (19), with $Pr_{t_\infty} = 0.85$. The good match between the experimental data and the calculated profiles in Fig. 5 indicates that this model is adequate, and suggests that pressure gradients alone do not significantly affect the turbulent Prandtl number distribution. In some flows, however, this distribution is expected to change. Kim et al. (1992) measured Pr_t directly and showed a rise in Pr_t for $y^+ > 100$. Probe size limitations prevent measurements within $y^+ < 100$ of their flow.

Conclusions

1. New formulations have been developed for mean velocity and temperature profiles in turbulent flows. The velocity profile is similar to one in the literature. No equivalent to the temperature formulation has been found in the literature. These profiles capture the effects of nonzero pressure gradients and match experimental data well.
2. The improvements to the velocity profiles allow an improved determination of skin friction coefficients from experimental data using a near-wall fitting technique. It was shown that "force fits" to the standard law of the wall can lead to errors of as large as 15 percent.
3. The profiles presented here are dependent on the mixing length model which assumes $\kappa = 0.41$ and are based upon a documented variable-A^+ model. As shown, inclusion of this variable-A^+ model is quite important. While this model appears to be adequate, further work to clarify the behavior of κ and A^+ under various conditions would be desirable.
4. The model has been tested through comparison to some data from pressure gradient flows. Further testing in both favorable and adverse pressure gradient cases would be useful.

Acknowledgment

This work was sponsored by the NASA Lewis Research Center under grant NASA/NAG3-881. The grant monitor is Fred Simon.

References

Blackwell, B. F., Kays, W. M., and Moffat, R. J., 1972, "The Turbulent Boundary Layer on a Porous Plate: an Experimental Study of the Heat Transfer Behavior with Adverse Pressure Gradients," HMT-16, Thermosciences Division, Mechanical Engineering Department, Stanford University, Stanford, Calif.

Blair, M. F., 1981, "Final Data Report: Vol. II—Velocity and Temperature Profile Data for Accelerating, Transitional Boundary Layers," United Technologies Research Center Report R81-914388-16.

Bradshaw, P., and Huang, G. P., 1994, "The Law of the Wall in Turbulent Flow," presented at the Osborne Reynolds Centenary Symposium, UMIST, Manchester, May 24, 1994.

Galbraith, R. A. McD., and Head, M. R. (1975), "Eddy Viscosity and Mixing Length from Measured Boundary Layer Developments," *Aeronautical Quarterly,* Vol. 26, pp. 133–154.

Hirt, F., and Thomann, H., 1986, "Measurement of Wall Shear Stress in Turbulent Boundary Layers Subject to Strong Pressure Gradients," *J. Fluid Mech.,* Vol. 171, pp. 547–562.

Huffman, G. D., and Bradshaw, P., 1972, "A Note on von Kármán's Constant in low Reynolds Number Turbulent Flows," *J. Fluid Mech.,* Vol. 53, pp. 45–60.

Julien, H. L., Kays, W. M., and Moffat, R. J., 1971, "Experimental Hydrodynamics of the Accelerated Turbulent Boundary Layer With and Without Mass Injection," ASME JOURNAL OF HEAT TRANSFER, Vol. 93, pp. 373–379.

Jones, W. P., and Launder, B. E., 1972, "Some Properties of Sink-Flow Turbulent Boundary Layers," *J. Fluid Mech.,* Vol. 56, pp. 337–351.

Kays, W. M., 1994, "Turbulent Prandtl Number—Where Are We?" ASME JOURNAL OF HEAT TRANSFER, Vol. 116, pp. 284–295.

Kays, W. M., and Crawford, M. E., 1993, *Convective Heat and Mass Transfer,* McGraw-Hill Book Co. Inc., New York.

Kearney, D. W., Moffat, R. J., and Kays, W. M., 1970, "The Turbulent Boundary Layer: Experimental Heat Transfer with Strong Favorable Pressure Gradients and Blowing," HMT-12, Thermosciences Division, Mechanical Engineering Department, Stanford University, Stanford, Calif.

Kim, J., Simon, T. W., and Russ, S. G., 1992, "Free-Stream Turbulence and Concave Curvature Effects on Heated, Transitional Boundary Layers," ASME JOURNAL OF HEAT TRANSFER, Vol. 114, pp. 338–347.

McDonald, H., 1969, "The Effect of Pressure Gradient on the Law of the Wall in Turbulent Flow," *J. Fluid Mech.,* Vol. 35, pp. 311–336.

Nagano, Y., Tagawa, M., and Tsuji, T., 1992, "Effects of Adverse Pressure Gradient on Mean Flows and Turbulence Statistics in a Boundary Layer," *Turbulent Shear Flows 8,* F. Durst et al., eds., Springer-Verlag, Berlin.

Rued, K., 1987, "Transitional Boundary Layers Under the Influence of High Free Stream Turbulence, Intensive Wall Cooling and High Pressure Gradients in Hot Gas Circulation," NASA TM 88254.

Samuel, A. E., and Joubert, P. N., 1974, "A Boundary Layer Developing in an Increasingly Adverse Pressure Gradient," *J. Fluid Mech.,* Vol. 66, pp. 481–505.

Spalart, P. R., 1986, "Numerical Study of Sink-Flow Boundary Layers," *J. Fluid Mech.,* Vol. 172, pp. 307–328.

Spalart, P. R., and Watmuff, J. H., 1993, "Experimental and Numerical Study of a Turbulent Boundary Layer with Pressure Gradients," *J. Fluid Mech.,* Vol. 249, pp. 337–371.

Thielbahr, W. H., Kays, W. M., and Moffat, R. J., 1969, "The Turbulent Boundary Layer: Experimental Heat Transfer with Blowing, Suction, and Favorable Pressure Gradient," HMT-5, Thermosciences Division, Mechanical Engineering Department, Stanford University, Stanford, Calif.

van Driest, E. R., 1956, "On Turbulent Flow Near a Wall," *J. Aero. Sci.,* Vol. 23, pp. 1007–1011.

Volino, R. J., and Simon, T. W., 1995, "Measurements in Transitional Boundary Layers Under High Free-Stream Turbulence and Strong Acceleration Conditions," NASA CR 198413, Appendix A.

Effects of Partial Inlet Blockages on High-Velocity Flow Through a Thin Rectangular Duct: Experimental and Analytical Results

T. K. Stovall
ASME Member.
stovalltk@ornl.gov

J. A. Crabtree

D. K. Felde

G. Farquharson

J. E. Park
ASME Member.

Oak Ridge National Laboratory,
PO Box 2008,
Oak Ridge, TN 37831-6092

The Advanced Neutron Source (ANS) reactor was designed to provide a research tool with capabilities beyond those of any existing reactors. One portion of its state-of-the-art design required high velocity fluid flow through narrow channels between the fuel plates in the core. Experience with previous reactors had shown that fuel plate damage could occur if debris became lodged at the entrance to these channels. Such debris disrupts the fluid flow to the plate surfaces and could prevent adequate cooling of the fuel. Preliminary ANS designs addressed this issue by providing an unheated entrance length for each fuel plate so that any flow disruption would have time to recover before reaching the heated portions of the fuel plates further downstream. As part of the safety analysis, the adequacy of this unheated entrance length was assessed using both analytical models and experimental measurements. The Flow Blockage Test Facility (FBTF) was designed and built to conduct experiments in an environment closely matching the ANS channel geometry. The FBTF permitted careful measurements of both heat transfer and hydraulic parameters. In addition to these experimental efforts, a thin rectangular channel was modeled using the FLUENT computational fluid dynamics computer code. The numerical results were compared to the experimental data to benchmark the hydrodynamics of the model. After this comparison, the model was extended to include those elements of the safety analysis difficult to measure experimentally. These elements included the high wall heat flux pattern and variable fluid properties.

Background

The Advanced Neutron Source (ANS) reactor was under development to provide a research tool with capabilities beyond those of any existing reactors. One portion of its original design required high velocity coolant (D_2O at 25 m/s) flow through a large number of very narrow channels between fuel plates. These fuel plates produce a very high heat flux, averaging 6 MW/m^2. Experience with previous reactors had shown that fuel plate damage could occur if debris became lodged at the entrance to the cooling channels between the fuel plates. Such debris could disrupt the fluid flow to the plate surfaces and prevent adequate cooling of the fuel. Preliminary ANS designs addressed this issue by providing an unheated entrance length for each fuel plate so that any flow disruption would have time to recover before reaching the heated portions of the fuel plates further downstream. This design concept for the ANS was evaluated to determine the relationship between maximum survivable blockage size and the length of the unheated entrance region.

Reactor safety analysis often relies on computer models to explore accident conditions that are difficult or dangerous to explore experimentally. Such computer models must be carefully designed and benchmarked against appropriate experimental or operational data. Therefore, the work described in this article was directed at understanding the behavior of high speed fluid flow within a partially blocked thin rectangular channel. An extensive literature search was made to find pertinent data to describe such an arrangement. Only one experiment was found that came close to the ANS conditions. Sparrow and Cur performed a series of detailed mass transfer experiments for a rectangular channel with 25 percent and 50 percent of the channel's entrance blocked (Sparrow and Cur, 1983; Cur, 1982). In addition to this empirical resource, many researchers have produced numerical models of a backward-facing step or sudden flow expansion. However, none of these models were applicable to the extreme aspect ratio found in the narrow ANS cooling channels. These models also failed to capture the three-dimensional effect of a partial blockage located at the channel entrance.

Therefore, the efforts described here were planned to expand on the information available from previous work in several ways. First, the partial entrance blockage size and placement were varied. Second, experimental measurements were made to characterize both velocity fields and channel wall heat transfer coefficients. Third, benchmarked numerical models were developed and used to predict wall temperatures under reactor operating conditions.

Several computational fluid dynamic (CFD) computer codes were available for performing flow blockage analysis. Each code solves a complex system of equations, thereby describing fluid flow behavior on a highly localized basis for any number of geometrical configurations. These codes varied in their mathematical approach, using either a finite difference or finite element approach, and offered a variety of solution techniques. In the Sparrow and Cur experiment, the blockage was positioned to one side, or at the edge, of the channel, and their data show a very long recirculation region behind the

Contributed by the Heat Transfer Division for publication in the JOURNAL OF HEAT TRANSFER. Manuscript received by the Heat Transfer Division June 21, 1996; revision received April 25, 1997; Keywords: Enclosure Flows; Flow Separation; Forced Convection. Associate Technical Editor: T. J. Rabas.

blockage, with greatly reduced mass transfer coefficients in this region. This experimental data resource was used to test a number of CFD codes, turbulence models, grid refinements, and geometrical simplifications of channel inlet and outlet regions (Stovall et al., 1995; Meyer et al., 1992). Based on this review, the FLUENT computer code and the renormalized group (RG) turbulence model were selected for use on the ANS flow blockage evaluation (Stovall et al., 1995; Fluent, Inc., 1993; Choudhury et al., 1993).

An experimental evaluation of flow blockage phenomena within the ANS channel was planned to provide both direct information for the ANS safety analysis and an independent check to benchmark the related numerical modeling effort. A parallel effort to identify potential blockage material, and possible blockage sizes, was also made. Because the possible blockage sizes were not identified when this task began, several blockage sizes were considered. The Flow Blockage Test Facility (FBTF) did not include the high heat fluxes expected during ANS operation but was used to define the fluid velocity field and wall heat transfer coefficients within the cooling channel for a number of blockages. After comparison to the experimental results, the numerical models were used to predict wall temperatures and fluid flow patterns under ANS operating conditions.

Facility Description

Two experimental measurement techniques were chosen to measure the fluid behavior within the narrow channel. The first used thermochromic liquid crystals (TLC) and a small heater plate to measure channel wall temperatures. The second used laser Doppler velocimetry (LDV) to monitor the fluid flow within the channel. The experimental facility shown in Fig. 1 was designed to accommodate both techniques with approximately the same channel dimensions as the proposed ANS fuel channel: an 84 mm span (perpendicular to the plane of Fig. 1), a 1.27 mm gap (horizontal on Fig. 1), and a 500 mm channel length (vertical on Fig. 1). Because of the large pressure drop (up to 1.5 MPa) associated with high speed fluid flow through the narrow channel, the lexan channel walls, each approximately 50 mm thick, were further supported by a strong steel case, shown as the shaded region in the side view of the test section in Fig. 1. This figure also shows the windows for video camera and LDV access that were cut through the steel case. The channel walls were formed by the machined-flat lexan surfaces and the channel gap was established by inserting a steel gasket with a thickness of 1.27 mm between the two lexan plates. This gasket extended below the entrance plenum and above the exit plenum.

The pump was sized to provide the full flow rate of water at 25 m/s in an unblocked channel. Temperature sensors, pressure sensors, and flow meters were included, where shown on Fig. 1, to characterize the test conditions for the bulk fluid flow with accuracies of ± 1.2°C, $< \pm 1$ percent, and ± 1 percent, respectively. The heat exchanger shown in this figure was used to maintain the water at the ambient temperature by removing the small amount of energy added to the water by the pump.

Water enters near the bottom of the test section in the center (spanwise) side of an inlet plenum, 180 mm long by 84 mm wide by 25 mm thick, at an angle of 30 deg. The top of the inlet plenum narrows at a 45 deg angle so that the gap is reduced from 25 mm to 2.54 mm. The 2.54 mm gap is maintained for 35 mm. At this point the channel entrance is defined by an abrupt (90 deg) symmetric change in the channel gap to 1.27 mm. Numerical models indicate that this flow conditioning produces uniform flow at the channel inlet in the absence of any blockage (Stovall et al., 1995). The exit plenum is an abrupt expansion in the gap from 1.27 mm to 25 mm. Because the channel length is equal to about 200 hydraulic diameters (d_h = 2.5 mm), the flow was able to return to a uniform velocity profile before the channel exit for all blockage sizes tested.

The flow blockage assembly was designed so that the blockage width and position could be easily changed. Figure 2 shows the side view of the channel entrance region, and the scale has been distorted to display both the blockage configuration and the heater plate installation in more detail. The blockage position was varied in the plane perpendicular to this figure to place it at either the center or edge of the channel's 84 mm width. The blockage width (again, perpendicular to Fig. 2) was varied from 10 percent to 50 percent of the channel's width, i.e., from 8.4 to 42 mm. The thickness of the blockage (in the direction of the flow) was 10 mm.

Thermochromic liquid crystals were used indirectly to measure the channel wall temperature. These crystals respond to temperature changes by changing color, and are available for a wide range of temperatures and a variety of resolutions. A stainless steel heater strip was imbedded in the wall of the channel to provide the uniform surface heat flux required for the TLC tests, as shown in Figs. 1 and 2. The heater started 4.4 mm ($1.76 d_h$) from the downstream side of the blockage assembly, covered the entire width of the channel, 30 mm ($12 d_h$) of the channel's length, and was 1 mm (± 1 percent) thick. To avoid electrical and thermal effects, the assembly design isolated the heater strip from both the structural steel case and the steel gasket used to form the channel side walls. After removal from the test facility, the heater strip was immersed in water and the electrical resistivity was measured (± 3 percent) to be from 0.00219 to 0.00229Ω as the voltage was varied from 0.25 to 1 V. A value of 0.0022Ω was used for all data analyses. During flow tests, the DC electrical current was measured (± 1 percent accuracy) for each test so that the heat flux from the heater

Nomenclature

B^k = bias uncertainty of turbulence measurement
B^U = bias uncertainty of velocity measurement
d_h = hydraulic diameter was 2.50 mm, equal to four times the cross sectional area divided by the wetted perimeter
h = convective heat transfer coefficient
k_{heater} = heater thermal conductivity, 14 W/m-°C
k = turbulent kinetic energy, m^2/s^2
L = channel length
Nu = Nusselt number
Pr = Prandtl number
q'' = heat flux
Re = Reynolds number
t = thickness of heater plate, 1 mm
T = temperature
T_{bulk} = fluid bulk temperature
$T_{crystal}$ = temperature recorded by TLC field
T_{wall} = wall temperature facing fluid flow
U = velocity
U_o = average exit fluid velocity, volumetric flow rate divided by channel cross sectional area
u_i = velocity vector at a point
$\bar{u}_i$ = time averaged velocity vector
u_i' = fluctuating velocity vector component, or velocity perturbation
w = channel span, also heater width, 84 mm
x = axial position
y = span-wise position
y^+ = position relative to boundary layer thickness
z = position within the gap

Greek Symbols

ρ = density
ξ = friction factor

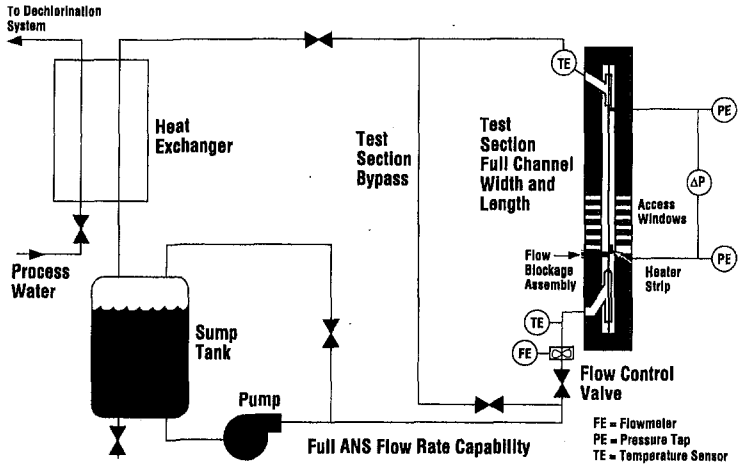

Fig. 1 Flow blockage test facility schematic

surface could be calculated based on the current and resistivity. The Watt meter on the power supply was not used because that measurement included the power lost in the wires that connected the supply to the heater strip.

Thermochromic liquid crystals are rather fragile and any direct exposure to channel flow would wash the crystals away from the heater surface. Therefore, the crystals were painted (over a thin base coat of black paint) on the back side of the heater plate, where they would not be in contact with the flowing water and would be visible through the clear lexan. The heater power was adjusted for each test to produce heater wall temperatures within the measurable band, from 30 to 45°C for the selected crystals.

A color video camera and data conversion system were installed to record the temperature field. System components, calibration, and accuracy are described fully in earlier papers (Stovall et al., 1995; Crabtree, 1994). The calibration procedure was performed with the heater strip in place to account for any color distortion that might be introduced by the lexan window. An evaluation of system accuracy showed that the recorded thermochromic liquid crystal temperature measurements were accurate to within 0.2°C, which can be compared to the ~10°C difference between the average heater surface temperature and the bulk fluid temperature and to the typical range of 3 to 5°C over the recorded temperature field. The access window for the video camera penetrated the test section's 50 mm thick steel case giving a viewing area large enough to cover the heater surface of 30 mm by 84 mm. Both lights and the camera lens were directed into this window. Although a diffuse light source was used, some reflections from the 50 mm thick side wall of the access window were unavoidable. These reflections affected a small area very near the edge of the field.

The LDV technology uses intersecting laser beams and advanced optical data collection and processing equipment (see Table 1) to measure the motion of individual minute particles (naturally present in water delivered through aging metal pipes) as they pass through the created fringe pattern. The heater plate used for the TLC tests was not used for LDV testing; instead, a smooth lexan side wall was fabricated and used for all the

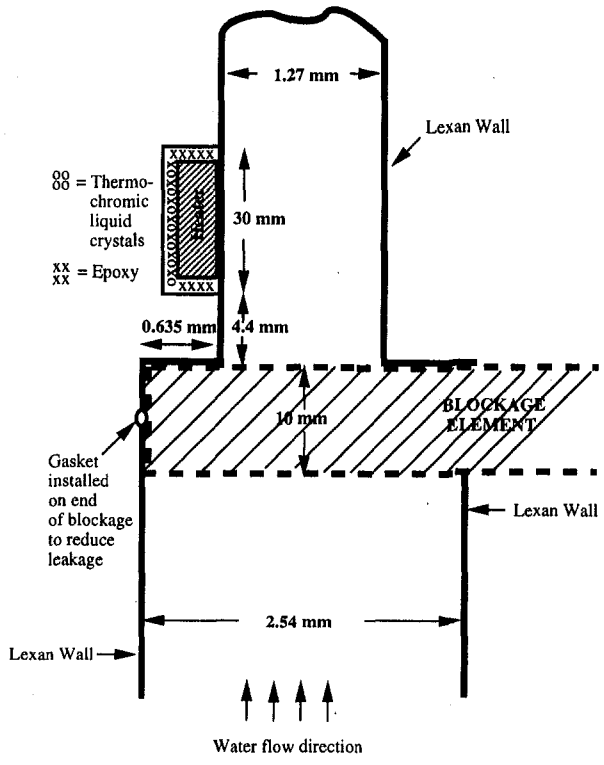

Fig. 2 FBTF channel side view (not drawn to scale)

Table 1 Optics configuration and processor settings (TSI, Inc., 1993)

	Processor 1	Processor 2
Processor model	TSI, Inc. IFA 750	
Analysis software	TSI, Inc. FIND, Version 4.0	
Fringe spacing (microns)	1.984	1.8818
Frequency Shift (MHZ)	40.0	40.0
Wavelength (Nanometers)	514.5	488.0
Half Angle	7.45	
Focal Length (mm)	122	
Beam Spacing (mm)	35	
Rotation x-y plane (deg)	−45	
Tilt y-z plane (deg)	0.0	
Frequency range	300 Hz to 100 MHZ	
Resolution	0.1 percent of reading	
Signal-to-noise ratio	−12 dB	
Samples per burst	256	
Samples per cycle	10–20	
Burst SNR detection	Automatic, realtime burst correlation	
Burst detection rate	500,000 bursts/s at >35 MHZ; 350,000 bursts/s at <35 MHZ	
Sampling rate	Automatic; adjusts to Doppler frequency; max. 1 Gigahertz (effective)	
Autocorrelation rate	120,000 measurements/s for 256 samples (one channel); 128 autocorrelation coefficients	

LDV experiments. To compare data from LDV and TLC testing, we assume that the isothermal and the nonisothermal flows have the same velocity fields, which is reasonable for the limited fluid temperature range of these experiments. Two LDV signal processors were used to provide axial and span velocity components. No measurements were made of the velocity component in the narrow gap direction. A beam retroreflector was used to increase the data collection rate.

The LDV system optical components were carefully chosen so that the measurement volume (i.e., the region where the laser beams intersect and moving particles are monitored) would fit within the confined gap of the FBTF channel. All the optical equipment was mounted on a three-dimensional traversing system able to position the measurement volume with an accuracy of 0.01 mm in each direction. The measurement volume diameter was 34 μm. The length of the measurement volume in the channel gap direction was 0.27 mm, or about one fifth of the total channel gap. The measurement volume was positioned in the center of the channel's gap for all measurements. The center was located by adjusting the traversing system until the measurement volume included the channel wall, which was indicated by a sharp spike in zero velocity measurements and by the decreased data collection rate. After the position of both bounding walls was identified in this manner, the traversing system was adjusted to place the measurement volume at the midpoint. Approximately 50 to 80 locations across the 84 mm channel span were monitored at each of the six observation windows. The number varied according to the observed flow phenomena so that measurements were concentrated in areas of rapidly changing velocities.

Data Analysis

Thermochromic Liquid Crystal Experiments. If the fluid temperature within the channel is constant and there is a constant heat flux over the surface of the channel wall, then the wall temperature field will reflect the variations in the convective heat transfer coefficient over the wall surface. For small heat flux values and large fluid flow rates, this assumption of constant fluid temperature is a good approximation. For the maximum experimental heat flux and the design flow rate, the calculated bulk fluid temperature rise would be only 0.03°C. For a localized area in the center of a recirculation pattern behind a flow blockage, the fluid temperature could become elevated to some level greater than the bulk temperature. Then the wall temperature will reflect the combined effect of elevated fluid temperature and reduced fluid velocity. For these small areas, the assumption of constant fluid temperature will produce a heat transfer coefficient less than the actual local value. This error will therefore be conservative and will also be reduced by high levels of turbulence.

A constant wall heat flux can be closely approximated using electrical resistance heating within the wall material. The electrical resistivity of stainless steel is a function of temperature, and the heat flux is proportional to the resistivity. The assumption of uniform internal heat generation, and therefore a constant heat flux over the heater surface, was carefully evaluated. For the temperatures experienced within the heater strip, the electrical resistivity will vary less than 2 percent, and a detailed electrical analysis showed that the internal heat generation will vary less than 3 percent. The heat flux was therefore assumed constant.

Because the crystals were located on the back of the heater strip, i.e., the side of the heater strip away from the channel flow, the recorded colors reflect the wall temperature after heat conduction through the heater strip and the paint. Any heat conduction through the thick lexan window on the lexan side of the plate will be negligible compared to the convective heat transfer on the channel side of the plate. Also, temperature change across the thin coat of paint was assumed to be negligible. The dimensions of the heater strip (1 mm × 30 mm × 84 mm), the low total heat generation (less than 300 W), and the resulting small temperature gradients (measured temperature differences were usually less than 3°C) assure that any conduction along the width or length of the heater strip will be considerably less than that through the much smaller thickness. This assumption is considered in more detail below.

Based on the assumptions of constant bulk fluid temperature, uniform internal heat generation, uniform heat flux, negligible heat transfer through the lexan window (i.e., the outside surface of the heater plate is adiabatic), and one-dimensional heat transfer through the heater, the wall temperature and heat transfer coefficient are related as shown in Eqs. 1 and 2. Considering uncertainties of ±3 percent for the heat flux, ±1 percent for the plate thickness, and ±6 percent for the thermal conductivity, the calculated temperature difference would have an uncertainty, based on the root-sum-square of the individual uncertainties, of ~7 percent. Using the same approach, the uncertainty in the Nusselt Number or heat transfer coefficient would then be ~±8 percent. Using this model, the recorded crystal temperature is about 4°C hotter than the channel wall temperature for a heat flux of 119 kW/m^2 (300 W uniformly distributed over the heater surface).

$$T_{\text{crystal}} - T_{\text{wall}} = \frac{q'' \times t}{2.0 \times k_{\text{heater}}} \tag{1}$$

$$h = \frac{q''}{T_{\text{wall}} - T_{\text{bulk}}} \tag{2}$$

An assessment of the one-dimensional heat transfer model was made by comparing the temperature gradient across the heater's thickness to that occurring across the heater's face. The greatest lateral temperature gradient would correspond to a sharp convective heat transfer coefficient gradient (10,000 W/m^2·K per mm), such as that found in the center of the recirculation region behind the blockage. At this location, the temperature gradient across the heater's thickness (~4°C/mm) is still about seven times the local lateral gradient. The average lateral temperature gradient over the entire heater face is less than 0.1°C/mm. The assumption of one-dimensional heat transfer, with a heater strip conductivity of 14 W/m·°C, was therefore used for all data analyses. The only locations at which this assumption might cause measurable errors are near the edges of the heater, where thick electrical assemblies can act as heat sinks. However, lighting difficulties near these edges make the color data less accurate in these regions, negating any advantage that could be gained from a more rigorous treatment of the internal heat conduction in this region.

Laser Doppler Velocimetry Experiments. Sophisticated statistical methods were employed to evaluate the large amount of data, about 1000 data points, produced by the LDV system for each observation point. The FIND analysis software evaluated these data values to calculate the mean, standard deviation, skewness, flatness, and turbulence intensity for the velocity in each of the two measured directions (TSI, Inc., 1993). The raw data values were also saved and used separately to calculate the turbulent kinetic energy. The turbulent kinetic energy is defined from the LDV data by using the absolute value of the flow perturbation for each data point to calculate the average perturbation magnitude. This value was then used, as shown in Eq. 3, to determine the turbulent kinetic energy for each velocity component. A detailed error analysis for LDV systems was made in 1985 (Patrick). For highly turbulent separated flow with a well-designed LDV system incorporating a frequency shift, the total uncertainty was calculated to be −2 percent to +3 percent. The precision error associated with the data processing for the LDV system used here would be ±0.5 percent for the mean velocity and ±2 percent for the turbulence. Another significant source of uncertainty is related to the positioning

accuracy (±4 percent of the gap dimension) of the measurement volume. This bias uncertainty is shown in Eq. 4 and is estimated to be less than 1 percent, based on velocity profile observations within the gap.

$$k_i = \tfrac{1}{2}(\overline{u_i'})^2 \tag{3}$$

$$B^U = \frac{\delta U}{\delta z}\Delta z \quad \text{and} \quad B^k = \frac{\delta k}{\delta z}\Delta z \tag{4}$$

Flow rates and kinetic energy terms were normalized relative to the average fluid velocity at the channel exit, i.e., the volumetric flow rate divided by the channel's cross sectional area. Considering that the bulk fluid temperature was held constant during these tests, the only uncertainty inherent in the Reynolds Number is in the velocity measurement, which has an uncertainty of ±1 percent.

Experimental Results

An unblocked experiment was made to compare the conditions within the FBTF to the design parameters of the ANS fuel channel. A pressure drop of 1.44 MPa produced the design flow rate of 25 m/s through the unblocked channel. This corresponds well to the design value of 1.4 MPa for the preliminary ANS design. Tests were then made for a variety of blockage sizes, in both center and edge locations. These tests include cases with an unblocked channel, edge blockages of 10 and 25 percent, and central blockages of 35 and 40 percent. Tests were made for Reynolds numbers (based on average axial velocity at the channel exit) varying from 16,000 to 86,000.

During the initial unblocked TLC tests, a small region of highly elevated heat transfer (or reduced wall temperature) was found very near the lip of the heater plate on the left side of the span. This anomaly was attributed to a slight elevation, approximately 0.08 mm, of the heater surface. This elevation caused a variance of 6 percent in the channel gap at that location, causing a redistribution of the cooling water flow and a region of enhanced heat transfer in all the test data. As expected, the heat transfer coefficients calculated from the measured wall temperatures for an unblocked test were depressed near the side walls. For the unblocked case at a Reynolds number of ~81,000, the average Nusselt number for the latter two thirds of the heater plate (axial locations from 6 to $14d_h$) was 438 (with a standard deviation of 62.5). For comparison, Petukhov's (1970) correlation for convective heat transfer, shown in Eqs. 5 and 6, with properties for water at room temperature and the design velocity of 25 m/s, produces a Nusselt number of 413.

$$\xi = (1.82 \log \mathrm{Re} - 1.64)^{-2} \tag{5}$$

$$\mathrm{Nu} = \frac{(\xi/8)\mathrm{Re}\,\mathrm{Pr}}{1.07 + 12.7(\xi/8)^{1/2}(\mathrm{Pr}^{2/3} - 1)} \tag{6}$$

Each TLC test showed a distinct region of reduced heat transfer behind the blockage. The region of reduced heat transfer has a relatively constant width over the first 34 mm of the channel's length and is approximately equal to the width of the blockage itself for almost every central and edge blockage size tested. The one exception was the 10 percent edge blockage where the experimental data show an affected region about twice as wide as the blockage itself. These results are questionable because of the light reflections near the channel edge discussed previously.

The temperature difference across the surface of the heater plate ranged from 1 to 3°C for most of the test results. When using these results, the accuracy of the crystals (±0.2°C) must be kept in mind. Also, the 6 percent distortion of the channel gap has an effect on the results. With these caveats, there is still some useful qualitative information available from the TLC

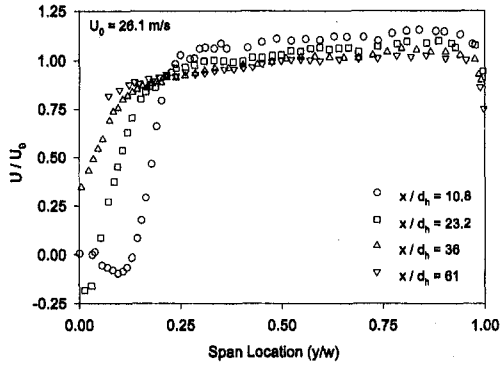

Fig. 3 Axial velocity profiles-25 percent edge blockage at Re = 85,000

test data. For the 25 percent edge blockage at a Reynolds number of 79,000, the minimum heat transfer coefficient behind the blockage is about $\frac{1}{4}$ that in the unblocked channel. For the same blockage at lower Reynolds numbers, the ratio of minimum to maximum heat transfer on the heater surface was about $\frac{1}{3}$.

The availability of LDV data for both edge and central blockage cases allows a more detailed look at the flow phenomena. Figures 3 and 4 show the axial and span-wise velocities measured by the LDV for a 25 percent edge blockage (located from $y/w = 0$ to $y/w = 0.25$) at a Reynolds number of 85,000. The LDV data bracket the reattachment, or transition to fully forward flow, between observation windows 2 and 3, indicating an axial position between 20 to $36d_h$ from the blockage. This test was repeated and showed consistent results. Sparrow and Cur found reattachment for a 25 percent edge blockage occurred at about $20d_h$ for an Re of 35,000, which could indicate that the reattachment length is relatively insensitive to Reynolds number over the range from 35,000 to 85,000 (Sparrow and Cur, 1983). The kinetic energy terms from the LDV data at $11d_h$ for the 25 percent edge case (where again the blockage is located from $y/w = 0$ to $y/w = 0.25$) range from 0.2 to 4.6 m^2/s^2, with the axial component about twice the span-wise kinetic energy over most of the channel's width, as shown in Fig. 5.

Figures 6 and 7 show the normalized axial and span-wise velocity profiles for two 35 percent center (from $y/w = 0.325$ to $y/w = 0.675$) blockage tests at Reynolds numbers of 35,000 and 81,000. As with the edge blockage, the results show very little change across this range of fluid velocities. For both cases, the flow was negative in the center of the first observation window but fully forward before the second, showing that the flow recovery occurs further upstream than for a smaller (25 percent) blockage in the edge position. The velocity profile was nearly uniform at $49d_h$, indicating that the flow disturbance will be fully recovered before the channel exit at $200d_h$. The water

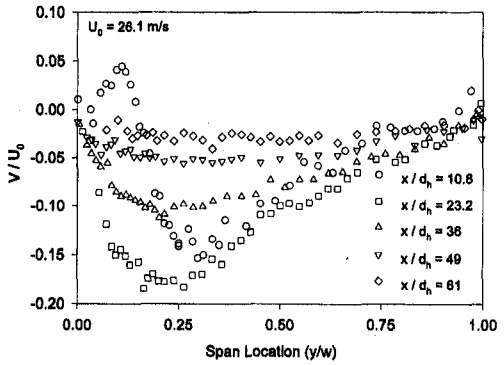

Fig. 4 Spanwise velocity profiles-25 percent edge blockage at Re = 85,000

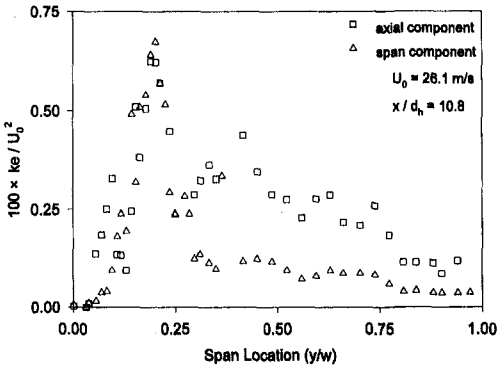

Fig. 5 Turbulent kinetic energy-25 percent edge blockage at Re = 85,000

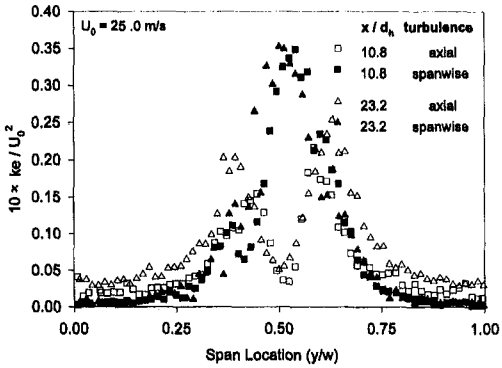

Fig. 8 Turbulent kinetic energy-35 percent center blockage at Re = 85,000

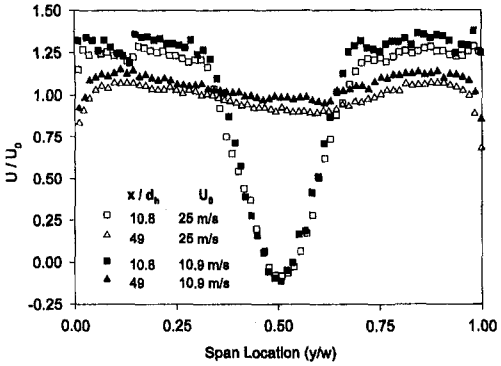

Fig. 6 Axial velocity profiles-35 percent center blockage at Re = 35,000 and 81,000

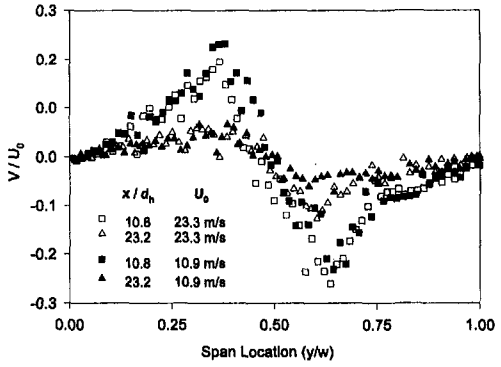

Fig. 7 Spanwise velocity profiles-35 percent center blockage at Re = 35,000 and 81,000

flowing from the edge regions toward the center of the channel produces the symmetric velocity profiles in Fig. 7, where the spanwise velocity is counted positive as it flows from left to right.

The turbulent kinetic energy for the 35 percent center blockage, located from $y/w = 0.325$ to $y/w = 0.675$, is shown in Fig. 8. There is little change in the turbulent kinetic energy distribution from the first to the second observation window, or from 11 to $23d_h$. The span-wise component peaks near the center of the channel at about 22 m^2/s^2. The axial component peaks at the edges of the recirculation region, directly behind the edges of the blockage, at about the same value. In the free-flow regions of the channel away from the blockage, the axial turbulent kinetic energy is greater than the span-wise, although they are both less than 3 m^2/s^2.

Numerical Model Description

The governing equations, mathematical formulations of turbulence models and numerical algorithms for the FLUENT code, are all described in the code's Users Guide (Fluent). For any analysis based on CFD, important issues must be addressed including (1) proper modeling of the inlet and outlet regions and all boundary conditions, (2) the computational grid definition, (3) the proper selection of a turbulence model, and (4) benchmark comparisons with experimental data.

Most of the CFD models developed during this analysis reflect the FBTF geometry. These models are primarily used to benchmark the models for the ANS channel geometry. Since the FBTF itself was designed to match ANS cooling channel geometry, this should provide a sound basis for the safety analysis. The pressure sensors on the FBTF were located in the entrance plenum and within the cooling channel, 469 mm from the channel inlet. The length of the channel in the CFD model was therefore set equal to 469 mm, giving a length to gap ratio of 370. The span and gap were set equal to the FBTF dimensions, giving a span to gap ratio of 66. The model's L/d_h ratio was 188 and the w/d_h ratio was 35.

Since the downstream pressure measurement was made within the channel, the outlet boundary condition was defined by the pressure at this location and the exit plenum was not modeled. The inlet boundary condition was specified by the pressure and temperature of the fluid at the plenum inlet. The channel side walls (1.27 mm high by 469 mm long) were considered adiabatic for all analyses. Boundary conditions for the wall representing the fuel plate (84 mm wide) varied among the models. For cases where the heater plate was installed, the uniform heat flux provided by the heater plate in the TLC tests was modeled. For the LDV tests, the wall was considered to be adiabatic, which is appropriate for the lexan walls. Finally, for a few cases run after the benchmarking efforts were complete, one representative heat flux pattern from the ANS design data was mapped onto the wall.

All fluid properties for the cases compared to experimental data were those of water at room temperature. This was appropriate because the water temperature was maintained at ambient conditions. For those cases designed to mimic ANS conditions with higher wall heat fluxes, temperature-dependent properties for liquid D_2O were used. The liquid D_2O property relations were developed for the ANS program and have an accuracy better than ±1 percent over a temperature range from 50 to 250°C, compared to tabular data from Atomic Energy of Canada Limited (Crabtree and Simantov, 1993; Hill et al., 1981). These relations are represented within the numerical model by a set of piecewise linear approximations based on 16 data points for each property over a temperature range from 50 to 150°C. The piecewise linear approximations match the ANS equations within ±0.5 percent.

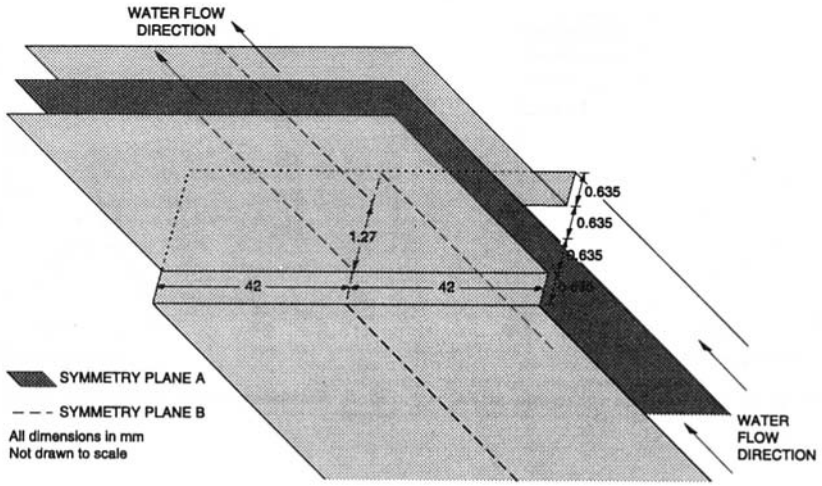

Fig. 9 Numerical model geometry at the channel inlet

Every blockage considered was assumed to cover the entire width of the gap (1.27 mm) and to cover at least three adjacent fuel channels. This conservative assumption provides symmetric boundary conditions along the center plane of the channel, as shown by symmetry Plane A in Fig. 9. An additional plane of symmetry, parallel to Plane A and located 0.635 mm away from the channel's wall surface, passes through the center of the fuel plate. Another plane of symmetry for unblocked or central blockage models is located at the center of the channel's span, as shown by Plane B in Fig. 9. Recognizing these symmetrical physical conditions permits a more efficient computational model.

As a result of studies examining the inlet plenum region, a region 50 mm long was used to model the inlet plenum upstream of the fuel channel (Stovall et al., 1995). This region includes the 10 mm thick blockage element. The plane of symmetry through the fuel plate extends out into the entrance plenum region. This symmetry within the plenum region is an accurate representation of the ANS geometry. However, the FBTF geometry is limited to one flow channel so that the bounding conditions in the plenum are side walls (because the FBTF plenum gap thickness is twice the channel gap thickness). The pressure drop due to wall friction in the plenum region is negligible compared to the pressure drop at the channel entrance and that due to wall friction within the channel. Nevertheless, one blockage model included the plenum wall boundary, confirming the insensitivity of the results to this factor.

The grid dimensions for the FLUENT CFD models were primarily determined by the small gap dimension. Because wall functions are used with FLUENT's RG turbulence model, the cell nearest the wall must be large enough to extend beyond the laminar sublayer of the boundary layer. Fluid velocities in the recirculation region behind a blockage are much lower than those in the rest of the channel. The code accounts for this variability by iteratively calculating the nondimensional distance y^+ for each cell near a wall. If this value indicates that the border of the computational cell is within the laminar sublayer, laminar correlations are used to calculate the local velocity vectors. When five equal elements were used across the half-gap distance of 0.635 mm, the turbulent wall functions were appropriate for most of the channel. Laminar conditions typically occurred in only a few cells at the center of the recirculation region and near the reattachment point. Grid densities in the remaining two directions were chosen to provide reasonable aspect ratios for the cells near the channel entrance.

Because the channel is so much longer than it is thick, the cell aspect ratio was allowed to grow farther away from the entrance to reduce computational requirements. Preliminary two-dimensional models were used to investigate the impact of grid variations in the axial and gap-directions and the adequacy of the 50 mm inlet region before the fuel plate. These models showed that five cells in the gap direction and 150 cells in the axial direction produced the expected mass flow rate for the specified pressure drop and converged well. Eight cells were used across the 1.27 mm gap in the inlet region. For unblocked and center blockage cases, 28 cells were used across the half-span of 42 mm. This grid performed well in matching the expected mass flow and heat transfer coefficients on the channel walls for the unblocked case. The span-wise cell divisions were spaced to provide smaller cells near the side walls and near the blockage. For edge blockages, 56 cells were used across the full span width of 84 mm and again, the grid was nonuniform in order to place smaller cells near the channel edges and in the region behind the blockage. The span-wise grid arrangement was doubled for several cases to investigate the grid's adequacy.

The RG turbulence model developed by Princeton researchers and implemented within the FLUENT code was used for most of the CFD models. Like the standard k-ϵ model, the RG model is a two-equation simplification and assumes isotropic stress fields (Fluent, Inc., 1993). A Reynolds Stress Model (RSM) is much more computationally intensive but allows the calculation to consider nonisotropic turbulent stresses. The RSM model was used for a few selected cases to evaluate the acceptability of the RG model and for direct comparison to experimental results. The results of this comparison are discussed later in this paper.

Within the FLUENT code, turbulence conditions at an inlet are defined by the turbulence intensity, the ratio of the turbulent fluctuations in velocity to the mean flow velocity, and a characteristic length, representative of the model's geometry. The turbulence intensity is used to calculate the turbulent kinetic energy, which is in turn used with the characteristic length to calculate the turbulent energy dissipation rate. For most of the numerical models constructed, the turbulence intensity at the inlet plenum was set at 10 percent and the characteristic length was set equal to the channel gap, 1.27 mm. For a few cases, the turbulence intensity was set at 2 percent to investigate the sensitivity of the results to this parameter. Comparing these cases, the point of flow reattachment was unchanged. Also, the turbulent kinetic energy peak value and overall distribution within the channel were unchanged. Apparently, the turbulence generated as the flow enters the channel and flows around the blockage element dwarfed any effect of the assumed turbulence at the plenum entrance.

Numerical Model Results

Numerical simulations corresponding to a large number of the experiments were completed using the FLUENT CFD code.

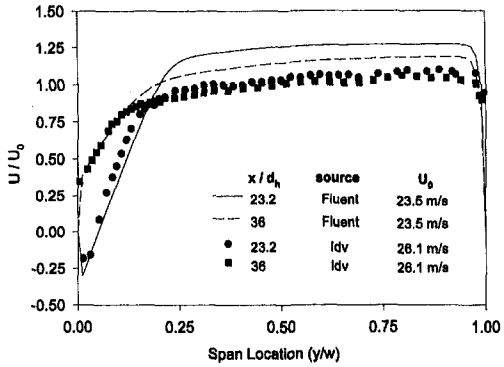

Fig. 10 Comparison of experimental and CFD results for axial velocity profiles, 25 percent edge blockage at Re = 85,000

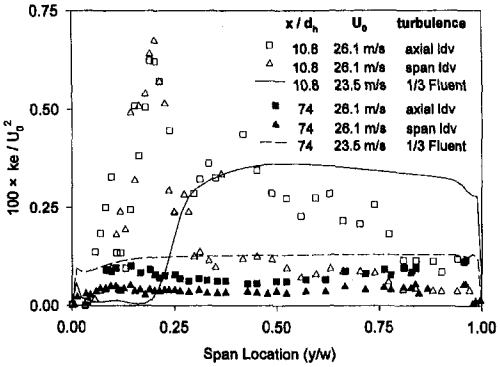

Fig. 11 Comparison of experimental and CFD results for kinetic energy, 25 percent edge blockage at Re = 85,000

There are several points at which direct comparisons are possible between the experimental results and the CFD code predictions. Velocity vectors from the CFD results for the computational nodes near the center of the gap can be compared to those measured within the LDV measurement volume. The LDV velocity vectors can also be used to help locate the boundaries of the recirculation region and the velocities within this region. Calculated wall temperatures and heat transfer coefficients from the TLC experiments can also be compared to results from the FLUENT models. Trends in turbulent kinetic energy distribution can also be considered from the LDV data analysis and the FLUENT models.

From the TLC test for the unblocked case, the average Nusselt number for axial locations from 6 to $14d_h$ was 438 (with a standard deviation of 62.5). The CFD model for this same case showed a heat transfer coefficient in this region of 438 and matched the total channel flow within 3 percent.

Each TLC test with an inlet blockage showed that the region of reduced heat transfer behind the blockage had a relatively constant width over the first $14d_h$ of the channel's length, approximately equal to the width of the blockage itself. The CFD models for these tests show similar behavior. Over all these tests, the CFD models and experimental results for the total mass flow through the channel agreed to within 1 to 6 percent. This indicated that the numerical method accurately emulated the pressure drops due to both the inlet obstruction and the channel wall friction.

The CFD models consistently predicted lower heat transfer coefficients than the TLC experimental data on the heater surface in the region behind the blockage. The average heat transfer coefficients over the heater surface were always well matched, as would be expected given the good agreement in the channel mass flow. For 10 and 25 percent edge blockages, the measured wall temperatures (which can be seen in Stovall et al., (1995)) in the region behind the blockage indicated heat transfer at a rate two to four times greater than predicted by the CFD models.

The LDV data was also used to benchmark the CFD models. Figure 10 shows the axial velocity measured by the LDV and the corresponding results from the CFD model, both for a 25 percent edge blockage (located between $y/w = 0$ and $y/w = 0.25$) and a Reynolds number of 85,000. The recirculation region is closely matched in size and in the predicted fluid velocity within this part of the profile. The CFD model shows reattachment, or the return to fully forward flow, occurring $26d_h$ downstream from the channel inlet. The LDV data corroborate this location by bracketing the reattachment between windows 2 and 3, indicating an axial position between 20 and $36d_h$ down the channel. The kinetic energy terms from the LDV data for the 25 percent edge case were also compared to the CFD model as shown in Fig. 11. The isotropic RG turbulence model in the FLUENT code produces a single kinetic energy term representing the sum of the kinetic energy terms in all three dimensions.

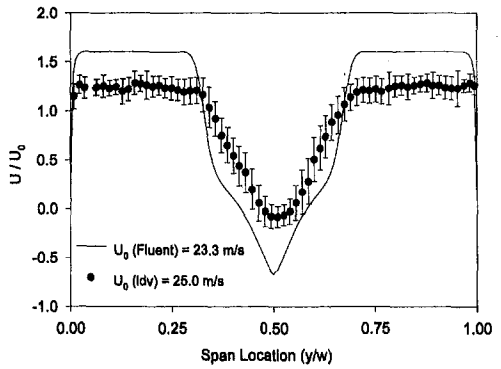

Fig. 12 Comparison of experimental and CFD results for axial velocity, 35 percent center blockage at Re = 85,000

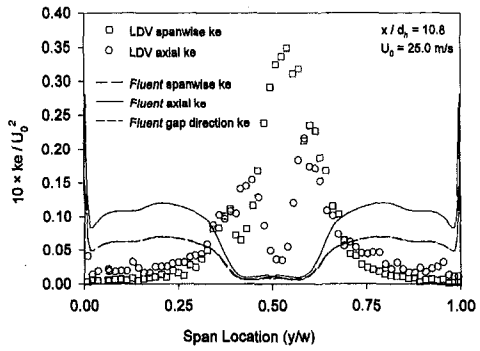

Fig. 13 Comparison of experimental and CFD results for kinetic energy, 35 percent center blockage at Re = 85,000

One third of this total is therefore used for a rough comparison to the directional LDV data. The isotropic kinetic energy from the CFD model should fall between the directional values obtained from the LDV data, where the axial and span-wise kinetic energy values range from 0.2 to 4.6 m^2/s^2, with the axial component about twice the span-wise kinetic energy. The CFD model, with values ranging from 0 to 2 m^2/s^2, matches the LDV data best in the free channel region. It estimates a smaller magnitude for the kinetic energy peak measured by the LDV at the edge of the recirculation region.

The comparison between LDV data and CFD model predictions for the 35 percent central blockage at a Reynolds number of 85,000 is shown in Fig. 12 for a location $11d_h$ downstream from the back of the blockage. Here the blockage was located from $y/w = 0.325$ to $y/w = 0.675$ and standard error bars are shown on the LDV data to show the range of velocities measured at each location. The larger standard errors correspond to

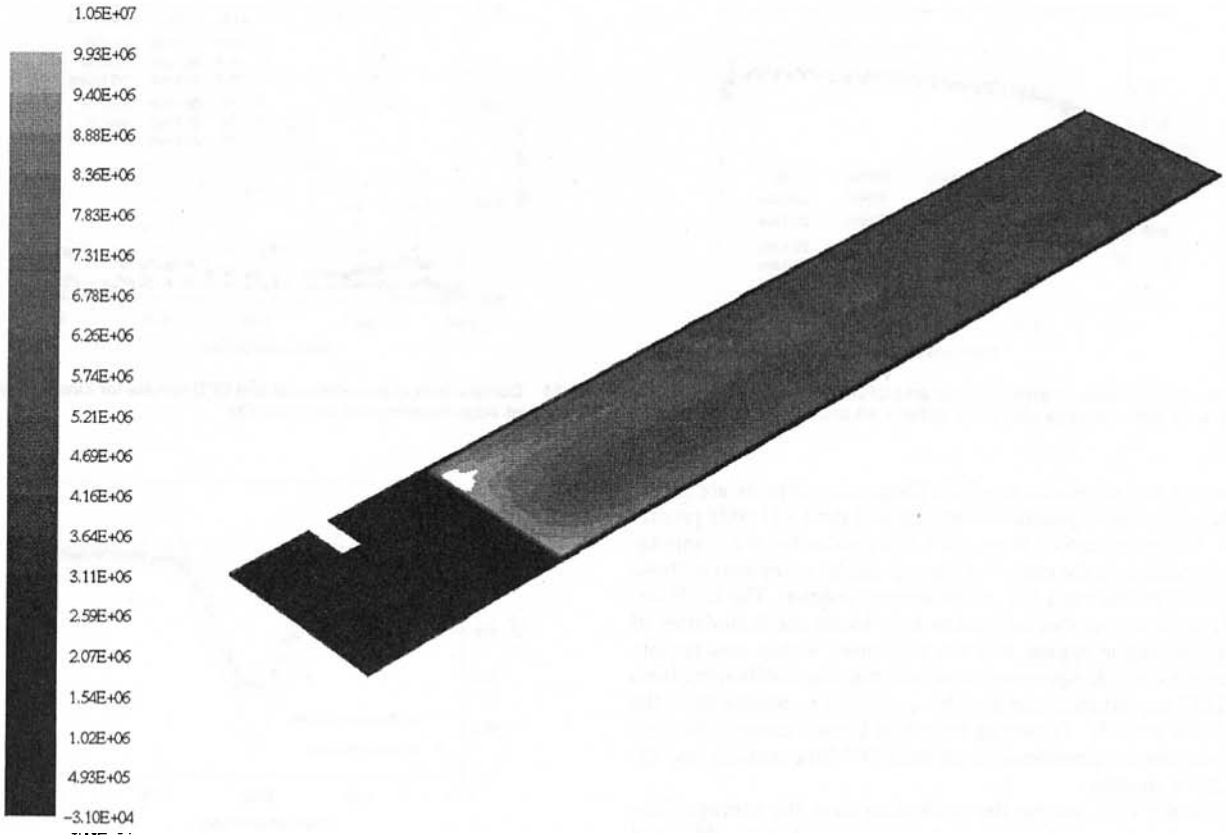

Fig. 14 "Worst case" heat flux imposed on channel wall (W/m^2)

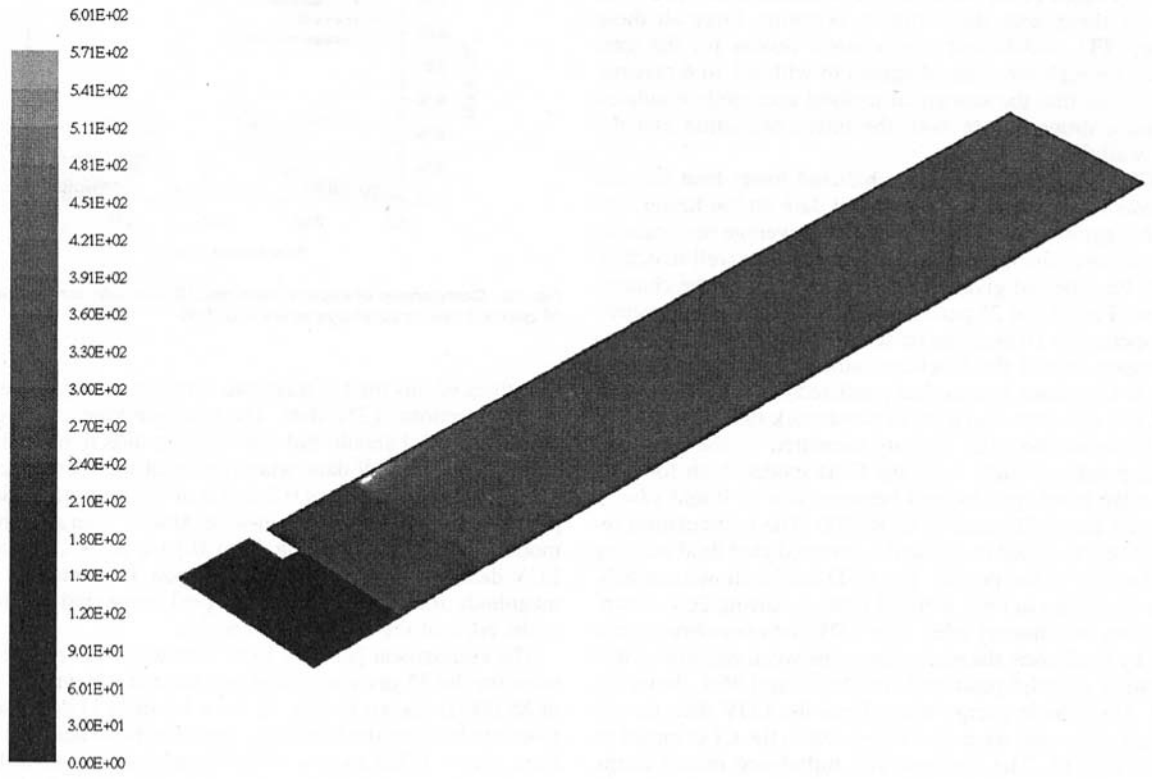

Fig. 15 Wall temperature for "worst case" heat flux with 50 mm unheated entrance-25 percent edge blockage (K)

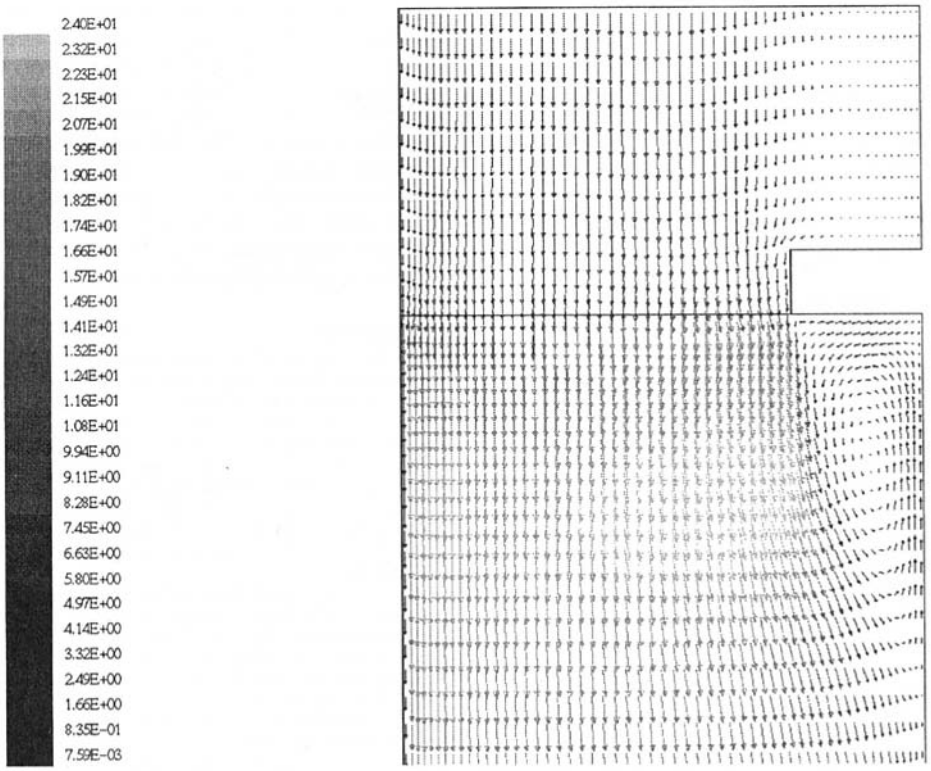

Fig. 16 Velocity vectors for "worst case" heat flux with 50 mm unheated entrance-25 percent edge blockage (m/s)

the regions of higher turbulence near the edges of the recirculation region. The LDV data and CFD model show a similar flow pattern, although the flow is closer to recovery, or less negative, in the experimental data. Indeed, the CFD model predicts a large recirculation region, about $23\,d_h$, very similar to that seen for the edge blockages. The experimental data show the return to fully forward axial flow occurring in a shorter length, somewhere between the first and second observation windows, or between 11 and $23\,d_h$.

The differences between the numerical model's prediction and the measured data were carefully examined. Experimental factors, including possible leakage around the blockage assembly, were explored (Stovall et al., 1995). Several modeling factors were also considered. Working with the 35 percent central blockage, numerous grid refinements were made including doubling the span-wise grid, and refining the grid in the inlet plenum. All these model changes caused only small incremental changes to the results, the best of which have been cited here. All the numerical models discussed here employed wall functions, i.e., the boundary layer was not resolved. This choice was made based on computer capabilities, considering that the model already used more than 300,000 cells. However, wall functions may not offer the best solution for strong recirculation zones, where the friction velocity changes between positive and negative values.

The more rigorous RSM turbulence model was used to determine whether the isotropic turbulence treatment inherent in the RG model was responsible for some portion of the differences. The RSM kinetic energy in the span and gap dimensions are almost identical. The axial kinetic energy is about twice that in the span dimension. The LDV data also show the axial kinetic energy to be about twice the span-wise kinetic energy in the free channel regions (see Fig. 13), but show the span-wise turbulence to be greater than the axial turbulence in the center of the channel. At $11\,d_h$, both the RG and the RSM turbulence models predicted span-wise turbulence values of about 2 m^2/s^2, compared to the LDV values ranging from less than 1 m^2/s^2 near the wall to 22 m^2/s^2 at the center of the channel. The RSM axial turbulence ranges from 1 to 7 m^2/s^2, and does well compared to the LDV values ranging from about 3 to 10 m^2/s^2. The overall comparison of the RG and RSM results showed that the RSM did only a slightly better job of capturing the kinetic energy peak associated with the edge of the recirculation region and reduced the length of the recirculation region from 23 to $21\,d_h$.

Extension of Numerical Models to Expected Operating Conditions

A comparison between experimental and numerical model results was very good for edge blockages, considering the factors of velocity direction, velocity magnitude, and reattachment length. The heat transfer comparison was less satisfactory, but it did show that the numerical model was conservative compared to the experimental data. The central blockage model did not match the experimental data as well as the edge model, but it did predict the appropriate flow pattern and was conservative in its prediction of the reattachment length. Both the numerical and experimental data indicated that the edge blockage presented the more limiting case for the safety evaluation because its recirculation region was much longer than that for the central blockage. Based on these benchmarking comparisons for water at room temperature with little or no wall heat flux, the numerical models were extended to model those aspects of ANS operating conditions difficult to test experimentally.

Two of the most important differences between the FBTF test conditions and ANS operating conditions are: (1) the high wall heat flux and power distribution, and (2) the temperature-dependent fluid properties of D_2O expected in the actual reactor. A simple, two-dimensional model of the unblocked channel was developed to test the ability of the CFD model to capture the effects of these two changes. This simplified model used a constant wall heat flux of 6 MW/m^2. The results closely matched the design data, showing the expected increase in

Reynolds number at the channel exit due to the increased velocity of the hotter, less dense fluid.

The heat flux on the fuel plate surface would not be constant but would vary with position and time. A "worst case" heat flux, shown in Fig. 14, was selected from the neutronics analysis and patched into the three-dimensional numerical model as a wall boundary condition for several edge blockage cases. Temperature-dependent fluid properties for D_2O were used for all of these models. These cases included 10 percent, 12 percent, and 25 percent edge blockages with unheated entrance lengths of 4 and $20d_h$.

There are several ways to define "survivable" blockage events. All design calculations were based on single-phase flow, i.e., vapor generation was equated to fuel-plate failure. Boiling was conservatively assumed to occur whenever the wall temperature was greater than the saturation temperature for the local pressure. Figures 15 and 16 show results for a case with a 25 percent edge blockage, variable D_2O properties, and with the wall heat flux shown in Fig. 14. Figure 15 shows that unacceptable wall temperatures are predicted even with a $20d_h$ unheated entrance length. Figure 16 shows the velocity vectors of the fluid near the channel wall in the recirculation region. When similar models were made for both 10 percent and 12 percent blockage sizes, they showed acceptably cooler wall surface temperatures for the same wall heat flux pattern.

Summary and Conclusions

Extrapolation from existing data in the literature indicated a need for further evaluation of potential entrance blockages for the ANS core. The experimental program included the application of two measurement techniques for measuring the downstream effects of entrance blockages. Thermochromic liquid crystals were used to measure wall temperatures on a diagnostic heater and a laser Doppler velocimeter system was employed to measure span-wise and axial velocity profiles and associated turbulence parameters.

Comparison of experimental data and CFD results for edge blockage cases shows that the CFD models are accurate in their representation of the fluid velocity vectors and provide a conservative estimate of heat transfer (i.e., they underestimate the heat transfer) behind the blockage. Both experimental data and CFD models show that the edge blockage generates the longer recirculation region, making the well-benchmarked edge blockage the limiting case for any safety analysis. Given this careful validation of the FBTF edge blockage models, extension of these models to incorporate variations in wall heat flux and temperature-dependent fluid properties is reasonable. Results from the empirical data and modeling evaluation show that blockage elements equal to 25 percent of the channel span would create a region of reduced velocity, and therefore reduced heat transfer, that extends about $50d_h$ downstream. The data from this experimental program will be preserved for future use in examining flow phenomena within thin rectangular channels.

References

Choudhury, D., Kim, S.-E., and Flannery, W. S., 1993 "Calculation of Turbulent Separated Flows Using a Renormalization Group Based k-ϵ Turbulence Model," FED-Vol. 149, *Separated Flows,* ASME, New York.

Crabtree, J. A., 1994, "Use of Image Processing Techniques for Heat Transfer Measurements Using Thermochromic Liquid Crystals," HTD-Vol. 279, *Optimal Design of Thermal Systems and Components,* L. A. Haas and R. S. Downing, eds., Book No. H00910, ASME, New York.

Crabtree, J. A., and Siman-Tov, M., 1993, *Thermophysical Properties of Saturated Light and Heavy Water for Advanced Neutron Source Application,* ORNL/TM-12322, Martin Marietta Energy Systems, Inc., Oak Ridge National Laboratory, Oak Ridge, TN.

Cur, N., 1982, "Local Turbulent Heat Transfer Coefficients in a Symmetrically or Asymmetrically Heated Flat Rectangular Duct With Either Uniform or Nonuniform Inlet Velocity," Ph.D. thesis, Department of Mechanical Engineering, University of Minnesota, Minneapolis, MN.

Fluent, Inc., 1993, *FLUENT User's Guide,* Version 4.2, Lebanon, NH.

Hill, P. G., MacMillan, R. D., and Lee, V., 1981, Tables of Thermodynamic Properties of Heavy Water in SI Units, AECL 7531, Atomic Energy of Canada Limited, Mississauga, Ontario.

Meyer, J. E., Kwak, S. M., and Shubert, T. D., 1992, *Narrow Channel Turbulence Modeling Project Final Report,* MITNE-299, Massachusetts Institute of Technology, Boston, MA.

Patrick, W. P., 1985, "Error Analysis for Benchmark Fluid Dynamic Experiments, Part I: Error Analysis Methodology and the Quantification of Laser Velocimeter Error Sources," R85-151772, United Technologies Research Center, East Hartford, CN.

Petukhov, B. S., 1970, "Heat Transfer and Friction in Turbulent Pipe Flow with Variable Physical Properties," *Advances in Heat Transfer,* Vol. 6, Academic Press, New York.

Sparrow, E. M., and Cur, N., 1983, "Maldistributed Inlet Flow Effects on Turbulent Heat Transfer and Pressure Drop in a Flat Rectangular Duct," ASME JOURNAL OF HEAT TRANSFER, Vol. 105, pp. 527–535.

Stovall, T. K., Crabtree, J. A., Felde, D. K., Park, J. E., 1995, Flow Blockage Analysis of the Advanced Neutron Source Reactor, ORNL/TM-6860, Oak Ridge National Laboratory, Oak Ridge, TN.

TSI, Inc., 1993, Flow Information Display (FIND) Software, Version 4.0, St. Paul, MN.

D. L. Quintana

M. Amitay

A. Ortega

I. J. Wygnanski

Department of Aerospace and Mechanical Engineering, The University of Arizona, Tucson, AZ 85721
www.ame.arizona.edu

Heat Transfer in the Forced Laminar Wall Jet

The mean and fluctuating characteristics of a plane, unsteady, laminar, wall jet were investigated experimentally for a constant wall-temperature boundary condition. Temperature and streamwise velocity profiles, including the downstream development of the thermal and hydrodynamic boundary layer thicknesses, were obtained through simultaneous hot and cold wire measurements in air. Even at relatively low temperature differences, heating or cooling of a floor surface sufficiently altered the mean velocity profile in the inner, near-wall region to produce significant effects on the jet stability. Selective forcing of the flow at the most amplified frequencies produced profound effects on the temperature and velocity fields and hence the time-averaged heat transfer and shear stress. Large amplitude excitation of the flow (up to 2 percent of the velocity measured at the jet exit plane) at a high frequency resulted in a reduction in the maximum skin friction by as much as 65 percent, with an increase in the maximum wall heat flux as high as 45 percent. The skin friction and wall heat flux were much less susceptible to low-frequency excitation.

Introduction

A wall jet is a thin jet of fluid blown tangentially along a surface. The free stream is often either co-flowing or quiescent. The wall jet is a fascinating flow; it provides an example of a flow field consisting of two primary, unstable shear layers which are associated with two different kinds of instability modes: the viscous (inner) mode associated with the inner near-wall region, and the inviscid (outer) mode associated with the inflection point in the outer region of the velocity profile (Mele et al., 1986). Wall jets also have important technological applications in heat and mass transfer (see review by Launder and Rodi, 1983) such as evaporation enhancement and in film cooling.

Probably the most widespread use of the wall jet for evaporation enhancement is in the automobile demister system. Windshields and windows that suffer from icing or fogging are exposed to a heated wall jet which significantly augments heat and mass transfer with the surface. Other applications are found in the complex field of film cooling where turbulent wall jets are used to shield the lining walls of combustion chambers in gas turbines, and to protect turbine blades and other surfaces exposed to either hot or corrosive gases in the free stream. The wall jet, which is cooler than the external stream, acts as a protective buffer for the surface. The success of this buffer is dependent on many variables (Simoneau, 1996): the free-stream turbulence, the upstream wakes, the rotational forces, engine vibrations, secondary flows, and the details of the flow out of the injection holes. It is not surprising that traditional predictive codes significantly underpredict the heat transfer in an actual film-cooling environment. It is evident that a detailed investigation of a wall jet flow subjected to external disturbances could significantly contribute to the physical understanding of these complex heat-transfer problems.

In previous explorations of turbulent wall jets, Katz et al. (1992) and Zhou et al. (1993) found that among other effects, significant reductions (up to 20 percent) in average skin friction can be obtained by exciting the flow at its dominant mode. Given the importance of the wall jet in the transport of heat and mass to or from surfaces, it is equally important to determine the related effects of forcing on the convective transport. Although most of the examples listed above incorporate turbulent wall jets with or without a free stream, an appropriate starting point for understanding the physical mechanisms associated with external excitation is the laminar wall jet. The subject of this paper is hence the heat transfer in a laminar wall jet, with and without external excitation, and in the absence of a free stream. This flow has allowed the examination of the effects of excitation on the coherent structures without the additional complexities associated with a turbulent flow. It will be shown that the evolution of embedded coherent vortices in the wall jet produce profound changes in the heat transfer, a fact that will be critical in studying the turbulent wall jet.

The first theoretical investigation of the incompressible, isothermal, laminar wall jet was done by Tetervin (1948). He predicted that the boundary layer thickness of the wall jet grows and the local maximum of velocity decays with downstream distance as $x^{3/4}$ and $x^{-1/2}$, respectively. Glauert (1956) obtained the solution in a closed form, and his results were substantiated by the hot-wire measurements of Bajura and Szewezyk (1970). Cohen et al. (1992) theoretically investigated the effects of subjecting an incompressible laminar wall jet to small amounts of blowing or suction. They found a new family of self-similar solutions in which Glauert's solution is a member. These self-similar solutions were later confirmed experimentally by Amitay and Cohen (1993).

The self-similar solutions of the temperature field for a low speed, laminar, incompressible wall jet with constant physical properties were obtained by Schwarz and Caswell (1961) for the special cases of constant wall temperature, varying wall temperature, and constant wall heat flux. Temperature profiles and heat fluxes were evaluated for a variety of Prandtl numbers. Mitachi and Ishiguro (1974) also performed a theoretical investigation of the laminar wall jet with different wall boundary conditions. They addressed the unheated starting length problem by using a coordinate transformation to obtain self similar solutions. These investigations were carried out with the assumption that there is no property dependence on fluid temperature. Riley (1958) theoretically investigated the compressible, radial wall jet assuming the dynamic viscosity was linearly dependent on temperature. He showed that a similarity solution for the velocity distribution exists which is expressible in terms of the corresponding incompressible wall jet solution. The energy equation was also studied for different Prandtl numbers and for different wall temperatures.

Contributed by the Heat Transfer Division for publication in the JOURNAL OF HEAT TRANSFER. Manuscript received by the Heat Transfer Division June 21, 1996; revision received April 29, 1997; Keywords: Augmentation & Enhancement; Flow Instability; Transient & Unsteady Heat Transfer. Associate Technical Editor: B. W. Webb.

The first linear stability analysis on the wall jet was a temporal study performed by Chun and Schwarz (1967). By solving the Orr-Sommerfeld equation, they predicted that the critical Reynolds number for which small amplitude disturbances become unstable is 57 (Reynolds number based on local maximum velocity U_m and local hydrodynamic boundary layer thickness δ_v, defined as the point where the velocity equals half of the local maximum velocity in the outer region). They were also the first to reveal the existence of a second unstable mode at relatively high Reynolds numbers. Bajura and Szewezyk (1970) subjected the wall jet to two-dimensional excitations and showed that the fluctuating velocity distribution contains two large peaks and another small peak. One peak is located in the near-wall (inner) region where the local velocity is equal to 0.5 of the local maximum. The second peak, which is initially larger, is located in the vicinity of the inflection point in the outer region where the velocity is equal to 0.8 of the local maximum velocity. An additional weak peak was observed in the outer region where the velocity equals 0.06 of the local maximum velocity. They claimed that the existence of this peak was attributed to convective air currents in their laboratory.

Bajura and Catalano (1975) investigated the transition to turbulence in two-dimensional, plane wall jets, using flow visualization in a water tunnel. They showed that the initial stages of transition are two-dimensional in nature and are dominated by the mechanism of vortex pairing, which is commonly observed in free shear flows. A clarifying physical explanation of the existence of the two modes was given by Mele et al. (1986). They demonstrated theoretically that the low frequency mode (inviscid mode for large-scale disturbances) is associated with the outer inflection point while the high frequency mode (viscous mode for small-scale disturbances) is related to the mean velocity gradient in the vicinity of the wall. These results were theoretically and experimentally verified by Amitay and Cohen (1997) who also investigated the effects of wall blowing and suction on the stability of the wall jet. They found that blowing stabilizes the inviscid (outer) mode and destabilizes the viscous (inner) mode (reducing wall shear stress), while suction destabilizes the inviscid mode and stabilizes the viscous mode (increasing wall shear stress). Furthermore, blowing and suction tend to increase and decrease, respectively, the ratio of the outer to inner amplitude maxima of the streamwise fluctuation of velocity. Likhachev and Tumin (1996) performed a linear stability analysis for a compressible wall jet with several heat transfer boundary conditions. They showed, for the constant temperature surface, that cooling the surface has the same effect as wall suction and heating the surface has the same effect as wall blowing.

An investigation of the effects of low and high acoustic excitation levels on the velocity and temperature fields of a two-dimensional, laminar wall jet flowing over a constant temperature surface is presented in the current paper. The steady, unforced wall jet was examined first, in order to qualify the experiment against existing theories for heat transfer in wall jets with constant properties. This was followed by an examination of the effects of forcing on the time-averaged wall shear stress and heat transfer and on the fluctuating components of streamwise velocity and temperature. In the present investigation, the free stream was quiescent and isothermal with respect to the jet exit temperature. The forced wall jet with heat transfer is currently under analytical, numerical, and experimental investigation in the authors' research group in a long term effort to gain a broader understanding of the control of heat transfer in laminar and turbulent wall jet flows with and without a free stream.

Test Apparatus and Instrumentation

Experimental Apparatus. The experiments were performed in a thermally controlled, closed return, low speed, air wind tunnel. The test section was 711 mm wide, 165 mm high, and 2,362 mm long. A slot type wall jet apparatus was used which essentially duplicates the design of Zhou et al. (1993). This apparatus consisted of a 0.5 HP centrifugal blower, acoustic muffler, air-water heat exchanger, a diffuser fitted with an acoustic speaker, three screens of 30, 40, and 50 mesh size and a contraction nozzle having a variable area ratio. In these experiments, the area ratio was 28:1 resulting in a jet slot width b of 3.2 mm and a jet exit velocity U_j of 1.5 m/s. These parameters were kept constant throughout the experiments. The apparatus was designed to fit in the test section floor of an existing closed return wind tunnel which will provide the free-stream flow in future experiments (see Fig. 1).

Test Surface. The flow exited the wall jet apparatus adhering to a 50.8 mm diameter aluminum Coanda cylinder and flowed tangentially over an isothermal heat transfer surface. The effective jet exit angle was approximately 40°. Since the test

Nomenclature

b = wall jet slot width, m
C_f = local friction coefficient = $[\mu(\partial u/\partial y)|_{y=0}]/(1/2)\rho U_j^2$
c_p = specific heat of air at free stream, J/kg-K
f_{ex} = excitation frequency, Hz
g = gravitational constant, m/s^2
Gr_δ = local Grashof number = $g\delta_v^3(T_w - T_o)/T_o\nu^2$
$\langle\hat{\mathbf{J}}\rangle$ = scaled local integrated kinetic energy of fluctuating velocity = $\int_0^{Y_m} u'^2 \cdot dy/U_j^2 \cdot b$
k = thermal conductivity, W/m-K
Re_δ = Reynolds number based on local quantities = $\rho U_m \delta_v/\mu$
Re_j = Reynolds number measured at exit plane = $\rho U_j b/\mu$
Ri_δ = local Richardson number = $\mathrm{Gr}_\delta/\mathrm{Re}_\delta^2$
St = local Stanton number = $[-k(\partial T/\partial y)|_{y=0}]/\rho U_j c_p(T_w - T_o)$
t' = fluctuating temperature, K
T = local mean temperature, K
T_j = jet exit plane temperature, K
T_o = free-stream temperature, K
T_w = wall temperature, K
u' = fluctuating streamwise velocity, m/s
U = local streamwise mean velocity, m/s
U_j = uniform jet exit velocity, m/s
U_m = local maximum streamwise velocity, m/s
U_o = free-stream velocity, m/s
v' = fluctuating transverse velocity, m/s
x, y = coordinates, m
Y_m = maximum normal distance from the wall (for the integration domain), m

Greek Symbols

β = Strouhal number at the jet exit plane = $f_{ex}b/U_j$
δ = boundary layer thickness, m
δ_v = local hydrodynamic boundary layer thickness, m
δ_t = local thermal boundary layer thickness, m
μ = free-stream dynamic viscosity, N-s/m^2
ν = kinematic viscosity = μ/ρ, m^2/s
ρ = free-stream density, kg/m^3

Subscripts

ex = excitation
j = jet exit plane
m = local maximum
o = free stream
t = thermal
ν = hydrodynamic
w = wall

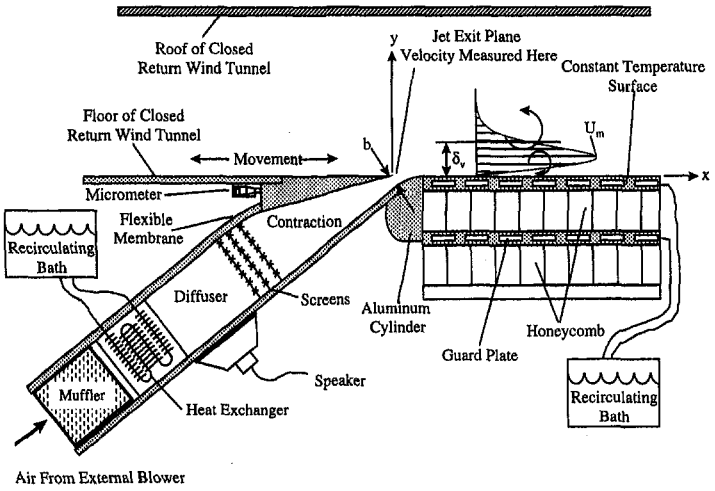

Fig. 1 Experimental apparatus

surface is placed downstream of the jet exit plane, an unheated starting length exists in the system which must be accounted for in theoretical comparisons. The surface consisted of a 19 mm thick, 508 mm wide and 1219 mm long (streamwise length) highly polished aluminum tooling plate which was held at constant temperature by means of cooled/heated water from a recirculating chiller that counterflowed through milled slots inside the plate. Surface temperatures were measured with Type K thermocouples that were potted into the surface with an aluminum epoxy. A 50.8 mm thick sheet of honeycomb was placed beneath the plate and served as an insulator and as a rigid support for the top plate. Another plate with unidirectional flow (at room temperature, 22°C) was placed beneath the honeycomb to stabilize any backside thermal losses. This experimental configuration allowed for independent variation of surface, jet, and free-stream temperatures. In the present investigation, no external mechanism supplied a free-stream flow, although there was a minor free stream induced by the wall jet entrainment in the closed return facility. The free-stream and jet exit temperatures were equal to within ±0.5°C.

Instrumentation. The measurements of the streamwise velocity and temperature were conducted using two side-by-side (7 mm apart in spanwise direction) standard Disa Model 55-P11 single hot and cold wire probes with a 5 μm diameter tungsten sensor having length-to-diameter ratio of 300. A probe holder was constructed that allowed the probes to be traversed in the test section simultaneously at the same streamwise and transverse coordinate. The hot wire was kept at an over-heat ratio of 1.6 and had a maximum frequency response of 30 kHz. The frequency response of the cold wire was 600 Hz. Both the hot and cold wire bridges were manufactured by AA Lab Systems (model AN-1003). The cold wire was calibrated against a NIST traceable lab standard thermistor probe (Thermometric Model ES210). The hot wire was calibrated in the exit plane of a thermally controlled vertical axisymmetric jet against a standard Pitot tube used in conjunction with an MKS Baratron (Model 398HD) pressure transducer. Seven velocities, at a constant temperature, were used for calibration, and a fourth order polynomial fit was used to generate the calibration curve. Due to temperature gradients in the flow field, the hot-wire output voltage required temperature compensation. The hot-wire output voltage was thus calibrated at different velocities for the range of temperatures which were used in the experiment. This produced an approximately linear relationship between voltage and temperature for each velocity. The slope was averaged for the range of velocities and thus used to find the temperature compensated voltage. Using this method, the error between the compensated velocity and the actual velocity (obtained by the Baratron) was less than 0.5 percent. The raw data from the hot and cold-wire anemometers and the pressure transducer were acquired and processed using National Instrument's LabVIEW programming language on a 486 personal computer.

In order to observe the effects of external forcing on the velocity and temperature fields, pressure fluctuations were artificially introduced into the wall jet with a 304.8 mm speaker cone placed in the diffuser section (Fig. 1). A digital-to-analog converter was used to generate the forcing signal, which was passed through an amplifier before it was used to activate the speaker. The desired forcing frequencies were determined from linear stability theory (Cohen et al., 1992), and the excitation level measured at the jet exit plane was incrementally varied from 0.6 to 2.0 percent of the jet exit velocity measured at the jet exit plane. In this investigation, the forcing frequencies were fixed at 44 Hz and 21 Hz, corresponding to the inner and outer modes of instability. The corresponding Strouhal numbers defined at the jet exit plane ($\beta = f_{ex}b/U_j$) were $\beta = 0.094$ and $\beta = 0.045$, respectively. Likhachev and Tumin (1996), using linear stability analysis, showed that when the wall is significantly heated or cooled these frequencies will vary; however, the small temperature differences used in this experiment (5–8°C) produced negligible effects on these forcing frequencies.

In order to retain phase information, the phased locked technique was used in which the hot wire, the cold wire, and the function generator records were sequentially digitized (4 μs delay between channels) 54,000 times (at a sampling rate that is 35 times higher than the frequency of the subharmonic of the excited wave) at each y location and saved in the memory buffer. The amplitude and phase of the fluctuating velocity and temperature components were obtained in the following manner. First, the local mean velocity and temperature were subtracted from the time dependent signals, then, a direct Fourier transform was performed on two periods of the function generator signal in order to retain amplitude and phase information on the fundamental as well as the sub-harmonic. Amplitudes and phases were then averaged for all the two-period calculations in the 54,000 point set. In the event that vortex pairing was present in the measurement domain under high levels of excitation, (as was noticed by the flow visualization studies of Bajura and Catalano (1975) and Amitay (1994)) the amplitude and phase of the sub-harmonic was available for future analysis.

Experimental Uncertainty. The uncertainty in each of the variables and in any calculated variables or parameters was determined by methods outlined by Kline and McClintock (1953). The relative uncertainty in the absolute surface temper-

ature was ±0.2°C. The uncertainty in the mean air temperature measured with the cold wire by sampling 54,000 points at a scan rate which was 35 times higher than the frequency of the sub-harmonic of the excited wave, was ±0.2°C. The cold wire was calibrated against a NIST traceable lab standard thermistor probe with an uncertainty of ±0.05°C. The free-stream temperature was kept constant within ±0.5°C by the low velocity external flow achieving a thermal equilibrium in the closed return wind tunnel with the air-conditioned laboratory. Mean velocity measurements were calibrated against a Baratron pressure transducer and 54,000 points were sampled at a sampling frequency of 35 times the sub-harmonic frequency to obtain an uncertainty of ±1 percent of the jet exit plane velocity.

The fluctuating temperature and velocity were measured at a sampling rate which was 35 times higher than the frequency of the sub-harmonic of the excited wave, giving a cyclic resolution of 10 deg relative to the sub-harmonic component of the phase-locked signal. The sampling time, defined by the sampling frequency and the number of points, was chosen so that the uncertainty in the maximum amplitude of the fluctuating component of the streamwise velocity was less than ±1 percent at the exit plane. The uncertainty in the near-wall velocity and temperature gradients was estimated to be less than ±10 percent of the unforced gradients at the first measured streamwise location. The normal distance from the wall was obtained by extrapolating the near-wall velocity gradient, giving an uncertainty of less than ±0.1 mm.

Results

Undisturbed Mean Flow. Three sets of experiments were conducted corresponding to three temperature ratios denoted by T_w/T_o (measured in Kelvin, where T_w is the wall temperature and T_o is the free-stream temperature): wall cooling with $T_w/T_o = 0.98$, wall heating with $T_w/T_o = 1.03$, and the neutral case with $T_w/T_o = 1$ in which the surface, jet exit, and free-stream temperatures were all the same. Throughout the experiments the jet-exit Reynolds number ($\mathrm{Re}_j = \rho U_j b/\mu$, where ρ is the free-stream density, U_j is the exit plane velocity, and μ is the free-stream dynamic viscosity) remained fixed at 320 ± 5, and the free stream was at rest. However, due to the presence of the wall jet in a closed return wind tunnel, a constant, low velocity flow was induced in the free stream (less than 0.1 m/s) which helped to keep the free-stream temperature in a range of ±0.5°C.

For all of the data presented, $b = 3.2$ mm, and the last measurement station was $x = 64$ mm downstream of the jet exit plane. Although the plate was 1219 mm in length, the measurements were confined to the leading 5 percent of the plate. The plate overheat was 8°C and the jet exit velocity maximum was 1.5 m/s. A local Richardson number ($\mathrm{Gr}_\delta/\mathrm{Re}_\delta^2$) at the farthest downstream station was evaluated by using as the length scale (for both the Reynolds number and the Grashof number) the local hydrodynamic boundary layer thickness δ_v which was on the order of 5 mm. It is appropriate to use this length scale in the Grashof number in comparing the local upward buoyant force to the force of the horizontal jet flow. The local Richardson number was of order (0.001), certainly indicating that the local buoyant mechanisms are negligibly weak by comparison to the local forced convection jet flow in the region of interest.

The normalized mean profiles of the streamwise velocity measured for the three thermal cases mentioned previously, and at three normalized streamwise locations ($x/b = 12$, 16, and 20), are shown in Fig. 2. Here, x is the streamwise distance measured from the wall jet exit plane and y is the normal distance measured from the wall. The local maximum velocity U_m and the local thickness of the hydrodynamic boundary layer δ_v were used to render all variables dimensionless. Figure 2(a) shows full velocity profiles for all cases, while Figs. 2(b), 2(c), and 2(d) present the inner region in more detail for the cooling, neutral, and heating cases, respectively. The symbols represent the experiments while the solid line corresponds to Glauert's (1956) theoretical prediction. Center-dot, solid, and center-cross symbols correspond to the cases of $T_w/T_o = 0.98$, $T_w/T_o = 1$, and $T_w/T_o = 1.03$, respectively. Squares, circles, and triangles correspond to $x/b = 12$, 16, and 20, respectively. The agreement between the experiments and the theory for the neutral case is good except in the inner region where the velocity gradient of the experimental data is higher, Fig. 2(c). This may be due to the relatively high turbulence level (0.5 percent) of the jet. When cooling is applied (Fig. 2(b)), the inner velocity gradient increases and the maximum velocity is shifted closer to the surface. Heating the surface (Fig. 2(d)), appears to have the opposite effect, but the differences in the heated case compared to the neutral case cannot be claimed to be outside of the range of experimental uncertainty. These effects are probably due to the temperature dependence of air viscosity. As will be shown, despite very small changes in the mean velocity due to heating and cooling, a more significant effect is observed on the fluctuating streamwise velocity distribution.

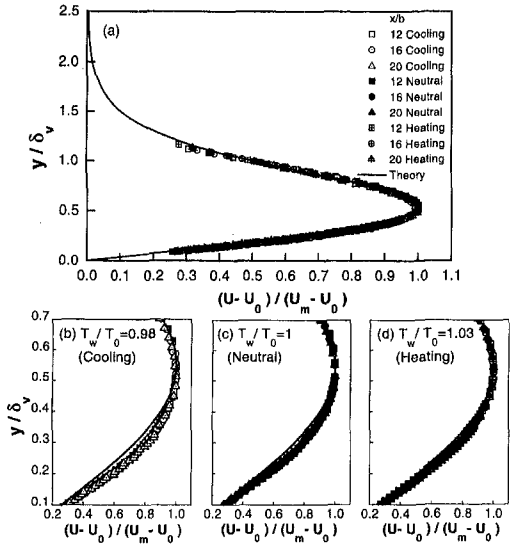

Fig. 2 Comparison of normalized velocity profiles at three x/b locations and for $T_w/T_o = 0.98$, 0, and 1.03; (a) full profile; (b), (c), and (d), near-wall region

The downstream development of the hydrodynamic and the thermal boundary layers are plotted in Fig. 3. Here, δ_t is defined as the distance from the wall to the place where the normalized temperature, $(T - T_w)/(T_o - T_w)$, is equal to 0.5. Figure 3(a) presents the dimensional form in order to observe the relative magnitudes of the boundary layer thicknesses, while Fig. 3(b) displays the boundary layer thickness normalized by the first measurement point displaying the spread rate of the two scales. As can be seen from Fig. 3(a), heating and cooling have no significant effect on the hydrodynamic boundary layer; however, heating produces a thicker thermal boundary layer. As shown in Fig. 3(b), the growth rate of the thermal boundary layer is greater than the hydrodynamic boundary layer, consistent with the existing theory of Mitachi and Ishiguro (1974) for Prandtl number less than unity.

The normalized temperature profiles for different scaling lengths and at three downstream stations are shown in Fig. 4. The hydrodynamic boundary layer thickness δ_v was used as the normalizing scale in Figs. 4(a) and 4(b), and the thermal boundary layer thickness δ_t was used in Figs. 4(c) and 4(d). Figures 4(a) and 4(c) present the full temperature profiles, while 4(b) and 4(d) show the inner region near the wall in more detail. The symbols represent the experimental data which

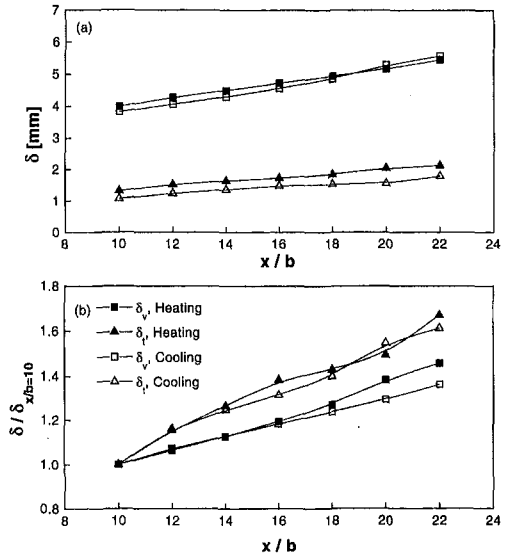

Fig. 3 The downstream development of the different boundary layer thicknesses; (*a*) dimensional and (*b*) normalized

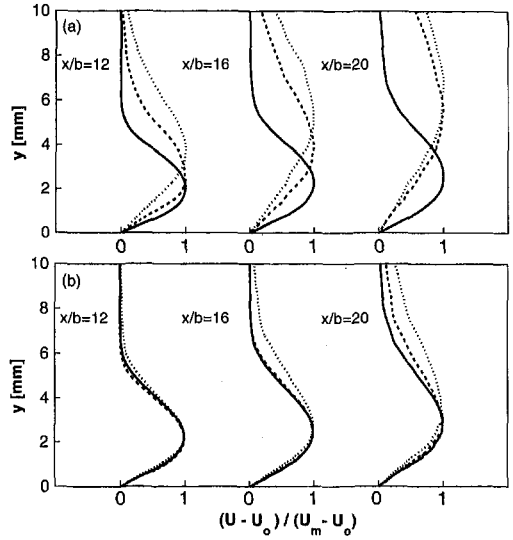

Fig. 5 Mean velocity profiles for various excitation levels and downstream locations; (*a*) $\beta = 0.094$ and (*b*) $\beta = 0.045$ forcing for $T_w/T_o = 1.03$, ——— Unforced, – – – 1 percent forcing, ----- 2 percent forcing

show good agreement with the solid lines, which correspond to the theory developed by Mitachi and Ishiguro (1974) for different temperature ratios and entry lengths. Using δ_v as the length scale causes the data to collapse on two curves, one for the cooling case and one for the heating case. These two curves correspond to two different unheated starting lengths which were used for a coordinate transformation in the Mitachi and Ishiguro (1974) theory.

As is shown in Fig. 3(*b*), the spreading rate for the thermal boundary layer thickness is approximately the same for heating and cooling but the magnitude is different (Fig. 3(*a*)). The virtual origin of the thermal boundary layer for the heating case therefore is shifted farther upstream and thus the corresponding unheated starting length is smaller. This results in a thicker temperature profile for wall heating, as is evident in Figs. 4(*a*) and 4(*b*). On the other hand, scaling on δ_t collapses the two cases onto one curve, shown in Figs. 4(*c*) and 4(*d*). These are not surprising results since the ratio of the thermal and the hydrodynamic boundary layers is different for the two cases above, mainly because the changes in δ_t are more significant than changes in δ_v, as was shown in Fig. 3. It is believed that these differences in the thermal boundary layer thicknesses as well as the normalized temperature profiles are due to the upstream conduction effects on the aluminum Coanda cylinder. The absolute temperature difference for the heating case ($T_w - T_o$) was 3°C larger than for the cooling case. This caused enough upstream conduction to allow the thermal boundary layer to develop further upstream and provide the noticeable differences in Figs. 3 and 4.

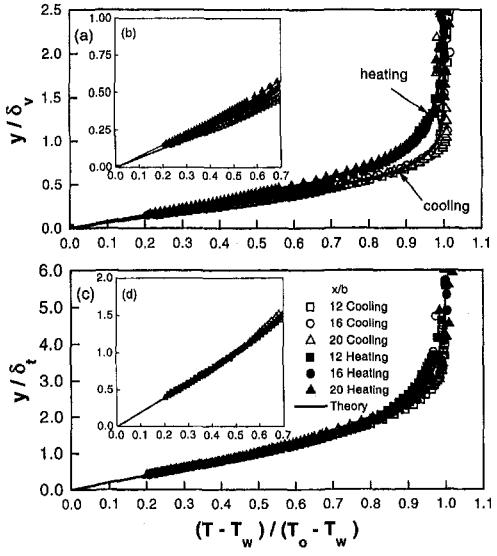

Fig. 4 Normalized temperature profiles; (*a*) scaled by δ_v and (*c*) scaled by δ_t, where (*b*) and (*d*) are the corresponding near-wall regions

Mean Flow Field Subjected to External Forcing. The mean velocity and temperature fields were also investigated under actively controlled conditions. Disturbances were introduced into the flow by a speaker at two frequencies (Strouhal numbers of 0.045 and 0.094) and three excitation levels (0.6 percent, 1.0 percent, and 2.0 percent). The excitation level introduced by the speaker is defined at the jet exit plane ($x/b = 0$) as $100 \cdot u'_m/U_j$, where u'_m is the maximum fluctuating streamwise velocity measured at the exit plane. Three cases, corresponding to the three values of T_w/T_o, were studied. In this section only the results for the heating case are presented, however, similar results were obtained for the other cases mentioned.

Mean profiles of the streamwise velocity measured for the heating case and at three normalized streamwise locations ($x/b = 12$, 16, and 20) are shown in Fig. 5. Figure 5(*a*) presents the case in which the flow is excited with a high frequency disturbance ($\beta = 0.094$) while Fig. 5(*b*) corresponds to a low frequency disturbance ($\beta = 0.045$). The solid, dashed, and dotted lines correspond to the unforced, 1 percent excitation level and 2 percent excitation levels, respectively. As is shown in Fig. 5(*a*), when high frequency forcing is applied, the velocity field is dramatically altered. The effects become more pronounced as the downstream distance increases. The effect of low frequency forcing is not as dramatic because the initial growth rates associated with the outer mode are smaller than the inner mode growth rates, as predicted by the theory (see Amitay and Cohen, 1997).

In order to see the effects of forcing on the wall shear stress, the near-wall region of the mean velocity field was replotted and is presented in Fig. 6. Seven cases, corresponding to the unforced case, high and low frequency forcing with 0.6 percent, 1 percent, and 2 percent excitation levels, are presented. Figures 6(*a*), 6(*b*), and 6(*c*) represent the experimental data taken at $x/b = 12$, 16, and 20, respectively. For low levels of excitation, the scaled velocity gradient near the wall is negligibly affected.

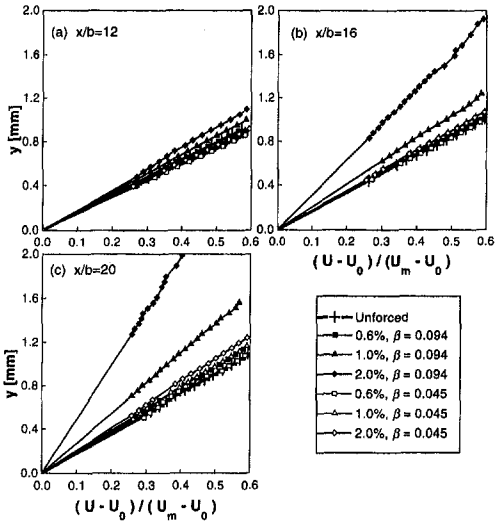

Fig. 6 Near-wall velocity comparison for different excitation levels and frequencies at x/b of (*a*) 12, (*b*) 16, (*c*) 20, and for $T_w/T_o = 1.03$

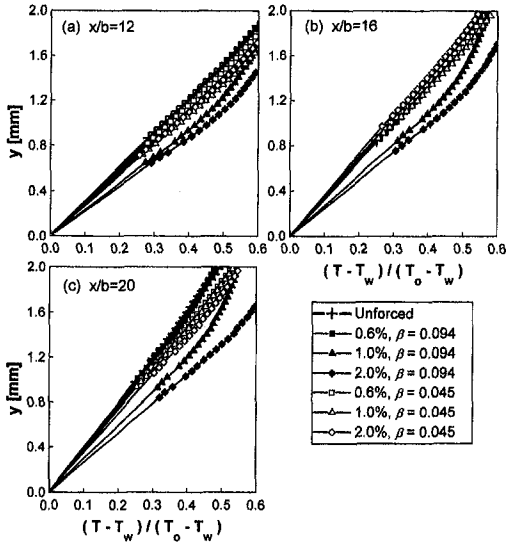

Fig. 8 Near-wall temperature comparison for different excitation levels and frequencies at x/b of (*a*) 12, (*b*) 16, (*c*) 20, and for $T_w/T_o = 1.03$

As the excitation level is increased up to 2 percent, the scaled velocity gradient near the wall is decreased by up to 15 percent (with respect to the unforced case at $x/b = 20$) for the low frequency forcing and by up to 65 percent for the high frequency forcing.

The normalized mean temperature profiles measured for the heating case at $x/b = 20$ are shown in Figs. 7(*a*) and 7(*b*) for high and low frequency forcing, respectively. As was observed for the velocity field, for low excitation levels the effect of forcing on the temperature profile is negligible. As the excitation level is increased, the temperature gradient near the wall increases and an inflection point is formed on the temperature profile. Again, the effect of the high frequency forcing is much more significant. Measurement of the normal component of the fluctuating velocity v' may help to clarify the formation of the inflection point in the temperature profile. However, since the boundary layer thickness was on the order of 5 mm, it was extremely difficult to measure v' using conventional X-wire techniques.

The effect of forcing on the near-wall region of the temperature profile is presented in Fig. 8. Profiles measured at three normalized streamwise locations ($x/b = 12$, 16, and 20) are shown in Figs. 8(*a*), 8(*b*), and 8(*c*), respectively. Low excitation levels do not significantly alter the temperature gradient near the wall, while increasing the excitation level causes an increase in the temperature gradient. Low and high frequency forcing (at 2 percent excitation level and at x/b of 20) increase the temperature gradient by up to 20 percent and 45 percent, respectively. This augmentation in the heat-transfer rate is accompanied by a net reduction in the time-averaged wall drag, a result which was not anticipated.

The integrated effect of forcing, with different frequencies and amplitudes, on the normalized total skin friction drag and the total heat flux, is presented in Figs. 9(*a*) and 9(*b*), respectively. Here, x_1 is the first measured downstream station (corresponding to $x/b = 12$), C_f is the friction coefficient

$$\left(C_f = \left[\mu \left. \frac{\partial u}{\partial y} \right|_{y=0} \right] \Big/ \frac{1}{2} \rho U_j^2 \right)$$

and St is the Stanton number

$$\left(\mathrm{St} = \left[-k \left. \frac{\partial T}{\partial y} \right|_{y=0} \right] \Big/ \rho U_j c_p (T_w - T_o) \right).$$

The total effect of low frequency forcing is weak and within 5 percent of the unforced curves. The effect of high frequency

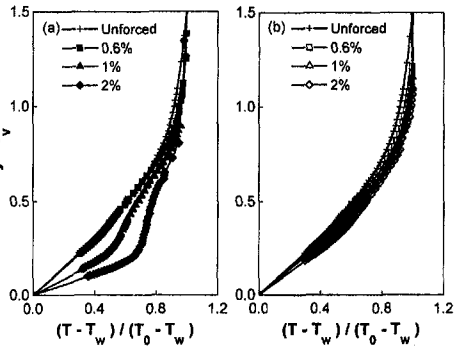

Fig. 7 Comparison of normalized temperature profiles measured at $x/b = 20$ and for different excitation levels for (*a*) $\beta = 0.094$ and (*b*) $\beta = 0.045$ (for $T_w/T_o = 1.03$)

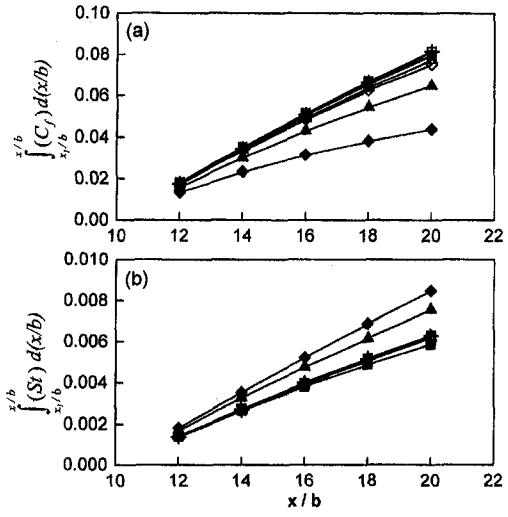

Fig. 9 Integrated (*a*) friction coefficient and (*b*) Stanton number for $T_w/T_o = 1.03$, and for various forcing conditions: – + – Unforced, – ■ – 0.6 percent, $\beta = 0.094$, – ▲ – 1.0 percent, $\beta = 0.094$, – ♦ – 2.0 percent, $\beta = 0.094$, – □ – 0.6 percent, $\beta = 0.045$, – △ – 1.0 percent, $\beta = 0.045$, – ◇ – 2.0 percent, $\beta = 0.045$

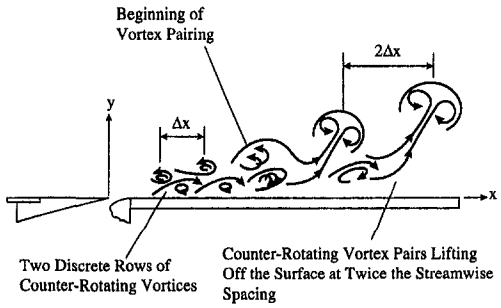

Fig. 10 Evolution of the vortices in the streamwise direction

forcing is much more significant, with a 45 percent reduction of the total skin friction drag and a 20 percent increase of the total heat transfer at x/b of 20.

As is shown in Fig. 5, high levels of forcing introduce nonlinear effects as observed by a dramatic thickening of the boundary layer. This is consistent with the observations of Bajura and Catalano (1975) and Amitay (1994) who noticed that the forced transition into turbulence is two-dimensional in nature. It begins with the formation of two discrete rows of counter-rotating vortices (which are not in phase) in the outer and inner regions of the wall jet (see Fig. 10). This is followed by simultaneous vortex pairing of adjacent vortices in both regions and a subsequent "lift off" of the combined vortex system from the surface into the ambient fluid. The space between the vortex pairs is twice the initial space before pairing, resulting in halving the original frequency. These paired vortices significantly widen the boundary layer and are responsible for the transport of energy and momentum away from the wall. A plausible explanation may be that the outer paired vortex system transports fluid away from the wall to the outer region (which is at a different temperature) and also entrains fluid towards the wall. This motion may also explain the large increase in the temperature gradient occurring at y/δ_v of about 0.2, as seen in Fig. 7(a), since the unsteady upward advective transport is increased compared to diffusive transport in this region. This enhanced thermal mixing is also manifested in the observed increase in the wall temperature gradient and thus the wall heat flux.

Fluctuating Quantities. Since the addition of controlled disturbances is apparently a primary factor in augmenting the heat transfer, the structure and evolution of the temperature and streamwise velocity fluctuations were further investigated. Data were measured and analyzed for low and high levels of excitation corresponding to the two modes of instability associated with the wall jet flow. These levels of excitation correspond to the linear and nonlinear transitional behavior of the flow. Figure 11 shows the normalized fluctuating temperature distribution versus the dimensional normal distance from the wall. Here, the fluctuating temperature is normalized by the low frequency ($\beta = 0.045$) maximum of the fluctuating temperature profile, $t'_m(\beta = 0.045)$. Measurements were taken at $x/b = 20$ for $T_w/T_o = 1.03$ and for three excitation levels of (a) 0.6 percent, (b) 1 percent, and (c) 2 percent. A single peak is present for 0.6 percent forcing, as is shown in Fig. 11(a). This peak is located at approximately the same distance from the wall for both high and low frequency forcing (within 0.25 mm of each other). The magnitude of this peak for high frequency forcing is larger due to higher initial growth rates associated with this mode. As the level of forcing is increased (from 0.6 percent to 2 percent), a second peak is formed on the distribution very close to the wall. This second peak occurs at the same location as the inflection point in the mean temperature profile. Similar trends occurred when the wall was cooled (not shown here).

Figure 12 shows the normalized distribution of the fluctuating fundamental streamwise velocity for low frequency forcing at an excitation level of 0.6 percent and for both (a) wall heating, and (b) wall cooling. The distribution contains two large peaks corresponding to the velocity gradient near the wall and the inflection point in the outer region of the velocity profile, as was explained by Mele et al. (1986). The fluctuating velocity is normalized by the value of the maximum of the outer peak, u' (outer). The outer peak is initially larger and has a broader disturbed region than the inner peak because the low forcing frequency ($\beta = 0.045$) has a more significant effect on the row of vortices in the outer region. For both cases, as the downstream distance increases, the ratio of the outer to inner amplitude maxima decreases, which is consistent with linear stability theory and experimental data, as shown by Amitay and Cohen (1997). According to the linear stability theory, as the downstream distance is increased, smaller scales (associated with high frequencies) in the near-wall region experience a larger growth rate. For a fixed downstream location, the ratio of the outer to inner amplitude maxima is smaller for the cooling case because of the higher velocity gradient near the wall (see Fig. 2).

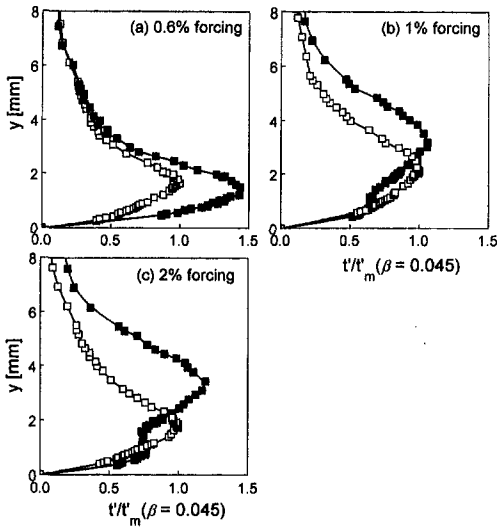

Fig. 11 Fluctuating temperature distribution for high and low frequency forcing for (a) 0.6 percent, (b) 1.0 percent, and (c) 2.0 percent excitation levels ($x/b = 20$, $T_w/T_o = 1.03$, – ■ – $\beta = 0.094$, and – □ – $\beta = 0.045$)

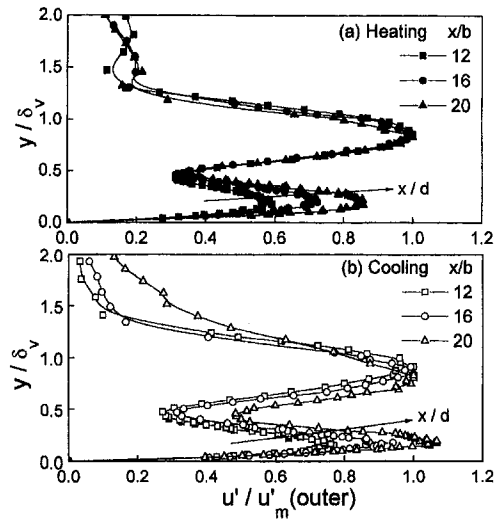

Fig. 12 Normalized fluctuating streamwise velocity comparison at three x/b locations for $\beta = 0.045$ at an excitation level of 0.6 percent; (a) wall heating and (b) wall cooling

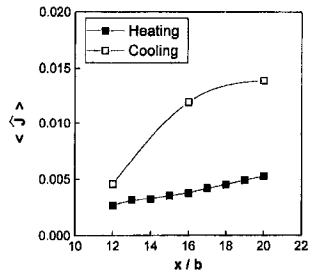

Fig. 13 Downstream development of the integrated kinetic energy of the fluctuating velocity for 0.6 percent excitation level and $\beta = 0.094$; $T_w/T_o = 1.03$ and 0.98

Another way to observe the difference between heating and cooling is to plot the integrated kinetic energy of the fluctuating streamwise velocity

$$\left(\langle \hat{\mathbf{J}} \rangle = \int_0^{Y_m} u'^2 \cdot dy \Big/ U_j^2 \cdot b\right)$$

as a function of the downstream distance for heating and cooling, as in Fig. 13. As can be seen, both the magnitude and the growth rate for the cooling case are higher than the heating case. This behavior is related to the apparently small but non-negligible increase and decrease of the slope of the mean velocity profile at the wall when cooling and heating are applied. The same effects were reported by Amitay and Cohen (1997) for wall blowing or suction, and by Likhachev and Tumin (1996) for wall heating and cooling. It is apparent that cooling and heating in the present study substantiate the theoretical predictions of Likhachev and Tumin (1996) and have a similar effect as suction and blowing in the investigation by Amitay and Cohen (1996).

Concluding Remarks

To better understand the heat and momentum transfer associated with an externally excited wall jet, a plane laminar, acoustically forced wall jet was investigated experimentally for the constant wall temperature boundary condition. No external mechanism supplied a free-stream flow, and as a simplification, both the free stream and the jet exit temperatures were equal (within ±0.5°C). Controlled acoustic disturbances were introduced into the flow in an attempt to influence the wall heat transfer by taking advantage of the two instability modes associated with the wall jet.

Measured streamwise mean flow velocity profiles for the unforced case for small temperature differences (5–8°C) were in good agreement with the theoretical predictions. Although the temperature difference between the surface and the jet was small, heating or cooling of the plate changed the mean velocity profile predominately in the inner region. When cooling was applied, the inner velocity gradient was the highest and the maximum velocity was shifted closer to the surface, while heating the surface had the opposite effects. Previous theoretical models require that the thermal and hydrodynamic boundary layers originate at the same location for full similarity; however, as is shown in Fig. 1, an unheated starting length exists in the experimental apparatus. The analytical solution of Mitachi and Ishiguro (1974), which accounts for the unheated starting length, was employed to compare the experimental results for the temperature field. It was found that using the thermal boundary layer thickness δ_t as the length scale collapsed the data for heating and cooling on a single theoretical solution.

Acoustic disturbances were introduced at excitation levels of 0.6 percent, 1 percent, and 2 percent and at two forcing frequencies corresponding to the inner and outer modes associated with the wall jet stability. It was found that the high levels of forcing (1 percent and 2 percent) greatly altered the velocity and temperature profiles. The most significant effects occurred for high frequency forcing where there was a 65 percent reduction in local skin friction and a 45 percent increase in the local wall heat flux measured at x/b of 20. At the same location, the total skin friction drag (integrated effect) was reduced by 45 percent and the total heat flux was increased by 20 percent. The skin friction and wall heat flux were less susceptible to low frequency excitation but the trends were not altered. The same results occurred for both heating and cooling of the surface.

The fluctuating temperature as well as the fluctuating streamwise component of velocity were measured. It was found that in the fluctuating temperature distribution, a large peak was located at $y/\delta_v = 0.5$. A second peak was formed on the distribution very close to the wall ($y/\delta_v = 0.2$) for high excitation levels and high frequency forcing ($\beta = 0.094$). This peak occurred at the same location as the inflection point in the mean temperature profile. The fluctuating velocity distribution contained two peaks associated with the inner and outer regions of the wall jet where the ratio of the outer to inner amplitude maxima was less when cooling was applied due to higher velocity gradients at the wall.

High frequency forcing had the most significant effects on the velocity and temperature fields. The emergence of paired vortices is evident in the observed increase in boundary layer thickness. It is these large scale and low frequency paired vortices that receive most of the energy under high levels of forcing; therefore, they increase the boundary layer thickness and decrease the velocity gradient near the wall. These large-scale vortex pairs enhance thermal mixing and produce the observed increase in the temperature gradient near the wall. One can immediately see the benefits of introducing controlled disturbances at a known frequency and excitation level to the flow of an automobile demister system. For film-cooling applications, the desired effect is a decrease in the heat-transfer rate to the surface. Although the present investigation shows that forcing could be detrimental to film cooling, the fact that there are select frequencies and excitation levels which must be accounted for in predictive models is also of value.

Acknowledgments

This work was supported, in part, by the United States Department of Energy under grant number DE-FG03-93ER14396, the Air Force Office of Scientific Research under grant number F49620-94-1-0131, and NASA Lewis Research Center under the Graduate Student Researchers Program, grant number NGT-70403#1.

References

Amitay, M., 1994, "Theoretical and Experimental Investigations of a Laminar Two-Dimensional Wall Jet," *Ph. D. thesis,* Faculty of Aerospace Engineering, Technion, Israel Institute of Technology, Haifa, Israel.

Amitay, M., and Cohen, J., 1993, "The Mean Flow of a Laminar Wall Jet Subjected to Blowing or Suction," *Phys. Fluids,* Vol. A5, pp. 2053–2057.

Amitay, M., and Cohen, J., 1997, "Instability of a Two-Dimensional Plane Wall Jet Subjected to Blowing or Suction," *J. Fluid Mech,* in press.

Bajura, R. A., and Catalano, M. R., 1975, "Transition in a Two-Dimensional Plane Wall Jet," *J. Fluid Mech.,* Vol. 70, Part 4, pp. 773–799.

Bajura, R. A., and Szewezyk, A., 1970, "Experimental Investigation of a Laminar Two-Dimensional Plane Wall Jet," *Phys. Fluids,* Vol. 13, pp. 1653–1664.

Chun, D. H., and Schwarz, W. H., 1967, "Stability of the Plane Incompressible Viscous Wall Jet Subjected to Small Disturbances," *Phys. Fluids,* Vol. 10, 5, pp. 911–915.

Cohen, J., Amitay, M., and Bayly, B. J., 1992, "Laminar-Turbulent Transition of wall Jet Flows Subjected to Blowing and Suction," *Phys. Fluids,* Vol. A4, pp. 283–289.

Glauert, M. B., 1956, "The Wall Jet," *J. Fluid Mech,* Vol. 1, pp. 625–643.

Katz, Y., Horev, E., and Wygnanski, I., 1992, "The Forced Turbulent Wall Jet," *J. Fluid Mech,* Vol. 242, pp. 577–609.

Kline, S. J., and McClintock, F. A., 1953, "Describing Uncertainties in Single Sample Experiments," *Mechanical Engineering,* Vol. 75, Feb., pp. 3–8.

Launder, B. E., and Rodi, W., 1983, "The Turbulent Wall Jet-Measurements and Modeling," *Ann. Rev. Fluid Mech.,* Vol. 15, pp. 429–459.

Likhachev, O., and Tumin, A., 1996, "Stability of a Compressible Laminar Wall Jet with Heat Transfer," *J. Fluids Engineering,* Vol. 118, pp. 824–828.

Mele, P., Morganti, M., Scibillia, M. F., and Lasek, A., 1986, "Behavior of Wall Jet in Laminar-to-Turbulent Transition," *AIAA Journal,* Vol. 24, pp. 938–939.

Mitachi, K., and Ishiguro, R., 1974, "Heat Transfer of Wall Jets," *Heat Transfer: Japanese Research,* Vol. 3, pp. 27–40.

Riley, N., 1958, "Effects of Compressibility on a Laminar Wall Jet," *J. Fluid Mech.,* Vol. 4, pp. 615–628.

Schwarz, W. H., and Caswell, B., 1961, "Some Heat Transfer Characteristics of the Two-Dimensional Laminar Incompressible Wall Jet," *Chemical Engineering Science,* Vol. 16, pp. 338–351.

Simoneau, R. J., 1996, "Research Strategy for Modeling the Complexities of Turbine Heat Transfer," *NASA Tech. Memo. 107161, The International Conference on Turbulent Heat Transfer,* R.M.C. So, ed., San Diego, CA.

Tetervin, N., 1948, "Laminar Flow of a Slightly Viscous Incompressible Fluid that Issues from a Slit and Passes over a Flat Plate," *NACA TN,* No. 1644.

Zhou, M. D., Heine, C., and Wygnanski, I., 1993, "The Forced Wall Jet in an External Stream," AIAA paper 93-3250, *AIAA Shear Flow Conference,* Orlando, FL.

Experimental Studies and Correlations of Convective Heat Transfer in a Radially Rotating Serpentine Passage

G. J. Hwang
Professor.
ASME Fellow.
gihwang@tmp.nthu.edu.tw

C. R. Kuo
Department of Power Mechanical Engineering,
National Tsing Hua University,
Hsinchu 30043, Taiwan

The present paper investigates experimentally the effects of rotation on the convective heat transfer of air flow in a radially rotating three-passage serpentine square channel. Due to rotation, the cross-stream and radial secondary flows are induced by the Coriolis force and the centrifugal-buoyancy force, respectively. The channel walls were made of low thermal conductivity material for suppressing wall heat conduction. The wall surfaces were heated individually by four separate stainless-steel film heaters to distinguish the local heat transfer rates. The hydraulic diameter and the mean rotational radius of the flow passages were 4 and 180 mm, respectively. The governing parameters are the through-flow Reynolds number Re, the rotation number Ro, the buoyancy parameter Gr, and the main flow direction. The results show that the local heat transfer rate was enhanced by rotation on the trailing side for outward flow and on the leading side for inward flow. In the first and third passages, the effect of rotation on heat transfer is relatively prominent. The buoyancy effect is favorable to the heat transfer enhancement on four sides of these passages. The data of Nu_Ω/Nu_0 are correlated on the leading and trailing sides of these passages.*

Introduction

High turbine inlet temperature has essential advantages for improving the thermodynamic efficiency and reducing the specific fuel consumption rate for a gas turbine. A vital part of going to high turbine inlet temperature is the technology of turbine blade cooling. The coolant air-flow rate currently required on new aircraft engines may be as high as 20 percent of the compressor discharge flow rate. The large quantity of air flow has two defects that tend to reduce the advantages of using high turbine inlet temperature. The mainstream turbine air flow, mixed with coolant air flow, causes additional aerodynamic losses and a drop in the turbine inlet temperature. Both of these defects are harmful and cannot be overlooked. Therefore, vigorous steps have been taken to minimize both the quantity of coolant air and the associated aerodynamic losses.

To increase the heat transfer with a given volume of coolant air, the flow passages should be intricate for increasing the turbulent mixing and the heat transfer area. A new manufacturing technique has changed the methods for producing more intricate and finer flow passages. The state-of-the-art cooling design by channeling compressor-bled air into radially rotating flow passages has been acquired. For decades, a number of theoretical and experimental studies have been investigating the influence of rotation and duct geometry on the flow and heat transfer characteristics in radially rotating passages.

Recently, researchers are interested in the hydrodynamic and thermal behaviors of air flow in serpentine flow passages. Wagner et al. (1991a, b) investigated the local heat transfer for radially outward and inward flows in rotating serpentine passages with hydraulic diameter D = 12.7 mm, maximum rotational speeds Ω = 1100 rpm, eccentricity ϵ = 26 and 42, and uniform wall temperature thermal boundary condition. They found that buoyancy was favorable for heat transfer on both the trailing and leading sides. However, the increase in the heat transfer for inward flow was relatively less than that for outward flow. Yang et al. (1992) investigated the heat transfer in a rotating 4-pass serpentine passage of square cross-section. The results showed that the heat transfer was enhanced at all sharp turns. The rotation effect on the local heat transfer performance was apparent, but the effect on the average heat transfer performance was minor. Han and Zhang (1992) and Han et al. (1993) revealed the effects of uneven wall temperature on the heat transfer in a rotating two-pass square channel with D = 12.7 mm, Ω(max.) = 800 rpm, and ϵ = 24. They studied three cases of thermal boundary conditions: four walls at the same temperature, four walls at the same heat flux, and the trailing wall hotter than the leading one with side walls unheated and insulated. Mochizuki et al. (1994) studied experimentally the heat transfer characteristic of a three-pass serpentine flow passages with D = 20 mm, Ω(max.) = 500 rpm, ϵ = 38.5, and nearly uniform wall heat flux. They found that the heat transfer rate in the radially outward flow passages diminished on the leading side, but increased on the trailing side, with an increase in the rotational speed. The trend was reversed for the radially inward flow. Since the heat transfer rate in the 180 deg bend was substantially higher than that in the straight sections, the average heat transfer rate over the entire flow passage is greatly increased. Kuo and Hwang (1996) summarized the experimental data and presented correlation equations on the leading and trailing sides for the outward and inward flows in a radially rotating single passage. A comparison of their experimental data with those of correlation equations, and data of Wagner et al. (1991a, b) and Han and Zhang (1992) was made.

The objective of this study is to examine experimentally the rotation effects on the local heat transfer in a rotating three-passage serpentine channel by varying the rotational speeds, through-flow Reynolds numbers, and heat flux. The rotation effects on the heat transfer may also depend on the main flow directions in these three passages. A channel of small hydraulic diameter was constructed for simulating a real engine with a

Contributed by the Heat Transfer Division for publication in the JOURNAL OF HEAT TRANSFER. Manuscript received by the Heat Transfer Division February 9, 1996 and presented in part at The ASME 1994 International Congress and Exposition, Chicago, IL, November 6–11, 1996; revision received April 21, 1997; Keywords: Mixed Convection; Reacting Flows; Turbines. Associate Technical Editor: R. D. Boyd.

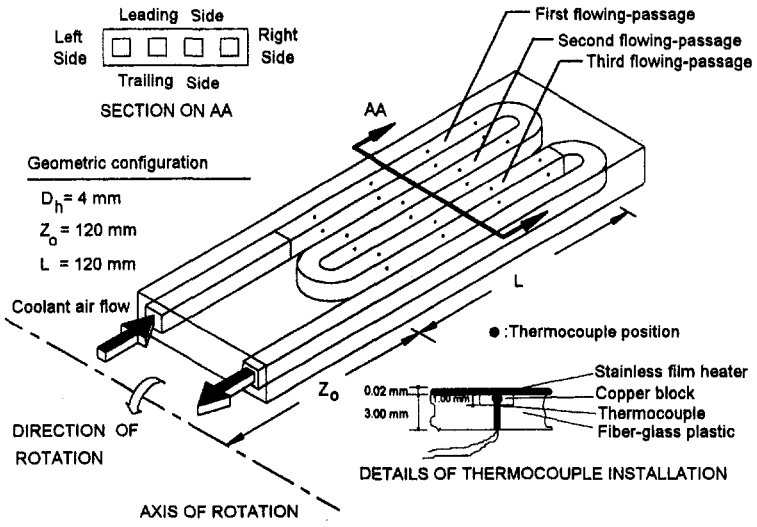

Fig. 1 Physical model of the test section

higher wall-to-coolant temperature difference when the centrifugal-buoyancy effect was examined. The four channel walls were made of a low conductivity material and heated separately by stainless-steel film heaters for suppressing the circumferential wall conduction and distinguishing the local heat transfer rate on the four side walls. One of the major attempts in the present study is also to summarize the present results and the existing experimental data by fitting with correlation equations for heat transfer in the three-passage serpentine channel.

Governing Parameters

The physical model of the test section is shown in Fig. 1. The heated length for the first passage starts at $Z_0 = 120$ mm. The heated surfaces include three straight sections of 120 mm length each and two curved sections with an inner radius of 4 mm. The heated length for the third passage ends at $Z_0 + L = 240$ mm. As shown in Fig. 2, the velocity profiles depict the rotation effects on the outward and inward air flows in a radially rotating channel. Since $W \gg V$ and $Z \gg X$ and Y, the dominant forces due to rotation are the force vectors of $2\rho\Omega W$ and $\rho\Omega^2 Z$, as seen in the force diagram. The Coriolis force $2\rho\Omega W$ distorts the axial velocity and moves the maximum velocity toward the trailing side in the outward flow passage, but toward the leading side in the inward flow passage. On the other hand, the centrifugal-buoyancy force $\rho\Omega^2 Z$ accelerates the less dense air near the heated wall toward the rotating axis for both the outward and the inward flows.

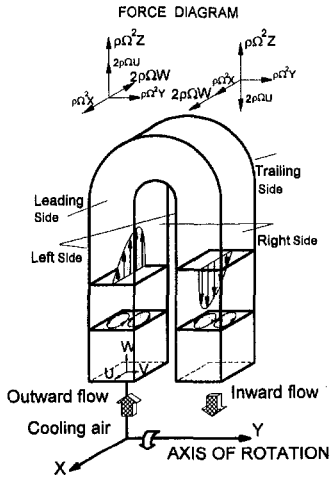

Fig. 2 Velocity profiles and coordinate system

Nomenclature

c_p = specific heat, J/(kg°C)
D = hydraulic diameter, mm
Gr_Ω = rotational Grashof number = $\beta(T_{w,z} - T_{b,z})[\epsilon + z/D]\,\mathrm{Re}^2\,\mathrm{Ro}^2$
Gr^* = rotational buoyancy parameter = $\mathrm{Gr}_\Omega/\mathrm{Re}^2$
L = actively heated length of duct, mm
Nu_0 = Nusselt number for non-rotating condition = $[q_{\mathrm{net},z}/(T_{w,z} - T_{b,z})]_0 D/k$
Nu_f = Nusselt number for fully developed flow in a non-rotating circular tube
Nu_Ω = Nusselt number for rotating condition = $[q_{\mathrm{net},z}/(T_{w,z} - T_{b,z})]_\Omega D/k$
Pr = Prandtl number = $c_p\mu/k_{\mathrm{air}}$
q_{net} = net wall heat flux, W/m^2
R = mean rotational radius = $Z_0 + L/2$, mm
Re = through-flow Reynolds number = $\rho W_0 D/\mu$
Re_Ω = rotational Reynolds number = $\rho\Omega D^2/\mu$
Ro = rotation number = $\mathrm{Re}_\Omega/\mathrm{Re}$ = $\Omega D/W_0$
$T_{b,i}$ = inlet coolant bulk temperature, °C
$T_{b,o}$ = outlet coolant bulk temperature, °C
$T_{b,z}$ = local coolant bulk temperature, °C
$T_{w,z}$ = local passage wall temperature, °C
W_0 = mean coolant velocity, m/s
U, V, W = velocity component, m/s
z = coordinate for outward flow passage measured from Z_0
$\bar{z}$ = coordinate for inward flow passage measured from $Z_0 + L$ to the axis
Z_0 = distance between rotating axis and heater minimum radius, mm
X, Y, Z = system coordinates

Greek Symbols

β = volume expansion coefficient, 1/K
ϵ = eccentricity = Z_0/D
μ = coolant dynamic viscosity, kg/m s
ρ = coolant density, kg/m^3
Ω = rotational speed, rpm

Table 1 Ranges of the experimental variables

VARIABLES	RANGES
rpm	0, 270, 800, 1300, 1800
D (mm)	4
T_w (°C)	30 - 90
$T_{b,o} - T_{b,i}$ (°C)	15, 30, 40
ε	30
R/D	45
L/D	30
z/D	2.5, 10.0, 17.5, 25.0
Pr	0.72
Re	5000, 10000, 15,000, 20,000
Ro	0 - 0.032
Gr*	0 - 0.01

A dimensional analysis of the flow governing equations reveals that the heat transfer coefficient in the rotating channel is functionally influenced in the following form (Morris and Ayhan, 1979):

$$\mathrm{Nu}_\Omega = f(\mathrm{Re}, \mathrm{Ro}, \mathrm{Gr}^*, \mathrm{Pr}, R/D, z/D) \quad (1)$$

where the definitions of these nondimensional parameters are listed in the nomenclature. In the present study, air with Pr = 0.72 was used as the coolant. The ratio of the mean rotational radius to the hydraulic diameter R/D = 45 was also fixed. Accordingly, Eq. (1) is reduced to

$$\mathrm{Nu}_\Omega = f(\mathrm{Re}, \mathrm{Ro}, \mathrm{Gr}^*, z/D). \quad (2)$$

In Eq. (2), the Reynolds number Re indicates the forced convection effect. The rotation number Ro represents the effect of Coriolis force on the main flow forced convection. The rotational buoyancy parameter Gr* denotes the effect of centrifugal-buoyancy effect. The thermophysical properties were evaluated at the local bulk temperature $T_{b,z}$.

For scaling the effects of rotation and deducing the heat transfer performance from the experimental data, the nondimensional parameters listed in Table 1 were applied. The ranges of the experimental variables are also shown in this table. The experiments were performed by varying one parameter while keeping the others unchanged to determine the heat transfer performance along the streamwise position of the serpentine channel.

Experimental Facilities and Test Procedure

The experimental setup for determining the local heat transfer in a rotating three-passage heated serpentine channel was illustrated previously in Kuo and Hwang (1996). It consists of four major parts: coolant air supply, test section, motor with speed controller, and data acquisition system. Coolant air was supplied from a compressor through flow meters, ranging from 0.2 to 8.0 m^3/h, and rotary seal assembly to the test section.

The test section has two outward flow passages, the first and the third, and one inward flow passage, the second, along with three 180 degree turn sections. For distinguishing the local heat transfer rates due to the effects of the secondary flows, the wall heat conduction was deliberately suppressed by using material of low thermal conductivity to construct the channel walls. The four channel walls were directly plated by stainless-steel film heaters of thickness 0.02 mm. They were separately heated by electrical power supplies through slip rings to approximately approach a uniform heat flux boundary condition. A further discussion on the wall-condition parameter can be seen in Kuo and Hwang (1996). A thermocouple was located at the air inlet of the actively heated region for measuring the inlet coolant bulk temperature. A mixing chamber, installed with staggered rod bundles for providing a well mixed condition, was attached to the exit plane for measuring the outlet bulk temperature. At a certain axial location, the temperature on each wall was measured by a thermocouple firmly attached to a copper block for measuring the local regional average temperature at that location. The copper block is electrically insulated from the film heaters. The estimated temperature drop between the heat transfer surface and the thermocouple is less than 1 percent of the bulk temperature difference. The test section had a relatively small hydraulic diameter of 4 mm and a mean rotational radius of 180 mm. The mean rotational radius-to-hydraulic diameter ratio was 45, which was reasonably large as compared with the ratio in a gas turbine and an electrical machine. The detailed drawing of the test section was shown in Fig. 1. The model of test section was firmly encased in a stainless-steel rectangular case. The whole module was bolted perpendicularly to the rotating shaft.

When the temperature measurement was carried out at a large flow rate or a large rotational rate, the compressibility correction including the effects of flow speed and the rotational potential must be made. A maximum temperature correction of 5°C was found for Re = 20,000 ($M \approx 0.289$) and 0.8°C for Ω = 188 rad/s (2000 rpm) in the present study. The correction for the temperature readings, the calculation of heat transfer coefficients, and the heat loss estimation can also be referred to Kuo and Hwang (1996).

According to uncertainty analysis introduced by Kline and McClintock (1953), most of the estimated uncertainties in the rotational Nusselt number come from the local wall-to-coolant temperature difference and the rest of them from the net heat flux in the present study. It is found that for Re = 5000, the lowest wall-to-coolant temperature difference occurred at the exit of the third passage. At this position, a highest uncertainty of 15 percent was estimated. At other positions, the estimated uncertainties were less than 10 percent. When Reynolds numbers were higher than 10,000, the uncertainties at all the measured positions were less than 10 percent.

Results and Discussion

To set up a bench mark, experiments were first conducted to determine the local Nusselt numbers of the three flow passages for the case of Ω = 0. Figure 3 gives the results at Re = 5000, 10,000, and 20,000, and shows a comparison with the Dittus-Boelter correlation (Dittus and Boelter, 1930)

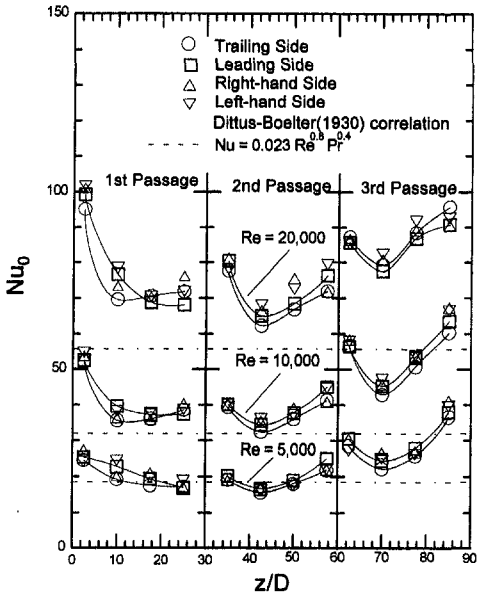

Fig. 3 Local heat transfer in the streamwise direction for the case of Ω = 0

$$Nu_f = 0.023\ Re^{0.8}\ Pr^{0.4} \quad (3)$$

which is for fully developed turbulent flow in a smooth circular pipe with uniform wall temperature condition. Note that the difference between the values of heat transfer coefficient in a circular pipe and a square duct is not significant. The Dittus-Boelter correlation has also been used for noncircular ducts (Holman, 1992) with Reynolds number evaluated on the basis of hydraulic diameter. The values of Nusselt number on the four sides of these flow passages increase with the increase in Re. Due to the entrance effect, the Nusselt number in the first flow passage decreases with the increase in z/D and approaches the fully developed value of Eq. (3) at around $z/D = 25$. The Nusselt numbers at the second and third passages do not show this tendency. At two ends of the second and third passages, the increase in the heat transfer coefficients is due to the combined effect of the 180 deg bend of coolant air flow and the radial wall heat conduction in these regions.

Figure 4 shows the rotation effect on the wall temperature distribution for Re = 5000, Ro = 0.034 and Re = 20000; Ro = 0.009. The wall temperature difference between the leading side and trailing side is caused by Coriolis force induced secondary flow. When the coolant air flow passes a 180 deg bend, the strength of secondary flow may be attenuated by the Coriolis force acting in the opposite direction and the centrifugal force in a direction normal to that of Coriolis force. Thus, the wall temperature difference between the leading sides and trailing sides of the second and third passages are smaller than that of the first passage. In the first and the third passages, the leading side temperature was higher than the trailing side temperature; however, in the second passage, the leading side temperature was lower than the trailing side temperature. This is due to that the direction of the Coriolis-induced cross-stream for the outward flow is opposite to that for the inward flow. Accordingly, the potential hot spots exist on the leading side for outward flow and on the trailing side for inward flow. This phenomena must be considered seriously for developing the cooling technology for the turbine blades. The bulk temperature $T_{b,z}$ was obtained by using an energy balance along the main flow direction. The net heat input at each main flow position was evaluated by subtracting the heat loss from the electrical power input. The heat loss depending on the wall temperature may be different from position to position. Therefore, the gradient of the bulk temperature along the flow in the third passage differs

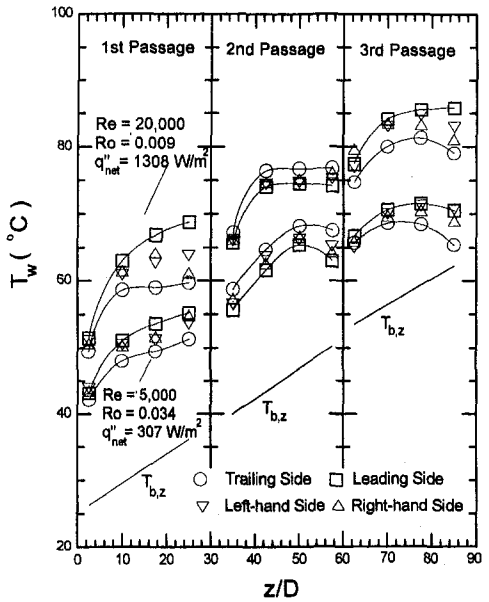

Fig. 4 Rotation effect on the streamwise temperature distribution

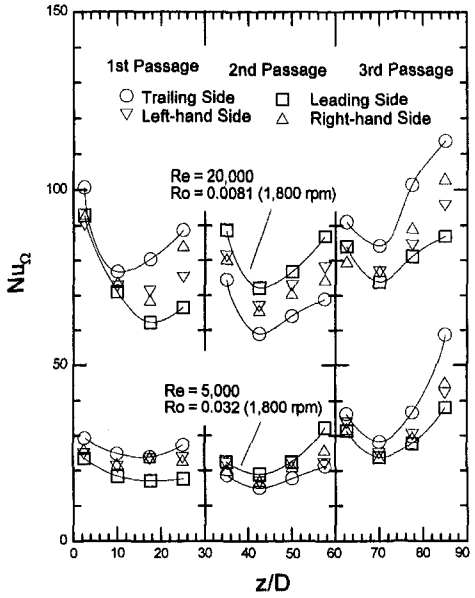

Fig. 5 Rotation effect on the streamwise heat transfer rate

from that in the first and second passages. It is also noted that the larger wall temperature is observed for Re = 20,000 because of using a higher wall heat flux in the test.

Since the wall heat flux was kept approximately constant, the local Nusselt number may be inversely proportional to the bulk temperature difference $T_{w,z} - T_{b,z}$ shown in Fig. 4. Figure 5 illustrates the rotation effect on the local Nusselt numbers. In the first flow passage, the Nusselt numbers along the trailing side are higher than that along the leading side. In the second flow passage, the heat transfer enhancement on the leading side is higher than that on the trailing side. The different values of heat transfer coefficients on the trailing and the leading sides are explained in Fig. 4. Figure 5 also shows that the heat transfer performance in the first flow passage is influenced more by rotation. The higher heat transfer rates at both ends of straight sections of the second and third passages are again observed as explained in Fig. 3. It is noted that the values of heat transfer of two side walls lie between those of the trailing and leading sides.

By varying the rotational speed, Fig. 6 reveals the effect of rotation number on the Nusselt number ratios for Re = 5000 and 20,000. The Nusselt number ratios on the trailing side for outward flow and on the leading side for inward flow are increased with the increase in the rotation number. This increased rotation number intensifies the Coriolis-induced cross-stream secondary flow and hence the heat transfer. The effects of rotation number on the heat transfer coefficients are attenuated by increasing the through-flow Reynolds number due to the forced convection effects.

Figure 7 shows the variations of the Nusselt number ratio with the rotation number in the streamwise direction at selected local positions for Re = 5000, 10,000, 15,000 and 20,000. In the entry region, the observed enhancement in heat transfer at smaller z/D is less than that at higher z/D. This result is consistent with the experiment of Metzger and Stan (1977) for entry region heat transfer in rotating radial tube. It is also noted that the Ro effect on the heat transfer rates in the second and third passage are suppressed. When the coolant air flow passes a 180 deg bend, the strength of secondary flow may be attenuated by the Coriolis force acting in the opposite direction and the centrifugal force in a direction normal to that of Coriolis force. After the cancellation of Coriolis force in the first and second passages, the secondary flow may restart in the third passage. It is seen that the difference between the values of heat transfer

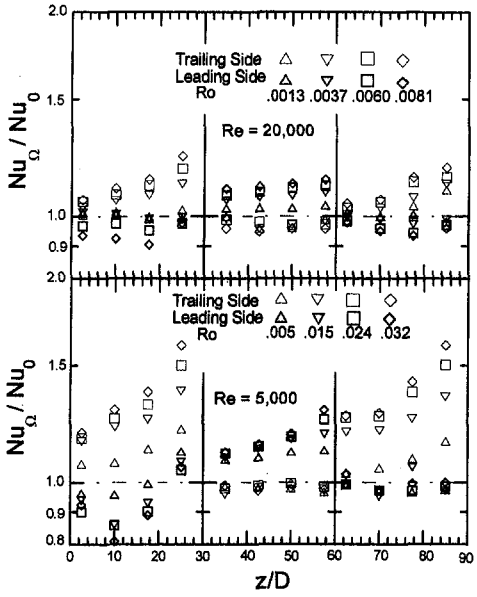

Fig. 6 Variations of Nusselt number ratio by varying rotational rate

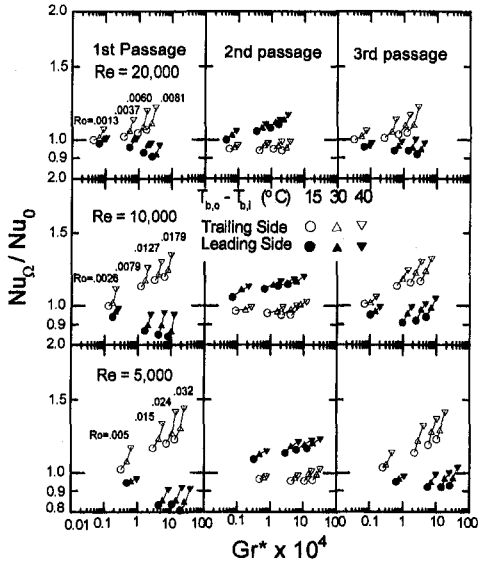

Fig. 8 Effect of centrifugal buoyancy on the heat transfer rate at $z/D = 10$

ratio at the leading and trailing sides is enlarged again in the third passage. The heat transfer characteristic shown in Fig. 7 gives a clue to the correlations of the results shown in Fig. 9.

The effect of centrifugal-buoyancy on the forced main flow is characterized by the rotational-buoyancy parameter, $Gr^* = Gr/Re^2$. As shown in Nomenclature, the rotational buoyancy parameter can be further decomposed into the thermal expansion coefficient, the wall-to-coolant temperature difference, the eccentricity and the local position, and the square of rotation number. The centrifugal force causes less dense fluid to move toward the axis of rotation and generates radial secondary flows. To highlight the salient features of the effect of centrifugal-buoyancy radial secondary flows, the experiments were conducted by keeping the outlet and inlet temperature difference

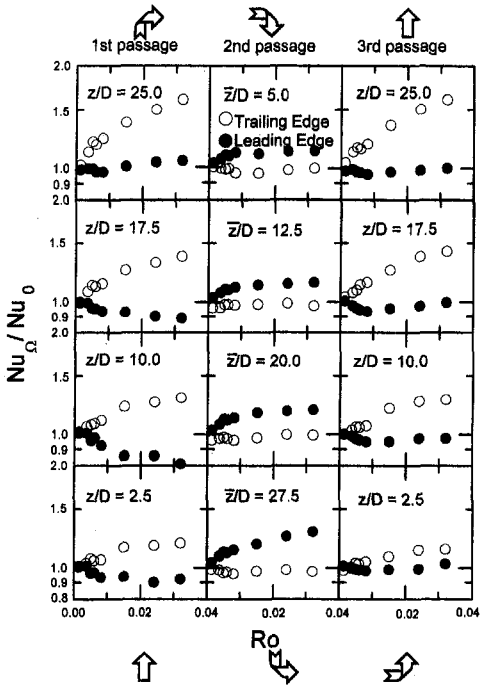

Fig. 7 Variations of Nu_Ω/Nu_0 with varying Ro along the streamwise direction

$T_{b,o} - T_{b,i}$ = 15, 30, 40°C while other operating parameters were held constant during each test. Since $T_{w,z} - T_{b,z} \sim W_0(\partial T/\partial z) \sim W_0(T_{b,o} - T_{b,i})$, varying the outlet and inlet temperature is as effective as varying the bulk temperature difference under the condition of constant mean coolant velocity.

Figure 8 shows the variations of Nusselt number ratio with the rotational Buoyancy parameters at axial location of z/D = 10. The increasing heat flux (or the outlet and inlet temperature difference) in the first passage increases the Nusselt number on both the trailing and the leading sides. The heat transfer enhancement is gradually decreased for a decreased Ro at higher Reynolds numbers. However, in the second passage, the heat transfer rates are not significantly influenced by the increasing temperature differences. The directions of main flow and buoyancy flow attribute to the difference of the results. In the outward flow passage, the direction of forced flow opposes the buoyancy flow (opposing flow) which introduces more disturbed flow in the turbulent flow regime. However, in the inward-flow passage, these two directions are parallel to each other (aiding flow). The acceleration of the flow suppresses the turbulence but increases the flow speed in the second passage. The combined effect on the heat transfer rate is obtained in Fig. 8. In the third passage, the centrifugal-buoyancy is seen to enhance the heat transfer again as in the first passage. These phenomena can be found by analyzing mixed convection of the buoyancy-induced opposing and aiding flows in a vertical heated tube (Buhr et al., 1974; Abdelmeguid and Spalding, 1979; Cotton and Jackson, 1987). With the increasing centrifugal-buoyancy parameter in the outward flow passage, the increased tendency on heat transfer was found by Wagner et al. (1991a, b), Morris and Ghavami-Nasr (1991), and Han and Zhang (1992).

Figure 9 shows the correlations of heat transfer data for the serpentine flow passage. Kuo and Hwang (1996) correlated the data of outward and inward flows on the leading and trailing sides of single straight tube, including those of Wagner et al. (1991a) and Han and Zhang (1992) for outward flow in a single passage. The present data for the first and third passages can also be correlated by using that of the single outward flow passage (Kuo and Hwang, 1996) within 1.15 percent rms differences as indicated. Due to the effects of the first passage and the 180 degree bend, the correlation of inward flow (Kuo and Hwang, 1996) cannot be used for the second passage. However, new correlations are derived to fit the data of the inward flow, and rms differences of 0.39 percent and 0.61 percent are found

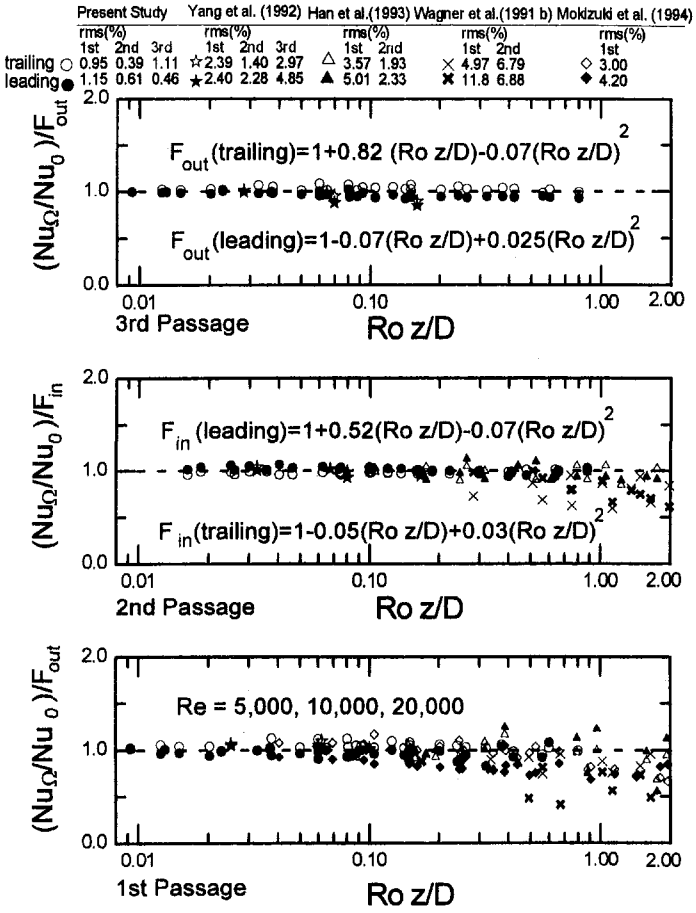

Fig. 9 Correlations of heat transfer data for $T_{b,o} - T_{b,i} = 30°C$

for the trailing and leading side, respectively. The experimental data of Wagner et al. (1991b) for uniform wall temperature and Yang et al. (1992), Han et al. (1993), and Mochizuki et al. (1994) for uniform wall heat flux are also plotted with these correlations. The data of Yang et al. (1992), Han et al. (1993), and Mochizuki et al. (1994) fit well generally with the present correlations on both the trailing and leading sides. Possibly due to the designed thermal boundary condition of constant wall temperature, the centrifugal-buoyancy on the leading side of the first passage and the trailing side of the second passage is weaker than that for constant wall heat flux. Therefore, the data of Wagner et al. (1991b) show lower heat transfer ratios than those of the present correlations. Note that the correlations in Fig. 9 are for the outlet and inlet bulk temperature difference $T_{b,o} - T_{b,i} = 30°C$.

Concluding Remarks

This investigation has presented the rotational effects on convective heat transfer in a rotating square serpentine channel with two radially outward flow and one radially inward flow passages. The channel walls were constructed out of material of low thermal conductivity to suppress the wall heat conduction in the circumferential direction. The walls were heated by four stainless steel film heaters of 0.02 mm thickness which were directly plated on the interior wall surfaces of the test section to achieve the uniform wall heat flux boundary conditions. The results obtained in this experiment are as follows:

1 For radially outward flow, the cross-stream secondary flow creates additional mixing to enhance the heat transfer on the trailing side. For radially inward flow this trend is reversed. The rotation effects are gradually attenuated with the increasing through-flow Reynolds number. The rotation effect on heat transfer for the second and third flow passages are relatively small compared with that for the first flow passage.

2 The rotation number indicates the effect of the Coriolis-induced cross-stream secondary flow on the forced main flow. The higher the rotation number is, the stronger the Coriolis-induced cross-stream secondary flow is. Due to the direction of the Coriolis force, the heat transfer enhancement is more prominent on the trailing side for radially outward flow and on the leading side for radially inward flow.

3 The effect of centrifugal-buoyancy was examined by varying the wall-to-coolant bulk temperature while keeping other operating parameters unchanged during each experiment. The rotational buoyancy parameter increases the heat transfer on both the trailing side and leading side for the first and third outward flow passages but has little influence on the heat transfer for the second inward flow passage.

4 To summarize the heat transfer results, the Nusselt number ratios on the trailing and leading sides for these three flow passages are correlated by four different equations. The equations for the first passage are the same as that for the single outward flow passage. But the correlations in the second passage are not the same as that for the single inward flow passage due to different inlet conditions. The correlations for the first passage can also be used for the third passage.

Acknowledgment

The authors wish to express their appreciation to the National Science Council, Taiwan (Grant No. NSC-81-0401-E007-04), for their financial support.

References

Abdelmeguid, A. M., and Spalding, D. B., 1979, "Turbulent Flow and Heat Transfer in Pipes with Buoyancy Effects," *Journal of Fluid Mechanics,* Vol. 94, pp. 383–400.

Buhr, H. O., Horsten, E. A., and Carr, A. D., 1974, "The Distortion of Turbulent Velocity and Temperature Profiles on Heating for Mercury in a Vertical Pipe," ASME JOURNAL OF HEAT TRANSFER, Vol. 96, pp. 152–158.

Cotton, M. A., and Jackson, J. D., 1987, "Calculation of Turbulent Mixed Convection in a Vertical Tube Using a Low-Reynolds-Numerical κ-ϵ Turbulence Model," presented at the 6th Symposium on Turbulent Shear Flows, Toulouse, France.

Dittus, P. W., and Boelter, L. M. K., 1930, "Heat Transfer in Automobile Radiators of the Tubular Type," *University of California Publications in Engineering,* Vol. 2, No. 13, pp. 443–461, reprinted in *Int. Comm. Heat Mass Transfer,* Vol. 12, pp. 3–22, 1985.

Han, J. C., and Zhang, Y., 1992, "Effect of Uneven Wall Temperature on Local Heat Transfer in a Rotating Square Channel with Smooth Walls and Radial Outward Flow," ASME JOURNAL OF HEAT TRANSFER, Vol. 114, pp. 850–858.

Han, J. C., Zhang, Y. M., and Kalkuehler, K., 1993, "Uneven Wall Temperature Effect on Local Heat Transfer in a Rotating Two-Pass Square Channel with Smooth Walls," ASME JOURNAL OF HEAT TRANSFER, Vol. 115, pp. 912–920.

Holman, J. P., 1992, *Heat Transfer,* 7th ed., McGraw Hill, Singapore, pp. 316–317.

Kline, S. J., and McClintock, F. A., 1953, "Describing Uncertainties in Single Sample Experiments," *Mechanical Engineering,* January, pp. 3–8.

Kuo, C. R., and Hwang, G. J., 1996, "Experimental Studies and Correlations of Radially Outward and Inward Air-Flow Heat Transfer in a Rotating Square Duct," ASME JOURNAL OF HEAT TRANSFER, Vol. 118, pp. 23–30.

Metzger, D. E., and Stan, R. L., 1977, "Entry Region Heat Transfer in Rotating Radial Tubes," AIAA Paper No. 77–189.

Mochizuki, S., Yamawaki, S., and Yang, W. J., 1994, "Heat Transfer in Serpentine Flow Passages with Rotation," *ASME Journal of Turbomachinery,* Vol. 116, pp. 133–140.

Morris, W. D., and Ayhan T., 1979 "Observations on the Influence of Rotation on Heat Transfer in the Coolant Channels of Gas Turbine Rotor Blades," *Proc. Inst. Mech. Engrs.,* Vol. 193, pp. 303–311.

Morris, W. D., and Ghavami-Nasr, G., 1991, "Heat Transfer in Rectangular Channel With Orthogonal Mode Rotation," *ASME Journal of Turbomachinery,* Vol. 113, pp. 339–345.

Wagner, J. H., Johnson, B. V., and Hajek, T. J., 1991a, "Heat Transfer in Rotating Passages With Smooth Walls and Radial Outward Flow," *ASME Journal of Turbomachinery,* Vol. 113, pp. 42–51.

Wagner, J. H., Johnson, B. V., and Kopper, F. C., 1991b, "Heat Transfer in Rotating Serpentine Passages With Smooth Walls," *ASME Journal of Turbomachinery,* Vol. 113, pp. 321–330.

Yang, W. J., Ahang, N, and Chiou, J., 1992, "Local Heat Transfer in a Rotating Serpentine Flow Passage," *ASME Journal of Heat Transfer,* Vol. 114, pp. 354–361.

The Effects of Prandtl Numbers on Local and Average Convective Heat Transfer Characteristics in Helical Pipes

R. C. Xin

M. A. Ebadian
ASME Fellow.

ebadian@eng.fiu.edu
Hemispheric Center for Environmental Technology,
Florida International University,
Miami, FL 33199

To investigate the effects of the Prandtl number and geometric parameters on the local and average convective heat transfer characteristics in helical pipes, experiments with three different fluids—air, water, and ethylene glycol—were carried out on five uniformly heated helical pipes. The test sections were made from 22.9 mm I.D. and 10.2 mm I.D. 304 stainless steel pipes. The ratios of the pipe diameter and pitch to coil diameter (d/D and b/D) ranged from 0.0267 to 0.0884 and 0.20 to 2.56, respectively. The peripheral and average, fully developed Nusselt numbers were evaluated in the experiments. Experimental findings indicate that after two turns ($X > 2$) the temperature distributions along the wall are almost parallel to the linear fluid bulk temperatures, and all dimensionless peripheral wall temperatures are nearly identical, implying that both the flow and temperature distribution within the helical pipes are fully developed. These results reveal that the peripheral Nusselt number varies significantly for higher Prandtl numbers and Dean numbers in the laminar flow region. A new set of empirical expressions for the average fully developed Nusselt number has therefore been regressed based on the present data and some data from previous investigations. No obvious effects of the coil pitch or torsion were observed in the scope of this investigation.

Introduction

Because of the existence of secondary flow, the special transition phenomena, and high heat transfer effectiveness, fluid flow and heat transfer in curved and helical pipes have frequently been studied numerically and experimentally in the last several decades (Yang and Chang, 1993; Yamamoto et al., 1995; Wang and Andrews, 1995). Previous experimental studies have focused on the average pressure drop and heat transfer rate (Seban and McLaughlin, 1963; Mori and Nakayama, 1965; Schmidt, 1967; Dravid et al., 1971; Kalb and Seader, 1972; Janssen and Hoogendoorn, 1978). Some early theoretical and numerical investigations described the secondary flow and its effects on the pressure drop and heat transfer (Dean, 1928; Kalb and Seader, 1972; Patankar et al., 1974). Shah and Joshi (1987) summarized most of the results and recommended some correlations to predict the friction factor and Nusselt number. Numerical investigations were then made on the combined effect of the centrifugal and buoyancy forces on the flow and heat transfer (Futagami and Aoyama, 1988; Prusa and Yao, 1982). Recent studies have focused on the torsion effect (Austin and Soliman, 1988; and Yamamoto et al., 1995).

Few of the experimental investigations on the heat transfer in curved and helical pipes have discussed the effect of the Prandtl number (Dravid et al., 1971; Janssen and Hoogendoorn, 1978). Dravid et al. (1971) measured the heat transfer of five liquids from a uniformly heated copper tube. The peripheral wall temperature was found to be essentially uniform. However, this study was somewhat limited in that only one coil was tested, and the heat transfer was not fully developed for most of the test cases where the oscillations of the axial local Nusselt number had not totally decayed. Janssen and Hoogendoorn (1978) later measured the local Nusselt number variation along the flow direction using constant heat flux boundary condition in a Prandtl number range of 20 to 450. The average Nusselt number for three different fluids was also measured using steam condensation as a heating method at Reynolds numbers less than 1000. The results and correlations reported by these investigators were inconsistent regarding the Prandtl number dependence. No systematic investigations of the effect of Prandtl number on heat transfer in curved and helical pipes for different geometries and a large Dean number range have been reported.

The heat transfer relations previously reported show a significant diversity in heat transfer coefficient calculations even for the same boundary condition, and especially in the case of high Prandtl and Reynolds numbers. This often makes it very difficult to make a good prediction for heat transfer in practical applications.

More flow structure information derived from numerical simulation and velocity measurement has been obtained. However, data on local heat transfer, especially the peripheral distribution, are very limited in the literature (Mikaila and Poskas, 1990; Kalb and Seader, 1983).

In this experimental investigation, five stainless steel coil configurations were tested for three different fluids (air, distilled water, and ethylene glycol) to study the effect of the Prandtl number on the local and average heat transfer characteristics. The effects of torsion (pitch) and curvature were also addressed.

Experimental Facility and Procedure

Figure 1 presents a schematic view of the flow loop featuring its main components and instrumentation. A three-meter-long straight entrance section was used to provide a well developed and stable inlet velocity distribution. Two sets of flow meters were installed to enable the measurement of different fluids and different flow rate ranges. Inlet and outlet plenums were used to dampen the flow fluctuations. A relief valve was positioned on the top of the inlet plenum to discharge the air in the flow system. A control valve

Contributed by the Heat Transfer Division for publication in the JOURNAL OF HEAT TRANSFER. Manuscript received by the Heat Transfer Division June 28, 1996; revision received April 3, 1997; Keywords: Augmentation & Enhancement; Forced Convection; Heat Exchangers. Associate Technical Editor: A. S. Lavine.

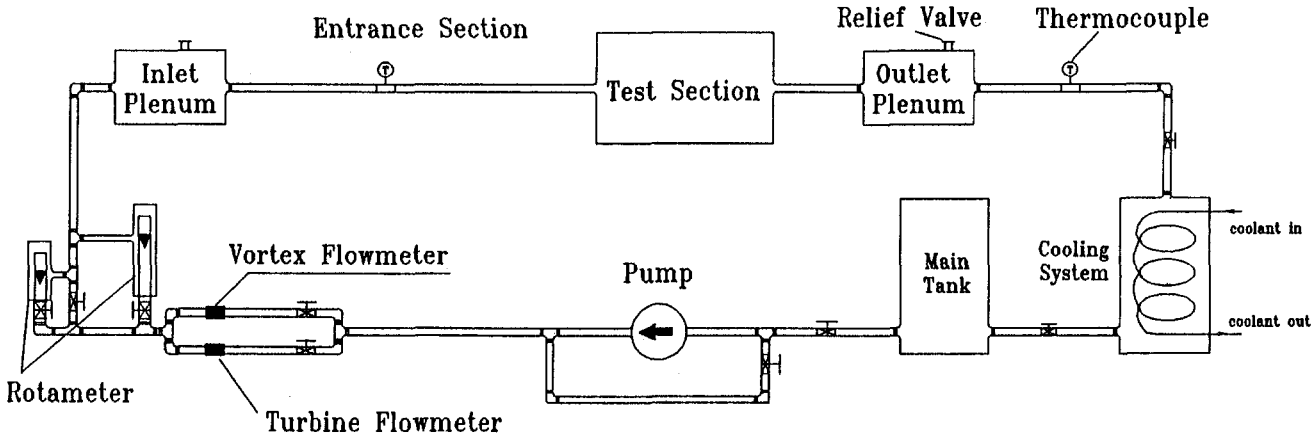

Fig. 1 Schematic view of the test loop

was placed beyond the exit of the test section to ensure that the working fluid would operate at a pressure higher than atmospheric pressure, thus preventing the formation of air bubbles in the system downstream of the inlet plenum. To maintain the inlet temperature, a cooling system was used to remove the heat added to the test section during the experiment. The air flow experiments were conducted in the system described by Awwad et al. (1995).

Five stainless steel helical test sections were used in the experiments. The test sections were constructed of 22.9 mm I.D. and 10.2 mm I.D. 304 stainless steel pipes. The ratios of the pipe diameter and pitch to coil diameter (d/D and b/D) ranged from 0.0267 to 0.0884, and 0.20 to 2.56, respectively. Initially, coils with ten turns were fabricated to ensure the full development of the fluid flow. However, after several measurements it was found that five turns of the coil sufficed to conduct the experiments and measure the fully developed heat transfer coefficient. The details of the geometry of the helical pipes are illustrated in Fig. 2. The geometric parameters of the test sections are provided in Table 1.

The test sections were heated directly by passing an electric current through the coils. The constant heating current was provided by a direct current (DC) power supply that allowed for adjusting the output current to vary the heating power. The boundary condition of a uniform heat flux could reasonably be assumed for the current test. The heat flux of the series of experiments ranged from 1.6 to 11.0 kW/m^2. To minimize the variation of the fluid properties and the effect of natural convection, the bulk temperature increases during the experiments were strictly controlled within the range of 5° to 20°C. The average thermal properties of the working fluid were maintained almost constant for each test run by a combination of adjusting the inlet temperature and varying the heat flux.

During the experiments, the tube wall temperature distribution was measured along the heated length utilizing E-type thermocouples. Starting from the entrance of the coil, two thermocouples were installed at every one-quarter turn (90 deg), one on the coil inner wall, and one on the coil outer wall. In the fully developed region of the coil ($X > 2$), four to eight thermocouples were installed in all four cross sections in one specified turn to measure the peripheral temperature distributions as well as the axial wall temperature distributions. The test coils were wrapped and insulated with fiberglass insulation tape.

Before installation, all thermocouples were calibrated against a precision thermometer and demonstrated an accuracy of ±0.1°C. After the thermocouples were installed, the test section was covered with three layers of one-half-inch thick fiberglass insulation material. Prior to testing, the thermocouples on the insulated test section were calibrated again in situ at three fixed temperatures between 20°C and 60°C. This re-calibration was accomplished by passing preheated water at a high flow rate through the test section without electric heating. Under such conditions, readings of all wall temperatures and the inlet and outlet bulk temperatures should be equal or very similar. A criterion of ±0.2°C was set for all readings. If the difference was higher than that criterion, small corrective differentials, repair, or replacement of the thermocouple was performed. All thermocouples were connected to a Hewlett Packard data acquisition system, and all temperatures were recorded automatically.

Based on the measurements of different variables, the major parameter uncertainties were estimated by the method recommended by Moffat (1988). The results are summarized in Table 2. The uncertainties of flow rate, temperature, and heat flux

Nomenclature

b = coil pitch, m
D = coil diameter, m
De = Dean number = $\mathrm{Re}(d/D)^{1/2}$
d = inner diameter of the tube, m
d_o = outer diameter of the tube, m
g = gravitational acceleration, m/s^2
k = fluid thermal conductivity, W/(m°C)
L = tube length of one turn of the coil, m
Nu = Nusselt number = $\alpha d/k$
q'' = heat flux, W/m^2
Pr = Prandtl number = α/ν
Ra = Rayleigh number = $\beta q'' d^4/(k\nu^2)\mathrm{Pr}$
Re = Reynolds number = $U_m d/\nu$
T = temperature, °C
U_m = mean fluid velocity, m/s
X = dimensionless distance = x/L
x = distance from the curve entrance of the helical pipe, m

Greek Symbols

α = heat transfer coefficient, W/(m^2 °C)
β = coefficient of thermal expansion, 1/°C
ϕ = dimensionless temperature = $(T_w - T_{\text{outer}})/(T_{\text{inner}} - T_{\text{outer}})$
θ = dimensionless temperature = $(T_w - T_{b,\text{in}})/(T_{b,\text{out}} - T_{b,\text{in}})$
ν = fluid kinematic viscosity, m^2/s
ρ = fluid density, kg/m
ψ = peripheral angle

Subscripts

av = peripheral average
b = fluid bulk
in = inlet of the test section
inner = inner coil wall ($\psi = 3\pi/2$)
out = outlet of the test section
outer = outer coil wall ($\psi = \pi/2$)
w = coil wall

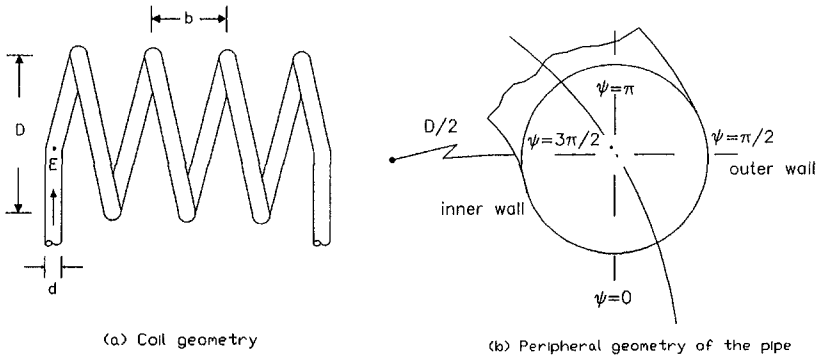

Fig. 2 Geometry of the test sections

resulted from the accuracy of the flow meter, thermocouples, and ampere/volt meters. The uncertainties of the thermoproperties were determined by comparing the correlations used in data reduction with the tabulated values in handbooks plus the uncertainties of the original data if available.

Results and Discussion

In the current investigation, the temperature distributions along the coils were measured. The fully developed average Nusselt number and Nusselt number distribution in the peripheral direction were evaluated. The test sections were also oriented at different angles—0 deg (horizontal), 60 deg (inclined), and 90 deg (vertical). To identify the buoyancy force effect, the peripheral temperature distribution in the fully developed region was examined. If the distribution is symmetric about the center line from the inner coil wall ($\psi = 3\pi/2$) to the outer coil wall ($\psi = \pi/2$) of the cross section, the buoyancy effect can be considered negligible. The flow regime map from Prusa and Yao (1982) was also used to make judgments. It was found that because of the high Prandtl number and large tube diameter, most cases of water and ethylene glycol flow in the fifth test section were in the mixed convection regime. Due to the limited scope of this paper, these mixed convection results will not be presented here. However, the Rayleigh number is still indicated in the figures. It is defined as:

$$\mathrm{Ra} = (g\beta q'' d^4)/(k\nu^2)\mathrm{Pr} \qquad (1)$$

The Wall Temperature Distributions. Both the inner and outer coil wall temperatures were measured along the coil for different Reynolds or Dean numbers for different working fluids. The following definitions were used for the dimensionless variables, X and θ:

$$X = x/L \quad \text{and} \quad \theta = \frac{T_w - T_{b,\mathrm{in}}}{T_{b,\mathrm{out}} - T_{b,\mathrm{in}}} \qquad (2)$$

where x denotes the distance from the entrance of the helical pipe; L represents the tube length of one turn of the test section; T_w is the wall temperature at the location of x; and $T_{b,\mathrm{in}}$ and $T_{b,\mathrm{out}}$ are the inlet and outlet bulk temperatures, respectively.

Table 2 Experimental uncertainties

Pipe diameter	2%	Viscosity	1.0%
Flow rate	0.1%	Velocity	1.5%
Temperature	±0.2%	Reynolds number	2.4%
Heat flux	5%	Dean number	2.6%
Density	0.25%	Nusselt number	12%
Conductivity	1.0%		

Figure 3 illustrates the typical wall temperature distributions along the inner and outer walls of the horizontally oriented test section for air, water, and ethylene glycol (Pr = 0.7, 5, and 120). It can be noted from the results that the achievement of the fully developed temperature field is indicated by the inner and outer wall temperatures rising steadily parallel to the linearly increasing fluid bulk temperature. Some wall temperature fluctuations that may result from the flow instability caused by secondary flow can be observed in Fig. 3(*c*).

The typical peripheral wall temperature distributions at $X > 2$ for three working fluids are shown in Fig. 4 which demonstrates that the peripheral temperature distributions are roughly sinusoidal and identical in dimensionless form $[\phi = (T_w - T_{\mathrm{outer}})/(T_{\mathrm{inner}} - T_{\mathrm{outer}})]$ for the different working fluids. This indicates that the flow patterns within the pipe are almost identical and that the temperature distribution is symmetric about the centerline from the inner coil wall ($\psi = 3\pi/2$) to the outer coil wall ($\psi = \pi/2$) of the cross section. As reported by Kalb and Seader (1972), if the buoyancy force is significant, the highest and lowest temperature locations should shift clockwise from the centerline.

Table 1 Geometrical parameters of the test sections and working fluids

Test Sect.	d (mm)	d_o (mm)	D (mm)	b (mm)	d/D	b/D	# of Turns	Fluids Tested
1	10.16	12.7	381	381.00	0.0267	1.000	7	air, water and ethylene glycol
2	10.16	12.7	381	76.00	0.0267	0.200	10	air, water and ethylene glycol
3	10.16	12.7	127	325.00	0.0800	2.560	10	air, water and ethylene glycol
4	10.16	12.7	127	76.00	0.0800	0.600	10	air, water and ethylene glycol
5	22.90	25.4	259	62.50	0.0884	0.241	5	air

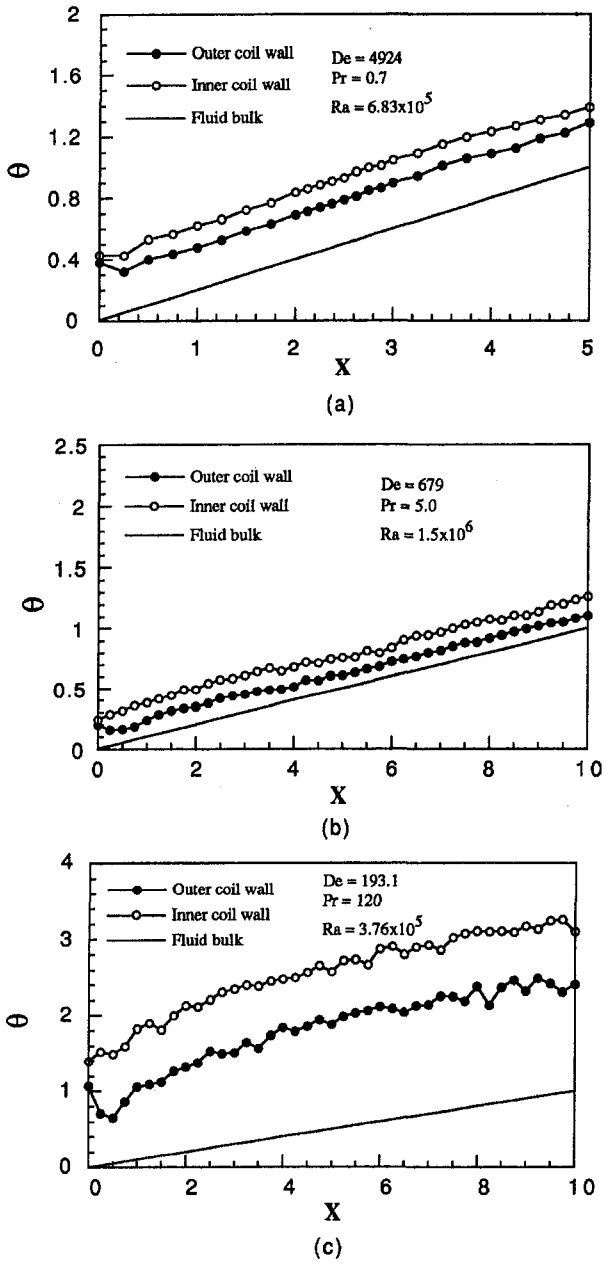

Fig. 3 Dimensionless wall temperature distributions along the coil

These findings have confirmed that natural convection can be neglected. Average wall temperature, according to the sinusoidal distribution, was applied to calculate the average Nusselt number in the fully developed region of the helical pipe. Test results indicate that the temperature difference between the inner and outer wall increases as the Reynolds (or Dean) number increases. This is consistent with the findings reported by Seban and McLaughlin (1963).

Peripheral Nusselt Number Distribution. For the constant heat flux boundary condition, the local Nusselt number is defined as:

$$\mathrm{Nu}_{\psi} = \frac{q'' d}{k(T_w - T_b)} \tag{3}$$

where T_w is the local wall temperature and T_b is the fluid bulk temperature at the same cross section. In the fully developed region, the average Nusselt number can be determined by the following equation:

$$\mathrm{Nu} = \frac{q'' d}{k\Delta T_{av}} \tag{4}$$

where ΔT_{av} is the average temperature difference at the fully developed region.

The distributions of the ratio of the peripheral Nusselt numbers to their average value for three different kinds of working fluids (Pr = 0.7, 5, and 120) are presented in Fig. 5, where $\psi = \pi/2$ and $\psi = 3\pi/2$ represent the outer and inner wall of the coil, respectively, as shown in Fig. 2. It is demonstrated that the variation of the peripheral Nusselt number can be seen only for a Dean number as high as 2000 for a low Prandtl number fluid such as air (Pr = 0.7), whereas for a higher Prandtl number fluid such as ethylene glycol (Pr = 120), the variation of the peripheral Nusselt number can be clearly observed for a Dean number of 29.

In the laminar flow region, the variation of the relative Nusselt number becomes stronger as the Dean number and Prandtl number increase. For laminar flow, as with the main velocity profile, the secondary flow distorts the temperature profiles, pushing the temperature peak toward the outer wall of the tube; this results in a higher heat transfer coefficient at the outer wall than at the inner wall. This distortion is much stronger for high Prandtl number fluids than for low Prandtl number fluids, as indicated by the temperature distributions presented by Shah and Joshi (1987). Increasing the Dean number therefore augments secondary flow, while increasing the Prandtl number augments thermal convection. However, in the turbulent flow region, the variation of the relative Nusselt number becomes stronger as the Dean number increases for a very low Prandtl number fluid such as air (Pr = 0.7) (Fig. 5(*a*)), whereas it decreases as the Dean number increases for a higher Prandtl number fluid (Pr = 5) (Fig. 5(*b*)). For a higher Prandtl number fluid, as the Dean number increases, the secondary flow becomes stronger; however, the main flow velocity profile becomes flat; and the average Nusselt number increases. As the combined effect, the relative Nusselt number variation decreases as the Dean number increases. This phenomenon should be true for the ethylene glycol flow, but due to the high viscosity and heat flux limitations, turbulent flow could not be reached in the present experimental system for ethylene glycol. The variations of the peripheral Nusselt number for different Prandtl numbers have been regressed and are listed in Table 3.

Figure 6 illustrates the peripheral Nusselt number for different Prandtl numbers for a fixed Dean number (De ≈ 1000). These results verify that for laminar flow, as the Prandtl number increases, the peripheral Nusselt number distribution changes

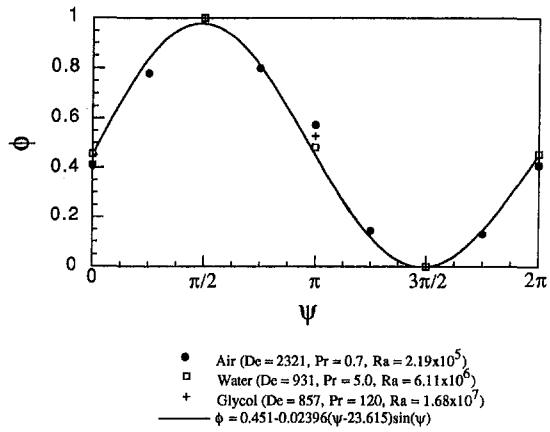

Fig. 4 Universal peripheral dimensionless temperature curve for different Dean and Prandtl numbers

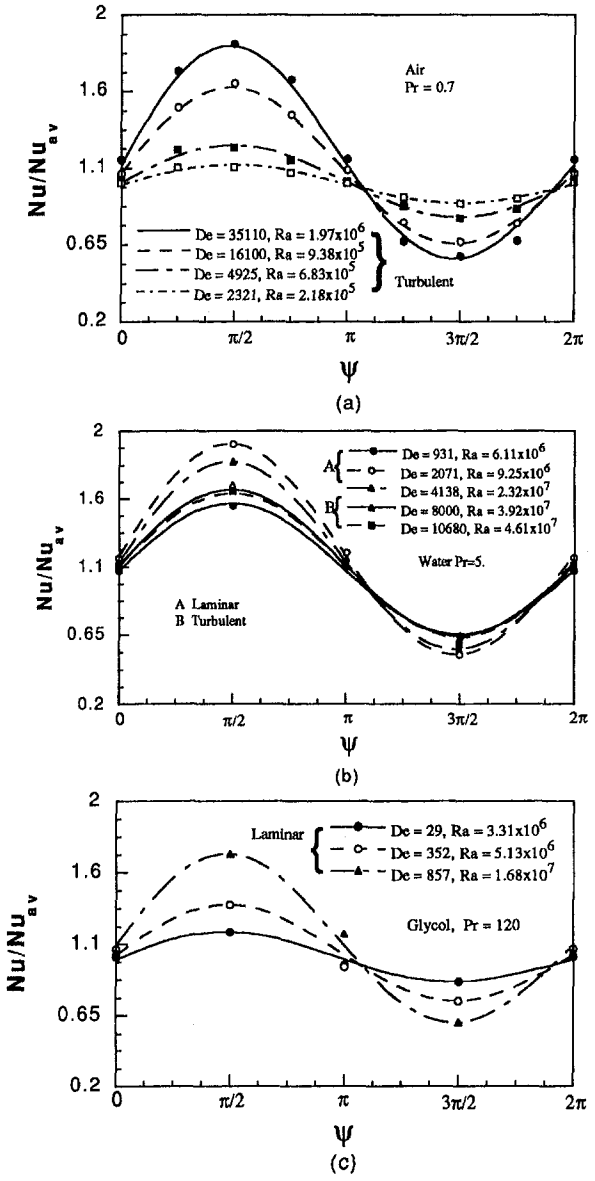

Fig. 5 Peripheral relative Nusselt number distributions for different fluids

vigorously, especially the values near the outer coil wall. Since the thermal boundary layer on the outer wall is much thinner than that on the inner wall, a small shift of the peak of the temperature distribution to the outer wall causes the temperature gradient to increase dramatically near the outer wall. This is

Table 3 Regressed expression for the peripheral Nusselt numbers

Fluid	De	Nu/Nu_{av}
air	35116	1.0-0.043(ψ-16.1)sinψ
	16100	1.0-0.026(ψ-19.2)sinψ
	4925	1.0-0.004(ψ-54.7)sinψ
	2321	1.0-0.002(ψ-64.6)sinψ
water	10680	1.0-0.0042(ψ-106)sinψ
	8000	1.0-0.011(ψ-43.1)sinψ
	4138	1.0-0.028(ψ-23.2)sinψ
	2071	1.0-0.027(ψ-25.4)sinψ
	931	1.0-0.008(ψ-52.3)sinψ
ethylene glycol	857	1.0-0.026(ψ-21.5)sinψ
	352	1.0-0.008(ψ-38.0)sinψ
	29	1.0-0.011(ψ-17.4)sinψ

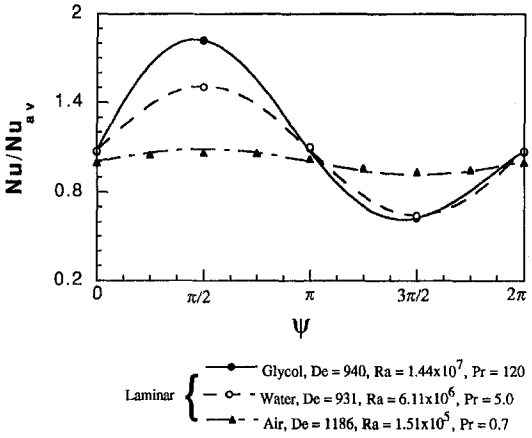

Fig. 6 Comparison of the peripheral relative Nusselt number distributions for different Prandtl numbers at a fixed Dean number

consistent with the temperature distribution results reported by Shah and Joshi (1987).

Fully Developed Nusselt Number. The wall temperature distributions recorded in these experiments show that the flow within the coils was fully developed after a certain distance from the entrance of the curved portion. The average Nusselt number in the fully developed flow region is evaluated by Eq. (3). In order to obtain an accurate correlation, it is useful to examine the effect of each parameter on the average Nusselt number.

Test Section Orientation. Figure 7 shows the results of water flow in Test Section 4 with different orientation angles. It can be observed that the orientation position has almost no effect on the average Nusselt number of the fully developed region in the present experimental range since the inertial and centrifugal forces are dominant and overwhelm the gravity and buoyancy forces. These findings verify that natural convection can be neglected.

Coil Pitch. Torsion may have a significant effect on the flow structure and friction factor at very large torsion, as indicated by Yamamoto et al. (1995). As shown in Fig. 8, no apparent pitch or torsion effect on the average Nusselt number for different Prandtl numbers can be observed, at least within the range tested in this study. This is consistent with the conclusion reported by Austen and Soliman (1988) based on their experimental findings for water and the theoretical findings of Manlapaz and Churchill (1981).

Curvature. Curvature is an essential parameter of a helical pipe. It creates the secondary flow inside the pipe and causes the main flow velocity profile to shift to the outer wall of the coil. Curvature also causes fluid flow in helical pipes to have a

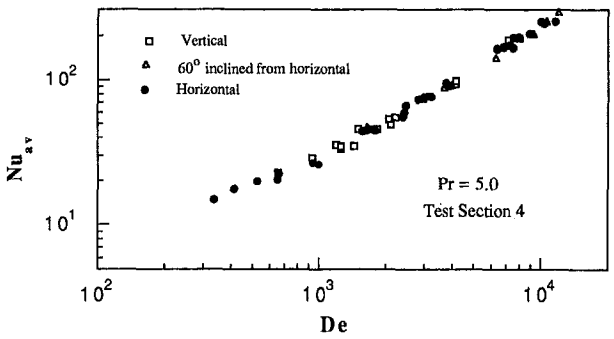

Fig. 7 Effect of inclination angle

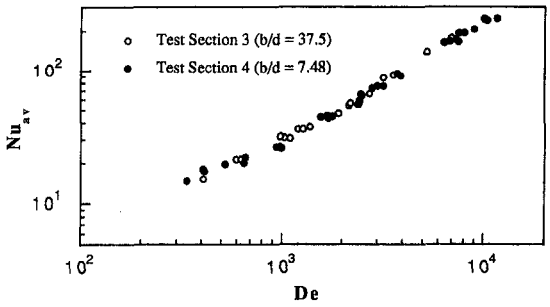

Fig. 8 Effect of pitch (D/d = 12.5)

higher heat transfer coefficient. The effect of curvature can be seen in Fig. 9 in which a correlation for straight pipes is also presented (Gnielinski, 1976). It can be observed that the higher the curvature ratio (d/D), the larger the average Nusselt number, based on the same torsion and Reynolds number. This effect can be correlated into a Dean number in the laminar flow region. Nevertheless, the Nusselt number is dependent on the curvature ratio in addition to the Dean number in the turbulent flow region, as described in the correlations below.

Prandtl Number Effect And Correlations. As previously stated, several correlations have been proposed for the Nusselt number prediction; however, they show significant diversity with respect to the heat transfer coefficient calculations even in the case of the same boundary condition, and especially in the case of a high Prandtl number. The authors believe that this diversity results from the fact that either natural convection was significant or the flow was not fully developed in some of the experimental data. After examining most experimental data in the literature, some data in which either natural convection was significant or the flow was not fully developed were disregarded. A well-selected data set and our new experimental data (Fig. 10) were regressed to propose a new set of correlations. Our new regressions for both laminar and turbulent regimes are the following:

$$\mathrm{Nu}_{av} = (2.153 + 0.318\ \mathrm{De}^{0.643})\mathrm{Pr}^{0.177}$$

$$20 < \mathrm{De} < 2000, \quad 0.7 < \mathrm{Pr} < 175, \quad 0.0267 < d/D < 0.0884 \tag{5}$$

$$\mathrm{Nu}_{av} = 0.00619\ \mathrm{Re}^{0.92}\mathrm{Pr}^{0.4}(1 + 3.455d/D)$$

$$5 \times 10^3 < \mathrm{Re} < 10^5, \quad 0.7 < \mathrm{Pr} < 5, \quad 0.0267 < d/D < 0.0884. \tag{6}$$

These correlations are based on more and better-selected data and cover most of the practical application parameter ranges.

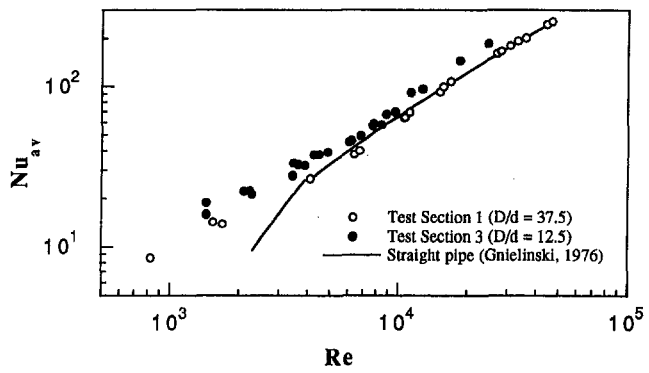

Fig. 9 Effect of curvature (b/d = 32–37.5)

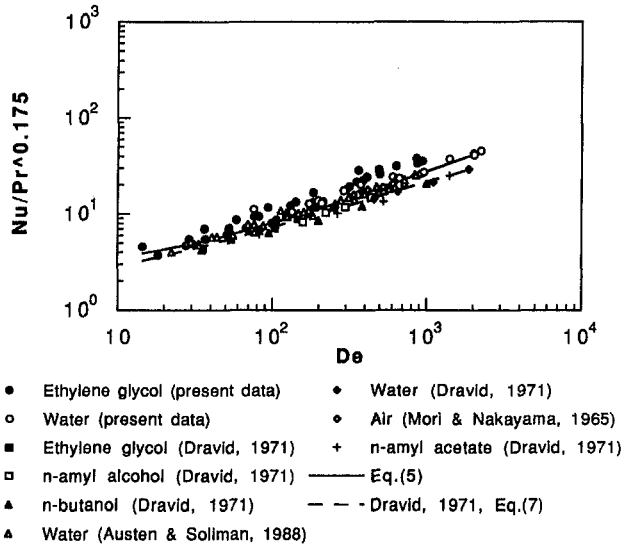

(a) Laminar flow

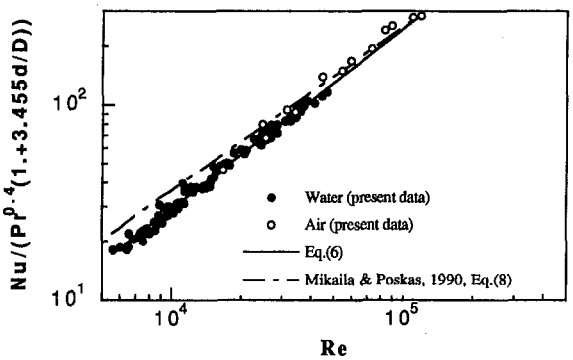

(b) Turbulent flow

Fig. 10 Fully developed average Nusselt number results and correlations

The root mean square (RMS) deviations of these correlations with the experimental data are 18 percent and 6 percent, respectively. In the correlation for laminar flow, the dependence of Prandtl number agrees quite well with the data for the high Prandtl number provided by Dravid et al. (1971). It can be concluded that the average Nusselt number is proportional to $\mathrm{Pr}^{0.177}$. All of our data are consistent with the results for air and water reported by Mori and Nakayama (1965) and Austen and Soliman (1988), which are roughly 20 percent higher than the prediction given by Dravid et al. (1971). The correlation proposed by Dravid et al. (1971) follows:

$$\mathrm{Nu} = (0.76 + 0.65\ \mathrm{De}^{1/2})\mathrm{Pr}^{0.175}. \tag{7}$$

The results in the turbulent regime have also been formulated and compared to the expression provided by Mikaila and Poskas (1990):

$$\mathrm{Nu} = 0.0266[\mathrm{Re}^{0.85}(d/D)^{0.15} + 0.225(D/d)^{1.55}]\mathrm{Pr}^{0.4}. \tag{8}$$

Because of the high viscosity and Prandtl number, no further results for ethylene glycol were obtained in the turbulent regime in this experiment.

Concluding Remarks

In this study, five helical pipes with different torsions and curvature ratios were tested for three kinds of fluid to investigate the local and average heat transfer characteristics of forced

convection in helical pipes. The experimental results suggest the following:

1 After two turns ($X > 2$), the temperature distributions along the wall are almost parallel to the linear fluid bulk temperatures, and the peripheral wall temperature distributions for different Dean number and Prandtl number can be represented as one-dimensionless single curve in the laminar flow regime. These findings suggest that the flow and temperature within the helical pipes are fully developed.
2 For laminar flow, as the Dean and Prandtl numbers increase, the peripheral variation of the relative Nusselt number becomes stronger. In the turbulent flow region this variation becomes stronger as the Dean number increases for a low Prandtl number fluid (air), but it decays as the Dean number increases for a higher Prandtl number fluid (water).
3 The effects of torsion and coil orientation were not observed in our experimental range.
4 A new set of correlations of fully developed average Nusselt number is suggested in Eqs. (5) and (6). These correlations are based on more and better selected data, and cover most practical application parameter ranges.

Acknowledgment

The results presented in this paper were obtained in the course of research sponsored by the National Science Foundation under Grant No. CTS-9017732.

References

Awwad, A., Xin, R. C., Dong, Z. F., Ebadian, M. A., and Soliman, H. M., 1995, "Measurement and Correlation of the Pressure Drop in Air-Water Two-Phase Flow in Horizontal Helical Pipes," *Int. J. Multiphase Flow,* Vol. 21, No. 4, pp. 607–619.

Austen, D. S., and Soliman, H. M., 1988, "Laminar Flow and Heat Transfer in Helically Coiled Tubes with Substantial Pitch," *Expl. Thermal Fluid Sci.,* Vol. 1, pp. 183–194.

Dean, W. R., 1928, "The Stream-Line Motion of Fluid in a Curved Pipe," *Philos. Mag., Ser. 7,* Vol. 5, No. 30, pp. 673–695.

Dravid, A. N., Smith, K. A., Merrill, E. W., and Blian, P. L. T., 1971, "Effect of Secondary Fluid Motion on Laminar Flow Heat Transfer in Helically Coiled Tubes," *AIChE J.,* Vol. 17, No. 4, pp. 1114–1122.

Futagami, K., and Aoyama, Y., 1988, "Laminar Heat Transfer in a Helically Coiled Tube," *Inter. J. Heat Mass Transfer,* Vol. 31, No. 2, pp. 387–396.

Gnielinski, V., 1976, "New Equations for Heat and Mass Transfer in Turbulent Pipe and Channel Flow," *Int. Chem. Eng.,* Vol. 16, pp. 359–368.

Janssen, L. A. M., and Hoogendoorn, C. J., 1978, "Laminar Convective Heat Transfer in Helical Coiled Tubes," *Int. J. Heat Mass Transfer,* Vol. 21, pp. 1197–1206.

Kalb, C. E., and Seader, J. D., 1972, "Heat and Mass Transfer Phenomena for Viscous Flows in Curved Circular Tubes," *Int. J. Heat Mass Transfer,* Vol. 15, pp. 801–817.

Kalb, C. E., and Seader, J. D., 1983, "Entrance Region Heat Transfer in a Uniform Wall Temperature Helical Coil with Transition from Turbulent to Laminar Flow," *Int. J. Heat Mass Transfer,* Vol. 26, No. 1, pp. 23–32.

Manpalaz, R. L., and Churchill, S. W., 1981, "Fully Developed Laminar Convection From a Helical Coil," *Chem. Eng. Commun.,* Vol. 9, pp. 185–200.

Mikaila, V. A., and Poskas, P. S., 1990, "Local Heat Transfer in Coiled Tubes at High Heat Fluxes," *Heat Transfer—Soviet Research,* Vol. 22, No. 6, pp. 713–727.

Moffat, R. J., 1988, "Describing Uncertainties in Experimental Results," *Expl. Thermal Fluid Sci.,* Vol. 1, pp. 3–7.

Mori, Y., and Nakayama, W., 1965, "Study on Forced Convective Heat Transfer in Curved Pipes (1st Report, Laminar Region)," *Int. J. Heat Mass Transfer,* Vol. 8, pp. 67–82.

Patankar, S. V., Pratap, V. S., and Spalding, D. B., 1974, "Prediction of Laminar Flow and Heat Transfer In Helically Coiled Pipes," *J. Fluid Mech.,* Vol. 62, pp. 539–551.

Prusa, J., and Yao, L. S., 1982, "Numerical Solution for Fully Developed Flow in Heated Curved Tubes," *J. Fluid Mech.,* Vol. 123, pp. 503–522.

Schmidt, E. F., 1967, "Wärmeübergang and Drukverlust in Rohrschlangen," *Chem. Ing. Tech.,* Vol. 13, pp. 781–789.

Seban, R. A., and McLaughlin, E. F., 1963, "Heat Transfer in Tube Coils with Laminar and Turbulent Flow," *Int. J. Heat Mass Transfer,* Vol. 6, pp. 387–395.

Shah, R. K., and Joshi, S. D., 1987, "Convective Heat Transfer in a Curved Duct," Chap. 5, in *Handbook of Single-Phase Convective Heat Transfer,* S. Kakac, R. K. Shah, and W. Aung, eds., Wiley, New York.

Wang, J. W., and Andrews, J. R. G., 1995, "Numerical Simulation of Flow in Helical Ducts," *AIChE J.,* Vol. 41, No. 5, pp. 1071–1080.

Yamamoto, K., Akita, T., Ikeuchi, H., and Kita, Y., 1995, "Experimental Study of the Flow in a Helical Circular Tube," *Fluid Dynamics Research,* Vol. 16, No. 4, pp. 237–249.

Yang, R., and Chang, S. F., 1993, "Numerical Study of Fully Developed Laminar Flow and Heat Transfer in a Curved Pipe with Arbitrary Curvature Ratio," *Inter. J. Heat Fluid Flow,* Vol. 4, No. 2, pp. 138–145.

Experimental Study of the Effect of Transverse Oscillation on Convection Heat Transfer From a Circular Cylinder

C.-H. Cheng

H.-N. Chen

Department of Mechanical Engineering,
Tatung Institute of Technology,
Taipei, Taiwan,
Republic of China

W. Aung
Fellow, ASME
waung@nsf.gov

Division of Engineering Education
and Centers,
National Science Foundation,
4201 Wilson Boulevard,
Arlington, VA 22230

The present study is concerned with heat transfer characteristics of forced convective flows over a transversely oscillating cylinder. The effect of oscillation of the cylinder on heat transfer coefficient and flow pattern is evaluated by experimental measurement. A modified transient test method and a flow visualization technique are employed to determine the heat transfer coefficient and to observe the flow pattern, respectively, for various dimensionless oscillation frequencies (S_c), dimensionless oscillation amplitudes (A/D), and Reynolds numbers (Re). The ranges of these parameters considered in this study are $0 \leq S_c \leq 0.65$, $0 \leq A/D \leq 0.628$, and $0 \leq Re \leq 4000$. Results show that the heat transfer coefficient can be significantly increased by the oscillation of the cylinder. Two effects that enhance the heat transfer performance are found, namely, the lock-on effect and the turbulence effect. A maximum of 34 percent increase in heat transfer is found within the parameter ranges considered in this study. Agreement of the present data is found with previous numerical studies; however, an existing approximate method, which ignores the lock-on phenomenon but which is commonly used to estimate the effect of oscillation on heat transfer, is found to be inapplicable in this study.

Introduction

Heat transfer between a stationary circular cylinder and its surrounding viscous fluid stream has been a problem of great interest in the past several decades. This problem is frequently encountered in thermal devices such as heat exchangers, nuclear reactors, and hot-wire anemometers. The understanding of the vortex-shedding phenomenon behind the cylinder is one of the fundamental challenges to fluid-dynamics researchers and, hence, has been pursued extensively. It is recognized that the Reynolds number is a dominant parameter governing the flow pattern, and in the range $5 < Re < 50$, there exists a pair of steady and symmetric laminar vortices behind the cylinder. For $Re > 50$, the flow acquires an unsteady and asymmetric feature. The vortex pairs appear to periodically shed downstream, and a vortex street is formed in the wake of the cylinder. The predominant frequency of vortex shedding which is referred to as the natural shedding frequency (f) may be measured to determine the Strouhal number. The Strouhal numer, defined by fD/u_0, is essentially a function of Reynolds number; nevertheless, it is nearly a constant with a value of 0.2 over a range of Reynolds number varying from 300 to 10^4 (Blevins, 1977). A review of the literature pertinent to the unsteady wake is provided by Griffin and Hall (1991).

As the cylinder is forced to oscillate transversely in a direction normal to the flow stream, a nonlinear interaction occurs, particularly as the cylinder oscillation frequency (s_c) approaches the natural shedding frequency (f). This interaction involves two major phenomena. Firstly, in the wake, the natural shedding frequency is suppressed and the vortex shedding occurs at the same frequency as that of the cylinder, and the resonance will be maintained over a certain range of forced frequency. Secondly, the drag force is appreciably increased with the maximum value found near the midpoint of the resonance regime. This is known as the lock-on phenomenon that has been studied by many authors (for example, Griffin and Ramberg, 1974; Hurlbut, Spaulding and White, 1982; Chilukuri, 1987; Karniadakis and Triantafyllou, 1989), and the resonance regime is often referred to as the lock-on regime. However, when the cylinder is forced to oscillate at a frequency higher than the lock-on frequencies, vortices will again be shed at the natural shedding frequency, independent of the oscillation of the cylinder.

Since the oscillation of the cylinder has a profound influence on vortex shedding and on the drag force exerted on the cylinder, one may reasonably expect that the effect of cylinder oscillation on heat transfer will be likewise appreciable. To evaluate this effect, Martinelli and Boelter (1938) oscillated a circular cylinder of 19 mm diameter in water and found a 500 percent increase in heat transfer for free convection.

For forced convection, Kezios and Prasanna (1966) reported a 20 percent increase in the average heat transfer coefficient from a cylinder vibrating transversely in cross-flow. Saxena and Laird (1978) considered a 22 mm diameter cylinder transversely oscillating in an open water channel for a flow at Re = 3500. They observed a 60 percent increase in heat transfer. In an earlier study performed by Sreenivasan and Ramachandran (1961), a copper cylinder, 8.7 mm in diameter, was forced to oscillate transversely in an air stream with a velocity varying from 5.78 to 28.05 m/s. The double amplitude of oscillation ranged from 0.75 to 3.2 cm and the oscillation frequency from 200 to 2800 cycles/min. No appreciable change in the heat transfer coefficient was observed. Leung, Ko, and Ma (1981) found that for $Re < 15{,}000$, heat transfer may be enhanced as either oscillation frequency or amplitude is increased; however, the oscillation effect becomes weaker as the Reynolds number is increased. On the other hand, numerical solutions have also been presented in a few reports. Karanth et al. (1994) provided the data for the flows over an in-line or transversely oscillating

Contributed by the Heat Transfer Division for publication in the JOURNAL OF HEAT TRANSFER. Manuscript received by the Heat Transfer Division September 20, 1995; revision received January 17, 1997; Keywords: Flow Visualization, Forced Convection, Measurement Techniques. Associate Technical Editor: S. Ramadhyani.

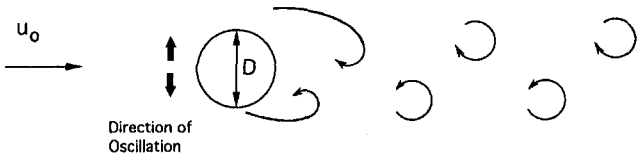

Fig. 1 A circular cylinder oscillating in a uniform stream

cylinder under a condition that exactly lies within the lock-on regime at Re = 200. Cheng, et al. (1997) predicted both the lock-on and unlock-on flows at Re < 300 and found a 13 percent increase in the heat transfer caused by the lock-on effect. To the authors' knowledge, the numerical studies by Karanth et al. (1994) and Cheng et al. (1997) probably are the only published numerical reports regarding the effects of oscillation on the heat transfer. Although limited to low Reynolds number flows, these two studies have provided numerical data which are valuable toward understanding the augmentation mechanism for heat transfer.

Based on the aforementioned studies, it may be concluded that the oscillation effect on heat transfer can be significant under certain conditions. The existing information, however, is still insufficient for practical application since the mechanisms of heat transfer enhancement are not fully understood. Moreover, some inconsistency remains in the data reported by the various authors.

The present study is thus conducted to investigate experimentally the heat transfer enhancement mechanisms caused by cylinder oscillation and to provide the first confirmation of the numerical predictions on the lock-on effects presented by Karanth et al. (1994) and Cheng et al. (1997). For these purposes, a modified version of the transient test method adopted by Sreenivasan and Ramachandran (1961), Scott (1970), and Ahmed et al. (1982) is employed in this study for measuring the heat transfer coefficient. To clearly observe the flow pattern, especially the lock-on phenomenon, the flow field is visualized by using smoke generated by means of kerosene oil. A comparison is provided between the present experimental data and those from the previous studies.

A schematic diagram for the present problem is shown in Fig. 1. A circular cylinder of diameter D is oscillating transversely in a uniform fluid stream. Three dominant parameters are varied in this investigation. The Reynolds number, representing quantitatively the strength of the air flow, ranges from 0 to 4000 (with air velocity u_0 ranging from 0 to 4 m/s). According to the existing information (e.g., Blevins, 1977), the transition range from unsteady laminar to turbulent flow in the wake of a stationary cylinder is $150 \leq \mathrm{Re} \leq 300$. The wake may become fully turbulent when $300 \leq \mathrm{Re} \leq 300{,}000$. However, the turbulence may appear earlier when the cylinder is oscillating. At a fixed Reynolds number, the turbulence intensity in the wake is increased with either the frequency or amplitude. Therefore, it is expected that the critical Reynolds number for the turbulence to occur will be reduced when the cylinder is oscillating. The range of the Reynolds number considered in this study is $0 \leq \mathrm{Re} \leq 4000$, which is designed to be located in the transition range so that both the lock-on and turbulence effects may be observed.

The second parameter is the dimensionless frequency of oscillation of the cylinder (S_c), which is varied in the range $0 \leq S_c \leq 0.65$ (with oscillation frequency s_c varied from 0 to 25 Hz). The third parameter, the dimensionless oscillation amplitude (A/D), is in the range $0 \leq A/D \leq 0.628$. The diameter of the cylinder is fixed at 16 mm.

Experimental Apparatus and Procedure

Experimental Apparatus. The layout of the wind tunnel is given in Fig. 2. In order to visualize the flow, the test section of this suction-type wind tunnel, which has a 300 mm × 300 mm cross section, is made with transparent perspex plates of 10 mm thickness. An entrance contraction section and a two-stage honeycomb section are placed in front of the test section. The honeycomb section contains about 4000 subchannels, each with a length-to-diameter ratio of 20. The air velocity may be varied in the range 0 ~ 4.0 m/s by means of a frequency regulator connected to the fan motor.

The time histories of the temperatures of the cylinder, measured by three K-type thermocouples distributed at three different longitudinal locations along the cylinder, are recorded in a personal computer for later data analysis. The thermocouples are mounted on the downstream face of the cylinder to eliminate possible disturbance to the incoming fluid flow. The cylinder is made of pure copper so that the entire cylinder is maintained at a uniform temperature in the cooling process. Bakelite caps are attached to both ends of the cylinder to reduce heat losses from the ends. Figure 3 shows the layout of the test cylinder as well as the installation and the longitudinal locations of the thermocouples. The length and the diameter of the cylinder are 250 mm and 16 mm, respectively, with a length-to-diameter ratio greater than 15. Temperature measurements along the longitudinal direction on the cylinder show that the error associated with a two-dimensional assumption is within 1.4 percent. The cylinder is heated by an electric heater until a sufficiently high temperature is reached. Both the cylinder and the electric heater are initially placed inside the wind tunnel; however, once the cylinder is hot enough, the heater is taken out from the wind tunnel and the test starts. The electric heater is composed of two symmetrical upper and lower halves. Each half is composed of a heating plate and a copper block. The copper blocks, inserted between the heating plates and the cylinder, are designed to yield uniform heating.

Nomenclature

A = amplitude of oscillation of cylinder
A_c = surface area of cylinder
Bi = Biot number, $\bar{h}D/k_c$
c = heat capacity of cylinder material
D = cylinder diameter
f = natural shedding frequency of fluid
h = heat transfer coefficient
$\bar{h}$ = time-averaged heat transfer coefficient
k_c = thermal conductivity of cylinder
k_f = thermal conductivity of fluid
L = cylinder length
m = mass of cylinder
Nu = overall Nusselt number, $\bar{h}D/k_f$
Nu_{PL} = peak value of Nusselt number in lock-on regime
Nu_0 = overall Nusselt number for a stationary cylinder
Re = Reynolds number, u_0D/ν
s_c = frequency of oscillation of cylinder
S_c = dimensionless frequency of oscillation of cylinder, s_cD/u_0
S_{c0} = dimensionless natural shedding frequency or dimensionless oscillation frequency at the peak of lock-on regime
St = Strouhal number, fD/u_0
t = time
T = temperature of cylinder
T_a = ambient temperature
T_i = initial temperature of cylinder
T_f = film temperature, $(T_i + T_a)/2$
$\bar{T}$ = time-averaged temperature
u_0 = free stream velocity
V_V = vibrational velocity of cylinder
V_R = resultant velocity

Greek Symbol

ν = kinematic viscosity of fluid

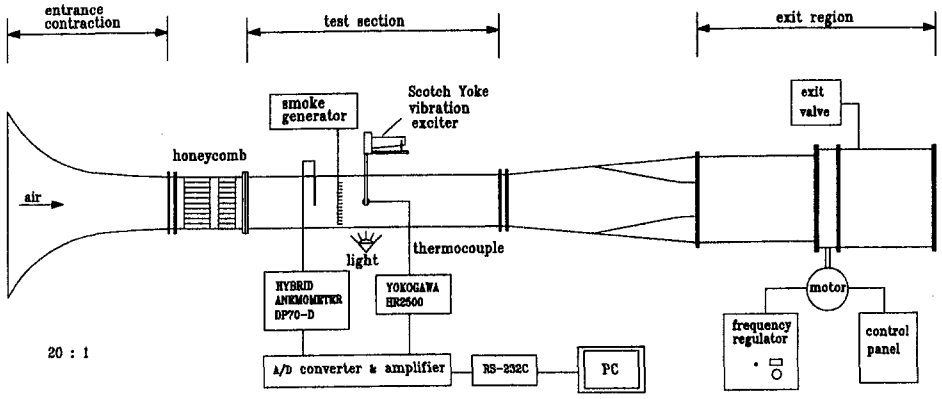

Fig. 2 Schematic diagram of the test system

The free stream velocity in the test section is measured by a hot-wire velocimeter that has been carefully calibrated and is valid for velocity measurement in the range of 0.1 ~ 50 m/s. A Scotch-Yoke oscillation exciter is designed to carry the cylinder and produce a sinusoidal oscillation of 0 ~ 10 mm in amplitude and 0 ~ 20 Hz in frequency. The arm of the exciter is extended into the test section from the top to oscillate the cylinder. The turbulence intensity inside the test section is obviously influenced by the oscillation of the cylinder even though care has been taken to reduce the disturbance from the oscillation exciter and the fan motor. The intensity of turbulence measured at the inlet of the test section is approximately 0.005 at Re = 4000, S_c = 0.3, and A/D = 0.628.

Numerous methods have been developed for air flow visualization. Smoke flow visualization is one of the most effective techniques that has been widely used in low Reynolds number flows. In this study, smoke is produced in a smoke generator by vaporizing kerosene oil and introducing it into the flow through a smoke rake placed in front of the test section. The photographs of the visualized flow patterns are taken by using a camera and a light unit installed outside the test section.

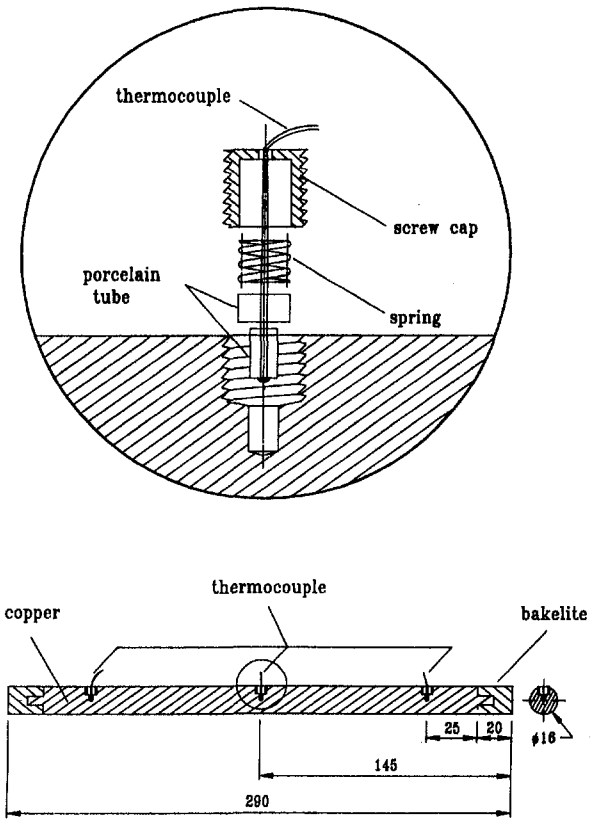

Fig. 3 Layout of cylinder and the installation of thermocouples

Measurement Procedure. The frequency regulator and the exit valve are adjusted to set the air velocity for a desired Reynolds number. The cylinder is initially heated by an electric heater to reach a sufficiently high temperature (say 85°C). The Scotch-Yoke oscillation exciter imparts a sinusoidal oscillation to the cylinder at a desired oscillation condition, and then the cooling process starts. The personal computer receives the temperature and velocity data from the thermocouples and the velocimeter, respectively, and records the thermal history of the cylinder until the latter is cooled to the ambient temperature. The values of $\bar{h}$ and then Nu are calculated for each test by using the temperature data recorded in the computer. The frequency and amplitude of the oscillation can be varied and displayed digitally. For flow visualization, the smoke generator is switched on. It only takes several minutes for the initiation of the kerosene smoke. The smoke is fed to the smoke rake placed in front of the test section. Clear smoke filaments may be obtained by properly adjusting the mass flow rate of the smoke and the position of the rake.

Data Reduction. The transient test method adopted in this study for determining the heat transfer coefficients is a modified version of the method used by Sreenivasan and Ramachandran (1961), Scott (1970), and Ahmed et al. (1982). The theory underlying this method has been described in these previous studies; however, some modifications are needed when applying the method to the measurement of heat transfer from a periodically oscillating body.

In describing the cooling process of an oscillating cylinder, it is convenient to separate the temperature and the heat transfer coefficient each into a time-averaged quantity and a periodically fluctuating component. Denoting the time-averaged temperature and time-averaged heat transfer coefficient by $\bar{T}$ and $\bar{h}$, and their fluctuations by T' and h', respectively, one may write:

$$T(t) = \bar{T}(t) + T'(t) \tag{1a}$$

$$h(t) = \bar{h}(t) + h'(t) \tag{1b}$$

with

$$\bar{T} = \frac{1}{\Delta t}\int_0^{\Delta t} T dt \tag{2a}$$

$$\bar{h} = \frac{1}{\Delta t}\int_0^{\Delta t} h dt \tag{2b}$$

where the time interval Δt must be taken sufficiently large compared with the time scale of an oscillation cycle; however, in order to provide enough data points for further analysis, Δt should not be too large. Typically, in this study, Δt varies from 5 to 20 seconds depending on the oscillation frequency, covering a number of oscillation cycles. The magnitudes of the fluctuation terms T' and h' in the above equations were evaluated numerically by Cheng et al. (1997). If there is no vibration, $T' = h' = 0$, and the problem becomes that of a stationary cylinder.

It is important to note that for the physical conditions considered in this study, the Biot number Bi is of order 10^{-3}. This implies that the internal conductive resistance of the cylinder is much lower than the external convective resistance. Recall that, generally, if Bi < 0.1, the temperature distribution becomes nearly uniform throughout a solid. It is commonly accepted that the error caused by such a "lumped-capacity-body" assumption is less than five percent provided that Bi is less than 0.1 (Ozisik, 1985).

The energy equation for the cylinder at any instant in the cooling process is

$$mc\frac{dT}{dt} + hA_c(T - T_a) = 0. \tag{3}$$

Taking the time average for Eq. (3) and introducing Eqs. (1a) and (1b) into the result lead to:

$$mc\frac{d\bar{T}}{dt} + \bar{h}A_c(\bar{T} - T_a) = 0 \tag{4}$$

in which the second-order fluctuation term has been neglected and the time averages of the fluctuation quantities,

$$\frac{1}{\Delta t}\int_0^{\Delta t} T'dt \quad \text{and} \quad \frac{1}{\Delta t}\int_0^{\Delta t} h'dt$$

have been set equal to zero.

The initial condition of Eq. (4) is

$$\bar{T} = T_i \quad \text{at} \quad t = 0 \tag{5}$$

where T_i is the initial temperature of the cylinder provided by the electric heater before a test starts.

Equation (4) is integrated and, by using Eq. (5), we obtain the following:

$$\ln(\bar{T} - T_a) = -\frac{\bar{h}A_c}{mc}t + \ln(T_i - T_a). \tag{6}$$

The measured time history of the time-averaged temperature of the cylinder is used in conjuction with the theoretical solution given by Eq. (6) to determine the time-averaged heat transfer coefficient $\bar{h}$ for each case. Once the time-averaged heat transfer coefficient ($\bar{h}$) is obtained, the overall Nusselt number given by

$$\mathrm{Nu} = \frac{\bar{h}D}{k_f} \tag{7}$$

can be calculated, and the dependence of the overall Nusselt number on Re, S_c, and A/D may then be evaluated. Note that all the properties of the fluid and the copper cylinder appearing in the above equations are evaluated at the film temperature

$$T_f = \frac{(T_i + T_a)}{2}. \tag{8}$$

Experimental Results and Discussion

Heat Transfer Performance. For each of the more than two hundred data runs executed, the overall Nusselt number has been evaluated. The experimental results are first verified by comparing them with the existing information. The overall Nusselt number for the stationary cylinders is compared with the data provided by McAdams (1954). As shown in Fig. 4, Nu is treated as a function of Re. It is observed that the present experimental results are in good agreement with the existing data. Based on the present experimental results, a correlation formula expressing the relationship between the Nusselt number and the Reynolds number for a stationary cylinder is obtained as

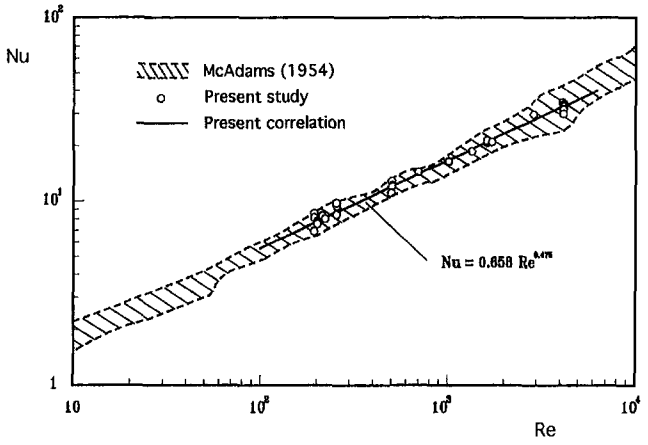

Fig. 4 Nusselt number as a function of Reynolds number for stationary cylinder

$$\mathrm{Nu} = 0.658\ \mathrm{Re}^{0.475} \tag{9}$$

which is valid for $100 \le \mathrm{Re} \le 4000$. Note that Eq. (9) does not reflect the Prandtl number effect; therefore, it may be applied only to air flows.

Figure 5 shows the influence of oscillation frequency (S_c) and amplitude (A/D) of the cylinder on the overall Nusselt number at Re = 200. The measured data are correlated by means of a least square regression method described by Benedict (1969). Note that the data at $S_c = 0$ are associated with the stationary cylinder. It is observed that at $A/D = 0.138$, it is only when the cylinder oscillates at a frequency close to the natural shedding frequency (in this case, $S_c = 0.16$), that the Nusselt number is appreciably increased. Outside this regime the heat transfer is almost unaffected by the oscillation. A similar feature is found also for $A/D = 0.314$. This phenomenon illustrates the fact that at Re = 200 basically the entire flow field is unsteady but laminar as long as the cylinder is forced

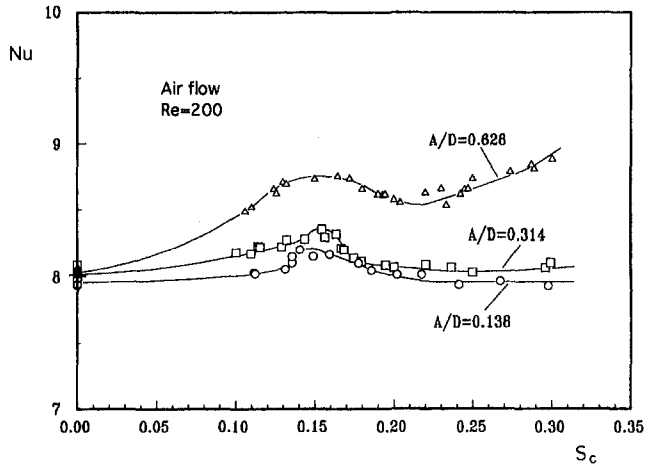

Fig. 5 Variation of Nusselt number with dimensionless oscillation frequency and amplitude at Re = 200

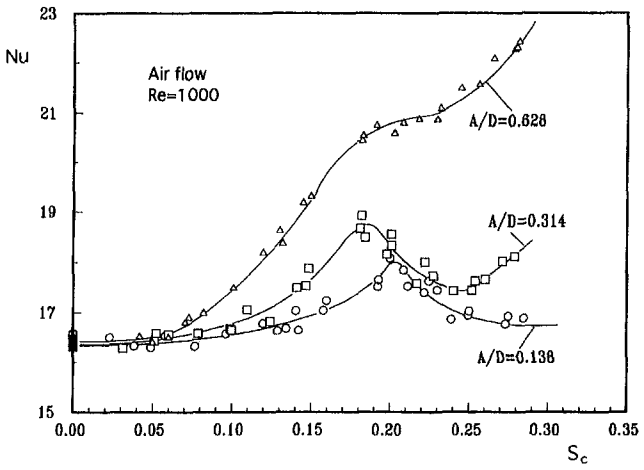

Fig. 6 Variation of Nusselt number with dimensionless oscillation frequency and amplitude at Re = 1000

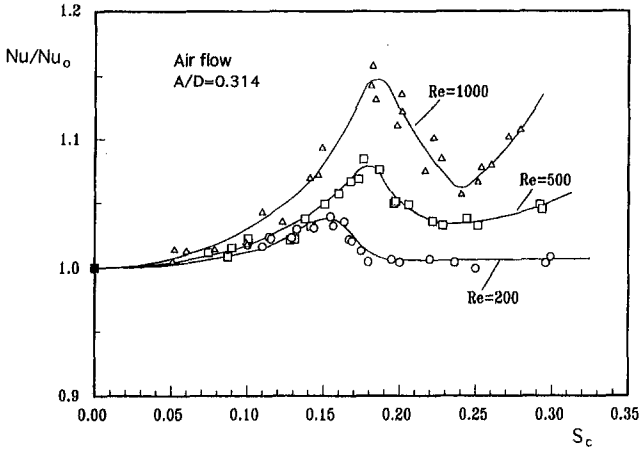

Fig. 7 Variation of Nusselt number with dimensionless oscillation frequency under various Reynolds numbers at A/D = 0.314

to oscillate at a small amplitude. In these situations the lock-on effect is the dominant mechanism enhancing the heat transfer. However, when the cylinder is forced to oscillate at a sufficiently high amplitude or frequency the wake of the cylinder may become turbulent. Note that when the amplitude is elevated to 0.628, the curve still exhibits a peak value in the lock-on regime; however, here, as the frequency is increased past the natural shedding frequency ($S_c > 0.23$), the magnitude of the Nusselt number first decreases and then increases to an even higher value. This indicates a second heat transfer augmenting mechanism that appears at higher frequencies and amplitudes. The most likely factor leading to the increase of the heat transfer is turbulence, which may be caused by a higher relative velocity between the fluid and the cylinder. The turbulent wake of the cylinder oscillating at higher frequency will be observed later by means of the flow visualization technique. It is important to note that the turbulence effect may produce a greater heat transfer increase than the lock-on effect.

To provide further insight into the heat transfer augmenting mechanisms, Fig. 6 shows the experimental results of Nu at various values of S_c and A/D for Re = 1000. As in Fig. 5, the lock-on effect plays a dominant role in heat transfer enhancement in the low-amplitude case ($A/D = 0.138$); however, when A/D is increased to 0.314, the effect of turbulence becomes important when S_c is greater than approximately 0.25. Moreover, at $A/D = 0.628$, the turbulence effect dominates the heat transfer behavior of the cylinder throughout the entire range of S_c, and as a result no lock-on effect can be found. Further, in this particular case Nu increases monotonically with S_c and a maximum of 34 percent increase in heat transfer is reached at $S_c = 0.3$.

In Fig. 5 it is found that for $A/D = 0.138$, the peak value of the lock-on regime occurs at a frequency slightly lower than that observed for $A/D = 0.314$. However, as will be seen in the section on uncertainty analysis, the uncertainty in dimensionless frequency (S_c) may reach 10.21 percent at Re = 200. The unavoidable uncertainty may be one of the possible factors leading to the slight difference in peak values for $A/D = 0.138$ and $A/D = 0.314$. On the other hand, from Fig. 6, which shows the data for a higher Reynolds number (Re = 1000), it seems that the trend is reversed and for $A/D = 0.138$ the peak occurs at a frequency higher than that for $A/D = 0.314$. However, the heat transfer mechanisms are very different for these two cases. Obviously, for $A/D = 0.138$ the lock-on effect is the only mechanism enhancing heat transfer, while for $A/D = 0.314$, turbulence appears to be the second major factor. The mixed effect of lock-on and turbulence in the intermediate regime is an area that requires further studies. Therefore, the inversion in the peak values for $A/D = 0.138$ and $A/D = 0.314$ found in Figs. 5 and 6 cannot yet be fully explained, and one should be very careful in drawing any conclusion at this time.

Figure 7 shows the dependence of the overall Nusselt number on the oscillation frequency at $A/D = 0.314$ under various Reynolds numbers. Plotted in Fig. 7 is the quantity Nu/Nu_0, where Nu_0 denotes the overall Nusselt number for the stationary cylinder case. Three observations may be made with regard to Fig. 7. Firstly, it is obvious that at the lowest Reynolds number (Re = 200), no change in Nu can be seen outside the lock-on regime; however, at Re = 1000, the turbulence effect produces a significant increase at high-frequency cases, even outside this regime. Secondly, if S_c and A/D are fixed, the Nusselt number increases with the Reynolds number. Thirdly, the value of S_c, corresponding to the peak of lock-on regime of each curve, indicates the natural shedding frequency (S_{c0}), which is a function of the Reynolds number. The measured data for S_{c0} at different Reynolds numbers are displayed in Fig. 8. These data are found to be close to the existing information on the natural shedding frequency provided by Blevins (1977).

Detailed information on the increase in the Nusselt number caused by the lock-on effect is given in Table 1. This table shows the peak values of the Nusselt number in the lock-on region, in terms of Nu_{PL}/Nu_0, at different Reynolds numbers and amplitudes. A maximum of 16 percent increase in the Nusselt number at Re = 1000 and $A/D = 0.314$ is observed. As noted previously, the turbulence effect may produce a higher

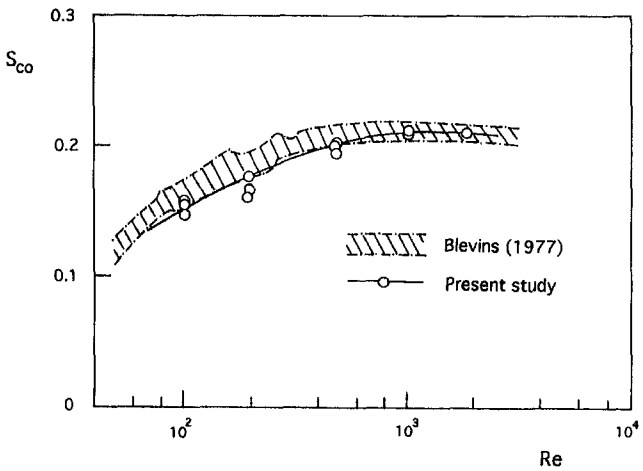

Fig. 8 Dimensionless natural shedding frequency as a function of Reynolds number, compared with the data of Blevins (1977)

Table 1 Data of Nu_{PL}/Nu_0 at different Re and A/D

Re	Nu_{PL}/Nu_0 $A/D = 0.138$	$A/D = 0.314$
200	1.03	1.04
500	1.05	1.08
1000	1.09	1.16

Nusselt number once the Reynolds number or the dimensionless amplitude is further increased.

The numerical predictions performed by Karanth et al. (1994) and Cheng et al. (1997) are also verified with the present experimental data. Since the solutions in these studies are limited to the low Reynolds number regime, only the data in the lower Reynolds number range should be used for comparison. Figure 9 displays the comparison of the lock-on effects between the numerical predictions by Cheng et al. (1997) and the present experimental data, at Re = 200 and $A/D = 0.138$, in the form of Nu/Nu_0 versus S_c/S_{c0} plots. Each of these two sets of data exhibits a distinctive jump in the heat transfer in the lock-on regime, even though the predicted values are, in general, slightly lower than the measured results. The discrepancy between the numerical and the experimental results indicates a complicated interaction in the lock-on regime between the fluid flow and the oscillating cylinder, which is inherently difficult to predict exactly by means of numerical methods. Inspite of this, the agreement is good. Comparison at other Reynolds numbers also show similar agreement but will not be discussed here.

The data of Nu_{PL}/Nu_0 at Re = 200 presented by Karanth et al. (1994) and Cheng et al. (1997) are given in Table 2. The present experimental results are also shown for comparison. It is found that the numerical predictions match the experimental data quite well.

In accordance with the numerical data presented by Cheng et al. (1997), a correlation formula expressing the dependence of Nu_{PL} on the Reynolds number and the dimensionless amplitude may be obtained as

$$Nu_{PL} = 0.68\ Re^{0.485}\ Pr^{0.4}[1 + 0.0944(A/D) + 0.118(A/D)^2] \quad (10)$$

which is valid for $80 \le Re \le 300$ and $0 \le A/D \le 0.7$. Note that if the oscillation parameters and the Reynolds number are further increased, turbulence may become the major mechanism enhancing the heat transfer. More theoretical and experimental information regarding the turbulence effects is definitely needed.

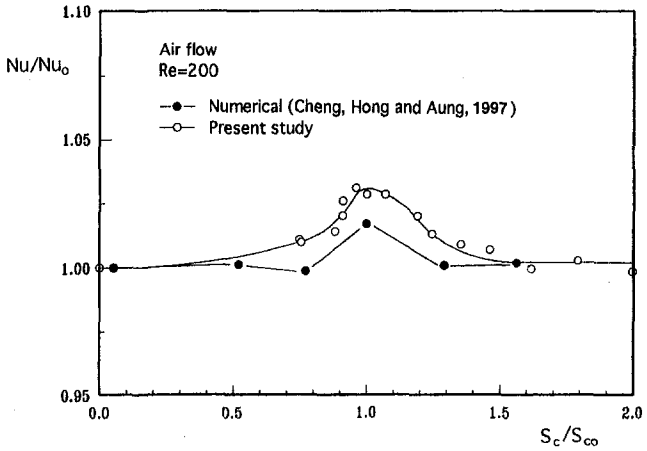

Fig. 9 Comparison on the lock-on effect between the experimental data and the numerical solutions of Cheng, et al. (1997), at Re = 200 and $A/D = 0.138$

Table 2 Comparison of lock-on heat transfer at Re = 200 between the present experimental data and existing numerical solutions (Karanth et al., 1994; Cheng et al., 1997)

A/D	Nu_{PL}/Nu_0 Present experimental data	Karanth et al. (1994)	Cheng et al. (1997)
0	1	1	1
0.14	1.03	—	1.016
0.2	—	1.016*	—
0.3	1.04	—	1.0388
0.4	—	1.05*	—
0.5	—	—	1.075
0.63	1.10	—	—
0.7	—	—	1.125

* Values taken from Fig. 8 presented by Karanth et al. (1994).

Attention is now directed at an approximate method proposed by Van Der Hegge Zijnen (1958) and Sreenivasan and Ramachandran (1961), which is commonly used to yield a fast estimate for the oscillation effect on heat transfer. In this approximate method, the analysis starts from the correlation formula between Nu and Re for the stationary cylinders. Recall that Eq. (9) is valid for $100 \le Re \le 4000$. We follow this approach and start from this equation.

Following Van Der Hegge Zijnen (1958) and Sreenivasan and Ramachandran (1961), Eq. (9) may be rearranged as

$$Nu = Cu_0^{0.475} \quad (11)$$

with $C = 0.658\ (D/\nu)^{0.475}$; u_0 is the free stream velocity.

Upon imposing a vibrational velocity V_V, the resultant velocity of fluid, as seen by the oscillating cylinder, is

$$V_R = \sqrt{(u_0^2 + V_V^2)}.$$

Replacing u_0 in Eq. (11) with V_R, we obtain

$$Nu = C(u_0^2 + V_V^2)^{0.237} \quad (12a)$$

or

$$Nu = Cu_0^{0.475}\left[1 + \left(\frac{V_V}{u_0}\right)^2\right]^{0.237}. \quad (12b)$$

Writing the binomial expansion for the terms in the parentheses, and neglecting the third and succeeding terms of this expansion, we have

$$Nu = 0.658\ Re^{0.475}\left[1 + 0.237\left(\frac{V_V}{u_0}\right)^2\right]$$

or

$$Nu/Nu_0 = \left[1 + 0.237\left(\frac{V_V}{u_0}\right)^2\right]. \quad (13)$$

The value of V_V is calculated with $V_V = 2As_c$.

Equation (13) may be used to estimate the heat transfer coefficient for an oscillating cylinder. The accuracy of this method is tested with the present experimental data. Figure 10 shows the comparison between the results calculated by Eq. (13) and the experimental data for a typical case at Re = 500 and $A/D = 0.628$. A remarkable discrepancy is seen. No appreciable change in the heat transfer coefficient calculated by Eq. (13) is found. According to the experimental data, the heat transfer performance is vastly underestimated by Eq. (13). Additional checks using the experimental data shown in Figs.

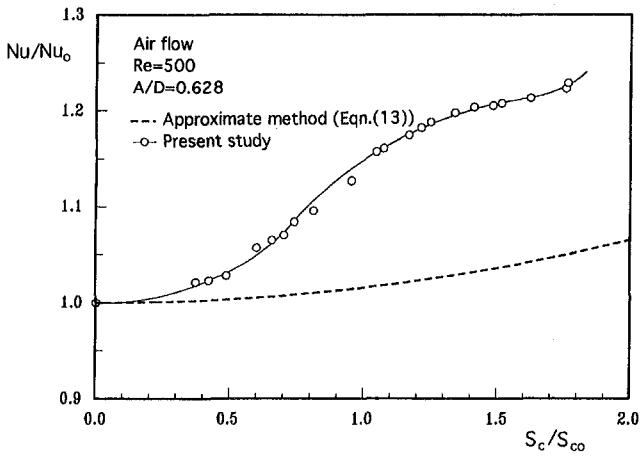

Fig. 10 Discrepancy between the vibrational-velocity approximation and the experimental data, at Re = 500 and A/D = 0.628

Table 3 Uncertainty analysis for measured parameters

Parameter	Typical value x	Uncertainty* δx	Relative uncertainty* $\delta x/x$
u_0	0.03–1.0 m/s	—	10.2 percent
	1.0–4.0 m/s		5.1 percent
T	50–85°C	0.1°C	0.2 percent
T_a	25°C	0.1°C	0.4 percent
s_c	20 Hz	0.1 Hz	0.5 percent
A	10 mm	0.05 mm	0.5 percent
D	16 mm	0.01 mm	0.06 percent
L	250 mm	0.05 mm	0.02 percent
m	0.449 kg	0.001 kg	0.22 percent
Re	0–4000	—	10.4 percent[1]
			5.48 percent[2]
S_c	0–0.65	—	10.21 percent[1]
			5.12 percent[2]
Nu	7.0–35.2	—	4.9 percent

* All estimated with 95 percent confidence.
[1] For 0.03 m/s < u_0 < 1.0 m/s.
[2] For u_0 > 1.0 m/s.

5 to 7 have also been made. Clearly, the approximate method, represented by Eq. (13), cannot reflect the influence of the lock-on and the turbulence effects shown in these figures.

Flow Visualization. Photographs showing the flow patterns in the cylinder wakes are given in Fig. 11. In this figure, Re and A/D are fixed at 330 and 0.628, respectively. Note that at Re = 330, the Strouhal number (St) is approximately 0.2; therefore, as S_c approaches this value, a lock-on phenomenon is expected.

Figure 11(a) illustrates the flow pattern of vortex shedding behind a stationary cylinder (S_c = 0). In this and in each of the remaining photographs shown in Fig. 11, the cylinder is partly visible on the left side of the photograph and air flows from left to right. The structure of vortex shedding can be clearly observed. The natural shedding frequency may be detected by using the hot-wire velocimeter placed at a proper distance behind the cylinder.

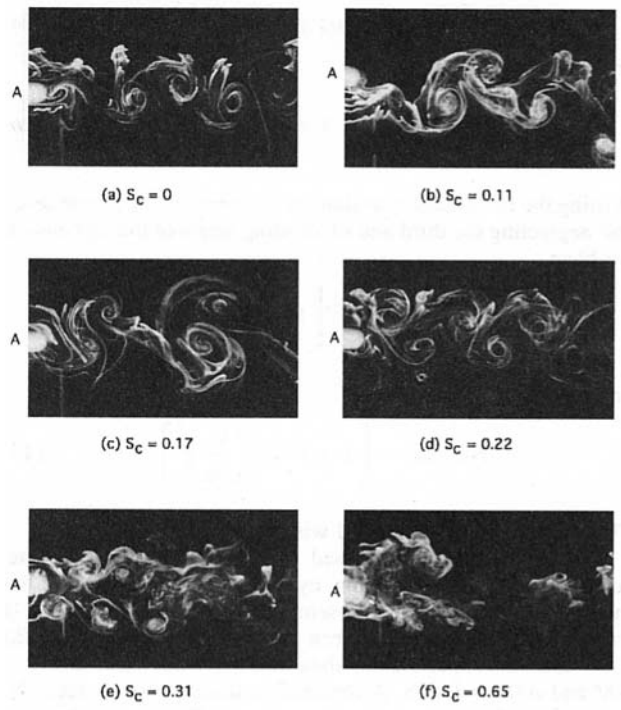

Fig. 11 Flow patterns of vortex shedding behind an oscillating cylinder, at Re = 330 and A/D = 0.628, at various dimensionless frequencies of oscillation (S_c); (Main air flow is from left to right; cylinder location is at A.)

Figure 11(b) shows the flow pattern behind an oscillating cylinder with a dimensionless frequency of S_c = 0.11. Even though the flow pattern in this figure is obviously different from that shown in Fig. 11(a) for a stationary cylinder, the predominant frequency of the vortex shedding is still approximately equal to the natural shedding frequency, as may be seen from the roughly equal spacing between the vortices in the two photographs or the approximately equal number of vortices within a given distance behind the cylinders.

When S_c is elevated to be 0.17, close to the Strouhal number of 0.2, the lock-on phenomenon takes place. As represented in Fig. 11(c), the vortex shedding frequency is reduced from the natural shedding frequency to the oscillation frequency of cylinder. The reduction of the shedding frequency may be observed from the reduced number of vortices behind the cylinder.

Figure 11(d) shows the results when the value of S_c is further elevated to 0.22. It may be seen that the vortex shedding frequency has also increased. This is evidenced by the greater number of vortices found behind the cylinder within the same distance.

Figure 11(e) shows the flow pattern for S_c = 0.31. The increase in shedding frequency with S_c continues; however, the effect of turbulence is starting to appear in the wake. The turbulent motion enhances the diffusion of the smoke filaments and hence makes the observation more difficult.

In this particular case, it may be concluded that a laminar lock-on regime exists for S_c = 0.17 ~ 0.3. For S_c higher than this range, the wake becomes turbulent and the smoke filaments cannot be seen clearly. The turbulent wake resulting from a higher relative velocity between the fluid and the cylinder, in cases with high frequency, high amplitude, or high Reynolds number, may produce a significant increase in the heat transfer, as already discussed in the preceding sections. A typical turbulent flow pattern at S_c = 0.65 is given in Fig. 11(f).

The heat transfer behavior is of major emphasis in the present study, and Fig. 11 displays the lock-on and the turbulent phenomena in the wake, both of which affect the heat transfer significantly. More detailed information for the flow structure and the frequency spectrum in a lock-on or unlock-on wake of an oscillating cylinder can be found in a number of reports, for example, Griffin and Ramberg (1974), Ongoren and Rockwell (1988), Karniadakis and Triantafyllou (1989), and Lecointe and Piquet (1989).

Uncertainty Analysis. An uncertainty analysis has been carried out and the results are summarized in Table 3. Uncertainty may be caused by many sources. In this study, these

sources are basically divided into three categories: calibration uncertainty, data acquisition uncertainty, and data reduction uncertainty. The uncertainty interval for each measured parameters is estimated with a 95 percent confidence using a standard single-sample analysis described by Kline and McClintock (1953) and Moffat (1985, 1988). It is observed in Table 3 that the air velocity contributes by far the largest relative uncertainty in the entire experiment, especially for the lower velocity cases. For 0.03 m/s $< u_0 <$ 1 m/s, the relative uncertainty in velocity measurement reaches 10.2 percent; however, only approximately 5.1 percent is found for velocities higher than 1 m/s. In addition, the thermal properties of air and copper may be determined from numerous existing sources (for example, CRC Handbook of Chemistry and Physics, 1993). However, the data from different existing sources are somewhat scattered, and moreover, the uncertainty of temperature measurement could also produce error in the determination of the properties. Thus, the uncertainty of the thermal properties may be treated as a combination of a random uncertainty of the scattered data and a fixed uncertainty caused by the error of temperature measurement. The combining uncertainty is calculated by applying the methods described by Moffat (1988). It is found that if estimated at the typical film temperature of 55°C, the uncertainties of the thermal conductivity and kinematic viscosity of air (k_f and ν) are 2.1 percent and 2.0 percent, respectively. For the heat capacity of copper (c), it is 0.9 percent.

Furthermore, Moffat (1985) employed a root sum-square method, which was advanced by Kline and McClintock (1953), to perform an uncertainty analysis for the heat transfer coefficient (h), obtained by using the transient test method. By following a similar procedure, the uncertainty of the time-averaged heat transfer coefficient ($\bar{h}$) of the present study is calculated. And as a result, a 4.4 percent relative uncertainty in $\bar{h}$ is found.

It is then necessary to determine how the uncertainties propagate into these dominant dimensionless parameters. By definition, $\mathrm{Re} = u_0 D/\nu$, $S_c = s_c D/u_0$, and $\mathrm{Nu} = \bar{h} D/k_f$. As suggested by Kline and McClintock (1953) and Moffat (1985, 1988), the relative uncertainties of these dimensionless parameters are calculated by

$$\frac{\delta\,\mathrm{Re}}{\mathrm{Re}} = \left[\left(\frac{\delta u_0}{u_0}\right)^2 + \left(\frac{\delta D}{D}\right)^2 + \left(\frac{\delta \nu}{\nu}\right)^2\right]^{1/2} \qquad (14a)$$

$$\frac{\delta S_c}{S_c} = \left[\left(\frac{\delta s_c}{s_c}\right)^2 + \left(\frac{\delta D}{D}\right)^2 + \left(\frac{\delta u_0}{u_0}\right)^2\right]^{1/2} \qquad (14b)$$

and

$$\frac{\delta\,\mathrm{Nu}}{\mathrm{Nu}} = \left[\left(\frac{\delta \bar{h}}{\bar{h}}\right)^2 + \left(\frac{\delta D}{D}\right)^2 + \left(\frac{\delta k_f}{k_f}\right)^2\right]^{1/2}. \qquad (14c)$$

Introduction of the known uncertainties of the measured parameters and the thermal properties into the above equations yields the relative uncertainty interval of the dimensionless parameters. Results are displayed in Table 3. Note that the contribution of the uncertainty of air velocity in the errors of Re and S_c is significant. The relative uncertainties of Re and S_c are approximately equal to 10.4 percent and 10.21 percent, respectively, with u_0 in the range 0.03 ~ 1 m/s; however, the relative uncertainties are reduced to within 5.5 percent when u_0 is greater than 1 m/s. On the other hand, for the measured Nusselt number, the relative uncertainty is approximately 5.0 percent in this study. The magnitudes of the uncertainties of the major parameters are basically reasonable since the uncertainty of the most widely used data of the Nusselt number and Strouhal number for the nonoscillating cylinders may vary by 10 percent. In fact, the existing information shown in Figs. 4 and 8, from McAdams (1954) and Blevins (1977), respectively, demonstrates this fact.

Concluding Remarks

The present study is concerned with the forced convection of air flowing over a transversely oscillating circular cylinder. The heat transfer enhancement due to the oscillation of the cylinder has been studied by experimental measurement. A transient test technique is employed to determine the average heat transfer coefficient under various oscillation conditions and physical configurations. The smoke flow visualization method is adopted to observe the vortex shedding in the wake, particularly the lock-on phenomenon in which the vortex shedding is in resonance with the oscillation of the cylinder. The conclusions reached in this study are summarized as follows:

1 Two mechanisms that could significantly enhance forced convection are found in this study, namely the lock-on effect and the turbulence effect. For a cylinder oscillating at low frequency and amplitude in a low Reynolds number laminar air flow, the heat transfer coefficient is increased only in the lock-on regime. On the other hand, if the oscillation parameters and the Reynolds number are sufficiently high, the heat transfer may be further augmented by the turbulence effect resulting from a higher relative velocity between the fluid and the oscillating cylinder. In this study, it is found that a maximum of a 34 percent increase in the heat transfer may be attributed to the turbulence effect.
2 The Nusselt number (Nu) exhibits a strong dependence on the Reynolds number (Re), the oscillation frequency (S_c), and the oscillation amplitude (A/D). In general, Nu increases with each of these parameters.
3 The numerical predictions performed by Karanth et al. (1994) and Cheng et al. (1997) for the lock-on effect on the heat transfer at Re = 200 have been confirmed with the present measurements. Agreement of the present data is found with the existing numerical predictions.
4 The approximate method, introducing a vibrational velocity concept into the heat transfer analysis, but neglecting the lock-on and the turbulence effects, may lead to a significant error in the estimate of heat transfer performance.

Acknowledgement

The financial support of this work by the National Science Council, Republic of China, under Grant NSC81-0401-E-036-02, is greatly acknowledged.

References

Ahmed, I. Y., Barrow, H., and Dixon, S. L., 1982, "An Experiment on Transient Heat and Mass Transfer in Humid Air Flow," *Heat Recovery System,* Vol. 2, pp. 3–11.

Benedict, R. P., 1969, "Engineering Analysis of Experimental Data," *J. Engineering for Power,* Vol. 90, pp. 21–30.

Blevins, R. D., 1977, *Flow-Induced Vibration,* Van Nostrand Reinhold Company, New York, Chap. 3, pp. 11–54.

Cheng, C. H., Hong, J. L., and Aung, W., 1997, "Numerical Prediction of Lock-on Effect on Convective Heat Transfer From a Transversely Oscillating Circular Cylinder," *Int. J. Heat Mass Transfer,* Vol. 40, pp. 1825–1834.

Chilukuri, R., 1987, "Incompressible Laminar Flow Past a Transversely Vibrating Cylinder," *ASME Journal of Fluids Engineering,* Vol. 109, pp. 166–171.

CRC Handbook of Chemistry and Physics, 1993, 74th edition, D. R. Lide, ed., CRC Press, London.

Griffin, O. M., and Hall, M. S., 1991, "Review-Vortex Shedding Lock-on and Flow Control in Bluff Body Wakes," ASME *Journal of Fluids Engineering,* Vol. 113, pp. 526–537.

Griffin, O. M., and Ramberg, S. E., 1974, "The Vortex-Street Wakes of Vibrating Cylinders," *J. Fluid Mech.,* Vol. 66, pp. 553–576.

Hurlbut, S. E., Spaulding, M. L., and White, F. M., 1982, "Numerical Solution for Laminar Two-Dimensional Flow about a Cylinder Oscillating in a Uniform Stream," ASME *Journal of Fluids Engineering,* Vol. 104, pp. 214–222.

Karniadakis, G. E., and Triantafyllou, G. S., 1989, "Frequency Selection and Asymptotic States in Laminar Wakes," *J. Fluid Mech.,* Vol. 199, pp. 441–469.

Karanth, D., Rankin, G. W., and Sridhar, K., 1994, "A Finite Difference Calculation of Forced Convection Heat Transfer From an Oscillating Cylinder," *Int. J. Heat Mass Transfer,* Vol. 37, pp. 1619–1630.

Kezios, S. P., and Prasanna, K. V., 1966, "Effect of Vibration on Heat Transfer From a Cylinder in Normal Flow," *Trans. ASME,* Paper No. 66-WA/HT-43.

Kline, S. J., and McClintock, F. A., 1953, "Describing Uncertainties in Single-Sample Experiments," *Mechanical Engineering,* Vol. 75, pp. 3–8.

Lecointe, Y., and Piquet, J., 1989, "Flow Structure in the Wake of an Oscillating Cylinder," ASME *Journal of Fluids Engineering,* Vol. 111, pp. 139–148.

Leung, C. T., Ko, N. W. M., and Ma, K. H., 1981, "Heat Transfer from a Vibrating Cylinder," *J. of Sound and Vibration,* Vol. 75, pp. 581–582.

Martinelli, R. C., and Boelter, L. M. K., 1938, "The Effect of Vibration on Heat Transfer by Free Convection from a Horizontal Cylinder," Proc. 5th Int. Congress, *Applied Mech.,* p. 578.

McAdams, W. H., 1954, *Heat Transmission,* 3rd ed., McGraw-Hill, New York.

Moffat, R. J., 1985, "Using Uncertainty Analysis in the Planning of an Experiment," ASME *Journal of Fluids Engineering,* Vol. 107, pp. 173–178.

Moffat, R. J., 1988, "Describing the Uncertainties in Experimental Results," *Experimental Thermal and Fluid Science,* Vol. 1, pp. 3–17.

Ongoren, A., and Rockwell, D., 1988, "Flow Structure From an Oscillating Cylinder: Part 2. Mode Competition in the Near Wake," *J. Fluid Mech.,* Vol. 191, pp. 225–245.

Ozisik, M. N., 1985, *Heat Transfer—A Basic Approach,* McGraw-Hill, New York, pp. 104–114.

Saxena, U. C., and Laird, A. D. K., 1978, "Heat Transfer From a Cylinder Oscillating in a Cross-Flow," ASME JOURNAL OF HEAT TRANSFER, Vol. 100, pp. 684–689.

Scott, C. J., 1970, "Transient Experimental Techniques for Surface Heat Flux Rates," *Measurement in Heat Transfer,* E. R. G. Eckert, and R. J. Goldstein, eds., Hemisphere, New York, pp. 375–395.

Sreenivasan, K., and Ramachandran, A., 1961, "Effect of Vibration on Heat Transfer From a Horizontal Cylinder to a Normal Air Stream," *Int. J. Heat Mass Transfer,* Vol. 3, pp. 60–67.

Van Der Hegge Zijnen, B. G., 1958, "Heat Transfer From Horizontal Cylinder to a Turbulent Air Flow," *Appl. Sci. Res.,* A 7, pp. 205–223.

Buoyancy Induced Convection in a Narrow Open-Ended Annulus

K. Vafai
Professor, Fellow ASME
Department of Mechanical Engineering,
The Ohio State University,
Columbus, OH 43210
vafai.l@osu.edu

C. P. Desai
BF Goodrich Aerospace,
Troy, OH 45373

S. V. Iyer
Department of Mechanical Engineering,
The Ohio State University,
Columbus, OH 43210

M. P. Dyko
ABS Corporation,
Akron, OH 44306

Results from a combined experimental and numerical investigation of buoyancy driven flow and heat transfer in a narrow annular gap between co-axial, horizontal cylinders are presented in this work. The annulus is open at both ends through which the ambient fluid can interact with the fluid inside the gap. In the experimental study, a constant heat flux was utilized to simulate buoyancy induced convection in an open ended annular cavity with a low gap to inner cylinder radius ratio; local surface temperature measurements were made to determine heat transfer characteristics of the convective flow. The heat transfer results are correlated by $Nu = 0.134(Ra^*)^{0.264}$ *for the range of Rayleigh numbers considered (*$7.09 \times 10^8 \leq Ra^* \leq 4.76 \times 10^9$*) in the experiments. In the numerical investigation, solutions to the three-dimensional time-averaged (Reynolds) steady-state equations of fluid motion and heat transfer were obtained using a finite element analysis. Results of the conjugate study including the local temperature distributions, heat transfer coefficients, and the flow field showing the interactions between the ambient and cavity flow fields agree favorably with experimental results. An investigation was also carried out to study the effect of axial length and the gap width of the annulus. A correlation for the average Nusselt number as a function of Rayleigh number, axial length and gap width has been obtained. The present work provides, for the first time, an experimental and numerical study of turbulent buoyancy induced flows in a narrow open-ended annulus.*

1 Introduction

Studies in natural convection in open-ended structures have received a great deal of attention in recent years, as they could serve as a valuable design aid in fire research, passive solar heating, energy conversion in buildings, and cooling of electronic components to name a few. The free convection in an annulus open at both ends, which constitutes a basic geometry, is strongly dependent upon the interactions of the inner (inside the cavity) and outer (the open region) flow and temperature fields.

In the analysis of open cavity problems, there is the inherent challenge of specifying boundary conditions at the open end. A number of numerical studies on two-dimensional rectangular open cavities have utilized the standard (and more viable) approach of performing calculations in a computational domain extended beyond the cavity and applying the far field conditions at the boundaries of the extended domain (Le Quere et al., 1981; Penot, 1982; Chan and Tien, 1985; Humphrey and To, 1986; and Vafai and Ettefagh, 1990). It has been shown by Vafai and Ettefagh (1990) that the extent of the enlarged computational domain has a considerable effect on the results. Due to the difficulty in controlling the ambient conditions, only a few experimental studies of natural convection in rectangular cavities have been reported. Bejan and Kimura (1981) did an experimental investigation to validate their theoretical study of free convection penetration into a rectangular cavity. The studies of Sernas and Kyriakides (1982), Hess and Henze (1984), and Chan and Tien (1986) provided further insight into two-dimensional rectangular open cavity natural convection through their experimental studies. Desai and Vafai (1996) provided experimental and numerical results for buoyancy induced flow and heat transfer in an annular cavity open at one end and closed at the other.

Of late, three-dimensional phenomenon of natural convection in open annular cavities has been gaining attention. Vafai and Ettefagh (1991) numerically studied the three-dimensional natural convection in an annulus in which the inner cylinder was maintained at a constant higher temperature while the outer cylinder was maintained at the lower ambient temperature. Several fundamental aspects of the flow field, such as the recirculating nature of the classical annular natural convection flow coupled with the strong axial convective effects induced by the open end, were revealed in their laminar, transient three-dimensional analysis.

An experimental investigation of turbulent natural convection in an annulus open at both ends has not been studied to date, nor has there been any relevant numerical study in the turbulent regime. In the present work, results from a combined experimental and numerical study of natural convection flow and heat transfer within and around an annulus open at both ends are analyzed. Experiments were performed and heat transfer correlations obtained for the range of heating conditions representative of several applications. A finite element model was also developed to simulate conditions in the experimental investigation. The numerical and experimental results are shown to be in excellent agreement. This investigation provides validated heat transfer data and improved physical understanding of fundamental aspects of natural convection in an annulus open at both ends.

2 Experimental Investigation

The purpose of the present experimental investigation is to simulate well-controlled buoyancy induced convection in an open ended annulus between co-axial horizontal cylinders. The quantitative output required from the experiments were temperature distributions and the heat transfer coefficients associated with the free convective flow around the open-ended annulus.

2.1 Test-Section Assembly. A schematic representation of the test-section assembly used in the present experimental study is shown in Fig. 1. The outer cylinder, inner cylinder, and the vertical faces on either side of the inner cylinder were

Contributed by the Heat Transfer Division for publication in the JOURNAL OF HEAT TRANSFER. Manuscript received by the Heat Transfer Division September 13, 1996; revision received April 3, 1997; Keywords: Augmentation & Enhancement; Conjugate Heat Transfer; Natural Convection. Associate Technical Editor: Y. Jaluria.

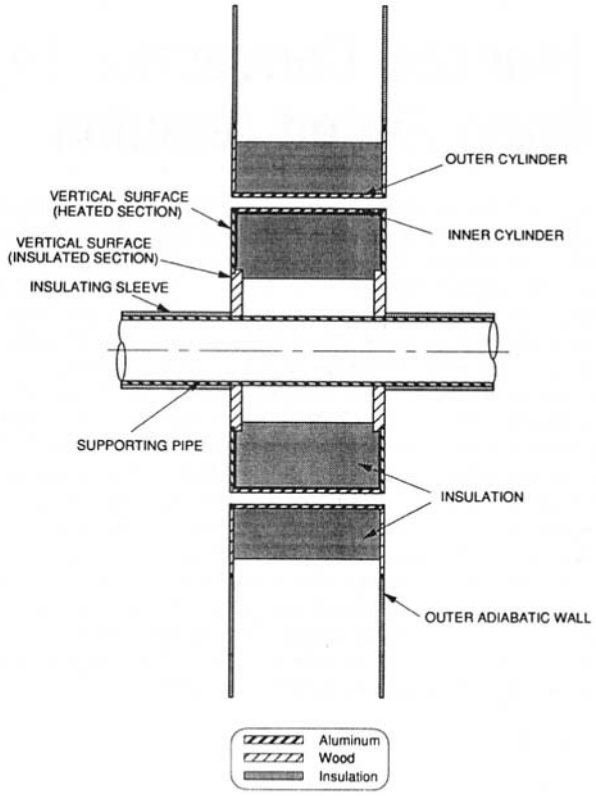

Fig. 1 Schematic of the test section used in the experimental study

machined from aluminum alloy (6061-T6) plates of thickness 0.25 in (6.35 mm). The inner cylinder was machined into a tube of OD 18.28 in. (46.43 cm), while the outer cylinder had an ID 20 in. (50.8 cm). The lengths of the inner and outer cylinders were 9.6 in. (24.38 cm) and 9.75 in. (24.77 cm), respectively. The two vertical faces (annular plates) were bolted to the inner cylinder on either side. Each vertical face had an OD = 18.28 in. (46.43 cm) and ID = 10 in. (25.4 cm). Wooden rings were bolted to the heated (aluminum) vertical surfaces of the inner cylinder in order to support the inner cylinder while preventing conductive heat losses from the vertical surfaces to the supporting pipe. The vertical insulated wall was fabricated by assembling two rings—the inner ring was made of masonite wood while the outer ring was made of lexan. These walls (one on either side) were connected to the outer cylinder by means of only four screw fasteners to minimize conduction losses to the supports.

One major objective in the present experimental study was to study the interaction between the inner and outer flow fields near the opening. To obtain meaningful experimental data, it was necessary to ensure that extraneous influences from the surroundings were minimized. Hence, a special supporting mechanism for the test section was designed to ensure that the effect of any external supports on the flow and temperature fields around the annular region of interest would be minimized. A schematic sketch of the supporting mechanism is shown in Fig. 2. The inner cylinder was supported by means of a central aluminum pipe which was mounted on two adjustable supports, one on either side of the inner cylinder and equidistant from it. These supports were placed at a sufficient distance from the test section to minimize its effect on the flow field. The diameter of the aluminum pipe was large enough to withstand the weight of the inner cylinder. Furthermore, to prevent heat transfer from air to the supporting pipe, a sleeve made of insulating PVC material was mounted on either side of the inner cylinder. Finally, longitudinal slots were milled in the supporting aluminum pipe to allow access to the thermocouple and heater lead wires. Also, the entire room in which the experiments were done was totally cut off from any air-conditioning currents.

2.2 Heating and Temperature Measurement System. The constant heat flux thermal boundary conditions on the inner cylinder and the two vertical aluminum faces were applied by means of flexible silicon rubber thermofoil heaters. The heaters, capable of raising the temperature to 260°C, were attached to the back side of the aluminum components by means of a high conductivity pressure sensitive adhesive (PSA) to provide good thermal contact. The backside of the heaters was insulated using

Nomenclature

A = exposed surface area of component under consideration
A_h = surface area of the heater on a particular component
b = gap width between inner and outer cylinders, $R_o - R_i$
dA = elemental surface area
g = gravitational acceleration
g^* = dimensionless gap width
h = heat transfer coefficient
h_m = average heat transfer coefficient
k = turbulent kinetic energy
k_C = thermal conductivity of annulus wall
k_W = thermal conductivity of outer wall
k_f = thermal conductivity of the fluid
L = length of the open annular cavity
L_e = length of the extended computational domain
$\underline{\mathrm{Nu}}$ = Nusselt number = hR_o/λ
$\overline{\mathrm{Nu}}$ = Average Nusselt number
Nu_b = Nusselt number based on gap width = hb/λ
Pr = Prandtl number = υ/α
p = pressure
Q = total power supplied to the heaters
Q_{loss} = heat loss from the insulation and radiation heat loss from the test section
q = applied heat flux
q_c = convected heat flux
Ra = Rayleigh number = $g\beta(T_m - T_\infty)R_o^3/\alpha\nu$
Ra_b = Rayleigh number based on gap width = $g\beta(T_m - T_\infty)b^3/\alpha\nu$
Ra* = modified Rayleigh number = $g\beta qR_o^4/\lambda\alpha\nu$
R_i = outer radius of the inner cylinder
R_o = inner radius of the outer cylinder
R_e = radius of the extended computational domain
r = radial coordinate
T = temperature
T_c = temperature at surface of annulus wall
T_m = average cavity temperature
T_w = temperature at surface of wooden wall
T_i = temperature at surface of inner cylinder
T_∞ = ambient temperature
t = thickness of the cavity components
U = characteristic velocity of the natural convection flow
u = velocity
u_r = radial velocity
u_θ = azimuthal velocity
u_z = axial velocity
x = cartesian coordinate
x^* = dimensionless length of annulus
z = axial location

Greek symbols

α = thermal diffusivity
β = volume expansion coefficient
ϵ = dissipation of turbulent K.E.
ν = kinematic viscosity
μ = dynamic viscosity
μ_{eff} = effective viscosity
μ_t = turbulent viscosity
λ = thermal conductivity
λ_{eff} = effective thermal conductivity
λ_t = turbulent thermal conductivity
θ = angular location measured from the top

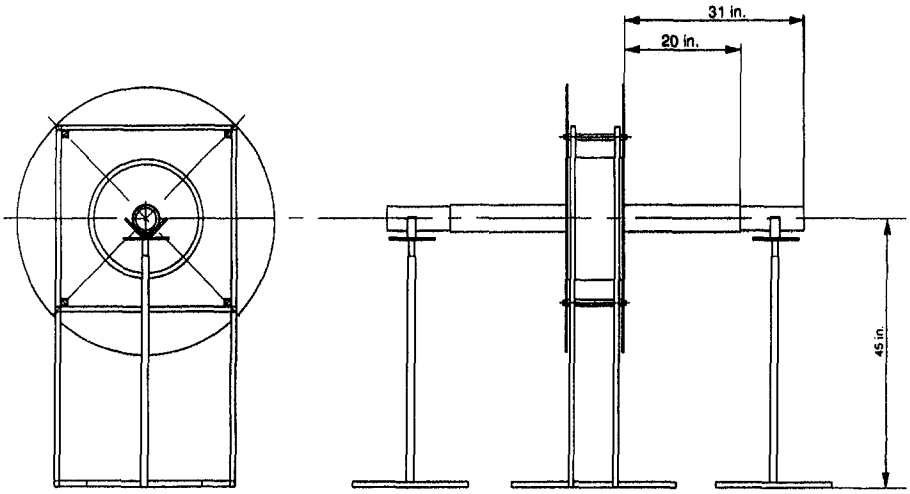

Fig. 2 Schematic of the supporting mechanism for the test-section assembly

Fiberfrax Durablanket insulation. This material provides excellent insulation characteristics due to its low thermal conductivity ($0.029\ \mathrm{W\ m^{-1}\ K^{-1}}$). With this arrangement, the maximum heat loss incurred was of the order of 4 percent of the total power supplied to the heaters.

A total of ninety-six holes (each 3 mm dia.) for thermocouple insertion were drilled into the test-section components to within 0.15 mm of the surface in contact with the surrounding air. AWG K-type thermocouples were inserted in these holes and held in place by high thermal conductivity cement. Each hole was completely filled with the high conductivity cement to minimize the effects of removing the material from the test section. Care was taken to ensure that the tip of the thermocouple was in contact with the bottom of the hole. The temperature reading which is obtained can be assumed to be indeed the temperature of the surface in contact with the surrounding air. In addition, two thermocouples were always used to measure the temperature drop across the insulation on the backside of the heaters. These temperature measurements were necessary to determine the heat loss through the insulation and thus, the actual heat supplied to the test section. Finally, one thermocouple continuously measured the temperature of the ambient air in the room.

A DC power supply capable of supplying up to 10 kW was used to provide the requisite power to the heaters. The voltage and current through the heaters was measured by means of a voltmeter and ammeter built into the power supply. The temperature data was recorded using a data acquisition/control unit and a high accuracy digital voltmeter. The heating and data acquisition procedures were fully automated.

2.3 Experimental Procedure. The experimental site was an isolated room with precise control over the air circulation. The supply of air to the room was completely shut off at least an hour prior to the start of each experimental run. To begin the experiments, the required amount of power was supplied to the heaters by means of the DC power supply. The voltage and current through the heaters for a given run were recorded for heat flux calculations. The data acquisition unit scanned all the thermocouples while the digital voltmeter measured the thermocouple output (in volts). At the end of each complete scan, the temperature values (the surface temperatures of the test section, the temperatures across the insulation, and the ambient temperature) were written to disk before the next scan was initiated. The total time per scan was approximately 20 seconds, producing three sets of temperature readings per minute. Data was taken continuously without interruption until steady state was reached. The requirement to obtain steady state was satisfied as follows: the experiment was allowed to run for at least 5 hours and steady state was assumed to be reached when the thermocouple variations were no more than ±0.1°C for at least a time span of 30 min. Duplicate experimental runs were performed at each Rayleigh number to verify repeatability of results. Results were found to be repeatable within ±1°C and even these differences were mainly due to the change in ambient temperature. At the end of each experimental run, the heater power and temperature data was stored for subsequent data reduction and analysis.

2.4 Data Reduction and Uncertainty Analysis. The Nusselt number and modified Rayleigh number are defined as

$$\mathrm{Nu} = \frac{hR_o}{\lambda} \quad \text{and} \tag{1}$$

$$\mathrm{Ra}^* = \frac{g\beta q R_o^4}{\lambda \alpha \nu} \tag{2}$$

where the heat transfer coefficient is defined as the ratio of the convected heat flux to the difference in temperatures between the mean temperature (T_m) and the ambient temperature (T_∞). The convected heat flux is calculated by subtracting the radiation heat loss from the total heat input from the power supply. Heat loss by radiation occurs from the test section and from the backside of the heaters (through the insulation). The mean temperature (T_m) is the weighted-area average temperature. The thermophysical properties of air were evaluated at the film temperature, which is defined as the average of the mean cavity surface temperature (T_m) and the temperature of the ambient air (T_∞).

The temperature measurement capabilities were within ±0.2°C. The outputs of the thermocouple were measured within ±0.01 μV, which corresponded to a sensitivity of 2.5×10^{-4}°C. The uncertainties in the measurement of the applied heat flux and that in the measurement of the heater current and voltage were 4 to 6 percent and ±1.5 percent, respectively. The length scale used in the current study had an uncertainty of ±0.1 mm associated with it, while an uncertainty of ±3.0 percent was assigned to the thermophysical properties of air (based on the observed variations in the reported values in the literature). The above uncertainties resulted in the uncertainty in the experimental Nusselt number to lie between 5.1 and 7.2 percent and in the modified Rayleigh number to lie between 7.9 and 9.1 percent.

3 Numerical Analysis

3.1 Physical Model and Assumptions. In the numerical study, the physical model, as illustrated in Fig. 3, was used.

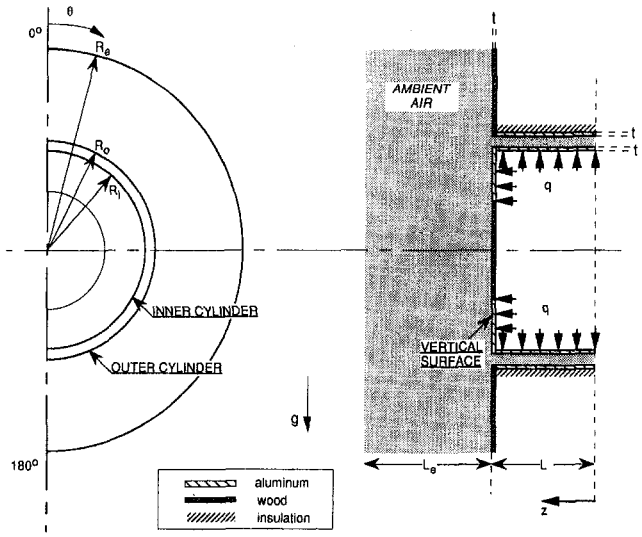

Fig. 3 Physical model and computational domain for the open-ended annulus

The computational domain includes the solid walls of thickness t and the extensions beyond the open end required to simulate the far-field boundary conditions. The annulus is bounded by aluminum walls in addition to the wall which extends into the ambient surroundings. The constant heat flux applied on the walls of the annulus causes natural convection currents to develop in the surrounding fluid. It is assumed in the analysis that the thermophysical properties of the walls and fluid are independent of temperature. The flow is in the turbulent regime for the range of Rayleigh numbers considered in the present study. The fluid is Newtonian, incompressible, and satisfies the Boussinesq approximation. This study concentrates only on the natural convection phenomenon within and outside the annulus. Hence, the contribution due to radiation heat transfer has been subtracted from the experimental data for subsequent comparisons. The physical model and coordinate system used for studying the effect of variations in geometric parameters is the same as before except that a constant temperature is applied on the surface of the inner cylinder.

3.2 Governing Equations. The governing equations are the Reynolds' time-averaged equations of fluid motion coupled with the energy equation in the fluid and in the solid walls of the computational domain. The k-ϵ model is used to simulate turbulence characteristics of the convective flow. The governing equations, using indicial notation, are written as follows:

For the Fluid.

Continuity:

$$u_{i,i} = 0 \tag{3}$$

Momentum:

$$\sqrt{\frac{\mathrm{Ra}^*}{\mathrm{Pr}}}\, u_j u_{i,j} = -p_{,i} - \sqrt{\frac{\mathrm{Ra}^*}{\mathrm{Pr}}}\, g_i T + \{\mu_{\mathrm{eff}}(u_{i,j} + u_{j,i})\}_{,j} \tag{4}$$

Energy:

$$\sqrt{\mathrm{Ra}^*\mathrm{Pr}}\,(u_j T_{,j}) = (\lambda_{\mathrm{eff}} T_{,j})_{,j} \tag{5}$$

Kinetic Energy:

$$\sqrt{\frac{\mathrm{Ra}^*}{\mathrm{Pr}}}\, u_j k_{,j} = \left[\left(1 + \frac{\mu_t}{\sigma_k}\right) k_{,j}\right]_{,j} + \frac{\mu_t}{\mathrm{Pr}_t}\, g_j T_{,j} + \mu_t \Phi - \sqrt{\frac{\mathrm{Ra}^*}{\mathrm{Pr}}}\, \epsilon \tag{6}$$

Dissipation:

$$\sqrt{\frac{\mathrm{Ra}^*}{\mathrm{Pr}}}\, u_j \epsilon_{,j} = \left[\left(1 + \frac{\mu_t}{\sigma_\epsilon}\right)\epsilon_{,j}\right]_{,j} + c_1(1 - c_3)\frac{\epsilon}{k}\frac{\mu_t}{\mathrm{Pr}_t}\, g_j T_{,j} + c_1 \frac{\epsilon}{k}\mu_t \Phi - \sqrt{\frac{\mathrm{Ra}^*}{\mathrm{Pr}}}\, c_2 \frac{\epsilon^2}{k} \tag{7}$$

For the Solid Walls.

Conduction:

$$T_{,j,j} = 0 \tag{8}$$

All variables in the above equations are nondimensionalized as follows (superscripts have been dropped, except for Ra*, for convenient):

$$x_i^* = \frac{x_i}{R_o} \quad u_i^* = \frac{u_i}{U} \quad T^* = \frac{T - T_\infty}{(qR_o/\lambda)} \quad p^* = \frac{pR_o}{\mu U}$$

$$k^* = \frac{k}{U^2} \quad \epsilon^* = \frac{\epsilon}{U^3/R_o} \quad \Phi^* = \frac{\Phi}{U^2/R_o^2}.$$

Further, the turbulent and effective viscosities are, respectively, given as

$$\mu_t^* = C_\mu \frac{k^{*2}}{\epsilon^*}\sqrt{\frac{\mathrm{Ra}^*}{\mathrm{Pr}}}, \quad \mu_{\mathrm{eff}}^* = 1 + \mu_t^*$$

while the turbulent and effective thermal conductivities are, respectively, given as

$$\lambda_t^* = \frac{\mu_t^*}{\mathrm{Pr}_t}\mathrm{Pr}, \quad \lambda_{\mathrm{eff}}^* = 1 + \lambda_t^*$$

and

$U = (\alpha/R_o)\sqrt{\mathrm{Ra}^*\mathrm{Pr}}$ is the characteristic velocity of the buoyancy induced flow.

The values of the constants appearing in the governing equations are $c_1 = 1.44$, $c_2 = 1.92$, $c_3 = 1.44$, $c_\mu = 0.09$, $\mathrm{Pr}_t = 1.0$, $\sigma_k = 1.0$, and $\sigma_\epsilon = 1.3$. Excluding c_3, all the preceeding constants are well-established from data obtained for turbulent forced convection flows. A sensitivity analysis of c_3 was carried out alone since this constant influences the buoyancy contribution in the ϵ equation. The results of this analysis revealed very little change in the Nusselt number and flow variables with a significant variation of c_3.

As mentioned before, the study of the effect of the geometric parameters is carried out up to a Rayleigh number of 10^6. The Rayleigh number used in this portion of the study is defined as

$$\mathrm{Ra}_b = \frac{g\beta(T_i - T_\infty)b^3}{\nu\alpha}.$$

3.3 Turbulence Model. The main challenge associated with the simulation of turbulent flows using the k-ϵ model is the resolution of sharp gradients of the flow variables in the near-wall region. A large number of grid points would be required in the viscous sublayer close to solid boundaries leading to a tremendous increase in CPU time and storage. Another difficulty stems from the fact that the standard k-ϵ approach (essential to model the high Reynolds number flow in the fluid outside the viscous sublayer) cannot be used to model the effects of viscosity on the turbulence field in the viscous sublayer (the low Reynolds number effects on turbulence).

In the scheme used in the present work, the fully turbulent outer flow field and the physical boundary are "bridged" by using a single layer of specialized wall elements. The interpolation functions in these wall elements are based on universal near-wall profiles. They are functions of the characteristic turbulent Reynolds numbers which accurately resolve the local flow

and temperature profiles. The turbulent diffusivity in the near-wall region is calculated by using Van Driest's mixing length approach. The standard k-ϵ equations are solved in the part of the computational domain excluding the wall element region. The elliptic form of the mean conservation equations are solved throughout the computational domain. However, the k-ϵ model is applied only up to and excluding the wall elements. Further details of the turbulence model can be found in the FIDAP Theory Manual (1993).

3.4 Boundary Conditions. Considering the symmetry in the flow and the temperature fields, only half the annulus in the angular direction and the axial direction were considered in the present study (Fig. 3), as was also confirmed by the experimental results. Based on physical considerations, it was assumed that no exchange of energy occurs across the vertical symmetry plane as well as the mid-axial symmetry plane of the annulus. Therefore, the boundary conditions at these symmetry planes are:

$$u_\theta = 0, \quad \frac{\partial u_r}{\partial \theta} = \frac{\partial u_z}{\partial \theta} = \frac{\partial T}{\partial \theta} = \frac{\partial k}{\partial \theta} = \frac{\partial \epsilon}{\partial \theta} = 0 \quad \text{at}$$

$$\theta = 0, \pi \text{ (angular symmetry)} \quad (9)$$

$$u_z = 0, \quad \frac{\partial u_r}{\partial z} = \frac{\partial u_\theta}{\partial z} = \frac{\partial T}{\partial z} = \frac{\partial k}{\partial z} = \frac{\partial \epsilon}{\partial z} = 0 \quad \text{at}$$

$$z = 0 \text{ (mid-axial symmetry)} \quad (10)$$

The no-slip boundary condition for velocity was applied at all the solid walls of the computational domain.

As mentioned earlier, a lot of care has to be exercised in specifying the boundary conditions at the aperture plane where fluid enters and leaves the annulus. The following alternate approaches can be used: (i) specifying boundary conditions at the aperture plane itself, and (ii) specifying the far-field conditions at the boundaries of an extended computational domain.

Approach (i) does not account for the outer region conditions. More realistic results are obtained using the second approach, especially near the opening of the annulus, as it has the advantage of including the aperture plane in the computations. Hence, in the present work, the second approach has been adopted. The extension to the computational domain is basically a cylinder of radius R_e and length L_e, as shown in Fig. 3.

Extensive numerical experimentation was done to arrive at the most appropriate set of far-field boundary conditions. At the radial boundary of the computational domain, the temperature gradient was imposed as zero while a constant ambient temperature was applied at the axial end of the computational domain. This is expressed as

$$\frac{\partial T}{\partial r} = 0 \quad \text{at} \quad r = \frac{R_e}{R_o} \quad \text{and}$$

$$T = 0 \quad \text{at} \quad z = \frac{(L + L_e)}{R_o}. \quad (11)$$

It was further determined that the following boundary conditions on velocity resulted in the most realistic simulation of far field conditions:

$$u_z = 0, \quad \frac{\partial u_r}{\partial r} = \frac{\partial u_\theta}{\partial r} = 0 \quad \text{at} \quad r = \frac{R_e}{R_o} \quad \text{and}$$

$$u_r = u_\theta = 0, \quad \frac{\partial u_z}{\partial z} = 0 \quad \text{at} \quad z = \frac{(L + L_e)}{R_o}. \quad (12)$$

For kinetic energy and dissipation, zero normal gradient was imposed on both the radial as well as axial boundaries of the domain.

$$\frac{\partial k}{\partial r} = 0, \quad \frac{\partial \epsilon}{\partial r} = 0 \quad \text{at} \quad r = \frac{R_e}{R_o} \quad \text{and}$$

$$\frac{\partial k}{\partial z} = 0, \quad \frac{\partial \epsilon}{\partial z} = 0 \quad \text{at} \quad z = \frac{(L + L_e)}{R_o}. \quad (13)$$

In order to arrive at the size of the extended computational domain, computations were performed with various axial and radial extension lengths of the computational domain. By comparing the results from these cases, an extended domain of size equal to three times the annulus size (i.e., the diameter of the annulus) was found to yield satisfactory results and hence, all calculations in the present work have been performed with this size of the computational domain.

Finally, the following interfacial boundary conditions need to be satisfied: at the interface of the annulus walls and the fluid

$$T_c = T, \quad \left(\frac{k_c}{k_f}\right)\frac{\partial T_c}{\partial n} = \frac{\partial T}{\partial n} \quad \text{at}$$

$$r = \frac{R_i}{R_o}, 1; \quad 0 \le z \le \frac{L}{R_o} \quad \text{and} \quad \frac{1}{2} \le r \le \frac{R_i}{R_o}; z = \frac{L}{R_o} \quad (14)$$

at the interface of the wall (vertical surface) and the fluid

$$T_w = T, \quad \left(\frac{k_w}{k_f}\right)\frac{\partial T_w}{\partial n} = \frac{\partial T}{\partial n} \quad \text{at} \quad z = \frac{L}{R_o}; \quad 1 \le r \le \frac{R_e}{R_o} \quad (15)$$

and at the interface of the annulus wall and the wall (vertical surface)

$$T_c = T_w, \quad \left(\frac{k_c}{k_w}\right)\frac{\partial T_c}{\partial n} = \frac{\partial T_w}{\partial n} \quad \text{at}$$

$$\frac{(L - t)}{R_o} \le z \le \frac{L}{R_o}; \quad r = 1 + \frac{t}{R_o}. \quad (16)$$

where n is the normal to the surface. In the above equations, the subscript c denotes the annulus walls (made of aluminum), and the subscript w denotes the other wall (made of masonite wood). Also, "annulus wall" refers to the curved surfaces, i.e., the convex surface of the inner cylinder and the concave surface of the outer cylinder.

In the study of the influence of geometric parameters, the nondimensionalization of the length-scale was carried out using the inner radius (R_i) instead of the outer radius (R_o). To study the effects of axial and gap width variations, the following eight boundary conditions were employed.

1 For the axial symmetry plane:

$$\text{at } z = 0 \quad \text{and} \quad 1 \le r \le \frac{R_o}{R_i},$$

$$u_z = 0, \quad \frac{\partial u_r}{\partial z} = \frac{\partial u_\theta}{\partial z} = \frac{\partial T}{\partial z} = 0 \quad (17)$$

2 For the curved surface of the inner cylinder:

$$\text{at } r = 1 \quad \text{and} \quad 0 \le z \le \frac{L}{R_i},$$

$$u_r = u_\theta = u_z = 0, \quad T = \frac{T_i - T_\infty}{T_i - T_\infty} = 1 \quad (18)$$

3 For the vertical surface of the inner cylinder:

$$\text{at } z = \frac{L}{R_i} \quad \text{and} \quad 0 \le r \le 1,$$

$$u_r = u_\theta = u_z = 0, \quad \frac{\partial T}{\partial z} = 0 \quad (19)$$

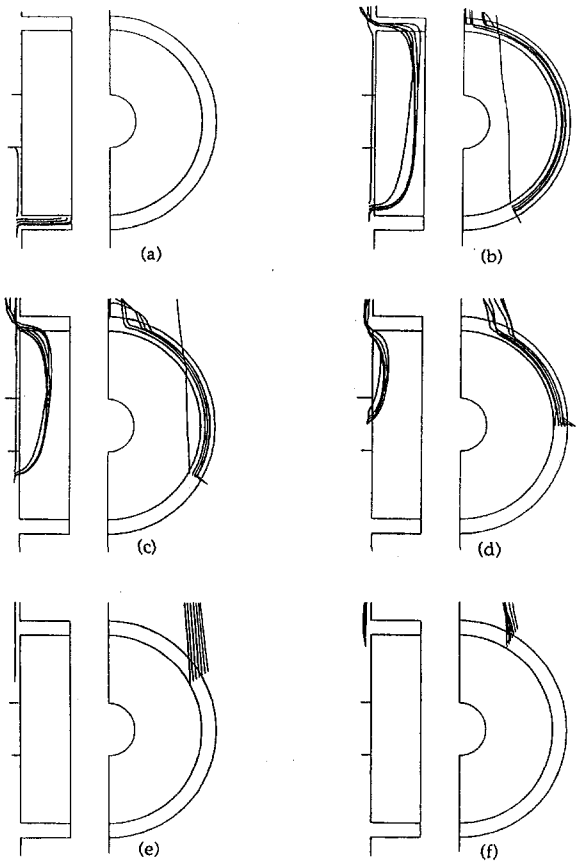

Fig. 4 Particle path plots around the annular gap ($Ra^* = 1.82 \times 10^9$), particles introduced at $z = 0.525$, $0.9 \le r \le 1.1$, and (*a*) $\theta = 180°$, (*b*) $\theta = 150°$, (*c*) $\theta = 120°$, (*d*) $\theta = 90°$, (*e*) $\theta = 60°$, and (*f*) $\theta = 30°$

4 For the curved surface of the outer cylinder:

$$\text{at } r = \frac{R_o}{R_i} \quad \text{and} \quad 0 \le z \le \frac{L}{R_i},$$

$$u_r = u_\theta = u_z = 0, \quad \frac{\partial T}{\partial r} = 0 \tag{20}$$

5 For the curved surface of the extension:

$$\text{at } r = \frac{R_e}{R_i} \quad \text{and} \quad \frac{L}{R_i} \le z \le \frac{(L + L_e)}{R_i},$$

$$u_z = 0, \quad \frac{\partial u_r}{\partial r} = \frac{\partial u_\theta}{\partial r} = 0, \quad \frac{\partial T}{\partial r} = 0 \tag{21}$$

6 For the vertical surface of the extension:

$$\text{at } z = \frac{(L + L_e)}{R_i} \quad \text{and} \quad 0 \le r \le \frac{R_e}{R_i},$$

$$u_r = u_\theta = 0, \quad \frac{\partial u_z}{\partial z} = 0 \quad T = 0 \tag{22}$$

7 For the vertical surface of the extension at the plane of the opening of the annulus:

$$\text{at } z = \frac{L}{R_i} \quad \text{and} \quad \frac{R_o}{R_i} \le r \le \frac{R_e}{R_i},$$

$$u_r = u_\theta = u_z = 0, \quad \text{and} \quad \frac{\partial T}{\partial z} = 0 \tag{23}$$

8 For the angular symmetry plane:

$$u_\theta = 0 \quad \text{and} \quad \frac{\partial u_r}{\partial \theta} = \frac{\partial u_z}{\partial \theta} = \frac{\partial T}{\partial \theta} = 0 \tag{24}$$

3.5 Numerical Scheme. A finite element formulation based on the Galerkin method of weighted residuals was used to solve the discretized set of governing equations (Eq. (3)–(8)) along with the boundary conditions. The highly coupled and nonlinear algebraic equations resulting from these discretizations are solved by using an iterative solution scheme based on the segregated solution algorithm which involves decomposition of the entire system of equations into smaller subsystems corresponding to each independent variable. An iterative solver based on a combination of the conjugate residual and conjugate gradient schemes is then used to solve each of the above subsystems. When the relative change in variables between consecutive iterations was 10^{-3}, convergence was assumed to have been reached.

4 Results and Discussion

A number of experiments were performed for the test section at different levels of power input resulting in average cavity temperatures ranging from 37°C to 166°C. During the experimental runs, the ambient air temperature was between 23°C and 24°C. The experiments thus covered a modified Rayleigh number of $Ra^* = 7.09 \times 10^8$ to 4.76×10^9.

In order to ensure that the results do not change with respect to the grid size, various combinations of grid size were tested. A systematic grid refinement procedure was used. This procedure consisted of varying the number of grid points in the radial and the angular direction one at a time while the other one was kept fixed, following this, the number of grid points in all the three

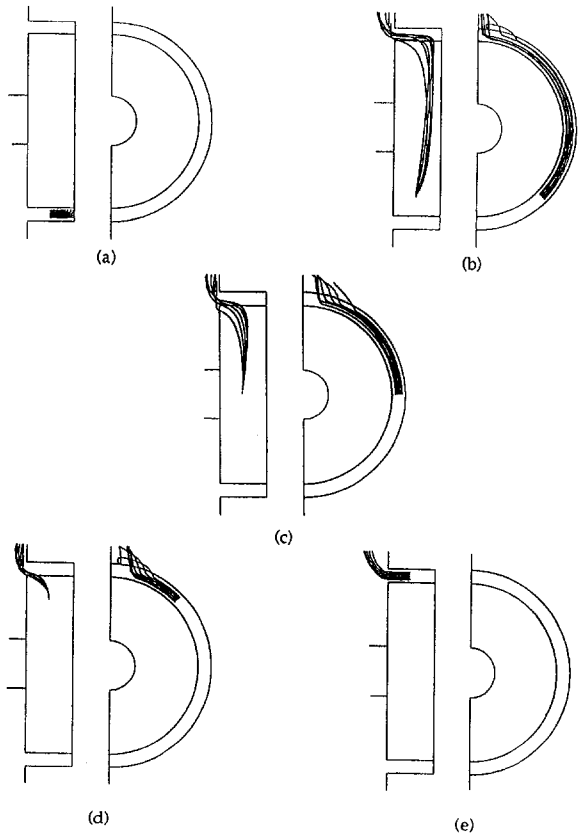

Fig. 5 Particle path plots around the annular gap ($Ra^* = 1.82 \times 10^9$), particles introduced at $z = 0.25$, $0.92 \le r \le 0.99$, and (*a*) $\theta = 180°$, (*b*) $\theta = 135°$, (*c*) $\theta = 90°$, (*d*) $\theta = 45°$, and (*e*) $\theta = 0°$

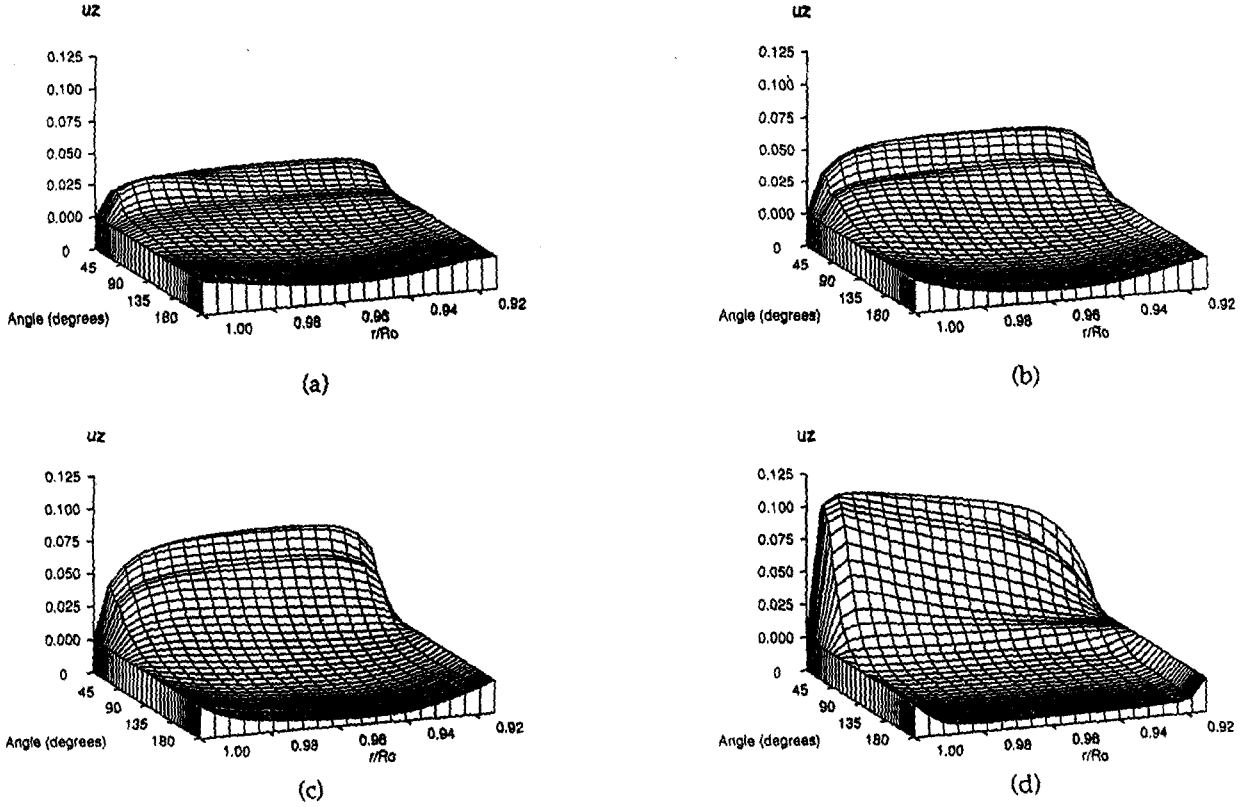

Fig. 6 Axial velocity distribution in different planes of the cavity; $Ra^* = 1.82 \times 10^9$: (*a*) $z = L/4$, (*b*) $z = L/2$, (*c*) $z = 3L/4$, and (*d*) $z = L$ (aperture plane)

directions were increased from the above values to determine the grid size required to obtain a grid-independent solution. It should be noted that a minimum of three grid points (and in most cases five points) were always used in the solid wall thickness of the computational domain. Furthermore, in the fluid region, a variable mesh strategy was adopted. The mesh was always finer near the walls (typically the mesh size near the walls was one half the size of the mesh in the interior of the domain). In the domain extension beyond the open end of the cavity, the maximum mesh size (i.e., the mesh size at the far-field locations) was about ten times the mesh size inside the cavity.

Both two-dimensional and three-dimensional analyses of turbulent buoyancy driven flow in an annulus were conducted to rigorously check the turbulence modeling approach. The Rayleigh numbers investigated ranged from 10^6 to 10^9, and good agreement was obtained between the results from the present

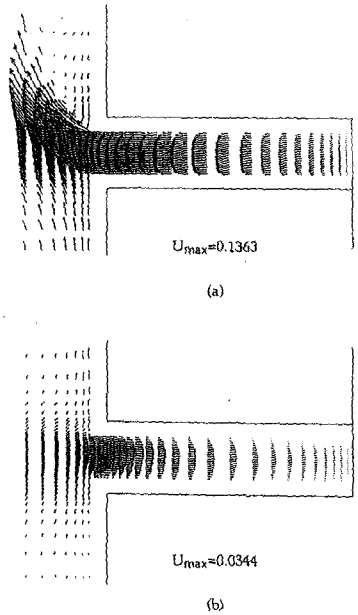

Fig. 7 Velocity vector field in the vertical symmetry plane of the cavity; $Ra^* = 1.82 \times 10^9$: (*a*) Upper half and (*b*) Lower half

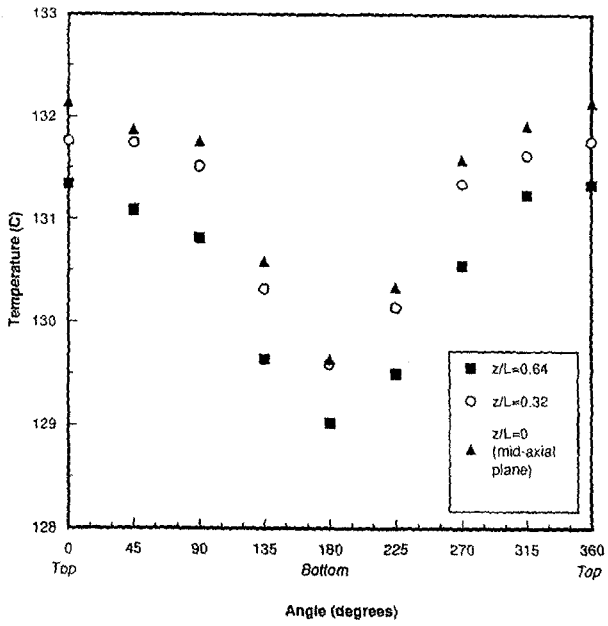

Fig. 8 Experimental temperature distribution for the inner cylinder; $Ra^* = 4.29 \times 10^9$

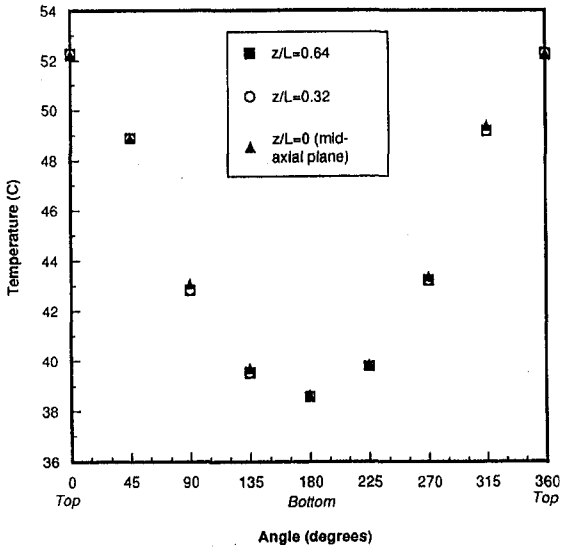

Fig. 9 Experimental temperature distribution for the outer cylinder; Ra* = 4.29 × 10⁹

investigation and previous works (Kuehn and Goldstein, 1976; Farouk and Guceri, 1982; Fukuda et al., 1990, 1991; and Desai and Vafai, 1994). There was also good agreement of the three-dimensional model with experimental results of McLeod and Bishop (1989). The results obtained from the numerical study were checked to verify that the conservation of mass principle was satisfied. This check was done by integrating the velocity field across different axial planes, and each of them was found to integrate to zero.

4.1 Flow Field. In the open annular cavity considered in the present study, the driving potential for the buoyancy induced flow is provided by the heated inner cylinder and its two vertical surfaces. As will be shown later, the steady state temperature attained by the outer cylinder is above the ambient temperature and therefore, also contributes to the buoyancy effects to some extent. Figures 4 and 5 depict the fluid particle paths obtained from the numerical results for $Ra^* = 1.82 \times 10^9$. The trajectories of fluid particles injected into the flow field is shown by these pathlines. In Fig. 4, the particles were assumed to be introduced in the flow field just outside the cavity at $z = 0.525$ at angular locations 30 deg apart and radii $r = 0.9$ to 1.1 ($\Delta r = 0.1$). These radii were chosen judiciously so as to cover the entire radial extent of the annular gap ($R_i - R_o$) as well as one grid point on either side. In general, it appears that the bulk flow is characterized by cold, ambient fluid entering the cavity axially through the lower regions of the aperture plane (the "suction" effect) and hot fluid leaving the cavity from the top (the "ejection" effect). The maximum penetration of ambient fluid into the cavity is through the lowermost angular location (180 deg); it diminishes in the upward direction. However, a significant amount of axial penetration is also observed up to the 90 deg location (Fig. 4(d)). The narrow gap precludes any local outflow below the inner cylinder or local inflow above it, which were observed in the air flow around annular cavities with wider gaps. Fluid particles also rise along the heated vertical surface and finally get entrained into the buoyant flow exiting from the top of the cavity. The pathlines originating at $r = 0.9$ show the buoyant plume rising along the vertical surface. To gain an understanding of the flow field inside the cavity, pathlines originating at $z = 0.25$ ($= L/2$) are also shown in Fig. 5. To generate these pathlines, it was assumed that particles are injected in the flow at angular locations 45 deg apart with radii $r = 0.92$ to 0.99. This figure further clarifies the axial flow toward the mid-axial symmetry plane through the lower regions of the cavity and flow toward the exit plane in the upper regions. In the $r - \theta$ planes, the pathlines inside the cavity are concentric circles, indicating a flow pattern similar to that in a narrow channel.

Figure 6 shows the axial velocity distribution in four planes of the cavity located one-fourth of the annulus length apart, measured from the mid-axial symmetry plane up to and including the exit plane. This figure, as well as subsequent figures showing the flow field, present the nondimensional velocities (with respect to the characteristic velocity $U = (\alpha/R_o)\sqrt{Ra^*Pr}$). The solid walls of the cavity are identified by the zero velocity reference plane in the surface plots. The values above the reference plane indicate positive axial velocities (flow away from the mid-axial plane, i.e., toward the exit) while the negative axial velocities indicate flow entering the cavity. The maximum and minimum values of the axial velocity in each plane are given in the figure. The axial velocity distribution in the exit plane (Fig. 6(d)) indicates that air enters the gap through approximately the lower two thirds of the aperture plane. From Fig. 6(d) it is also observed that the axial velocities of the entering fluid are significantly lower than those of the fluid leaving the cavity. It should also be noted that the "vena contracta" effect causes increased resistance to the flow field at the inlet, as compared to that at the outlet. It is observed that the axial velocity magnitudes increase continuously from the interior of the cavity toward the exit plane. The fluid attains maximum axial velocities in the exit plane through which it "gushes" out of the annular cavity into the ambient surroundings.

The velocity vector field in the upper and lower halves of the vertical symmetry plane (Fig. 7) clearly shows the axial flow effects induced by the open end of the cavity. At the exit plane, the velocity profile at the top of the cavity is significantly different. The angular velocity component of the fluid diminishes significantly as fluid leaves the restrictive outer cylinder surface and ejects as a buoyant jet from the top of the cavity.

4.2 Heat Transfer Results. Thermocouples were installed at eight different angular locations 45 deg apart on the inner and outer cylinder surfaces. For the vertical surfaces on either side of the inner cylinder, the four angular locations were 90 deg apart. For the inner and outer cylinders, the thermocouples were installed at five different axial locations, while for the vertical surfaces, two radii were chosen to install the thermocouples.

Figures 8–10 illustrate the experimental steady-state surface temperatures for the three components of the test section, i.e.,

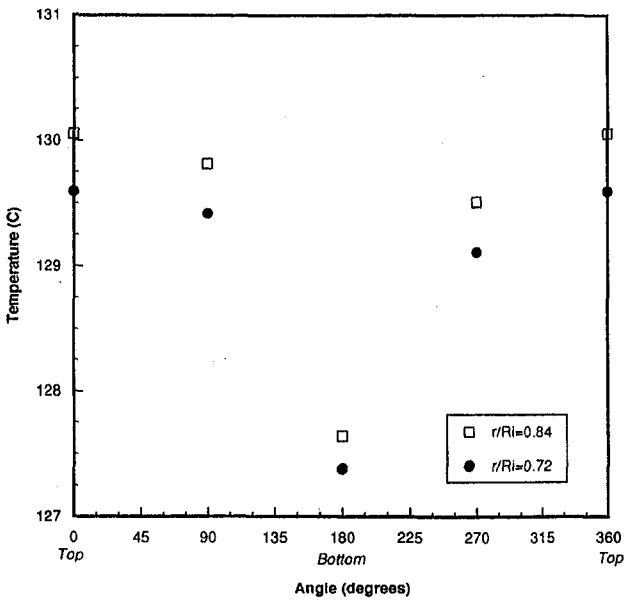

Fig. 10 Experimental temperature distribution for the vertical surface; Ra* = 4.29 × 10⁹

Table 1 Experimental mean heat transfer results

Ra*	Ra	Pr	Mean temperature (°C)				$\overline{Nu}$ (Inner cylinder and vertical surface)
			Inner cylinder	Outer cylinder	Vertical surface	Inner cylinder and vertical surface	
7.09×10^8	1.40×10^4	0.705	38.9	27.3	38.6	38.8	29.9
1.22×10^9	2.13×10^4	0.705	47.1	27.6	46.6	46.9	33.6
1.82×10^9	2.86×10^4	0.704	56.8	29.1	56.2	56.6	37.4
2.33×10^9	3.45×10^4	0.703	70.7	33.1	69.7	70.3	39.8
3.20×10^9	4.36×10^4	0.702	89.8	34.9	88.3	89.3	43.2
3.42×10^9	4.61×10^4	0.701	97.8	37.2	96.3	97.2	43.7
3.81×10^9	4.97×10^4	0.700	113.9	41.0	112.1	113.2	45.2
4.29×10^9	5.32×10^4	0.699	130.6	44.1	128.3	129.8	47.5
4.55×10^9	5.50×10^4	0.698	147.4	47.5	144.8	146.5	48.7
4.76×10^9	5.63×10^4	0.696	164.6	50.9	161.7	163.6	49.8

the inner cylinder, the vertical surfaces, and the outer cylinder. In each figure, the 0 deg location denotes the uppermost angular plane of the cavity. It can be seen that the temperature distribution over each of the components exhibits a good degree of symmetry in the angular direction about the vertical plane of the cavity. Also, for the inner and outer cylinders it was observed that the results were symmetric in the axial direction with respect to the mid-axial symmetry plane. However, to clarify the axial trends in the temperature profiles the thermocouple outputs at three axial locations have been presented in these figures.

For the inner cylinder (Fig. 8), the temperature values were lower near the open end of the cavity, as compared to locations in the interior portions of the cavity. The difference in temperatures is more pronounced near the bottom angular position (θ = 180 deg) because penetration of cold ambient fluid into the cavity is primarily through the lower half of the annulus. As fluid penetrates the cavity through the opening, its bulk temperature increases because it gains energy from the inner cylinder.

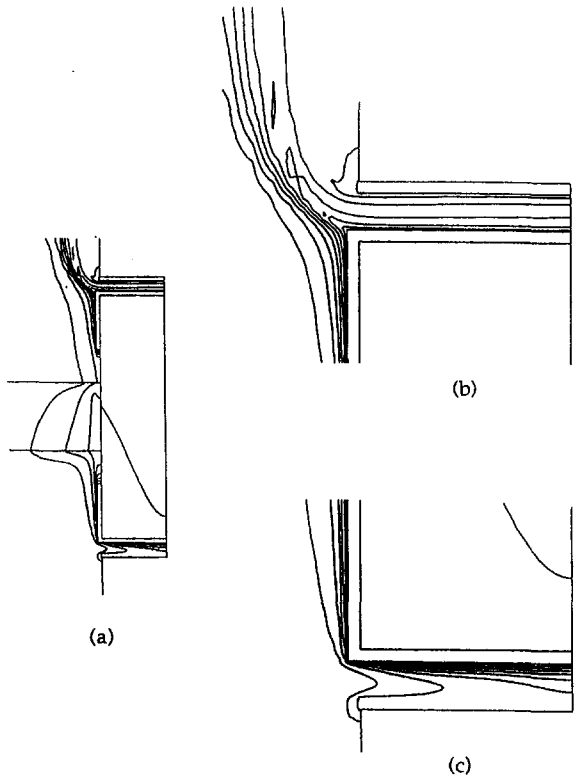

Fig. 11 Isotherms in the symmetry plane of the cavity; Ra* = 1.82 × 10^9: (*a*) Symmetry plane, (*b*) Upper half, and (*c*) Lower half

Hence, the heat transfer rates from the inner cylinder decrease as the distance from the mid-axial plane decreases. The temperature distribution over the outer cylinder (Fig. 9) indicates that the axial variation of temperature was negligible. The increase in temperature in angular direction was observed for the outer cylinder also because of the increase in the bulk fluid temperature. This is due to the flow which moves primarily from the bottom of the cylinder upwards. Furthermore, the difference between the maximum and minimum temperature in the angular direction for the outer cylinder was considerably higher than the corresponding temperature difference for the inner cylinder.

The temperature distribution over each vertical surface (Fig. 10) was found to be identical, further verifying the axial symmetry condition. Similar to the inner cylinder temperature distribution, for each vertical surface the trend of increasing temperature in the angular direction was observed. The temperatures over the vertical surface are highest at the top (θ = 0 deg) since the air is hottest at the top after gaining heat continuously as it convects heat from the vertical surface. As far as the trends in the radial direction are concerned, it was observed that the surface temperatures at the outer radius were higher than those at the location near the center line. In the present case, there was an unheated area over the aluminum portion of the vertical surface since the heater could not be placed directly in contact with the wooden portion of the vertical surface. This causes the lower temperatures near the inner radii as the temperatures near this unheated area are lower than at the outer radial locations.

In the experimental investigation, a wide range of Rayleigh numbers was considered ($7.09 \times 10^8 < Ra^* < 4.76 \times 10^9$) which corresponded to average inner cylinder surface temperatures ranging from 37°C to 166°C. The trends in the steady-state temperature distribution over the entire range of Rayleigh numbers were similar to the case described above. However, the difference between the maximum and minimum temperatures were found to increase at higher power inputs. For example, the outer cylinder temperatures ranged from 26°C to 28°C at the lowest Rayleigh number, while for the highest Rayleigh number the temperatures vary from 41°C to 57°C. The same effect was observed in the axial direction for the inner cylinder, i.e., the temperature difference in the axial direction increases with an increase in Rayleigh number. For the aluminum portions of the vertical surfaces, the temperature differences increase in the radial direction for the higher power inputs.

The mean Nusselt number is a measure of the convective heat transfer rates from the inner cylinder and its two vertical surfaces. The averaged quantities including the mean Nusselt number from the experimental runs for different heating conditions are given in Table 1. A power law correlation for the experimental heat transfer results was obtained as

$$\overline{Nu} = 0.134(Ra^*)^{0.264} \quad \text{for}$$

$$7.09 \times 10^8 \leq Ra^* \leq 4.76 \times 10^9. \quad (25)$$

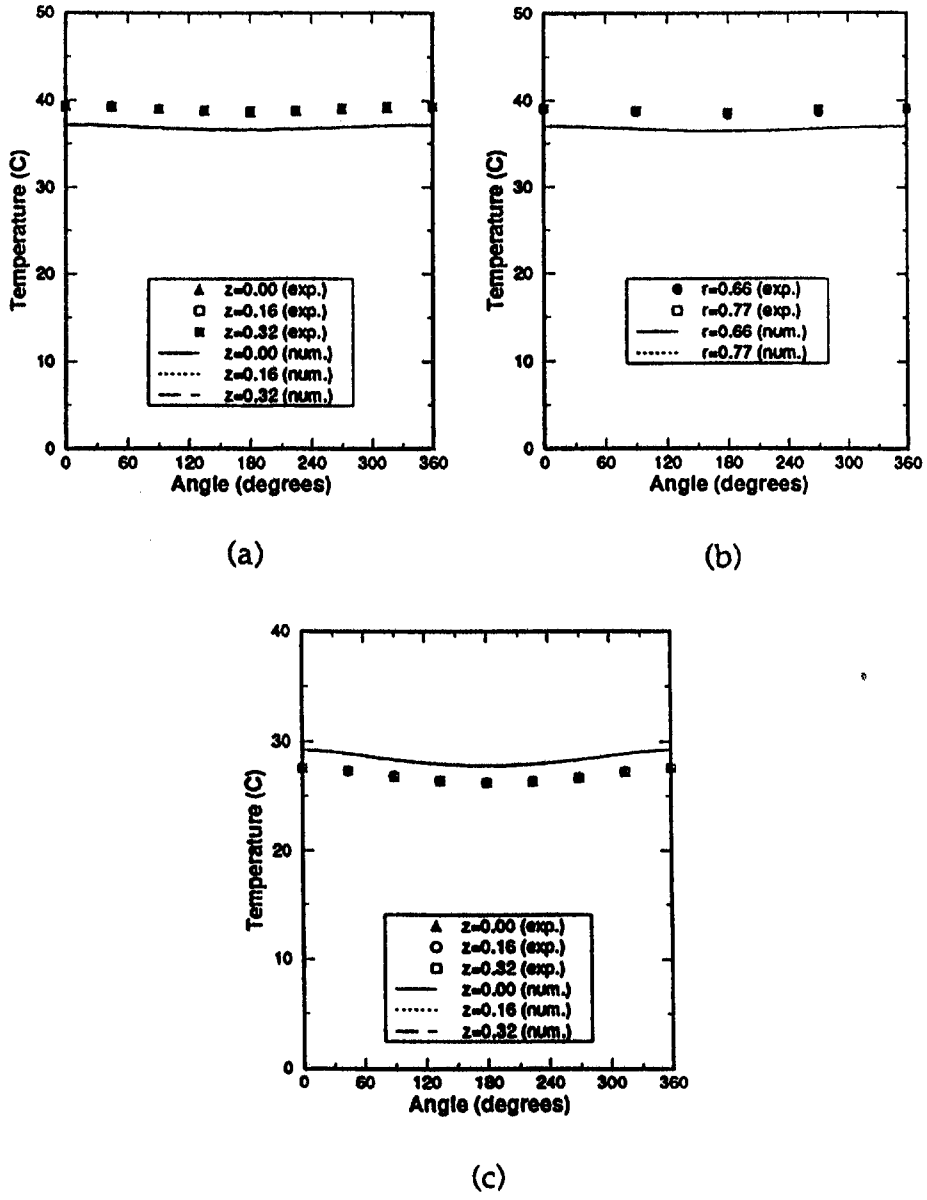

Fig. 12 Comparison between experimental and numerical results; Ra* = 7.09 × 10^8: (*a*) Inner cylinder, (*b*) Vertical surface, and (c) Outer cylinder

Figure 11 shows the isotherms for Ra* = 1.82 × 10^9 predicted by the numerical model. The temperature values in the figure have been nondimensionalized using $(T - T_\infty)/(qR_o/k)$. The isotherms in the lower half of the symmetry plane indicate the penetration of cold ambient fluid through the open end in the lower half of the cavity. The increase in the thermal boundary layer thickness from the open end toward the mid-axial symmetry plane is also apparent from the figure. At the top of the cavity, the distortion of isotherms near the open end indicates the buoyant jet leaving the cavity.

A comparison between the numerical and experimental results is shown in Fig. 12. One of the initial checks done for the numerical heat transfer calculations consisted of verifying that the amount of heat coming from the inner cylinder and that leaving the aperture plane at $z = L/R_o$ are the same. The local temperature distribution over the inner cylinder, the outer cylinder, and the vertical surface are compared for the heating condition corresponding to Ra* = 7.09 × 10^8. The temperature values agree within 15 percent, even for the highest Rayleigh number. Upon closer examination of the temperature values from the numerical and experimental results, it was observed that they display precisely the same trend at different axial and radial locations. A comparison between the experimentally and numerically predicted mean component temperatures under different heating conditions is shown in Table 2. It can be seen that the results showed excellent agreement (approximately 5 percent) at the lowest Rayleigh number considered while the agreement deteriorated slightly, but was still within 13 percent for the highest Rayleigh number case studied. It should be noted that the agreement was better for the outer cylinder temperatures. The Nusselt number results also displayed similar agreement.

4.3 Variation of Key Geometric Parameters. The geometric parameters which will be considered are the length of the annular cavity and the gap width between the cylinders. The physical model used for the analysis is the same as before. The only change is that the curved surface of the inner cylinder is maintained at a constant temperature while the vertical face of the inner cylinder and the curved surface of the outer cylinder are assumed to be insulated. Dimensionless parameters used in characterizing the effects of the geometric parameters identified

Table 2 Comparison between experimental and numerical results

Ra*	Ra	Method	Temperature (°C)		
			Inner cylinder	Outer cylinder	Vertical surface
7.09×10^8	1.40×10^4	Experimental	38.9	27.3	38.6
		Numerical	36.8	28.4	36.6
		Percent difference	−5.4	+4.1	−5.2
1.82×10^9	2.86×10^4	Experimental	56.8	29.1	56.2
		Numerical	50.7	30.1	50.2
		Percent difference	−10.7	+3.4	−10.7
3.20×10^9	4.36×10^4	Experimental	89.8	34.9	88.3
		Numerical	78.1	36.4	77.2
		Percent difference	−13.0	+4.3	−12.6

above are now given. The dimensionless length of the annulus in the axial direction is given by

$$x^* = \frac{L}{R_i} \tag{26}$$

where L is the length of the annulus and R_i is the radius of the inner cylinder. The dimensionless gap width is given by

$$g^* = \frac{R_o - R_i}{R_i} \tag{27}$$

where R_i and R_o are the radii of the inner and the outer cylinder, respectively. In order to study the effects of these geometric parameters, several cases were investigated. For each case, the average Nusselt number was compared with that for a baseline configuration. The geometric parameters for the baseline configuration and that for the different cases which were studied are summarized in the following table:

	x^*	g^*
Baseline	0.500	0.100
Case 1	0.375	0.100
Case 2	0.250	0.100
Case 3	0.500	0.075
Case 4	0.500	0.050

The results obtained are shown in Fig. 13 in terms of the percentage change in average Nusselt number between each of the cases identified above and the baseline case. The studies were carried out up to a Rayleigh number of 1×10^6 and at any given Rayleigh number, the average Nusselt number was found to increase with an increase in the gap width between the inner and the outer cylinders. The average Nusselt number was found to decrease by about 60 percent (as compared to the baseline case for a dimensionless width of 0.075) and by about 80 percent for a gap width of 0.05. As seen in Fig. 13, the effect of the gap width increases with Rayleigh number up to 2×10^5. Above that, the effect of the width does not change appreciably with the Rayleigh number. The study of the effect of the length of the annulus revealed a strong dependency on the Rayleigh number. For a length of 0.25, the average Nusselt number was found to be higher than that for the baseline case having a length of 0.5 up to a Rayleigh number of about 6×10^5, and the trend reverses beyond that. This behavior was expected because at lower Rayleigh numbers reduced length results in greater interaction between the fluid inside the annulus and the ambient fluid. However, at higher Rayleigh numbers, the higher velocity of the influx fluid results in a greater penetration and hence increased interaction between the fluid inside the annulus and the ambient fluid. A similar behavior was found for a length of 0.375, but the change in trends was observed at a Rayleigh number of 2×10^5. Thus, the increase in the average Nusselt number at lower Rayleigh numbers is caused by the reduced length and at higher Rayleigh numbers by the increased length which results in a higher heat transfer area. These two conflicting factors suggest the existence of an optimum length at which the heat transfer rate can be maximized. The results can be well correlated by the following equation:

$$\overline{\mathrm{Nu}} = 0.292(\mathrm{Ra})^{0.48}(0.02 - 0.09x^*)(-0.12 + 2.61g^*) \tag{28}$$

which is valid for a Rayleigh number up to 1×10^6. Equation (28), which is obtained by using a curve-fitting procedure, captures the effects of all the pertinent geometric parameters as well as the Rayleigh number variations.

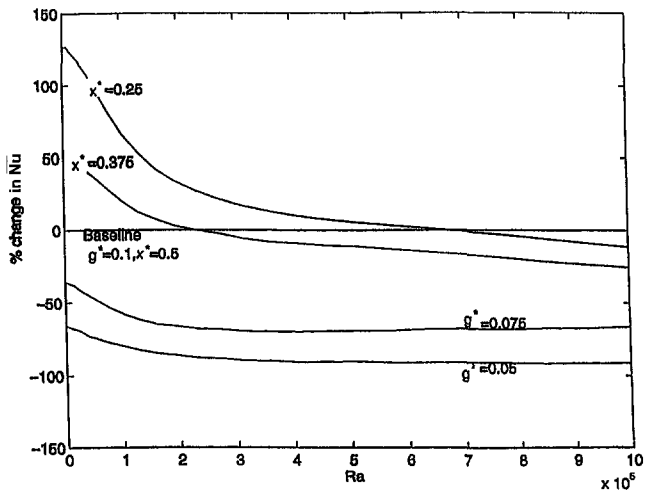

Fig. 13 Effect of variations in key geometric parameters

5 Conclusions

In the present study, the buoyancy driven fluid flow and heat transfer characteristics of a narrow annular gap open at both ends and bounded by co-axial horizontal cylinders have been investigated. The numerical results provide insight into the basic mechanisms underlying buoyancy induced flow in open ended cavities. The flow field results indicate the strong influence of the open end on the flow field within the cavity. The bulk flow is characterized by the suction of cold fluid into the lower portions of the cavity and the ejection of hot fluid, as a buoyant jet, from the top of the cavity. This interaction between the inner and outer flow fields is responsible for enhanced heat transfer rates from open ended cavities. These observations are consistent with the flow patterns obtained earlier for open annular cavities. The inner cylinder temperatures are lowest near the open end of the gap and increase continuously toward the mid-axial plane of the gap. Furthermore, buoyancy effects result in higher temperatures in the upper regions of the cavity.

The experimental investigation confirmed the trends in the temperature distribution obtained from the numerical results. Experiments were carried out over a wide range of heating

conditions ($7.09 \times 10^8 < \mathrm{Ra}^* < 4.76 \times 10^9$) and heat transfer correlations were obtained to predict the heat losses from the inner cylinder and its vertical side-faces.

References

Bejan, A., and Kimura, S., 1981, "Penetration of Free Convection Into a Lateral Cavity," *Journal of Fluid Mechanics,* Vol. 103, pp. 465–478.

Chan, Y. L., and Tien, C. L., 1985, "A Numerical Study of Two-Dimensional Natural Convection in Square Open Cavities," *Numerical Heat Transfer,* Vol. 8, pp. 65–80.

Chan, Y. L., and Tien, C. L., 1986, "Laminar Natural Convection in Shallow Open Cavities," ASME JOURNAL OF HEAT TRANSFER, Vol. 108, pp. 305–309.

Desai, C. P., and Vafai, K., 1994, "An Investigation and Comparative Analysis of Two-Dimensional and Three-Dimensional Turbulent Natural Convection in a Horizontal Annulus," *International Journal of Heat and Mass Transfer,* Vol. 37, pp. 2475–2504.

Desai, C. P., and Vafai, K., 1996, "Experimental and Numerical Study of Buoyancy Induced Flow and Heat Transfer in an Open Annular Cavity," *International Journal of Heat and Mass Transfer,* Vol. 39, pp. 2053–2066.

Farouk, B., and Guceri, S. I., 1982, "Laminar and Turbulent Natural Convection in the Annulus Between Horizontal Concentric Cylinders," ASME JOURNAL OF HEAT TRANSFER, Vol. 104, pp. 631–636.

FIDAP Theory Manual, 1993, Fluid Dynamics International, Evanston, IL.

Fukuda, K., Miki, Y., and Hasegawa, S., 1990, "Analytical and Experimental Study on Turbulent Natural Convection in a Horizontal Annulus," *International Journal of Heat and Mass Transfer,* Vol. 33, pp. 629–639.

Fukuda, K., Miki, Y., Taniguchi, N., Morita, K., and Hasegawa, S., 1991, "Direct Simulation and Large Eddy Simulation of Turbulent Natural Convection in a Horizontal Annulus," Memoirs of Faculty of Engineering, Kyushu University, Vol. 51, pp. 355–369.

Hess, C. F., and Henze, R. H., 1984, "Experimental Investigation of Natural Convection Losses From Open Cavities," ASME JOURNAL OF HEAT TRANSFER, Vol. 106, pp. 333–338.

Humphrey, J. A. C., and To, W. M., 1986, "Numerical Simulation of Buoyant Turbulent Flow—II. Free and Mixed Convection in a Heated Cavity," *International Journal of Heat and Mass Transfer,* Vol. 29, pp. 593–610.

Kline, S. J., and McClintock, F. A., 1953, "Describing Uncertainties in Single Sample Experiments," *Mechanical Engineering,* pp. 3–8.

Kuehn, T. H., and Goldstein, R. J., 1976, "An Experimental and Theoretical Study of Natural Convection in the Annulus Between Horizontal Concentric Cylinders," *Journal of Fluid Mechanics,* Vol. 74, pp. 695–719.

Le Quere, P., Humphrey, J. A. C., and Sherman, F. S., 1981, "Numerical Calculation of Thermally Driven Two-Dimensional Unsteady Laminar Flow in Cavities of Rectangular Cross Section," *Numerical Heat Transfer,* Vol. 4, pp. 249–283.

McLeod, A. E., and Bishop, E. H., 1989, "Turbulent Natural Convection of Gases in Horizontal Cylindrical Annuli at Cryogenic Temperatures," *International Journal of Heat and Mass Transfer,* Vol. 32, pp. 1967–1978.

Moffat, R. J., 1988, "Describing the Uncertainties in Experimental Results," *Experimental Thermal and Fluid Science,* Vol. 1, pp. 3–17.

Penot, P., 1982, "Numerical Calculation of Two-Dimensional Natural Convection in Isothermal Open Cavities," *Numerical Heat Transfer,* Vol. 5, pp. 421–437.

Sernas, V., and Kyriakides, I., 1982, "Natural Convection in an Open Cavity," *Proc. 7th International Heat Transfer Conference,* Munich, Germany, Vol. 2, pp. 275–286.

Vafai, K., and Ettefagh, J., 1990, "The Effects of Sharp Corners on Buoyancy Driven Flows with Particular Emphasis on Outer Boundaries," *International Journal of Heat and Mass Transfer,* Vol. 33, pp. 2311–2328.

Vafai, K., and Ettefagh, J., 1991, "Axial Transport on Natural Convection Inside of an Open Ended Annulus," ASME JOURNAL OF HEAT TRANSFER, Vol. 113, pp. 627–634.

Effects of Surface Properties on Radiative Transfer in a Cylindrical Tube With a Nonparticipating Medium

Y. R. Sivathanu
sivathan@ecn.purdue.edu

J. P. Gore

Thermal Sciences and Propulsion Center,
School of Mechanical Engineering,
Purdue University,
West Lafayette, IN 47907-1003

Radiative heat transfer inside a cylindrical tube is modeled using a statistical method called the discrete probability function (DPF) method. The DPF method involves solution of the equation of radiative heat transfer using Lagrangian simulations of representative photon trajectories on a discrete spatial grid. The DPF method is different from the Markov Chain method in terms of associating a probability with each state of the photon rather than a transition from one state to another. The advantages and disadvantages of the DPF method in comparison to the Markov Chain method are demonstrated in this paper using two practical applications of the cylindrical tube radiative heat transfer problem. The cylindrical tube has a hot source at one end and a detector at the other end. The cylindrical wall absorbs and reflects (both diffusely and specularly) the radiation incident on it. The present calculations have applications in: (1) intrusive pyrometry with collimating light guides, and (2) measurement of the spectral absorption and reflection coefficients of coatings using two, coated cylindrical tubes as specimen. The results show that: (1) the effect of light guide surface properties on errors in pyrometry must be carefully assessed, and (2) the method can be used for a convenient evaluation of radiative properties of coatings.

Introduction

The calculation of radiative transfer in enclosures with and without participating media is of considerable engineering interest. Solutions to the equation of radiative transfer in enclosures have been obtained using a wide variety of methods. Pioneering computations (Hottel, 1954; Oppenheim, 1956; and Sparrow et al., 1961) involved solutions to the radiative transfer equations for diffuse surfaces. Eckert and Sparrow (1961) pioneered the use of the angle-factor method for analyzing radiative transfer in enclosures with specular surfaces. Subsequently, different approximate methods based on extensions of the angle factor, or the script-F method, have been used to analyze radiative transfer in enclosures having specular and diffuse surfaces (Sparrow et al., 1962; Bobco, 1964; Bevans and Edwards, 1965; and Sarofim and Hottel, 1966). In addition, analytical methods for the calculation of radiative heat transfer for simple surfaces such as cylindrical and conical cavities (Lin and Sparrow, 1965) and axisymmetric passages (Rabl, 1977; and Mahan et al., 1979) have been developed.

Statistical methods for the calculation of radiative heat transfer in enclosures using Monte Carlo simulations have been published a few decades ago (Howell and Perlmutter, 1964; and Perlmutter and Howell, 1964). Initially, unbiased or Direct Monte Carlo (Corlett, 1966; and Toor and Viskanta, 1968) simulations were used to calculate the thermal radiation in enclosures with mixed specular/diffuse surfaces. A review of the earlier Monte Carlo simulations of radiative transfer problems is found in Howell (1968).

Direct Monte Carlo methods are computer intensive, and therefore fully vectorized or parallelized codes are very helpful in reducing the costs associated with long run times. Monte Carlo algorithms for an irregular enclosure with arbitrary values for surface properties (transmitivity, specular, and diffuse reflectivity) have been implemented using fully vectorized codes (Burns and Pryor, 1989). The accuracy and convergence of direct Monte Carlo algorithms have been documented (Maltby and Burns, 1991). A grid shading algorithm (Burns and Pryor, 1989) was shown to reduce computational time significantly. For complex two-dimensional and three-dimensional heat transfer problems, similar changes in the photon tracking kernel are necessary to obtain reasonable computational efficiency, and the authors (Burns and Pryor, 1989) suggested a weighted, moving average process to reduce the number of photon trajectories required in such calculations.

There are several methods of reducing the sample size in Monte Carlo methods such as importance sampling and correlation and statistical estimation techniques (Kahn and Marshall, 1953). For radiative transfer calculations, weighting and biasing individual photons (Lanore, 1971) and importance sampling in conjunction with angular discretization (Burgart and Stevens, 1970) have shown to reduce the computational time and increase accuracy for deep penetration problems.

Other schemes for improving accuracy, such as the energy partition method (Shamsundar et al., 1972; and Modest, 1978), have been used to combine deterministic elements with a Monte Carlo simulation of radiative transfer calculations. Haji-Sheikh (1988) and Burns et al. (1990) provide a detailed literature review of the more recent Monte Carlo simulations of radiative transfer. Haji-Sheik (1988) provides a very thorough exposition of the importance sampling method in radiative heat transfer problems for variance reduction. Monte Carlo methods are currently being used in a variety of problems demonstrating their applicability for irregular shapes (Parthasarathy et al., 1994), discrete arrays (Drost and Welty, 1992), and diffuse and specular reflectance and transmittance in axisymmetric enclosures (Burns et al., 1992). Recent papers (Tong and Skocypec, 1992)

Contributed by the Heat Transfer Division for publication in the JOURNAL OF HEAT TRANSFER. Manuscript received by the Heat Transfer Division June 12, 1996; revision received March 3, 1997; Keywords: Measurement Techniques, Numerical Methods, Radiation Interactions. Associate Technical Editor: B. W. Webb.

have shown that application of similar Monte Carlo approaches to a bench mark problem can result in differences in solutions that are up to factors of 2 to 3.

Markov chain theory (Naraghi and Chung, 1984; and Billings et al., 1991) has been used to calculate the radiation interchange in enclosures with a finite number of isothermal diffuse and specular surfaces. Similar to the exodus modification of the Monte Carlo method (Emery and Carson, 1968), Markov chain theory does not need random number generators, eliminating one source of statistical fluctuations in the solutions. For single parameter state definition of the Markov chains, the calculation of the transition probability matrix for multiple (more than twice) reflected photons, or for arbitrarily varying specular reflectivity, proves to be challenging. A two-parameter state definition in conjunction with the Markov chain method (Billings et al., 1991) makes it easier to treat specular reflections in enclosures. Billings et al. (1991) modeled the radiative heat transfer in a two-dimensional square enclosure using this method. The biggest advantage of the Markov chain method is the ability to reuse the probability transition matrix.

Recently, to address the disadvantages associated with the use of random number generators in the Monte Carlo methods, we developed a Discrete Probability Function (DPF) method to calculate the spectral radiation intensity leaving a representative path in a flame (Sivathanu and Gore, 1993). The DPF method involves discretization of the probability density functions (PDFs) of the initial and boundary conditions of a variable into a finite number of bins (histogram representation). The governing equations are then applied to the individual bin values. Application of the governing equations to individual bin values is similar to their application to randomly selected values in the Monte Carlo method. In the DPF method, the values and probabilities associated with the solutions of the governing equations obtained are rebinned to provide the PDF of the solution. In the Monte Carlo method, the random sampling algorithm selects more of the higher-probability values and less of the lower-probability values of the initial and boundary conditions and source functions. The application of the governing equations to the resulting realizations leads to solutions that upon binning yield their PDF.

The DPF method was subsequently applied to the calculation of the view factors in a cylindrical tube with diffusely reflecting surfaces (Sivathanu and Gore, 1994). The computational cost of carrying the information concerning the probabilities was found to be less than that of considering a large number of random realizations required for Monte Carlo calculations in these two applications (Sivathanu and Gore, 1993; Sivathanu and Gore, 1994).

The two objectives of the present paper are: (1) to present an application of the DPF method for the calculation of radiative transfer in a cylindrical tube with specular and diffuse reflections, and (2) to provide two practical applications of the calculations involving error estimation in two-wavelength pyrometry and the inverse determination of the optical properties of commercial paints and coatings. The similarities and differences between the Markov chain and the Discrete Probability Function methods are also highlighted.

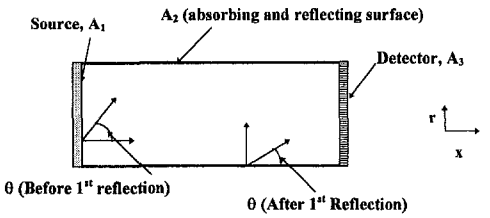

Fig. 1 The cylindrical tube used for simulating photon transport

Theoretical Methods

In intrusive two-wavelength pyrometry (Sivathanu et al., 1991), a long stainless steel tube is used to collimate and guide the radiation intensity from a source at one end of the tube onto a detector placed at the other end. The radiation intensities (i_λ) at the detector end of the tube at two wavelengths (λ_1 and λ_2) are measured and used to obtain the apparent source temperature as (in the limit of large λT):

$$T = \frac{C_2(1/\lambda_2 - 1/\lambda_1)}{\ln\left(\frac{i_{\lambda 1}}{i_{\lambda 2}}\frac{\lambda_1^5}{\lambda_2^5}\frac{\epsilon_{\lambda 2}}{\epsilon_{\lambda 1}}\right)} \quad (1)$$

where C_2 is the second radiation constant and $\epsilon_{\lambda i}$ is the spectral emissivity at wavelength λ_i.

The cylindrical surface of the tube (length = L, radius = R) absorbs some of the radiation intensity incident on it and reflects the rest specularly and diffusely, as shown in Fig. 1. As a result of the wavelength dependent reflections on the cylindrical surface, the spectral content of the radiation incident on the detector is different than that of the source. In the present work, the errors in pyrometric temperature measurements, caused by the interaction of the photons with the cylindrical surface, are modeled. For this purpose, a hot emitting surface of known temperature is located at one end of the tube (surface A_1 in Fig. 1), and a cold and nonreflecting detector surface (surface A_2) is placed at the other end. The cold cylindrical curved wall (surface A_3) absorbs part of the radiation, and the remainder is reflected diffusely and specularly. The trajectories of emitted photons representing bin values in the probability distribution functions of location and angles of emissions are followed. A representative temperature value of 1500 K and spectral emissivity values of 0.111 and 0.10 at 900 and 1000 nm wavelengths

Nomenclature

B = number of bins in the DPF of azimuthal angle
C_2 = second radiation constant
$f(\phi)$ = probability density function of variable ϕ
i = radiation intensity
L = length of the tube
l = direction cosine
M = number of bins in the DPF of polar angle
m = direction cosine
N = number of bins in the DPF of position
n = direction cosine
$P(\phi)$ = discrete probability function of variable ϕ
R = radius of the tube
l, m, n = direction cosines
r = radial coordinate
x = axial coordinate

Greek

ϵ = emissivity
ϕ = azimuthal angle
μ = cosine of the polar angle
θ = polar angle
ρ = hemispherical reflectivity
ρ_s = hemispherical specular reflectivity
ρ_d = hemispherical diffuse reflectivity

Subscripts

λ = wavelength
λ_1 = first measurement wavelength (1000 nm)
λ_2 = second measurement wavelength (900 nm)
i, j, k = subscripts for bin values

were chosen for the source. These values yield spectral emission intensities from the hot surface that are of similar magnitude to the average intensities leaving luminous flames (Sivathanu et al., 1991).

The surfaces and angles shown in Fig. 1 are discretized to obtain surface and angular ranges, similar to the method of Billings et al., 1991. The source surface A_1 is divided into N annular subsurfaces, each of equal width Δr. The polar angle θ, and the azimuthal angle ϕ (with respect to a normal to the surface A_1 at location r) are divided into M and B equal angle ranges, $\Delta\theta$ and $\Delta\phi$, respectively.

The normalized probability density function (PDF) of a photon leaving surface A_1 at a radius r, and in a direction with polar and azimuthal angles θ and ϕ, is given by (Sivathanu and Gore, 1994)

$$f(r, \mu, \phi) = f(r)f(\mu)f(\phi) \tag{2}$$

$$f(r) = 2r/R^2 \tag{3}$$

$$f(\mu) = 2\mu \tag{4}$$

$$f(\phi) = 1/2\pi \tag{5}$$

where μ is equal to $\cos\theta$ and R is the radius of the cylinder. Equations (2–5) represent Lambertian emission from the surface A_1. We have chosen Lambertian emission because it provides the angular emission characteristics of a black body. For real surfaces, a different angular distribution could be used (if available), but for the purposes of the present study it was deemed to be an unnecessary complication.

Following Sivathanu and Gore (1993), the three PDFs associated with the emission of the photons from surface A_1 are discretized to obtain their respective DPFs $P(r)$, $P(\mu)$, and $P(\phi)$ as

$$P(r) = (r_i; P_{ri}); \quad i = 1, N \tag{6}$$

$$P(\mu) = (\mu_j; P_{\mu j}); \quad j = 1, M \tag{7}$$

$$P(\phi) = (\phi_k; P_{\phi k}); \quad k = 1, B \tag{8}$$

where

$$P_{\Phi i} = \int_{\Phi_i - \Delta\Phi/2}^{\Phi_i + \Delta\Phi/2} f(\Phi)d\Phi \tag{9}$$

Φ represents one of the three variables r, μ, or ϕ and P_{ri}, $P_{\mu j}$ and $P_{\phi k}$ are the probabilities that a photon is emitted from the surface range r_i, polar angular range θ_j, and azimuthal angular range ϕ_k.

The photon emitted from r_i, θ_j, and ϕ_k intersects the cylinder at an x-location (x^1):

$$x^1 = \frac{l_j[r_i m_{jk} + \{R^2(m_{jk}^2 + n_{jk}^2) - r_i^2 n_{jk}^2\}^{1/2}]}{m_{jk}^2 + n_{jk}^2} \tag{10}$$

where the superscript 1 represents the first interaction of the photon with the cylindrical surface and l_j, m_{jk}, and n_{jk} are the direction cosines given by

$$l_j = \cos\theta_j; \; m_{jk} = \sin\theta_j \cos\phi_k; \; n_{jk} = \sin\theta_j \sin\phi_k. \tag{11}$$

If x^1 is greater than the length of the tube, the photon strikes the detector. Otherwise, it intersects the wall where it undergoes a diffuse or a specular reflection. The photons which leave surface A_1 and strike the wall are characterized by a location given by the surface range x_i^1 (which is on surface A_2), and new polar and azimuthal angles given by θ_j^1, and ϕ_k^1. The angles are determined by whether the photon is specularly or diffusely reflected. This is identical to the two state parameters in the Markov chain method of Billings et al. (1991) and x_i^1, θ_j^1, and ϕ_k^1 can be considered to be the new three-parameter state of the photon. The point of departure from the Markov chain method is that each of these states have a probability associated with them through the DPF calculations, rather than the probability being associated with the transition of a photon from the old state of r_i, μ_j, and ϕ_k to the new state of x_i^1, μ_j^1, and ϕ_k^1.

The probabilities associated with the photon at the new state (x^1) (treated as "reemission") are found by summing up the probabilities associated with all possible combinations of the old states, and can be expressed as (Sivathanu and Gore, 1994)

$$P(x^1) = (x_i^1; P_{x_i}^1); \; i = 1, N \tag{12}$$

where

$$P_{x_i}^1 = \sum_{i=1}^{N}\sum_{j=1}^{M}\sum_{k=1}^{B} \delta(x^1)P_{ri}P_{\mu j}P_{\phi k}\rho_\lambda \tag{13}$$

where $\delta(x^1) = 1$ if $x_i - \Delta x_i/2 \le x^1 \le x_i + \Delta x_i/2$; $\delta(x^1) = 0$. x^1 is obtained from Eq. (10). To maintain a high degree of accuracy, the probabilities are divided among two neighboring bins (δ takes a fractional value between 0 and 1 for the $i-1$, i, and $i+1$ bins depending on the proximity of x^1 to x_i). Physically, Eqs. (10–13) imply that the probability of a photon starting from surface range x_i^1 is the sum of the products of the probabilities that the photon started from r_i, θ_j, and ϕ_k and intersected the curved surface between $x_i - \Delta x_i/2$ and $x_i + \Delta x_i/2$ multiplied by the spectral reflectivity (ρ_λ). The factor ρ_λ accounts for the fraction absorbed by the curved surface. Of the reflected photons, a certain fraction are specularly reflected, and the remainder are diffusely reflected. It is noted that for each value of i, j, and k under the summation signs, the product $\delta(x^1)P_{ri}P_{\mu j}P_{\phi k}\rho_\lambda$ is identical to the transition probability of the photon going from states r_i, μ_j, and ϕ_k to the new state after interaction with the surface.

It is slightly more difficult to calculate the probabilities for the angles of departure of the specularly reflected fraction of the photons, since these probabilities depend on the angle of incidence. If the surface is totally diffuse (Sivathanu and Gore, 1994), these probabilities are independent of the location x_i and are identical to the probabilities of Lambertian emission. However, for the present problem, the surface reflects specularly and diffusely; therefore, a joint-probability density function for the angles of reemission, and the location of the photon after reflection, is needed. The method of calculating these joint-probability density functions are, in principle, identical to those given in Eqs. (10–13). For the polar angle θ^1 and axial location x^1, the joint discrete probability function of reemission, is defined as

$$P(\mu^1, x^1) = ((\mu_j^1, x_i^1); P_{\mu_j x_i}^1); \quad j = 1, M; \quad i = 1, N \tag{14}$$

where $P_{\mu_j x_i}^1$ is the probability that a photon is emitted from the surface range x_i in the polar angle range θ_j after 1 interaction with the wall. For specular reflection, the new polar angle of emission of the reflected photon, which is incident at an angle of θ_j, is given by

$$\theta^1 = \theta_j. \tag{15}$$

The probability associated with the photons reemitted in the θ_j^1 direction consists of both a specular component $P_{\mu_j x_i}^{1s}$ which is given by

$$P_{\mu_j x_i}^{1s} = \sum_{i=1}^{N}\sum_{j=1}^{M}\sum_{k=1}^{B} \delta(x^1)\delta(\theta^1)P_{ri}P_{\mu j}P_{\phi k}\rho_{s\lambda} \tag{16}$$

where $\delta(\theta^1) = 1$ if $\mu_j - \Delta\mu_j/2 \le \cos(\theta^1) \le \mu_j + \Delta\mu_j/2$, and $\delta(\theta^1) = 0$. The superscript "s" implies that only the specular component has been used for calculating these probabilities. The last term in Eq. (16) represents the fraction of photons that undergo specular reflection. The probability of the fraction which are diffusely reflected is added to that of the specular component to obtain the joint discrete probability function of a

photon emitted from the surface range x_i in the polar angle range θ_j after 1 interaction with the wall

$$P^1_{\mu_j x_i} = P^{1s}_{\mu_j x_i} + 2\mu_j * \Delta\mu_j \left(P^1_{x_i} - \sum_{j=1}^{M} P^{1s}_{\mu_j x_i} \right). \quad (17)$$

The second term in Eq. (17) distributes the probabilities associated with the diffuse component to the different θ_j directions based on Lambertian emission given by Eq. (4).

Finally, the joint DPF of axial location, polar, and azimuthal angle $P^1_{\phi_k \mu_j x_i}$ after 1 interaction with the wall is calculated in a similar manner. For specular reflection, the azimuthal angle of emission ϕ^1 after one reflection, for a photon which was emitted from surface A_1 in the range ϕ_k, is

$$\phi^1 = \phi_k \quad (18)$$

and the associated probability is given by

$$P^1_{\phi_k \mu_j x_i} = \sum_{i=1}^{N} \sum_{j=1}^{M} \sum_{k=1}^{B} \delta(x^1)\delta(\theta^1)\delta(\phi^1) P_{ri} P_{\mu j} P_{\phi k} \rho_{s\lambda} \quad (19)$$

where $\delta(\phi^1) = 1$ if $\phi_k - \Delta\phi_k/2 \le \phi^1 \le \phi_k + \Delta\phi_k/2$, and $\delta(\phi^1) = 0$. As before, we add the probabilities associated with the diffuse component of reflection (Eq. 5) as

$$P^1_{\phi_k \mu_j x_i} = P^{1s}_{\phi_k \mu_j x_i} + \frac{\Delta\phi}{2\pi} \left(P^1_{\mu_j x_i} - \sum_{k=1}^{N} P^1_{\phi_k \mu_j x_i} \right). \quad (20)$$

At the end of the above procedure, Eq. (20) represents the probability associated with the photon reemission from surface A_2 (see Fig. 1) in the surface range x_i, and angular ranges μ_j and ϕ_k, after one reflection. Summing up these probabilities for all the surface and angular ranges yields the total probability that a photon initially emitted from surface A_1 will interact with the surface A_2. The remaining probabilities represent the view factor (Sivathanu and Gore, 1994) from the hot end of the cylinder to the cold end.

The next step in the process is to calculate the subsequent trajectories for the photons that have undergone one reflection at the wall. The radial location of the photons is no longer an independent variable since all the photons now start from the wall with radius R; however, their axial location varies from 0 to L. The photons are started from all the N bins of x_i^1, μ_j^1, and ϕ_k^1. The x-coordinates of the second (and subsequent) intersections are given by

$$x^2 = x_i^1 + 2l_j \{ Rm_{jk}/(m_{jk}^2 + n_{jk}^2) \} \quad (21)$$

where the superscript "2" is a counter, indicating the second interaction of the photon with the wall. The probabilities associated with each photon that undergoes this interaction are given by $P^1_{\phi_k \mu_j x_i}$. These probabilities are rebinned using the procedure explained in Eqs. (13, 17, and 20) to obtain $P^2_{\phi_k \mu_j x_i}$. The solution procedure is carried forward to obtain $P^3_{\phi_k \mu_j x_i}$, $P^4_{\phi_k \mu_j x_i}$, ... The process is terminated when more than 99.5 percent of the photons have been absorbed by the cylindrical surface or leave the tube through the right and left ends.

The simulations to calculate the intensity incident on the detector were carried out with 50 annular rings and 50 ranges of polar and azimuthal angles. For the Markov chain method, for even one interaction (e.g., the $n-1$ to the n^{th} interaction) the transition probability matrix would have $50 \times 50 \times 50$ elements, with each element containing the probability of transition from x_i^{n-1}, θ_j^{n-1}, ϕ_k^{n-1} to x_i^n, θ_j^n, ϕ_k^n. These probabilities are difficult to compute when n is greater than 2 for such a large number of surface and angular ranges. In the DPF method, the probabilities associated with each interaction Eqs. (13, 17, and 20) were obtained by tracking a total of 125,000 photons through just one interaction with the wall. It is noted that the recursive nature of the algorithm results in a computational advantage over explicit solutions since the probabilities are always rebinned after one interaction with the wall. Even with specular/diffuse surfaces and the three dimensional trajectory, the total number of calculations are restricted to $N \times M \times B$ (125,000 in the present case). In addition, all possible photon trajectories (resolved to the surface and angular ranges), which have a probability of greater than 1 in 1000, are computed. This feature provides solutions with a high degree of accuracy. The method can be extended to participating media and other geometries since the probabilities are associated primarily with the photons and it is not necessary to compute transition probabilities explicitly.

The disadvantage over the Markov chain method is that since the transition probabilities are not explicitly stored, any surface property changes will require the simulation to be repeated. However, if only the temperature of the source is changed, the probabilities can be explicitly used to find the intensity incident on the detector.

Table 1 Comparison between solutions obtained for sample calculations using the DPF and analytical method

Reflectivity	Specular component	Analytical solution	DPF method
0.00	N/A	0.09167	0.09138
1.00	1.00	1.000	0.9992

Results and Discussion

The improved accuracy of the DPF method over direct simulation Monte-Carlo for higher order moments has been shown in our previous work (Sivathanu and Gore, 1994). For example, in view-factor calculations using the DPF method, the accuracy is better than 1 part in 1000 (Sivathanu and Gore, 1994). This is because a large number of subsurfaces and subangles (50 each) are used. In addition, the statistical noise (which is evident primarily for the higher order moments of the solutions) resulting from the use of a random number generator is avoided (Sivathanu and Gore, 1994). For mean properties, very high accuracy can be achieved with both the DPF method and the direct simulation Monte-Carlo method. Table 1 illustrates the accuracy of the DPF method for two limiting cases where analytical solutions are available.

Inverse Determination of Optical Properties of Coatings. The normalized intensities incident on the detector for three different reflectivities of the cylindrical surface with the specular component varying from 0 percent to 100 percent are shown in Fig. 2. The aspect (length to radius) ratio of the cylinder is 3. The normalized intensity increases as the specular component of the reflectivity increases. When the cylindrical surface is specular, and the reflectivity is unity, all the radiation emitted by the source is incident on the detector as expected. There is a wide variation in the intensity that reaches the detector, even for a small aspect ratio of 3, depending on the surface properties of the cylindrical tube. For a totally reflecting surface, the normalized intensities vary from 0.444 to 1 when the specular component is varied from 0 percent to 100 percent. Therefore, the specular component of the reflectivity of a coating with a known reflectivity can be measured using an inverse method with a high degree of accuracy utilizing a coated tube and a detector.

Alternatively, tubes with two different L/R ratios (3 and 6) can be used to measure the reflectivity and its specular component. The ratio of the intensities at the end of the two different tubes (with aspect ratios of 3 and 6) for the three different reflectivities is shown in Fig. 3. For determining the reflectivity of the coating and its specular component, two intensity measurements are required.

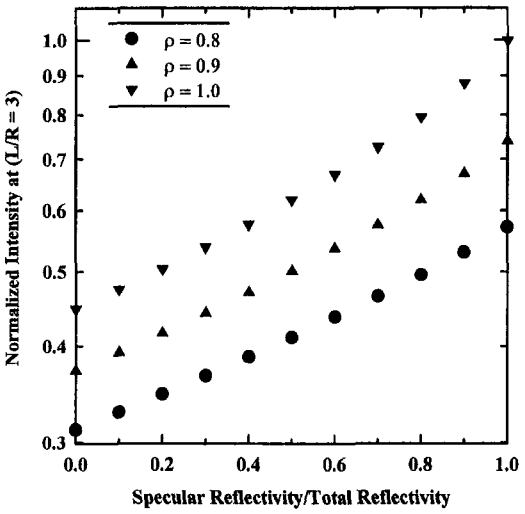

Fig. 2 The variation of normalized intensity with the specular component of reflectivity

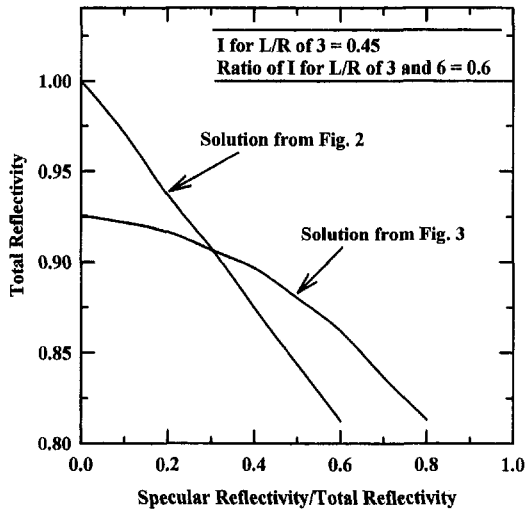

Fig. 4 Inverse graphical determination of the reflective properties of a coating

For example, let the normalized intensity at the end of the coated tube (with L/R of 3) be 0.45 and the ratio of intensities measured for the two coated tubes, with aspect ratios of 3 and 6, be 0.6. An inverse graphical determination of the total reflectivity and its specular component is illustrated in Fig. 4. For a normalized intensity of 0.45 at the end of the tube with $L/R = 3$, the different possible combinations of total reflectivity and its specular component can be obtained from Fig. 2. Further, for a given ratio of intensities at the end of the two tubes, a different combination of reflectivity and total reflectivity can be obtained from Fig. 3. These two possible combinations are shown by the solid lines in Fig. 4. The intersection of these two lines simultaneously provides the reflectivity (approximately 0.91) and the specular component (approximately 0.31).

Effect of Coating Property on Two-Wavelength Pyrometry. The effect of aspect ratio on the apparent source temperature in two wavelength optical pyrometry is shown in Fig. 5. If the coating is gray ($\rho_{\lambda 1} = \rho_{\lambda 2}$), the apparent temperature is accurate (same as the source temperature) for all aspect ratios. However, if the coating on the cylindrical walls has a reflectivity which varies inversely with wavelength, typical of pigments used in commercial paints, errors are introduced in the estimated

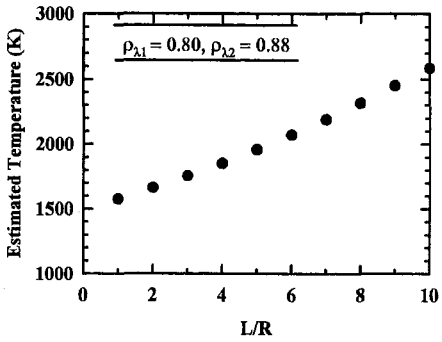

Fig. 5 Estimated temperatures as a function of aspect ratio

temperature for tubes of all aspect ratios greater than zero. When the aspect ratio is zero, the apparent temperature is 1500 K since only direct radiation is incident on the detector. The radiation which was not absorbed was assumed to be reflected diffusely (specular component = 0) with the transmitivity of the coating being zero. The total reflectivity of the coating was assumed to be 0.8 at 1000 nm. Table 2 shows the properties of the tube coating as a function of wavelength used for the calculations shown in Figs. 5–7. As the aspect ratio of the tube increases, the radiation incident on the detector consists of photons that have undergone multiple reflections with the cylindrical walls of the tube. Therefore, the longer wavelength radiation is preferentially absorbed, leading to higher estimates for the apparent source temperatures. At an aspect ratio of 5, more that 70 percent of the photons have undergone at least five or more interactions with the wall coating, and the measured source temperature is higher by approximately 500 K than the actual value. Therefore, in two wavelength pyrometry, it is crucial to have a coating with a very high absorption coefficient. If the coating has an absorptivity of nearly one, or a reflectivity

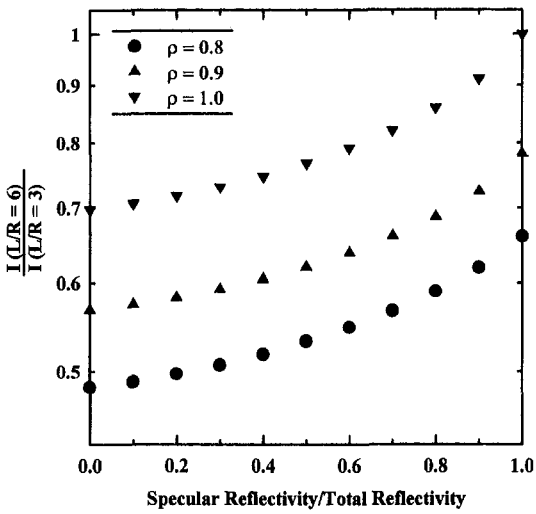

Fig. 3 The variation in ratio of intensities obtained at the end of two tubes with different values of reflectivity

Table 2 Surface properties used for estimating the errors caused by a pyrometer with sighting tube

Properties used	Reflectivity at 900 nm	Reflectivity at 1000 nm	Specular component
Fig. 5	0.88	0.80	0.00
Fig. 6	0.88	0.80	0.00 to 1.00
Fig. 7	0.556 to 1.00	0.50 to 0.90	0.40

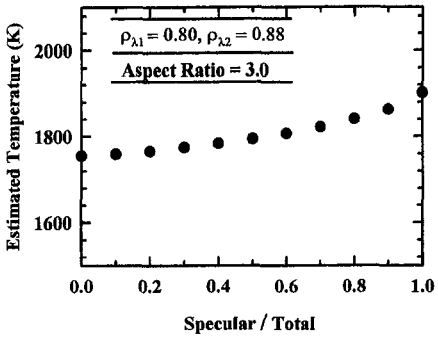

Fig. 6 Variation in estimated temperatures with the specular component of reflectivity

of zero, then the apparent temperature obtained from the two-wavelength pyrometer is 1500 K (or equal to the source temperature) since only direct radiation from the source is incident on the detector.

The effect of the specular component of the reflectivity on the apparent temperatures is shown in Fig. 6 for a tube with $L/R = 3$. The effect of reflectivity depends on the number of interactions the photons undergo with the wall. An increase in the specular component increases the number of photons that reach the detector after an interaction with the wall. Therefore, the temperatures estimated by the detector are higher since this larger fraction of the photons have undergone preferential longer wavelength absorption. When the specular reflection is unity, approximately 85 percent of the radiation incident on the detector is from photons that have undergone multiple reflections at the wall.

The variation in the apparent temperatures with reflectivity of the cylindrical surface is shown in Fig. 7. The ratio of specular to total reflectivity of the surface was set at 0.4. As the reflectivity of the cylindrical surface is decreased, a larger fraction of the photons are absorbed at the cylindrical surface and a higher percentage of the radiation incident on the detector is from direct radiation, leading to a better estimate of the source temperature.

If the optical properties of the tube coating are known, then the source temperature can be inferred using the apparent temperature. The source temperatures for different apparent temperatures, when the reflectivity of the tube ($L/R = 3$) varies from 0.2 to 0.8 and the specular component varies from 0.0 to 1.0, are shown in Fig. 8. As expected, when the reflectivity of the tube is higher, the apparent temperatures are also much higher than the source temperatures. This is due to the greater number of reflected photons (which have a preferential absorption for the longer wavelength) reaching the detector. Similarly, when the specular component of the reflection increases, the ratio of reflected photons to total photons at the detector increases, causing a greater upward bias in the apparent temperatures.

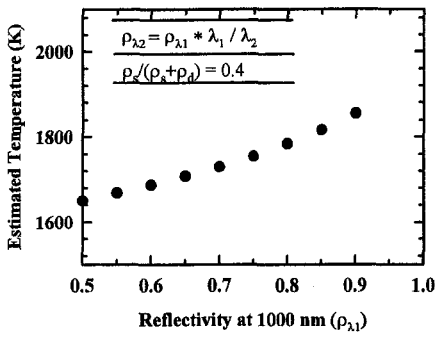

Fig. 7 The effect of reflectivity on the estimated temperatures.

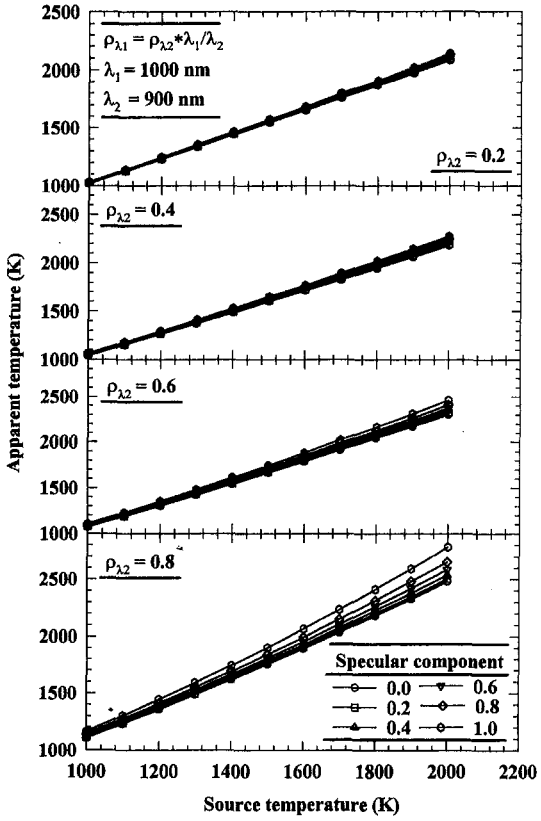

Fig. 8 Locus of apparent source temperatures for different values of reflectivity and its specular component

Conclusions

The conclusions of the present study are:

1 The Discrete Probability Function method is applicable to specular and diffuse reflections and absorption in an axisymmetric cylindrical enclosure. The specific differences between the DPF method and the Markov Chain method are presented.
2 A novel inverse method for the evaluation of reflective properties of coatings, including a delineation of the diffuse and specular components, has been discovered using the present analysis. The method requires very simple specimen (two coated tubes with different aspect ratios) and instrumentation.
3 The apparent temperatures measured using intrusive two-wavelength pyrometry could be significantly biased (by as much as 40 percent) if the reflectivity of the interior wall of the collimating tubes is high. Coating such tubes with highly absorbing paints is therefore crucial.

Acknowledgment

This work was performed under the sponsorship of the U.S. Department of Commerce, National Institute of Standards and Technology under Grant No. 60NANB5D0113 with Dr. William Grosshandler serving as the federal Program Officer. Partial support of this work by the National Science Foundation under grant number CTS-9157920 with Dr. Milton Linevsky serving as Program Director is also acknowledged.

References

Bevans, J. T., and Edwards, D. K., 1965, "Radiation Exchange in an Enclosure With Directional Wall Properties," ASME JOURNAL OF HEAT TRANSFER, Vol. 87, pp. 388–396.

Billings, R. L., Barnes, J. W., Howell, J. R., and Slotboom, O. E., 1991, "Markov Analysis of Radiative Transfer in Specular Enclosures," ASME JOURNAL OF HEAT TRANSFER, Vol. 113, pp. 429–436.

Bobco, R. P., 1964, "Radiation Heat Transfer in Semigray Enclosures with Specularly and Diffusely Reflecting Surfaces," ASME JOURNAL OF HEAT TRANSFER, Vol. 86, pp. 123–130.

Burgart, C. E., and Stevens, P. N., 1970, "A General Method of Importance Sampling the Angle of Scattering in Monte Carlo Calculations," *Nucl. Sci. Eng.*, Vol. 42, pp. 306–323.

Burns, P. J., and Pryor, D. V., 1989, "Vector and Parallel Monte Carlo Radiative Heat Transfer Simulation," *Numerical Heat Transfer,* Vol. 16, pp. 97–124.

Burns, P. J., Maltby, J. D., and Christon, M. A., 1990, "Large-Scale Surface to Surface Transport for Photons and Electrons via Monte Carlo," *Computing Systems in Engineering,* Vol. 1, pp. 75–99.

Burns, P. J., Loehrke, R. I., Dolaghan, J. S., and Maltby, J. D., 1992, "Photon Tracing in Axisymmetric Enclosures," *Developments in Radiative Heat Transfer,* HTD-Vol. 23, ASME, New York, pp. 93–99.

Corlett, R. C., 1966, "Direct Monte Carlo Calculation of Radiative Heat Transfer in Vacuum," ASME JOURNAL OF HEAT TRANSFER, Vol. 88, pp. 376–382.

Drost, M. K., and Welty, J. R., 1992, "Monte Carlo Simulation of Radiation Heat Transfer in Arrays of Fixed Discrete Surfaces using Cell-to-Cell Photon Transport," *Developments in Radiative Heat Transfer,* HTD-Vol. 203, ASME, New York, pp. 85–91.

Eckert, E. R. G., and Sparrow, E. M., 1961, "Radiative Heat Exchange Between Surfaces with Specular Reflection," *Int. J. Heat Mass Transfer,* Vol. 3, pp. 42–54.

Emery, A. F., and Carson, W. W., 1968, "A Modification to the Monte Carlo Method-The Exodus Method," ASME JOURNAL OF HEAT TRANSFER, Vol. 90, pp. 328–332.

Haji-Sheik, 1988, "Monte Carlo Methods," *Handbook of Numerical Heat Transfer,* W. J. Minkowsycz et al., eds., John Wiley & Sons Inc., New York.

Hottel, H. C., 1954, *Heat Transmission,* McGraw-Hill Book Co., New York, NY.

Howell, J. R., 1968, "Application of Monte Carlo to Heat Transfer Problems," *Advances in Heat Transfer,* Vol. 5, pp. 1–54, T. F. Irvine Jr. and J. P. Harnett, eds., Academic Press, New York.

Howell, J. R., and Perlmutter, M., 1964, "Monte Carlo Solution of Thermal Transfer Through Radiant Media Between Gray Walls," ASME JOURNAL OF HEAT TRANSFER, Vol. 86, pp. 116–122.

Kahn, H., and Marshall, A. W., 1953, "Methods of Reducing Sample Size in Monte Carlo Computations," *J. Operations Res. Society of America,* Vol. 1, pp. 263–278.

Lanore, J. M., 1971, "Weighting and Biasing of a Monte Carlo Calculation for Very Deep Penetration of Radiation," *Nucl. Sci. Eng.*, Vol. 45, pp. 66–72.

Lin, S. H., and Sparrow, E. M., 1965, "Radiant Exchange Among Curved Specularly Reflecting Surfaces-Application to Cylindrical and Conical Cavities," ASME JOURNAL OF HEAT TRANSFER, *Trans. ASME,* Series C, Vol. 87, pp. 123–130.

Mahan, J. R., Kingsolver, J. B., and Mears, D. T., 1979, "Analysis of Diffuse-Specular Axisymmetric Surfaces with Application to Parabolic Reflectors," ASME JOURNAL OF HEAT TRANSFER, Vol. 101, pp. 689–694.

Maltby, J. D., and Burns, P. J., 1991, "Performance, Accuracy, and Convergence in a Three-Dimensional Monte Carlo Radiative Heat Transfer Simulation," *Numerical Heat Transfer,* Vol. 19, pp. 191–209.

Modest, M. F., 1978, "Three-Dimensional Radiative Exchange Factors for Non-Gray, Non-Diffuse Surfaces," *Numerical Heat Transfer,* Vol. 1, pp. 403–416.

Naraghi, M. H. N., and Chung, B. T. F., 1984, "A Stochastic Approach for Radiative Exchange in Enclosures with Nonparticipating Medium," ASME JOURNAL OF HEAT TRANSFER, Vol. 106, pp. 690–698.

Oppenheim, A. K., 1956, "Radiation Analysis by the Network Method," *Trans. ASME,* Vol. 78, pp. 725–735.

Parthasarathy, G., Patankar, S. V., Chai, J. C., and Lee, H. S., 1994, "Monte Carlo Solutions for Radiative Heat Transfer in Irregular Two-Dimensional Geometries," Radiative Heat Transfer: Current Research, HTD-Vol. 276, ASME, New York, pp. 191–199.

Perlmutter, M., and Howell, J. R., 1964, "Radiant Transfer Through a Gray Gas Between Concentric Cylinders Using Monte Carlo," ASME JOURNAL OF HEAT TRANSFER, Vol. 86, pp. 169–179.

Rabl, A., 1977, "Radiation Transfer Through Specular Passages-A Simple Approximation," *Int. J. Heat Mass Transfer,* Vol. 20, pp. 323–330.

Sarofim, A. F., and Hottel, H. C., 1966, "Radiative Exchange Among Non-Lambert Surfaces," ASME JOURNAL OF HEAT TRANSFER, Vol. 88, pp. 37–44.

Shamsundar, N., Sparrow, E. M., and Heinish, R. P., 1972, "Monte Carlo Radiation Solutions-Effect of Energy Partitioning and Number of Rays," *Int. J. Heat Mass Transfer,* Vol. 16, pp. 690–694.

Sivathanu, Y. R., and Gore, J. P., 1993, "A Discrete Probability Function Method for the Equation of Radiative Transfer," *J. Quant. Spec. & Rad. Trans.,* Vol. 49, pp. 269–280.

Sivathanu, Y. R., and Gore, J. P., 1994, "A Discrete Probability Function Method for Radiation in Enclosures and Comparison with the Monte Carlo Method," *Radiative Heat Transfer: Current Research,* HTD-Vol. 276, ASME, New York, pp. 213–218.

Sivathanu, Y. R., Gore, J. P., and Dolinar, J., 1991, "Transient Scalar Properties of Strongly Radiating Jet Flames," *Combust. Sci. & Tech.*, Vol. 76, pp. 45–66.

Sparrow, E. M., Gregg, J. L., Szel, J. V., and Manos, P., 1961, "Analysis, Results, and Interpretation for Radiation Between Simply Arranged Gray Surfaces," ASME JOURNAL OF HEAT TRANSFER, Vol. 83, pp. 217–214.

Sparrow, E. M., Eckert, E. R. G., and Jonsson, V. K., 1962, "An Enclosure Theory for Radiative Exchange Between Specularly and Diffusely Reflecting Surfaces," ASME JOURNAL OF HEAT TRANSFER, Vol. 84, pp. 294–300.

Tong, T. W., and Skocypec, D. R., 1992, "Summary on Comparison of Radiative Heat Transfer Solutions for a Specified Problem," ASME HTD-Vol. 203, pp. 253–264.

Toor, J. S., and Viskanta, R., 1968, "A Numerical Experiment of Radiant Heat Interchange by the Monte Carlo Method," *Int. J. Heat Mass Transfer,* Vol. 11, pp. 883–897.

Radiative Transfer in Pulsed-Laser-Induced Plasma

X. Xu
xxu@ecn.purdue.edu

K. H. Song

School of Mechanical Engineering,
Purdue University,
1288 Mechanical Engineering Building,
West Lafayette, IN 47907

When a high-power pulsed laser interacts with materials, a plasma layer containing micrometer-size particles is formed above the target surface. The laser induced plasma changes the energy coupling mechanism between the laser beam and the target. This work investigates the radiative heat transfer process in the excimer laser generated plasma layer on the Ni specimen, in the laser fluence range between 1.5 and 5 J/cm^2. Novel diagnostic techniques are developed to measure transient transmission and scattering of the thin plasma layer within the duration of the laser pulse. Based on the measurement results, radiative heat transfer analysis is performed to evaluate the radiative properties of the plasma layer, including the optical depth, the absorption coefficient, the single scattering phase function, and the scattering size parameters. Knowledge of the radiative properties of the laser induced plasma helps to understand the energy transfer process during laser-materials interaction. Further, this work demonstrates the feasibility of using the transient scattering measurement for in situ monitoring of the size of the laser ejected particles.

Introduction

High-power pulsed lasers are used in a variety of applications in manufacturing and materials processing, including laser assisted machining, surface modification and pulsed laser deposition of thin films (Crafer and Oakley, 1992; Chrisey and Hubler, 1994). In these processes, the laser beam evaporates the target and ionizes the evaporants, creating a plasma layer between the laser and the target (Phypps and Dreyfus, 1993). The laser induced plasma layer greatly effects the mechanisms of energy transfer between the laser and the target. Understanding energy transfer in laser induced plasma is crucial for controlling laser/materials interaction.

The laser evaporation process is accompanied by ejection of particulates whose diameter is between sub-micrometers and several micrometers. Controlling the size of the particulates or eliminating these particulates is often desirable. For example, in pulsed laser deposition of thin films for microdevices fabrication, the presence of particulates can be problematic. The mechanisms of particulate formation and the transport process of the particulates in the laser ejected vapor plume need to be investigated.

A number of diagnostic methods have been developed and a large amount of research have been carried out to investigate the laser induced plasma, including mass spectroscopy, emission spectroscopy, Langmuir probes, the time-of-flight technique, and high-speed photography (e.g., papers in Braren et al., 1993). The ionization densities, velocity distributions, and chemical compositions of plasma are obtained using these techniques. However, these methods can only analyze the properties of the plasma plume after the laser pulse is terminated, therefore, they do not reveal energy transport modes between the laser and the target. The laser induced plasma propagates in a direction nearly normal to the target surface with a velocity between 10^3 to 10^4 m/s. For the time duration of the laser pulse, which is around tens of nanoseconds, the plasma front only travels a distance of a few hundred micrometers. Experimental investigations of the laser generated plasma and particulates within the laser pulse duration are hampered by the small dimension of the plasma layer before the termination of the laser pulse, its rapidly changing properties, and lack of in situ diagnostic tools. To date, few measurements were carried out to study the energy transport process in the laser induced plasma/vapor plume within the duration of the laser pulse. Time averaged absorption of the laser induced plasma was measured in the process of laser machining of ceramics (Tönshoff and Gedrat, 1990). The work by Callies et al. (1994) studied the transient transmissivity of laser induced plasma in the atmospheric environment.

This work conducted a series of experiments to investigate the transient radiative properties of the laser induced plasma and particulates layer within the laser pulse duration. Transient transmissivity and the scattering intensity of the laser induced plasma layer at the incident laser wavelength ($\lambda = 248$ nm) were measured. The energy loss due to plasma absorption, plasma scattering, and reflection at the target surface were also obtained. The test materials are thin Ni foils. Based on the measurement results, radiation transfer analysis was carried out to quantify the radiative properties of the laser induced plasma and particulates, including the transient optical depth, the absorption coefficient, the single scattering albedo, and the transient single scattering phase function. The energy coupling factors between the pulsed laser and the targets at different laser energy density were then calculated. Knowledge on these quantities enables a better understanding of laser/materials interaction. The measurement data can also be used as inputs for numerical modeling of the pulsed-laser evaporation process.

From the measured single scattering phase function, the size parameter $x\,(=\pi d/\lambda)$ of the laser ejected particulates was calculated using the Mie theory. The size of the particulates was also measured by SEM (scanning electron microscopy). It is shown that measuring the transient angular scattering intensity is a feasible method for in situ monitoring of the size of the laser ejected particulates.

Experimental Descriptions

Three experiments were designed and carried out to determine: (1) transient transmission of the laser beam through the laser induced plasma and particulates; (2) transient scattering of the laser beam from the laser induced plasma and particulates; and (3) the total energy loss to the ambient, which is due to scattering from the particulates and reflection from the specimen surface.

Figure 1 shows the experimental apparatus for measuring the transient transmission of the laser beam through a layer of laser

Contributed by the Heat Transfer Division for publication in the JOURNAL OF HEAT TRANSFER. Manuscript received by the Heat Transfer Division April 29, 1996; revision received November 14, 1996; Keywords: Laser Processing, Measurement Techniques, Radiation. Associate Technical Editor: B. Webb.

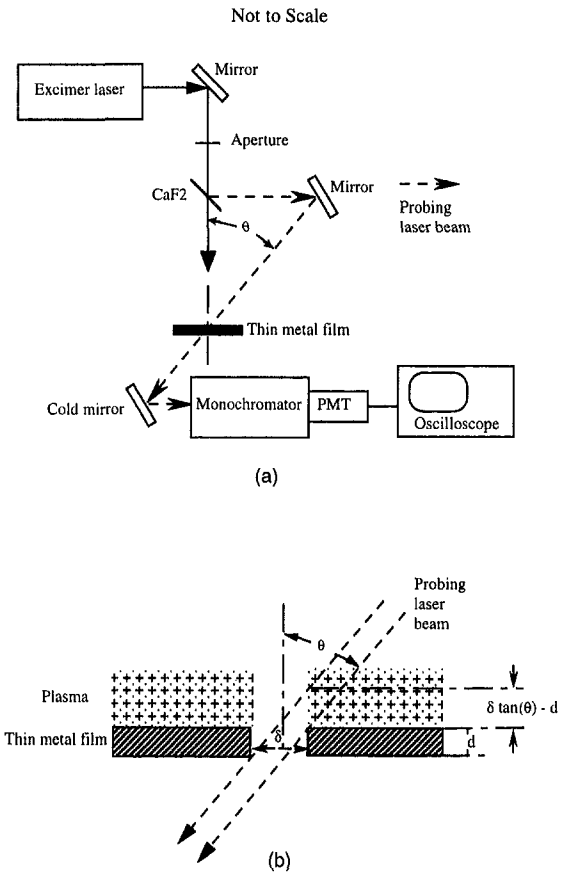

Fig. 1 Experimental set-up for measuring transient transmission of laser-induced plasma and particulates

generated plasma and particulates. Part of the description of this experiment has been reported elsewhere (Xu and Song, 1996). A KrF excimer laser beam with a pulse duration of 26 ns (FWHM) and a wavelength of 248 nm is used to evaporate the target surface. To ensure spatial uniformity of the KrF laser beam, only the center portion of the KrF laser beam is passed through a 10 mm by 5 mm aperture. This portion of the excimer laser beam is focused onto the specimen surface using a lens with a 50 mm focal length. The spot size at the specimen surface is adjusted from 1 mm by 0.5 mm to 2 mm by 1 mm. The energy of each laser pulse is monitored by a built-in energy meter of the laser, which is calibrated and converted to the energy density at the surface of the specimen.

A portion of the excimer laser beam is split from the incident laser beam by a CaF_2 plate, whose reflectivity is measured to be 8.0 percent at the excimer laser wavelength, to form a probing beam. The probing beam is then reflected by a UV mirror and directed towards the center of a several micron thick, free standing nickel specimen. A circular hole with a diameter, δ of 10 to 12 μm, is fabricated at the center of the nickel film. The transmission of the probing laser beam through the hole is measured. When a plasma layer is generated above the sample surface by excimer laser irradiation, the transient intensity of the probing beam is measured to determine its transmissivity at the excimer laser wavelength. It can be seen from Fig. 1(b) that, if the plasma layer is thicker than $\delta \tan(\theta) - d$, the entire probing laser beam passes through the plasma layer; the path length of the probing beam in the plasma layer can be determined using straight forward geometry manipulations. Here d, δ, and θ denote the thickness of the Ni film, the diameter of the hole, and the angle of the probing beam measured from the normal direction of the specimen, respectively. For a 5-μm-thick film with a hole diameter of 10 μm, and at the probing beam angle of 45 deg, transmission of the plasma layer with a minimum thickness of 5 μm ($\delta \tan(\theta) - d$) can be measured. Measurements of transmission at different angles are achieved by either moving the UV mirror, or by rotating the specimen.

A 'reference' signal is obtained by blocking the specimen from the heating laser beam and measuring the intensity of the probing beam. The ratio between the transmission through the laser induced plasma and the reference is the transmissivity. To

Nomenclature

a_l = coefficients of the Legendre polynomial
d = thickness of the specimen, diameter of the laser ejected particulates
E_1, E_2 = energy measured by energy meter 1 and 2 (Fig. 3)
E_o = energy loss to the ambient, ($=E_1 + E_2$)
F = fluence of laser irradiation
I = intensity
L = number of terms in the Legendre polynomial expansion
$M(\times 2)$ = order of the discrete ordinate approximation
N = total nodes for discretizing the optical depth, t
p = phase function
P_a = percentage of the absorbed laser energy
P_e = percentage of the laser energy extinction when the laser beam passes through plasma once
P_l = Legendre polynomial
P_o = percentage of the laser energy loss to the ambient
$P_{s,v}$ = percentage of the laser energy scattered by the laser ejected particulates
P_t = percentage of the laser energy reaching the surface of the specimen when the laser beam passes through plasma once
t = optical depth
t_p = pulse duration
w = weight of Gaussian integration
x = size parameter of the scattering center

Greek Symbols

α = absorption coefficient
δ = diameter of the hole fabricated at the center of specimens
θ = angle of incidence of the probing laser beam, polar angle in the discrete ordinate approximation
λ = wavelength
μ = cosine of the polar angle
μ' = cosine of the angle between the scattered light and the incident light
ρ = reflectivity
ρ_s = specular reflectivity
ρ_d = diffuse reflectivity
σ = scattering coefficient
τ = transmissivity
ϕ = angle between the direction of the incident excimer laser beam and the normal direction of the specimen
ω_o = single scattering albedo

Subscripts

a = absorption
i = discrete direction in the discrete ordinate method
l = Legendre polynomial
Ni = nickel
o = incident laser
s = scattering
v = laser ejected vapor and particulate

reduce and eliminate signals from plasma emission and scattering, the transmitted light is passed through a monochromator with a minimum wavelength bandwidth of 0.1 nm. The experiment showed that by blocking the probing beam, the measured signal is at the noise level. This indicates that the intensity of plasma emission and scattering within the wavelength bandwidth of 0.1 nm is negligible compared with the intensity of the probing laser beam. A photomultiplier tube (PMT) is used to capture the transmitted light through the monochromator. The use of the highly sensitive PMT is necessary since the diameter of the probing laser beam is less than 10 μm after passing through the hole. The time resolution of the PMT used in this work is about 3 ns. The signal from the PMT is recorded on a digital oscilloscope, which is operated at a sampling rate of 1 GHz. Therefore, the time resolution of the experiment is limited by the PMT.

The Ni specimen can survive more than ten laser pulses before the hole expands. The expansion of the hole is determined by measuring and comparing the intensity of the reference signal before and after the specimen is irradiated by each laser pulse.

There is substantial difference between plasma transmission obtained during the first few laser pulses. This is attributed to the contamination at the sample surface. The contaminants were removed by the first one or two laser pulses with low fluences (<2 J/cm^2). The difference between plasma transmission measurements after the second laser pulse is less than 3 percent. Observation of the surface of the specimen under the high resolution optical microscope confirms that the surface morphology of the specimen exhibits no distinguishable variation after the second laser pulse.

The experimental set up for measuring scattering from the plasma is shown in Fig. 2. Transient angular scattering at the excimer laser wavelength is measured by a detection system including a rotating rail, a light collimator, an optical fiber, a monochromator and a PMT system. Since the scattering intensity is weak, a larger hole ($\delta \approx 100$ μm) is fabricated on the specimen and a higher bias voltage is applied to the PMT to increase the measurement sensitivity. Measurements are performed at the polar angles between 20 and 70 degrees, with a ten degree increment. Diffracted radiation could be detected when the polar angle is small. Scattering can also be measured at the front side of the specimen ($\theta > 90$ deg), however, it was found that the signal obtained at those positions contains mostly diffusely reflected light from the specimen. Therefore, only the scattering intensities measured at the back side of the specimen are used to analyze the radiative properties of the laser ejected plasma and particulates.

In order to compare the intensity of scattering with the intensities of plasma emission, measurements are also taken at wavelengths other than the excimer laser wavelength. It was found that intensities at other wavelengths are at the noise level, therefore, plasma emission is insignificant compared with scattering.

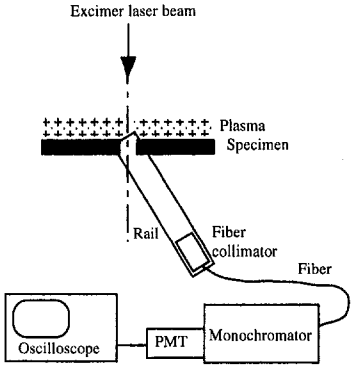

Fig. 2 Experimental set-up for measuring the transient scattering of the laser-induced plasma and particulates

Figure 3 shows the experimental apparatus for measuring the total laser energy loss to the ambient due to scattering from the laser induced plasma and particulates and reflection from the specimen surface. The specimen is positioned at the first focal point of an ellipsoidal reflector. The size of the specimen is chosen to be small, with a surface area of 3×3 mm^2, so that the specimen does not intercept the reflected light from the ellipsoidal reflector. Scattered and reflected light is collected by the ellipsoidal reflector and a CaF_2 plate, and is measured by two energy meters. The energy meter at the second focal point of the ellipsoidal reflector collects the light scattered from the plasma and diffusely reflected from the specimen. The energy meter under the CaF_2 plate measures scattered light from the plasma, and mostly specularly reflected light from the specimen. The total energy measured by the two energy meters is the total laser energy loss to the ambient. The resolution of the energy meter is 1 μJ, while the energy per laser pulse is about 80 mJ. The noise level is about 1 percent of the signal. The inner surface of the ellipsoidal is coated with UV enhance rhodium to ensure a 98 percent reflectivity at the wavelength of 248 nm.

An interference filter with a bandwidth of 3 nm and transmissivity of 13.2 percent is used to examine the radiation power from the plasma plume. The interference filter is positioned in front of the energy meter at the second focal point of the ellipsoidal reflector. It is found that the total radiation intensity outside the wavelength band of the filter is below the measurement sensitivity. Thus, thermal radiation from the plasma is again determined to be negligible compared with the reflected and scattered excimer laser intensity.

Reflectivity of liquid Ni is also measured by the set up in Fig. 3 by setting the laser fluence right below the evaporation threshold. The specular reflectivity, ρ_s, is measured to be 0.22, and the hemispherical reflectivity is measured to be 0.06 (the average diffuse reflectivity, $\rho_d = 0.06/\pi \approx 0.019/sr$). Therefore, the total reflectivity ρ_{Ni}, which includes both the specularly and diffusely reflected components, is 0.28.

Radiative Transfer Analysis

The experimental data obtained from the above measurements are used to derive the radiative properties of the laser generated plasma and particulates using the Radiative Transfer Equation (RTE) (Siegel and Howell, 1992). Transfer of the excimer laser light in the laser induced plasma layer can be modeled as a one-dimensional radiative transfer process with collimated incident radiation and anisotropic scattering. The one-dimensional approach is appropriate since within the laser pulse duration the thickness of the plasma/particulate layer in the direction normal to the sample surface is less than 200 μm, one order of magnitude smaller than the dimensions in the other two directions. When the incident collimated radiation is normal to the target surface, and the laser ejected particles are treated as randomly oriented particles, the radiative transfer process can be simplified as azimuthally independent. A RTE equation averaged over the azimuthal angle can be applied.

Scattering of the laser beam originates from both the atomic vapor and the large size particulates. However, the scattering intensity from the atomic vapor is much weaker. Therefore, a single-scattering phase function for the particulates is used in the RTE analysis, assuming that scattering from the particulates is dominant. This assumption is verified by the results of the RTE analysis, which shows that the diameter of the scattering center is about 130 nm.

The azimuthally averaged intensity I at the incident laser wavelength and at the direction of μ ($=\cos(\theta)$) is expressed by Eq. (1). In this equation, the incident collimated laser radiation is treated as an energy source term in the radiative transfer equation (Brewster, 1992):

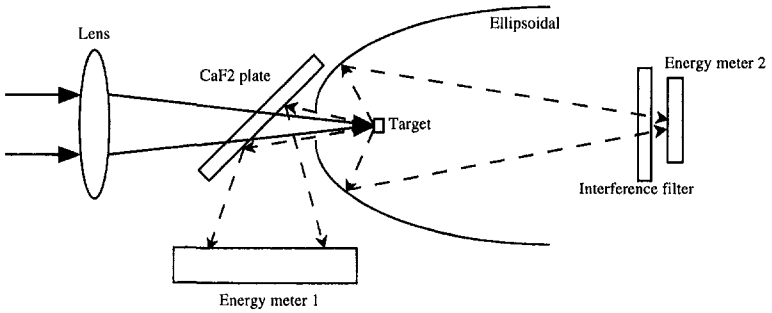

Fig. 3 Experimental set-up for measuring laser energy loss to the ambient

$$\mu \frac{dI(t, \mu)}{dt} + I(t, \mu) = \frac{\omega_o}{2} \int_{-1}^{1} I(t, \mu')p(\mu, \mu')d\mu' + \frac{\omega_o}{4\pi} I_o(\mu_o)p(\mu_o, \mu) \exp\left[-\frac{t}{\mu_o}\right] \quad (1)$$

where μ_o and I_o are cosine of the angle of the incident laser beam and the intensity of the incident laser light, respectively, $p(\mu_j, \mu_i)$ the slab phase function, and ω_o the single-scattering albedo. Since the intensity of plasma emission within the measured wavelength interval is negligible, blackbody emission is not included in Eq. (1). The optical depth, $t(x)$, is defined as $t(x) = \int_o^x [\alpha(x^*) + \sigma(x^*)]dx^*$, where α and σ are the absorption and scattering coefficient, respectively. The last term in Eq. (1) is the light intensity scattered from the collimated incident direction μ_o into the direction μ.

The boundary conditions at the top of the plasma layer, $t = t_v$, and at the surface of the target, $t = 0$, are

$$I(t_v, \mu > 0) = 0 \quad \text{at } t = t_v \quad (2a)$$

$$I(0, \mu < 0) = \rho_s \cdot I(0, -\mu) + 2\rho_d \int_{-1}^{1} I(t, \mu')d\mu' \quad \text{at } t = 0 \quad (2b)$$

where ρ_s and ρ_d are the measured specular and diffuse reflectivity of the specimen at the excimer laser wavelength, respectively.

Methods for solving RTE in a slab geometry have been described adequately in literature (e.g., Chandrasekhar, 1950). The discrete ordinates approximation is used in this work with a $2M$-order quadrature (Fig. 4). Therefore, the radiation intensity is calculated at discrete directions, μ_i (=cos (θ_i)). The Gaussian numerical quadrature is used to approximate the integrals in Eq. (1) and Eq. (2). The single scattering phase function is represented by the zero-order Legendre polynomial, i.e.,

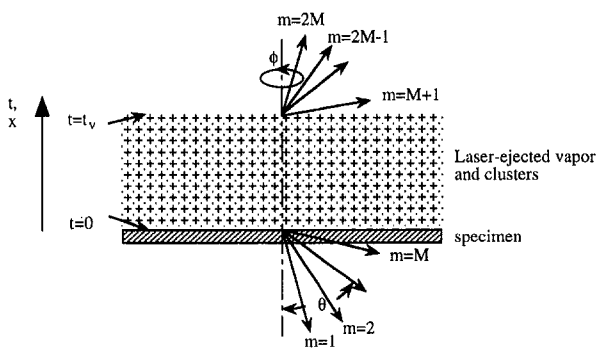

Fig. 4 Schematic of the discrete ordinate coordinates for the RTE calculation

$$p(\mu_j, \phi_j; \mu_i, \phi_i) = \sum_{l=0}^{L} a_l P_l(\mu') \quad (3a)$$

where μ is the cosine of the angle between the directions μ_i, ϕ_i and μ_j, ϕ_j. A finite number of terms of the Legendre polynomial are used to expand the phase function, with the coefficients a_1. The slab phase function in Eq. (1) is related to the single scattering phase function as

$$p(\mu_j; \mu_i) = \sum_{l=0}^{L} a_l P_l(\mu_j) P_l(\mu_i) \quad (3b)$$

and Eq. (1) is rewritten as

$$\mu_i \frac{dI(t, \mu_i)}{dt} + I(t, \mu_i) = \frac{\omega_o}{2} \sum_{j=1}^{2M} w_j I(t, \mu_j) \sum_{l=0}^{L} a_l P_l(\mu_j) P_l(\mu_i) + \frac{\omega_o}{4\pi} I_o(\mu_o) \sum_{l=0}^{L} a_l P_l(\mu_o) P_l(\mu_i) \exp\left[-\frac{t}{\mu_o}\right]. \quad (4)$$

Eq. (4) is solved numerically by the finite difference approach. The spatial variable t is discretized by dividing the total optical thickness of the plasma layer into N nodes. The abscissas and weights of the Gaussian quadrature, as well as the zero-order Legendre polynomials, are computed using standard numerical methods (Press et al., 1992). The accuracy of the finite difference scheme is verified by comparing this calculation with the results of Mengüç and Viskanta (1983) and Kumar et al. (1990). The same boundary conditions and radiative properties described by these authors were tested, including both a highly forward scattering phase function and a diffuse scattering phase function. Solutions obtained from this calculation are identical to those obtained by the above authors. The numerical scheme is also verified by the analytical solutions using a low-order numerical quadrature, $M = 1$.

The transmission, scattering, and energy loss experiments are performed on the same specimens with equivalent surface conditions, e.g., purity and the surface roughness. Therefore, these measurements results can be combined for the radiative transport analysis. Procedures of obtaining radiative properties and the size parameters of the laser ejected vapor and particulates are as follows:

1 The optical depth of the plasma plume at any instant in time is determined by the transmissivity measurement. The transmissivity τ is related to the optical depth, t, by the Beer's law, $\tau = \exp(-t/\mu)$, where μ is cosine of the angle of the probing beam. Beer's law is applicable since the intensities of plasma scattering and emission were found to be negligible compared with the intensity of plasma absorption.
2 The percentage of the total laser energy reaching the surface is obtained by integration of the transmissivity weighted by the laser intensity:

$$P_t = \frac{\int_o^{t_p} \tau(t) I_o(t) dt}{\int_o^{t_p} I_o(t) dt} \quad (5)$$

where $I_o(t)$ and t_p are the intensity and the pulse duration (50 ns) of the excimer laser, respectively. Since the experiment showed that the intensity of plasma scattering and emission is negligible compared with the intensity of the probing beam, extinction of the laser beam in the plasma when the laser beam passes through the plasma can be calculated as $P_e = 1 - P_t$.

3 The percentages of the laser energy absorbed and scattered by the plasma $P_{a,v}$, $P_{s,v}$ are calculated using P_e, P_t, the measured total energy loss to the ambient E_o ($=E_1 + E_2$, where E_1 and E_2 are energy loss measured by the energy meter in Fig. 3), and the measured surface total reflectivity, ρ_{Ni}. The absorption coefficient, the scattering coefficient, and the single scattering albedo are then calculated from $P_{a,v}$ and $P_{s,v}$.

4 The scattering phase function is obtained by a fitting procedure: a trial set of Legendre polynomial coefficients are assumed and the RTE, Eq. (4), is computed. The calculated angular scattering intensities are then compared with the measurements to determine the Legendre polynomial coefficients based on the least-square minimization method. Since the absolute values of the angular scattering intensities are not obtained in the experiments, both the measured scattering intensity and the calculated scattering intensity are normalized by the respective intensities at $\theta = 20°$. The Legendre polynomial coefficients of the scattering phase function are calculated by fitting the normalized intensities. Several schemes have been described in literature for deriving the Legendre polynomial coefficients from measurements. For instance, the Henyey-Greenstein phase function requires only one coefficient (the asymmetry factor) to be fitted with the experimental data (Modest, 1993). However, this approach does not yield satisfactory fit for the angular scattering data obtained in the experiment. Instead, a set of Legendre polynomial coefficients are simultaneously fitted with the experimental data. The phase function is truncated at $L = 3$ since the fourth term is calculated to be less than 0.01, which does not affect the comparison between the measurements and the results of RTE calculations.

5 Assuming a spherical geometry for the particles which scatter the laser beam, and using the refractive index of liquid Ni, $n = 1.5 + i2.7$ (Miller, 1969), the size of the scattering center is then computed from the fitted phase function based on the Mie scattering theory (Bohren and Huffman, 1983).

Results and Discussions

Figure 5 shows the signals recorded during a transmission measurement. The laser fluence is 4.2 J/cm^2 and the angle of incidence of the probing beam, $\theta = 45$ deg. The total time duration of the measurement is the laser pulse duration, approximately 50 ns with a FWHM of 26 ns. Both the transmission and the reference signals appear rather smooth. This is because of the relatively poor time resolution of the PMT, which is 3 ns. The negative voltage signal is a result of the PMT circuit. The solid line is the reference signal, while the dotted line is the intensity of the probing beam passing through the laser-induced plasma layer.

The ratio between the dotted and the solid lines is transmissivity, $\tau(t)$. Figure 6 shows transmissivity measured at several laser fluences. Transmissivity remains at '1' for the first several nanoseconds, which corresponds to the period before evaporation. This time period is also indicated in Fig. 5, which is the time duration when the reference signal and the transmission signal remain identical. However, it is noticed that the plasma

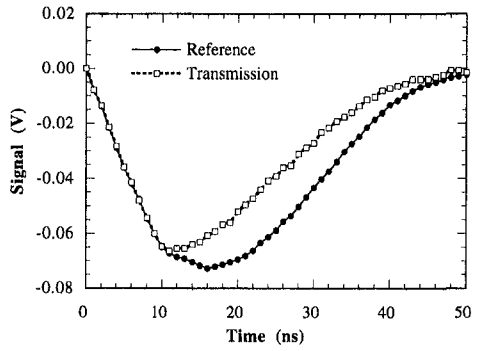

Fig. 5 Measured transmission and reference signals on Ni at F = 4.2 J/cm^2

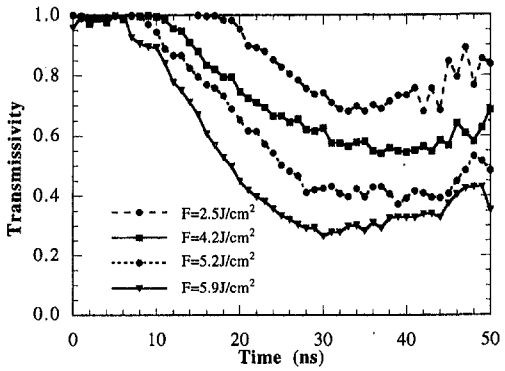

Fig. 6 Transient transmissivity of laser induced plasma on Ni

is not detected by the probing beam until the plasma has traveled a distance of about 5 μm, which corresponds to about 2 ns. As expected, transmissivity of the plasma layer is lower at higher laser fluences. Also, at higher laser fluences, transmissivity starts to decrease at an earlier time because evaporation of the target occurs earlier at higher laser fluences. Transmissivity decreases rapidly after plasma is formed and reaches a plateau at approximately 30 ns.

The percentage of the laser energy lost in the plasma when the laser beam travels through plasma once, P_e, is calculated using Eq. 5 and the relation $P_e = 1 - P_t$. Table 1 summarizes the measurement results of P_e, the laser energy lost to the ambient, P_o, and the measured total reflectivity of liquid Ni, ρ_{Ni}.

The data in Table 1 are used to calculate the percentages of the energy absorbed by plasma/particulates, $P_{a,v}$, scattered by particulates, $P_{s,v}$, absorbed by the specimen, $P_{a,Ni}$, and the scattering albedo, ω_o. It was found that for all the laser fluences used in this work, the total laser energy lost to the ambient, P_o, matches closely with the energy of the laser beam reflected from the specimen surface. This reflected energy from the specimen surface is calculated as $P_t \cdot \rho_{Ni} \cdot P_t$ since the laser beam passes through the plasma layer twice. For comparison, values of $P_t \cdot \rho_{Ni} \cdot P_t$ are also shown in Table 1. The close match between

Table 1 Measured total energy extinction in plasma and the total laser energy lost to the ambient

F (J/cm^2)	ρ_{Ni} (percent)	P_e (percent)	P_o (percent)	$P_t = 1 - P_e$ (percent)	$P_t \cdot \rho_{Ni} \cdot P_t$ (percent)
1.87	28	3.8	25.9	96.2	25.9
2.73		8.0	23.6	92.0	23.7
3.60		10.6	22.2	89.4	22.5
4.21		11.4	21.4	88.6	22.0
4.71		15.5	20.4	84.5	20.0

the total energy loss and the energy reflected from the surface indicates that the laser energy lost to the ambient is due to reflection at the specimen surface; the energy scattered from the plasma/particulates is negligible compared with the energy reflected from the specimen surface.

The percentage of laser energy absorbed by the Ni specimen can be calculated as $P_{a,\mathrm{Ni}} = (1 - P_e)\cdot(1 - \rho_{\mathrm{Ni}})$, and the energy absorbed by the laser induced plasma/particulates can be calculated as $P_{a,v} = P_e + (1 - P_e)\cdot\rho_{\mathrm{Ni}}\cdot P_e$. The calculated values of $P_{a,\mathrm{Ni}}$ and $P_{a,v}$, are shown in Fig. 7. An important result of the above calculations is that the requirement of conservation of energy, $P_{a,v} + P_{a,\mathrm{Ni}} + P_o = 1$, is satisfied (with $P_{s,v} \approx 0$), indicating that the measurements are reliable and accurate. Since the energy loss due to plasma scattering is below the measurement sensitivity, values of $P_{s,v}$ in Fig. 7 are the maximum values estimated based on the uncertainties in the $P_{a,v}$, $P_{a,\mathrm{Ni}}$, and P_o measurements. Figure 7 shows that, within the laser fluence range studied in this work, about 60 percent to 70 percent of the laser energy is absorbed by the Ni specimen, 5 percent to 20 percent is absorbed in the plasma, and 20 percent to 26 percent is lost to the ambient by reflection from the specimen surface. Absorption of laser energy by the specimen decreases as the laser energy increases, while absorption by plasma increases as the laser energy increases.

The value of ω_o is too small to be measured. Its maximum value is determined to be less than 0.05 when the energy fluence is larger than 2.5 J/cm^2. However, when ω_o is small, calculation of the scattering phase function based on the angular scattering intensities does not require the exact value of ω_o. Numerical calculations show that the ratio of scattering intensity at two polar angles varies less than 1 percent when the single scattering albedo is varied eight orders of magnitude, from 0.5×10^{-1} to 10^{-9}. Therefore, RTE calculations of the scattering phase function can be performed by assigning a small value to the scattering albedo; $\omega_o = 0.001$ is used in the calculation.

The coefficients of the Legendre polynomial of the scattering phase function are calculated based on the scatting intensities measured between 20 deg and 70 deg. Once the coefficients of the Legendre polynomial are obtained, the phase function can be calculated for any polar angle, using Eq. (3*b*). Figure 8 shows the scattering phase function at the laser fluence $F = 4.2$ J/cm^2 at five time steps. The scattering phase function does not vary significantly within the time duration of the laser pulse. The size parameter of the scattering center is then computed from the scattering phase function using the Mie theory. Figure 9 shows the calculated diameter of the scattering center. The size of the particulate is about 130 nm at 20 ns, while the plasma is formed at about 10 ns (Figs. 5 and 6). This implies that the particulates are ejected directly from the target surface by laser irradiation, since collision between the atomic vapor is not likely to form a 130 nm particulate within a 10 ns time duration. The

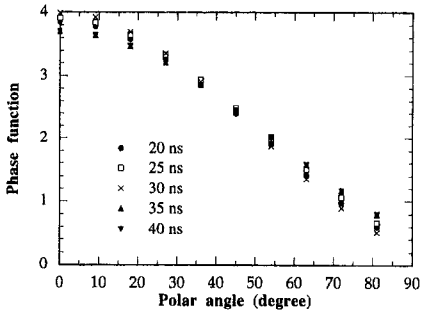

Fig. 8 Calculated scattering phase function based on angular scattering measurements

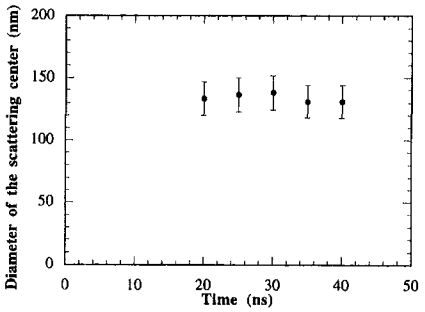

Fig. 9 Diameters of the laser ejected particulates at $F = 4.2$ J/cm^2

diameter of the particulate does not vary significantly as time progresses.

To evaluate the accuracy of the particle size calculation, the laser ejected particulates are collected on a glass plate. For SEM analysis, a layer of particulates rather than isolated particles is necessary. The SEM micrograph of the Ni Layer is shown in Fig. 10. The size of the particulates is about 100 nm, 30 percent lower than the size determined from the scattering measurement.

Error Analysis

Errors in determining the quantities of $P_{a,v}$, $P_{s,v}$, $P_{a,\mathrm{Ni}}$, and P_o originate from the experimental uncertainties. The energy of the laser pulse is stable, and the energy of each laser pulse is accurately measured. Therefore, the error from laser energy fluctuation is negligible. The light detection systems used in the experiment, including the PMT, the oscilloscope, and the energy meter have high resolutions. Based on the accuracy of these instruments, the signal-to-noise ratios of the measurements and the measurement repeatability, the error associated with the

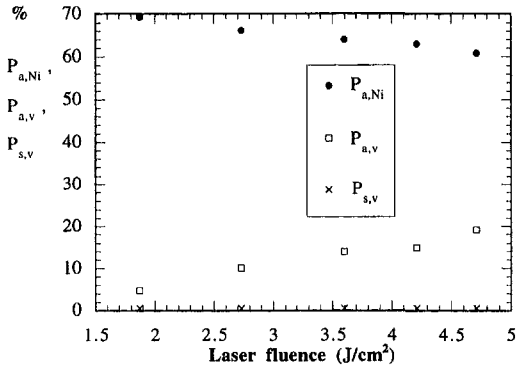

Fig. 7 Percentages of energy absorbed by vapor and specimen, and scattered by particulates

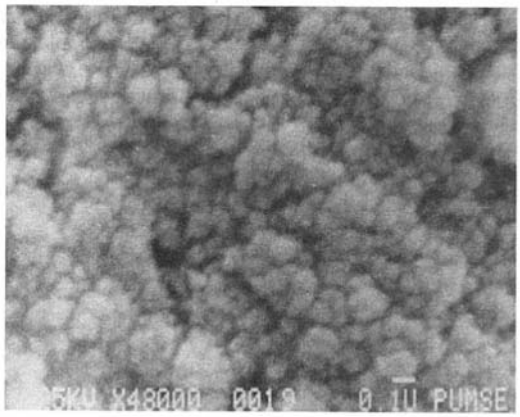

Fig. 10 SEM micrograph of the laser-ablated particulates

quantities of $P_{a,v}$, $P_{s,v}$, $P_{a,\mathrm{Ni}}$, and P_o is determined to be 1 percent at most laser fluences (i.e., P_o = 21.4 percent ± 1 percent at 4.21 J/cm^2), and about 2 percent when laser fluence is less than 2.5 J/cm^2. The measured values of $P_{a,v}$, $P_{s,v}$, $P_{a,\mathrm{Ni}}$, and P_o satisfy the overall energy conservation, indicating the accuracy of each measurements.

Errors in determining the scattering size parameter could originate from both the numerical scheme and the uncertainties in the input parameters of the numerical calculation. The numerical method for solving the RTE is shown to be accurate by comparing calculation results with bench mark solutions. The size of the particles produced by the laser irradiation ($x \approx 2$) is one order of magnitude larger than the particle size in the Rayleigh scattering regime ($x \approx 0.2$). Therefore, the angular scattering intensity varies dramatically with the size parameter. The least-square error used in the fitting procedure of the phase function is on the order of 10^{-3}. Therefore, the numerical scheme for particle-size fitting does not introduce significant error in computing the scattering phase function.

The input parameters of the phase function calculation include the surface reflectivity, the scattering albedo, the optical depth, and the transient angular scattering intensities. A numerical sensitivity study is carried out to evaluate the effect of the uncertainties of these input parameters on the phase function calculations. It is found that results of RTE calculations vary little when the input values of surface reflectivity, the optical depth, and the scattering albedo are varied within their measurement uncertainties. On the other hand, the transient scattering intensities measurement carries an uncertainty of 10 percent which is attributed to the randomness of particle generation. The numerical sensitivity calculation shows that the 10 percent uncertainty in the angular scattering intensity measurement corresponds to a 15 percent uncertainty in determining the scattering phase function and a 10 percent uncertainty in determining the scattering size parameter.

The discrepancy between the calculated and the SEM observed particle sizes is larger than the 10 percent uncertainty of calculation. This could be attributed to the nonuniformity of the particulate size, as shown in Fig. 10. The scattering intensity from a larger particle is stronger than that from a smaller particle. On the other hand, the optical refractive index used in the Mie scattering calculations is the refractive index of liquid Ni. The possible anomalous electrical states at the laser evaporated particle surface and its surroundings could alter the refractive index of the Ni particulates, which affects the particle size computation. However, prediction of the optical properties based on postulating a particle electrical state and an surrounding electrical field presents enormous difficulties. Assessment of the deviation of the optical properties of the charged particles in an electrical field is beyond the scope of this work.

Conclusions

This work developed novel experimental techniques to investigate the radiative transport process in a layer of plasma and particulates induced by high power, pulsed KrF excimer laser irradiation. Transient transmissivity and angular scattering intensity of plasma, and the energy loss to the ambient were measured. Based on the experimental data, radiative heat transfer analysis was performed to determine the scattering phase function and the scattering size parameter. Conclusions of this work, which apply to the range of the laser fluence used in the experiments, are:

1 Energy absorption in the laser-induced plasma increases as the laser intensity increases, and energy absorption in the specimen decreases as the laser intensity increases.
2 Scattering and re-radiation by the laser ejected plume are insignificant energy transport mechanisms compared with the absorption and surface reflection processes. The laser energy loss to the ambient is a result of reflection at the target surface.
3 Particulates are ejected from the specimen surface by laser irradiation. The size of the particulates does not change significantly within the laser pulse duration.
4 The transient scattering measurement is a possible method to estimate the size of the laser ejected particulates.

Acknowledgments

This work is partially supported by the National Science Foundation under grant number CTS-9624890.

References

Braren, B., Dubowski, J. J., and Norton, D. P., eds., 1993, "Laser Ablation in Materials Processing: Fundamentals and Applications," *Mat. Res. Soc. Symp. Proc.*, Vol. 285, MRS, New York.

Brewster, M. Q., 1992, *Thermal Radiative Transfer & Properties*, John Wiley & Sons, New York.

Bohren, C. F., and Huffman, D. R., 1983, *Absorption and Scattering of Light by Small Particles*, John Wiley and Sons, New York.

Callies, G., Berger, P., Kästle, J., and Hügel, H., 1995, "Excimer-Laser Induced Shock Waves in the Presence of External Gas Flows," *Proceedings of SPIE—The International Society for Optical Engineering*, Vol. 2502, pp. 706–711.

Chandrasekhar, S., 1950, *Radiative Transfer*, Oxford University Press, Glasgow.

Chrisey, D. B., and Hubler, G. K., eds., 1994, *Pulsed Laser Deposition of Thin Films*, John Wiley & Sons, New York.

Crafer, R. C., and Oakley, P. J., 1992, *Laser Processing in Manufacturing*, Chapman and Hall, New York.

Kumar, S., Majumdar, A., and Tien, C. L., 1990, "The Differential-Discrete-Ordinate Method for Solutions of the Equation of Radiative Transfer," ASME JOURNAL OF HEAT TRANSFER, Vol. 112, pp. 424–429.

Mengüç, M. P., and Viskanta, R., 1983, "Comparison of Radiative Transfer Approximations for a Highly Forward Scattering Planar Medium," *J. Quant. Spectrosc. Radiat. Transfer*, Vol. 29, pp. 381–394.

Miller, J. C., 1969, "Optical Properties of Liquid Metals at High Temperatures," *Phil. Mag.*, Vol. 20, pp. 1115–1132.

Modest, M. F., 1993, *Radiative Heat Transfer*, McGraw-Hill, New York.

Phypps, C. R., and Dreyfus, R. W., 1993, "The High Laser Irradiance Regime," *Laser Ionization Mass Analysis*, A. Vertes, et al., eds., John Wiley & Sons, New York.

Press, W. H., Teukolsky, S. A., Vetterling, W. T., and Flannery, B. P., 1992, *Numerical Recipes in FORTRAN*, 2nd ed., Cambridge University Press, MA.

Siegel, R., and Howell, J. R., 1992, *Thermal Radiation Heat Transfer*, 3rd. ed., Hemisphere Publishing, Washington.

Tönshoff, H. K., and Gedrat, O., 1990, "Absorption Behavior of Ceramic Materials Irradiated with Excimer-Lasers," *Excimer Laser Materials Processing and Beam Delivery System*, SPIE, Vol. 1377, pp. 38–44.

Xu, X., and Song, K. H., 1996, "Measurement of Radiative Properties of Pulsed Laser Induced Plasma," *Proceedings of the 31th National Heat Transfer Conference*, HTD-Vol. 327, pp. 11–18.

A General Semicausal Stochastic Model for Turbulence/Radiation Interactions in Flames

S. H. Chan
Wisconsin Distinguished Professor
shc@csd.uwn.edu
Fellow ASME

X. C. Pan
Graduate Student

Department of Mechanical Engineering,
The University of Wisconsin-Milwaukee,
Milwaukee, WI 53201

This paper presents a general two-dimensional non-stationary semicausal model for the simulation of mixture fraction, which improves our previous causal model. The proposed model includes not only the pre-correlation predictors (both in time space and geometric space) as well as the cross-correlation predictors, as in the causal model, but also post-correlation predictors. The latter makes possible the consideration of interactions of a scalar, such as mixture fraction, at a physical location with that of all its adjacent locations. It has also been shown that the complicated second- and higher-order correlation predictors can be neglected in the semicausal simulation of mixture fraction. To show the validity of the model, the stochastic mean and variance of the spectral intensities at different wavelengths were predicted and compared with detailed experimental data for turbulent carbon monoxide/hydrogen/air diffusion flames having different Reynolds numbers. These comparisons showed excellent agreement with existing data and the improvement over the prior causal model.

Introduction

Due to temperature and species concentration fluctuations and the nonlinear relationship among temperature, radiation properties, and radiation intensity, many theoretical and experimental studies have shown that the turbulence/radiation interactions in turbulent flames have a significant influence on radiation. Cox (1977), Kabashinikov and Myansnikova (1985), Grosshandler and Vantelon, (1985), Nelson (1989a, b), etc. studied turbulence effects on radiation by using simplified flame radiation models. Measurements of radiation properties of nonluminous and luminous turbulent diffusion flames have also been reported for burning different fuels in still air: hydrogen (Gore et al., 1987b; Kounalakis et al., 1988), carbon monoxide (Gore et al., 1987a), methane (Jeng and Faeth, 1984a, b), natural gas (Gore et al., 1987), ethylene (Gore and Faeth, 1986), and acetylene (Gore and Faeth, 1988). It was found that turbulence/radiation interactions caused more than 100 percent increases of mean radiation levels above estimates based on mean scalar properties, although this effect was small (20–110 percent) for some nonluminous flames (Kounalakis et al., 1989). In a highly turbulent combustor, Kock et al. (1994) recently reported the mean and the standard deviation of spectral radiative intensities in a confined turbulent diffusion flame burning lean propane with air. They reported that the fluctuations of time-resolved measurements of the spectral radiative intensity can be more than 30 percent of the mean value. For radiative fluxes, fluctuations can increase mean fluxes up to 2–3 times larger than estimates based on mean properties (Kabashnikov and Kmit, 1979), although smaller increases were reported by Song and Viskanta (1987). Recently, more modeling and implementation of turbulence-radiation interaction effects in confined flames (Hartick, et al., 1996) and furnaces (Adams and Smith 1994) have been reported. For turbulent flames described by flamelet models, radiation was found to have a significant effect on flamelet structures, e.g. more than 100 percent on thermal NO formation (Chan et al., 1995).

To explain the essence of turbulence/radiation interaction, it is noted that the energy equation, which is one of the conservation equations required for global flame calculation, calls for the local divergence of radiative flux, $\nabla \cdot q_R$. The latter is known if the radiation intensity field is determined. The radiation intensity is a function of temperature and species concentrations, which in turn are functions of other scalars. For example, the scalars can be mixture fraction z and scalar dissipation rate χ. Being turbulent, all scalars are fluctuating and are functions of local time, m, and the local geometric location, n, as shown in Fig. 1*C*. Furthermore, in truly turbulent flow the instantaneous scalar at (m, n) is affected by all that of the surrounding, namely, that at $(m, n + 1)$, $(m - 1, n + 1)$, etc. In other words, they are dependent on one another and are correlated. However, the existing models, including those reviewed here, cannot account for such dependence/correlation and often resort to the assumption that scalars are independent of one another. For this reason, a general semicausal stochastic model is proposed here to address the fundamental question of how to account for all correlations in the evaluation of the instantaneous (and mean) radiation intensity in turbulent flow. Once the instantaneous intensity is known, the instantaneous and mean radiative flux, etc., can be evaluated for global flame computation.

Among methods available, an effective method to treat turbulence/radiation interactions is by a stochastic model. A simple stochastic model was reported by Kounalakis et al. (1991). They began with the simulation of instantaneous mixture fraction distributions along a radiation path. This allowed radiation intensities to be calculated by solving the radiative transfer equation along the radiation path because properties, such as temperature and species concentrations, can be approximated as functions of mixture fraction alone. Such a simplification is valid for chemical equilibrium conditions and is reasonable for some major radiating species like H_2O in methane-air flames, even though reaction rates are finite. Then the radiation statistics can be readily computed from the instantaneous radiation intensities. Their work is, however, limited to Markov process while our recent (Chan et al., 1994) and the present work seek to advance beyond this simple limit. In their approach, it was necessary to assume that the two-dimensional random process was a combination of one-dimensional random processes in the

Contributed by the Heat Transfer Division for publication in the JOURNAL OF HEAT TRANSFER. Manuscript received by the Heat Transfer Division February 6, 1996; revision received January 30, 1997; Keywords: Combustion, Radiation, Turbulence. Associate Technical Editor: M. Modest.

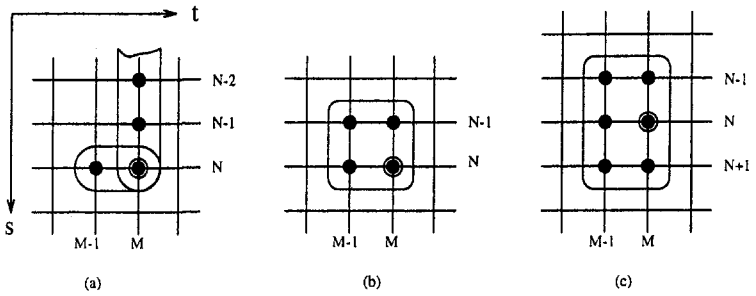

Fig. 1 The two-dimensional (time and geometric spaces) random field for a scalar in the existing and present models

t (time) and s (geometric) directions. The prediction of mixture fraction at (m, n) was then expressed as the sum of the one-dimensional predictions of mixture fraction in each direction, namely the prediction at $(m - 1, n)$ in the t direction and $(m, n - 1)$ and $(m, n - 2)$ etc., in the s direction (as shown in Fig. 1*a*). Consequently, the contribution from cross locations such as $(m - 1, n - 1)$ and post locations such as $(m, n + 1)$ cannot be accounted for since there was no consideration of temporal-spatial correlations. To account for contributions from cross locations (i.e., post correlations), a causal stochastic model (Fig. 1*b*) has recently been developed (Chan et al., 1994) but it still cannot account for post-correlations. For the most general model to be presented here, the contribution from the post locations such as $(m, n + 1)$ in the geometric space direction, s, in Fig. 1 is to be included. This change is significant since, in geometric space, a scalar or a vector quantity at any grid node is affected by all adjacent nodes and the correlation with all the adjacent nodes (as opposed to just nodes on one side of the node as in the causal model) should be considered. A new formulation, termed the semicausal model in the following, will be developed to account for pre and post-correlations in geometric space, in addition to pre-correlations in time space, and time-space cross-correlations (Fig. 1*c*). It is noted that pre and post-correlations are physically sensible for spatial correlations but not the post-correlations of temporal correlations since we do not know what will happen in the future. Thus, treating pre and post-spatial correlations in conjunction with pre-temporal correlations is a reasonable approach. Furthermore, in the simulation of mixture fraction distributions, the relative importance of second and higher-order correlations in comparison to the first-order correlations will be assessed in this study to yield a simpler and more practical form of the proposed model. Finally, to demonstrate the solution procedure, the present two-dimensional non-stationary semicausal model is applied to the prediction of mean and fluctuating spectral radiation intensities of carbon monoxide/hydrogen/air turbulent diffusion flames for which detailed data are available for comparison with predictions.

Two-Dimensional Semicausal Stochastic Model

Most existing stochastic models were essentially based on the concepts of time-series techniques intended for a one-dimensional process. The causal and the present semicausal models, however, are based on the recent advances in the field of image processing which has developed a model capable of simulating a two-dimensional random field (Jain, 1989). Nevertheless, the latter is for a stationary field, namely, the mean and variance of a scalar are treated as constants in the field. Even in steady combustion, the mean and variance of mixture fraction are still functions of space. Therefore, a two-dimensional model for a non-stationary random field suitable for general use in turbulent combustion is developed below.

Consider the instantaneous mixture fraction distributions along a radiation path as a two-dimensional (time space/geometric space) random field. Let $z(m, n)$ be a two-dimensional random field with a mean value $\bar{z}(m, n)$ and covariance $r(m, n; m - k, n - l)$. For the simulation of mixture fraction, m and n represent the locations of time space and geometric space, respectively. It is noted that m can also designate the location of another geometric space. For a two-dimensional non-stationary random field, the linear prediction of $z(m, n)$ under minimum variance representations is affected by that of all adjacent points and is simulated most generally as

$$z(m, n) = \sum_{(k,l)} \sum_{\epsilon \hat{S}} a(m - k, n - l) z(m - k, n - l) + \epsilon(m, n) \quad (1)$$

Nomenclature

$a(m - k, n - l)$ = predictor coefficients of random field
d = burner exit diameter
$E[\ ]$ = expectation
f = mixture fraction
i_λ = spectral radiation intensity
p, q = order of prediction
r = covariance of random field
$R(\Delta s)$ = spatial correlation
$R(\Delta t)$ = temporal correlation
s = geometric space coordinate
$\hat{S}$ = prediction region
t = time space coordinate
$\hat{W}$ = finite prediction region
x = axial distance from the burner exit
$z(m, n)$ = random field
$z(t, s)$ = unclipped mixture fraction distribution
α = prediction coefficient
β^2 = variance of prediction error
Γ = integral length scale
δ = Kronecker delta function
Δs = geometric space increment
Δt = time space increment
ϵ = prediction error
λ = wavelength
ρ = correlation
σ^2 = variance
τ = integral time scale
ϕ_{i1}, ϕ_{i2} = prediction coefficients

Subscripts

s = geometric space coordinate
t = time space coordinate
ϵ = prediction error

Superscripts

$( )'$ = instantaneous fluctuation from time-averaged mean value
$\overline{( )}$ = time-averaged mean quantities
$\sqrt{\overline{( )'^2}}$ = root-mean-squared fluctuating quantities

in which $\hat{S}$ is the prediction region, and the predictor coefficients a's are unknowns to be found and, unlike the prior work (Jain, 1989), are now allowed to be functions of $m - k$ and $n - l$. In the above equation, $\epsilon(m, n)$ is the zero mean prediction error that is governed by the present state (m, n) and is independent of all the other states, i.e., the following expectations hold,

$$E[\epsilon(m, n)] = 0 \tag{2}$$

$$E[\epsilon(m, n)z(m - k, n - l)] = \beta^2_{m,n}\delta(k, l) \tag{3}$$

in which $\beta^2_{m,n}$ is the variance of $\epsilon(m, n)$, i.e.,

$$\beta^2_{m,n} \equiv E[\epsilon(m, n)\epsilon(m, n)] \tag{4}$$

and $\delta(k, l) = 0$ when $k \neq 0 \cup l \neq 0$ and $\delta(k, l) = 1$ when $k = l = 0$. In general, we decompose $z(m, n)$ into mean and fluctuating parts as follows:

$$z(m, n) = \bar{z}(m, n) + z'(m, n). \tag{5}$$

It has been proven that $z(m, n)$ can be simulated based on the realization of $z'(m, n)$, which is another two-dimensional non-stationary random field with zero mean and covariance $r(m, n; m - k, n - l)$ (Chan et al., 1994), that is,

$$z'(m, n) = \sum_{(k,l)} \sum_{\epsilon\hat{S}} a(m - k, n - l)z'(m - k, n - l) + \epsilon(m, n). \tag{6}$$

This is the approach used in the present study.

Semicausal Prediction. The fluctuations of mixture fraction or any other variables of interest in turbulent flames can be considered as a random field. It is affected by its own fluctuation at previous times (pre-correlation in time) and by that of all surrounding points (pre and post-correlations in space) at the current time. Thus the general model needed is a semicausal model in which we seek a predictor to be expressed in terms of previous predictions in one of the coordinates and previous as well as future predictions in the other. In other words, the proposed two-dimensional stochastic model is causal in one dimension and noncausal in another dimension; its prediction region is (Fig. 2*a*)

$$\hat{S} = \{k \geq 1, \forall l\} \cup \{k = 0, l \neq 0\}. \tag{7}$$

In practice, only a finite neighborhood $\hat{W}$, $\hat{W} \subset \hat{S}$ is used in the prediction process, so Eq. (6) becomes

$$z'(m, n) = \sum_{(k,l)} \sum_{\epsilon\hat{W}} a(m - k, n - l)z'(m - k, n - l) + \epsilon(m, n) \tag{8}$$

in which W (Fig. 2*a*) can generally be described by

$$\hat{W} = \{0 \leq k \leq p, -q \leq l \leq q, (k, l) \neq (0, 0)\} \tag{9}$$

The semicausal simulations are semirecursive because they are recursive only in one dimension. The full vector $\mathbf{z}'_m = \{z'(m, n), \forall n\}$ can be calculated from the past output vector $\{\mathbf{z}'_i, i \leq m\}$ and all the past and present input vectors $\{\boldsymbol{\epsilon}_i, i \leq m\}$.

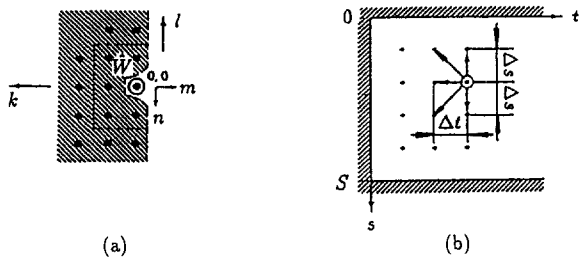

Fig. 2 (*a*) The semicausal prediction region *S* and the corresponding finite prediction region *W*, and (*b*) initial conditions for a semicausal system (Δt—time space increment, Δs—geometry space increment, *S*—radiation path length)

First-Order Semicausal Model. The first-order model is to include five immediate nodal points next to (m, n) as shown in Fig. 1*c*, namely, assigning $p = q = 1$. The higher-order model is presented in the Appendix to show that the first-order model is accurate and sufficient for practical purpose. From Eq. (8) we have the following first-order semicausal model for the simulation of the two-dimensional non-stationary random field:

$$\begin{aligned} z'(m, n) &= a(m - 1, n)z'(m - 1, n) \\ &+ a(m, n - 1)z'(m, n - 1) + a(m, n + 1)z'(m, n + 1) \\ &+ a(m - 1, n - 1)z'(m - 1, n - 1) \\ &+ a(m - 1, n + 1)z'(m - 1, n + 1) + \epsilon(m, n). \end{aligned} \tag{10}$$

Multiplying both sides of Eq. (10) by $z'(m - k, n - l)$ and then finding expectations yields the following:

$$\begin{aligned} r(m, n; m - k, n - l) &= a(m - 1, n)r(m - 1, n; m - k, n - l) \\ &+ a(m, n - 1)r(m, n - 1; m - k, n - l) \\ &+ a(m, n + 1)r(m, n + 1; m - k, n - l) \\ &+ a(m - 1, n - 1)r(m - 1, n - 1; m - k, n - l) \\ &+ a(m - 1, n + 1)r(m - 1, n + 1; m - k, n - l) \\ &+ r_\epsilon(m, n; m - k, n - l) \end{aligned} \tag{11}$$

where

$$r(m, n; m - k, n - l) \equiv E[z'(m, n)z'(m - k, n - l)] \tag{12}$$

$$r_\epsilon(m, n; m - k, n - l) \equiv E[\epsilon(m, n)\epsilon(m - k, n - l)]. \tag{13}$$

It is noted that

$$E[\epsilon(m, n)z'(m - k, n - l)] = E[\epsilon(m, n)\epsilon(m - k, n - l)] = \beta^2_{m,n}\delta(k, l). \tag{14}$$

Using the definition of the correlation at lags k and l,

$$\rho_{m,n;m-k,n-l} \equiv \frac{E[z'(m, n)z'(m - k, n - l)]}{\sqrt{E[z'^2(m, n)]E[z'^2(m - k, n - l)]}} = \frac{r(m, n; m - k, n - l)}{\sigma_{m,n}\sigma_{m-k,n-l}} \tag{15}$$

where $\sigma^2_{m,n}$ is the variance of $z'(m, n)$, Eq. (11) can be expressed as

$$\begin{aligned} \sigma_{m,n}\rho_{m,n;m-k,n-l} &= a(m - 1, n)\sigma_{m-1,n}\rho_{m-1,n;m-k,n-l} \\ &+ a(m, n - 1)\sigma_{m,n-1}\rho_{m,n-1;m-k,n-l} \\ &+ a(m, n + 1)\sigma_{m,n+1}\rho_{m,n+1;m-k,n-l} \\ &+ a(m - 1, n - 1)\sigma_{m-1,n-1}\rho_{m-1,n-1;m-k,n-l} \\ &+ a(m - 1, n + 1)\sigma_{m-1,n+1}\rho_{m-1,n+1;m-k,n-l} \\ &+ r_\epsilon(m, n; m - k, n - l). \end{aligned} \tag{16}$$

Substituting the five sets of k and l values for the five neighboring nodal points into Eq. (16), and using Eqs. (13–15) yield, respectively,

$$\begin{aligned} \sigma_{m,n}\rho_{m,n;m-1,n} &= a(m - 1, n)\sigma_{m-1,n} \\ &+ a(m, n - 1)\sigma_{m,n-1}\rho_{m,n-1;m-1,n} \\ &+ a(m, n + 1)\sigma_{m,n+1}\rho_{m,n+1;m-1,n} \end{aligned}$$

$$+ a(m-1, n-1)\sigma_{m-1,n-1}\rho_{m-1,n-1;m-1,n}$$
$$+ a(m-1, n+1)\sigma_{m-1,n+1}\rho_{m-1,n+1;m-1,n} \quad (k=1, l=0)$$

$$\sigma_{m,n}\rho_{m,n;m,n-1} = a(m-1, n)\sigma_{m-1,n}\rho_{m-1,n;m,n-1}$$
$$+ a(m, n-1)\sigma_{m,n-1} + a(m, n+1)\sigma_{m,n+1}\rho_{m,n+1;m,n-1}$$
$$+ a(m-1, n-1)\sigma_{m-1,n-1}\rho_{m-1,n-1;m,n-1}$$
$$+ a(m-1, n+1)\sigma_{m-1,n+1}\rho_{m-1,n+1;m,n-1} \quad (k=0, l=1)$$

$$\sigma_{m,n}\rho_{m,n;m,n+1} = a(m-1, n)\sigma_{m-1,n}\rho_{m-1,n;m,n+1}$$
$$+ a(m, n-1)\sigma_{m,n-1}\rho_{m,n-1;m,n+1} + a(m, n+1)\sigma_{m,n+1}$$
$$+ a(m-1, n-1)\sigma_{m-1,n-1}\rho_{m-1,n-1;m,n+1}$$
$$+ a(m-1, n+1)\sigma_{m-1,n+1}\rho_{m-1,n+1;m,n+1} \quad (k=0, l=-1)$$

$$\sigma_{m,n}\rho_{m,n;m-1,n-1} = a(m-1, n)\sigma_{m-1,n}\rho_{m-1,n;m-1,n-1}$$
$$+ a(m, n-1)\sigma_{m,n-1}\rho_{m,n-1;m-1,n-1}$$
$$+ a(m, n+1)\sigma_{m,n+1}\rho_{m,n+1;m-1,n-1}$$
$$+ a(m-1, n-1)\sigma_{m-1,n-1}$$
$$+ a(m-1, n+1)\sigma_{m-1,n+1}\rho_{m-1,n+1;m-1,n-1} \quad (k=1, l=1)$$

$$\sigma_{m,n}\rho_{m,n;m-1,n+1} = a(m-1, n)\sigma_{m-1,n}\rho_{m-1,n;m-1,n+1}$$
$$+ a(m, n-1)\sigma_{m,n-1}\rho_{m,n-1;m-1,n+1}$$
$$+ a(m, n+1)\sigma_{m,n+1}\rho_{m,n+1;m-1,n+1}$$
$$+ a(m-1, n-1)\sigma_{m-1,n-1}\rho_{m-1,n-1;m-1,n+1}$$
$$+ a(m-1, n+1)\sigma_{m-1,n+1} \quad (k=1, l=-1) \quad (17)$$

from which the predictor coefficients $a(m-k, n-l)$ can be readily solved in terms of variance $\sigma_{m,n}$ and correlation $\rho_{m,n;m-k,n-l}$. As in image processing (Jain, 1989), the correlation function $\rho_{m,n;m-k,n-l}$ is taken as separable,

$$\rho_{m,n;m-k,n-l} = \rho_{m,m-k}\rho_{n,n-l} \quad (18)$$

which is commonly made out of necessity because only data about non-cross-correlations, $\rho_{i,j}$'s are normally available. By substituting the above into Eq. (17) and solving for the coefficients, it yields

$$a(m-1, n) = \frac{\sigma_{m,n}}{\sigma_{m-1,n}}\rho_{m,m-1}$$

$$a(m, n-1) = \frac{\sigma_{m,n}}{\sigma_{m,n-1}}\frac{\rho_{n,n-1} - \rho_{n+1,n}\rho_{n+1,n-1}}{1-\rho^2_{n+1,n-1}}$$

$$a(m, n+1) = \frac{\sigma_{m,n}}{\sigma_{m,n+1}}\frac{\rho_{n+1,n} - \rho_{n,n-1}\rho_{n+1,n-1}}{1-\rho^2_{n+1,n-1}}$$

$$a(m-1, n-1) = -\frac{\sigma_{m,n}}{\sigma_{m-1,n-1}}\rho_{m,m-1}\frac{\rho_{n,n-1} - \rho_{n+1,n}\rho_{n+1,n-1}}{1-\rho^2_{n+1,n-1}}$$

$$a(m-1, n+1) = -\frac{\sigma_{m,n}}{\sigma_{m-1,n+1}}\rho_{m,m-1}\frac{\rho_{n+1,n} - \rho_{n,n-1}\rho_{n+1,n-1}}{1-\rho^2_{n+1,n-1}}. \quad (19)$$

Here, $\rho_{m-k,m} \equiv \rho_{m,m-k}$, $\rho_{n-l,n} \equiv \rho_{n,n-l}$ have been used. Therefore, by substituting Eq. (19) into Eq. (10), the two-dimensional non-stationary first-order semicausal model can be expressed as

$$z'(m, n) = \frac{\sigma_{m,n}}{\sigma_{m-1,n}}\rho_{m,m-1}z'(m-1, n)$$
$$+ \frac{\sigma_{m,n}}{\sigma_{m,n-1}}\alpha_{n-1}z'(n, n-1) + \frac{\sigma_{m,n}}{\sigma_{m,n+1}}\alpha_{n+1}z'(n, n+1)$$
$$- \left[\frac{\sigma_{m,n}}{\sigma_{m-1,n-1}}\rho_{m,m-1}\alpha_{n-1}z'(m-1, n-1)\right.$$
$$\left. + \frac{\sigma_{m,n}}{\sigma_{m-1,n+1}}\rho_{m,m-1}\alpha_{n+1}z'(m-1, n+1)\right] + \epsilon(m, n). \quad (20)$$

Consequently, the modeled covariance function of ϵ is obtained by multiplying $\epsilon(m-k, n-l)$ on both sides of Eq. (20) and by finding the expectation of the resulting equation

$$r_\epsilon(m, n; m-k, n-l)$$
$$= \sigma^2_{m,n}(1-\rho^2_{m,m-1})(1-\alpha_{n-1}\rho_{n,n-1} - \alpha_{n+1}\rho_{n+1,n})\delta(k)[\delta(l)$$
$$- \alpha_1\delta(l-1) - \alpha_2\delta(l+1)]. \quad (21)$$

In the above equations

$$\alpha_{n-1} = \frac{\rho_{n,n-1} - \rho_{n+1,n}\rho_{n+1,n-1}}{1-\rho^2_{n+1,n-1}},$$

$$\alpha_{n+1} = \frac{\rho_{n+1,n} - \rho_{n,n-1}\rho_{n+1,n-1}}{1-\rho^2_{n+1,n-1}}. \quad (22)$$

The semicausal model presented above is a first-order realization. In practice, the higher-order correlation predictors can be neglected since they have little effect on the simulation compared to the contributions of the first-order correlation predictors. This is proved in the Appendix by deriving a second-order realization model.

Mixture Fraction Stochastic Simulations

As in Eq. (5), the instantaneous mixture fraction distributions along the radiation path $z(s, t)$ can be decomposed as

$$z(t, s) = \bar{z}(s) + z'(t, s). \quad (23)$$

It is noted that the mean value of mixture fraction $\bar{z}$ depends on location s only (Fig. 2*b*). If $z'(s, t)$ is considered to be a first-order semicausal field and the correlation function is treated as separable, the above semicausal model is simplified to

$$z'(t, s) = R(\Delta t)z'(t-\Delta t, s)$$
$$+ \frac{\sigma_s}{\sigma_{s-\Delta s}}\alpha z'(t, s-\Delta s) + \frac{\sigma_s}{\sigma_{s+\Delta s}}\alpha z'(t, s+\Delta s)$$
$$- \left[\frac{\sigma_s}{\sigma_{s-\Delta s}}\alpha R(\Delta t)z'(t-\Delta t, s-\Delta s)\right.$$
$$\left. + \frac{\sigma_s}{\sigma_{s-\Delta s}}\alpha R(\Delta s)z'(t-\Delta t, s+\Delta s)\right] + \epsilon(t, s) \quad (24)$$

since the variance of mixture fraction σ^2 is only a function of location s, i.e., $\sigma_{t-\Delta t,s} = \sigma_{t,s} = \sigma_s$. In Eq. (24),

$$\alpha = \frac{R(\Delta s)}{1+R^2(\Delta s)} \quad (25)$$

and the temporal and spatial correlations $R(\Delta t) \equiv \overline{f'(t)f'(t-\Delta t)}/\overline{f'^2}$ and $R(\Delta s) \equiv \overline{f'(s)f'(s-\Delta s)}/(\sqrt{\overline{f'^2}(s)}\sqrt{\overline{f'^2}(s-\Delta s)})$, are equivalent to $\rho_{m,m-1}$ and $\rho_{n,n-1}$ in Eq. (20), respectively. In general, the temporal and spatial correlations can be expressed in terms of exponential forms as shown by experiments of Becker et al. (1967), Wygnanski and Fiedler (1969), and Frenkiel and Klebanoff (1973). The prediction error, $\epsilon(t, s)$, is chosen to be an uncorrelated Gaussian random variable with a zero mean and a variance as follows:

$$\beta_s^2 = \sigma_s^2[1 - R^2(\Delta t)]\frac{1 - R^2(\Delta s)}{1 + R^2(\Delta s)}. \quad (26)$$

The above equation is obtained from Eqs. (21) and (22) by setting $k = l = 0$.

The solution procedure of finding $z'(t, s)$ in the field is described next. Since the solution at (t, s) requires, for example, results from the solution at a post location $(s + \Delta s)$ (Fig. 2(*b*), which is unknown, they must be solved simultaneously. First, if $R(\Delta t)$, $R(\Delta s)$, and σ_s^2 are known and a *pdf* of ϵ is selected, $\epsilon(s, t)$ can be simulated from its zero mean and its variance β_s^2 given by Eq. (26). Then, the initial values $z'(0, s)$, $z'(t, 0)$, and $z'(t, S)$ along the computational boundaries shown in Fig. 2*b* can be simulated by using the one-dimensional time-series technique, and $N - 2$ equations can be set up for $N - 2$ unknowns of $z'(t, s_n)$, $n = 2$ to $N - 1$ at a given t for a radiation path $(0 - S)$ discretized as $s_1 \ldots s_n \ldots s_N$. The linear equations are solved simultaneously by an inversion technique to yield all unknowns, z', and therefore the desired instantaneous z by Eq. (23). Thus, such initial boundary-value problems are solved semirecursively, that is, recursively in t direction and nonrecursively in the other s direction. Finally, since the instantaneous mixture fraction has a clipped Gaussian probability density function, it can be obtained by modifying z as follows (Kounalakis, et al. 1991):

$$f = z, 0 \le z \le 1; \quad f = 0, \quad z \le 0; \quad f = 1, \quad z \ge 1. \quad (27)$$

Application

The present semicausal model is applied to buoyant turbulent round jet diffusion flames of a carbon monoxide/hydrogen mixture burning in still air since the detailed experimental data of such flames are available from Kounalakis (1990). The spectral intensities at the flame boundary for the radiation emitted radially outward from two turbulent diffusion flames are to be predicted and compared with data at various axial locations and wavelengths. The two flames considered have Reynolds numbers at the burner exit of 7400 and 12,700. The radial radiation paths are at $x/d = 30$, 40, and 50. The measured time-averaged mean and variance of mixture fraction distributions for the three radiation paths in each flame were reported. The measured temporal and spatial correlations, integral length scales, and integral time scales along the radiation paths of two flames were also available. These measured quantities are useful for the present validation of the proposed two-dimensional stochastic model.

The prediction of radiation statistics began with the simulation of instantaneous mixture fraction distributions along the radiation path, which was performed by the two-dimensional non-stationary first-order semicausal model. It was required to generate a set of random numbers ranging from 0–1. The random numbers were chosen from the cumulative distribution function of the unclipped Gaussian *pdf* of $\epsilon(s, t)$ with a zero mean and variance given by Eq. (26). The measured correlations $R(\Delta t)$ as a function of x/d and Δt, $R(\Delta s)$ as a function of x/d and Δs, and the variance of mixture fraction σ_s^2, taken from Kounalakis (1990), were used to evaluate Eq. (26). Given $\epsilon(s, t)$, Eq. (24) was solved to yield $z'(t, s)$. Then, the unclipped instantaneous mixture fraction z was computed from Eq. (23) in which the measured values (Kounalakis, 1990) of the mean mixture fraction $\overline{f(s)}$ were used. The clipped f was finally determined from Eq. (27). By following the procedure described by Chan et al. (1994), the instantaneous concentrations of radiating species and mixture temperature as a function of the mixture fraction were obtained from a radiating flamelet calculation with a scalar dissipation rate of $\chi = 1.0\ s^{-1}$. The flamelet with $\chi = 1.0\ s^{-1}$ was selected since it yields a 10 percent loss of heat of reaction by radiative transfer, which is the same percentage as that used by Kounalakis et al. (1991) who simply adopted equilibrium state relationships with a 10 percent radiative heat loss adjustment to the heat of reaction.

This simulation was made for the two carbon monoxide/hydrogen/air turbulent diffusion flames specified above. The radiation paths were discretized into 37 segments. The sampling frequency for the stochastic simulation was 20,000 Hz so that the frequency of experimental data up to 10,000 Hz could be resolved. Therefore, $\Delta t = 1/20{,}000$ was used in the simulation. The space increment was chosen to coincide with data locations, i.e., $\Delta s = 0.3d$, $0.4d$, and $0.5d$ for $x/d = 30$, 40, and 50, respectively. The total number of realizations was 2000 in order to yield stable radiation statistics. The mean radial spectral radiation intensities and their fluctuation intensities were calculated as follows:

$$i_\lambda = \sum_{j=1}^{M} e_{b\lambda}(T_j)(\tau_{\lambda,j} - \tau_{\lambda,j-1})/\pi$$

$$\bar{i}_\lambda = \frac{1}{N}\sum_{i=1}^{N} i_{\lambda i}$$

$$\overline{i'^2} = \frac{1}{N}\sum_{i=1}^{N} (i_{\lambda i} - \bar{i}_\lambda)^2$$

where M is the number of radial segments, N is the number of the realization, and $e_{b\lambda}$ is the Planck function. $\tau_{\lambda,j}$ is the transmittance up to segment j and is evaluated by the RADCAL algorithm, considering H_2O, CO_2, CO, and CH_4 as radiating species (Grosshandler and Joulain, 1987). The CPU time by convex computer was 1.5 hours, which was almost the same as the previous causal model though two extra terms are included in the simulation (Eq. 10). It implies that most of the time consumed was due to the use of RADCAL. RADCAL, which is based on a narrow-band model, is accurate but is computationally time consuming. The computing time can be reduced, for example, by using Planck mean absorption coefficients.

The two-dimensional non-stationary first-order semicausal predictions of the mean and fluctuating spectral radial radiation intensities are summarized in Table 1 together with the experimental data (Kounalakis, 1990) and the existing predictions using a two-dimensional causal model (Chan et al., 1994), and using the Markov approach (Kounalakis, 1990). The results are given for two spectral wavelengths, $\lambda = 2.8\ \mu$m and $\lambda = 4.5\ \mu$m. For each wavelength, the intensity at three axial locations ($x/d = 30$, 40, 50) are provided. The present predictions and the measured mean spectral radiation intensities in Table 1 are in good agreement, with an average error of roughly 5 percent. The predicted fluctuations of spectral radiation intensities in Table 1 also are close to the measured values with an average discrepancy of less than 15 percent. The error, though small, can be attributed to the use of the state relationships for mixture fractions mentioned earlier. Finally, Table 1 also shows apparent improvement of the present semicausal model compared with previous models.

Conclusions

1 The proposed two-dimensional non-stationary semicausal model makes possible the inclusion of the contributions to the mixture fraction simulation from past locations in geometric space. Thus, it is a general method because it accounts for fluctuation correlations with all adjacent points in geometric space and pre-locations in time space.
2 For the case of exponential correlation functions, the second-order and higher-order correlation predictors are negligible in the semicausal simulation of mixture fraction as proven in the Appendix. Thus, the first-order model is accurate enough for practical use.
3 The two-dimensional non-stationary semicausal model has been applied to the mixture fraction simulation for turbulent diffusion carbon monoxide/hydrogen/air flames. The predicted mean and fluctuating radiation properties agree well with measurements.

Table 1 Predicted and measured radiation properties

	$\bar{i}_\lambda$ (kW/m^2 μm sr)				$\sqrt{\overline{i_\lambda'^2}}/\bar{i}_\lambda$ (Percent)			
x/d	Data	Pred. two-dimensional semicausal	Pred. two-dimensional causal	Kounalakis et al. (1991)	Data	Pred. two-dimensional semicausal	Pred. two-dimensional causal	Kounalakis et al. (1991)
				(Re = 7,400, λ = 2.8 μm)				
30	2.6	2.5	2.2	2.3	24	25	25	23
40	2.9	2.7	2.5	2.7	27	30	30	29
50	2.8	2.8	2.7	2.5	35	33	35	36
				(Re = 7,400, λ = 4.5 μm)				
30	8.7	8.8	8.6	9.8	20	21	21	16
40	11.2	11.3	11.0	10.3	18	20	20	19
50	11.0	11.0	11.2	9.7	26	24	26	27
				(Re = 12,700, λ = 2.8 μm)				
30	2.2	2.1	1.8	2.5	25	26	31	21
40	3.3	3.1	2.4	3.4	22	26	28	21
50	3.6	3.5	2.9	3.3	26	27	29	27
				(Re = 12,700, λ = 4.5 μm)				
30	9.2	9.9	9.0	10.1	15	19	21	15
40	11.4	12.2	10.8	12.0	13	17	16	13
50	12.4	12.7	11.8	11.7	16	16	16	16

4 The present two-dimensional stochastic model can be extended easily to three and four-dimensional models, corresponding to directions (x, y, t) and (x, y, z, t), respectively, in order to simulate the mixture fraction distribution along a radiation path.

Acknowledgments

This research was sponsored by the Gas Research Institute under the technical management of Dr. B. Sarauskas.

References

Adams, B., and Smith, P., 1994, "Modeling Effects of Soot and Turbulence-Radiation Coupling on Radiative Transfer in an Industrial Furnace," *Radiative Heat Transfer: Current Research,* HTD-Vol. 276, ASME, New York.

Becker, H. A., Hottel, H. C., and Williams, G. C., 1967, "The Nozzle-Fluid Concentration Field of the Round, Turbulent, Free Jet," *J. Fluid Mech.,* Vol. 30, pp. 285–303.

Chan, S. H., Pan, X. C., and Abou-Ellail, M. M. M., 1995, "Flamelet Structure of Radiating CH_4-Air Flames," *Combustion and Flame,* Vol. 102, pp. 438–446.

Chan, S. H., Pan X. C., and Zhang, J., 1994, "A Two-Dimensional Non-Stationary Causal Stochastic Model for Turbulence/Radiation Interactions in Flames," *Twenty-Fifth Symp. (Int.) on Combustion,* pp. 1115–1123.

Cox, G., 1977, "On Radiant Heat Transfer in Diffusion Flame," *Combust. Sci. Tech.,* Vol. 17, pp. 75–78.

Frenkiel, F. N., and Klebanoff, P. S., 1973, "Probability Distributions and Correlations in a Turbulent Boundary Layer," *The Physics of Fluids,* Vol. 16, pp. 725–737.

Gore, J. P., and Faeth, G. M., 1986, "Structure and Spectral Radiation Properties of Turbulent Ethylene/Air Diffusion Flames," *Twenty-First Symp. (Int.) on Combustion,* The Combustion Institute, Pittsburgh, pp. 1521–1531.

Gore, J. P., and Faeth, G. M., 1988, "Structure and Radiation Properties of Luminous Turbulent Acetylene/Air Diffusion Flames," ASME JOURNAL OF HEAT TRANSFER, Vol. 110, pp. 173–181.

Gore, J. P., Faeth, G. M., Evans, D., and Pfenning, C., 1987, "Structure and Radiation Properties of Large-Scale Natural Gas/Air Diffusion Flame," *Fire and Materials,* Vol. 10, pp. 161–169.

Gore, J. P., Jeng, S.-M., and Faeth, G. M., 1987a, "Spectral and Total Radiation Properties of Turbulent Carbon Monoxide/Air Diffusion Flames," *AIAA J.,* Vol. 25, pp. 339–345.

Gore, J. P., Jeng, S.-M., and Faeth, G. M., 1987b, "Spectral and Total Radiation Properties of Turbulent Hydrogen/Air Diffusion Flames," ASME JOURNAL OF HEAT TRANSFER, Vol. 109, pp. 165–171.

Grosshandler, W. L., and Joulain, P., 1987, "Intermittency and Flame Radiation," *Tenth International Colloquium on Dynamics of Explosion and Reactive Systems,* J. R. Bowell et al., eds., AIAA, New York.

Grosshandler, W. L., and Vantelon, J. P., 1985, "Predicting Soot Radiation in Laminar Diffusion Flames," *Combus. Sci. Tech.,* Vol. 44, pp. 128–141.

Hartick, J. W., Neuber, A. A., Fournier, R., Hassel, E. P., and Janicka, J., 1996, "Modeling Turbulence-Radiation Interaction in Confined Diffusion Flames," *Transport Phenomena in Combustion,* S. H. Chan, ed., Taylor and Francise, Inc., Washington, DC.

Jain, A. K., 1989, *Fundamentals of Digital Image Processing,* Prentice-Hall, Englewood Cliff, New Jersey.

Jeng, S. M., and Faeth, G. M., 1984a, "Radiative Heat Fluxes Near Turbulent Buoyant Methane Diffusion Flames," ASME JOURNAL OF HEAT TRANSFER, Vol. 106, pp. 886–888.

Jeng, S. M., and Faeth, G. M., 1984b, "Species Concentrations and Turbulence Properties in Buoyant Methane Diffusion Flames," ASME JOURNAL OF HEAT TRANSFER, Vol. 106, pp. 721–727.

Kabashnikov, V. P., and Myasnikova, G. I., 1985, "Thermal Radiation in Turbulent Flows—Temperature and Concentration Fluctuations," *Heat Transfer—Soviet Research,* Vol. 17, No. 6. pp. 116–125.

Kabashnikov, V. P., and Kmit, G. I., 1979, "Influence of Turbulent Fluctuations on Thermal Radiation," *J. Applied Spectroscopy,* Vol. 31, pp. 963–967.

Kock, R., Krebs, W., Jeckel, R., Ganz, B., and Wittig, S., 1994, "Spectral and Time Resolved Radiation Measurements in Model Gas Turbine Combustor," *ASME Turo-Expo 94-Land, Sea, and Air,* Int. Gas Turbine Institute/ASME Int., The Hague, Netherlands, June 13–16.

Kounalakis, M. W., Gore, J. P., and Faeth, G. M., 1988, "Turbulence/Radiation Interactions in Nonpremixed Hydrogen/Air Flames," *Twenty-Second Symp. (Int.) on Combustion,* The Combustion Institute, Pittsburgh, pp. 1281–1290.

Kounalakis, M. E., Gore, J. P., and Faeth, G. M., 1989, "Mean and Fluctuating Radiation Properties of Nonpremixed Turbulent Carbon Monoxide/Air Flames," ASME JOURNAL OF HEAT TRANSFER, Vol. 111, pp. 1021–1030.

Kounalakis, M. E., 1990, "Structure and Radiation Properties of Turbulent Diffusion Flames," Ph.D. thesis, University of Michigan, Ann Arbor, Michigan.

Kounalakis, M. E., Sivathanu, Y. R., and Faeth, G. M., 1991, "Infrared Radiation Statistics of Nonluminous Turbulent Diffusion Flames," *ASME/JSME Thermal Engineering Proceedings,* Vol. 5, pp. 3–12.

Nelson, D. A., 1989a, "Band Radiation from a Nonhomogeneous Fluctuating Medium," *Heat Transfer Phenomena in Radiation, Combustion, and Fires,* R. K. Shah, ed., HTD-Vol. 106, ASME, New York, pp. 287–293.

Nelson, D. A., 1989b, "Band Radiation from a Fluctuating Medium," ASME JOURNAL OF HEAT TRANSFER, Vol. 111, pp. 131–134.

Song, T. H., and Viskanta, R., 1987, "Interaction of Radiation with Turbulence: Application to a Combustion System," *J. Thermophysics and Heat Transfer,* Vol. 1, No. 1, p. 56.

Wygnanski, I., and Fiedler, H., 1969, "Some Measurement in the Self-Preserving Jet," *J. Fluid Mech.,* Vol. 38, pp. 577–612.

Appendix — Higher-Order Model

A non-stationary second-order semicausal model can be obtained by setting $p = q = 2$ in Eq. (8). However, it has been proven that the second-order predictors in the time space of the causal model can be neglected if the correlations are exponential

(Chan et al., 1994). Thus, referring to Fig. 3, the presentation of the second-order semicausal model can be simplified by setting $p = 1$, and $q = 2$ in Eq. (8)

$$z'(m, n) = \sum_{i=-2, i\neq 0}^{2} a(m, n-i)z'(m, n-i) + \sum_{i=-2}^{2} a(m-1, n-i)z'(m-1, n-i) + \epsilon(m, n). \quad \text{(A1)}$$

Multiplying both sides of Eq. (A1) by $z'(m-k, n-l)$ and then finding the expected value yields

$$r(m, n; m-k, n-l) = \sum_{i=-2, i\neq 0}^{2} a(m, n-i)r(m, n-i; m-k, n-l) + \sum_{i=-2}^{2} a(m-1, n-i)r(m-1, n-i; m-k, n-l) + r_\epsilon(m, n; m-k, n-l). \quad \text{(A2)}$$

Similar to the first-order model, we assume that the correlation function is separable. Substituting Eqs. (15) and (18) into Eq. (A2) then yields

$$\sigma_{m,n}\rho_{m,m-k}\rho_{n,n-l} = \sum_{i=-2, i\neq 0}^{2} a(m, n-i)\sigma_{m,n-i}\rho_{m,m-k}\rho_{n-i,n-l} + \sum_{i=-2}^{2} a(m-1, n-i)\sigma_{m-1,n-i}\rho_{m-1,m-k}\rho_{n-i,n-l} + r_\epsilon(m, n; m-k, n-l). \quad \text{(A3)}$$

Using Eqs. (13–15), and applying different values of k and l ($k = 0, l = -2$; $k = 0, l = -1$; $k = 0, l = 1$; $k = 0, l = 2$; $k = 1, l = -2$; $k = 1, l = -1$; $k = 1, l = 0$; $k = 1, l = 1$; $k = 1, l = 2$) in Eq. (A3), yields a set of nine equations. Then solving these equations, after considerable manipulation yields

$$a(m, n-1) = \frac{\sigma_{m,n}}{\sigma_{m,n-1}}\phi_{n-1},$$

$$a(m-1, n-1) = -\frac{\sigma_{m,n}}{\sigma_{m-1,n-1}}\phi_{m-1}\phi_{n-1}$$

$$a(m, n-2) = \frac{\sigma_{m,n}}{\sigma_{m,n-2}}\phi_{n-2},$$

$$a(m-1, n-2) = -\frac{\sigma_{m,n}}{\sigma_{m-1,n-2}}\phi_{m-1}\phi_{n-2}$$

$$a(m, n+1) = \frac{\sigma_{m,n}}{\sigma_{m,n+1}}\phi_{n+1},$$

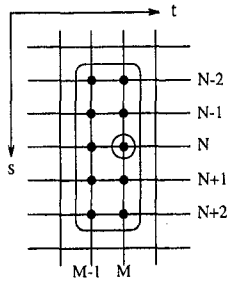

Fig. 3 The two-dimensional random field for the second-order semicausal model

$$a(m-1, n+1) = -\frac{\sigma_{m,n}}{\sigma_{m-1,n+1}}\phi_{m-1}\phi_{n+1}$$

$$a(m, n+2) = \frac{\sigma_{m,n}}{\sigma_{m,n+2}}\phi_{n+2},$$

$$a(m-1, n+2) = -\frac{\sigma_{m,n}}{\sigma_{m-1,n+2}}\phi_{m-1}\phi_{n+2}$$

$$a(m-1, n) = \frac{\sigma_{m,n}}{\sigma_{m-1,n}}\phi_{m-1} \quad \text{(A4)}$$

where

$$\phi_{m-1} = \frac{\rho_{m,m-1} - \rho_{m-1,m-2}\rho_{m,m-2}}{1 - \rho^2_{m-1,m-2}}$$

$$\phi_{n-1} = \begin{vmatrix} \rho_{n,n-1} & \rho_{n-2,n-1} & \rho_{n+1,n-1} & \rho_{n+2,n-1} \\ \rho_{n,n-2} & 1 & \rho_{n+1,n-2} & \rho_{n+2,n-2} \\ \rho_{n,n+1} & \rho_{n-2,n+1} & 1 & \rho_{n+2,n+1} \\ \rho_{n,n+2} & \rho_{n-2,n+2} & \rho_{n+1,n+2} & 1 \end{vmatrix} \Big/ |D_\rho|$$

$$\phi_{n-2} = \begin{vmatrix} 1 & \rho_{n,n-1} & \rho_{n+1,n-1} & \rho_{n+2,n-1} \\ \rho_{n-1,n-2} & \rho_{n,n-2} & \rho_{n+1,n-2} & \rho_{n+2,n-2} \\ \rho_{n-1,n+1} & \rho_{n,n+1} & 1 & \rho_{n+2,n+1} \\ \rho_{n-1,n+2} & \rho_{n,n+2} & \rho_{n+1,n+2} & 1 \end{vmatrix} \Big/ |D_\rho|$$

$$\phi_{n+1} = \begin{vmatrix} 1 & \rho_{n-2,n-1} & \rho_{n,n-1} & \rho_{n+2,n-1} \\ \rho_{n-1,n-2} & 1 & \rho_{n,n-2} & \rho_{n+2,n-2} \\ \rho_{n-1,n+1} & \rho_{n-2,n+1} & \rho_{n,n+1} & \rho_{n+2,n+1} \\ \rho_{n-1,n+2} & \rho_{n-2,n+2} & \rho_{n,n+2} & 1 \end{vmatrix} \Big/ |D_\rho|$$

$$\phi_{n+2} = \begin{vmatrix} 1 & \rho_{n-2,n-1} & \rho_{n+1,n-1} & \rho_{n,n-1} \\ \rho_{n-1,n-2} & 1 & \rho_{n+1,n-2} & \rho_{n,n-2} \\ \rho_{n-1,n+1} & \rho_{n-2,n+1} & 1 & \rho_{n,n+1} \\ \rho_{n-1,n+2} & \rho_{n-2,n+2} & \rho_{n+1,n+2} & \rho_{n,n+2} \end{vmatrix} \Big/ |D_\rho| \quad \text{(A5)}$$

with the determinant D_ρ defined as follows:

$$|D_\rho| \equiv \begin{vmatrix} 1 & \rho_{n-2,n-1} & \rho_{n+1,n-1} & \rho_{n+2,n-1} \\ \rho_{n-1,n-2} & 1 & \rho_{n+1,n-2} & \rho_{n+2,n-2} \\ \rho_{n-1,n+1} & \rho_{n-2,n+1} & 1 & \rho_{n+2,n+1} \\ \rho_{n-1,n+2} & \rho_{n-2,n+2} & \rho_{n+1,n+2} & 1 \end{vmatrix}.$$

Therefore, the two-dimensional non-stationary second-order semicausal model is expressed as

$$z'(m, n) = \frac{\sigma_{m,n}}{\sigma_{m,n-1}}\phi_{n-1}z'(m, n-1) + \frac{\sigma_{m,n}}{\sigma_{m,n-2}}\phi_{n-2}z'(m, n-2) + \frac{\sigma_{m,n}}{\sigma_{m,n+1}}\phi_{n+1}z'(m, n+1) + \frac{\sigma_{m,n}}{\sigma_{m,n+2}}\phi_{n+2}z'(m, n+2) + \frac{\sigma_{m,n}}{\sigma_{m-1,n}}\phi_{m-1}z'(m-1, n) - \left[\frac{\sigma_{m,n}}{\sigma_{m-1,n-1}}\phi_{m-1}\phi_{n-1}z'(m-1, n-1) + \frac{\sigma_{m,n}}{\sigma_{m-1,n-2}}\phi_{m-1}\phi_{n-2}z'(m-1, n-2) + \frac{\sigma_{m,n}}{\sigma_{m-1,n+1}}\phi_{m-1}\phi_{n+1}z'(m-1, n+1) + \frac{\sigma_{m,n}}{\sigma_{m-1,n+2}}\phi_{m-1}\phi_{n+2}z'(m-1, n+2)\right] + \epsilon(m, n). \quad \text{(A6)}$$

As in Eq. (24) for the simulation of mixture fraction fluctuations, Eq. (A6) can be simplified to the following:

$$z'(t,s) = \frac{\sigma_s}{\sigma_{s-\Delta s}}\phi_{s-\Delta s}z'(t,s-\Delta s) + \frac{\sigma_s}{\sigma_{s-2\Delta s}}\phi_{s-2\Delta s}z'(t,s-2\Delta s) + \frac{\sigma_s}{\sigma_{s+\Delta s}}\phi_{s+\Delta s}z'(t,s+\Delta s) + \frac{\sigma_s}{\sigma_{s+2\Delta s}}\phi_{s+2\Delta s}z'(t,s+2\Delta s) + \phi_{t-\Delta t}z'(t-\Delta t,s) - \left[\frac{\sigma_s}{\sigma_{s-\Delta s}}\phi_{t-\Delta t}\phi_{s-\Delta s}z'(t-\Delta t,t,s-\Delta s) + \frac{\sigma_s}{\sigma_{s-2\Delta s}}\phi_{t-\Delta t}\phi_{s-2\Delta s}z'(t-\Delta t,s-2\Delta s) + \frac{\sigma_s}{\sigma_{s+\Delta s}}\phi_{t-\Delta t}\phi_{s+\Delta s}z'(t-\Delta t,s+\Delta s) + \frac{\sigma_s}{\sigma_{s+2\Delta s}}\phi_{t-\Delta t}\phi_{s+2\Delta s}z'(t-\Delta t,s+2\Delta s)\right] + \epsilon(t,s) \quad \text{(A7)}$$

where

$$\phi_{t-\Delta t} = \frac{R(\Delta t)[1-R(2\Delta t)]}{1-R^2(\Delta t)}$$

$$\phi_{s-\Delta s} = \begin{vmatrix} R(\Delta s) & R(\Delta s) & R(2\Delta s) & R(3\Delta s) \\ R(2\Delta s) & 1 & R(3\Delta s) & R(4\Delta s) \\ R(\Delta s) & R(3\Delta s) & 1 & R(\Delta s) \\ R(2\Delta s) & R(4\Delta s) & R(\Delta s) & 1 \end{vmatrix} \Big/ |D_R|$$

$$\phi_{s-2\Delta s} = \begin{vmatrix} 1 & R(\Delta s) & R(2\Delta s) & R(3\Delta s) \\ R(\Delta s) & R(2\Delta s) & R(3\Delta s) & R(4\Delta s) \\ R(2\Delta s) & R(\Delta s) & 1 & R(\Delta s) \\ R(3\Delta s) & R(2\Delta s) & R(\Delta s) & 1 \end{vmatrix} \Big/ |D_R|$$

$$\phi_{s+\Delta s} = \begin{vmatrix} 1 & R(\Delta s) & R(\Delta s) & R(3\Delta s) \\ R(\Delta s) & 1 & R(2\Delta s) & R(4\Delta s) \\ R(2\Delta s) & R(3\Delta s) & R(\Delta s) & R(\Delta s) \\ R(3\Delta s) & R(4\Delta s) & R(2\Delta s) & 1 \end{vmatrix} \Big/ |D_R|$$

$$\phi_{s+2\Delta s} = \begin{vmatrix} 1 & R(\Delta s) & R(2\Delta s) & R(\Delta s) \\ R(\Delta s) & 1 & R(3\Delta s) & R(2\Delta s) \\ R(2\Delta s) & R(3\Delta s) & 1 & R(\Delta s) \\ R(3\Delta s) & R(4\Delta s) & R(\Delta s) & R(2\Delta s) \end{vmatrix} \Big/ |D_R|$$

$$|D_R| \equiv \begin{vmatrix} 1 & R(\Delta s) & R(2\Delta s) & R(3\Delta s) \\ R(\Delta s) & 1 & R(3\Delta s) & R(4\Delta s) \\ R(2\Delta s) & R(3\Delta s) & 1 & R(\Delta s) \\ R(3\Delta s) & R(4\Delta s) & R(\Delta s) & 1 \end{vmatrix} \quad \text{(A8)}$$

and the time space and geometric space increments are taken as constant. As noted above, both the spatial and temporal correlations often have exponential form, that is, $R(\Delta t) = \exp(-\Delta t/\tau)$ and $R(\Delta s) = \exp(-\Delta s/\Gamma)$. Γ and τ are the spatial integral scale and the temporal integral scale, respectively. Therefore,

$$R(k\Delta t) = \exp(-k\Delta t/\tau) = R^k(\Delta t),$$
$$R(l\Delta s) = \exp(-l\Delta s/\Gamma) = R^l(\Delta s). \quad \text{(A9)}$$

Substituting Eq. (A9) into Eq. (A8) yields

$$\phi_{t-\Delta t} = R(\Delta t), \quad \phi_{s-\Delta s} = \phi_{s+\Delta s} = \frac{R(\Delta s)}{1+R^2(\Delta s)},$$
$$\phi_{s-2\Delta s} = \phi_{s+2\Delta s} = 0. \quad \text{(A10)}$$

Therefore, the second, forth, seventh and ninth terms on the right side of Eq. (A7) become zero. Equation (A7) is then simplified to

$$z'(t,s) = \frac{\sigma_s}{\sigma_{s-\Delta s}}\frac{R(\Delta s)}{1+R^2(\Delta s)}z'(t,s-\Delta s) + \frac{\sigma_s}{\sigma_{s+\Delta s}}\frac{R(\Delta s)}{1+R^2(\Delta s)}z'(t,s+\Delta s) + R(\Delta t)z'(t-\Delta t,s) - \left[\frac{\sigma_s}{\sigma_{s-\Delta s}}R(\Delta t)\frac{R(\Delta s)}{1+R^2(\Delta s)}z'(t-\Delta t,s-\Delta s) + \frac{\sigma_s}{\sigma_{s+\Delta s}}R(\Delta t)\frac{R(\Delta s)}{1+R^2(\Delta s)}z'(t-\Delta t,s+\Delta s)\right] + \epsilon(t,s)$$

which is identical to Eq. (24), the first-order semicausal model. Therefore, it is concluded that the terms involving second-order correlations, namely, those second, fourth, seventh and ninth terms of Eq. (34), can be neglected in the mixture fraction simulation. It is also shown that the contributions of the first-order correlations and the first-order cross-correlation are more important to the simulation than that of second-order correlations or second-order cross-correlations. It can be proven that the same conclusion is also valid for higher-order realizations.

Suppression of Flow Boiling Nucleation

G. E. Thorncroft

J. F. Klausner
klaus@nersp.nerdc.ufl.edu

Department of Mechanical Engineering,
University of Florida,
Gainesville, FL 32611-6300

R. Mei
Department of Aerospace Engineering,
Mechanics, and Engineering
Science,
University of Florida,
Gainesville, FL 32611-6250

A simple model is presented for estimating the ratio of the maximum to minimum cavity radius required for ebullition in two-phase flow with heat transfer. The resulting dimensionless parameter, r_{max}/r_{min}, is demonstrated to correlate flow boiling nucleation site density. As the convective heat transfer associated with bulk turbulence in two-phase flow is enhanced, $r_{max} \rightarrow r_{min}$, and the probability of finding surface cavities whose radii lie between r_{max} and r_{min} is reduced. Thus, active nucleation sites become deactivated. A vertical flow boiling facility was fabricated in which the nucleation suppression point can be measured. Experiments conducted for mass flux ranging from 183–315 kg/m^2-s and inlet quality ranging from 0–0.151, along with data available from the literature, suggest that r_{max}/r_{min} is the leading order dimensionless parameter on which the complete suppression of nucleation sites depends. Although the suppression of nucleation sites also depends, to a certain extent, on the surface/fluid combination and heat flux, it is found that complete suppression occurs for r_{max}/r_{min} ranging from 40 to 120. This is proposed as a criterion to discriminate the purely convective regime from the nucleate boiling regime.

1 Introduction

Over the past four decades, the heat transfer rates associated with forced convection boiling have been investigated by hundreds of researchers. Perhaps the first investigators to propose a correlation for predicting flow boiling heat transfer rates were Dengler and Addoms (1956). Since then many other flow boiling heat transfer correlations have been proposed, many of which have been summarized by Gungor and Winterton (1986). The type of correlation which has been used the most was first proposed by Chen (1966) and takes the following form:

$$h_{2\phi} = h_{\text{mac}} + h_{\text{mic}} \tag{1}$$

where $h_{2\phi}$ is the two-phase heat transfer coefficient, h_{mac} is the macroconvection heat transfer coefficient due to bulk turbulent transport, and h_{mic} is the microconvection heat transfer coefficient due to the ebullition process. Klausner (1989) examined various correlations which take the same form as Eq. (1) and found they predict that the macroconvection component of heat transfer is the dominant heat transfer mechanism, and the microconvection component of heat transfer typically does not contribute significantly to the total two-phase heat transfer. One notable exception is the correlation proposed by Kandlikar (1990), which predicts that microconvection can be a considerable portion of the total heat transfer. Zeng and Klausner (1993a) measured the microconvection component of heat transfer for horizontal flow boiling of refrigerant R113 and demonstrated that under certain flow and thermal conditions it contributes significantly to the total two-phase heat transfer, as demonstrated in Fig. 1. Others who have reported finding microconvection heat transfer to be significant over a range of flow and thermal conditions include Blatt and Adt (1964), Staub and Zuber (1966), Frost and Kippenhan (1967), Kenning and Cooper (1989), Cooper (1989), Klausner (1989), and Tran et al. (1993).

In order to understand the discrepancy, it is instructive to consider the saturated vertical upflow boiling experiments by Kenning and Cooper (1989). Over the range of flow and thermal conditions tested, two flow boiling regimes were identified: the apparently convective regime and the apparently nucleate boiling regime. In the apparently convective regime, the measured two-phase heat transfer coefficient appears to be independent of the heat flux and heating surface conditions and can be predicted within an uncertainty of approximately ±10 percent. In this regime, it appears that the boiling activity has been completely suppressed. In the apparently nucleate boiling regime, the measured heat transfer coefficients are essentially independent of mass flux, vapor quality, and flow regime. They tend not to be repeatable due to variations in surface conditions and gas entrainment, and they are difficult to predict.

The importance of the two flow boiling regimes identified by Kenning and Cooper cannot be underestimated. When nucleation sites are completely suppressed and heat transfer is dominated by bulk turbulence and liquid film evaporation, as occurs in the convective regime, the physics governing the heat transfer are completely different than that in the nucleate boiling regime in which heat transfer is mainly controlled by the incipience, growth, and departure of vapor bubbles. As demonstrated in Fig. 1, as soon as incipience occurs, microconvection strongly contributes to the total two-phase heat transfer. Moreover, without a clear distinction between the two regimes, experimental data used to construct empirical heat transfer correlations can contain convective data interspersed with nucleate boiling data. This can bias a correlation toward one regime, making it incapable of satisfactorily predicting the heat transfer in the other. Therefore, it is of critical importance to be able to predict which heat transfer regime is present for a given set of flow conditions.

The objective of this work is to understand the fundamental mechanisms controlling the suppression of nucleation sites in flow boiling inside channels or tubes with net vapor generation, which establishes the transition point between the convective and nucleate boiling regimes. Based on thermodynamic relations and physical reasoning, a dimensionless parameter is identified to serve as a criterion for predicting when nucleation sites become completely suppressed. It is tested and calibrated using experimental heat transfer data obtained in this work, flow boiling nucleation site density data of Zeng and Klausner (1993b), and heat transfer data of Kenning and Cooper (1989) and Jallouk (1974). The working fluids considered are water, R113, R114, and FC-87.

2 Nucleation Sites in Flow Boiling

An extensive experimental investigation of nucleation site density in horizontal flow boiling with refrigerant R113 was

Contributed by the Heat Transfer Division for publication in the JOURNAL OF HEAT TRANSFER. Manuscript received by the Heat Transfer Division June 18, 1996; revision received February 24, 1997; Keywords: Boiling, Forced Convection, Multiphase Flows. Associate Technical Editor: M. D. Kelleher.

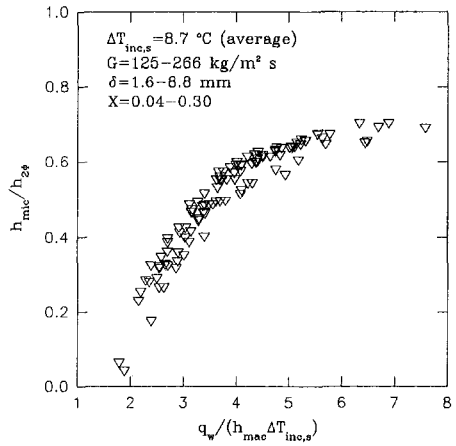

Fig. 1 Ratio of microconvection heat transfer coefficient to total two-phase heat transfer coefficient for different flow boiling conditions (from Zeng and Klausner; 1993a)

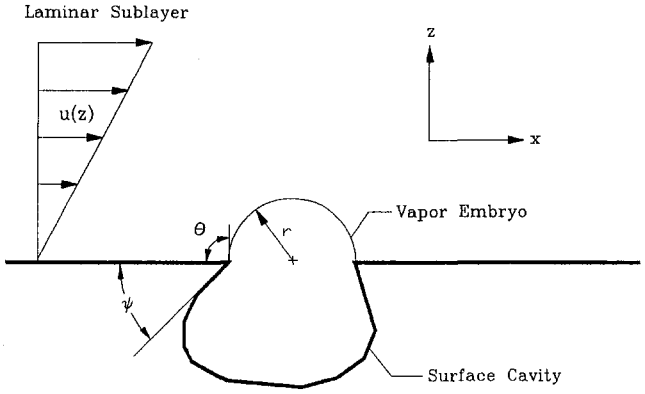

Fig. 2 Idealized sketch of a vapor embryo embedded in shear flow protruding a surface cavity

reported by Zeng and Klausner (1993b). They demonstrated that the behavior of the nucleation site density is significantly different than that found in pool boiling, and although the nucleation site density data show dependence on the critical (minimum) cavity radius, it is insufficient for correlating the data. They observed a strong dependence on heat flux and mean vapor velocity. As the mean vapor velocity increased, the nucleation site density decreased until complete suppression of nucleation sites occurred. No generalized correlation for the data was suggested. In general, the formation of nucleation sites is highly dependent upon the size and geometry of the microscopic scratches and pits on the heating surface, the wettability of the fluid, the amount of foreign contaminants on the surface, and the material from which the surface was fabricated. Here, the data of Zeng and Klausner (1993b) are reexamined based on theoretical considerations.

It has long been recognized that surface cavities which become active nucleation sites must be capable of trapping vapor (Corty and Foust, 1955). Wang and Dhir (1993) suggested that only those cavities with $\theta > \psi_{min}$ are capable of trapping vapor, in which θ is the liquid-solid contact angle and ψ_{min} is the minimum cavity side angle, or in the case of spherical cavities, ψ_{min} is the mouth angle. Using this vapor trapping criterion and the nucleation site density model proposed by Yang and Kim (1988) for pool boiling, the nucleation site density for either pool or flow boiling may be calculated from

$$\frac{n}{A} = \frac{N}{A}\int_{r_{min}}^{r_{max}} f_1(r)\,dr \int_0^{\theta} f_2(\psi_{min})\,d\psi_{min} \qquad (2)$$

where n/A is the nucleation site density, N/A is the number of cavities per unit area on the heating surface, f_1 is the probability density function of finding cavities with mouth radius r, f_2 is the probability density function of finding cavities with minimum side angle ψ_{min}, and r_{min} and r_{max} are the respective minimum and maximum mouth cavity radii within which incipience will occur. The use of Eq. (2) assumes a statistically homogeneous distribution of cavities on the heating surface and statistical independence of r and ψ_{min}.

Although the applicability of Eq. (2) to flow boiling has yet to be experimentally verified, it is quite useful in understanding the nucleation site density data presented by Zeng and Klausner (1993b) in which n/A is observed to decrease rapidly with increasing vapor velocity. Increasing the mean vapor velocity results in enhanced two-phase bulk turbulence and thus reduces the thermal boundary layer thickness. The temperature field which is seen by a vapor embryo protruding a surface cavity, as sketched in Fig. 2, is strongly influenced by the bulk turbulence. A vapor embryo will grow and establish a nucleation site only if there is sufficient energy from the surroundings to sustain growth. If a vapor embryo is too large, which might occur in a cavity with a large diameter, it will protrude into the colder region of the liquid, which reduces the vapor temperature to

Nomenclature

$f_1(r)$ = probability density function for finding cavities with mouth radius r
$f_2(\psi_{min})$ = probability density function for finding cavities with minimum side angle, ψ_{min}
G = mass flux (kg/m^2-s)
h = heat transfer coefficient (W/m^2-K)
h_{fg} = latent heat of vaporization (J/kg)
k = thermal conductivity (W/m-K)
n/A = nucleation site density (cm^{-2})
N/A = number of surface cavities per unit area (cm^{-2})
P_{sat} = saturation pressure (Pa)
q_w = heat flux (W/m^2)
r = cavity mouth radius (m)
r_{max} = maximum cavity radius allowed for nucleation (m)
r_{min} = minimum cavity radius required for nucleation (m)
R_v = engineering gas constant (J/kg-K)
Re_l = liquid Reynolds number based on liquid fraction flowing
$T_l(z)$ = liquid temperature profile near wall (C)
T_w = average wall temperature (C)
T_v = vapor temperature (C)
T_{sat} = saturation temperature (C)
ΔT_{sat} = wall superheat (C)
$\Delta T_{inc,s}$ = incipient wall superheat (C)
u = liquid velocity (m/s)
x = vapor quality
z = distance from heating surface (m)

Greek Symbols

θ = liquid/solid contact angle
ρ = density (kg/m^3)
σ = surface tension (N/m)
ψ_{min} = minimum cavity side angle

Subscripts

i = inlet
l = liquid
mac = macroconvection
mic = microconvection
sup = nucleation suppression point
v = vapor
2ϕ = two-phase

below the value required by the Clapeyron equation for the equilibrium of the two phases. Therefore, in addition to a minimum cavity radius required for incipience, there also exists a maximum cavity radius above which the incipience is inhibited. As the bulk turbulence is enhanced, the thermal boundary layer becomes thinner and $r_{max} \rightarrow r_{min}$, and thus the nucleation sites become suppressed, as suggested by Eq. (2). The distinct difference in the formation of nucleation sites between pool and flow boiling lies in the fact that r_{max} in flow boiling is typically much less than that in pool boiling due to a much thinner thermal boundary layer. In fact, Wang and Dhir (1993) were able to adequately predict pool boiling nucleation site density by assuming $r_{max} \rightarrow \infty$. As will be demonstrated, such an assumption is not valid for flow boiling.

2.1 Estimating r_{min} and r_{max} in Flow Boiling. In order to estimate r_{max} and r_{min} for saturated flow boiling, consideration is given to a hemispherical vapor embryo which protrudes a surface cavity as shown in Fig. 2, for which the following assumptions are made: (1) the static vapor embryo is embedded in a saturated liquid shear flow with a temperature profile governed by macroconvection heat transfer, and (2) the embryo radius is typically much less than the liquid film thickness, and the temperature profile in the vicinity of the embryo may be approximated as linear. Following Zeng and Klausner (1993a), the near wall liquid temperature profile, $T_l(z)$, is approximated as

$$T_l(z) = T_w - \frac{h_{mac} z}{k_l} \Delta T_{sat} \tag{3}$$

where T_w is the mean wall temperature, ΔT_{sat} is the wall superheat, and k_l is the thermal conductivity of the liquid. During vapor bubble growth under saturated conditions, energy is transferred to the vapor through the liquid microlayer which resides beneath the bubble. However, prior to growth no liquid microlayer can be established, and thus energy is transferred to the embryo from the surrounding liquid and the solid heating surface beneath the embryo. A physically sound criterion for vapor embryo growth to continue is that there must exist net heat transfer into the embryo from the surroundings. Resolution of the temperature field in the vicinity of the embryo requires a three-dimensional, three-phase heat transfer analysis. Because of the complexity of such an analysis, the problem is greatly simplified by approximating the liquid temperature profile near the wall to be linear as given by Eq. (3), and the incipience criterion proposed by Bergles and Rohsenow (1964) is instituted: vapor bubble growth will proceed only when the liquid temperature, T_l, at the top of the hemispherical embryo exceeds the vapor temperature, T_v. It is assumed that the vapor embryo temperature T_v is uniform, which is computed from the Clapeyron equation as

$$T_v - T_{sat} = \frac{T_v T_{sat} R_v}{h_{fg}} \ln\left(1 + \frac{2\sigma}{r P_{sat}}\right) \tag{4}$$

where R_v is the engineering gas constant, σ is the surface tension, P_{sat} is the pressure in the liquid phase, and h_{fg} is the latent heat. Thus, the maximum and minimum cavity radii which can sustain an active nucleation site may be estimated by setting $T_l = T_v$ and $z = r$ in Eq. (3) and solving Eq. (3) and Eq. (4) for r. An approximation for r can be made by noting that $\ln(1 + (2\sigma/rP_{sat})) \approx (2\sigma/rP_{sat})$ for many cases of practical interest. Implementing the perfect gas law and combining Eqs. (3) and (4) results in

$$\frac{h_{mac} r}{k_l} = 1 - \frac{T_{sat} 2\sigma}{h_{fg} \rho_v \Delta T_{sat} r} . \tag{5}$$

Equation (5) is quadratic in r, and the two solutions give the respective maximum and minimum cavity radii, r_{max} and r_{min}. Simplification of the solutions to Eq. (5), by noting that $(T_{sat} 2\sigma h_{mac}/h_{fg} \rho_v \Delta T_{sat} k_l)$ is small compared with unity for many cases of interest, results in approximate expressions for r_{max} and r_{min}:

$$r_{max} = \frac{k_l}{h_{mac}} \tag{6}$$

and

$$r_{min} = \frac{2\sigma T_{sat}}{\Delta T_{sat} h_{fg} \rho_v} . \tag{7}$$

A straightforward result of this analysis is the identification of the dimensionless parameter r_{max}/r_{min}, which is referred to as the cavity size ratio,

$$\frac{r_{max}}{r_{min}} = \frac{\Delta T_{sat} k_l \rho_v h_{fg}}{h_{mac} T_{sat} 2\sigma} . \tag{8}$$

In cases where the approximations leading to Equations (6)–(8) cannot be satisfied, it is only necessary to use an iterative technique to simultaneously solve Eqs. (3) and (4) for r_{max} and r_{min}. It is noted that variations of the Bergles-Rohsenow incipience criterion have appeared in the literature, but inherent assumptions are used in all of these. In light of the assumptions used in the incipience criterion, the assumptions used to arrive at Eq. (8), and the nonuniform geometry of most nucleation sites, r_{max}/r_{min} should be viewed as a dimensionless variable on which the formation and suppression of nucleation sites depends.

As implied by Eq. (2), the probability of finding cavities on the heating surface which have mouth radii which fall between r_{max} and r_{min} decreases as $r_{max} \rightarrow r_{min}$. Specifically, it is noted that $r_{max}/r_{min} = 4$ is the limit allowed by the Bergles-Rohsenow incipience criterion. This suggests that r_{max}/r_{min} may serve as a useful correlating parameter for the nucleation site density. In fact, when $r_{max}/r_{min} = 4$ it is not physically possible to maintain heterogeneous boiling; however, this is too restrictive a condition to use as a suppression criterion since it is possible for nucleation sites to become completely suppressed for $r_{max}/r_{min} > 4$, depending on the distribution of cavity mouth radii on the heating surface. It is expected that the topography of the heating surface plays some role, as do the wetting characteristics of the fluid. The usefulness of r_{max}/r_{min} as a dimensionless variable to characterize nucleation suppression will be demonstrated empirically.

2.2 Nucleation Site Density. Figure 3 shows the flow boiling nucleation site density data, measured by Zeng and Klausner (1993b) using R113 in horizontal stratified flow over a smooth nichrome heating strip, displayed as a function of r_{max}/r_{min} for two different heat fluxes, q_w = 19.3 and 13.8 kW/

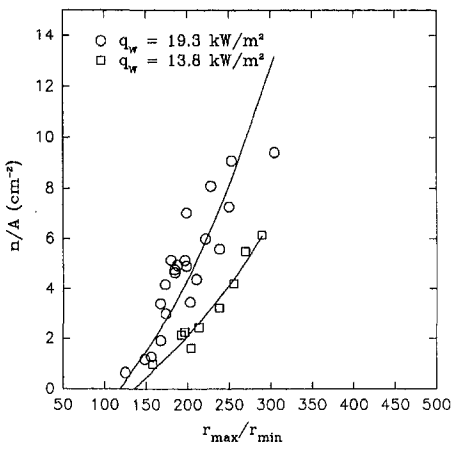

Fig. 3 Nucleation site density data of Zeng and Klausner (1993b) shown as a function of r_{max}/r_{min}

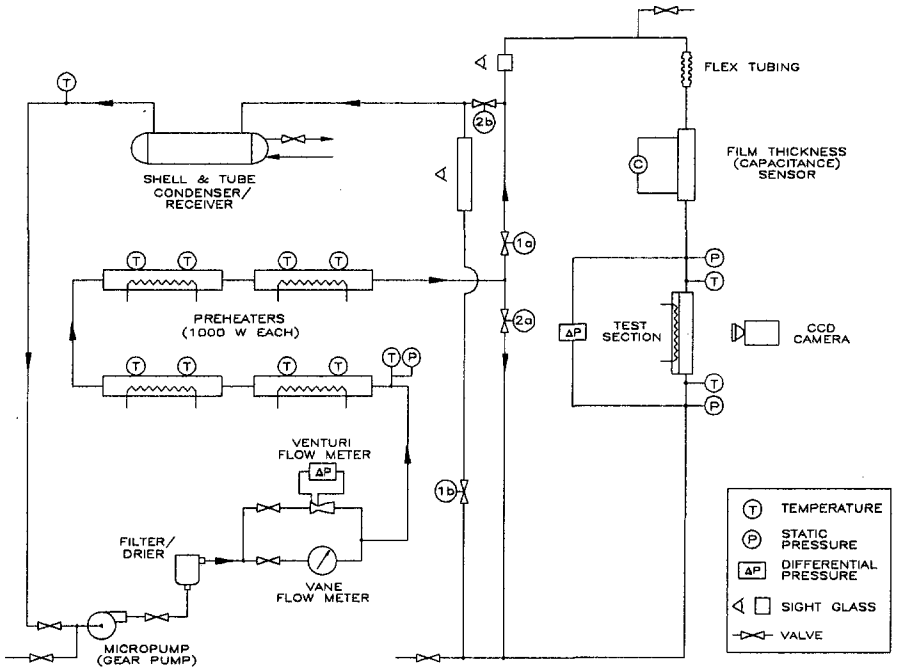

Fig. 4 Schematic diagram of vertical flow boiling facility

m^2. In these data the mass flux, vapor quality, liquid film thickness, and wall superheat varied. The lines through the data are merely curve fits. In computing r_{max}/r_{min}, experimental values for h_{mac} were used. It is seen that for a given heat flux the data collapse into a single curve. It is noted that Zeng and Klausner were unable to correlate their nucleation site density data with r_{min} alone. For the data shown in Fig. 3, r_{min} does not change appreciably, while r_{max} varies significantly. Thus, the variation in r_{max}/r_{min} is primarily controlled by r_{max}, which suggests that r_{max} has a controlling influence on flow boiling nucleation site density. This is significant because r_{max} has historically been ignored in correlating n/A.

According to Eq. (2), the nucleation site density as a function of r_{max}/r_{min} should not be heat flux dependent. The heat flux dependence shown in Fig. 3 may be due to the fact that Eq. (3) and Eq. (8) assume a uniform wall temperature. In fact, in the presence of heterogeneous boiling, the thermal field on the heating surface is highly nonuniform with large temperature gradients beneath nucleation sites, which are more pronounced at higher heat fluxes. As the nucleation site density is reduced, the temperature nonuniformities should be less pronounced and the observed convergence of the data in Fig. 3 is expected. The heat flux dependence displayed in Fig. 3 may also be a result of the simplified incipience criterion used to compute r_{max}/r_{min}.

When nucleation is completely suppressed, the wall temperature should be uniform (within the length scale of the bubble size) and the two curves fitted to the data are expected to intersect at $n/A = 0$. Although they do not exactly intersect at $n/A = 0$, $(r_{max}/r_{min})_{sup} = 117$ for $q_w = 19.3$ KW/m^2, which is close to $(r_{max}/r_{min})_{sup} = 130$ for $q_w = 13.8$ KW/m^2, where the subscript "sup" denotes the point of suppressed nucleation.

A result which makes clear the limitations of the Bergles-Rohsenow incipience criterion is that $(r_{max}/r_{min})_{sup}$ is much

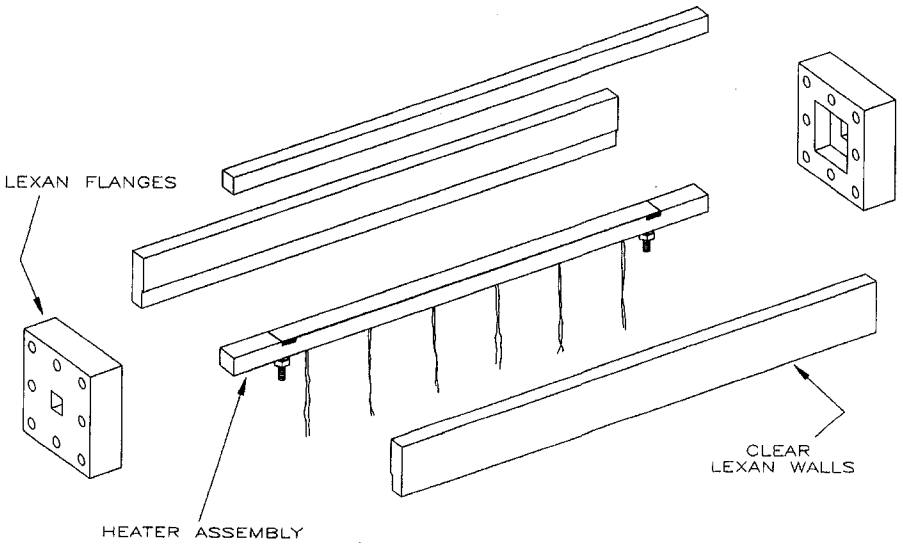

Fig. 5 Exploded view of visual test section

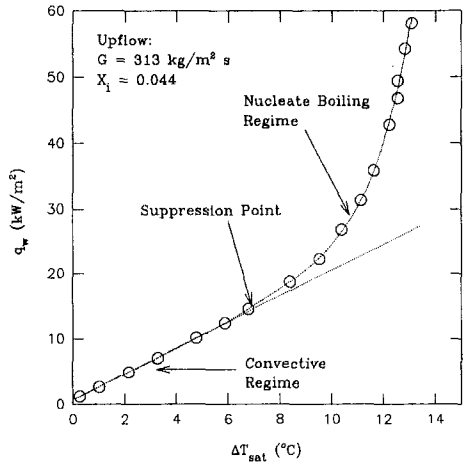

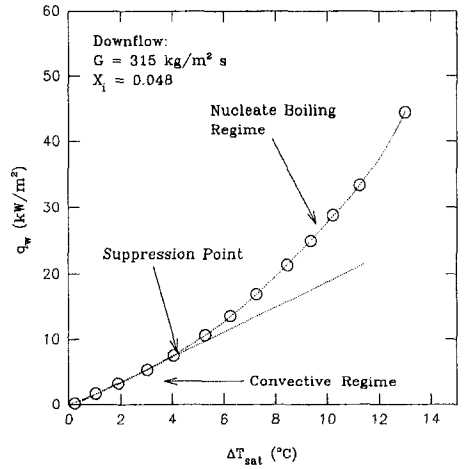

Fig. 6 Boiling curves for vertical annular upflow and downflow, illustrating nucleation suppression point

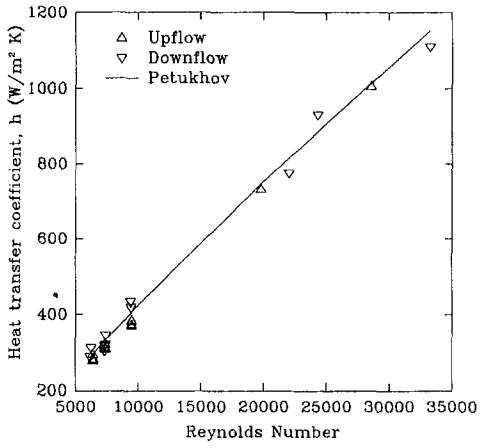

Fig. 7 Comparison of measured single-phase heat transfer coefficient to Petukhov's (1970) model

greater than unity. Although the magnitude of r_{max}/r_{min} is high, its value as a correlating parameter will be further demonstrated. In order to further test the applicability of correlating the cavity size ratio with the point of suppressed nucleation, a vertical forced convection boiling facility has been constructed in which measurements of the flow boiling nucleation suppression point have been made for vertical upflow and downflow over a wide range of flow and thermal conditions. A perfluorocarbon fluid, FC-87, having similar surface wetting characteristics as R113, was used as the working fluid, and nichrome was again used as the heating surface. Suppression point data have been obtained for mass flux, G, ranging from 183 to 315 kg/m^2-s; inlet quality, x_i, ranging from 0 to 0.151; and heat flux, q_w, ranging from 1.20 to 16.95 kW/m^2.

3 Experiment Description

3.1. Flow Boiling Facility. A schematic diagram of the experimental facility used in this work is shown in Fig. 4. FC-87, a perfluorocarbon fluid, was selected as the working fluid for its low latent heat and moderate saturation temperature. A variable speed Micropump drives the working fluid through the facility. Following the pump, the fluid is filtered to eliminate contaminants. The fluid is degassed thoroughly before testing by bleeding gas off the system through a valve at the top of the facility. The volumetric flow rate is measured using either a Venturi or vane-type flow meter, each used to measure a different range of flow rates (Venturi, 0.0–1.8 *l*/min; vane, 3.0–9.0 *l*/min). Both meters were calibrated in the laboratory and are accurate to within ±0.5 percent of their respective full scale. The fluid is preheated via four preheaters to achieve a saturated two-phase mixture, then routed by a series of valves (1a and b, 2a and b) to obtain vertical upflow or downflow in the test section. The square test section uses a DC-powered nichrome heating strip, on which the average wall temperature and heat flux can be measured. After exiting the test section the flow enters a water-cooled, shell and tube condenser/receiver which returns the fluid to a subcooled state. Measurements of pressure, temperature, flow rate, and capacitance were recorded by a multiplexed 12-bit analog-to-digital converter attached to a personal computer. Since two-phase flows are inherently unsteady, 500 samples per channel were obtained over a period of 5 seconds and averaged to achieve repeatable measurements.

An important component of the boiling facility is the transparent test section, illustrated in Fig. 5. The walls of the test section and the heater assembly are constructed of $\frac{1}{2}$ inch thick cast Lexan plate; these are bonded together with methacrylate resin to form a 12.7 × 12.7 mm square duct. Cast Lexan was chosen for its optical clarity and strength. A 30 cm long, 12.7 mm wide, 0.15 mm thick nichrome strip, clamped and adhered to one wall, is used as the heating surface. To measure the average heater surface temperature, six equally spaced type E thermocouples are attached to the underside of the nichrome strip, and lead out through holes in the base. The thermocouples have an accuracy of ±0.5°C and are repeatable to within ±0.1°C. Two 1 inch thick Lexan flanges are sleeved over the ends of the duct and bonded with the resin. The test section connects to the rest of the facility by flange connections employing double O-ring face seals.

Electric power to the test section heater is supplied by a 0–50 V, 120 A DC rectifier. A digital voltmeter records the voltage across the heater with an uncertainty of ±0.04 V. The electric current through the heater is determined by measuring the voltage drop across a 1 Ω shunt connected in series with the heater, and the resulting uncertainty is ±0.09 A. The heat loss through the test section is determined via calibration. Following Kline and McClintock (1953), the maximum uncertainty in heat flux is approximately ±1 percent.

Two Viatran model 2416 static pressure transducers are installed immediately before and after the test section, both accurate to within ±400 Pa. Two type-E thermocouples are also installed before and after the test section, and are used to measure bulk flow temperature. The resulting wall superheat, ΔT_{sat}, is obtained by subtracting the saturation temperature from the average wall temperature, with an estimated uncertainty of ±0.5°C.

Table 1 Point of suppressed nucleation heat transfer data from present work

G (kg/m^2-s)	x_i	δ (mm)	q_w (kW/m^2)	ΔT_{sat} (°C)	h_{mac} (W/m °C)	$(r_{max}/r_{min})_{sup}$
			upflow			
200	0.045	1.60	16.18	8.00	2022	54.8
201	0.052	1.68	16.36	8.01	2043	53.2
200	0.057	1.54	16.62	8.25	2015	56.6
201	0.087	1.41	15.52	7.54	2059	50.5
201	0.120	1.21	16.23	7.75	2094	51.5
200	0.151	1.11	15.55	7.46	2084	49.5
260	0.023	1.75	16.21	7.94	2041	54.2
261	0.062	1.39	16.51	7.66	2155	50.0
260	0.087	1.31	16.27	7.58	2147	50.2
261	0.109	1.15	16.67	7.49	2225	48.7
262	0.137	1.07	18.67	8.17	2285	52.5
311	0.025	1.65	15.57	7.41	2101	50.1
314	0.044	1.48	16.36	7.58	2158	50.6
314	0.067	1.31	16.50	7.48	2206	49.5
314	0.102	1.14	17.52	7.41	2364	47.3
			downflow			
183	0.060	0.851	7.00	5.12	1367	51.8
202	0.062	0.829	8.15	5.07	1608	44.5
236	0.054	0.892	8.52	4.97	1714	41.2
237	0.075	0.889	6.53	4.21	1550	38.5
238	0.128	0.860	6.04	4.05	1492	39.9
237	0.151	0.829	6.82	4.43	1540	43.0
284	0.023	0.940	8.06	4.48	1798	36.0
280	0.048	0.939	7.91	4.56	1734	38.3
280	0.076	0.927	9.19	5.05	1819	39.6
280	0.109	0.900	8.23	4.82	1707	42.6
315	0.026	0.981	9.41	4.74	1986	34.6
314	0.049	0.968	8.78	4.67	1881	36.6
313	0.073	0.951	8.19	4.50	1819	37.0
311	0.106	0.919	7.73	4.30	1798	36.8

3.2 Data Collection and Analysis. The nucleation site density suppression point data were obtained from the boiling facility in the following manner: for a given mass flux and inlet vapor quality at the test section, sufficient power was applied to the heater to achieve vigorous boiling. The power input to the test section heater was then stepped down in small increments, and measurements of heat flux, mass flux, wall superheat, vapor quality, liquid film thickness, and saturation pressure and temperature were obtained. Decreasing wall heat flux was used in order to avoid boiling hysteresis. A flow boiling curve (q_w versus ΔT_{sat}) was generated for the given flow conditions. Typical flow boiling curves for vertical upflow and downflow are illustrated in Fig. 6. The suppression point is determined from the flow boiling curve by observing that in the convective regime the heat transfer coefficient is independent of heat flux, and q_w varies linearly with ΔT_{sat}. The suppression point is therefore taken to be the point at which the heat flux curve departs from linearity as shown in Fig. 6. The value of ΔT_{sat} for which nucleation suppression is established has an estimated uncertainty of ±0.5°C. The macroconvection heat transfer coefficient, h_{mac}, is the slope of the q_w versus ΔT_{sat} curve in the convective regime. Following Kline and McClintock (1953), h_{mac} is determined with an uncertainty of ±5 percent. In order to validate the heat transfer coefficient measurements, single-phase flow heat transfer coefficients were measured over a range of Reynolds number. The results are compared against Petukhov's

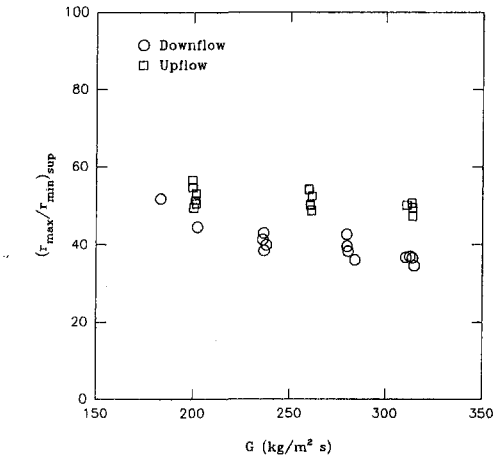

Fig. 8 Suppression point cavity ratio, $(r_{max}/r_{min})_{sup}$, as a function of mass flux

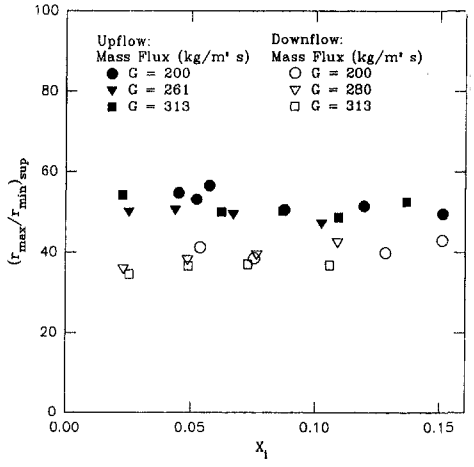

Fig. 9 Suppression point cavity ratio, $(r_{max}/r_{min})_{sup}$, as a function of test section inlet quality

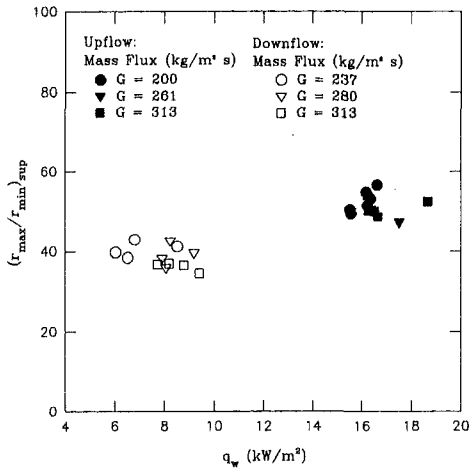

Fig. 10 Suppression point cavity ratio, $(r_{max}/r_{min})_{sup}$, as a function of wall heat flux

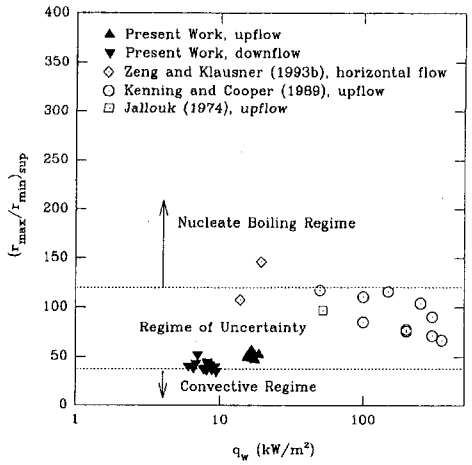

Fig. 11 Identification of two-phase heat transfer regimes based on point of suppressed nucleation

(1970) single-phase flow heat transfer correlation in Fig. 7. It is seen that the agreement is good.

4 Results

In the present work, a set of 29 suppression points were determined from vertical upflow and downflow boiling curves. Using flow conditions and properties obtained from the experiment, the cavity size ratio at the point of suppression, $(r_{max}/r_{min})_{sup}$, was calculated using Eq. (8). In determining $(r_{max}/r_{min})_{sup}$, experimental values of h_{mac} (the slope of the q_w versus ΔT_{sat} curve in the convective regime) were used. A summary of the suppression point data and thermal and flow conditions at the point of suppression are displayed in Table 1.

Figures 8, 9, and 10 show the variation of $(r_{max}/r_{min})_{sup}$ for vertical upflow and downflow with mass flux, inlet quality, and wall heat flux, respectively. According to Eq. (2), $(r_{max}/r_{min})_{sup}$ should be independent of these parameters. Furthermore, for a specific heating surface and fluid combination, $(r_{max}/r_{min})_{sup}$ should be invariant. As shown in Figs. 8, 9, and 10, the measured values for $(r_{max}/r_{min})_{sup}$ are scattered slightly over a narrow range, $40 < (r_{max}/r_{min})_{sup} < 60$, and show no dependence on inlet quality and very little dependence on mass flux, which qualitatively supports the theory. However, Fig. 10 shows a slight dependence of $(r_{max}/r_{min})_{sup}$ on heat flux, particularly in upflow. Although the dependence on heat flux is not strong, it may be indicative of some thermal phenomena which the theory does not take into account. Whether this is due to the assumed uniform wall superheat in Eq. (8) or the use of the Bergles-Rohsenow incipience criterion is not currently known and requires further scrutiny. Again it is observed that $(r_{max}/r_{min})_{sup}$ is much greater than unity, although within the same order of magnitude of the suppression point data of Zeng and Klausner (1993b).

The point of suppressed nucleation can also be determined from the heat transfer data of Kenning and Cooper (1989), obtained from vertical upflow boiling of water on cupronickel tubing. The values of $(r_{max}/r_{min})_{sup}$ based on their measured heat transfer data are summarized in Table 2. Additionally, the R114 heat transfer data measured inside a copper tube by Jallouk (1974) can be used to determine that $(r_{max}/r_{min})_{sup} = 112$ for $q_w = 19$ kW/m^2. These $(r_{max}/r_{min})_{sup}$ data, as well as those obtained using the current experimental facility, are summarized in Fig. 11 as a function of the heat flux.

It is seen that the data demonstrate a slight dependence on heat flux, but are generally scattered between $(r_{max}/r_{min})_{sup} = 40-120$. In general, the point of suppressed nucleation depends on the fluid/surface combination and the wetting characteristics of the fluid; however, despite vastly different flow configurations and fluid/surface combinations, Eq. (8) yields suppression point cavity size ratios within the same order of magnitude. In this study, both highly wetting fluids (FC-87, R113, R114) and an intermediate wetting fluid (water) have been considered. As indicated in Fig. 11, three regimes may be identified based on r_{max}/r_{min}:

Regime I: $r_{max}/r_{min} < 40$, Convective Regime (suppressed nucleation)

Regime II: $40 \le r_{max}/r_{min} \le 120$, Regime of Uncertainty (nucleation may or may not be sustainable)

Regime III: $r_{max}/r_{min} > 120$, Nucleate Boiling Regime (nucleation is sustained)

Thus, Fig. 11 may be used as a flow boiling regime map to determine whether the flow and thermal conditions correspond to sustained nucleation or purely forced convection. The purpose of the flow boiling regime map is to provide guidance to practitioners, experimenters, and theoreticians as to which regime is most probable for specific operating conditions.

Table 2 Point of suppressed nucleation from Kenning and Cooper (1989) heat transfer data

$(r_{max}/r_{min})_{sup}$	q_w (kW/m^2)	G (kg/m^2-s)
108	50	304
90	100	304
103	100	123
111	150	123
74	200	304
74	200	203
99	250	123
69	300	304
89	300	123
63	350	123

5 Discussion

The cavity size ratio, r_{max}/r_{min}, has been demonstrated to correlate nucleation site density as well as to distinguish between the convective and nucleate boiling regimes in flow boiling. Experimental data from this work, along with data obtained from the literature, are used to examine $(r_{max}/r_{min})_{sup}$ and identify the transition between the two regimes. The values of $(r_{max}/r_{min})_{sup}$ are much greater than unity; however, data taken over a wide range of flow conditions, heating surfaces, and working fluids all fall within the same order of magnitude. This suggests

that the cavity size ratio is, to the leading order, the most important dimensionless parameter in characterizing the suppression of nucleation sites.

The cavity size ratio identified in this work is intended as a first step toward a better understanding of flow boiling nucleation and the development of a flow boiling regime map. This work also provides direction for future flow boiling nucleation investigations. An incipience criterion based on conservation of energy which provides a realistic description of the thermal boundary layer in the vicinity of the vapor embryo may give an improved estimate for r_{max}. Equation (2) dictates that the heating surface topography and fluid/surface wetting characteristics play a role in the formation and suppression of nucleation sites, both of which require improved understanding.

Acknowledgments

This work was partially funded by the Florida Space Grant Consortium and the Exxon Education Foundation under Grant No. 04/1995. The authors also wish to thank the 3M Corporation Specialty Fluids Division for supplying the perfluorocarbon fluids used in this work.

References

Bergles, A. E., and Rohsenow, W. M., 1964, "The Determination of Forced-Convection Surface-Boiling Heat Transfer," ASME JOURNAL OF HEAT TRANSFER, Vol. 86, pp. 365–372.

Blatt, T. A., and Adt, R. R. Jr., 1964, "An Experimental Investigation of Boiling Heat Transfer and Pressure-Drop Characteristics of Freon 11 and Freon 113 Refrigerants," *AIChE Journal,* Vol. 10, No. 3, pp. 369–373.

Chen, J. C., 1966, "Correlation for Boiling Heat Transfer to Saturated Fluids in Convective Flow," *I&EC Proc. Design and Development,* Vol. 5, No. 3, pp. 322–329.

Cooper, M. G., 1989, "Flow Boiling—the "Apparently Nucleate" Regime," *Int. J. Heat Mass Transfer,* Vol. 32, No. 3, pp. 459–464.

Corty, C., and Foust, A., 1955, "Surface Variables in Nucleate Boiling," *Chem. Eng. Prog. Symp. Series,* No. 51, Vol. 17, pp. 1–12.

Dengler, C. E., and Addoms, J. N., 1956, "Heat Transfer Mechanism for Vaporization of Water in a Vertical Tube," *Chem. Eng. Prog. Symp. Series,* No. 18, Vol. 52, pp. 95–103.

Frost, W., and Kippenhan, C. J., 1967, "Bubble Growth and Heat Transfer Mechanisms in the Forced Convection Boiling of Water Containing a Surface Active Agent," *Int. J. Heat Mass Transfer,* Vol. 10, pp. 931–949.

Gungor, K. E., and Winterton, R. H. S., 1986, "A General Correlation for Flow Boiling in Tubes and Annuli," *Int. J. Heat Mass Transfer,* Vol. 29, No. 3, pp. 351–358.

Jallouk, P. A., 1974, "Two-Phase Flow Pressure Drop and Heat Transfer Characteristics of Refrigerants in Vertical Tubes," Ph.D. thesis, University of Tennessee at Knoxville, TN.

Kandlikar, S. G., 1990, "A General Correlation for Saturated Two-Phase Flow Boiling Heat Transfer Inside Horizontal and Vertical Tubes," ASME JOURNAL OF HEAT TRANSFER, Vol. 112, pp. 219–228.

Kenning, D. B. R., and Cooper, M. G., 1989, "Saturated Flow Boiling of Water in Vertical Tubes," *Int. J. Heat Mass Transfer,* Vol. 32, No. 3, pp. 445–458.

Klausner, J. F., 1989, "The Influence of Gravity on Pressure Drop and Heat Transfer in Flow Boiling," Ph.D. thesis, University of Illinois at Urbana-Champaign, IL.

Kline, S. J., and McClintock, F. A., 1953, "Describing Uncertainties in Single-Sample Experiments," *Mechanical Engineering,* Vol. 75, Jan., pp. 3–8.

Petukhov, B. S., 1970, "Heat Transfer and Friction in Turbulent Pipe Flow with Variable Properties," *Advances in Heat Transfer,* J. P. Harnett and T. F. Irvine, eds. Vol. 6, pp. 503–564.

Staub, F. W., and Zuber, N., 1966, "Void Fraction Profiles, Flow Mechanisms, and Heat Transfer Coefficients for Refrigerant 22 Evaporating in a Vertical Tube," *ASHRAE Trans.,* Vol. 72, Part 1, pp. 130–146.

Tran, T. N., Wambsganss, M. W., France, D. M., and Jendrzejczyk, J. A., 1993, "Boiling Heat Transfer in a Small, Horizontal, Rectangular Channel," *AIChE Symp. Series,* Vol. 89, pp. 253–261.

Wang, C. H., and Dhir, V. K., 1993, "On the Gas Entrapment and Nucleation Site Density During Pool Boiling of Saturated Water," ASME JOURNAL OF HEAT TRANSFER, Vol. 115, pp. 670–679.

Yang, S. R., and Kim, R. H., 1988, "A Mathematical Model of the Pool Boiling Nucleation Site Density in Terms of Surface Characteristics," *Int. J. Heat Mass Transfer,* Vol. 31, No. 6, pp. 1127–1135.

Zeng, L. Z., and Klausner, J. F., 1993a, "Heat Transfer, Incipience, and Hysteresis in Saturated Flow Boiling," *AIChE Sypmp. Series,* Vol. 115, pp. 215–221.

Zeng, L. Z., and Klausner, J. F., 1993b, "Nucleation Site Density in Forced Convection Boiling," ASME JOURNAL OF HEAT TRANSFER, Vol. 115, pp. 215–221.

Numerical Simulation of Saturated Film Boiling on a Horizontal Surface

G. Son

V. K. Dhir
vdhir@seas.ucla.edu

Mechanical and Aerospace Engineering Department,
University of California, Los Angeles
Los Angeles, CA 90095

The past efforts in applying linear Taylor instability theory to the prediction of heat transfer during film boiling on a horizontal surface have suffered from the fact that empirical correlations must be used to define the shape of vapor-liquid interfaces and to determine the transport of mass and heat across these interfaces. The objective of this study is to clarify the physics of film boiling and to predict heat transfer coefficients through complete numerical simulation of the evolving interface between superposed layers of immiscible fluids. A coordinate transformation technique supplemented by a numerical grid generation method and a second-order projection method are combined to solve for the flow and temperature fields associated with an evolving interface. From the numerical simulation, the film thickness and, in turn, the heat transfer coefficient are found to vary both spatially and temporally. Increased wall superheat not only thickens the vapor film in the valley but also enlarges the vapor bulge. The effect of increased system pressure is to slow down the growth of the interface.

Introduction

Film boiling is characterized by the existence of a continuous vapor layer between a heated surface and a liquid layer. The evolution of the vapor-liquid interface during film boiling on a horizontal surface is determined by Taylor instability.

Zuber (1959) was the first to apply the concept of Taylor instability to predict maximum and minimum heat fluxes in pool boiling. He proposed that vapor bubbles were spaced a distance bounded between the "critical" and "most dangerous" Taylor wavelengths. By assuming that two bubbles were released per cycle from a square cell, he predicted the minimum heat flux.

Subsequently, Berenson (1961) obtained an expression for the heat transfer coefficient during saturated film boiling on horizontal surfaces. Berenson assumed that vapor bubbles were placed on square grid with a spacing equal to two-dimensional "most dangerous" Taylor wavelength, λ_{d2}, and a thin vapor film of uniform thickness connected the neighboring bubbles. By further assuming that mean bubble height and bubble diameter were proportional to the bubble spacing and two bubbles were supported per λ_{d2}^2 area of the heater, he predicted the Nusselt number for film boiling as

$$\mathrm{Nu} = 0.42\left[\frac{\rho_v(\rho_l-\rho_v)gh_{fg}}{k_v\mu_v\Delta T}\right]^{1/4}\left[\frac{\gamma}{g(\rho_l-\rho_v)}\right]^{3/8}. \quad (1)$$

In Eq. (1) all of the properties were evaluated at the mean film temperature. Equation (1) was derived from a static model which did not account for the time variation of the bubble height or bubble diameter and the flow field in the liquid. Heater surface temperature was assumed to remain constant with time and space. In reality, the interface is dynamic and temperature and local heat flux can vary during the evolution of the interface. The predictions from Eq. (1) were, however, found to compare well with Berenson's data. The two-dimensional wave configuration used by Zuber and Berenson was improved by Sernas et al. (1973) while carrying out three-dimensional Taylor instability analysis. They showed that using the three-dimensional Taylor wavelength, λ_{d3}, which is $\sqrt{2}$ times larger than the two-dimensional Taylor wavelength, four bubbles were released per cycle on λ_{d3}^2 area. Therefore, two bubbles are generated per cycle on λ_{d2}^2 area. However, at any instant there will be only one bubble per λ_{d2}^2 that will be growing.

Hosler and Westwater (1962) experimentally studied film boiling of water and Freon-11 and found the heat transfer data and bubble spacing to show a large variability. The mean of the data, however, tended to show a good agreement with the predictions made from Eq. (1).

Film boiling on a liquid metal surface has been studied by Henry et al. (1974) and Greene and Irvine (1986). In the work of Greene and Irvine, substantial quasi-static heat transfer data for film boiling of R-11 on liquid metal surfaces of lead, bismuth, and Wood's metal were taken. Temporal fluctuations in the readings of the thermocouples placed in molten metal pools were observed and data were reduced by using mean values of the temperature. It was concluded that all of the data could be correlated within 20 percent of that predicted from Berenson's Eq. (1).

Ramilison and Lienhard (1987) reproduced Berenson's experiment with a reduced thermal resistance in the heater to improve accessibility to transition boiling regime. By decreasing the heater temperature from the film boiling side, they obtained the film and transition boiling data for Freon-113, acetone, benzene and *n*-pentane on surfaces with different finishes. They correlated data in film boiling and found that in the transition film boiling regime the heat transfer coefficient deviated strongly from Berenson's Eq. (1) and the deviations depended on the surface conditions. The temperature for onset of the transition from pure film boiling was found to correlate with the advancing contact angle.

Klimenko (1981) has carried out a somewhat generalized analysis of film boiling on horizontal flat plates. Employing a basic formulation similar to that of Berenson, Klimenko has developed a correlation that includes data for a variety of liquids, including cryogen. In a subsequent work, Klimenko and Shelepen (1982) broadened the data base of their original correlation. According to their correlation, the Nusselt number for

Contributed by the Heat Transfer Division for publication in the JOURNAL OF HEAT TRANSFER. Manuscript received by the Heat Transfer Division September 3, 1996; revision received February 7, 1997; Keywords: Boiling, Multiphase Flows, Phase-Change Phenomena. Associate Technical Editor: M. Kaviany.

film boiling on an upward facing horizontal surface is expressed as

$$\mathrm{Nu} = 3.02 \times 10^{-2}\,\mathrm{Ar}^{1/3}\,\mathrm{Pr}^{1/3} f_1(\beta); \quad \text{for} \quad \mathrm{Ar} < 10^8 \quad (2)$$

$$\mathrm{Nu} = 1.37 \times 10^{-3}\,\mathrm{Ar}^{1/2}\,\mathrm{Pr}^{1/3} f_2(\beta); \quad \text{for} \quad \mathrm{Ar} > 10^8 \quad (3)$$

where

$$f_1 = 1 \quad \text{for} \quad \beta > 0.71$$
$$= 0.89\beta^{-1/3} \quad \text{for} \quad \beta < 0.71$$
$$f_2 = 1 \quad \text{for} \quad \beta > 0.50$$
$$= 0.71\beta^{-1/2} \quad \text{for} \quad \beta < 0.50.$$

Equations (2) and (3) suggest that for small values of superheat parameter, β ($=c_{pv}\Delta T/h_{fg}$), the heat transfer coefficient should vary as $\Delta T^{-1/3}$ or $\Delta T^{-1/2}$, depending on the magnitude of Archimedes number Ar. For a high values of β, the heat transfer coefficient is predicted to be independent of wall superheat.

Dhir et al. (1977) studied pseudo film boiling during sublimation of a slab of dry ice placed beneath a pool of warm liquid. The heat transfer rate was determined by noting a change in the enthalpy of the overlying liquid pool. Data were found to compare favorably with prediction from an equation similar to Eq. (1) when the lead constant was reduced to 0.36. It was argued that reduction of about 15 percent in the lead constant resulted from the fact that during sublimation only one bubble was supported per λ_{d2}^2 area instead of $\lambda_{d2}^2/2$ as assumed by Berenson. This was based on their experimental observation that the bubbles were released from the same location rather than alternately from nodes and antinodes as observed during film boiling on flat plates or during early period of sublimation. Subsequently Taghavi-Tafreshi et al. (1979) studied melting of a slab of frozen olive oil placed under a pool of water and again found their data to correlate well with predictions from an equation similar to Eq. (1). However, the lead constant had to be reduced by almost a factor of 2. The reduction in the lead constant was rationalized on the basis that growth rate of the melt droplets was very slow and the time averaged height of the droplets was much smaller than that of a bubble in film boiling. This reduction in lead constant demonstrates that density difference between the phases or components is an independent parameter in addition to the thermophysical properties already contained in the expression given by Eq. (1).

The studies described above have provided us with data and semiempirical models for description of film boiling on flat plates. However, many of the assumptions made in the models (e.g., constant film thickness between bubbles as assumed in Berenson's model for heat transfer coefficient in film boiling) remain not validated. It is believed that headway in further clarifying the physics of film boiling can be made if we employ a tool that has, so far, not been used, i.e., complete numerical simulation of the evolving interface between two immiscible fluids. The objective of this work is to carry out such a simulation. The simulation is applied to film boiling on a horizontal plate.

Analysis

Figure 1 shows the configuration used in this study to simulate the instability of the interface between two superposed horizontal layers of immiscible fluids. The computations are performed for two-dimensional incompressible flow which is described in axisymmetric coordinates. The bubble configuration during film boiling was described in Fig. 1(*a*), which is based on three-dimensional Taylor stability theory (Sernas et al., 1973). The bubbles (or valleys) are spaced a distance equal to λ_{d2} ($=2\pi\sqrt{3\gamma/g(\rho_l - \rho_v)}$). One bubble is released alternatively from the node and the antinode per λ_{d2}^2 area of the heater during each half of the cycle. The three-dimensional computation for a square grid on the horizontal heated surface can be

Nomenclature

Ar = Archimedes number, $(2\pi)^3 g l_o^3 \rho_v(\rho_l - \rho_v)/\mu_v^2$
B = radiation parameter defined as Eq. (45)
C = differential operator including convection terms
c_p = specific heat at constant pressure
g = gravitational acceleration
h_{fg} = latent heat of evaporation
J = Jacobian of transformation, $x_\xi y_\eta - x_\eta y_\xi$
k = thermal conductivity
L = differential operator including diffusion terms
l_o = characteristic length, $\sqrt{\gamma/g(\rho_l - \rho_v)}$
M, N = differential operator including pressure terms
$\dot{m}$ = vapor generation rate
Nu = Nusselt number, $l_o q_w/k_v\Delta T$
$\overline{\mathrm{Nu}}$ = Nusselt number averaged over a cell
P = control function for grid generation
p = pressure
p' = pressure correction
Pr = Prandlt number, $c_{pv}\mu_v/k_v$
Q = control function for grid generation
q = heat flux
q_{co} = film boiling heat flux without radiation
q_r = radiative heat flux
R = radius of each circular region ($=\lambda_{2d}/\sqrt{2\pi}$)
r = radial coordinate, $R - |x|$
r_1, r_2 = radial coordinates in two-circular regions as shown in Fig. 1
Re = Reynolds number, $\rho u_o l_o/\mu$
S = source term
T = temperature
ΔT = temperature difference, $T_w - T_{\mathrm{sat}}$
t_o = characteristic time, $\sqrt{l_o/g}$
u = velocity in x-direction
$\bar{u}$ = contravariant velocity component
u_o = characteristic velocity, $\sqrt{gl_o}$
v = velocity in y-direction
$\bar{v}$ = contravariant velocity component
x = horizontal coordinate
y = vertical coordinate
β = the ratio of sensible heat to latent heat
γ = surface tension
δ = vapor film thickness
ϵ = radiation emissivity
η = transformed coordinate
θ = dimensionless temperature
κ = interfacial curvature
λ_{c2} = two-dimensional "critical" wavelength
λ_{d2} = two-dimensional "most dangerous" wavelength
λ_{d3} = three-dimensional "most dangerous" wavelength
μ = viscosity
ξ = transformed coordinate
ρ = density
σ = dimensionless viscous normal stress
σ_s = Stefan-Boltzmann constant
τ = dimensionless shear stress
ϕ = general dependent variable

Superscripts

n = time step of $n\Delta t$
$\hat{}$ = property ratio of vapor to liquid

Subscripts

l, v = liquid, vapor
w, sat = wall, saturation
t = partial differentiation with respect to t
x, y = partial differentiation with respect to x, y
ξ, η = partial differentiation with respect to ξ, η

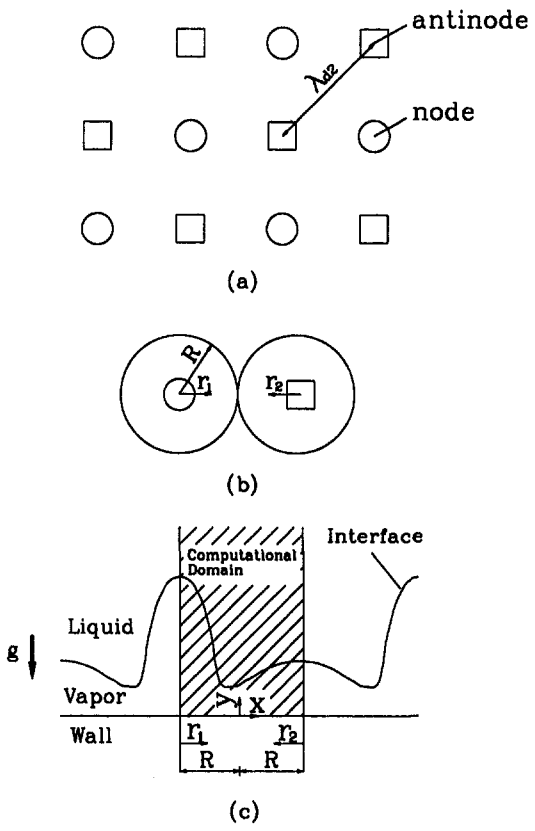

Fig. 1 Two-circular regions used in numerical simulation for film boiling

a really huge one. Also, a three-dimensional grid system aligned with a complex interface should be constructed by solving three coupled nonlinear elliptic equations at every time step. The authors believe that the three-dimensional computation for film boiling is one of the most challenging numerical problem still remaining to be solved. As such, in this study, two-circular regions shown in Fig. 1 are chosen as the computation domain. Each circle has an area $\lambda_{d2}^2/2$ and its origin is located on the center of a node and an antinode. By using this geometry it is possible not only to describe vapor bubbles as spherical rather than cylindrical but also to compute the cyclic release of bubbles. This axisymmetric approximation is not expected to be so restrictive for vapor bubbles during film boiling. As has been verified from the experimental observations, vapor bubbles during film boiling are nearly axisymmetric due to strong effect of surface tension. For convenience the horizontal coordinate x is defined as

$$x = r_1 - R \quad \text{for} \quad 0 \le r_1 \le R \tag{4}$$

$$x = R - r_2 \quad \text{for} \quad 0 \le r_2 \le R \tag{5}$$

where

$$R = \lambda_{d2}/\sqrt{2\pi}\,.$$

In carrying out numerical simulation, characteristic length l_o, characteristic time t_o, and characteristic velocity u_o are defined as

$$l_o = \sqrt{\frac{\gamma}{g(\rho_l - \rho_v)}}\,; \quad t_o = \sqrt{\frac{l_o}{g}}\,; \quad u_o = \frac{l_o}{t_o}\,. \tag{6}$$

Also, vapor and liquid pressures are nondimensionalized with $\rho_v u_o^2$ and $\rho_l u_o^2$, respectively, and dimensionless temperature is defined as

$$\theta = \frac{T_v - T_{\text{sat}}}{T_w - T_{\text{sat}}}\,. \tag{7}$$

In dimensionless form the equations governing the conservation of mass, momentum, and energy for vapor and liquid are written as

$$(ru)_x + (rv)_y = 0 \tag{8}$$

$$\frac{Du}{Dt} = -p_x + \frac{1}{\text{Re}}\left(\nabla^2 u - \frac{u}{r^2}\right) \tag{9}$$

$$\frac{Dv}{Dt} = -p_y + \frac{1}{\text{Re}}\nabla^2 v \tag{10}$$

$$\frac{D\theta}{Dt} = \frac{1}{\text{Pr Re}_v}\nabla^2\theta \tag{11}$$

where p is a pressure modified to remove the body force term in the momentum equation and for the general dependent variable ϕ, which represents dependent variables u, v, p, and θ,

$$\frac{D\phi}{Dt} = \frac{\partial\phi}{\partial t} + u\frac{\partial\phi}{\partial x} + v\frac{\partial\phi}{\partial y} \tag{12}$$

$$\nabla^2\phi = \frac{1}{r}\frac{\partial}{\partial x}\left(r\frac{\partial\phi}{\partial x}\right) + \frac{\partial^2\phi}{\partial y^2} \tag{13}$$

also

$$\text{Pr} = \frac{c_{pv}\mu_v}{k_v}$$

$$\text{Re} = \text{Re}_v = \frac{\rho_v u_o l_o}{\mu_v} \quad \text{for vapor,}$$

$$\text{Re} = \text{Re}_l = \frac{\rho_l u_o l_o}{\mu_l} \quad \text{for liquid.}$$

Since an interface cannot be described in a simple manner in (x, y) coordinates, the following coordinate transformation is used:

$$\xi = \xi(x, y, t); \quad \eta = \eta(x, y, t) \tag{14}$$

where the interface is described by η = constant. Using the above transformation and the chain rule of partial differentiation, the following equations are obtained: for the continuity equation, the momentum equations and the energy equation, respectively,

$$(ry_\eta u - rx_\eta v)_\xi + (rx_\xi v - ry_\xi u)_\eta = 0 \tag{15}$$

$$rJu_t + rJp_x = L(u) - C(u) + S_u \tag{16}$$

$$rJv_t + rJp_y = L(v) - C(v) \tag{17}$$

$$rJ\theta_t = \text{Pr}^{-1}L(\theta) - C(\theta) \tag{18}$$

where

$$J = x_\xi y_\eta - x_\eta y_\xi$$

$$L(\phi) = \text{Re}^{-1}J\nabla^2\phi$$

$$C(\phi) = [ry_\eta(u - x_t) - rx_\eta(v - y_t)]\phi_\xi + [rx_\xi(v - y_t) - ry_\xi(u - x_t)]\phi_\eta$$

$$S_u = -(\text{Re}r)^{-1}Ju.$$

In this study, a staggered grid system is used in which the locations for velocity components are displaced from those for pressure and temperature. This is done to avoid the difficulty caused by pressure boundary conditions. Also, contravariant velocity components which are naturally dependent variables

describing the continuity equation are used as dependent variables. They are defined in this study as

$$\bar{u} = \frac{y_\eta u - x_\eta v}{\sqrt{x_\eta^2 + y_\eta^2}}; \quad \bar{v} = \frac{-y_\xi u + x_\xi v}{\sqrt{x_\xi^2 + y_\xi^2}}. \tag{19}$$

The governing equations for contravariant velocity components are obtained by following the procedure similar to that used by Karki and Patankar (1988). First, the differential equations for cylindrical velocity components which are supposed to be located at the same grid points with contravariant velocity components are discretized spatially using a central difference scheme. Thereafter, the discretized governing equations for contravariant velocity components are obtained by algebraic manipulation. When discretizing governing equations temporally, the diffusion terms are treated by a fully implicit scheme. The convection, grid curvature, and source terms are treated by a first-order explicit method. Then, the discretized governing equations are expressed as

$$rJ\frac{\bar{u}^{n+1}}{\Delta t} = -rJM(p^{n+1}) + L(\bar{u}^{n+1}) + S_{\bar{u}}^n \tag{20}$$

$$rJ\frac{\bar{v}^{n+1}}{\Delta t} = -rJN(p^{n+1}) + L(\bar{v}^{n+1}) + S_{\bar{v}}^n \tag{21}$$

where

$$M(p) = \frac{1}{\sqrt{x_\eta^2 + y_\eta^2}}\left(\frac{x_\eta^2 + y_\eta^2}{J}p_\xi - \frac{x_\xi x_\eta + y_\xi y_\eta}{J}p_\eta\right)$$

$$N(p) = \frac{1}{\sqrt{x_\xi^2 + y_\xi^2}}\left(-\frac{x_\xi x_\eta + y_\xi y_\eta}{J}p_\xi + \frac{x_\xi^2 + y_\xi^2}{J}p_\eta\right)$$

$$S_{\bar{u}} = -L(\bar{u}) - \frac{x_\eta}{\sqrt{x_\eta^2 + y_\eta^2}}\left[L(v) + rJ\frac{v}{\Delta t} - C(v)\right] + \frac{y_\eta}{\sqrt{x_\eta^2 + y_\eta^2}}\left[L(u) + rJ\frac{u}{\Delta t} - C(u) + S_u\right]$$

$$S_{\bar{v}} = -L(\bar{v}) + \frac{x_\xi}{\sqrt{x_\xi^2 + y_\xi^2}}\left[L(v) + rJ\frac{v}{\Delta t} - C(v)\right] - \frac{y_\xi}{\sqrt{x_\xi^2 + y_\xi^2}}\left[L(u) + rJ\frac{u}{\Delta t} - C(u) + S_u\right]$$

where superscript ^{n} and $^{n+1}$ represent n and $n+1$ time steps, respectively, and geometric functions are evaluated at the current time step. In order to obtain a governing equation for pressure which achieves mass conservation, the fractional-step method, or projection method, is used. This method has been developed by Chorin (1968), Kim and Moin (1985), Bell et al. (1989), Rosenfeld et al. (1991), and Jin and Braza (1993). Using contravariant velocities as dependent variables, Rosenfeld et al. applied the fractional-step method to generalized coordinate systems. A variation of that method is used in the present study.

$$rJ\frac{\theta^{n+1} - \theta^n}{\Delta t} = \mathrm{Pr}^{-1}L(\theta^{n+1}) + S_\theta^n \tag{22}$$

$$rJ\frac{\hat{\bar{u}}}{\Delta t} = -rJM(p^n) + L(\hat{\bar{u}}) + S_{\bar{u}}^n \tag{23}$$

$$rJ\frac{\hat{\bar{v}}}{\Delta t} = -rJN(p^n) + L(\hat{\bar{v}}) + S_{\bar{v}}^n \tag{24}$$

$$\bar{u}^{n+1} = \hat{\bar{u}} - \Delta tM(p') \tag{25}$$

$$\bar{v}^{n+1} = \hat{\bar{v}} - \Delta tN(p'). \tag{26}$$

The momentum equations are decomposed into two fractional steps. First, the momentum Eqs. (23) and (24) are solved using pressure evaluated at the previous time step. Then, the resulting velocities, $\hat{\bar{u}}$ and $\hat{\bar{v}}$, which do not satisfy the continuity equation, are corrected, as given by Eqs. (25) and (26). A pressure correction, p', is estimated as

$$p^{n+1} = p^n + p' + O(p'\Delta t). \tag{27}$$

Using Eqs. (25), (26), and continuity Eq. (15), the governing equation for pressure correction is obtained as

$$rJ\nabla^2 p' = \frac{1}{\Delta t}[(ry_\eta\hat{u} - rx_\eta\hat{v})_\xi + (rx_\xi\hat{v} - ry_\xi\hat{u})_\eta]. \tag{28}$$

At the interface, the matching conditions for velocities and stresses are

$$u_l - u_v = (1 - \hat{\rho})\frac{y_\xi\dot{m}}{\sqrt{x_\xi^2 + y_\xi^2}} \tag{29}$$

$$v_l - v_v = -(1 - \hat{\rho})\frac{x_\xi\dot{m}}{\sqrt{x_\xi^2 + y_\xi^2}} \tag{30}$$

$$\frac{1}{\hat{\mu}}\tau_l - \tau_v = 0 \tag{31}$$

$$\frac{1}{\hat{\rho}}p_l - p_v = \frac{1}{\mathrm{Re}_v}\left(\frac{1}{\hat{\mu}}\sigma_l - \sigma_v\right) + \frac{(1 - \hat{\rho})}{\hat{\rho}}(y - \kappa) + (1 - \hat{\rho})\dot{m}^2. \tag{32}$$

In the above equations

$$\hat{\rho} = \frac{\rho_v}{\rho_l}; \quad \hat{\mu} = \frac{\mu_v}{\mu_l}$$

$$\dot{m} = \frac{c_{pv}\Delta T}{h_{fg}\,\mathrm{Pr}\,\mathrm{Re}_v}\frac{\sqrt{x_\xi^2 + y_\xi^2}}{J}\theta_\eta$$

$$\tau = \frac{x_\xi^2 + y_\xi^2}{J}\frac{x_\xi u_\eta + y_\xi v_\eta}{x_\xi^2 + y_\xi^2} + \frac{x_\xi v_\xi - y_\xi u_\xi}{x_\xi^2 + y_\xi^2} - \frac{x_\xi x_\eta + y_\xi y_\eta}{J}\frac{x_\xi u_\xi + y_\xi v_\xi}{x_\xi^2 + y_\xi^2}$$

$$\sigma = -\frac{2u}{r} - \frac{2(x_\xi u_\xi + y_\xi v_\xi)}{x_\xi^2 + y_\xi^2}$$

$$\kappa = -\frac{x_\xi y_{\xi\xi} - y_\xi x_{\xi\xi}}{(x_\xi^2 + y_\xi^2)^{3/2}} - \frac{y_\xi}{r\sqrt{x_\xi^2 + y_\xi^2}}.$$

Since the interface is maintained at the saturation temperature,

$$\theta = 0. \tag{33}$$

At the wall

$$u = v = 0; \quad \theta = 1. \tag{34}$$

At the locations of symmetry with respect to y-axis,

$$u = v_x = \theta_x = 0. \tag{35}$$

Far away from the interface,

$$u_y = v_y = 0. \tag{36}$$

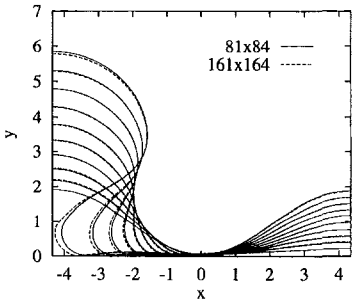

Fig. 2 Evolution of the interface with time intervals of 0.4 at ΔT = 200°C using different mesh sizes

After solving the temperature and flow field, the interface is advanced in an explicit manner:

$$x^{n+1} = x^n + \Delta t x_t^n \tag{37}$$

$$y^{n+1} = y^n + \Delta t y_t^n \tag{38}$$

where x_t and y_t are x and y-directional components of the normal interfacial velocity and are expressed as

$$x_t = -\frac{y_\xi(\bar{v}_v - \dot{m})}{\sqrt{(x_\xi^2 + y_\xi^2)}}; \quad y_t = \frac{x_\xi(\bar{v}_v - \dot{m})}{\sqrt{(x_\xi^2 + y_\xi^2)}}. \tag{39}$$

When the interface is deformed significantly, interior grid points are difficult to determine algebraically. As such, a grid system aligned with a complex interface is generated numerically by solving Poisson's equations (Thompson et al., 1985). The grid generation equation is

$$\nabla^2\xi = P(\xi_x^2 + \xi_y^2); \quad \nabla^2\eta = Q(\eta_x^2 + \eta_y^2) \tag{40}$$

where P and Q are functions which control the spacing and curvatures of η and ξ grid lines. Without the control functions, interior grid points would be uniformly spaced away from the boundary regardless of the boundary grid point distribution because of the strong smoothing tendencies of Laplace equations. The control functions P and Q are evaluated in the same manner as was done by Thompson (1982) and Thompson et al. (1985). They are expressed as

$$P = -\frac{x_\xi x_{\xi\xi} + y_\xi y_{\xi\xi}}{x_\xi^2 + y_\xi^2} - \sqrt{x_\xi^2 + y_\xi^2}\,\frac{y_\eta x_{\eta\eta} - x_\eta y_{\eta\eta}}{(x_\eta^2 + y_\eta^2)^{1.5}} \tag{41}$$

$$Q = -\frac{x_\eta x_{\eta\eta} + y_\eta y_{\eta\eta}}{x_\eta^2 + y_\eta^2} - \sqrt{x_\eta^2 + y_\eta^2}\,\frac{x_\xi y_{\xi\xi} - y_\xi x_{\xi\xi}}{(x_\xi^2 + y_\xi^2)^{1.5}}. \tag{42}$$

The first and second terms of Eqs. (41) and (42) control the spacing and curvatures of grid lines, respectively. These functions are evaluated at the boundary first and are then interpolated linearly into the computational domain.

In this study, the discretized equations are solved iteratively by a line-by-line TDMA (Tridiagonal-Matrix Algorithm) supplemented by Gauss-Seidel method which was suggested by Patankar (1980). To enhance the rate of iteration convergence, a relaxation factor obtained from orthogonal-residual method (Streett and Hussaini, 1987) is used. During computations, this optimal relaxation factor enhanced the rate of iteration convergence significantly compared with the initially specified and fixed relaxation factor.

The numerical method described above was first tested for its accuracy by comparing the predicted growth rate of the interface with that determined from the linear Taylor instability theory for a two-dimensional interface. For this exercise, an adiabatic condition was used for the rigid wall bounding the lower layer. The numerical errors were less than 1.05 percent, when using the mesh points of 32 × 64 (Son, 1996). Also, the computations with a heated wall were made to check grid resolutions with mesh points of 81 × 84 and 161 × 164. The numerical results are plotted in Fig. 2. The interface shape obtained with 81 × 84 mesh points almost overlaps the interface shape obtained with 161 × 164, except at the locations with negative curvature during the late period of the evolution of the interface. The time and area averaged Nusselt number, computed with 81 × 84 mesh points, is 9.63. This is 1.04 percent larger than that computed with 161 × 164 mesh points. Most of computations in this study were performed with 81 × 84 grid points to save the computing time without any loss in accuracy of numerical results. During the computations, time steps were chosen to satisfy the CFL condition due to the explicit treatment of the convection terms, and the condition that the numerical results should not change if the time steps are reduced. An appropriate time step is determined as

$$\Delta t = \min\left[0.7\left(\frac{|u|}{\Delta x} + \frac{|v|}{\Delta y}\right), 10^{-3}\right].$$

Generally, it took about four hours CPU time on CRAY C90 to calculate one cycle of the evolution of the interface.

Results and Discussion

Figure 3 shows the evolution of the interface for different wall superheats (ΔT) at one atmosphere pressure. Properties of water and steam evaluated at one atmosphere pressure and the mean film temperature were used for the upper and lower layers, respectively. It is seen that the time at which the upward moving portion of the interface attains a certain height decreases with increase in wall superheat. The base of the vapor bulge is also seen to widen as the wall superheat increases. This in turn reduces the extent of the thin film region. The widening of the base of the vapor bulge is consistent with the observation made by Lienhard and Dhir (1973) during film boiling on horizontal cylinders.

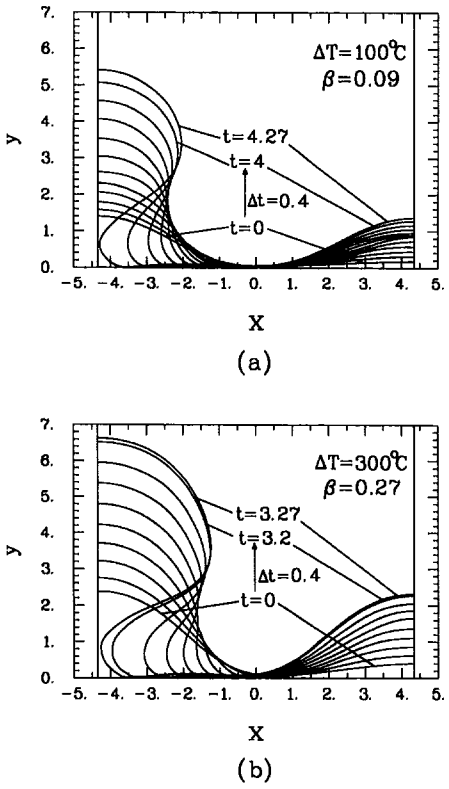

Fig. 3 Evolution of the interface with time intervals of 0.4 at different wall superheats

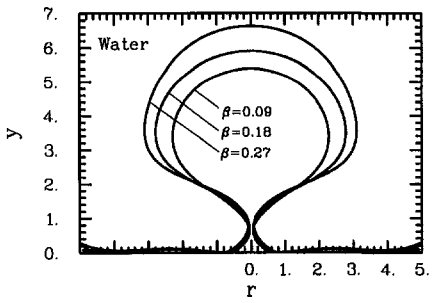

Fig. 4 Comparison of the bubble shapes just prior to departure for different wall superheats

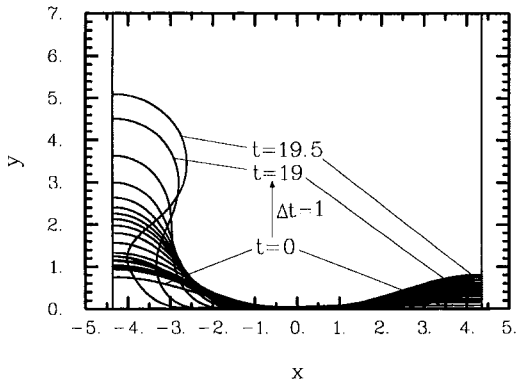

Fig. 5 Evolution of the interface for water at 100 atm. and ΔT = 100°C

The bubble shapes at departure for different wall superheats are compared in Fig. 4. As the wall superheat increases, the bubble becomes larger and the shape is closer to a mushroom rather than a sphere. The calculated height and the effective radius of bubbles are listed in Table 1. Here, the effective radius is estimated by assuming the bubble to be a sphere. The bubble break off radius predicted numerically is found to compare well with the observations of Berenson (1961) and Lienhard and Dhir (1980). However, the bubble radii reported by Hosler and Westwater (1962) are much larger than those reported by others and obtained from the present calculations. The bubble height at departure is a function of wall superheat, and is comparable to that reported by Lienhard and Dhir during film boiling of acetone on cylinders. Lienhard and Dhir did not report the wall superheat, hence a direct comparison is not possible. Bubble release period predicted from the numerical analysis is also listed in Table 1. It is noted that the predicted values for water are comparable to those reported by Hosler and Westwater. While comparing the bubble radii and heights predicted numerically with those obtained experimentally, the possibility of presence of radiation in the experiments was checked. According to Siviour and Ede (1970), the film boiling heat transfer rate including the radiation effect is expressed as

$$q = q_{co} + q_r \tag{43}$$

$$q_r = B\epsilon_w\sigma_s(T_w^4 - T_{\text{sat}}^4) \tag{44}$$

$$B = \frac{3}{4} + \frac{1}{4}\frac{q_r}{q_{co}}\left[2.62 + \frac{q_r}{q_{co}}\right]^{-1} \tag{45}$$

where q_{co} is film boiling heat flux without radiation, q_r is radiative heat flux, and ϵ_w is the emissivity of the surface. In Eq. (44), the radiation absorptivity of liquid was assumed to be 1. Usually, the heat transfer surface used in the film boiling experiments such as those referred to in Table 1 is well polished. The radiative emissivities of polished metal surfaces, such as copper and inconel, are less than 0.2 (Siegel and Howell, 1981). If $\epsilon_w = 0.2$, q_r/q_{co} is 1.8 percent for water at ΔT = 100°C. When the wall superheat is increased to 300°C, q_r/q_{co} is increased to 4.3 percent. Even if $\epsilon_w = 0.5$, q_r/q_{co} is less than 11 percent at the highest superheat investigated in this work. Therefore, as long as the wall superheat is not very high and the surfaces are not dirty, the radiation effect can be neglected.

To study the effect of change of system pressure on film boiling, calculations were carried out using properties of steam and water at 100 atmosphere pressure. Figure 5 plots the evolution of the interface for ΔT = 100°C. At the higher pressure the growth of the interface has been found to slow down. Comparison of the bubble size at departure with that for one atmosphere pressure (see Table 1) shows a reduction in bubble height and radius with system pressure. This is consistent with visual observations which indicate that with a decrease in density difference between heavier and lighter fluid, the bubbles acquire a shape similar to that of droplets.

A comparison of the predicted amplitude of the interface disturbance η, at the peak with the data (Son, 1996), is made in Fig. 6. In obtaining the data, the experiments, and in making the predictions, the numerical simulation were performed for pseudo film boiling during sublimation of a horizontal slab of dry ice placed beneath a pool of warm water. The evolution of the interface during early period of sublimation is nearly similar to that for film boiling because during the early period the solid surface is flat and gas-liquid density and viscosity ratios are quite similar in both cases. The data were obtained by measuring the height of the bubble that was recorded with a movie camera. The data are normalized with initial amplitude η_o of the interface, which was set equal to 0.25. The predictions are seen to be in good agreement with the data, in both the linear as well as the nonlinear growth periods. In linear Taylor instability theory, the interface disturbance is predicted to grow symmetrically in the peak and valley regions. However, from the numerical simulation of film boiling it is found that while the growth of the interface disturbance in the peak region is pronounced, the interface in the valley region is nearly stationary due to the presence of the wall. Without the effect of vapor generation due to heat transfer, the vapor volume in the vapor layer will be conserved. As a result, the upward movement of the interface in the peak region slows down and finally stops to conserve

Table 1 Height and radius of bubble at departure

Fluid	ΔT (°C)	Height (λ_{d2})	Radius (λ_{d2})	Bubble release period (s)	Reference
water	100	0.50	0.20	0.14	present work
water	200	0.54	0.23	0.12	present work
water	300	0.61	0.26	0.10	present work
benzene	120	0.52	0.22	0.10	present work
R-113	100	0.51	0.21	0.08	present work
n-pentane			0.22		Berenson
water	158		0.35	0.20 ± 0.10	Hosler and Westwater
acetone		0.65	0.25		Lienhard and Dhir
water (100 atm.)	100	0.47	0.16	0.46	present work

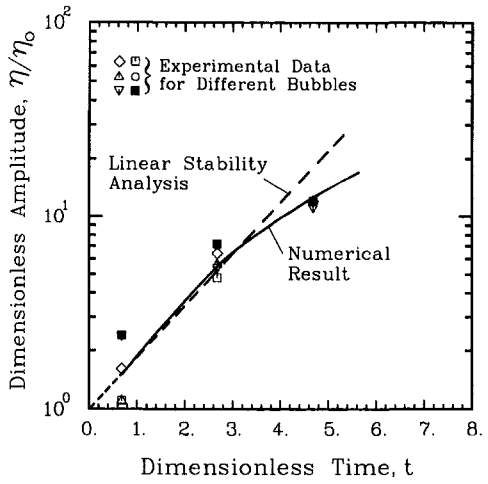

Fig. 6 Comparison of the predicted and observed disturbance amplitude with time for pseudo film boiling during sublimation of a horizontal slab of dry ice

volume. Thus, the vapor generation allows the interface to continuously evolve. Also, the vapor generation allows cyclic bubble release during film boiling by providing the vapor volume removed by the bubbles that break off. The numerical results show that the speed with which the average film thickness increases is less than 6.4 percent of the interfacial velocity in the peak region. Initially, the disturbance grows exponentially as plotted in Fig. 6. Unlike the prediction from the linear stability analysis, the slope is seen to slightly vary with time. This is

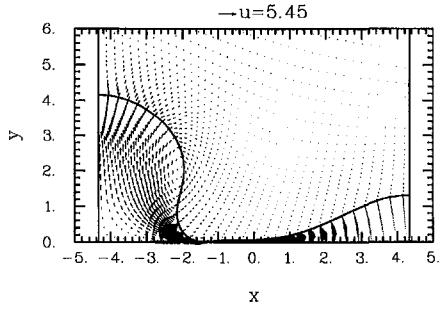

Fig. 7 Velocity vectors at t = 2.3 for ΔT = 200°C

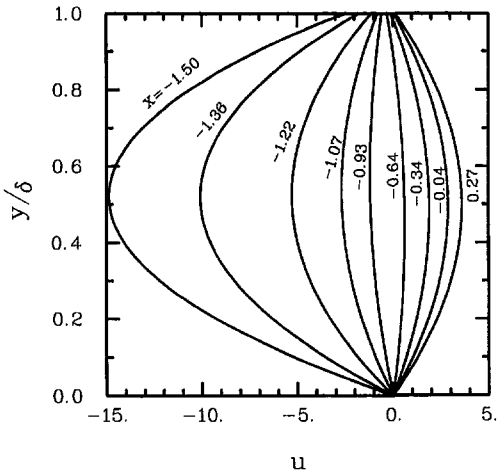

Fig. 8 Radial velocity profiles at t = 2.3 for ΔT = 200°C

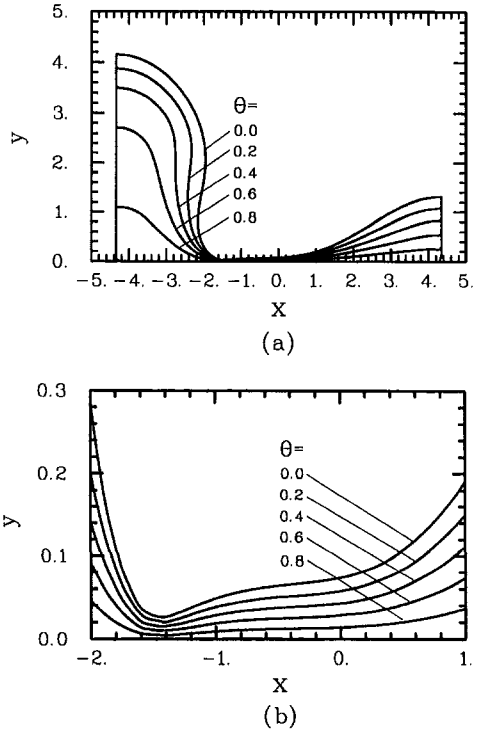

Fig. 9 Isotherms at t = 2.3 for ΔT = 200°C: (*a*) in the vapor over the computational domain, and (*b*) in expanded region near the location of minimum thickness

caused by the variation in the average film thickness during the evolution of the interface. At ωt = 2, the growth rate starts to decrease due to the nonlinear effect of liquid inertia rather than

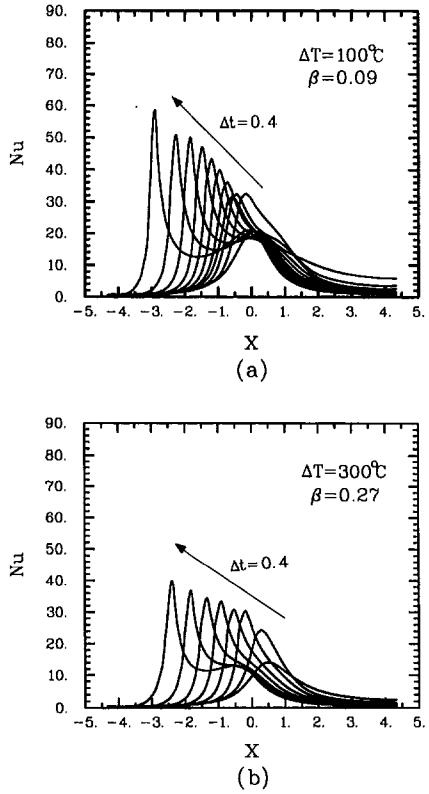

Fig. 10 Variation of Nusselt number with radial position for different wall superheats

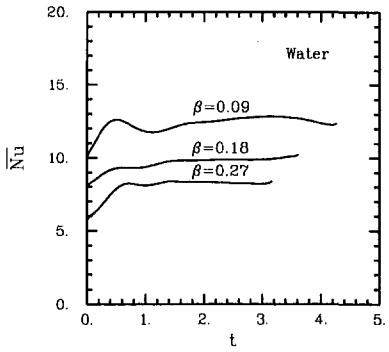

Fig. 11 Nusselt numbers based on heat transfer coefficient averaged over the cell area for different wall superheats

the wall. If the vapor generation was not included, the nonlinear effect due to the presence of the wall would appear earlier and manifest itself more strongly.

In Fig. 7 the velocity vectors at $t = 2.3$ during film boiling of water, for $\Delta T = 200°C$ and one atmosphere pressure, are plotted. It is seen that upward movement of the interface is much stronger in the primary bubble region (near $x = -R$) than in the secondary bulge (near $x = R$). The vapor injected into the primary bubble through the thin film induces a clockwise vortex motion near the interface. The liquid flow induced by the evolving interface decays with elevation.

The x-direction velocity profiles in the thin film region are plotted in Fig. 8. The maximum velocity occurs at the location ($x = -1.5$) where the film is thinnest. As x increases, the magnitude of horizontal velocity decreases due to increases in the film thickness, and is zero near $x = -0.64$ where the direction of x-directional velocity changes. This indicates that at $t = 2.3$, the vapor generated at the interface is fed into the primary and the secondary bubble, but is not symmetrical. Also, the vapor velocity profiles are found almost parabolic and symmetric with respect to $y = 0.5\delta$. The boundary condition at the vapor-liquid interface is closer to the no-slip condition rather than the slip condition. This is expected from the fact that the liquid viscosity and density are much larger than the vapor viscosity and density.

The isotherms in the vapor are shown in Fig. 9. Each isotherm almost follows the interface. The spacing between isotherms is uniform, except in the primary bubble where isotherms are a little more closely packed near the interface due to the upward vapor flow. Figure 9(b) shows the isotherm pattern in an expanded region near the location of minimum thickness. The uniform spacing between isotherms indicates that the energy transfer during film boiling is governed mainly by conduction rather than convection, as the vapor film is very thin.

Figure 10 shows dependence of the Nusselt number on radial position with time for different wall superheats. The Nusselt number is defined as a dimensionless heat flux from the heater to the vapor layer:

$$\mathrm{Nu} = \frac{l_o q_w}{k_v \Delta T} = -\left.\frac{\partial \theta}{\partial y}\right|_{y=0}.$$

Most of the heat is transferred in the thin film region and in the bubble region in the vicinity of the point of the minimum film thickness. Under the bubble core, little heat transfer takes place. The location of maximum heat transfer coefficient moves radially inwards with time, while increase in the magnitude of the maximum heat transfer coefficient is observed with time. These observations are not in agreement with Berenson's assumption of uniform heat flux in the film region and zero heat flux under the bubble. For a constant heat flux surface this also implies that the heater surface temperature at a given location will oscillate with time. The magnitude of oscillation will, however, depend on the thermal properties and thickness of the heater. It is interesting to note that the magnitude of the maximum heat transfer rate increases as the wall superheat decreases. Since the film is thinnest where the heat transfer rate is highest, the magnitude of the minimum thickness decreases with a decrease in wall superheat. At a certain superheat, the film may become so thin that it may rupture. Any perturbations near the interface will accelerate the rupture process. In this work, the film rupture conditions have not been identified.

Nusselt numbers, based on heat transfer coefficient averaged over the cell area, are plotted in Fig. 11. As the wall superheat increases, the film thickness increases and the extent of the thin film region decreases. As a result, the heat transfer coefficients are observed to decrease with increase in wall superheat. It is interesting to note that average Nusselt number also shows some dependence on time but is much less than that seen in the local heat transfer coefficient.

Table 2 shows a comparison of the Nusselt numbers based on time and area averaged heat transfer coefficients obtained from the present work and those obtained from Berenson's model (Eq. 1) and the correlation of Klimenko (Eq. 2 or Eq. 3). Upper and lower bounds of the data obtained by Hosler and Westwater, and the data of Ramilison and Lienhard (1987), are also listed in Table 2. In evaluating the Nusselt number, in all cases, vapor properties were evaluated at the average temperature in the vapor film. The Nusselt numbers predicted from Klimenko's correlation are about 32 percent higher than those given by Berenson's model, whereas Nusselt numbers obtained from the present analysis are about 34 percent lower than those obtained from Berenson's model. The Nusselt numbers obtained from the present analysis are near the lower limit of Hosler and Westwater's data for water, and are about 36 percent lower than the data of Ramilison and Lienhard (1987). However, the dependence of the Nusselt number obtained from the present work on wall superheat is consistent with Berenson's prediction: the Nusselt numbers obtained from the present work and Berenson's model, when property dependence on temperature is included, vary as $\Delta T^{-0.37}$ and $\Delta T^{-0.40}$, respectively. One possible reason for under prediction of the heat transfer rate from present analysis could be due to the existence in the experiments, as has been noted by Hosler and Westwater, of wave-

Table 2 Predicted average Nusselt numbers

Fluid	ΔT (°C)	Berenson's correlation	Klimenko's correlation	Experimental data	Present work
water	100	19.2	27.3		12.3
water	158	16.4	22.0	13.0–21.6[a]	10.6
water	200	14.7	19.0		9.6
water	220	14.0	17.8	10.9–20.4[b]	9.2
water	300	12.1	14.7		8.0
benzene	120	14.7	16.5	15.4[b]	10.1
R-113	100	14.3	15.8	15.6[b]	9.7
water (100 atm.)	100	22.2	38.9		15.2

[a] Denotes the data by Hosler and Westwater (1962).
[b] Denotes the data by Ramilison and Lienhard (1987).

lengths shorter than the "most dangerous" wavelength. Some shrinking of cell size can occur because of the wall effects. Generally, the smaller cell size leads to increased heat transfer rate because the ratio of the area occupied by the thin vapor film to the cell area increases. Also, the axisymmetric assumption of the interface possibly causes under prediction of the heat transfer rate. In reality, the vapor film thickness can vary circumferentially as well as radially. If the interface is disturbed circumferentially while keeping the average level of the interface position constant, the heat transfer rate increases. The additional variation in interface position will probably provide more efficient flow patterns for vapor removal. However, the nonaxisymmetric effect of the interface on the Nusselt number can be estimated quantitatively only when three-dimensional computations are performed, which were not carried out in this work.

Conclusions

1 A numerical simulation of the evolution of the vapor-liquid interface during saturated film boiling on a horizontal surface has been carried out.
2 Film thickness and heat transfer coefficient are found to vary spatially and temporally during the growth of the interface.
3 The Nusselt numbers for film boiling obtained in the present work are about 34 percent lower than those obtained from Berenson's model. However, the bubble size at breakoff predicted from numerical analysis compares well with that observed in the experiments.
4 The effect of wall superheat and system pressure on the shape of the vapor bulge during film boiling is consistent with visual observations reported in the literature.

Acknowledgment

This work received support from the National Science Foundation.

References

Bell, J. B., Colella, P., and Glaz, H. M., 1989, "A Second-Order Projection Method for the Incompressible Navier-Stokes Equations," *J. of Comput. Phys.*, Vol. 85, pp. 257–283.

Berenson, P. J., 1961, "Film Boiling Heat Transfer From a Horizontal Surface," ASME JOURNAL OF HEAT TRANSFER, Vol. 83, pp. 351–362.

Chorin, A. J., 1968, "Numerical Solution of the Navier-Stokes Equations," *Math. Comput.*, Vol. 22, pp. 745–762.

Dhir, V. K., Castle, J. N., and Catton, I., 1977, "Role of Taylor Instability on Sublimation of a Horizontal Slab of Dry Ice," ASME JOURNAL OF HEAT TRANSFER, Vol. 99, pp. 411–418.

Greene, G. A., and Irvine, T. F., 1986, "Film Boiling of R-11 on Liquid Metal Surfaces," *Proceedings of the Eighth International Heat Transfer Conference*, Vol. 4, C. L. Tien et al., eds., San Francisco, CA. pp. 2049–2054.

Henry, R. E., Quinn, D. J., and Spleha, E. A., 1974, "An Experimental Study of the Minimum Film Boiling Point for Liquid-Liquid Systems," *Proceedings of the Fifth International Heat Transfer Conference*, Tokyo, Japan. Vol. 4, Paper No. B 3.5.

Hosler, E. R., and Westwater, J. W., 1962, "Film Boiling on a Horizontal Plate," *ARS J.*, Vol. 32, pp. 553–560.

Jin, G., and Braza, M., 1993, "A Nonreflecting Outlet Boundary Condition for Incompressible Unsteady Navier-Stokes Calculations," *J. of Comput. Phys.*, Vol. 107, pp. 239–253.

Karki, K. C., and Patankar, S. V., 1988, "Calculation Procedure for Viscous Incompressible Flows in Complex Geometries," *Numerical Heat Transfer*, Vol. 14, pp. 295–307.

Kim, J., and Moin, P., 1985, "Application of a Fractional-Step Method to Incompressible Navier-Stokes Equations," *J. of Comput. Phys.*, Vol. 59, pp. 308–323.

Klimenko, V. V., 1981, "Film Boiling on a Horizontal Plate-New Correlation," *Int. J. Heat Mass Transfer*, Vol. 24, pp. 69–79.

Klimenko, V. V., and Shelepen, A. G., 1982, "Film Boiling on a Horizontal Plate-A Supplementary Communication," *Int. J. Heat Mass Transfer*, Vol. 25, pp. 1611–1613.

Lienhard, J. H., and Dhir, V. K., 1973, "Extended Hydrodynamic Theory of the Peak and Minimum Pool Boiling Heat Fluxes," NASA CR-2270.

Lienhard, J. H., and Dhir, V. K., 1980, "On the Prediction of the Minimum Pool Boiling Heat Flux," ASME JOURNAL OF HEAT TRANSFER, Vol. 102, pp. 457–460.

Patankar, S. V., 1980, *Numerical Heat Transfer and Fluid Flow*, Hemisphere, Washington, D.C.

Ramilison, J. M., and Lienhard, J. H., 1987, "Transition Boiling Heat Transfer and the Film Transition Regime," ASME JOURNAL OF HEAT TRANSFER, Vol. 109, pp. 746–752.

Rosenfeld, M., Kwak, D., and Vinokur, M., 1991, "A Fractional Step Solution Method for the Unsteady Incompressible Navier-Stokes Equations in Generalized Systems," *J. of Comput. Phys.*, Vol. 94, pp. 102–137.

Sernas, V., Lienhard, J. H., and Dhir, V. K., 1973, "The Taylor Wave Configuration During Boiling From a Flat Plate," *Int. J. Heat Mass Transfer*, Vol. 16, pp. 1820–1821.

Siegel, R., and Howell, J. R., 1981, *Thermal Radiation Heat Transfer*, Hemisphere, Washington, DC.

Siviour, J. B., and Ede, A. J., 1970, "Heat Transfer in Subcooled Pool Film Boiling," *Proceedings of the Fourth International Heat Transfer Conference*, Vol. 5, Paper No. B3.12, U. Grigull and E. Hahne, eds., Paris-Versailles, France.

Son, G., 1996, *Numerical Simulation of Nonlinear Taylor Instability with Application to Film Boiling, Melting and Sublimation*, Ph.D. dissertation, University of California, Los Angeles.

Streett, C. L., and Hussaini, M. Y., 1987, "Finite Length Effects on Taylor-Couette Flow," *Stability of Time-Dependent and Spatially Varying Flows*, D. L. Dwoyer, and M. Y. Hussaini, eds., Springer-Verlag, New York.

Taghavi-Tafreshi, K., Dhir, V. K., and Catton, I., 1979, "Thermal and Hydrodynamic Phenomena Associated With Melting of a Horizontal Substrate Placed Beneath a Heavier Immiscible Liquid," ASME JOURNAL OF HEAT TRANSFER, Vol. 101, pp. 318–325.

Thompson, J. F., 1982, *Numerical Grid Generation*, Elsevier Science Publishing Co., New York.

Thompson, J. F., Warsi, Z. U. A., and Mastin, C. W., 1985, *Numerical Grid Generation, Foundations and Applications*, Elsevier Science Publishing Co., North-Holland.

Zuber, N., 1959, *Hydrodynamic Aspects of Boiling Heat Transfer*, Ph.D. dissertation, University of California, Los Angeles.

Modeling the Characteristics of Thermally Governed Transient Flow Surges in Multitube Two-Phase Condensing Flow Systems With Compressibility and Thermal and Flow Distribution Asymmetry

G. L. Wedekind
Professor of Engineering.
wedekind@oakland.edu

C. J. Kobus
Graduate Assistant.
Member ASME

B. L. Bhatt
Professor and Associate Dean
of Engineering.
Member ASME

Department of Mechanical Engineering,
Oakland University,
Dodge Hall of Engineering,
Rochester, MI 48309-4401

In a tube-type condenser involving complete condensation, small changes in the inlet vapor flow rate momentarily cause very large transient surges in the outlet mass flow rate. An Equivalent Single-Tube Model (ESTM), based on the System Mean Void Fraction Model, is developed that predicts these transient flow surges for a multitube system; including the effects of compressibility as well as thermal and flow distribution asymmetry. The model is verified theoretical and experimentally. From a design perspective, the significant value of the ESTM is that it includes the primary physical mechanisms involved in such complex flow transients, yet is simple enough to be solved on typical "spreadsheet" software.

Introduction

This paper is concerned with multiple in-tube condensing flow systems involving complete condensation, the transient characteristics of which are important in a broad spectrum of energy transport and conversion processes, ranging from reheat, reboiler, and submerged evaporator systems associated with nuclear and conventional power plants, to applications in the process and chemical industries, as well as systems associated with refrigeration, air conditioning, and space power generation. Large flow excursions could substantially affect the performance and control of the processes taking place within the devices, cause damage to mechanical equipment and components, and endanger the safety of such systems. For example, large flow oscillations in the subcooled liquid at the end of the condensation process, including possibilities of flow reversals, are likely to cause process control problems and/or large impulse loads that may result in substantial damage to various system components. Specific examples have been cited in earlier publications (Wedekind and Bhatt, 1977; Wedekind et al., 1978; Rabas and Minard, 1987).

Motivation for the present research was generated in part by the successful results of earlier experimental and theoretical studies on transient flow surges in multitube condensing flow systems (Wedekind and Bhatt, 1989), influence of compressibility (Bhatt and Wedekind, 1980a), and self-sustained limit-cycle type flow instabilities (Bhatt and Wedekind, 1980b), including the effects of two-phase pressure drop (Bhatt et al., 1989); the latter three papers involving single-tube condensing flow systems. Although other researchers have investigated condensing flow transients (Liao et al., 1988; Liao and Wang, 1990), to the best knowledge of the authors, there do not appear to be any theoretical models in the literature addressing the effects of compressibility on the transient flow surges in multitube condensing flow systems.

The primary purpose of the research described in this paper was to extend the predictive capability of the Equivalent Single-Tube Model (ESTM), which was developed for the case of incompressible condensing flow in multitube systems (Wedekind and Bhatt, 1989), to include the effects of compressibility, which had been done earlier for single-tube systems (Bhatt and Wedekind, 1980a). The approach will be to first summarize the formulation of the governing equations for a generalized multitube condensing flow system. Next, an ESTM will be presented for an n-tube condensing flow system, which includes the effects of compressibility as well as thermal and flow distribution asymmetry. Finally, the predictive capability of the ESTM will be verified both theoretically and with existing experimental data.

Formulation of System Mean Void Fraction Model

Central in the development of the governing equations of the System Mean Void Fraction (SMVF) Model, which is a one-dimensional, two-fluid, distributed parameter integral model describing the primary physical mechanisms in the two-phase region[1], is the concept of a nonfluctuating system mean void fraction, $\bar{\alpha}$, defined as

$$\bar{\alpha} \equiv \frac{1}{\eta(t)} \int_{z=0}^{\eta(t)} \alpha(z, t)\, dz \qquad (1)$$

Contributed by the Heat Transfer Division for publication in the JOURNAL OF HEAT TRANSFER. Manuscript received by the Heat Transfer Division June 17, 1996; revision received April 29, 1997; Keywords: Condensation; Multiphase Flows; Transient & Unsteady Heat Transfer. Associate Technical Editor: T. J. Rabas.

[1] The System Mean Void Fraction Model is in the same category as that of von Karman's integral model for describing the viscous effects within a viscous boundary layer.

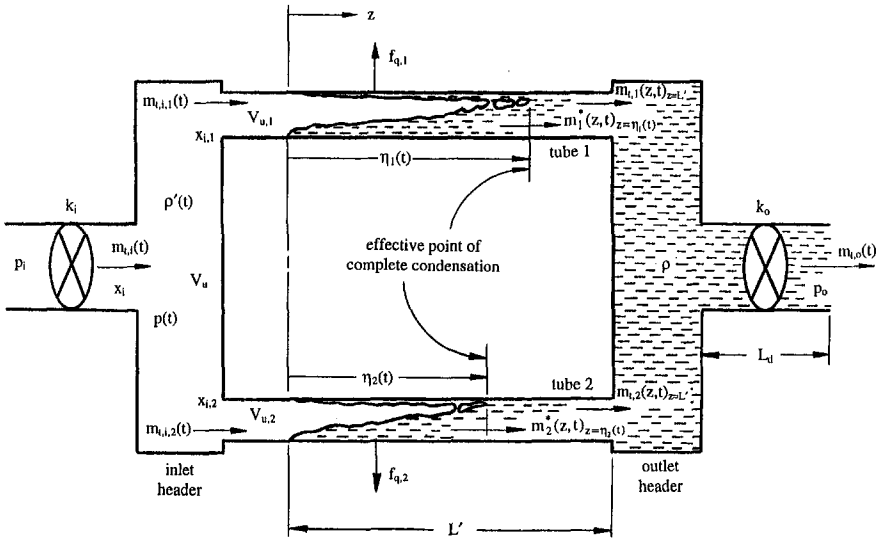

Fig. 1 Schematic of a horizontal two-tube condensing flow system

where $\eta(t)$ is the effective point of complete condensation in the individual condenser tube.

A schematic of a two-tube condensing flow system is depicted in Fig. 1. The mass flow rate, heat flux, and cross-sectional geometry of each channel is allowed to be different; however, the length of the channels is assumed to be the same. Viscous dissipation, longitudinal heat conduction, and changes in kinetic energy are neglected. The spatially averaged heat flux for the entire two-phase region[2] is assumed to be invariant with time. Since thermodynamic equi-

[2] Since the condenser tubes were water-cooled and in a concentric-tube configuration, the method utilized in this study for obtaining the spatially averaged heat flux is described by Bhatt and Wedekind (1984).

Nomenclature

$A_{t,j}$ = total cross-sectional area of tube j, m^2

$A_{t,o}$ = total cross-sectional area of system outlet, m^2

$\bar{f}_{q,j}$ = spatially averaged heat flux from tube j, W/m^2

h = enthalpy of saturated liquid, J/kg

k_o = lumped effective outlet orifice coefficient, $\Delta p/\rho v^2$

k' = flow resistance coefficient, $N \cdot s^2/m^2 \cdot kg^2$

k_o^* = linearized flow resistance at outlet, $kN \cdot s/m^2 \cdot g$

L' = length of condenser tube bundle, m

$m_{t,j}(z, t)$ = local instantaneous total mass flow rate of fluid in channel j, kg/s

$m_{t,j}^*(z, t)_{z=\eta j(t)}$ = mass flow rate leaving the two-phase region of tube j, kg/s

$m_{t,i}$ = initial steady-state total mass flow rate, kg/s

$m_{t,i}(t)$ = total time-dependent mass flow rate at system inlet, kg/s

$m_{t,i,j}(t)$ = total mass flow rate entering condenser tube j; kg/s

$m_{t,f}$ = final steady-state total mass flow rate, kg/s

$m_{t,o}(t)$ = total time-dependent mass flow rate at system outlet, kg/s

$p(t)$ = condensing flow system pressure, N/m^2

P_j = inside circumference of flow channel j, m

$\bar{v}$ = mean velocity, m/s

V_u = upstream vapor volume in inlet header assembly, m^3

$V_{u,j}$ = upstream vapor volume in condenser channel j, m^3

$V_{u,t}$ = total upstream vapor volume, m^3

x = flow quality; ratio of vapor mass flow rate to total mass flow rate

x_i = quality of flow entering at the system inlet

z = axial position coordinate from beginning of condensation process, m

$\alpha(z, t)$ = local area void fraction

$\bar{\alpha}$ = system mean void fraction

β = thermal/geometric asymmetry parameter

β^* = variation of saturated liquid enthalpy with pressure, dh/dp, $J \cdot m^2/kg \cdot kN$

β_o = dimensionless thermodynamic parameter

Δp = total system pressure drop, N/m^2

γ = flow distribution asymmetry parameter

γ^* = vapor compressibility coefficient; $d\rho'/dp$, $kg/m \cdot kN$

$\eta_j(t)$ = position of effective point of complete condensation in tube j, m

$\eta_{j,i}$ = initial position of effective point of complete condensation in channel j, m

$\eta_{j,f}$ = final position of effective point of complete condensation in channel j, m

ρ = density of saturated liquid, kg/m^3

$\tau_{c,j}$ = condensing flow system time constant for channel j, s

$\tau_{c,s}$ = effective condensing flow time constant for entire multitube system, s

$\tau_{f,j}$ = compressible flow system time constant for channel j, s

$\tau_{f,s}$ = effective compressible flow system time constant for entire multitube system, s

τ_m = time constant for inlet flow rate variation, s

$'$ = Primed symbols of quantities refer to saturated vapor. Symbols of quantities generally refer to time-averaged quantities where the averaging time is small enough so as to just eliminate the inherent fluctuations but not interfere with the deterministic transient.

librium is assumed to exist in the two-phase region, all thermodynamic properties are assumed to be saturated properties, independent of axial position, and evaluated at the mean condensing system pressure which is, however, allowed to vary with time. The region upstream of the heat transfer (two-phase) region in and upstream of the individual condenser tubes is assumed to be adiabatic and saturated. Also, the inlet flow quality into each individual tube is assumed to be the same as that into the condenser system; that is, $x_{i,1} = x_{i,2} = x_i$.

Two-Phase Region: Conservation of Mass and Energy. Applying the integral form of the conservation of mass and energy principles to the two-phase region of a representative jth-tube, utilizing the concept of a system mean void fraction, $\bar{\alpha}$, respectively yields, after considerable algebraic rearrangement,

$$A_{t,j}\{\rho(1-\bar{\alpha}_j)+\rho'\bar{\alpha}_j\}\frac{d\eta_j(t)}{dt} - A_{t,j}(\rho-\rho')\eta_j(t)\frac{d\bar{\alpha}_j}{dt} + A_{t,j}\bar{\alpha}_j\eta_j(t)\frac{d\rho'}{dt} = m_{t,j}(z,t)_{z=0} - m_j^*(z,t)_{z=\eta_j(t)} \quad (2)$$

$$A_{t,j}\{\rho h(1-\bar{\alpha}_j)+\rho'h'\bar{\alpha}_j\}\frac{d\eta_j(t)}{dt} + A_{t,j}(\rho'h'-\rho h)\eta_j(t)\frac{d\bar{\alpha}_j}{dt} + A_{t,j}\{\beta_{o,j}(h'-h)+\bar{\alpha}_j h'\}\eta_j(t)\frac{d\rho'}{dt} = -\bar{f}_{q,j}P_j\eta_j(t) + [h(1-x_i)+h'x_i]m_{t,j}(z,t)_{z=0} - m_j^*(z,t)_{z=\eta_j(t)}h \quad (3)$$

where

$$\beta_{o,j} = \frac{\rho(1-\bar{\alpha}_j)}{(h'-h)}\left(\frac{\beta^*}{\gamma^*}\right). \quad (4)$$

For a two-tube system, $j = 1, 2$. The quantity β_o is a thermodynamic parameter[3] composed of fluid properties and the system mean void fraction, $\bar{\alpha}$, and accounts for property variations with pressure changes.

The combined conservation of mass and energy equations for the two-phase region may be obtained by multiplying Eq. (2) by the enthalpy of saturated liquid, h, and subtracting from Eq. (3). Thus,

$$A_{t,j}(h'-h)\rho'\left\{\bar{\alpha}_j\frac{d\eta_j(t)}{dt}+\eta_j(t)\frac{d\bar{\alpha}_j}{dt}\right\} + A_{t,j}(h'-h)(\bar{\alpha}_j+\beta_{o,j})\eta_j(t)\frac{d\rho'}{dt} = -\bar{f}_{q,j}P_j\eta_j(t) + x_i m_{t,j}(z,t)_{z=0}(h'-h). \quad (5)$$

Upstream Vapor Volume: Conservation of Mass. The conservation of mass equations, first applied to the vapor volume in the representative jth-tube, as depicted in Fig. 1, then to the inlet header assembly[4] and combined in such a way as to eliminate the unknown mass flow rate entering the condenser tube, $m_{t,i,j}(t)$, yields

$$(\gamma_j V_u + V_{u,j})\frac{d\rho'}{dt} = \gamma_j m_{t,i}(t) - m_{t,j}(z,t)_{z=0} \quad (6)$$

where the flow distribution parameter, γ_j, is defined as

$$\gamma_j \equiv \frac{m_{t,i,j}(t)}{m_{t,i,c}(t)}; \quad m_{t,i,c}(t) = \sum_{j=1}^{n} m_{t,i,j}(t). \quad (7)$$

Physically, the flow distribution parameter is defined as the fraction of the total mass flow rate entering a representative jth tube. In general, $0 \le \gamma_j \le 1$ and the sum of the flow distribution parameters for all of the tubes is unity. Flow distribution symmetry for an n tube system is assured when $\gamma_j = 1/n$.

Subcooled Liquid Region: Conservation of Mass. The conservation of mass principle, applied to the subcooled liquid region of the representative jth-tube, yields

$$-\rho A_{t,j}\frac{d\eta_j(t)}{dt} = m_j^*(z,t)_{z=\eta_j(t)} - m_{t,j}(z,t)_{z=L'}. \quad (8)$$

The total mass flow rate leaving the system, $m_{t,o}(t)$, is the sum of the flow rates leaving the individual tubes, $m_{t,j}(z,t)_{z=L'}$, again as a consequence of the conservation of mass principle. Thus,

$$m_{t,o}(t) = \sum_{j=1}^{n} m_{t,j}(z,t)_{z=L'}. \quad (9)$$

Subcooled Liquid Region: Momentum Principle. The pressure drop may be obtained by applying the integral form of the momentum principle to the subcooled liquid region of each tube as well as the outlet header assembly. Thus, when the effects of inertia are negligible,

$$p(t) - p_o = \frac{k_o}{\rho A_{t,o}^2} m_{t,o}^2(t). \quad (10)$$

Here, k_o is a total effective outlet orifice coefficient consisting of all of the flow resistances, including those due to friction in the outlet header and tubing as well as the fittings, valves, and an equivalent resistance due to the individual resistances in the parallel condenser channels[5]. This total outlet resistance can be viewed to be lumped into an effective flow resistance located at the outlet of the downstream header assembly, where the mass flow rate, $m_{t,o}(t)$, leaves the system. In terms of the compressibility coefficient, γ^*, and pressure, the vapor compressibility, $d\rho'/dt$, incorporating Eq. (10), is

$$\frac{d\rho'}{dt} = \gamma^*\frac{dp(t)}{dt} = \frac{2k_o\gamma^*}{\rho A_{t,o}^2} m_{t,o}(t)\frac{dm_{t,o}(t)}{dt}. \quad (11)$$

In order to obtain a differential equation governing the motion of the effective point of complete condensation in each condenser tube, $\eta_j(t)$, the unknown mass flow rate entering the two-phase region of each individual tube, $m_{t,j}(z,t)_{z=0}$, is eliminated by substituting Eq. (6) into (5). Thus,

$$\tau_{c,j}\frac{d\eta_j(t)}{dt} + \eta_j(t) = x_i\frac{(h'-h)}{\bar{f}_{q,j}P_j}\gamma_j m_{t,i}(t) - \frac{(h'-h)}{\bar{f}_{q,j}P_j}\{(V_{u,j}+\gamma_j V_u)x_i + (A_{t,j}\bar{\alpha}_j)\eta_j(t)\}\frac{d\rho'}{dt} \quad (12)$$

where

$$\tau_{c,j} = \frac{\rho'\bar{\alpha}_j A_{t,j}}{\bar{f}_{q,j}P_j}(h'-h) \quad (13)$$

[3] The manner in which β_o is defined here varies slightly from the version presented by Bhatt and Wedekind (1980a). Variations in liquid density, ρ, were not considered in the prior work. However, when such variations are considered, the numerical difference in β_o between the prior and present research is less than 10 percent.

[4] Referring to Fig. 1, the inlet header assembly includes the common inlet header, where the flow is divided among the individual condenser tubes, and includes any piping upstream to the point where the total inlet mass flow rate, $m_{t,i}(t)$, enters the system.

[5] For a detailed discussion on the determination of an equivalent flow resistance for a multitube system, refer to the Appendix.

and where it was assumed[6] that

$$\frac{1}{\bar{\alpha}_j}\frac{d\bar{\alpha}_j}{dt} \approx -\frac{1}{\rho'}\left(\frac{\beta_{o,j}}{\bar{\alpha}_j}\right)\frac{d\rho'}{dt}. \quad (14)$$

To obtain the governing equation for the mass flow rate leaving the representative jth tube, $m_{t,j}(z, t)_{z=L'}$, Eqs. (2), (6), and (8) are added together so as to eliminate the unknown mass flow rates entering and leaving the two-phase region, $m_{t,j}(z, t)_{z=0}$ and $m_j^*(z, t)_{z=\eta_j(t)}$, respectively. Thus,

$$m_{t,j}(z, t)_{z=L'} = \gamma_j m_{t,i}(t) - [(V_{u,j} + \gamma_j V_u) + (A_{t,j}\bar{\alpha}_j)\eta_j(t)]\frac{d\rho'}{dt} + A_{t,j}(\rho - \rho')\left\{\bar{\alpha}_j\frac{d\eta_j(t)}{dt} + \eta_j(t)\frac{d\bar{\alpha}_j}{dt}\right\}. \quad (15)$$

In an effort to obtain a differential equation involving the outlet mass, $m_{t,o}(t)$, Eqs. (6) and (5) are combined so as to eliminate the unknown mass flow rate entering the two-phase region, $m_{t,j}(z, t)_{z=0}$. Substituting the result into Eqs. (11) and then (15) yields

$$\left(\frac{\rho}{\rho'}\right)\left\{\left(\frac{\rho'}{\rho}\right)\{[(\rho/\rho') - 1]x_i + 1\}(V_{u,j} + \gamma_j V_u) + (A_{t,j}\bar{\alpha}_j)\eta_j(t) + A_{t,j}\beta_{o,j}\eta_j(t)\right\} \times \frac{2k_o\gamma^*}{\rho A_{t,o}^2}m_{t,o}(t)\frac{dm_{t,o}(t)}{dt} + m_{t,j}(z, t)_{z=L'} = \{[(\rho/\rho') - 1]x_i + 1\}\gamma_j m_{t,i}(t) - [(\rho/\rho') - 1]\frac{\bar{f}_{q,j}P_j\eta_j(t)}{(h' - h)}. \quad (16)$$

Equation (16) not only involves the total outlet mass flow rate, $m_{t,o}(t)$, but also the unknown flow rate leaving the representative jth tube, $m_{t,j}(z, t)_{z=L'}$, as well as the motion of the effective point of complete condensation, $\eta_j(t)$.

Combined Condensing Flow System Equations. Equations (9), (11), (12), and (16) form a complete set of differential equations governing the deterministic flow transient. However, many of the coefficients in each of the last three equations are time dependent. Time-varying quantities, where they appear as coefficients, will be approximated by their mean value over the transient to linearize the equations. Thus, Eq. (11) becomes

$$\frac{d\rho'}{dt}\gamma^* k_o^*\frac{dm_{t,o}(t)}{dt}; \quad k_o^* = \frac{2k_o}{\rho A_{t,o}^2}\bar{m}_{t,o}. \quad (17)$$

The linearized differential equation governing the motion of the effective point of complete condensation for a representative jth tube, Eq. (12), becomes

$$\tau_{c,j}\frac{d\eta_j(t)}{dt} + \eta_j(t) = x_i\frac{(h' - h)}{\bar{f}_{q,j}P_j}\gamma_j m_{t,i}(t) - \frac{(h' - h)}{\bar{f}_{q,j}P_j}\{(\forall_{u,j} + \gamma_j\forall_u)x_i + (A_{t,j}\bar{\alpha})\bar{\eta}_j\}\frac{d\rho'}{dt}. \quad (18)$$

[6] Justification for this simplification is discussed in detail by Bhatt (1978) for a single tube. Normally, the system mean void fraction is assumed to be time invariant (Wedekind and Bhatt, 1989) when compressibility effects are negligible. However, when compressibility effects are significant, the time variation in $\bar{\alpha}$, as depicted in Eq. (14), appears to exist, although the system mean void fraction may be considered time-invariant everywhere else.

Eq. (18) represents a System Mean Void Fraction (SMVF) Model similar to that developed by Wedekind and Bhatt (1989), except for the final term, which accounts for vapor compressibility. In the case of complete condensation, the system mean void fraction, $\bar{\alpha}$, may be determined[7] from the following expression:

$$\bar{\alpha} = \frac{1}{(1 - a)} + \frac{a}{x_i(1 - a)^2}\text{Ln}\left|\frac{a}{a + (1 - a)x_i}\right|; \quad a = (\rho'/\rho)^{2/3}. \quad (19)$$

The linearized differential equation governing the outlet mass flow rate, Eq. (16), becomes

$$\tau_{f,j}\frac{dm_{t,o}(t)}{dt} + m_{t,j}(z, t)_{z=L'} = \{[(\rho/\rho') - 1]x_i + 1\}\gamma_j m_{t,i}(t) - [(\rho/\rho') - 1]\frac{\bar{f}_{q,j}P_j\eta_j(t)}{(h' - h)} \quad (20)$$

where

$$\tau_{f,j} = (\rho/\rho')\{(\rho'/\rho)\{[(\rho/\rho') - 1]x_i + 1\}(\forall_{u,j} + \gamma_j\forall_u) + (A_{t,j}\bar{\alpha})\bar{\eta}_j + A_{t,j}\beta_o\bar{\eta}_j\}\gamma^* k_o^*. \quad (21)$$

In their present form, Eqs. (9), (17), (18), and (20) form a complete set of linear differential equations which must be solved simultaneously to predict the response of the outlet mass flow rate, $m_{t,o}(t)$, to any inlet vapor flow rate variation, $m_{t,i}(t)$.

Solution of Governing Equations

Two-Way Coupling. Equation (20), which governs the outlet mass flow rate, $m_{t,o}(t)$, is dependent upon the motion of the effective point of complete condensation, $\eta_j(t)$, which in turn is dependent upon the outlet mass flow rate through the mechanism of vapor compressibility, Eq. (17); therefore, the system is two-way coupled. To combine the general set of governing equations, Eq. (20) was solved for the effective point of complete condensation and substituted, along with Eq. (17), into Eq. (18). This yields n-coupled, second-order differential equations governing the response of the outlet mass flow rate, $m_{t,o}(t)$, to an inlet flow rate variation, $m_{t,i}(t)$. Adding these equations yields

$$\left[\sum_{j=1}^{n}\tau_{c,j}\tau_{f,j}\right]\frac{d^2m_{t,o}(t)}{dt^2} + \left[\sum_{j=1}^{n}(\tau_{f,j} - \tau_{v,j})\right]\frac{dm_{t,o}(t)}{dt} + m_{t,o}(t) + \sum_{j=1}^{n}\left\{\tau_{c,j}\frac{dm_{t,j}(z, t)_{z=L'}}{dt}\right\} = m_{t,i}(t) + \left[\sum_{j=1}^{n}\gamma_j\tau_{c,j}\right]\frac{dm_{t,i}(t)}{dt} \quad (22)$$

where the time constant, $\tau_{v,j}$, is the direct result of the two-way coupling and is defined as

$$\tau_{v,j} = [(\rho/\rho') - 1][(\gamma_j V_u + V_{u,j})x_i + (A_{t,j}\bar{\alpha})\bar{\eta}_j]\gamma^* k_o^*. \quad (23)$$

Equation (22) cannot be solved in its present form because there are too many $(n - 1)$ unknowns, except for the situation

[7] The particular void fraction model used in the present research is that proposed by Zivi (1964). It was chosen for reasons of simplicity and proven accuracy for these types of flow problems. However, any void fraction relationship that is valid over the full range of flow quality would yield similar results. Since the system mean void fraction is dependent on the inlet flow quality, x_i, which is the same for each tube, the system mean void fraction will be the same in each tube; $\bar{\alpha}_j = \bar{\alpha}$.

where thermal/geometrical symmetry[8] exists, which would result in the condensing flow system time constant of each individual condenser tube, $\tau_{c,j}$, being the same. Obviously, however, such a solution would be incapable of providing any insight into the effects of thermal asymmetry.

One-Way Coupling. The motion of the effective point of complete condensation in each individual condenser tube, $\eta_j(t)$, may be uncoupled from the outlet mass flow rate, $m_{t,o}(t)$, if the last term in Eq. (18) is negligible. However, the outlet mass flow rate is still dependent on the motion of the effective point of complete condensation, thus the one-way coupling. Making the above assumption, Eq. (18) reduces to

$$\tau_{c,j}\frac{d\eta_j(t)}{dt} + \eta_j(t) = x_i\frac{(h' - h)}{\bar{f}_{q,j}P_j}\gamma_j m_{t,i}(t). \quad (24)$$

Equation (20) may be added for $j = 1$ to n, producing

$$\tau_{f,s}\frac{dm_{t,o}(t)}{dt} + m_{t,o}(t) = \{[(\rho/\rho') - 1]x_i + 1\}m_{t,i}(t) - [(\rho/\rho') - 1]\sum_{j=1}^{n}\frac{\bar{f}_{q,j}P_j\eta_j(t)}{(h' - h)} \quad (25)$$

where the total compressible flow system time constant, $\tau_{f,s}$, is expressed as

$$\tau_{f,s} = \sum_{j=1}^{n}\tau_{f,j} = \left(\frac{\rho}{\rho'}\right)\left\{\left(\frac{\rho'}{\rho}\right)\{[(\rho/\rho') - 1]x_i + 1\}V_{u,t} + (\bar{\alpha} + \beta_o)\sum_{j=1}^{n}A_{t,j}\bar{\eta}_j\right\}\gamma^* k_o^*; \quad V_{u,t} = V_u + \sum_{j=1}^{n}V_{u,j}. \quad (26)$$

The inlet flow rate, $m_{t,i}(t)$, is needed to solve the above differential equations. Consider the special flow situation where the time varying total inlet flow rate, $m_{t,i}(t)$, is an exponential function[9]; thus,

$$m_{t,i}(t) = m_{t,f} - (m_{t,f} - m_{t,i})e^{-t/\tau_m}. \quad (27)$$

Substituting Eq. (27) into (24), a closed form solution may be obtained for the motion of the effective point of complete condensation in the representative jth tube—subject to the initial condition obtained from the steady-state form of Eqs. (24). Thus,

$$\frac{\bar{f}_{q,j}P_j\eta_j(t)}{(h' - h)} = x_i\gamma_j m_{t,f} - x_i\frac{\gamma_j(m_{t,f} - m_{t,i})}{[1 - (\tau_{c,j}/\tau_m)]} \times \{e^{-t/\tau_m} - (\tau_{c,j}/\tau_m)e^{-t/\tau_{c,j}}\}. \quad (28)$$

Substituting Eq. (28) into (25) yields a first-order, ordinary differential equation governing the response of the outlet mass flow rate, $m_{t,o}(t)$,

$$\tau_{f,s}\frac{dm_{t,o}(t)}{dt} + m_{t,o}(t) = m_{t,f} - (m_{t,f} - m_{t,i})e^{-t/\tau_m} + x_i(m_{t,f} - m_{t,i})[(\rho/\rho') - 1] \times \sum_{j=1}^{n}\left\{\frac{\gamma_j\beta_j(\tau_{c,1}/\tau_m)(e^{-t/\tau_m} - e^{-t/\beta_j\tau_{c,1}})}{[\beta_j(\tau_{c,1}/\tau_m) - 1]}\right\} \quad (29)$$

where the thermal/geometrical asymmetry parameter, β, is expressed as

$$\beta_j \equiv \frac{\tau_{c,j}}{\tau_{c,1}} = \left(\frac{\bar{f}_{q,1}}{\bar{f}_{q,j}}\right)\left[\left(\frac{P_1}{P_j}\right)\left(\frac{A_{t,j}}{A_{t,1}}\right)\right]. \quad (30)$$

Here, β is the product of the heat flux ratio between any tube in the condensing flow system, and a reference tube (designated as tube 1), and a geometrical ratio. In general, $\beta \geq 0$. Also, $\beta_j = 1$ signifies thermal\geometrical symmetry throughout the condensing flow system.

Although the model allows for geometrical variations in the individual tubes, they will not be considered here since they would rarely be encountered. Therefore, for most practical applications the quantity β_j will be considered a thermal asymmetry parameter where

$$\beta_j = (\bar{f}_{q,1}/\bar{f}_{q,j}). \quad (31)$$

In this phase of the model development, both the thermal and flow distribution asymmetry parameters, γ and β, respectively, are considered to be system parameters in the classical sense; that is, they are assumed to be known and independent of one another. However, it is recognized that the flow distribution in each tube will be governed by the momentum principle and thus dependent upon the flow resistances in each condenser tube as well as the rest of the condensing flow system, including the two-phase pressure drop, which in turn is affected by the heat flux (Wedekind et al., 1989). Thus, the flow distribution parameter, γ, may be coupled to the thermal asymmetry parameter, β, albeit weakly. For this research, in the present scope of the model, the thermal and flow distribution parameters need to be determined independently. The purpose of this approach is to ascertain the primary physical mechanisms involved and the magnitude of the influence of thermal and flow distribution asymmetry on the deterministic flow transients under investigation—not to model the thermal and flow distribution parameters themselves; thus the reference to them as parameters.

It should be pointed out that in computing the linearized outlet flow resistance, k_o^*, for an exponential flow rate variation, the value of the average flow rate in Eq. (17) is approximated quite well by the final flow rate, $m_{t,f}$, especially when appreciable flow resistance is present. Thus,

$$k_o^* \cong \frac{2k_o}{\rho A_{t,o}^2}m_{t,f} \quad (32)$$

and also,

$$\bar{\eta}_j = (\eta_{j,i} + \eta_{j,f})/2. \quad (33)$$

The solution of Eq. (29) consists of a complimentary and n-particular solutions. Since the differential equation is linear, the method of superposition may be used and a separate particular solution may be found for each individual forcing function. The solution may therefore be obtained by adding the complimentary and particular solutions, subject to the initial outlet mass flow rate, and can be expressed as

$$\frac{m_{t,o}(t) - m_{t,i}}{m_{t,f} - m_{t,i}} = 1 - e^{-t/\tau_{f,s}} + \sum_{j=1}^{n}\left\{\frac{\gamma_j[\{[(\rho/\rho') - 1]x_i + 1\}\beta_j(\tau_{c,1}/\tau_m) - 1]}{[\beta_j(\tau_{c,1}/\tau_m) - 1][(\tau_{f,s}/\tau_m) - 1]} \times (e^{-t/\tau_m} - e^{-t/\tau_{f,s}})\right.$$

[8] As can be seen in Eq. (13), for a two-tube system, $(A_{t,1}/P_1) = (A_{t,2}/P_2)$ represents geometric symmetry and $f_{q,1} = f_{q,2}$ represents thermal symmetry.

[9] An exponential inlet flow rate variation was chosen here because of its commonality and simplicity. It would be a reasonable approximation for many practical situations, having the capability of ranging from very fast (step transients) to slow transients. However, any form of the inlet flow rate variation may be used.

$$+ x_i \frac{\gamma_j\beta_j(\tau_{c,1}/\tau_m)[(\rho/\rho') - 1]}{[\beta_j(\tau_{c,1}/\tau_m) - 1][1 - (\tau_{f,s}/\beta_j\tau_{c,1})]} \times (e^{-t/\beta_j\tau_{c,1}} - e^{-t/\tau_{f,s}})\Bigg\}. \quad (34)$$

The above expression describes the transient flow surge in the outlet mass flow rate, $m_{t,o}(t)$, for a multitube condensing flow system consisting of any number of individual condenser tubes, with or without compressibility, and including the effects of both thermal and flow distribution asymmetry.

Asymptotic Solutions. As a means of validating the above multitube compressible model, asymptotic solutions will be investigated and compared to previously published models. One such asymptotic solution to Eq. (34) is when compressibility effects are negligible, $\tau_{f,s} \cong 0$. Thus,

$$\frac{m_{t,o}(t) - m_{t,i}}{m_{t,f} - m_{t,i}} = 1 + e^{-t/\tau_m} + x_i \sum_{j=1}^{n} \left\{ \frac{\gamma_j\beta_j(\tau_{c,1}/\tau_m)[(\rho/\rho') - 1]}{[\beta_j(\tau_{c,1}/\tau_m) - 1]} \times (e^{-t/\tau_m} - e^{-t/\beta_j\tau_{c,1}}) \right\}. \quad (35)$$

Equation (35) is a more general expression of the two-tube incompressible model developed by Wedekind and Bhatt (1989).

Another asymptotic solution of Eq. (34) occurs for the case of a single tube, $n = 1$. In this case, the summation in Eq. (34) becomes just its argument, with $\gamma_j = \gamma_1 = 1$ and $\beta_j = \beta_1 = 1$. With these simplifications, Eq. (34) reduces to the compressible model for a single tube (Bhatt and Wedekind, 1980a).

One other asymptotic solution occurs when the inlet flow quality, x_i, approaches zero, corresponding to pure liquid flowing into the condenser, where the condenser tubes are simply a network of liquid pipes. In this case, the compressible flow system time constant, $\tau_{f,s}$, expressed by Eq. (26), will be zero, and Eq. (34) reduces to Eq. (27), describing the total inlet flow rate variation, $m_{t,i}(t)$. Therefore, the outlet flow rate exactly matches the inlet flow rate; $m_{t,o}(t) = m_{t,i}(t)$.

Influence of Thermal and Flow Distribution Asymmetry: Two-Tube System. The purpose of this section is to ascertain the magnitude of the influence of the thermal and flow distribution asymmetry parameters on the transient flow surge characteristics. A parametric study of the response of the outlet mass flow rate, $m_{t,o}(t)$, is depicted in Fig. 2 for a wide range of the thermal and flow distribution parameters, β and γ, respectively.

Referring to Fig. 2, it is seen that thermal and flow distribution asymmetry can have a significant influence on the characteristics of the transient flow surge. The symmetric case is when $\beta_2 = 1.0$ and $\gamma_1 = 0.5$. It is interesting to point out that in the case of thermal symmetry, $\beta_2 = 1$, flow distribution has no influence on the characteristics of the flow surge. The peak of the flow surge is approximately 30 percent higher than that of the symmetric case when $\beta_2 = 2.0$ and $\gamma_1 = 0.25$, corresponding to tube 2 having half the heat flux of tube 1, but 75 percent of the total flow rate. Also, the peak of the flow surge is approximately 30 percent lower than that of the symmetric case when $\beta_2 = 0.5$ and $\gamma_1 = 0.25$, corresponding to tube 2 having twice the heat flux of tube 1 and 75 percent of the total flow rate.

Although the above n tube model governing the outlet mass flow rate, $m_{t,o}(t)$, is useful, it becomes computationally complex because of the summations, especially when large numbers of tubes are present. This complexity is the impetus for a simpler model.

Equivalent Single-Tube Model

Wedekind and Bhatt (1989) demonstrated a method of approximating an n-tube condensing flow system with an Equivalent Single Tube Model (ESTM). The concept of the ESTM is to obtain an equivalent single-tube condensing flow system time constant, $\tau_{c,s}$, which is simply a weighted average of the time constants in the individual condenser tubes. Thus,

$$\tau_{c,s} \cong \sum_{j=1}^{n} \gamma_j\tau_{c,j} = \tau_{c,1} \sum_{j=1}^{n} \gamma_j\beta_j. \quad (36)$$

It is interesting to note that this approximation is already present in the coefficient of the last term in Eq. (22). As will be shown later, the above simplification is most accurate when the tubes are nearest to thermal symmetry, $\beta_j \cong 1$.

Utilizing the above approximation, a solution may be obtained in the same manner as was done earlier for the multitube system: first solve the differential equation governing the motion of the effective point of complete condensation, $\eta(t)$, Eq. (24), for an equivalent single-tube and substitute the result into the equivalent single-tube differential equation governing the outlet mass flow rate, $m_{t,o}(t)$. Substituting this solution into Eq. (20), which is now also a single equation governing the response of the outlet mass flow rate, and solving, yields

$$\frac{m_{t,o}(t) - m_{t,i}}{m_{t,f} - m_{t,i}} = 1 - e^{-t/\tau_{f,s}} + \frac{\{[(\rho/\rho') - 1]x_i + 1\}(\tau_{c,s}/\tau_m) - 1}{[(\tau_{c,s}/\tau_m) - 1][(\tau_{f,s}/\tau_m) - 1]}(e^{-t/\tau_m} - e^{-t/\tau_{f,s}}) + x_i \frac{(\tau_{c,s}/\tau_m)[(\rho/\rho') - 1]}{[(\tau_{c,s}/\tau_m) - 1][1 - (\tau_{f,s}/\tau_{c,s})]} \times (e^{-t/\tau_{c,s}} - e^{-t/\tau_{f,s}}) \quad (37)$$

where

$$\tau_{c,s} = \tau_{c,1} \sum_{j=1}^{n} \gamma_j\beta_j \quad \text{and}$$

$$\tau_{f,s} = \left(\frac{\rho}{\rho'}\right)\left\{\left(\frac{\rho'}{\rho}\right)\{[(\rho/\rho') - 1]x_i + 1\}V_{u,t} + (\bar{\alpha} + \beta_o)\sum_{j=1}^{n} A_{t,j}\bar{\eta}_j\right\}\gamma^* k_o^*. \quad (38)$$

Note that, although the effective condensing flow system time constant, $\tau_{c,s}$, is a weighted function, where the weighting parameters are the thermal and flow distribution asymmetry of the multitube system, β and γ, respectively, the total compressible flow system time constant, $\tau_{f,s}$, is not weighted at all but rather is cumulative.

It can clearly be seen that the above ESTM is much simpler than the n-tube model given earlier. However, the ESTM retains the primary physical mechanisms responsible for the transient characteristics of the flow surge, including the effects of compressibility[10], as well as thermal and flow distribution asymmetry.

Theoretical Verification of the ESTM. The validity of the ESTM is established by comparing its predictive capability with that of the n-tube model, in the case of two tubes for a wide range of thermal and flow distribution asymmetry. As can be clearly seen in Fig. 2, for the case of thermal symmetry, $\beta_2 =$

[10] The attenuating characteristics, due to compressibility, for a multitube system, are similar to those of a single tube system, which were explored in considerable detail by Bhatt and Wedekind (1980a).

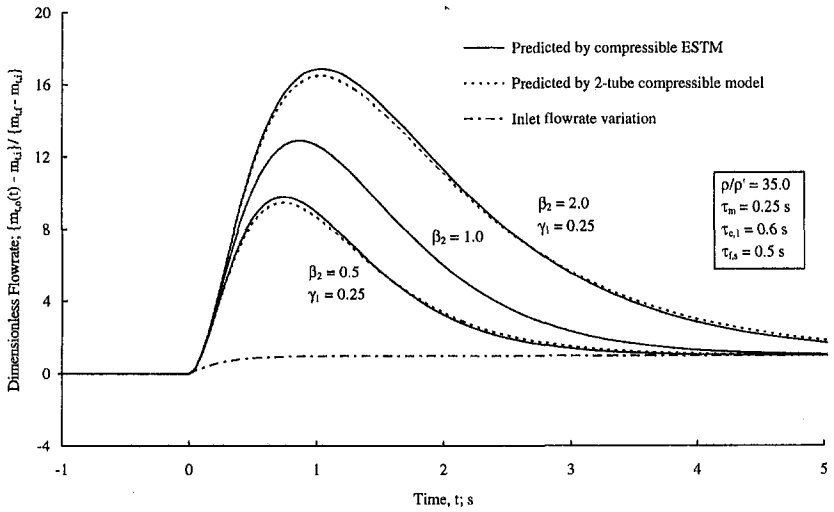

Fig. 2 Response of outlet liquid flow rate relative to inlet vapor flow rate for a two-tube condensing flow system; comparison of Equivalent Single-Tube Model (ESTM) with Two-Tube Model

1, the predictions of the ESTM and the two-tube model are identical. In the case of thermal asymmetry, the ESTM is seen to agree very closely with the two-tube solution for the range of thermal and flow distribution parameters presented—a range that would probably cover most practical applications. It seems reasonable that as the number of individual condenser tubes increases, the predictive capability of the ESTM would probably improve in accuracy. Therefore, it may very well be that the above two-tube system with significant thermal asymmetry represents a worst-case situation.

Comparison of ESTM with Existing Experimental Data: Two-Tube System

The theoretical predictions of the transient flow surges in the outlet mass flow rate for a two-tube condensing flow system are compared in Figs. 3–5 with existing experimental data[11] for three different flow situations. The theoretical predictions are that of the current compressible ESTM. Also, as a point of reference for the effects of compressibility, the incompressible ESTM (Wedekind and Bhatt, 1989) is superimposed for all three cases. A comparison of the theoretical prediction of the ESTM with existing experimental measurements in complete thermal and flow distribution symmetry ($\beta_2 = 1$, $\gamma_l = 0.5$) is shown in Fig. 3. A similar comparison is depicted in Fig. 4, but with only thermal asymmetry, while flow distribution symmetry was maintained ($\beta_2 = 0.72$, $\gamma_l = 0.5$). Similarly, Fig. 5 shows a comparison for a slight thermal and moderate flow distribution asymmetry ($\beta_2 = 1.03$, $\gamma_l = 0.38$).

The agreement between the experimental data and the theoretical predictions of the ESTM is very encouraging, especially when consideration is given to the complexity of the physical mechanisms involved and the relative simplicity of the model, complete with its ability to predict not only the influence of thermal and flow distribution asymmetry, but the effects of compressibility as well. It should be noted that in every case the incompressible ESTM predicted a peak in the flow rate surge that was higher than what was measured

[11] The experimentally measured transient flow surges presented here are the same as those presented by Wedekind and Bhatt (1989). Therefore, details of the experimental apparatus and measurements will not be repeated.

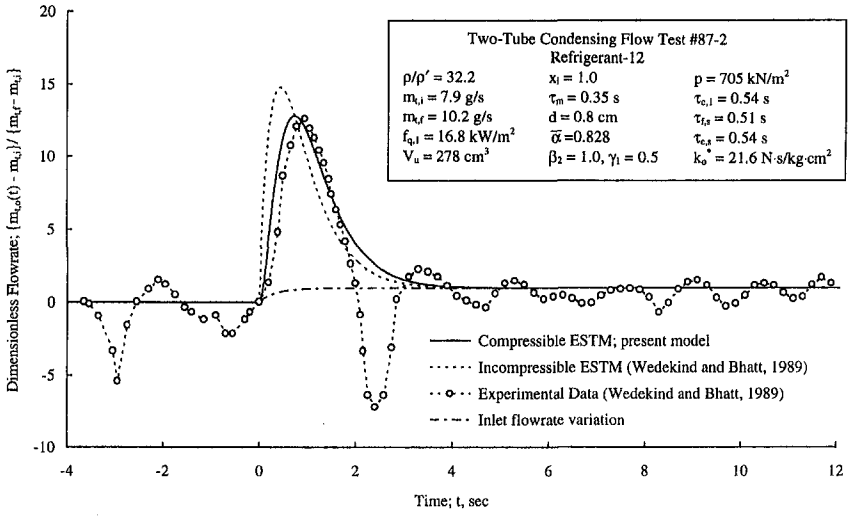

Fig. 3 Response of outlet liquid flow rate to an increase in the inlet vapor flow rate for a two-tube condenser; thermal and flow distribution symmetry

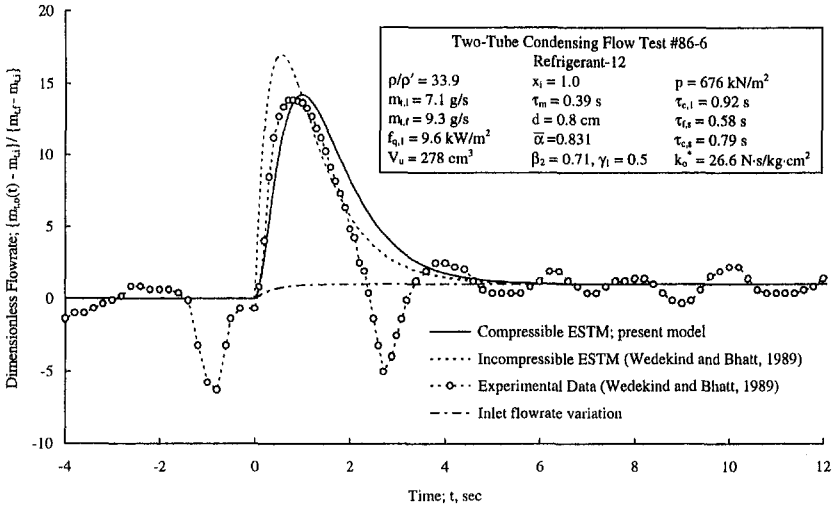

Fig. 4 Response of outlet liquid flow rate to an increase in the inlet vapor flow rate for a two-tube condenser; thermal asymmetry and flow distribution symmetry

experimentally. However, the present compressible ESTM correctly predicts the experimentally measured attenuating effects.

As was mentioned by Wedekind and Bhatt (1989), it is significant to note that the outlet flow rate data in Figs. 3 and 4 tends to exhibit larger than normal oscillations, especially immediately following the flow surge. This was characteristic of being near the boundary for the onset of a self-sustained oscillatory instability (Bhatt and Wedekind, 1980b) investigated earlier for a single-tube condenser. Such experimental evidence suggests a strong possibility of being able to further develop the ESTM to the point where it will not only predict the flow instability, but also the corresponding stability boundary for multitube condensing flow systems. This is the subject of ongoing research.

Summary and Conclusions

An Equivalent Single Tube Model (ESTM) has been developed for predicting thermally governed transient flow surges in multitube condensing flow systems undergoing complete condensation. This multitube model, based on the System Mean Void Fraction Model, has the capability of predicting the influence of thermal and flow distribution asymmetry, as well as the effects of compressibility.

The predictive capability of the ESTM was verified both analytically, by comparison with a two-tube model, and by comparison with existing experimental data, for a two-tube system. Excellent agreement was seen to exist, especially when consideration is given to the complexity of the physical mechanisms involved and the relative simplicity of the model. From a design perspective, the major value of the ESTM is that it has the capability of predicting, and graphically demonstrating, the relative influence of various fluid, system, and design parameters on the characteristics of transient flow surges. Therefore, since the model is simple enough to be put on "spreadsheet" software, the design engineer can obtain valuable design insight into the physical mechanisms involved, and can also evaluate the range of possible flow surges that might be anticipated, and then make changes in system design parameters which would reduce or minimize the surges as appropriate.

There is some very sophisticated but, because of its complexity, not so "user friendly" computer software available to design engineers who are working with two-phase evaporating

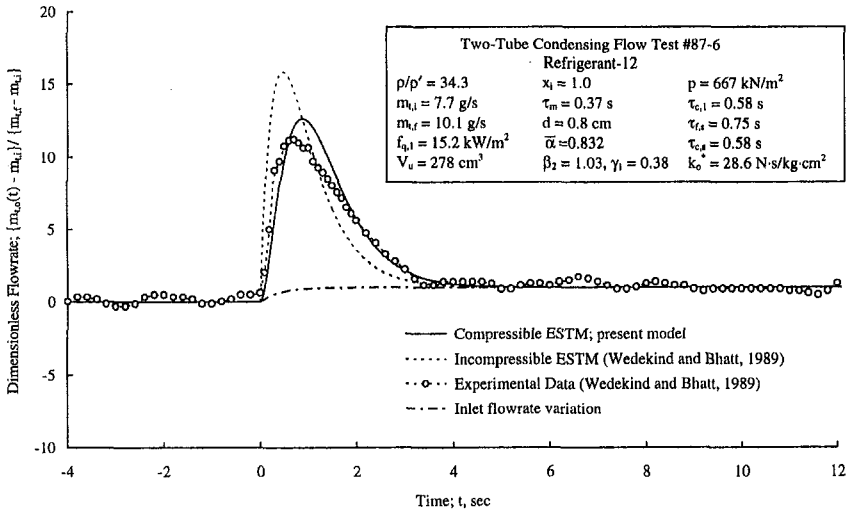

Fig. 5 Response of outlet liquid flow rate to an increase in the inlet vapor flow rate for a two-tube condenser; thermal symmetry and flow distribution asymmetry

and condensing flow equipment. It is recognized that the utilization of this type of software may be both necessary and appropriate in some instances. However, the Equivalent Single-Tube Model (ESTM) presented in this paper offers the design engineer another tool which, because of its simplicity, should have a place in the overall design process of two-phase, in-tube condensing flow equipment.

Acknowledgments

The authors would like to acknowledge the National Science Foundation, Thermal Transport and Thermal Processing Program, Division of Chemical and Transport Systems, for its part in the support of this research under Grant No. CTS-9420853.

References

Bhatt, B. L., 1978, "An Experimental and Theoretical Study of Various Transient and Oscillatory Flow Phenomena in Two-Phase Condensing Flow Systems," Ph.D. thesis, School of Engineering, Oakland University, Rochester, MI.

Bhatt, B. L., and Wedekind, G. L., 1980a, "Transient and Frequency Response Characteristics of Two-Phase Condensing Flows: With and Without Compressibility," ASME JOURNAL OF HEAT TRANSFER, Vol. 102, No. 3, pp. 595–600.

Bhatt, B. L., and Wedekind, G. L., 1980b, "A Self-Sustained Oscillatory Flow Phenomenon in Two-Phase Condensing Flow Systems," ASME JOURNAL OF HEAT TRANSFER, Vol. 102, No. 4, pp. 695–700.

Bhatt, B. L., and Wedekind, G. L., 1984, "An Experimental and Theoretical Study into the Determination of Condensing Length," *Basic Aspects of Two-Phase Flow and Heat Transfer, 22nd National Heat Transfer Conference,* V. K. Dhir, and V. E. Schrock, eds., Niagara Falls, N.Y., pp. 179–183.

Bhatt, B. L., Wedekind, G. L., and Jung, K., 1989, "Effects of Two-Phase Pressure Drop on the Self-Sustained Oscillatory Instability in Condensing Flow," ASME JOURNAL OF HEAT TRANSFER, Vol. 111, pp. 538–545.

Liao, N. S., and Wang, C. C., 1990, "Transient Response Characteristics of Two-Phase Condensing Flows," *International Journal of Heat and Mass Transfer,* Vol. 16, No. 1, pp. 139–151.

Liao, N. S., Wang, C. C., and Tien, C. L., 1988, "Analysis of Transient Flow Surge Phenomena in a Single-Tube Condenser," *International Communications in Heat and Mass Transfer,* Vol. 15, No. 3, pp. 257–268.

Rabas, T. J., and Minard, P. G., 1987, "Two Types of Flow Instabilities Occurring Inside Horizontal Tubes with Complete Condensation," *Heat Transfer Engineering,* Vol. 8, No. 1, pp. 40–49.

Wedekind, G. L., and Bhatt, B. L., 1977, "An Experimental and Theoretical Investigation into Thermally Governed Transient Flow Surges in Two-Phase Condensing Flow," *Preceedings of the Two-Phase Flow and Heat Transfer Symposium-Workshop,* Ft. Lauderdale, FL., Vol. 11, pp. 691–711. Also in, ASME JOURNAL OF HEAT TRANSFER, Vol. 99, No. 4, pp. 561–567.

Wedekind, G. L., and Bhatt, B. L., 1989, "Modeling the Thermally Governed Transient Flow Surges Multitube Condensing Flow Systems with Thermal and Flow Distribution Asymmetry," ASME JOURNAL OF HEAT TRANSFER, Vol. 111, No. 3, pp. 786–791.

Wedekind, G. L., Bhatt, B. L., and Beck, B. T., 1978, "A System Mean Void Fraction Model for Predicting Various Transient Phenomena Associated with Two-Phase Evaporating and Condensing Flows," *International Journal of Multiphase Flow,* Vol. 4, pp. 97–114.

Wedekind, G. L., Bhatt, B. L., and Roslund, G. L., 1989, "An Experimental and Theoretical Study of Transient Pressure Drop in Two-Phase Condensing Flow," ASME JOURNAL OF HEAT TRANSFER, Vol. 111, pp. 546–551.

Zivi, S. M., 1964, "Estimation of Steady-State Steam Void Fraction by Means of the Principle of Minimum Entropy Production," ASME JOURNAL OF HEAT TRANSFER, Vol. 86, p. 247.

APPENDIX

Obtaining the Effective Outlet Orifice Coefficient, k_o: Multitube System. To obtain the effective outlet orifice coefficient for the entire condensing flow system, including the equivalent flow resistance in the multiple channels as well as any resistance in and downstream of the outlet header, the total effective pressure drop must be obtained, where the total pressure drop is the sum of an equivalent pressure drop in the condenser tubes themselves, Δp_c, and the pressure drop downstream of the condenser tubes, Δp_d. Thus,

$$\Delta p = \Delta p_c + \Delta p_d. \tag{A1}$$

The nonlinear pressure drop downstream of the condenser tubes may be obtained either theoretically by classical[12] means or through calibration measurements. Thus,

$$\Delta p_d = k'_{o,d} m^2_{t,o} \tag{A2}$$

where $k'_{o,d}$ is a type of flow resistance coefficient downstream of the condenser tubes, which includes the equivalent length due to friction in straight tubing as well as fittings and valves downstream of the outlet header assembly.

It can be seen from Fig. 1 that, because there is a common condensing pressure, the pressure drop over the entire multitube system is a constant for a given flow rate. Therefore, the pressure drop across any individual tube must be the same. The linearized pressure drop[13] across a representative jth-tube may be expressed as

$$\Delta p_j = (k'_j \bar{m}_j) m_j \tag{A3}$$

where $\bar{m}_j$ is a mean value of the mass flow rates in tube j. Also, k'_j includes the equivalent length of the respective tube, consisting of flow resistance due to friction in the subcooled liquid region and the two-phase pressure drop[14]. Solving Eqs. (A3) for the individual mass flow rates, m_j, substituting this into Eq. (11), and utilizing the flow distribution parameter, γ, for the linearized mass flow rate,

$$m_{t,o} = \frac{\Delta p_n}{\bar{m}_{t,o}} \sum_{j=1}^{n} \frac{1}{\gamma_j k'_j} = \frac{\Delta p_n}{k'_n \bar{m}_{t,o}}. \tag{A4}$$

Rearranging Eq. (A4) to solve for the pressure drop, and adding this to the linearized pressure drop equivalent of Eq. (A2), Eq. (A1) becomes

$$\Delta p = [(k'_n + k'_{o,d})\bar{m}_{t,o}] m_{t,o}. \tag{A5}$$

The mean outlet mass flow rate, $\bar{m}_{t,o}$, can be approximated with the final flow rate, $m_{t,f}$, which is consistent with how the effective outlet resistance is linearized in Eq. (19). Referring to Eq. (A4), the effective n-tube resistance coefficient, k'_n is expressed as

$$\frac{1}{k'_n} = \sum_{j=1}^{n} \frac{1}{\gamma_j k'_j}. \tag{A6}$$

In the case of thermal and flow distribution symmetry, the resistance coefficient of any tube in the multitube system will be

[12] Friction factor, equivalent length, Moody diagram, etc.

[13] It is interesting to point out that the form of Eq. (A3) is the same as Ohm's Law for linear circuit analysis, where the pressure drop is analogous to the voltage drop, the mass flow rate is analogous to electrical current, and the term in parenthesis is seen to be a linearized resistance analogous to a linear electrical resistor. The electric circuit analog may be helpful to the reader in the succeeding analysis as they are quite similar.

[14] Transient two-phase condensing pressure drop, including friction, flow acceleration and inertia have been specifically studied for a single-tube condenser by Wedekind et al. (1989). The System Mean Void Fraction Model was used successfully in predicting the experimentally measured total pressure drop. It was from this work that a subsequent study was carried out involving the "Effects of Two-Phase Pressure Drop on the Self-Sustained Oscillatory Instability in Condensing Flow," Bhatt et al. (1989). As a result of the above study, it was determined that, in so far as modeling the average pressure within the two-phase region during a flow transient is concerned, the effects of the transient two-phase pressure drop could be adequately predicted by incorporating the two-phase pressure drop into an effective outlet flow resistance for the system. Thus, only the steady-state pressure drop is required. The same approach, which appears to be sufficient in predicting the effects of compressibility on transient flow surges, is being followed in the current paper.

the same. Thus for a two-tube system, $k'_2 = k'_1/4$; for a three-tube system, $k'_3 = k'_1/9$; for a four-tube system, $k'_4 = k'_1/16$. It is apparent that a type of recursion relationship appears. For a multitube system consisting of any number of individual condenser tubes, the total effective pressure drop may be approximated for thermal and flow distribution asymmetry by the following relationship:

$$\Delta p = [(\bar{k}'_n/n^2 + k'_{o,d})m_{s,f}]m_{t,o} = [k'_o m_{s,f}]m_{t,o} \quad \text{(A7)}$$

where

$$k'_o = \bar{k}'_n/n^2 + k'_{o,d} \quad \text{(A8)}$$

and where $\bar{k}'_n$ is the algebraic mean of the flow resistance coefficients in the individual condenser tubes. The dimensionless orifice coefficient, k_o, may then be calculated by the following expression:

$$k_o = \frac{\Delta p}{\rho \bar{v}^2} = \rho A_{t,o}^2 k'_o. \quad \text{(A9)}$$

Modeling of Transient Turbulent Natural Convection in a Melt Layer With Solidification

T. H. Fan

F. B. Cheung
fxc4@psu.edu

Department of Mechanical Engineering,
The Pennsylvania State University,
University Park, PA 16802

The phenomenon of turbulent natural convection in a horizontal heat-generating melt layer with solidification taking place at the cooled upper and lower boundaries is investigated theoretically. The objective is to determine the transient behavior of the crust at the upper and lower surfaces and the effect of crust formation on the turbulent natural convection process in the melt layer. Various surface temperatures, latent heats, and the heat source strengths are considered along with the effects of the Stefan number and Rayleigh number. Special attention is given to the interaction between the melt pool heat transfer and the crust dynamics. Numerical results are presented for the transient crust thickness, transient temperature distribution, eddy heat transport, and the heat transfer characteristics at the solid-liquid interface during the freezing process. The present study provides basic information needed to predict the transient behavior of a melt pool in a reactor lower head following a severe core-meltdown accident.

Introduction

The process of natural convection in a volumetrically heated fluid has been investigated quite extensively in the past three decades or so, mainly because of its relevance to the cooling of core melt under severe accident conditions in a nuclear reactor (Theofanuous et al., 1995). Early studies by Roberts (1967), Tritton and Zarraga (1967), Thirlby (1970), and Schwiderski and Schwab (1971) focused primarily on the post stability regime and the laminar natural convection flow patterns. Turbulent natural convection in a horizontal heat-generating layer under steady-state conditions was first investigated by Fielder and Wille (1970) and later by Kulacki and Emara (1977), Kulacki and Goldstein (1972), Kulacki and Nagle (1975), Mayinger et al. (1976), Cheung (1977, 1980a), Steinberner and Reineke (1978), Cheung et al. (1992), Arpaci (1995), Nourgalier and Dinh (1996), and Dinh and Nourgalier (1997). Steady natural convection in a semicircular or hemispherical heat-generating melt pool was studied by Jahn and Reineke (1974), Min and Kulacki (1978), Gabor et al. (1980), Asfia and Dhir (1994), Tan et al. (1994), and Kymalainen et al. (1994). For the case of transient natural convection in a volumetrically heated layer, works were performed by Kulacki and Emara (1977), Cheung (1978, 1980b), and Keyhani and Kulacki (1983).

In all the above studies, solidification of the core melt at the cooled boundaries was not considered, and the volume occupied by the heat-generating fluid was assumed to remain unchanged. The effect of crust formation on the core melt heat transfer was completely ignored. Under severe accident conditions, a crust of core material is bound to form on the inner wall of the reactor lower head. This is because the inner wall temperature is well below the freezing temperature of the core melt. The formation of a crust layer at the cooled boundaries would affect the system behavior in three different ways. First, it would render the process of heat transfer in the system highly transient. Second, the growth of the crust represents a moving boundary at the solid-liquid interface. This would change the hydrodynamic boundary conditions for the melt pool which, in turn, would alter the natural convection heat transfer in the core melt. Third, as the crust grows thicker at the cooled boundaries, the depth of the melt pool would become smaller. This could considerably reduce the magnitude of the internal Rayleigh number which is proportional to the fifth power of the pool depth. Hence, the convective heat flux would decrease. Thus far, the crust dynamics and the crust effects on the core melt heat transfer have not been seriously explored by previous investigators.

In this work, the process of transient turbulent natural convection in a horizontal, heat-generating melt layer that is cooled from the top and bottom below its freezing temperature, is studied theoretically, taking full account of the crust formation at the lower and upper boundaries. The eddy heat transport model of Cheung (1977) is employed to describe the local turbulent heat transfer characteristics of the flow in the thermally unstable upper portion of the melt layer. An interface immobilization technique is used to transform the governing equations and the boundary conditions to immobilize the moving fronts of the lower and upper solid-liquid interfaces in the transformed space. In the meantime, a moving grid concept is applied to trace the unknown location between the thermally stable and unstable regions of the melt layer. The transient upper and lower surface heat fluxes are computed by solving the governing system using a fully implicit finite-difference scheme, whereas the instantaneous thicknesses of the lower and upper crusts are determined by integrating the interface energy balance equations using the fourth-order Runge-Kutta method. Special attention is given to the mutual interaction between the crust dynamics and the transient melt layer heat transfer.

Mathematical Formulation

The system under consideration is shown in Fig. 1. A horizontal layer with uniform volumetric heat sources is cooled from the upper and lower surfaces. Initially, no crust is present at the boundaries, and the liquid layer is at a steady state with the surface temperatures maintained at the freezing point of the liquid. At time zero, the temperatures at the upper and lower surfaces are suddenly lowered to a constant value below the freezing point of the liquid. The upper and lower crusts begin to grow at the cooled boundaries. While the rates of growth of the crusts depend on the heat transfer in the liquid layer, the latter, in turn, can be affected by the moving solid-liquid bound-

Contributed by the Heat Transfer Division for publication in the JOURNAL OF HEAT TRANSFER. Manuscript received by the Heat Transfer Division August 16, 1996; revision received March 8, 1997; Keywords: Natural Convection, Phase-Change Phenomena, Transient & Unsteady Heat Transfer. Associate Technical Editor: T. L. Bergman.

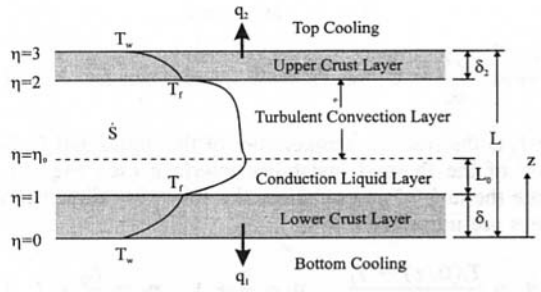

Fig. 1 Schematic of the heat-generating horizontal melt layer with solidification at the cooled upper and lower boundaries

aries associated with the crust growth process. To formulate the problem, the flow and heat transfer are treated as one-dimensional, and the strength of the heat sources is assumed to be constant.

Liquid Region in the Melt Layer. As shown in Fig. 1, the liquid occupies the region between $z = \delta_1(t)$ and $z = L - \delta_2(t)$, where δ_1 and δ_2 are the instantaneous thicknesses of the lower and the upper crusts, respectively. The temperature stratification is stable in the lower portion of the liquid layer ($\delta_1 < z < \delta_1 + L_0$), whereas in the upper liquid portion ($\delta_1 + L_0 < z < L - \delta_2$), the temperature stratification is unstable. To model the local heat transfer, it is necessary to separate the liquid region into the upper and the lower layers.

Upper Liquid Layer. Using the Boussinesq approximation, the ensemble averaged energy equation can be written as

$$\frac{\partial \bar{T}_l}{\partial t} = \frac{\partial}{\partial z}\left(\alpha_l \frac{\partial \bar{T}_l}{\partial z}\right) - \frac{\partial \overline{wT'}}{\partial z} + \frac{\dot{S}}{\rho_l C_{P_l}} \tag{1}$$

where $\overline{wT'}$ is the turbulent eddy heat flux. This quantity can be expressed in terms of the eddy diffusivity for heat α_t by

$$\overline{wT'} = -\alpha_t \frac{dT_l}{dz}. \tag{2}$$

Equation (1) becomes

$$\frac{\partial T_l}{\partial t} = \frac{\partial}{\partial z}\left(\alpha_{\text{eff}} \frac{\partial T_l}{\partial z}\right) + \frac{\dot{S}}{\rho_l C_{P_l}} \tag{3}$$

where

$$\alpha_{\text{eff}} = \alpha_l + \alpha_t \tag{4}$$

is the effective thermal diffusivity which includes the molecular and turbulent effects. The eddy heat transport model developed by Cheung (1977) will be employed to determine the local value of α_t. This will be done in the next section.

Lower Liquid Layer. Conduction is the dominated heat transfer mechanism in the lower part of the liquid layer. The energy equation is similar to Eq. (3), but there is no advection effect in this region. That is

$$\frac{\partial T_l}{\partial t} = \frac{\partial}{\partial z}\left(\alpha_l \frac{\partial T_l}{\partial z}\right) + \frac{\dot{S}}{\rho_l C_{P_l}}. \tag{5}$$

The initial and boundary conditions for the entire liquid region are

$$\begin{aligned} t = 0: \quad & T_l = T_l(0, z) \\ t > 0: \quad & T_l = T_f \quad \text{at} \quad z = \delta_1(t) \\ & T_l = T_f \quad \text{at} \quad z = L - \delta_2(t) \end{aligned} \tag{6}$$

where δ_1, δ_2 are given by the Stefan condition described below,

Nomenclature

C_{P_l}, C_{P_s} = specific heats of the liquid layer and crust layer
g = gravitational acceleration
h = heat transfer coefficient
k_{eff} = effective thermal conductivity of the melt layer
k_l, k_s = thermal conductivities of the liquid layer and crust layer
L = total layer thickness
L_0 = thickness of the thermally stable portion of the liquid layer
Nu = Nusselt number at the upper solid-liquid interface
q_1, q_2 = downward and upward heat fluxes at the boundaries
Ra* = local Rayleigh number
Ra_I = internal Rayleigh number
$\dot{S}$ = volumetric energy source
Ste_I = internal Stefan number
t = time
T_w = wall temperature at the upper and lower surfaces
T_f = freezing or melting temperature
$T_{\max}$ = maximum temperature in the melt layer
T_l, T_s = temperatures in the liquid layer and crust layer
$\overline{wT'_l}$ = eddy heat transport
$\overline{W\theta'_l}$ = dimensionless eddy heat transport
z = vertical coordinate

Greek Symbols

α_l, α_s = thermal diffusivities of the liquid layer and crust layer
α_{eff} = effective thermal diffusivity of the melt layer
α_t = turbulent eddy diffusivity for heat
β = coefficient of volumetric thermal expansion
ΔT^* = characteristic local temperature
$\Delta\tau$ = dimensionless time step
ΔH = latent heat of melting or solidification
δ_1, δ_2 = lower and upper crust thicknesses
$\tilde{\delta}_1$, $\tilde{\delta}_2$ = dimensionless lower and upper crust thicknesses
η_l = dimensionless spatial coordinate in the liquid layer
η_{s1}, η_{s2} = dimensionless spatial coordinates in the lower and upper crust layers
η_0 = location of the thermal instability interface
θ_w = dimensionless temperature at the upper and lower surfaces
$\theta_{\max}$ = maximum dimensionless temperature in the melt layer
θ_l, θ_s = dimensionless temperatures in the liquid layer and the crust layer
θ_{li} = initial dimensionless temperature
ν = kinematic viscosity
ρ_l, ρ_s = densities of the liquid layer and crust layer
τ = dimensionless time

Subscripts

I = internal heating
l = liquid phase
t = turbulence quantity
max = maximum value
s = solid phase

Superscripts

$'$ = fluctuating quantity
$\tilde{}$ = dimensionless quantity
$\bar{}$ = ensemble average
$(\ )'$ = correction value from grid point migration
$*$ = local variable

and the initial temperature distribution $T_l(0, z)$ is determined by the steady state solution for a volumetrically heated fluid layer without solidification.

Solid Regions at the Top and Bottom. The regions occupied by the lower and upper crusts are given by $0 \le z < \delta_1$ and $L - \delta_2 < z \le L$. The governing equations for the upper and lower crusts are the same by assuming constant properties for each, which can be written as

$$\frac{\partial T_s}{\partial t} = \alpha_s \frac{\partial^2 T_s}{\partial z^2} + \frac{\dot{S}}{\rho_s C_{P_s}} \tag{7}$$

$$t = 0: \quad \delta_1(0) = \delta_2(0) = 0$$

$$t > 0: \quad T_s = T_w < T_f \quad \text{at} \quad z = 0$$

$$T_s = T_f \quad \text{at} \quad z = \delta_1(t)$$

$$T_s = T_f \quad \text{at} \quad z = L - \delta_2(t)$$

$$T_s = T_w < T_f \quad \text{at} \quad z = L. \tag{8}$$

Stefan Condition at the Solid-Liquid Interfaces. The lower and upper crust thicknesses $\delta_1(t)$ and $\delta_2(t)$ are determined by considering the Stefan condition (interface energy balance) at the solidification fronts, taking into account the density variation during phase change. From mass and energy conservations at the solid-liquid interfaces, a control volume analysis gives

$$\rho_s \Delta H \frac{d\delta_1(t)}{dt} = k_s \left.\frac{\partial T_s}{\partial z}\right|_{z=\delta_1(t)^-} - k_l \left.\frac{\partial T_l}{\partial z}\right|_{z=\delta_1(t)^+}$$

$$\text{at} \quad z = \delta_1(t) \tag{9}$$

and

$$\rho_s \Delta H \frac{d\delta_2(t)}{dt} = k_l \left.\frac{\partial T_l}{\partial z}\right|_{z=[L-\delta_2(t)]^-} - k_s \left.\frac{\partial T_s}{\partial z}\right|_{z=[L-\delta_2(t)]^+}$$

$$\text{at} \quad z = L - \delta_2(t) \tag{10}$$

where ΔH is the latent heat, and the crust density, ρ_s, is allowed to be different than the liquid density, ρ_l. The initial conditions are

$$t = 0: \quad \delta_1(0) = \delta_2(0) = 0. \tag{11}$$

From Eqs. (9) to (11), the moving solidification fronts can be traced by integrating the instantaneous crust thicknesses with time.

Numerical Model

Steady State Analysis (Initial Condition). The initial condition corresponds to the steady-state solution for turbulent natural convection in a fluid layer with uniform volumetric energy sources. With cooling from the top and bottom, turbulent convection appears only in the upper portion of the liquid layer. The lower portion is dominated by conduction. Cheung (1977) developed an eddy heat transport model for high Rayleigh number thermal convection in a horizontal heated fluid layer with an adiabatic lower boundary and an isothermal upper wall. His model will be employed to the upper liquid layer in this study.

Governing System. Initially, no crust is present and the liquid layer is at a steady state. The temperature $T_l(0, z)$ is governed by

$$\frac{d}{dz}\left(\alpha_{\text{eff}} \frac{dT_l}{dz}\right) + \frac{\dot{S}}{\rho_l C_{P_l}} = 0 \quad \text{for} \quad 0 \le z \le L \tag{12}$$

$$T_l = T_f \quad \text{at} \quad z = 0$$

$$T_l = T_f \quad \text{at} \quad z = L$$

$$\frac{\partial T_l}{\partial z} = 0 \quad \text{or} \quad T_l = T_{\max} \quad \text{at} \quad z = L_0 \tag{13}$$

where T_f is the freezing temperature of the liquid and L_0 is the location of the thermal instability interface (see Fig. 1). To facilitate the task of computation, the following dimensionless variables are introduced:

$$\theta_{li} = \frac{T_l(0, z) - T_f}{\dot{S}L^2/2k_l}, \quad \eta_l = \frac{z}{L} + 1, \quad \eta_0 = \frac{L_0}{L} + 1. \tag{14}$$

The dimensionless initial liquid temperature θ_{li} is a function of η_l. The quantity η_0 is the unknown location that separates the lower (stable) and upper (unstable) liquid layers. In dimensionless form, Eq. (12) becomes

$$\frac{d}{d\eta_l}\left(\frac{\alpha_{\text{eff}}}{\alpha_l}\frac{d\theta_{li}}{d\eta_l}\right) + 2 = 0 \quad \text{for} \quad 1 \le \eta_l \le 2. \tag{15}$$

The boundary conditions are

$$\theta_{li} = 0 \quad \text{at} \quad \eta_l = 1$$

$$\theta_{li} = 0 \quad \text{at} \quad \eta_l = 2$$

$$\frac{\partial \theta_{li}}{\partial \eta_l} = 0 \quad \text{or} \quad \theta_{li} = \theta_{\max} \quad \text{at} \quad \eta_l = \eta_0 \tag{16}$$

where η_0 has a value bounded by $1 < \eta_0 < 2$.

Eddy Heat Transport Model. Cheung (1977) considered the eddy heat flux a function of the local Rayleigh number. The local Rayleigh number is defined in terms of a characteristic local length scale and a characteristic local buoyancy difference. Accordingly, the effective thermal diffusivity is given by

$$\frac{\alpha_{\text{eff}}}{\alpha_l} = 1 + a\,\text{Ra}^{*b} \tag{17}$$

where a and b are universal constants and Ra* is the local Rayleigh number given by

$$\text{Ra}^* = \frac{g\beta\Delta T^*(L - L_0)^3}{\alpha_l \nu}[\tilde{\eta}_l(1 - \tilde{\eta}_l)]^{(3/b)}$$

$$\text{for} \quad 0 \le \tilde{\eta}_l \le 1 \tag{18}$$

where $\tilde{\eta}_l = (z - L_0)/(L - L_0)$ is the dimensionless spatial coordinate in the thermally unstable region of the liquid layer for the case without solidification. It follows that α_t/α_l would vary according to the third power of the distance from the solid boundaries, i.e.,

$$\frac{\alpha_{\text{eff}}}{\alpha_l} = 1 + a\left(\frac{g\beta\Delta T^*(L - L_0)^3}{\alpha_l \nu}\right)^b [\tilde{\eta}_l(1 - \tilde{\eta}_l)]^3$$

$$\text{for} \quad 0 \le \tilde{\eta}_l \le 1. \tag{19}$$

In the above expressions, ΔT^* is the characteristic local temperature defined by

$$\Delta T^* = T_l - T_f. \tag{20}$$

The universal constants are given by $a = 0.051$ and $b = 0.87$. The eddy heat transport model is applied to the thermally unstable region where $L_0 \le z \le L$ or $\eta_0 \le \eta_l \le 2$. This is done by shifting the third order distance by algebra manipulation to maintain the same amplitude as the original one, i.e.,

$$[\tilde{\eta}_l(1-\tilde{\eta}_l)]^3 \underset{\text{shift}}{\rightarrow} \left[\left(\frac{\eta_l-\eta_0}{G}\right)\left(\frac{2-\eta_l}{G}\right)\right]^3$$

$$0 \le \tilde{\eta}_l \le 1 \quad \eta_0 \le \eta_l \le 2 \quad (21)$$

where η_0 will be located using a shooting method as described in the next section. The coefficient G is based upon the same maximum amplitudes as

$$G = 2 - \eta_0. \quad (22)$$

Modifying the third order distance function in the local Rayleigh number, Eq. (18) becomes

$$\mathrm{Ra}^* = \frac{g\beta\Delta T^*(L-L_0)^3}{\alpha_l\nu}(2-\eta_0)^{-(6/b)}[(\eta_l-\eta_0)(2-\eta_l)]^{3/b}$$

$$\text{for} \quad \eta_0 \le \eta_l \le 2. \quad (23)$$

Combining Eqs. (14), (20), and (23), the local Rayleigh number can be expressed by

$$\mathrm{Ra}^* = \mathrm{Ra}_l\theta_l(2-\eta_0)^{(3b-6)/b}[(\eta_l-\eta_0)(2-\eta_l)]^{3/b} \quad (24)$$

where Ra_l is the internal Rayleigh number given by

$$\mathrm{Ra}_l = \frac{g\beta\dot{S}L^5}{2k_l\alpha_l\nu}. \quad (25)$$

In the lower liquid layer $1 \le \eta_l \le \eta_0$ where there is no turbulent convection, the ratio $\alpha_{\text{eff}}/\alpha_l$ in Eq. (15) is equal to unity.

Numerical Analysis. Integrating Eq. (15) once using the boundary condition at η_0, the following equation is obtained for the upper liquid layer:

$$\frac{d\theta_{li}}{d\eta_l} = \frac{2(\eta_0-\eta_l)}{1+0.051\,\mathrm{Ra}_l^{0.87}\theta_{li}^{0.87}(2-\eta_0)^{-3.39}[(\eta_l-\eta_0)(2-\eta_l)]^3}$$

$$\text{for} \quad \eta_0 \le \eta_l \le 2$$

$$\theta_{li} = 0 \quad \text{at} \quad \eta_l = 2. \quad (26)$$

Similarly, the governing equation for the lower liquid layer is:

$$\frac{d\theta_{li}}{d\eta_l} = 2(\eta_0-\eta_l) \quad \text{for} \quad 1 \le \eta_l \le \eta_0$$

$$\theta_{li} = 0 \quad \text{at} \quad \eta_l = 1. \quad (27)$$

To determine the unknown location η_0 at which the liquid temperature is maximum, the coupled problem represented by Eqs. (26) and (27) are solved numerically by using the fourth-order Runge-Kutta integration and bisection shooting methods.

Steady State Temperature Profiles. The calculated steady state dimensionless temperature distributions at different internal Rayleigh numbers are shown in Fig. 2. The solid lines represent the result from numerical prediction; the data points are from the work of Kulacki and Goldstein (1972). Overall, the calculated results compare quite well with the experimental data, especially near the top and bottom surfaces. The differences between the predicted and the measured values in the core region could be due to the fact that the flow is not highly turbulent for a Rayleigh number on the order of 10^6. Note that as the internal Rayleigh number is increased, the temperature distributions become relatively flat in the upper liquid layer except in a region near the upper surface. Considerably smaller differences between the predicted and the measured values are obtained for the case of $\mathrm{Ra}_l = 8.76 \times 10^6$, relative to the case of $\mathrm{Ra}_l = 2.02 \times 10^6$. Due to the intensive turbulent mixing in the core, the thermal boundary layer is restricted to a very thin region at the upper surface where the temperature gradients are large. The location η_0 tends to shift toward the bottom with increasing internal Rayleigh number. This alters the upward and downward heat fluxes through the upper and lower surfaces accordingly. The estimated steady-state results will be used to specify the initial conditions for the transient problem.

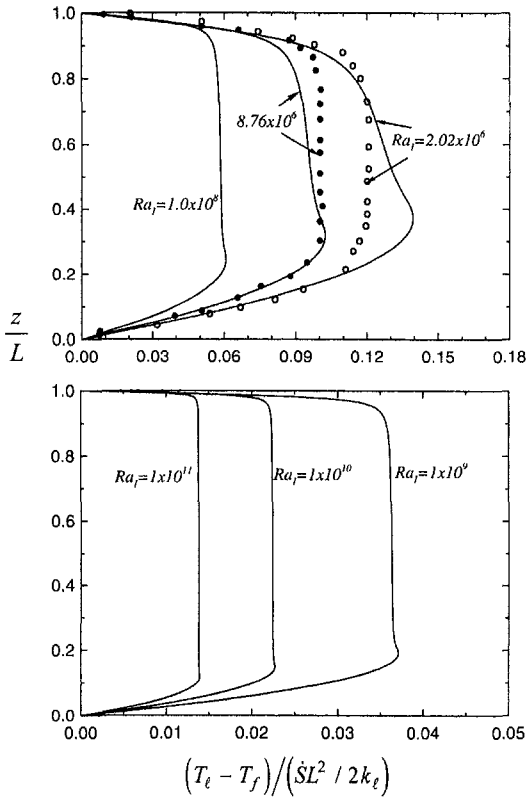

Fig. 2 Steady-state dimensionless temperature distributions at different internal Rayleigh numbers

Transient Analysis. To alleviate the need for tracking the moving fronts at the upper and lower solid-liquid interfaces, the governing differential equations along with the initial and boundary conditions are transformed into dimensionless forms.

Liquid Region. $\delta_1(t) < z < L - \delta_2(t)$ or $1 < \eta_l < 2$. The following dimensionless variables are introduced

$$\tau = \frac{\alpha_l t}{L^2}, \quad \eta_l = 1 + \frac{z-\delta_1(\tau)}{L-\delta_1(\tau)-\delta_2(\tau)},$$

$$\theta_l = \frac{T_l - T_f}{\dot{S}L^2/2k_l} \quad (28)$$

where the dimensionless temperature θ_l is function of the dimensionless time τ, and the dimensionless spatial variable η_l. Transforming Eq. (3) in terms of the dimensionless variables, the following equation can be obtained:

$$\frac{\partial\theta_l}{\partial\tau} + \frac{1}{1-\tilde{\delta}_1-\tilde{\delta}_2}\left[(\eta_l-2)\frac{d\tilde{\delta}_1}{d\tau} + (\eta_l-1)\frac{d\tilde{\delta}_2}{d\tau}\right]\frac{\partial\theta_l}{\partial\eta_l}$$

$$= 2 + \frac{1}{(1-\tilde{\delta}_1-\tilde{\delta}_2)^2}\frac{\partial}{\partial\eta_l}\left(\frac{\alpha_{\text{eff}}}{\alpha_l}\frac{\partial\theta_l}{\partial\eta_l}\right) \quad (29)$$

where $\tilde{\delta}_1$, $\tilde{\delta}_2$ are dimensionless lower and upper crust thicknesses defined by

$$\tilde{\delta}_1(\tau) = \frac{\delta_1(\tau)}{L}, \quad \tilde{\delta}_2(\tau) = \frac{\delta_2(\tau)}{L}. \quad (30)$$

Eddy Heat Transfer Model—Application to the Transient Problem. Based upon the concept of the eddy heat transport model, a transient local Rayleigh number can be introduced as follows:

$$\mathrm{Ra}^* = \frac{g\beta\Delta T^*[L - \delta_1(\tau) - \delta_2(\tau) - L_0(\tau)]^3}{\alpha_l \nu} \times [2 - \eta_0(\tau)]^{(-6/b)}\{[\eta_l - \eta_0(\tau)][2 - \eta_l]\}^{3/b} \quad \text{for} \quad \eta_0 < \eta_l < 2 \quad (31)$$

where

$$\eta_0(\tau) = 1 + \frac{L_0(\tau)}{L - \delta_1(\tau) - \delta_2(\tau)}. \quad (32)$$

From Eqs. (20), (28), (30), and (31), the local Rayleigh number is given by

$$\mathrm{Ra}^* = \mathrm{Ra}_l\theta_l[1 - \tilde{\delta}_1(\tau) - \tilde{\delta}_2(\tau)]^3[2 - \eta_0(\tau)]^{(3b-6)/b} \times \{[\eta_l - \eta_0(\tau)][2 - \eta_l]\}^{3/b}. \quad (33)$$

The effective thermal diffusivity in the upper (unstable) liquid layer is

$$\frac{\alpha_{\mathrm{eff}}}{\alpha_l} = 1 + 0.051\,\mathrm{Ra}_l^{0.87}\theta_l^{0.87}[1 - \tilde{\delta}_1(\tau) - \tilde{\delta}_2(\tau)]^{2.61} \times [2 - \eta_0(\tau)]^{-3.39}\{[\eta_l - \eta_0(\tau)][2 - \eta_l]\}^3 \quad \text{for} \quad \eta_0 < \eta_l < 2. \quad (34)$$

On the other hand, the effective thermal diffusivity in the lower (stable) liquid portion is

$$\frac{\alpha_{\mathrm{eff}}}{\alpha_l} = 1 \quad \text{for} \quad 1 < \eta_l \le \eta_0. \quad (35)$$

Substituting Eqs. (34) and (35) into Eq. (29), the following governing equations can be derived:

- Thermally unstable upper liquid layer, $\eta_0 < \eta_l < 2$

$$\frac{\partial\theta_l}{\partial\tau} + \frac{1}{1 - \tilde{\delta}_1 - \tilde{\delta}_2}\left[(\eta_l - 2)\frac{d\tilde{\delta}_1}{d\tau} + (\eta_l - 1)\frac{d\tilde{\delta}_2}{d\tau}\right]\frac{\partial\theta_l}{\partial\eta_l} = 2 + \frac{1}{(1 - \tilde{\delta}_1 - \tilde{\delta}_2)^2}\frac{\partial^2\theta_l}{\partial\eta_l^2} + \frac{0.051}{1.87}\mathrm{Ra}_l^{0.87}(1 - \tilde{\delta}_1 - \tilde{\delta}_2)^{0.61}(2 - \eta_0)^{-3.39} \times \left\{3[(\eta_l - \eta_0)(2 - \eta_l)]^2(2 + \eta_0 - 2\eta_l)\frac{\partial(\theta_l^{1.87})}{\partial\eta_l} + [(\eta_l - \eta_0)(2 - \eta_l)]^3\frac{\partial^2(\theta_l^{1.87})}{\partial\eta_l^2}\right\} \quad (36)$$

- Thermally stable lower liquid layer, $1 < \eta_l \le \eta_0$

$$\frac{\partial\theta_l}{\partial\tau} + \frac{1}{1 - \tilde{\delta}_1 - \tilde{\delta}_2}\left[(\eta_l - 2)\frac{d\tilde{\delta}_1}{d\tau} + (\eta_l - 1)\frac{d\tilde{\delta}_2}{d\tau}\right]\frac{\partial\theta_l}{\partial\eta_l} = 2 + \frac{1}{(1 - \tilde{\delta}_1 - \tilde{\delta}_2)^2}\frac{\partial^2\theta_l}{\partial\eta_l^2} \quad (37)$$

The boundary conditions are the same as those given in the steady state analysis, i.e., Eq. (16), with η_0 being a function of time in the transient problem.

Solid Regions (Lower and Upper Crust Layers). A coordinate transformation is applied to immobilize the solid-liquid interfaces at the spatial locations of $\eta = 1$ and $\eta = 2$. This is done by invoking the following dimensionless spatial variables and dimensionless temperature

$$\eta_{s1} = \frac{z}{\delta_1(\tau)} \quad \text{for} \quad 0 \le z < \delta_1(\tau) \quad \text{or} \quad 0 \le \eta_{s1} < 1,$$

$$\eta_{s2} = 3 - \frac{L - z}{\delta_2(\tau)} \quad \text{for} \quad L - \delta_2(\tau) < z \le L \quad \text{or} \quad 2 < \eta_{s2} \le 3,$$

$$\theta_s = \frac{T_s - T_f}{\dot{S}L^2/2k_s} \quad (38)$$

where θ_s is function of τ and η_s. Performing the coordinate transformation, Eq. (7) becomes

$$\frac{\partial\theta_s}{\partial\tau} - \left(\frac{\eta_{s1}}{\tilde{\delta}_1}\frac{d\tilde{\delta}_1}{d\tau}\right)\frac{\partial\theta_s}{\partial\eta_{s1}} = \left(\frac{\alpha_s}{\alpha_l}\frac{1}{\tilde{\delta}_1^2}\right)\frac{\partial^2\theta_s}{\partial\eta_{s1}^2} + 2\frac{\alpha_s}{\alpha_l} \quad \text{for} \quad 0 \le z < \delta_1(\tau) \quad \text{or} \quad 0 \le \eta_{s1} < 1 \quad (39)$$

$$\frac{\partial\theta_s}{\partial\tau} + \left(\frac{3 - \eta_{s2}}{\tilde{\delta}_2}\frac{d\tilde{\delta}_2}{d\tau}\right)\frac{\partial\theta_s}{\partial\eta_{s2}} = \left(\frac{\alpha_s}{\alpha_l}\frac{1}{\tilde{\delta}_2^2}\right)\frac{\partial^2\theta_s}{\partial\eta_{s2}^2} + 2\frac{\alpha_s}{\alpha_l} \quad \text{for} \quad L - \delta_2(\tau) < z \le L \quad \text{or} \quad 2 < \eta_{s2} \le 3. \quad (40)$$

The initial and boundary conditions are

$$\begin{aligned} &\tau = 0, \quad \tilde{\delta}_1(\tau) = 0, \quad \tilde{\delta}_2(\tau) = 0 \\ &\tau > 0, \quad \theta_s = -\theta_w \quad \text{at} \quad \eta_{s1} = 0 \\ &\qquad\quad \theta_s = 0 \quad \text{at} \quad \eta_{s1} = 1 \\ &\qquad\quad \theta_s = 0 \quad \text{at} \quad \eta_{s2} = 2 \\ &\qquad\quad \theta_s = -\theta_w \quad \text{at} \quad \eta_{s2} = 3 \end{aligned} \quad (41)$$

where

$$\theta_w = \frac{T_f - T_w}{\dot{S}L^2/2k_s} \quad (42)$$

is the dimensionless wall temperature at the upper and lower surfaces.

Stefan Condition at the Solid-Liquid Interfaces. The Stefan condition at the lower and upper solid-liquid interfaces are given by Eqs. (9) and (10) which can be transformed into the following forms:

$$\frac{d\tilde{\delta}_1}{d\tau} = \mathrm{Ste}_l\frac{\alpha_s}{\alpha_l}\left(\frac{1}{\tilde{\delta}_1}\frac{\partial\theta_s}{\partial\eta_{s1}}\bigg|_{\eta_{s1}=1^-} - \frac{1}{1 - \tilde{\delta}_1 - \tilde{\delta}_2}\frac{\partial\theta_l}{\partial\eta_l}\bigg|_{\eta_l=1^+}\right) \quad \text{at} \quad \eta_l = \eta_{s1} = 1 \quad (43)$$

$$\frac{d\tilde{\delta}_2}{d\tau} = \mathrm{Ste}_l\frac{\alpha_s}{\alpha_l}\left(\frac{1}{1 - \tilde{\delta}_1 - \tilde{\delta}_2}\frac{\partial\theta_l}{\partial\eta_l}\bigg|_{\eta_l=2^-} - \frac{1}{\tilde{\delta}_2}\frac{\partial\theta_s}{\partial\eta_{s2}}\bigg|_{\eta_{s2}=2^+}\right) \quad \text{at} \quad \eta_l = \eta_{s2} = 2 \quad (44)$$

where Ste_l is the internal Stefan number defined by

$$\mathrm{Ste}_l = \frac{C_{P_s}}{\Delta H}\left(\frac{\dot{S}L^2}{2k_s}\right). \quad (45)$$

Equations (43) and (44) are coupled first order nonlinear ordinary differential equations, which can be solved by the fourth-order Runge-Kutta time integration method. To handle the ini-

tial jump and to avoid the singularity points from zero crust thickness, Eq. (43) is multiplied by $\tilde{\delta}_1$ on both sides whereas Eq. (44) is multiplied by $\tilde{\delta}_2$. In so doing, the singularity points are removed from the right hand side of the equations whereas the left hand side becomes the time derivative of $\tilde{\delta}^2/2$.

Tracing of the Thermal Instability Interface. To trace the imaginary interface between the thermally stable and unstable liquid regions, it is assumed that the interface location corresponds to the maximum temperature location. A one-dimensional moving grid method is employed to account for the moving interface, where the grid point is fixed on the physical boundary and moving along with the migrating interface.

The grid point redistribution depends on the same dimensionless temperature profile. A correction can be made by simply using a Lagrangian polynomial formula expressed as

$$(\theta_i)' = \theta_1 \frac{[(\eta_i)' - \eta_2][(\eta_i)' - \eta_3][(\eta_i)' - \eta_4]}{(\eta_1 - \eta_2)(\eta_1 - \eta_3)(\eta_1 - \eta_4)} + \theta_2 \frac{[(\eta_i)' - \eta_1][(\eta_i)' - \eta_3][(\eta_i)' - \eta_4]}{(\eta_2 - \eta_1)(\eta_2 - \eta_3)(\eta_2 - \eta_4)} + \theta_3 \frac{[(\eta_i)' - \eta_1][(\eta_i)' - \eta_2][(\eta_i)' - \eta_4]}{(\eta_3 - \eta_1)(\eta_3 - \eta_2)(\eta_3 - \eta_4)} + \theta_4 \frac{[(\eta_i)' - \eta_1][(\eta_i)' - \eta_2][(\eta_i)' - \eta_3]}{(\eta_4 - \eta_1)(\eta_4 - \eta_2)(\eta_4 - \eta_3)} \quad (46)$$

where $(\ \ )'$ indicates the new nodal values, and the subscripts 1, 2, 3, 4 are the four grid points which have the nearest locations about the grid point i. Note that the subscript l is ignored since only the liquid region is being considered.

Computational Procedure. To discretize the governing equations, a fully implicit scheme with a first-order forward difference in time and a second-order central difference in space is developed. The finite difference form of Eq. (36) is algebraically nonlinear due to the differential term involving $\theta_l^{1.87}$ at the unknown time level. The Newton linearization procedure is used so that the system can be rearranged for the TDMA solver. Using the moving grid method to trace the location of η_0, the grid spacings in the upper and lower liquid portions are adjustable, and a nonuniform finite difference form is used for the location of thermally unstable interface.

Due to the strong coupling of the governing equations for each liquid portion with the two solid-liquid interface energy balance equations, iterations between the fully implicit and Runge-Kutta schemes are necessary in each time step. However, if the time step is small enough, using one iteration at each time step is acceptable but not encouraged, especially for the calculation near the initial jump. At the first time step, the crust thicknesses and solidification front velocities are computed before the temperature distributions, so that the singular points from zero crust thicknesses will only appear on the interface energy balance equations. On the other hand, there is no singular point once solidification has begun. As mentioned above, the singularity points in the first time step are conveniently removed by multiplying $\tilde{\delta}_1$, $\tilde{\delta}_2$ on both sides of Eqs. (43) and (44), respectively.

The transient heat transfer characteristics including the solid-liquid interface heat transfer coefficient, transient Nusselt number, melt layer turbulent intensity, and boundary heat fluxes are determined at the end of each time step along with the interface locations.

Results and Discussion

There are three major dimensionless parameters that control the transient behavior of the melt pool heat transfer and the crust dynamics. These are the internal Rayleigh number, Ra_l, the dimensionless wall cooling temperature, θ_w, and the internal Stefan number, Ste_l. Under steady-state conditions, however, the Stefan number is irrelevant. A value of $\alpha_s/\alpha_l = 0.9$ is used for the thermal diffusivity ratio of the reactor fuel, and the other thermal properties are treated constant in each phase. In addition, the solid and liquid densities are assumed to be equal in the numerical computation.

The optimized dimensionless time step $\Delta\tau$ and the grid point distribution depend on the magnitude of the internal Rayleigh number. At a moderate internal Rayleigh number of 1×10^7, a total of 111 grid points is applied for the entire computational domain with 30, 51, and 30 nodes for the lower crust, melt layer, and upper crust, respectively. A very small time step equal to 1×10^{-5} is used in order that the transient phenomena are clearly understood even around the initial jump condition. A much finer melt layer grid distribution is needed at very high internal Rayleigh numbers. Nevertheless, the order of magnitude of the characteristic time τ_∞ for a steady state to achieve is roughly equal to unity in all cases. To assure the accuracy of the numerical results, a global convergence criterion with a relative error of 1×10^{-9} is used. Numerical Experiments have been performed and the results have been found to be independent of the grid size. Further decrease in the grid size used in the present study would not improve the accuracy of the results (see Fan, 1996).

The idea of combining the Lagrangian and Eulerian approaches is successfully applied in this study. The solid-liquid interfaces are immobilized at the dimensionless locations $\eta = 1$ and $\eta = 2$ in order to trace the solidification fronts (fixed grids). Meanwhile, the thermal instability interface is traced by the maximum dimensionless temperature at location $\eta = \eta_0$. The grid spacings are adjustable in the liquid region (moving grids). The grid point migration is restricted to a small amount at each time step compared with the grid spacing in order to prevent wavy solutions due to numerical oscillation.

Before presenting the numerical results, it is necessary to justify the transient model (i.e., the eddy heat transport model) employed for the unstable melt region. Kulacki and Emara (1977), Cheung (1978, 1980b), and Keyhani and Kulacki (1983) studied the case of transient natural convection in a volumetrically heated horizontal fluid layer without solidification. In particular, they investigated the nature of developing and decaying turbulent convection in an internally heated fluid layer following a step change in volumetric energy generation. They found that the turbulent heat transport maintains its steady-state behavior during turbulent-to-turbulent transients despite any restructuring of the flow in the transient process. This quasi-steady behavior of the turbulent heat transport is due to the fact that the time scale of the turbulent natural convection flow is much smaller than the total time scale of the developing or decaying flow process. Thus, it is appropriate to extend the eddy heat transport model of Cheung (1977), which has been shown to correctly predict the steady turbulent natural convection behavior, to the case of transient flows. This is particular true for the case of solidification as the time scale of the turbulent natural convection flow is much smaller than the time scale of solidification. To further demonstrate this point, i.e., the validity of the eddy heat transport model, numerical calculations have been performed to simulate the turbulent decaying flow investigated in the experimental work of Kulacki and Emara (1977). Results for a decaying flow from an initial Rayleigh number of 8.55×10^5 are shown in Fig. 3. In this figure, the data points are from the work of Kulacki and Emara (1977) whereas the solid lines are the predictions of the present transient model without solidification. Overall, the agreement is quite satisfactory in spite of the fact that some deviation does exist. The present transient model correctly predicts not only the transient temperature distribution of the fluid layer but also the time scale of the decaying flow process.

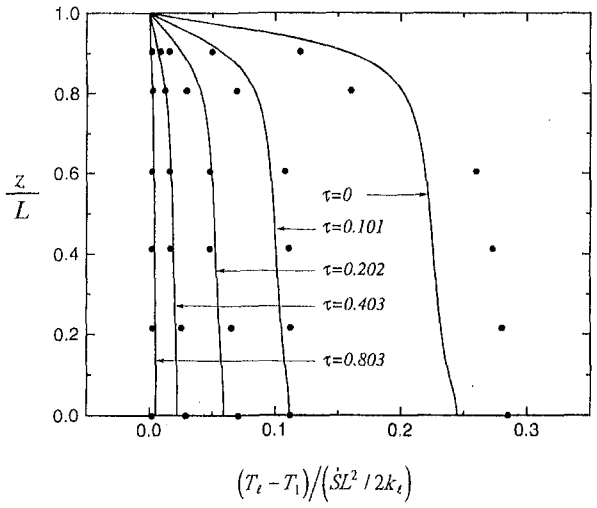

Fig. 3 Transient dimensionless temperature distributions following a flow decay from an initial internal Rayleigh number of 8.55 × 10^5 for the case without solidification

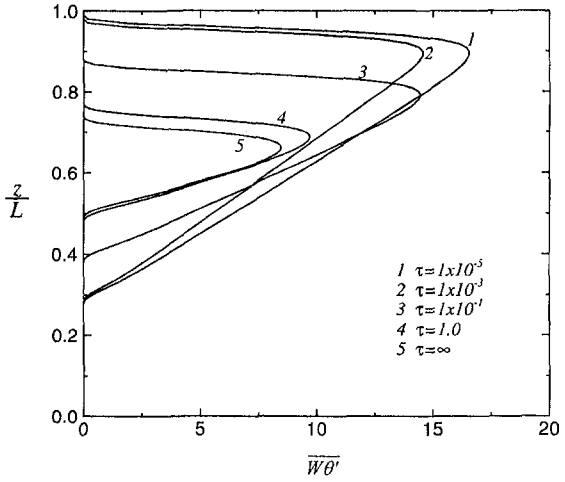

Fig. 5 Transient dimensionless eddy heat transport distributions for the case with solidification (Ra_l = 5 × 10^7; θ_w = 0.2; Ste_l = 1.0)

Figure 4 presents the transient temperature variation at a moderate internal Rayleigh number, 5 × 10^7, with a relatively strong cooling effect, θ_w = 0.2. The internal Stefan number is fixed at 1.0. To show the advancing fronts of the upper and lower solid-liquid interfaces, the physical distance along the vertical direction is plotted against the dimensionless temperatures at different time instants. The dashed line at zero-dimensionless temperature is the freezing interface which separates the solid and the liquid phases. Very large temperature gradients are present in the crust regions at small times. The initial temperature distribution is very close to the one given by Curve 1 and would not show any difference on the scale presented in the figure. Since the heat generated is removed instantly from the cooling boundaries, the crusts grow rapidly by releasing the latent heat in early stages. Due to the intensive turbulent mixing effect, the liquid temperature profile is relatively flat in the upper liquid layer where the temperature stratification is unstable. The local Rayleigh number decreases with time due to decrease in the local characteristic length. The thermal instability interface moves upward to a higher location in the melt layer region as time proceeds. Once a steady state is attained, the upper and lower crusts assume their maximum thicknesses. No additional latent heat is released in the system. It should be noted that the nonlinear temperature profiles in the crust regions are generated by the energy sources. The nonsymmetric temperature profiles in the crust regions imply different heat fluxes across the cooling boundaries. At steady state, the upper and lower heat flux ratio is the same as the ratio of the upper and lower layer thicknesses determined by the location η_0. The numerical data have been presented in tables by Fan (1996).

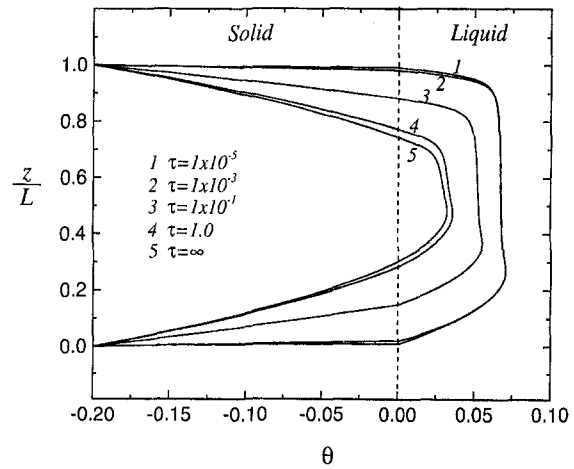

Fig. 4 Transient dimensionless temperature distributions for the case with solidification (Ra_l = 5 × 10^7; θ_w = 0.2; Ste_l = 1.0)

Figure 5 shows the transient dimensionless turbulent heat flux in the thermally unstable upper liquid layer where the dimensionless turbulent heat flux is defined by

$$\overline{W\theta_l'}(\tau, \eta_l) = \frac{\overline{wT_l'}}{\alpha_l(T_{\max} - T_f)/L}. \tag{47}$$

Physically, this dimensionless quantity represents the ratio of the turbulent heat flux to the conduction heat flux. The peak value is concentrated at the location just outside the upper thermal boundary layer. The mixing intensity decreases very rapidly due to the wall cooling effect. Throughout the transient, the turbulent mixing core is shrinking due to the inward growth of the two solidification fronts. The transient Rayleigh number decreases continuously with decreasing liquid layer thickness. At steady state, the peak turbulence intensity is about half of the initial value.

Figure 6 shows the upper and lower crust thicknesses at different cooling temperatures. The two solidification fronts move rapidly in the early stage. They eventually slow down and approach their steady-state thicknesses at large times. During the entire transient stage, the upper crust is thinner than the lower crust. This is because of a higher heat flux through the upper solid-liquid interface due to turbulent convection, which suppresses the latent heat release and the crust growth. In general, both the upper and lower crusts become thicker at a larger value of θ_w.

Due to the presence of turbulent thermal convection in the upper liquid layer, a higher heat flux is obtained at the upper solid-liquid interface. The transient Nusselt number at the upper surface is defined by

$$\mathrm{Nu}(t) = \frac{h(t)[L - \delta_1(t) - \delta_2(t) - L_0(t)]}{k_l} \tag{48}$$

where h is the heat transfer coefficient at the upper solid-liquid interface given by

$$h = \frac{1}{T_{\max} - T_f}\left(-k_l \frac{\partial T_l}{\partial z}\right)_{z=L-\delta_2}. \tag{49}$$

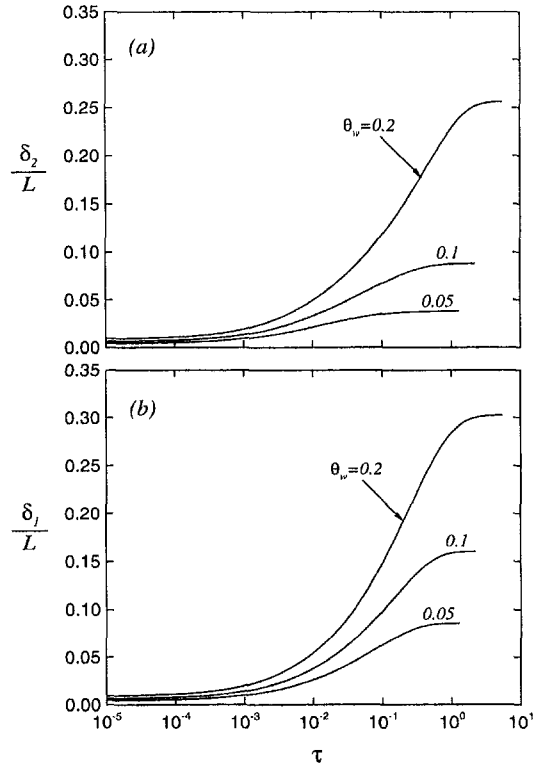

Fig. 6 Dimensionless thicknesses of the upper and lower crust layers for different cooling temperatures: (*a*) upper crust layer, and (*b*) lower crust layer ($Ra_l = 5 \times 10^7$; $Ste_l = 1.0$)

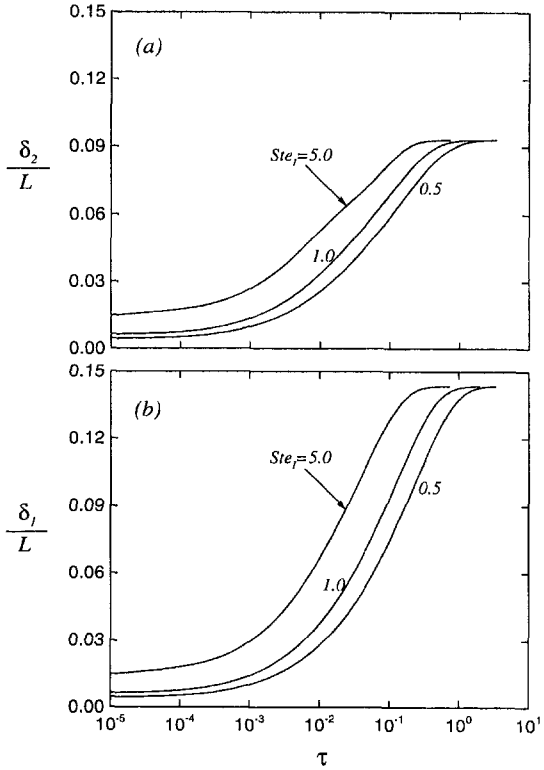

Fig. 8 Dimensionless thicknesses of the upper and lower crust layers for different Stefan numbers: (*a*) upper crust layer, and (*b*) lower crust layer ($Ra_l = 1 \times 10^7$; $\theta_w = 0.1$)

In dimensionless form, Eq. (48) becomes

$$\mathrm{Nu}(\tau) = \frac{-[2 - \eta_0(\tau)]}{\theta_{\max}(\tau)} \left.\frac{\partial \theta_l(\tau, \eta_l)}{\partial \eta_l}\right|_{\eta_l = 2^-} \qquad (50)$$

The transient Nusselt number at the upper solid-liquid interface normalized by the initial steady-state value, Nu_0, is presented in Fig. 7. During the early stage, Nu/Nu_0 is larger than unity. This early transient is a classical time-lag effect. It takes certain time for the inward movement of the cold upper solid-liquid interface to penetrate the entire length of the boundary layer, as clearly shown in Fig. 4. After the early stage of growth, the thickness of the thermally unstable upper liquid layer gradually decreases. This results in a lower Rayleigh number, leading to a decrease in the transient Nusselt number.

The internal Stefan number effect (i.e., the latent heat effect) is depicted in Figs. 8 and 9. In order to keep the same magnitudes of Ra_l and θ_w, all physical properties, initial liquid layer thickness, and energy sources are fixed at the same values. The Stefan number is varied mainly with the inverse of the latent heat. An increase in the internal Stefan number corresponds to a decrease in the latent heat which results in a rapid growth of crusts at the top and bottom boundaries. This in turn induces a higher convective heat transfer in the early stage of transient. As can be seen from Eqs. (43) and (44), the Stefan number only affects the transient solutions and the characteristic time τ_∞. As the new steady state is attained, all three cases have

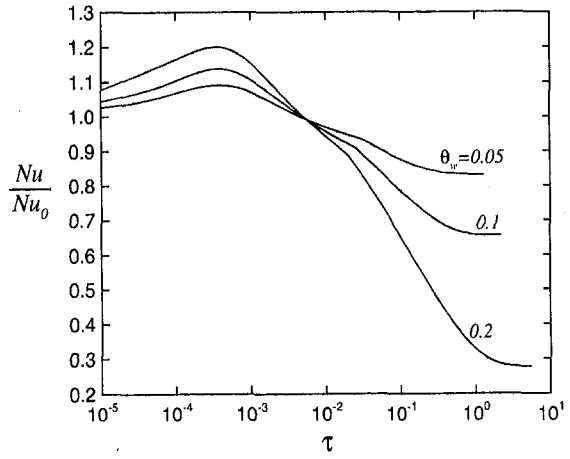

Fig. 7 Normalized Nusselt number at the upper solid-liquid interface for different wall cooling temperatures ($Ra_l = 5 \times 10^7$; $Ste_l = 1.0$)

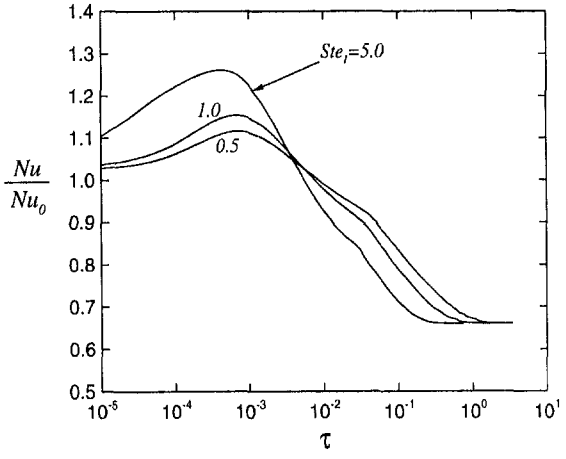

Fig. 9 Normalized Nusselt number at the upper solid-liquid interface for different Stefan numbers ($Ra_l = 1 \times 10^7$; $\theta_w = 0.1$)

the same final steady-state values, independent of the Stefan number.

Conclusions

A numerical model has been successfully developed to investigate the transient phenomenon of turbulent natural convection in a volumetrically heated horizontal melt layer, with solidification taking place at the cooled boundaries. Based upon the results obtained in this study, the following conclusions can be made:

1 The heat transfer in the melt layer is strongly coupled to the crust dynamics throughout the entire transient process. While the rate of solidification (i.e., crust growth) depends strongly on the boundary heat fluxes from the melt layer, the turbulent natural convection in the melt layer is strongly affected by the crust.
2 In the early stage of the transient process, the growth of the crust at the upper surface induces a wall suction effect on the melt layer which enhances the convective heat transfer at the upper solid-liquid interface. However, as the upper and lower crusts grow thicker in the later stage of the transient process, the depth of the liquid layer becomes smaller. This results in a large reduction in the magnitude of the transient Rayleigh number and thus the convective heat flux at the upper solid-liquid interface.
3 The presence of turbulent natural convection in the upper portion of the melt layer tends to suppress the crust growth at the upper boundary. As a result, the upper crust is considerably thinner than the lower crust. The difference in thickness between the upper and lower crusts becomes more pronounced as the internal Rayleigh number defined in terms of the initial depth of the melt layer is increased.
4 The transient thermal behavior of the system is controlled not only by the internal Rayleigh number but also by the internal Stefan number and the dimensionless surface cooling temperature. Higher rates of growth of the crusts are obtained as the Stefan number or the dimensionless cooling temperature is increased. The steady state upper and lower crust thicknesses, however, are dictated by the internal Rayleigh number and the dimensionless cooling temperature, independent of the Stefan number.
5 The crust dynamics, which has an important effect on the transient turbulent natural convection in the melt layer, needs to be taken into account in predicting the transient boundary heat fluxes from the heat-generating melt layer.

References

Arpaci, V. S., 1995, "Buoyant Turbulent Flow Driven by Internal Energy Generation," *Int. J. Heat Mass Transfer,* Vol. 38, pp. 2761–2770.

Asfia, F. J., and Dhir, V. K., 1994, "An Experimental Study of Natural Convection in a Volumetrically Heated Spherical Pool With Rigid Wall," *ASME Paper 94-WA/HT-26.*

Cheung, F. B., 1980a, "Heat-Source-Driven Thermal Convection at Arbitrary Prandtl Numbers," *J. Fluid Mech.,* Vol. 97, pp. 743–758.

Cheung, F. B., 1980b, "The Boundary Layer Behavior in Transient Turbulent Thermal Convection Flow," ASME JOURNAL OF HEAT TRANSFER, Vol. 102, pp. 373–375.

Cheung, F. B., 1978, "Turbulent Thermal Convection in a Horizontal Fluid Layer With Time Dependent Volumetric Energy Sources," *AIAA/ASME Thermophysics and Heat Transfer Conf.,* 78-HT-6, Palo Alto.

Cheung, F. B., 1977, "Natural Convection in a Volumetrically Heated Fluid Layer at High Rayleigh Numbers," *Int. J. Heat Mass Transfer,* Vol. 20, pp. 499–506.

Cheung, F. B., Shiah, S. W., Cho, D. H., and Tan, M. J., 1992, "Modeling of Heat Transfer in a Horizontal Heat-Generating Layer by an Effective Diffusivity Approach," *ASME/HTD,* Vol. 192, pp. 55–62.

Dinh, T. N., and Nourgalier, R. R., 1997, "On Turbulence Modeling in Large Volumetrically Heated Liquid Pools," *Nucl. Engng. Design,* in press.

Fan, T. H., 1996, "Heat Transport Phenomena of Turbulent Natural Convection in a Melt Layer With Solidification," M.S. thesis, The Pennsylvania State University, University Park, PA.

Fielder, H. E., and Wille, R., 1970, "Turbulante Freie Konvektion in Einer Horizontalea Flussigkeitsschicht mit Volumen-Warmequelle," Paper NC 4.5, *Proc. Fourth Int. Heat Transfer Conf.,* Vol. IV, pp. 1–12.

Gabor, J. D., Ellison, P. G., and Cassulo, J. C., 1980, "Heat Transfer From Internally Heated Hemispherical Pools," Presented at *the 19th National Heat Transfer Conference,* Orlando, FL.

Jahn, M., and Reineke, H. H., 1974, "Free Convection Heat Transfer With Internal Heat Sources, Calculations and Measurements," *Proc. 5th Int. Heat Transfer Conf.,* Paper NC2.8, Vol. III, Tokyo, Japan, pp. 74–83.

Keyhani, M., and Kulacki, F. A., 1983, "Experiments on Transient Thermal Convection with Internal Heat Sources—Large Time Results," ASME JOURNAL OF HEAT TRANSFER, Vol. 105, pp. 261–266.

Kulacki, F. A., and Emara, A. A., 1977, "Steady and Transient Thermal Convection in a Fluid Layer With Uniform Volumetric Energy Sources," *J. Fluid Mech.,* Vol. 83, pp. 375–395.

Kulacki, F. A., and Goldstein, R. J., 1972, "Thermal Convection in a Horizontal Fluid Layer With Uniform Volumetric Energy Sources," *J. Fluid Mech.,* Vol. 55, pp. 271–287.

Kulacki, F. A., and Nagle, M. Z., 1975, "Natural Convection in a Horizontal Fluid Layer With Volumetric Energy Sources," ASME JOURNAL OF HEAT TRANSFER, Vol. 97, 204–211.

Kymalainen, O., Tuomisto, H., Hongisto, O., and Theofanous, T. G., 1994, "Heat Flux Distribution From a Volumetrically Heated Pool With High Rayleigh Number," *Nuclear Engineering and Design,* 149, pp. 401–408.

Mayinger, F., Jahn, M., Reineke, H. H., and Steinbrenner, V., 1976, "Examination of Thermohydraulic Processes and Heat Transfer in a Core Melt," *BMFT RS 48/1,* Institute fur Verfanhrenstechnic der T. U., Hanover, Germany.

Min, J. H., and Kulacki, F. A., 1978, "An Experimental Study of Thermal Convection With Volumetric Energy Sources in a Fluid Layer Bounded From Below by a Segment of a Sphere," Presented at *the 6th International Heat Transfer Conference,* Toronto, Canada.

Nourgalier, R. R., and Dinh, T. N., 1996, "An Investigation of Turbulence Characteristics in an Internally Heated Unstable-Stratified Fluid Layer," *ANS Proceedings HTC,* Vol. 9, pp. 357–367.

Roberts, P. H., 1967, "Convection in Horizontal Layers With Internal Heat Generation—Theory," *J. Fluid Mech.,* Vol. 30, pp. 33–49.

Schwiderski, E. M., and Schwab, H. J., 1971, "Convection Experiments With Electrolytically Heated Fluid Layers," *J. Fluid Mech.,* Vol. 48, pp. 703–719.

Steinberner, U., and Reineke, H. H., 1978, "Turbulent Buoyancy Convection Heat Transfer With Internal Heat Sources," *Proc. 6th Int. Heat Transfer Conf.,* Vol. 2, pp. 305–310, Paper NC-21, Toronto, Canada.

Tan, M. J., Cho, D. H., and Cheung, F. B., 1994, "Thermal Analysis of Heat-Generating Pools Bounded From Below by Curved Surfaces," ASME JOURNAL OF HEAT TRANSFER, Vol. 116, pp. 127–135.

Theofanuous, T. G., Liu, C., Addition, S., Angelini, S., Kymalainen, O., and Salmassi, T., 1995, "In-Vessel Coolability and Retention of a Core Melt," *DOE/ID-10460,* U.S. Department of Energy.

Thirlby, R., 1970, "Convection in an Internally Heated Layer," *J. Fluid Mech.,* Vol. 44, pp. 673–693.

Tritton, D. J., and Zarraga, M. N., 1967, "Convection in Horizontal Fluid Layers With Heat Generation Experiments," *J. Fluid Mech.,* Vol. 30, pp. 21–32.

Melting in a Two-Component Packed Bed

J. Pak

O. A. Plumb
plumb@mme.wsu.edu

School of Mechanical and Materials Engineering, Washington State University, Pullman, WA 99164-2920

The melting of a multi-component mixture that consists of melting and nonmelting components is examined. A numerical solution is obtained by solving the energy equation and continuity equations for both solid and liquid phases for a one-dimensional system. Both constant volume and constant porosity melting models are explored. Experiments were conducted to confirm the numerical results. During the experiments, heat was applied at the bottom of a rectangular packed bed containing salol (benzoic acid 2-hydroxyphenylester) and glass beads. The experiments were conducted with various sizes of glass beads ranging from 120 μm to 450 μm in diameter with salol having an average diameter of 90 μm. During the melting process, the volume fraction of the phase-change material (salol), temperature, and applied heat flux were measured. The volume fraction of the salol was measured utilizing gamma attenuation. Upon melting, the salol moves as two fronts, one downward due to gravity and one upward due to capillary action. The constant porosity model yields results which compare well with the experimental data.

Introduction

Transport phenomena in porous media with phase change have been studied in a wide variety of both environmental and engineering systems during the past several decades. Examples of applications of interest include the freezing and melting of soils (Miller, 1980), thermal energy storage (Mechanical Engineering, 1983), and post-accident analysis of nuclear reactors (Dosanjh, 1989). These examples involve heat and mass transfer in porous media occupied by both vapor and liquid. In such systems, interstitial fluids are subject to vaporization, condensation, solidification, melting and transport due to pressure, temperature, and concentration gradients. The liquid-vapor, phase-change problem in porous media has been investigated by many researchers. Wang and Beckermann (1993) have developed a two-phase mixture model for liquid-vapor flow and heat transfer, and Udell (1985) has discussed heat and mass transfer in porous media saturated with liquid and vapor phases. Sahota and Pagni (1979) have reported the effects of a phase change on energy and mass transfer. Liquid-solid, phase-change processes in porous media have also received some attention. The melting of a frozen interstitial fluid in a porous medium has been studied by Weaver and Viskanta (1986). A combined numerical and experimental study of the liquid-solid, phase-change problem during solidification with natural convection has been reported by Beckermann and Viskanta (1988). Thermal densification of a porous matrix to net or near net shape during solid-liquid phase change has been investigated by Mughal and Plumb (1993). In this case, the porous matrix consisted of melting and nonmelting particles.

The present study focuses on the solid-liquid phase change occurring during the melting of a two component packed bed. Particular attention is paid to the redistribution of mass. In the previous study by Mughal and Plumb (1993) the melting particles were assumed to be much smaller than the nonmelting particles. For this case, the melting particles can be assumed to occupy the interstitial space resulting in no total volume change or subsidence for the packed bed during melting. In this study, we examine a bed packed with melting and nonmelting particles of similar size. Thus, a constant porosity model which allows for subsidence of the bed is developed. The results are applicable to the manufacture of powder-based composites, ceramic-metal or certain metal-metal combinations. Due to the process used in producing ceramics and advanced alloys, many of the raw materials utilized in advanced composites are powders. Several processing technologies are able to deal with specific combinations of ceramic and metal powders. Examples include the processes developed by the Lanxide Corporation (Lawrence, 1989) and combustion synthesis (Munir and Anselmi-Tamburim, 1989). For these processing techniques, fully analytical transport models, which can be used for design and control of the manufacturing process, are not available.

The objective of the present study is to extend the previous model of Mughal and Plumb (1993) to include particles of similar size and to present recent experimental results for such a system. The specific geometry studied is a packed bed heated from below. A one-dimensional, phase-change process is examined. The macroscopic energy equation and continuity equations for both the liquid and solid phases are solved numerically, and experiments are conducted to confirm the numerical results. The nonmelting particles used in the experiments are spherical glass beads. Salol (benzoic acid 2-hydroxyphenylester) was chosen as the phase change material because of its low melting temperature and available thermophysical properties. During the melting process, the redistribution of the salol was monitored utilizing gamma attenuation. The measurements are compared with the numerical results. The effects of varying the particle diameter and the geometric melting model from a constant volume model to a constant porosity model are discussed.

Problem Statement and Model Development

The one-dimensional transport of heat and mass in a packed bed is considered in the present study. The packed bed, as illustrated in Fig. 1, contains a mixture of particles of two materials, one which melts during the experiment while the other does not. The void space is occupied by air at atmospheric pressure. A macroscopic description of the transport phenomenon based on volume-averaged equations is employed in the mathematical model. In a previous study, Mughal and Plumb (1993), a constant volume model in which the porosity varies during melting was utilized to predict the redistribution of mass within the packed bed during melting. This approach is appropriate for situations where the melting phase consists of small particles which can occupy the interstitial space created by the

Contributed by the Heat Transfer Division for publication in the JOURNAL OF HEAT TRANSFER. Manuscript received by the Heat Transfer Division November 5, 1996; revision received January 17, 1997; Keywords: Packed & Fluidized Beds; Phase-Change Phenomena; Porous Media. Associate Technical Editor: M. Kaviany.

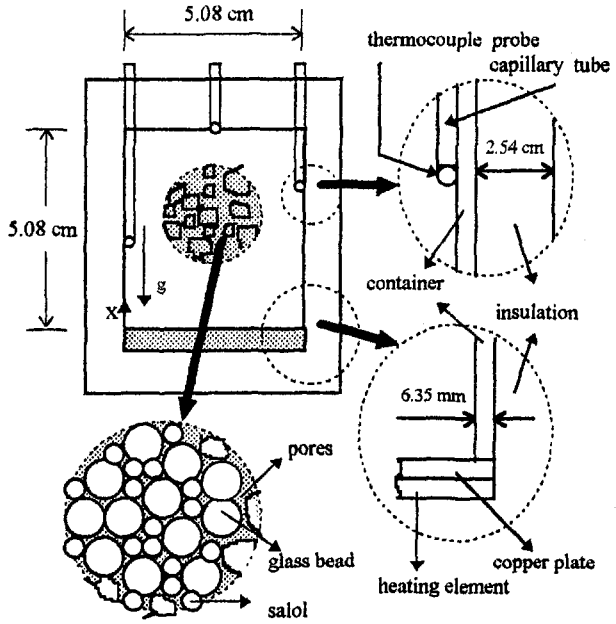

Fig. 1 Schematic of the experimental container

larger particles of the nonmelting phase. In the present study, we examine melting and nonmelting particle sizes of the same order of magnitude. For this situation, the porosity is assumed to remain constant while the bed volume continuously changes during melting. Several other assumptions are made in the present study including: (1) the initial distribution of the volume fraction of the melting material is uniform; (2) no heat loss occurs through the vertical and upper walls of the experimental container; (3) the heat flux applied in the experiment reaches a desired value instantaneously; (4) thermophysical properties are independent of temperature, except the surface tension of the melting component; (5) the particle diameter is taken to be much smaller than the length-scale characteristic of macroscopic changes in temperature and volume fraction of each species such that microscopic equations can be volume averaged to yield macroscopic governing equations; (6) inertial forces are neglected in modeling the liquid flow so that the linear Darcy's law can be utilized; (7) the melt is incompressible and evaporation is neglected; and (8) the gas phase pressure remains constant at one atmosphere.

By combining the volume-averaged conservation equations for each constituent, the macroscopic continuity equations for both liquid and solid phases are obtained as follows:

$$\rho_l \frac{\partial \phi_l}{\partial t} + \rho_l \frac{\partial u_l}{\partial x} = \dot{m} \tag{1a}$$

$$\phi_l = \epsilon S = \frac{V_l}{V_t} \tag{1b}$$

$$\rho_S \frac{\partial \phi_S}{\partial t} = -\dot{m} \tag{2a}$$

$$\phi_S = \frac{V_S}{V_t}. \tag{2b}$$

The local volume fraction of the liquid phase of a phase-change material (PCM), ϕ_l, can be expressed as the product of the local porosity, ϵ, which is assumed to remain constant, and the liquid saturation, S. ρ_l and ρ_s are the densities of the liquid and solid phases of the PCM, respectively. In arriving at Eq. (2*a*), it has been assumed that the velocity of the solid phase remains zero so that no convection results from the solid-phase motion during the melting process. The liquid-phase velocity is determined using Darcy's law for unsaturated flow.

$$u_l = -\frac{KK_{rl}}{\mu}\left(\frac{\partial p_l}{\partial x} + \rho_l g\right) \tag{3}$$

where K is the permeability of the porous medium, μ is the dynamic viscosity of the liquid phase of the PCM, g is the gravitational constant, K_{rl} is a relative permeability, and p_l is the liquid pressure. The value of the permeability, K, is obtained from the Carman-Kozeny equation.

$$K(d_p) = \frac{d_p^2 \epsilon^3}{180(1-\epsilon)^2} \tag{4a}$$

$$d_p = \begin{cases} d_{ps} & \text{imbibition} \\ d_{pg} & \text{drainage} \end{cases} \tag{4b}$$

where d_p is the mean particle size of the components. At any location where solid salol is present it is assumed that the permeability is controlled by the smaller salol particles (imbibition). In regions where the salol is completely melted, the glass beads are assumed to control the permeability (drainage). For a constant volume model the porosity varies continuously as melting takes place while it remains constant for the constant porosity model. The relative permeability is approximated using

$$K_{rl} = S_e^3 \tag{5}$$

Nomenclature

H = total enthalpy, J/m^3
K = permeability, m^2
L = bed height, m
L_p = path length for gamma beam, m
N = number of gamma counts
S = saturation
T = temperature, K
V = volume, m^3
d = diameter, m
d_{ps} = mean diameter of salol particles, m
d_{pg} = mean diameter of glass beads, m
g = gravitational constant, m/s^2
h = enthalpy, J/kg
k = thermal conductivity, W/m-K
$\dot{m}$ = mass production rate, kg/m^3-s
p = pressure, Pa
q = heat flux, W/m^2
u = superficial velocity, m/s
x = axial distance from heater, m

Greek symbols

ϵ = porosity
γ = attenuation coefficient
ϕ = volume fraction
μ = dynamic viscosity, kg/(m·s)
ρ = density, kg/m^3
σ = surface tension, N/m
ω = uncertainty

Subscripts

c = capillary or container (in Eq. 19)
e = effective
g = glass beads
ir = irreducible
l = liquid
o = original, initial
p = particle
pg = glass particle
ps = salol particle
rl = relative to liquid phase
s = solid
t = total
v = vapor

where S_e is the normalized saturation expressed as follows:

$$S_e = \frac{S - S_{ir}}{1 - S_{ir}} \tag{6}$$

and S_{ir} is the irreducible saturation.

The capillary pressure is defined as the difference between the liquid pressure, p_l, and the gas phase pressure, p_v.

$$p_c = p_v - p_l. \tag{7}$$

The derivative of the liquid pressure in Eq. (3) can be replaced with the derivative of the capillary pressure by taking the derivative of Eq. (7), with respect to axial distance x, under the assumption of constant vapor phase pressure

$$\frac{\partial p_l}{\partial x} = -\frac{\partial p_c}{\partial x}. \tag{8}$$

The capillary pressure is approximated using the Leverett function expressed as

$$p_c = J(S_e)\sigma\sqrt{\epsilon/K} \tag{9}$$

$$J(S_e) = a(S_e + b)^c \tag{10}$$

where σ is the surface tension and $a = 0.38$, $b = 0.014$, and $c = -0.27$ (Dosanjh, 1989). The Leverett function is the product of the mean interfacial curvature (inverse of the mean radius of curvature of the meniscus in the pore) p_c/σ and the pore-level length scale which is taken to be $\sqrt{K/\epsilon}$. The Leverett function is assumed to be a function of saturation only, although it can depend upon wettability (Kaviany, 1991).

The energy equation for the two-component porous matrix can be written

$$\frac{\partial}{\partial t}(\rho_s\phi_s h_s + \rho_g\phi_g h_g + \rho_l\phi_l h_l) = \frac{\partial}{\partial x}\left(k_e\frac{\partial T}{\partial x}\right) - \frac{\partial}{\partial x}(\rho_l u_l \phi_l h_l) \tag{11}$$

where h_g is the enthalpy of the nonmelting matrix which consists of glass beads in the present study. h_s and h_l are the enthalpies of the melting component in the solid and liquid phases, respectively. The geometric mean thermal conductivity of the mixture components is taken to obtain the effective thermal conductivity (Kaviany, 1991).

$$k_e = k_s^{\phi_s} k_l^{\phi_l} k_g^{\phi_g}. \tag{12}$$

Phase change occurs at a fixed temperature, T_m, for a pure substance, and the difference between the liquid and solid enthalpies is equal to the latent heat of fusion, h_{sl}. A volume element simultaneously occupied by liquid and solid should be at the melting temperature, T_m, since the phases are assumed to be in local thermal equilibrium. The thermophysical properties used in the calculations are shown in Table 1. Salol properties are from Dey and Sekhar (1993) with the exception of the surface tension. The surface tension of liquid salol is given at several temperatures in the International Critical Table of Numerical Data (1928). This data was curvefit to obtain the relationship for surface tension versus temperature for use in the model.

Table 1 Thermophysical properties of salol and glass beads

	Units	Salol	Glass beads
density (solid)	kg/m^3	1261.4	2500.0
density (liquid)	kg/m^3	1250.0	
melting point	K	314.7	
latent heat of fusion	J/kg	87204.17	
thermal conductivity (solid)	W/m-K	0.39	0.74
thermal conductivity (liquid)	W/m-K	0.13	
viscosity	kg/m-s	0.01	
surface tension	N/m	$(-9.14E\text{-}5)T + 4.54E\text{-}2$	

Solution Algorithm

The energy equation is solved using the enthalpy method (Voller and Cross, 1981) with a time-explicit, finite difference scheme. The temperature is calculated at each time step from the total enthalpy, H.

$$H = \rho_s\phi_s c_{ps}(T - T_{\text{ref}}) + \rho_g\phi_g c_{pg}(T - T_{\text{ref}}) + \rho_l\phi_l[c_{pl}(T - T_{\text{ref}}) + h_{sl}] \tag{13}$$

The temperature is determined at the center of each computational cell with the melting temperature of salol used as the reference temperature. The local temperature is determined from the total enthalpy as follows:

$$T = \begin{cases} \dfrac{H}{\rho_s\phi_s c_{ps} + \rho_g\phi_g c_{pg}} + T_m & H < 0 \\ T_m & 0 \le H \le \rho_l h_{sl} \\ \dfrac{[H + (c_{pl}T_m - h_{sl})\rho_l\phi_l + \rho_g\phi_g c_{pg}T_m]}{\rho_g\phi_g c_{pg} + \rho_l\phi_l c_{pl}} & \rho_l h_{sl} < H. \end{cases} \tag{14}$$

Neumann-type boundary conditions are applied at the bottom and the top of the domain of interest, $0 \le x \le L$.

$$k_e\frac{\partial T}{\partial x} + q = 0 \quad x = 0$$

$$k_e\frac{\partial T}{\partial x} = 0 \quad x = L \tag{15}$$

Here it should be noted that the bed height, L, decreases as melting occurs when the constant porosity model is implemented. The change of volume fraction of solid salol is obtained by solving for the mass source, $\dot{m}$, when the local temperature reaches the melting temperature, T_m, at a particular computational cell. It is necessary to select a time step sufficiently small to insure that the overall results are not affected by the melting or solidification front falling between grid lines (temperature change and melting both taking place during a single time step).

$$\dot{m}h_{sl} = \frac{\partial}{\partial x}\left(k_e\frac{\partial T}{\partial x}\right) + \frac{\partial}{\partial x}(\rho_l u_l \phi_l h_l) \tag{16}$$

The volume fraction of the glass beads at the new time step is calculated from the geometric constraint

$$\phi_g = 1 - \epsilon - \phi_s. \tag{17}$$

The liquid-phase continuity equation written in terms of saturation through the substitution of Eq. (3) into Eq. (1a),

$$\epsilon\frac{\partial S}{\partial t} = -\frac{\partial}{\partial x}\left[\frac{KK_{rl}}{\mu}\left(\frac{\partial p_c}{\partial x} - \rho g\right)\right] + \frac{\dot{m}}{\rho_l}, \tag{18}$$

is solved using the Crank-Nicholson method. The liquid-phase velocity is obtained from the calculated saturation at the boundaries of a computational cell using Darcy's law.

At the end of each time step, the size of each computational cell is recomputed. If the temperature of the cell is greater than or equal to the melting temperature, the new volume fraction of the glass beads is computed using Eq. (17). The grid size

is then adjusted to maintain a constant volume of glass beads within the cell. The instantaneous bed height can then be computed by summing all of the grid sizes. A total of 31 grids along with a time step of $\Delta t = 0.01$ s was utilized in the majority of the numerical simulations. Calculations were also performed with 61 grids and a time step of $\Delta t = 0.001$ s to examine the dependence of the solution on these parameters. The results of these calculations were in close agreement with those for 31 grids and $\Delta t = 0.01$ s.

Experiment

The volume fraction of salol, the applied heat flux, and the local temperature were monitored during the melting of packed beds of 120 μm, 180 μm, 250 μm, and 450 μm glass beads. The size distribution of the glass beads is shown in Table 2. For the glass beads designated as having a mean diameter of 120 μm, 10 percent pass an 85 μm screen, 50 percent pass a 108 μm screen, and 90 percent pass a 153 μm screen. The size of salol particles ranged from 80 μm to 105 μm with a mean value of 90 μm (measured). It should be noted that the shape of the salol particles was irregular because they were produced through grinding using a pestle and ceramic bowl and screening to obtain the desired particle size.

The cross-sectional area of the experimental container was 5.08 by 5.08 cm^2 and the height was 5.08 cm. Polystyrene insulation boards, 2.54 cm thick, were used to insulate the side walls and the top of the container to minimize the heat loss during melting. The container was constructed from PVDF (polyvinylidene fluoride) which resists chemical attack from the liquid salol. Details of design and dimensions of the experimental chamber are shown in Fig. 1.

The local volume fraction of salol was measured utilizing gamma attenuation (Plumb et al., 1984). A cylindrical Am-241 gamma source shielded by brass emits a beam through a slit 2.80 cm wide and 0.5 mm high. Thus, the resulting measurements are averaged over a slice of the material approximately 0.5 mm high and 2.80 cm wide. A NaTI scintillation crystal mounted to a photomultiplier tube detects the attenuated gamma energy as it emerges from the test cell. The detector is also shielded with a brass plate having a slit 0.5 mm high and 3.8 cm wide. The slit in the detector is aligned with the slit on the brass cover of the gamma source to minimize background radiation. The entire source/detector assembly is mounted on a vertical traverse mechanism which can be driven at 0.44 mm/step. The measurements of the amount of attenuation that results due to the container, dry glass beads, solid salol, and liquid salol are necessary to calculate the volume fraction of salol during the melting process. The uncertainty analysis for these measurements is discussed later in this section.

The bottom of the test cell consisted of a 1.65 mm thick copper plate. A heating element, 5.08 cm by 5.08 cm, was placed below the copper base. The heating element was constructed by embedding a serpentine of nichrome wire in a ceramic paste which was then cured. An RdF micro-foil™ heat flux sensor which consists of a total of 40 butt joined microfoil (12.7 μm thick) thermocouples connected in series across a sheet of Kapton™ polymide plastic was sandwiched between the heater and the copper plate. A T type thermocouple was built into the heat flux sensor to monitor its temperature. The entire assembly was approximately 3.048 mm thick.

Table 2 Geometric properties of glass beads

	Particle size distribution		
Mean diameter	10 percent	50 percent	90 percent
120 μm	85 μm	108 μm	153 μm
180 μm	116 μm	160 μm	285 μm
250 μm	164 μm	235 μm	382 μm
450 μm	337 μm	428 μm	552 μm

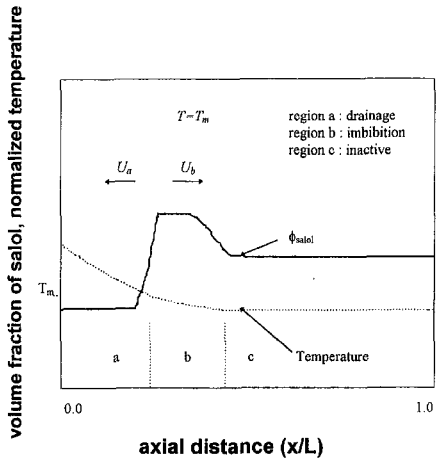

Fig. 2 Direction of liquid flow and salol volume fraction versus dimensionless axial distance near the melt front

The temperature distribution in the packed bed was measured using embedded copper-constantan thermocouples. The temperature was measured at three locations—$\frac{1}{3}$ of height, $\frac{2}{3}$ of height, and near the top of the packed bed as illustrated in Fig. 1. The thermocouple installation was made difficult by the corrosive nature of the salol and the desire to measure temperature without interfering with the gamma-attenuation measurements. To avoid these problems, the thermocouples were placed in a glass capillary tube having a diameter of 1.59 mm installed along the side walls of the test cell.

The uncertainty in the measurements of volume fraction was calculated using the method of Kline and McClintock (1953). The volume fraction of salol can be obtained from the following relationship:

$$\phi_{\text{salol}} = \frac{\left(\ln \frac{N_{c+g+\text{salol}}}{N_{c+g}} + \gamma_g \rho_g \phi_g L_p\right)}{(-\gamma_{\text{salol}} \rho_{\text{salol}} L_p)} \tag{19}$$

where $N_{c+g+\text{salol}}$ is the number of counts measured when salol is present, and N_{c+g} is the number of counts measured for the container and glass beads in the absence of salol. The uncertainty of the volume fraction of salol depends upon the measuring path length, attenuation coefficients for glass and salol, the volume fraction of glass, and the number of counts. For the 250 μm glass beads, the estimated uncertainty based on the experimental data on volume fraction was 4.2 percent. For these measurements a count time of 4 s was utilized, resulting in the number of counts being on the order of 5000. It should be noted that this measurement does not distinguish between liquid and solid salol since their attenuation coefficients are indistinguishable.

The maximum uncertainty in the heat flux is estimated to be ±6 percent. This is primarily the result of the measurement of the microvolt level output to ±1 μV, which is the last significant digit read from a data logger. Although the accuracy of the thermocouples can be assumed to be ±0.5°C, it is expected that the measured temperatures are slightly lower than the temperatures at the center of the bed because the heat losses through the insulation. These losses are estimated to be 2.8 percent of the power input, which leads to a calculated temperature difference between the center of the bed and the thermocouple locations of 2 K. These measurements may also be affected by the change in porosity and, hence, capillary pressure near the wall.

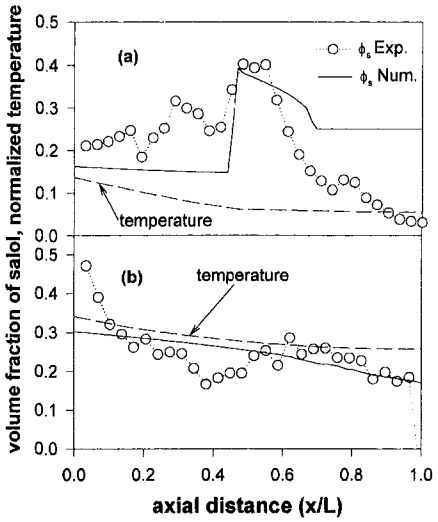

Fig. 3 Comparisons of measured salol volume fraction with numerical results (d_P = 120 μm, ϕ_s = 0.25, ϕ_g = 0.45, ϵ = 0.3): (*a*) t = 2000 s; (*b*) t = 6000 s

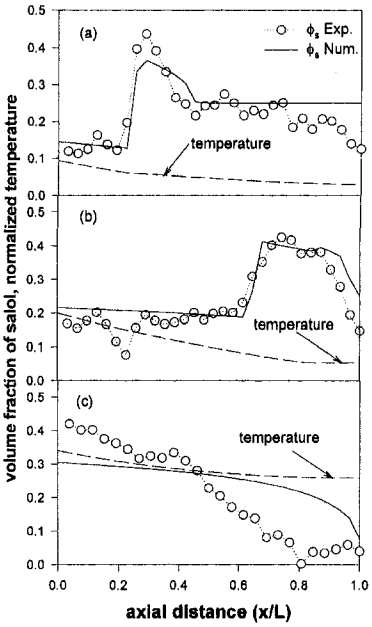

Fig. 5 Comparison of measured volume fraction of salol with predictions (d_P = 250 μm, ϕ_s = 0.25, ϕ_g = 0.45, ϵ = 0.3): (*a*) t = 1200 s; (*b*) t = 3000 s; (*c*) t = 6000 s

Results and Discussion

The numerical simulation was performed under the conditions corresponding as closely as possible to the experimental conditions. It is important to note that both the permeability and the capillary pressure should be expected to vary in the vicinity of the melting front. At the leading edge, the melting front interfaces with the matrix of the glass beads and the solid salol and this solid matrix imbibes a portion of the liquid salol produced as a result of melting. This results in an increase in the salol volume fraction (both measured and predicted) in the region where both solid and liquid salol are present. At the trailing edge of the melting front, which faces the bottom of the container, the melt drains through the matrix of the glass beads due to gravity. Figure 2 depicts the melting process schematically. The location of the volume elements which are at the melting temperature are indicated by dashed lines and designated region b. In region c, liquid salol is resolidified and the region b contains both solid and liquid salol. The velocity in region b within the melting zone (designated u_b) is positive, while the velocity u_a in region a is negative. The model predictions utilize different permeability values for regions a and b. The smaller interstitial space due to the presence of salol is assumed to dominate the flow in region b. In region a no solid salol particles exist, hence, the diameter of the glass beads was used to obtain the permeability from Eq. (4). For the constant volume model, the volume fraction of glass beads is constant throughout the bed. For the constant porosity model, the volume fraction of glass beads is higher in region a than the initial volume fraction which exists in region b. Thus, subsidence of the bed results during melting when using the constant porosity model.

Figures 3 through 5 compare the experimental data for the temperature and volume fraction of salol with the numerical simulation for two different sizes of the glass beads. For all of the results reported the initial volume fraction for the salol was 0.25; for the glass beads it was 0.45, resulting in a porosity of 0.30. In all of the figures, the axial distance is normalized with the instantaneous bed height. Temperatures are normalized using the initial temperature, T_o = 296.65 K. In Fig. 3(a), the experimental data does not agree well with the numerical simulation near the top of the container. The reason is that the actual initial distribution of the salol particles was not completely uniform, as assumed in the numerical model. The model accurately predicts the location of the melting front and the long time salol distribution for the 120 μm glass beads, as shown in Fig. 3(b). For the 250 μm glass beads, comparisons are shown in Figs. 4 and 5. In Fig. 4, the measured temperatures are compared with the numerical data at 1000, 3000, and 6000 s. Heat loss through the top of the container may cause the discrepancy between the numerical and experimental results at long time. The model accurately predicts the actual location of the melting front, as shown in Fig. 5. In this case, the long time distribution of the volume fraction of the salol is not well predicted. This is the likely result of the capillary function used in the model not being a good approximation to the equilibrium

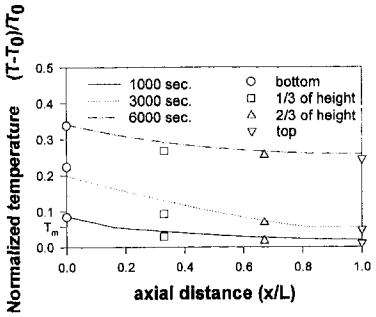

Fig. 4 Comparison of measured temperatures with predictions (d_P = 250 μm, ϕ_s = 0.25, ϕ_g = 0.45, ϵ = 0.3)

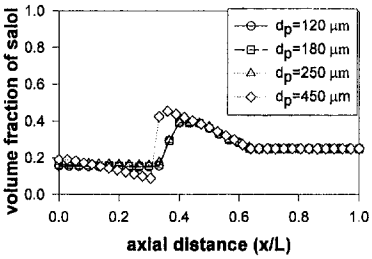

Fig. 6 Numerical results for volume fraction of salol for a range of glass bead sizes (t = 2000 s, ϕ_s = 0.25, ϕ_g = 0.45, ϵ = 0.3)

capillary pressure curve for the 250 μm beads. Some of the discrepancy may also be attributed to the geometric model.

Figure 6 shows model predictions for the four different sizes of glass beads at 2000 s. The effect of increasing the diameter of the glass beads is to increase the permeability after melting has taken place. This serves to accelerate the movement of the liquid salol toward the bottom of the container. For glass bead diameters ranging from 120 μm to 250 μm, the Bond number ($\rho_l g d_{pg}^2/\sigma$) ranges from 0.01 to 0.05 while for the 450 μm glass beads it is an order of magnitude higher (0.150). These results imply that gravitational forces have little effect for Bond numbers less than 0.10. The stronger effect of gravitational forces compared to capillary forces is indicated by the dip in the salol volume fraction immediately behind the melting front in the case of the 450 μm beads. The velocity of the melting front depends only on the applied heat flux, which was held constant in performing the calculations and in the experiments. This is because the effective thermal conductivity behind the melting front is not significantly different even though the liquid salol volume fraction behind the front is slightly higher for the larger diameter glass beads. In addition, the model assumes that the permeability ahead of the melting front is controlled by the smaller salol particles, which is 90 μm for all cases.

The effect of the assumed form of the capillary function is illustrated in Fig. 7. In this figure, results for a power-law-type function, given by Eq. (10), are compared with those for the polynomial function proposed by Udell (1985). The results lead to the conclusion that the model predictions for the melting front propagation and the salol volume fraction in the melt zone are not extremely sensitive to the precise form of the capillary function utilized. However, as indicated above, the salol distribution at the end of melting does depend strongly on the form of the capillary pressure versus saturation curve.

The validity of the constant porosity assumption is examined using Figs. 8 and 9. Figure 8 shows the change in bed height as a function of time for various sizes of glass beads. For three sizes of the glass beads, 120 μm, 180 μm, and 250 μm, the final volume measured experimentally ranges from 78.4 percent to 80.7 percent of the original volume while the final volume for the 450 μm glass beads is 93.8 percent of the original volume. The bed subsidence in the experiments tended to occur in steps, as opposed to the continuous change predicted by the model. The constant porosity model predicts a final bed height of 72.1 percent of the original. Hence, the redistribution of the glass beads is not "perfect," as predicted by the model. This leads to a higher final porosity which could be part of the explanation for the failure of the model to precisely predict the long time salol distribution.

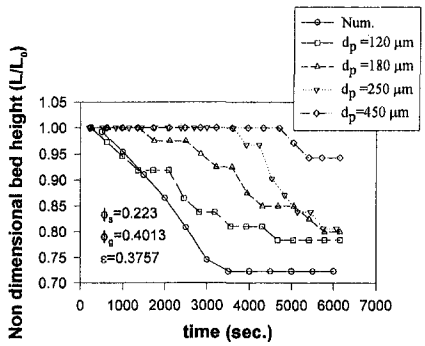

Fig. 8 Numerical and experimental results for bed subsidence

A comparison of the constant porosity model and the constant volume model with the experimental data is shown in Fig. 9. Details of the constant porosity model and the constant volume model are described by Plumb (1994). The constant volume model should be most accurate when the melting particles occupy only the interstitial space between the nonmelting particles. The porosity in the constant volume model increases as melting takes place until it reaches a maximum value. This results in a higher permeability than in the case of the constant porosity model. Hence, the velocity of the melting front for the constant volume model is greater than that for the constant porosity model. The constant volume model overpredicts the location of the melting front for the 250 μm glass beads. The numerical calculations for the constant porosity model result in the bed reaching its final volume more quickly than observed experimentally.

In Fig. 10, the two different geometric models are compared with the experimental results for the volume fraction of salol at 2000 s for the 450 μm glass beads. This plot illustrates that the constant volume model is more appropriate for the larger glass beads. In this case, the 90 μm salol particles are nearly small enough to occupy interstitial spaces and have a small effect on bed volume as melting occurs.

In many of the materials processing applications mentioned in the Introduction, the particle sizes are much smaller than those examined in this study. For smaller particles, gravity will play a smaller role in bed subsidence when compared to capillary forces. In addition, models that include reaction and/or diffusion between solid and liquid phases, and the entrapment of gases (leading to residual porosity), would be of interest.

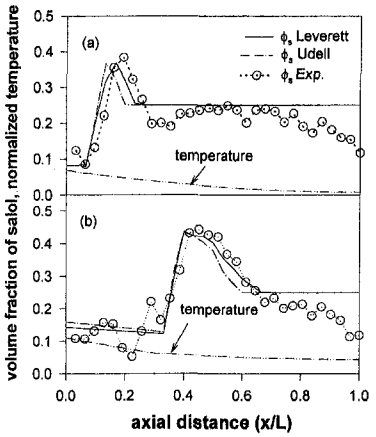

Fig. 7 The effect of capillary pressure function on numerical predictions (d_P = 250 μm, ϕ_s = 0.25, ϕ_g = 0.45, ϵ = 0.3): (*a*) t = 1000 s; (*b*) t = 2000 s

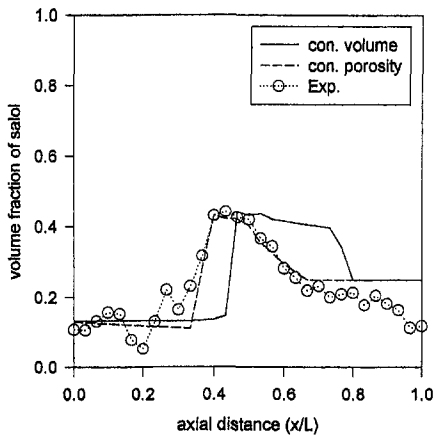

Fig. 9 Numerical predictions using the constant volume model and the constant porosity model compared with experimental results (t = 2000 s, d_P = 250 μm, ϕ_s = 0.25, ϕ_g = 0.45, ϵ = 0.3)

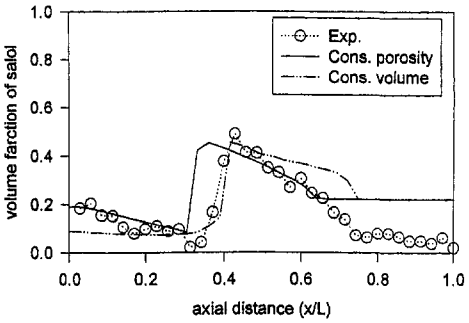

Fig. 10 Numerical predictions using the constant volume model and the constant porosity model compared with experimental results (t = 2000 s, d_P = 450 μm, ϕ_s = 0.25, ϕ_g = 0.45, ϵ = 0.3)

Conclusions

The solid-liquid phase change problem for a two-component packed bed has been investigated numerically and experimentally. Results include measurements and predictions of the redistribution of the melting component and the resulting volume change or subsidence for the bed. The results lead to the following conclusions:

1 The empirical relationships for relative permeability and capillary pressure which are commonly used in the literature appear to yield acceptable results in this situation where effective particle diameter is changing as the melt front progresses through the bed.
2 The constant porosity model predicts the velocity of the melt front and the melting phase distribution near the melt front reasonably well for glass beads of 120 μm, 180 μm, and 250 μm and for 90 μm salol particles. For 450 μm glass beads and 90 μm salol particles, the constant volume model is in better agreement with the experimental data.
3 The constant porosity model overpredicts the bed-height reduction or subsidence compared with the experimental data. However, it is superior to a constant volume model except in the case of the 450 μm beads.
4 The conventional capillary pressure model did not, in all cases, predict accurately the long time distribution of the melting phase. This is probably a combination of the inaccuracy of the model as well as the overprediction of the volume decrease by the constant porosity model.

Acknowledgment

This material is based upon work supported by the National Science Foundation under Grant No. CTS-9016104.

References

Beckermann, C., and Viskanta, R., 1988, "Natural Convection Solid/Liquid Phase Change in Porous Media," *Int. J. Heat Mass Transfer,* Vol. 31, No. 1, pp. 35–46.

Dey, N., and Sekhar, J. A., 1993, "Interface Configuration During the Directional Growth of Salol, 1. Morphology," *Acta Metallurgica. et Materialia,* Vol. 41, pp. 409–424.

Dosanjh, S. S., 1989, "Melting and Refreezing of Porous Media," *Int. J. Heat and Fluid Flow,* Vol. 10, No. 4, pp. 301–310.

International Critical Table of Numerical Data, Physics, Chemistry and Technology, National Research Council of the U.S.A., 1928, McGraw-Hill Book Co. Inc., New York, Vol. 4, pp. 461.

Kaviany, M., 1991, *Principles of Heat Transfer in Porous Media,* Springer-Verlag, New York.

Kline, S. J., and McClintock, F. A., 1953, "Describing Uncertainties in Single-Sample Experiments," *Mechanical Engineering,* ASME, New York, p. 3.

Lawrence, D. M., 1989, "Make Way for Engineered Ceramics," *Design News,* Vol. 45, No. 10, Rogers Pub. Co., Detroit, MI.

Miller, R. D., 1980, "Freezing Phenomena in Soils," *Applications of Soil Physics,* Academic Press, New York, pp. 254–318.

Mughal, M., and Plumb, O. A., 1993, "Thermal Densification of Metal-Ceramic Composites," *Scripta Metallurgica et Materialia,* Vol. 29, pp. 383–388.

Munir, Z. A., and Anselmi-Tamburim, U., 1989, "Self Propagating Exothermic Reactions: the Synthesis of High Temperature Materials by Combustion," *Material Science Reports,* Vol. 3, No. 7, 8, pp. 277–365.

Plumb, O. A., Brown, C. A., and Olmstead, B. A., 1984, "Experimental Measurements of Heat and Mass Transfer During Convective Drying of Southern Pine," *Wood Sci. Tech.,* Vol. 18, pp. 187–204.

Plumb, O. A., 1994, "Convective Melting of Packed Beds," *Int. J. Heat Mass Transfer,* Vol. 37, No. 5, pp. 829–836.

Sahota, M. S., and Pagni, P. J., 1979, "Heat and Mass Transfer in Porous Media Subject to Fires," *Int. J. Heat Mass Transfer,* Vol. 22, pp. 1069–1081.

Mechanical Engineering, *Seasonal Thermal Energy Storage,* 1983, Vol. 105, pp. 28–34.

Udell, K. S., 1985, "Heat Transfer in Porous Media Considering Phase Change and Capillarity—The Heat Pipe Effect," *Int. J. Heat Mass Transfer,* Vol. 28, No. 2, pp. 485–495.

von Rosenberg, D. U., 1969, *Methods for the Numerical Solution of Partial Differential Equations,* American Elsevier Publishing Company, New York.

Voller, V., and Cross, M., 1981, "Accurate Solutions of Moving Boundary Problems Using the Enthalpy Method," *Int. J. Heat Mass Transfer,* Vol. 24, pp. 545–556.

Wang, C. Y., and Beckermann, C., 1993, "A Two-Phase Mixture Model of Liquid-Gas Flow and Heat Transfer in Capillary Porous Media—1. Formulation," *Int. J. Heat Mass Transfer,* Vol. 16, No. 11, pp. 2747–2758.

Weaver, J. A., and Viskanta, R., 1986, "Melting of Frozen, Porous Media Contained in a Horizontal or a Vertical, Cylindrical Capsule," *Int. J. Heat Mass Transfer,* Vol. 29, pp. 1943–1951.

N.-H. Kim
knh0001@lion.inchon.ac.kr
Department of Mechanical Engineering,
University of Inchon,
Inchon, Korea

J.-H. Yun
Korea Academy of Industrial Technology,
Seoul, Korea

R. L. Webb
Department of Mechanical Engineering,
The Pennsylvania State University,
University Park, PA

Heat Transfer and Friction Correlations for Wavy Plate Fin-and-Tube Heat Exchangers

This paper deals with heat exchangers having plate fins of herringbone wave configuration. Correlations are developed to predict the air-side heat transfer coefficient and friction factor as a function of flow conditions and geometric variables of the heat exchanger. Correlations are provided for both staggered and in-line arrays of circular tubes. A multiple regression technique was used to correlate 41 wavy fin geometries by Beecher and Fagan (1987), Wang et al. (1995), and Beecher (1968). For the staggered layout, 92 percent of the heat transfer data are correlated within ±10 percent and 91 percent of the friction data are correlated within ±15 percent.

Introduction

Air cooled, finned-tube heat exchangers have been used for heat exchange between gases and liquids for many years. In forced convection heat transfer between a gas and a liquid, the heat transfer coefficient of the gas is typically 5–20 percent that of the liquid. The use of extended surfaces will reduce the gas-side thermal resistance. However, the resulting gas-side resistance may still exceed that of the liquid. In this case, it will be advantageous to use specially configured extended surfaces which provide increased heat transfer coefficients. Such special geometries may provide heat transfer coefficients 50–150 percent higher than those given by plain extended surfaces.

One of the popular enhanced fin geometries is the wavy fin. It has long been used in fin-tube heat exchangers because of the superior heat transfer performance. The fin geometry is illustrated in Fig. 1. There are two basic variants of the basic wavy fin geometry. They may have a smooth wave curve configuration, or they may have a herringbone wave configuration as illustrated in Fig. 1. The herringbone wave has flat sides.

Goldstein and Sparrow (1976) used a mass transfer technique to measure local and average mass transfer coefficients on a fin-tube model having the herringbone wave configuration. Their test simulated a one-row geometry having 606 fins/m on a 8.53 mm diameter tube. At a Reynolds number (based on fin spacing) of 1000, their measured average mass transfer coefficients were 45 percent higher than a flat fin design of the same basic geometry. They propose that the enhancement results from Goetler vortices that form as the flow passes over the concave wave surfaces. These are counter-rotating vortices which have a corkscrew-like flow pattern. The presence of the Goetler vortices was confirmed from the flow visualization studies by Ali and Ramadhyani (1992) in the corrugated channel.

Heat transfer or friction data on the wavy fin geometry are very limited, and only four studies are known to the authors. They are Beecher and Fagan (1987), Wang et al. (1995), Beecher (1968), and Mirth and Ramadhyani (1994). Of the four studies, the first three had herringbone wave configuration, and the last one had smooth wave configuration. Beecher and Fagan (1987) published heat transfer data for twenty three-row plate fin-and-tube geometries listed in Table 1. Their cores had staggered tube layout. The tests were conducted using a model consisting of a pair of brass plates that were machined to form the fin-channel geometry. The tubes were simulated by cylindrical cross sectional spacers inserted between the plates. The fins were electrically heated, and thermocouples were embedded in the plates to determine the plate surface temperature. The Nusselt number data were presented as Nu_a ($=h_a D_h/k$) versus the Graetz number $\mathrm{Gz} = \mathrm{Re}_h \mathrm{Pr} D_h/L$. The Nu_a was based on the arithmetic mean temperature difference (AMTD) rather than on the log mean temperature difference (LMTD). Beecher and Fagan did not provide pressure drop data. Webb (1990) developed multiple regression correlations of the Beecher and Fagan data. His correlating equations contains Nu_a and Gz.

Wang et al. (1995) recently published data on eighteen wavy fin configurations listed in Table 2. Their cores include both staggered and in-line tubes with one to four rows. Pressure drop data were also presented. They built sample cores, and experiments were conducted in a forced draft wind tunnel. Heat was supplied to the coil by circulating hot water. They presented the heat transfer data in the form of "j" versus Re_D. The Colburn "j" factor was reduced from the raw temperature data using the ϵ-NTU method. Additional pressure drop data on the herringbone wave fin geometry were available from Beecher (1968). His cores had three different fin pattern depths for a fixed fin pattern length $x_f = 4.58$ mm. Table 3 lists the geometry of the cores. The cores had eight rows.

Mirth and Ramadhyani (1994) tested five cores with two different types of wavy fin geometries. Three cores had a smooth continuous wave fin on 13.2 mm diameter tubes with a tube pitch (P_t) of 31.8 mm. The other two cores did not have a continuous wave fin. Instead, the fin had a relatively flat area between each pair of waves. The cores had four or eight rows with $P_t = 38.1$ mm. They developed a correlation from their own data.

Only one correlation is available for the herringbone wave fin configuration (Webb, 1990). His correlation is based on the Beecher and Fagan (1987) data, which is limited to three-row cores. Webb's correlation is given in the form of Nu_a and Gz, which is not as popular as "j" and Re_D. The purpose of this paper is to provide a new heat transfer correlation for the herringbone wave fin configuration. Both the Beecher and Fagan (1987), Wang et al. (1995), and Becher (1968) data are used. The correlation is developed in the form of j and Re_D. A friction correlation is also developed.

Heat Transfer and Friction Data

Beecher and Fagan (1987) tested 20 wavy fin cores. All the cores had a staggered tube configuration. Table 1 summarizes the geometries. They presented the results in the form of Nu_a versus Gz. Thus, it was necessary to manipulate their data in

Contributed by the Heat Transfer Division for publication in the JOURNAL OF HEAT TRANSFER. Manuscript received by the Heat Transfer Division July 25, 1996; revision received February 21, 1997; Keywords: Finned Surfaces, Forced Convection, Heat Exchangers. Associate Technical Editor: T. J. Rabas.

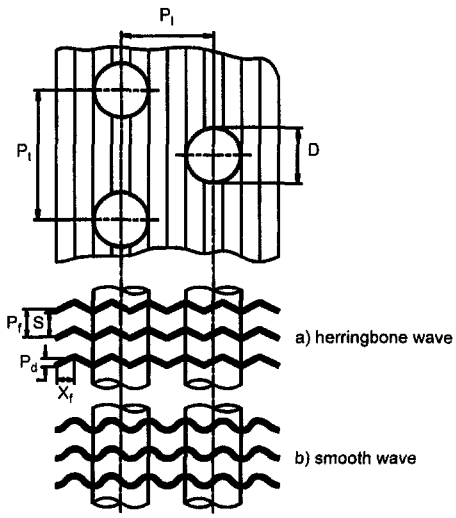

Fig. 1 Typical wavy fin configuration

the form of j versus Re_D. The Nu_a, Gz, Re_h defined by Beecher and Fagan are as follows:

$$\mathrm{Nu}_a = \frac{h_a D_{hv}}{k} \tag{1}$$

$$\mathrm{Gz} = \frac{\mathrm{Re}_h \, \mathrm{Pr} D_{hv}}{L} \tag{2}$$

$$\mathrm{Re}_h = \frac{\rho u_m D_{hv}}{\mu} . \tag{3}$$

The volumetric hydraulic diameter (D_{hv}) used in the equations above is defined as four times the open channel volume divided by the total surface area and is given by

$$D_{hv} = \frac{2s(1-\beta)}{(1-\beta)\sec\theta + 2s\beta/D} \tag{4}$$

where

$$\beta = \frac{\pi D^2}{4 P_t P_l} \tag{5}$$

and

$$\sec\theta = \frac{\sqrt{x_f^2 + p_d^2}}{x_f} . \tag{6}$$

The parameter β is the fraction of the channel volume occupied by the tube. The parameter sec θ accounts for the additional fin area provided by the waves, relative to a flat fin. For flat fins, the wave depth (p_d) is zero and sec θ is unity. The velocity u_m used in the Reynolds number is based on the weighted mean velocity in the actual channel volume, and is defined by

$$u_m = \frac{u_{fr}}{\sigma(1-\beta)} . \tag{7}$$

The contraction ratio (σ) is the fraction of the flow area reduced by the fin thickness, and is defined by

$$\sigma = \frac{s}{s+t} . \tag{8}$$

Note that u_m does not conform to the definitions conventionally employed.

Beecher and Fagan chose to use AMTD. The Nusselt number is traditionally based on the LMTD rather than the AMTD. The AMTD-based Nusselt number (Nu_a) may be converted to LMTD-based Nusselt number (Nu_l) using the following relationship (Beecher and Fagan, 1987).

$$\mathrm{Nu}_l = \frac{\mathrm{Gz}}{4} \ln \frac{1 + 2\mathrm{Nu}_a/\mathrm{Gz}}{1 - 2\mathrm{Nu}_a/\mathrm{Gz}} . \tag{9}$$

The present authors converted the Beecher and Fagan data to the j versus Re_D format. For a given Gz number, Re_D is obtained from the following equations:

$$\mathrm{Re}_D = \mathrm{Re}_h \frac{D}{D_{hv}} \frac{u_{\max}}{u_m} \tag{10}$$

$$\mathrm{Re}_h = \frac{\mathrm{Gz} L}{\mathrm{Pr} D_{hv}} . \tag{11}$$

Nomenclature

A = air-side surface area (fins and tubes), m^2
A_c = minimum flow area, m^2
$A_{c,t}$ = minimum flow area for tube bank, m^2
A_f = surface area of fins, m^2
D = tube outer diameter (including collar), m
D_h = hydraulic diameter ($=4LA_C/A$), m
D_{hv} = volumetric hydraulic diameter given by Eq. (4), m
f = fanning friction factor, dimensionless
f_f = friction factor associated with fin area, dimensionless
f_t = friction factor associated with tube area, dimensionless
Gz = Graetz number defined by Eq. (2), dimensionless
h_a = heat transfer coefficient based on AMTD, W/m^2K
h_l = heat transfer coefficient based on LMTD, W/m^2K
j = Colburn j factor
k = thermal conductivity, W/mK
K_c = entrance loss coefficient, dimensionless
K_e = exit loss coefficient, dimensionless
L = heat exchanger flow length, m
Nu_a = Nusselt number based on AMTD ($=h_a D_{hv}/k$), dimensionless
Nu_l = Nusselt number based on LMTD ($=h_l D_{hv}/k$) (dimensionless)
p_d = fin pattern depth, peak-to-valley excluding fin thickness, m
P_l = tube spacing in air flow direction, m
Pr = Prandtl number, dimensionless
P_t = tube spacing normal to flow, m
Re_D = Reynolds number based on D ($=\rho u_{\max} D/\mu$)
Re_h = Reynolds number based on u_m and D_{hv} ($=\rho u_m D_{hv}/\mu$)
s = spacing between adjacent fins, m
t = fin thickness, m
u_{fr} = frontal velocity, m/s
u_m = mean velocity defined by Eq. (7), m/s
$u_{\max}$ = maximum velocity based on A_C, m/s
x_f = projected fin pattern length for one-half wave length, m
β = geometric parameter defined by Eq. (5), dimensionless
ΔP = pressure drop across a heat exchanger, Pa
ΔP_t = pressure drop assignable to bare tube bank, Pa
ΔP_f = pressure drop assignable to fin area, Pa
θ = geometric parameters defined by Eq. (6), dimensionless
μ = dynamic viscosity, kg/m s
σ = fin contraction ratio defined by Eq. (8), dimensionless

Table 1 Geometry of sample configurations tested by Beecher and Fagan (1987)

No.	In-line or staggered	P_t (mm)	P_l (mm)	D (mm)	s (mm)	x_f (mm)	p_d (mm)	N
1	S	25.4	22.0	9.53	1.96	3.67	0.97	3
2	S	31.8	27.5	9.53	1.96	4.58	0.97	3
3	S	31.8	27.5	12.7	1.96	4.58	0.97	3
4	S	25.4	22.0	12.7	1.96	3.67	0.97	3
5	S	31.8	27.5	12.7	4.09	4.58	1.57	3
6	S	31.8	27.5	12.7	2.79	4.58	1.57	3
7	S	31.8	27.5	12.7	1.96	4.58	1.57	3
8	S	31.8	27.5	12.7	4.09	4.58	0.97	3
9	S	31.8	27.5	12.7	2.79	4.58	0.97	3
10	S	31.8	27.5	12.7	4.09	4.58	3.18	3
11	S	31.8	27.5	12.7	1.96	4.58	3.18	3
12	S	25.4	22.0	12.7	2.39	5.50	0.97	3
13	S	25.4	22.0	12.7	1.96	5.50	0.97	3
14	S	25.4	22.0	12.7	2.39	3.67	0.97	3
15	S	31.8	27.5	12.7	1.96	4.58	0.46	3
16	S	31.8	27.5	12.7	1.96	4.58	0.71	3
17	S	31.8	27.5	12.7	1.96	4.58	1.24	3
18	S	31.8	27.5	12.7	1.96	4.58	2.36	3
19	S	25.4	22.0	12.7	1.96	2.76	0.97	3
20	S	25.4	22.0	12.7	1.96	3.67	0.97	3

Here, u_{max} is the flow velocity at the minimum flow area. The j factor is defined as

$$j = \frac{\mathrm{Nu}_l}{\mathrm{Re}_D \, \mathrm{Pr}^{1/3}} \cdot \frac{D}{D_{hy}}. \tag{12}$$

The Nu_l is obtained from Eq. (9) for a given Gz, Nu_a.

Wang et al. (1995) tested 18 wavy fin cores listed in Table 2. Their cores include both staggered and in-line tubes with one to four rows. Their heat transfer data are provided in the form of j versus Re_D. Pressure drop data are also presented. Additional pressure drop data are provided by Beecher (1968).

Staggered Tube Layout

Heat Transfer Correlation. Heat transfer correlations for the staggered tube layout were developed based on the manipulated Beecher and Fagan data and the Wang et al. staggered tube data. The Beecher and Fagan data are limited to three-row cores while the Wang et al. data include one to four rows.

Table 2 Geometry of sample configurations tested by Wang et al. (1995)

No.	In-line or staggered	P_t (mm)	P_l (mm)	D (mm)	s (mm)	x_f (mm)	p_d (mm)	N
1	S	25.4	19.05	10.3	3.41	4.76	1.38	1
2	S	25.4	19.05	10.3	3.41	4.76	1.38	2
3	S	25.4	19.05	10.3	3.41	4.76	1.38	3
4	S	25.4	19.05	10.3	3.41	4.76	1.38	4
5	S	25.4	19.05	10.3	2.22	4.76	1.38	1
6	S	25.4	19.05	10.3	2.22	4.76	1.38	2
7	S	25.4	19.05	10.3	2.22	4.76	1.38	3
8	S	25.4	19.05	10.3	2.22	4.76	1.38	4
9	S	25.4	19.05	10.3	1.57	4.76	1.38	1
10	S	25.4	19.05	10.3	1.57	4.76	1.38	2
11	S	25.4	19.05	10.3	1.57	4.76	1.38	3
12	S	25.4	19.05	10.3	1.57	4.76	1.38	4
13	I	29.4	29.4	10.46	4.6	7.35	1.8	2
14	I	29.4	29.4	10.46	4.6	7.35	1.8	3
15	I	29.4	29.4	10.46	4.6	7.35	1.8	4
16	I	29.4	29.4	10.46	3.33	7.35	1.8	2
17	I	29.4	29.4	10.46	3.33	7.35	1.8	3
18	I	29.4	29.4	10.46	3.33	7.35	1.8	4

Table 3 Geometry of sample configurations tested by Beecher (1968)

No.	In-line or staggered	P_t (mm)	P_l (mm)	D (mm)	s (mm)	x_f (mm)	p_d (mm)	N
1	S	31.8	27.5	12.7	2.79	4.58	0.81	8
2	S	31.8	27.5	12.7	1.96	4.58	0.81	8
3	S	31.8	27.5	12.7	1.42	4.58	0.81	8
4	S	31.8	27.5	12.7	2.79	4.58	1.08	8
5	S	31.8	27.5	12.7	1.96	4.58	1.08	8
6	S	31.8	27.5	12.7	1.42	4.58	1.08	8
7	S	31.8	27.5	12.7	2.79	4.58	1.42	8
8	S	31.8	27.5	12.7	1.96	4.58	1.42	8
9	S	31.8	27.5	12.7	1.42	4.58	1.42	8

Inspection of the Wang et al. data showed that, for $Re_D \geq 1000$, the j factor increases as the row number increases. Three and four row data were approximately the same. For $Re_D < 1000$, the trend was reversed. Thus, the correlation was developed in two steps. The first step developed a correlation based on Beecher and Fagan's three-row data and Wang et al.'s three and four row data. This correlation is applicable to cores with larger than three rows. Then, a multiplier was developed based on Wang et al.'s one and two row data to account for the row effect. This procedure was used by Gray and Webb (1986) to develop their plain fin correlation.

A commercially available software package was used to perform a multiple linear regression analysis, which provided the best fit of the data. The accuracy of the correlation was evaluated using the "R-squared" value, which is defined as the fraction of the variability in the logarithm of the dependent variable (e.g., j-factor) that can be accounted for by means of the linear regression equation using the dimensionless geometric variables. The objective is to select dimensionless parameters that give the highest R-square value. This was done by trial and error. This method of correlating the data is strictly empirical and requires knowledge of the geometric and flow parameters that affect the heat transfer coefficient. The potentially significant variables are: flow variables (Re and Pr), tube bank geometric variables (D, P_t, P_l, N and tube layout), and fin geometry variables (s, x_f, p_d). Several different groupings of the dimensionless variables were tried in development of the correlation. The set finally chosen was based on the groupings that provided the best correlation.

When several data sets are available, it is important to check the consistency between the data set. One way of checking the consistency is to develop a correlation from one data set, and predict other data using the correlation. For the wavy fin correlation, two data sets—Beecher and Fagan, Wang et al.—are available. A heat transfer correlation was first developed using the Beecher and Fagan data. Then, Wang et al.'s data (three and four rows) were predicted by the correlation. An error plot is shown in Fig. 2. Most of Wang et al.'s data are predicted within ±10 percent. This suggests that the two data sets are consistent in spite of the distinctively different test methods involved. Beecher and Fagan simulated the fin-and-tube geometry by a pair of machined brass plates and spacers while Wang et al. tested sample cores. Several data points, which are 20 percent to 30 percent overpredicted, correspond to cores 11 and 12 in Table 2. Cores 11 and 12 have a relatively narrow interfin spacing ($s/x_f = 0.33$), which is outside of the applicable range ($0.36 \leq s/x_f \leq 0.89$) of the correlation based on Beecher and Fagan data. Corrugated channel is known to enhance the heat transfer by streamwise vortices formed from the concave wave surfaces as well as by spanwise eddies shed from the peaks

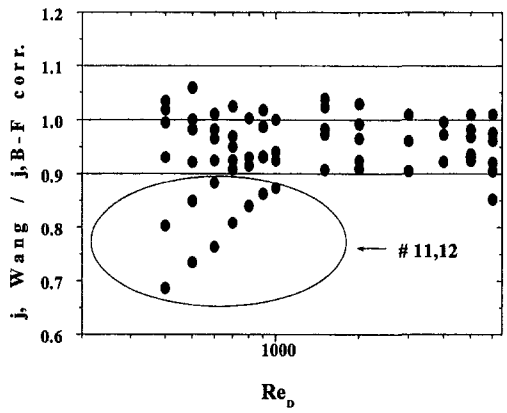

Fig. 2 Wang et al. (1995) three and four row data predicted by the correlation developed based on Beecher and Fagan (1987) data

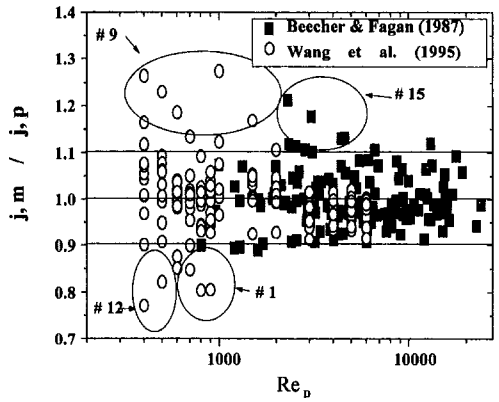

Fig. 3 Error plot of the "j" factor correlation (Eq. (13)) developed for the staggered tube layout

of corrugated facets. Particularly at low Reynolds numbers, spanwise vortices are important to the heat transfer enhancement. In a narrow interfin spacing spanwise vortices may not form, as was shown by Ali and Ramadhyani (1992). They claimed that, in a narrow channel, vorticity generated at the channel walls is convected and diffused sufficiently rapidly to preclude the formation of a concentrated roll-up vortex. This may explain the j-factor overprediction for cores 11 and 12 at low Reynolds numbers.

A correlation was then developed using both sets of data. The heat transfer correlation based on both data sets is

$$j_3 = 0.394\ Re_D^{-0.357}\left(\frac{P_t}{P_l}\right)^{-0.272}\left(\frac{s}{D}\right)^{-0.205}\left(\frac{x_f}{p_d}\right)^{-0.558}\left(\frac{p_d}{s}\right)^{-0.133} \quad (N \geq 3) \quad (13)$$

$$j_N = j_3(0.978 - 0.010N) \quad (Re_D \geq 1000,\ N = 1, 2)$$

$$j_N = j_3(1.350 - 0.162N) \quad (Re_D < 1000,\ N = 1, 2). \quad (14)$$

Figure 3 shows an error plot of the wavy fin heat transfer data, which include 32 wavy fin geometries. The above correlation predicts 92 percent of the data within ±10 percent. Several data points of Sample 9 of Wang et al. are approximately 20 percent underpredicted and several data points of Sample 1 are approximately 15 percent overpredicted. These samples correspond to one row configuration at low Reynolds numbers. Wang et al. reduced their data by the ϵ-NTU method. The experimental uncertainty gets larger for small row configuration at low Reynolds numbers. Wang et al. reported that the uncertainty on the j factor ranged 3.8 percent to 7.2 percent. Several data points of sample 12 of Wang et al. are approximately 20 percent overpredicted. The reason may be attributed to the narrow interfin spacing of Sample 12, which yields lower heat transfer coefficients at low Reynolds numbers. Several data points of Sample 15 of Beecher and Fagan are approximately 15 percent underpredicted. This sample has the smallest wave depth ($p_d = 0.46$ mm). The wave depth is so small that it may act as a "roughness" rather than altering the main flow direction. Surface roughening is not an effective way of enhancing the heat transfer when low Reynolds number flow is involved (Webb, 1994). Thus, the correlation may overpredict the data for Sample 15. Table 4 summarizes the limitations of the heat transfer correlation.

Goldstein and Sparrow (1976) measured the mass transfer coefficients of a one-row wavy fin sample with 606 fins per meter on 8.53 mm diameter tubes. Their model had $s/D = 0.193$, $x_f/p_d = 2.6$, and $p_d/s = 1.98$. The mass transfer coefficients were converted to heat transfer coefficients by invoking the heat and mass transfer analogy. Figure 4 shows the

Table 4 Limitations on correlations

Staggered Tube Layout–Heat Transfer Correlation
$500 \le \mathrm{Re}_D \le 6000, \quad 1 \le N \le 4,$
$1.16 \le \frac{P_t}{P_l} \le 1.33, \quad 0.15 \le \frac{s}{D} \le 0.33$
$1.44 \le \frac{x_f}{p_d} \le 10.0, \quad 0.23 \le \frac{p_d}{s} \le 1.21$
Staggered Tube Layout–Friction Correlation
$500 \le \mathrm{Re}_D \le 9000, \quad 1 \le N \le 8, \quad 1.16 \le \frac{P_t}{P_l} \le 1.33,$
$0.11 \le \frac{s}{D} \le 0.33, \quad 3.23 \le \frac{x_f}{p_d} \le 5.65, \quad 0.29 \le \frac{p_d}{s} \le 1.0$
In-line Tube Layout–Heat Transfer and Friction Correlations
$500 \le \mathrm{Re}_D \le 6000, \quad 1 \le N \le 4, \quad \frac{P_t}{P_l} = 1.0,$
$0.318 \le \frac{s}{D} \le 0.440, \quad \frac{x_f}{p_d} = 4.083, \quad 0.391 \le \frac{p_d}{s} \le 0.541$
$D = 10.46$ mm, $t = 0.2$ mm, $P_t = 29.4$ mm, $P_l = 29.4$ mm

Goldstein and Sparrow data compared with the predictions by Eqs. (13) and (14). For the Schmidt number exponent, a value of $\frac{1}{3}$ was used. Figure 4 shows that Goldstein and Sparrow's data are approximately 25 percent below the predicted value, based on Eqs. (13) and (14). In the experiment by Goldstein and Sparrow, the tubes were simulated by aluminum discs, which apparently did not participate in the mass transfer. In addition, the mass transfer from the surface results in a "boundary layer blowing" phenomena, which leads to lower heat transfer coefficients. This may partly explain the lower experimental values.

Friction Correlation. To date, the only correlation available for prediction of the friction factor of the wavy fin is by Mirth and Ramadhyani (1994). However, their correlation was developed based on their own data of the Fig. 1 smooth wave configuration. No friction correlations are reported for the herringbone geometry. A friction correlation applicable to the herringbone fin configuration was developed using the Wang et al. (1995) and Beecher (1968) data.

The friction correlation is based on a superposition model as discussed by Gray and Webb (1986). The total pressure drop ΔP is written as

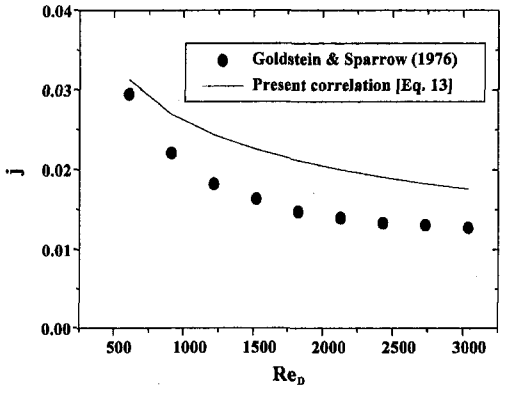

Fig. 4 Goldstein and Sparrow (1976) mass transfer data compared with the present correlation (Eq. (13))

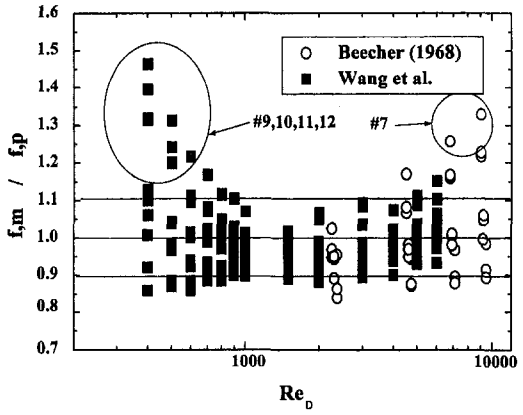

Fig. 5 Error plot of the friction factor correlation (Eq. (20)) developed for the staggered tube layout

$$\Delta P = \Delta P_f + \Delta P_t \tag{15}$$

where ΔP_t is the pressure drop component due to the drag force on the tubes, and ΔP_f is the pressure drop component due to the friction on the fins. One may write equations for ΔP_t and ΔP_f as

$$\Delta P = f \frac{A}{A_c} \frac{G_c^2}{2\rho} \tag{16}$$

$$\Delta P_f = f_f \frac{A_f}{A_c} \frac{G_c^2}{2r} \tag{17}$$

$$\Delta P_t = f_t \frac{A_t}{A_{c,t}} \frac{G_c^2}{2\rho}. \tag{18}$$

Some authors (e.g., Wang et al. (1995)) report friction data in a form different from Eq. (16). Their friction factor includes the entrance and exit loss coefficients K_c and K_e, as described by Kays and London (1984). It is estimated, however, that the difference between the two methods would be minor, as is evident from Fig. 5.3 of Kays and London (1984). Substituting Eqs. (16)–(18) into (15), and solving for f gives,

$$f = f_f \frac{A_f}{A} + f_t \left(1 - \frac{A_f}{A}\right)\left(1 - \frac{t}{p_f}\right). \tag{19}$$

Using f_t, as given by Zukauskas and Ulinskas (1983), Eq. (19) was solved for f_f. Zukauskas and Ulinskas provided equation from of the friction factor correlation across the tube bank. Then, the multiple regression method was used to develop the correlation for f_f. The Zukauskas and Ulinskas (1983) correlation is provided in the Appendix. The resulting correlation is given by

$$f_f = 4.467\ \mathrm{Re}_D^{-0.423} \left(\frac{P_t}{P_l}\right)^{-1.08} \left(\frac{s}{D}\right)^{-0.0339} \left(\frac{x_f}{p_d}\right)^{-0.672}. \tag{20}$$

Eq. (20) does not contain the dimensionless variables p_d/s. The effect of p_d/s was correlated by other variables such as Re_D, P_t/P_l, s/D and x_f/p_d. The friction factor of the finned tube heat exchanger is obtained by substituting Eq. (20) and Zukauskas's f_t into Eq. (19). Figure 5 shows the ability of the correlation to predict the heat exchanger friction factor. The figure shows that 82 percent of the data are predicted within ±10 percent, and 91 percent of the data are predicted within ±15 percent. Some data points are somewhat underpredicted. They correspond to the fin configuration samples 9, 10, 11, 12 in Table 2 and the fin configuration 7 in Table 3. Samples 9, 10, 11, 12 have the smallest fin pitch (p_f = 1.69 mm) and Sample 7 has relatively large fin pitch (p_f = 2.95 mm). For

both cases, the fin pattern (x_f and p_d) is approximately the same. It is not clear why the underprediction occurs for the small fin pitch at low Reynolds numbers while it occurs for the large fin pitch at high Reynolds numbers. Sparrow and Comb (1983) showed that the pressure loss of the corrugated duct drastically increased (more than tripled) as the interwall spacing was increased (1.5 times). The Reynolds numbers associated with their test were very high ($Re_{Dh} > 2000$). Limitations of the heat transfer and friction correlations are given in Table 4.

The present correlations are applicable to fins of herringbone wave configuration. Another variant is the smooth wave configuration reported by Mirth and Ramadhyani (1994). They tested two different smooth wavy fin geometries—one with continuous wave, the other with flat area between each pair of waves. The continuous smooth wavy fins shown in Fig. 1 correspond to the herringbone wavy fins considered in this study. The four row continuous smooth wavy fin data of Mirth and Ramadhyani were predicted by the present correlations (Eqs. (13), (14) and (20)). The heat transfer data were approximately 45 percent below the predicted values, and the friction data were approximately 75 percent below the predicted values. Sparrow and Hossfeld (1984) report that rounding of the protruding edges decreases the heat transfer coefficient and the friction factor in a corrugated duct. Hence, it appears that the herringbone pattern may yield substantially higher heat transfer coefficient than the smooth wave. However, the j/f ratio of the smooth wave may be much higher.

In-Line Tube Layout

Wang et al. (1995) also provides heat transfer and friction data for the wavy fin, in-line tube layout. The tested configurations are given in Table 2. Different from the staggered layout, the in-line data showed a negligible effect of row number at high Reynolds numbers ($Re_D \geq 2000$). At $Re_D < 2000$, the heat transfer coefficient decreased with increasing number of rows. Thus, a row effect multiplier was developed only for $Re_D < 2000$. The heat transfer correlation developed is

$$j = 0.37 Re_D^{-0.186} \left(\frac{s}{D}\right)^{-0.045} \quad (Re_D \geq 2000\ N = 2, 3, 4) \quad (21)$$

$$j_4 = 0.238\ Re_D^{-0.528} \left(\frac{s}{D}\right)^{-0.635} \quad (Re < 2000, N = 4)$$

$$\frac{j_N}{j_4} = 1.350 - 0.097N \quad (Re < 2000, N = 2, 3). \quad (22)$$

Eq. (21) does not contain the dimensionless variables x_f/p_d and p_d/s. The x_f/p_d was fixed at 4.083 in the Wang et al.'s data,

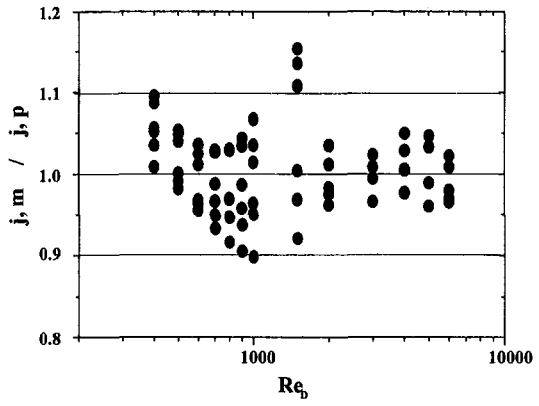

Fig. 6 Error plot of the "j" factor correlation (Eq. (21)) developed for the in-line tube layout

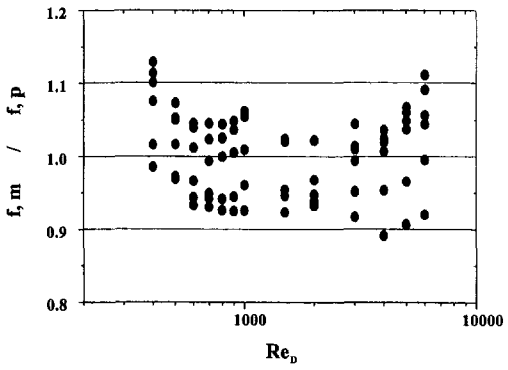

Fig. 7 Error plot of the friction factor correlation (Eq. (22)) developed for the in-line tube layout

and p_d/s was highly correlated by other variables. Figure 6 shows the ability of the correlation to predict the heat transfer coefficient. The figure shows that 96 percent of the data are predicted within ±10 percent. Limitations of the correlation are listed in Table 4.

The configuration of the tube layout may influence the heat transfer coefficient of wavy fin-and-tube heat exchangers. The heat transfer data of the in-line configuration were predicted by the staggered tube correlation (Eqs. (13) and (14)). The in-line heat transfer data were approximately 35 percent below the staggered tube correlation, which implies that the staggered configuration may yield much higher heat transfer coefficients than the in-line configuration. This result is in accordance with the behavior of plain finned tube banks. For plain circular finned tubes, Brauer (1964) obtained approximately 100 percent higher heat transfer coefficient for the staggered tube layout than that for the in-line tube layout. He argues that bypass effects in in-line tube arrangement are responsible for the poor performance. Note that the P_t/P_l value of the in-line cores ($P_t/P_l = 1.0$) is outside of the applicable range of the staggered tube correlation ($1.154 \leq P_t/P_l \leq 1.333$). The friction correlation was developed following the same procedure as was used for the staggered tube layout. The final correlation for f_f is

$$f_f = 0.571\ Re_D^{-0.601} \left(\frac{s}{D}\right)^{-0.82}. \quad (23)$$

Again, Eq. (23) does not contain the variable x_f/p_d because it was fixed at 4.083. Eq. (23) was developed assuming Jakob's (1938) bare tube bank correlation for f_t. Although Zukauskas's correlation is the state of the art, his correlation is limited to $P_t/D = 2.5$. Wang et al's P_t/D for in-line layout was 2.81. Jakob's correlation extends to $P_t/D = 3.0$. Jakob's correlation is provided in the Appendix. Figure 7 shows the ability of the correlation to predict the heat exchanger friction factor. The figure shows that 95 percent of the data are predicted within ±10 percent. Limitations of the correlation are listed in Table 4.

The configuration of the tube layout may also influence the friction factor of wavy fin-and-tube heat exchangers. The friction data of the in-line cores were compared with the friction factor of the corresponding staggered cores, which was obtained by substituting Eq. (20) and Jakob's f_t into Eq. (19). The in-line friction data were approximately 66 percent below the staggered tube values. Note that the in-line heat transfer data were approximately 35 percent below the staggered tube values. Again, the P_t/P_l value of the in-line cores is slightly outside of the applicable range of the staggered tube correlation. Figure 8 shows typical results. The j and f factor of in-line Sample 17 were compared with the staggered correlations (Eqs. (13) and (20)).

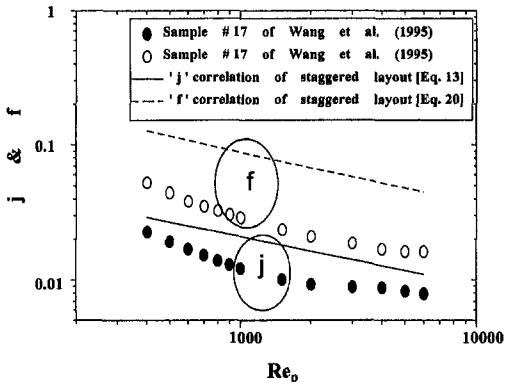

Fig. 8 Typical Wang et al. (1995) in-line data compared with staggered geometry correlations (Eqs. (13) and (20))

Conclusions

1 Air-side heat transfer and friction correlations were developed for plate-finned tube geometries of the herringbone wave configuration. Correlations encompass both staggered and in-line layout. Limitations on the correlations are provided in Table 4.
2 For the staggered tube layout, 92 percent of the heat transfer data are correlated within ±10 percent by Eq. (13), and 91 percent of the friction data are correlated within ±15 percent by Eq. (20).
3 The heat transfer coefficient and friction factor correlation for the in-line tube layout were also developed (Eqs. (21) and (23)). The correlations do not account for the effect of the wave geometry parameters x_f and p_d. This is because only one value of x_f/p_d was tested. More data are needed to determine the effect of the wave geometry parameters.
4 The herringbone pattern may yield a substantially higher heat transfer coefficient as compared to the smooth wave pattern. However, the j/f ratio of the smooth wave geometry may be much higher.
5 Staggered tube layout may yield a higher heat transfer coefficient as compared to the in-line layout. However, the j/f ratio of the in-line geometry may be higher.

References

Ali, M. M., and Ramadhyani, S., 1992, "Experiments on Convective Heat Transfer in Corrugated Channels," *Experimental Heat Transfer,* Vol. 5, pp. 175–193.

Beecher, D. T., 1968, "The Effects of Pattern Depth on the Performance of a Typical Air Conditioning Division Fin Tube Heat Exchanger," Westinghouse Research Lab Report 68-ID8-HEXDE-RI.

Beecher, D. T., and Fagan, T. J., 1987, "Effects of Fin Pattern on the Air-Side Heat Transfer Coefficients in Plate Finned-Tube Heat Exchangers," *ASHRAE Trans.,* Vol. 93, Pt. 2, pp. 1961–1984.

Brauer, H., 1964, "Compact Heat Exchangers," *Chemical Engineering Progress,* London, Vol. 45, No. 8, pp. 451–460.

Goldstein, L., and Sparrow, E. M., 1976, "Experiments on the Transfer Characteristics of a Corrugated Fin and Tube Heat Exchanger Configuration," ASME JOURNAL OF HEAT TRANSFER, Vol. 98, pp. 26–34.

Gray, D. L., and Webb, R. L., 1986, "Heat Transfer and Friction Correlations for Plate Fin—Tube Heat Exchangers Having Plain Fins," *Proceedings of the 9th International Heat Transfer Conference,* San Francisco, pp. 2745–2750.

Jacob, M., 1938, "Heat Transfer and Flow Resistance in Cross Flow of Gases over Tube Banks," *Trans. ASME,* Vol. 60, pp. 384.

Kays, W. M., and London, A. L., 1984, *Compact Heat Exchangers,* 3rd ed., McGraw-Hill Book Co., Inc., New York.

Mirth, D. R., and Ramadhyani, S., 1994, "Correlations for Predicting the Air-Side Nusselt Numbers and Friction Factors in Chilled Water Cooling Coils," *Experimental Heat Transfer,* Vol. 7, pp. 143–162.

Sparrow, E. M., and Comb, J. W., 1983, "Effect of Interwall Spacing and Fluid Flow Inlet Condition on a Corrugated-Wall Heat Exchanger," *Int. J. Heat Mass Trans.,* Vol. 26, No. 7, pp. 993–1005.

Sparrow, E. M., and Hossfeld, L. M., 1984, "Effect of Rounding of Protruding Edges on Heat Transfer and Pressure Drop in a Duct," *Int. J. Heat Mass Trans.,* Vol. 27, No. 10, pp. 1715–1723.

Wang, C. C., Fu, W. L., and Chang, C. T., 1995, "Heat Transfer and Friction Characteristics of Typical Wavy Fin-and-Tube Heat Exchangers," submitted to Exp. Thermal Fluid Sci.

Webb, R. L., 1990, "Air-Side Heat Transfer Correlations for Flat and Wavy Plate Fin-and-Tube Geometries," *ASHRAE Trans.,* Vol. 96, Pt. 2, pp. 445–449.

Webb, R. L., 1994, *Principles of Enhanced Heat Transfer,* John Wiley & Sons, Inc., New York.

Zukauskas, A., and Ulinskas R., 1983, "Banks of Plain and Finned Tubes," chap. 2.2.4, in *Heat Exchanger Design Handbook,* Vol. 2, pp. 72–80, Hemisphere Publishing Corp., Bristol, PA.

APPENDIX

Zukauskas and Ulinskas (1983) Correlation

Zukauskas and Ulinskas provided the tube bank friction factor equation for both in-line and staggered layout. They used the term Eu_N for the friction factor, which is related with the tube friction factor f_t as follows:

$$Eu_N = f_t \frac{A_t}{A_{c,t}} N. \tag{A1}$$

Here, Eu_N is the average friction factor for the first N tube rows. Eu_N is different from Eu which is the friction factor for large number of rows. Zukauskas and Ulinskas provided the following relationship for Eu_N.

$$Eu_N = K_N Eu \quad \text{and} \quad K_N = \frac{1}{N} \sum_{N=1}^{N} C_N \tag{A2}$$

Listed below are the C_N equations for the staggered layout.

For $\mathrm{Re}_D = 10$,

$$C_N = 1.065 - \frac{0.180}{N - 0.297} \quad C_N = 1, N \geq 3. \tag{A3}$$

For $\mathrm{Re}_D = 10^2$,

$$C_N = 1.798 - \frac{3.497}{N + 1.273} \quad C_N = 1, N \geq 4. \tag{A4}$$

For $\mathrm{Re}_D = 10^3$,

$$C_N = 1.149 - \frac{0.411}{N - 0.412} \quad C_N = 1, N \geq 3. \tag{A5}$$

For $\mathrm{Re}_D = 10^4$,

$$C_N = 0.924 + \frac{0.269}{N + 0.143} \quad C_N = 1, N \geq 3. \tag{A6}$$

For $\mathrm{Re}_D = 10^5$ and 10^6,

$$C_N = 0.62 + \frac{1.467}{N + 0.667} \quad C_N = 1, N \geq 4. \tag{A7}$$

The equations for Eu are

For $P_t/D = 1.25$, $3 < \mathrm{Re}_D < 10^3$:

$$\frac{Eu}{C_g} = 0.795 + \frac{0.247 \times 10^3}{\mathrm{Re}_D} + \frac{0.335 \times 10^3}{\mathrm{Re}_D^2} - \frac{0.155 \times 10^4}{\mathrm{Re}_D^3} + \frac{0.241 \times 10^4}{\mathrm{Re}_D^4}. \tag{A8}$$

For $P_t/D = 1.25$, $10^3 < \mathrm{Re}_D < 2 \times 10^6$:

$$\frac{Eu}{C_g} = 0.245 + \frac{0.339 \times 10^4}{\mathrm{Re}_D} - \frac{0.984 \times 10^7}{\mathrm{Re}_D^2} + \frac{0.132 \times 10^{11}}{\mathrm{Re}_D^3} - \frac{0.599 \times 10^{13}}{\mathrm{Re}_D^4}. \tag{A9}$$

For $P_t/D = 1.5$, $3 < \mathrm{Re}_D < 10^3$:

$$\frac{Eu}{C_g} = 0.683 + \frac{0.111 \times 10^3}{\mathrm{Re}_D} - \frac{0.973 \times 10^2}{\mathrm{Re}_D^2} + \frac{0.426 \times 10^3}{\mathrm{Re}_D^3} - \frac{0.574 \times 10^3}{\mathrm{Re}_D^4}. \quad \text{(A10)}$$

For $P_t/D = 1.5$, $10^3 < \mathrm{Re}_D < 2 \times 10^6$:

$$\frac{Eu}{C_g} = 0.203 + \frac{0.248 \times 10^4}{\mathrm{Re}_D} - \frac{0.758 \times 10^7}{\mathrm{Re}_D^2} + \frac{0.104 \times 10^{11}}{\mathrm{Re}_D^3} - \frac{0.482 \times 10^{13}}{\mathrm{Re}_D^4}. \quad \text{(A11)}$$

For $P_t/D = 2.0$, $7 < \mathrm{Re}_D < 10^2$:

$$\frac{Eu}{C_g} = 0.713 + \frac{0.448 \times 10^2}{\mathrm{Re}_D} - \frac{0.126 \times 10^3}{\mathrm{Re}_D^2} - \frac{0.582 \times 10^3}{\mathrm{Re}_D^3}. \quad \text{(A12)}$$

For $P_t/D = 2.0$, $10^2 < \mathrm{Re}_D < 10^4$:

$$\frac{Eu}{C_g} = 0.343 + \frac{0.303 \times 10^3}{\mathrm{Re}_D} - \frac{0.717 \times 10^5}{\mathrm{Re}_D^2} + \frac{0.88 \times 10^7}{\mathrm{Re}_D^3} - \frac{0.38 \times 10^9}{\mathrm{Re}_D^4}. \quad \text{(A13)}$$

For $P_t/D = 2.0$, $10^4 < \mathrm{Re}_D < 2 \times 10^6$:

$$\frac{Eu}{C_g} = 0.162 + \frac{0.181 \times 10^4}{\mathrm{Re}_D} + \frac{0.792 \times 10^8}{\mathrm{Re}_D^2} - \frac{0.165 \times 10^{13}}{\mathrm{Re}_D^3} + \frac{0.872 \times 10^{16}}{\mathrm{Re}_D^4}. \quad \text{(A14)}$$

For $P_t/D = 2.5$, $10^2 < \mathrm{Re}_D < 5 \times 10^3$:

$$\frac{Eu}{C_g} = 0.33 + \frac{0.989 \times 10^2}{\mathrm{Re}_D} - \frac{0.148 \times 10^5}{\mathrm{Re}_D^2} + \frac{0.192 \times 10^7}{\mathrm{Re}_D^3} - \frac{0.862 \times 10^8}{\mathrm{Re}_D^4}. \quad \text{(A15)}$$

For $P_t/D = 2.5$, $5 \times 10^3 < \mathrm{Re}_D < 2 \times 10^6$:

$$\frac{Eu}{C_g} = 0.119 + \frac{0.498 \times 10^4}{\mathrm{Re}_D} - \frac{0.507 \times 10^8}{\mathrm{Re}_D^2} + \frac{0.251 \times 10^{12}}{\mathrm{Re}_D^3} - \frac{0.463 \times 10^{15}}{\mathrm{Re}_D^4}. \quad \text{(A16)}$$

In the above equation, "C_g" is the geometry factor, which depends on the transverse to longitudinal pitch ratio (P_t/P_l). For an equilateral triangular array, $C_g = 1$. For other geometries, Zukauskas and Ulinskas proposed the following equations:

For $0.5 < P_t/P_l < 1.2$, $\mathrm{Re}_D = 10^3$:

$$C_g = Z^{-0.048} \quad \text{where } Z = P_t/P_l. \quad \text{(A17)}$$

For $0.45 < P_t/P_l < 3.5$, $\mathrm{Re}_D = 10^4$:

$$C_g = 1.28 - \frac{0.708}{Z} + \frac{0.55}{Z^2} - \frac{0.113}{Z^3}. \quad \text{(A18)}$$

For $0.45 < P_t/P_l < 3.5$, $\mathrm{Re}_D = 10^5$ and $0.45 < P_t/P_l < 1.6$, $\mathrm{Re}_D = 10^6$:

$$C_g = 2.016 - 1.675Z + 0.948Z^2 - 0.234Z^3 + 0.021Z^4. \quad \text{(A19)}$$

For $1.25 < P_t/P_l < 3.5$, $\mathrm{Re}_D = 10^2$:

$$C_g = 0.93Z^{0.48}. \quad \text{(A20)}$$

For $1.25 < P_t/P_l < 3.5$, $\mathrm{Re}_D = 10^3$:

$$C_g = 0.951Z^{0.284}. \quad \text{(A21)}$$

The above equations are for the staggered tube layout. Zukauskas and Ulinskas (1983) also provide the equations for the in-line geometry.

Jakob (1938) Correlation. Jakob (1938) provided the friction correlation for both in-line and staggered tube layout. His correlation extends to $P_t/D = 3.0$. Listed below is his correlation for the line-line tube layout.

$$E_u = 4 \times \left[0.044 + \frac{0.08 P_l/D}{[(P_t - D)/D]^{0.43 + 1.13 D/P_l}} \right] \mathrm{Re}_D^{-0.15} \quad \text{(A22)}$$

$$f_t = E_u \frac{A_{c,t}}{A_t N} \quad \text{(A23)}$$

Effect of Suspended Particles on Crystallization Fouling in Plate Heat Exchangers

B. Bansal[1]
Department of Chemical and Materials Engineering,
The University of Auckland,
New Zealand

H. Müller-Steinhagen
Department of Chemical and Process Engineering,
The University of Surrey,
England

X. D. Chen
Department of Chemical and Materials Engineering,
The University of Auckland,
New Zealand

The presence of suspended particles in solutions significantly affects the crystallization rate. This study investigates the effects of calcium sulphate (crystallizing) particles and alumina (noncrystallizing) particles on calcium sulphate crystallization fouling in a plate heat exchanger. Calcium sulphate particles are formed during the preparation of calcium sulphate solution due to breakage of calcium sulphate crystals growing on the heat transfer surface. These suspended particles settle on the heat transfer surface and act as nuclei. The availability of extra nucleation sites increases the crystallization rate significantly. These particles can be removed with a filter, and the removal of the particles prevents this extra assistance available for crystallization. Therefore, the crystallization rate is reduced markedly. Alumina particles were purposely added during the preparation of calcium sulphate solutions. These particles attach loosely to the heat transfer surface compared with crystalline deposits which adhere strongly. Therefore, calcium sulphate crystals growing on these particles are removed easily. Also, alumina particles settling on the growth faces of calcium sulphate crystals may act as a distorting agent. This slows down the growth of the crystals.

Introduction

Fouling is the formation of undesired deposits on heat transfer surfaces. Crystallization fouling is the precipitation of a dissolved substance from the solution onto the heat transfer surface. It occurs when the concentration of the dissolved material in the fluid near the heat transfer surface exceeds the solubility limit. There are various possibilities which can lead to supersaturation:

- Solution of normal solubility salt cooled below solubility temperature
- Solution of inverse solubility salt heated above solubility temperature
- Solution evaporated beyond the solubility limit of the dissolved substance
- Mixing of different solutions

Crystallization fouling of calcium sulphate, an inverse solubility salt, is a serious problem in various applications. In cooling towers, for instance, it presents a major problem along with calcium carbonate. During water desalination by reverse osmosis membranes, it blocks the membranes. Even small quantities in the boiler feed water can cause a significant increase in fuel consumption. In saline water distillation units, precipitation of calcium sulphate in sea water is a common problem.

Fouling-related costs in New Zealand are around 0.15% of its GDP (Müller-Steinhagen, 1993). By way of comparison, in countries such as USA, Germany, and Japan the fouling related costs are 0.25% of the countries' GDP because these countries are industrially more developed (Müller-Steinhagen, 1993). There are various ways to reduce fouling costs. In general, the most effective steps in controlling fouling are those taken during the design of heat exchangers. These are: selection of a suitable heat exchanger type, selection of favorable operating conditions (e.g., higher flow velocities, lower temperatures etc.), and selection of optimum heat exchanger design. No matter how well the operating conditions are maintained, if the design is not appropriate a considerable amount of fouling will take place. Gilmour (1965) reported that the degradation of heat transfer performance by fouling in shell and tube heat exchangers occurs mainly due to the poor shell side design. Plate heat exchangers are becoming more common because they foul significantly less compared with shell and tube heat exchangers (Branch et al., 1991; Cooper et al., 1980; Cross, 1979; Müller-Steinhagen, 1988; Müller-Steinhagen, 1993; Novak, 1982).

There are several methods available commercially to mitigate fouling. These methods can be classified into two basic categories: chemical methods and mechanical methods. Some of these methods are applied on-line and some are applied off-line. Chemical methods for mitigating crystallization fouling involve the addition of additives such as sequestering agents (ethylene diamine tetraacetate), threshold agents (polyphosphates and polyphosphonates), and crystal modifying agents (polycarboxylic acid) (Bott, 1981; Harris and Marshall, 1981; Krisher, 1978). Mechanical methods for mitigating crystallisation fouling involve an increase in flow velocity, reversal of flow direction, better quality heat transfer materials, smoother heat transfer surfaces, pulsating flow, turbulence promoters, transport of cleaning devices through tubes, etc. (Müller-Steinhagen, 1993).

It is well known that the rate of crystallization depends on the number of nucleation sites, as described by Eq. (1) (Amjad, 1988; Klima and Nancollas, 1981; Liu and Nancollas, 1970; Nancollas and Reddy, 1974):

$$\dot{m}_d = K_R \Delta c^n s \tag{1}$$

where $\dot{m}_d$ is the rate of crystallization, K_R is the reaction-rate constant, Δc is the concentration difference, n is the order of reaction, and s is a function of the number of nucleation sites. This means that the rate of crystallization increases with increasing number of nuclei. Nucleation sites may already exist at the heat transfer surface or may be generated by deposition of matter from the bulk stream. This can be a serious problem in industrial applications because there are always some particles present in industrial fluids. Note that fluid streams may also

[1] Current address: Natang Consultants, 5 Epsom Avenue, Epsom, Auckland, New Zealand.

Contributed by the Heat Transfer Division for publication in the JOURNAL OF HEAT TRANSFER. Manuscript received by the Heat Transfer Division August 11, 1996; revision received February 5, 1997; Keywords: Fouling, Heat Exchangers, Heat Transfer. Associate Technical Editor: S.-H. Chan.

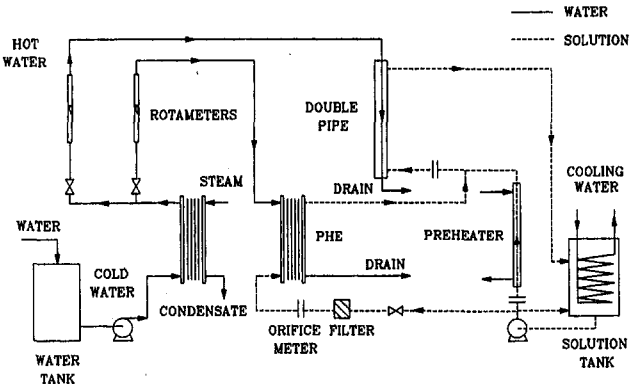

Fig. 1 Experimental set up

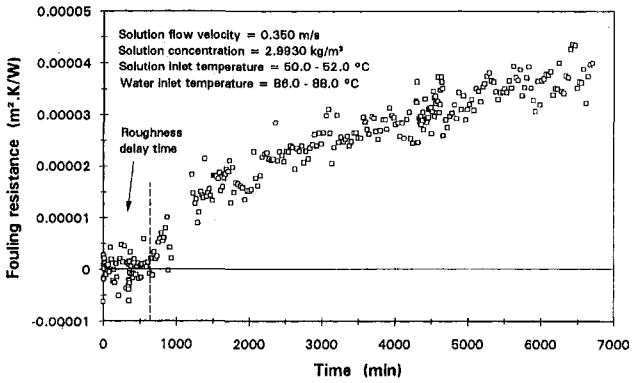

Fig. 2 Typical fouling curve

contain inert (noncrystallizing) contaminant particles. The present research work was carried out to investigate the effect of crystallizing and noncrystallizing particles on crystallization fouling of calcium sulphate during heat transfer in a plate heat exchanger.

Experimental Set Up

The experimental set up is illustrated in Fig. 1. The test plate heat exchanger consisted of only three flow channels to keep the set up as simple as possible. Calcium sulphate solution was present in the central channel and was heated by hot water flowing in the two adjacent channels. The solution was pumped to the plate heat exchanger from a 50 litre tank using a centrifugal pump. The hot water was prepared using steam in another heat exchanger. The hot solution leaving the plate heat exchanger was returned to the tank whose temperature was controlled using a cooling water coil. From the tank, the solution was pumped back to the plate heat exchanger.

The progress of the calcium sulphate crystallization process was monitored by measuring the increase in the resistance to heat transfer, i.e., the fouling resistance with deposit formation. The fouling resistance R_f can be derived from

$$R_f = \frac{1}{U} - \frac{1}{U_o} \tag{2}$$

where U_o and U are the overall heat transfer coefficients at time $t = 0$ and $t = t$, respectively. U is given by

$$U = \frac{\dot{Q}}{A\Delta T_{\log}} \tag{3}$$

where $\dot{Q}$ is the rate of heat gained by solution, A is the heat transfer area, and $\Delta T_{\log}$ is the log mean temperature difference. The heat flow rate $\dot{Q}$ is determined from

$$\dot{Q} = \dot{M}c_p(T_o - T_i) \tag{4}$$

where $\dot{M}$ is the mass flow rate, c_p is the specific heat of the solution, and T_i and T_o are the solution temperatures at the entrance and the exit of the plate heat exchanger, respectively.

By measuring the inlet and the outlet temperatures of the hot water and the solution streams, and the flow rate of the solution stream, the fouling resistance can be determined.

The measured temperatures are accurate within ±0.25°C. The maximum error in the flow measurements is ±1–2 percent. Therefore, the maximum error in the measured fouling resistances is less than ±5 percent.

Preparation of Calcium Sulphate Solution

The calcium sulphate solution was prepared using calcium nitrate ($Ca(NO_3)_2 \cdot 4H_2O$) and sodium sulphate (Na_2SO_4) instead of using calcium sulphate ($CaSO_4$) directly. Since both calcium nitrate and sodium sulphate have higher solubility than calcium sulphate, this indirect technique offered the following two advantages:

1 Highly supersaturated solutions with respect to calcium sulphate could be prepared without difficulty.
2 The amount of undissolved material was minimal.

The solutions used in the experiments were supersaturated in order to produce measurable fouling rates within short experimental times.

Results and Discussion

The results presented below provide understanding on the effect of suspended particles on crystallisation fouling. These results provide the general trend which should be applicable to other heat exchangers as well.

Fouling Resistance. The calcium sulphate crystallisation process was found to be second order reaction controlled, i.e., the exponent n in Eq. (1) had a value of 2 (Bansal, 1994). A typical fouling resistance curve is illustrated in Fig. 2. When the heat transfer process started, no deposition was observed for some time. This time period, known as initiation or delay

Nomenclature

A = area of heat transfer, m^2
c_p = specific heat of solution, kJ/kg·K
K_R = reaction rate constant, $m^4/kg \cdot s$
$\dot{m}_d$ = deposition rate, $kg/m^2 \cdot s$
$\dot{M}$ = solution mass flow rate, kg/s
n = order of reaction
$\dot{Q}$ = rate of heat gained by solution, kW
R_f = fouling resistance, $m^2 \cdot K/W$
s = function of nucleation sites (dependence of the rate of crystallisation on the number of nucleation sites)
t = experimental run time, s
T_i = solution temperature at the entrance of the plate heat exchanger, °C
T_o = solution temperature at the exit of the plate heat exchanger, °C
U = overall heat transfer coefficient at time $t = t$, $W/m^2 \cdot K$
U_o = overall heat transfer coefficient at time $t = 0$, $W/m^2 \cdot K$

Greek Symbols

Δc = concentration difference, kg/m^3
$\Delta T_{\log}$ = log mean temperature difference, °C

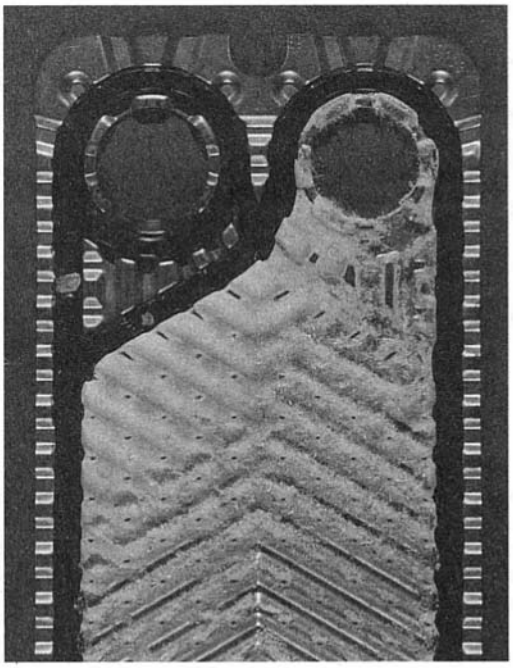

Fig. 3 Photograph of the fouled plate

period, was required for a minimum nuclei density before macroscopic crystallization could start. The fouling resistance remained unchanged during this period. The initial growth of deposit layer penetrated the viscous sublayer, which increased the turbulence (Schlichting, 1968). Therefore, the overall heat transfer coefficient increased, and the fouling resistance became negative. With further deposit formation, the increase in the thermal resistance overcame the advantage of higher turbulence and the fouling resistance became positive again. The time period from the start until the fouling resistance became positive, after being negative for some time, is called roughness delay time (Bansal and Müller-Steinhagen, 1993; Bansal and Müller-Steinhagen, 1996).

A photograph of a fouled plate is illustrated in Fig. 3. The solution entered at the bottom left side and exited at the top right side of the plate. The heating water in the surrounding channels entered at the top left side and exited at the bottom right side. Only the top portion of the plate was fouled. Various reasons for this are as follows:

1 The hot water entering at the top resulted in higher temperature in the upper part of the plate. Therefore, the local saturation concentration of calcium sulphate corresponding to the surface temperature was lower due to its inverse solubility. This increased the difference between the bulk concentration and the saturation concentration and hence, resulted in a higher driving force for crystallization (see Eq. (1)).
2 The crystallisation rate constant K_R increased—as it depends exponentially on the temperature (Arrhenius law).

Within the upper portion of the plate, the regions near the top left corner, and the areas near the contact points between adjacent plates, had comparatively more deposition. The peculiar geometry of these regions resulted in lower flow velocities and hence, higher temperatures. The higher temperature would increase the deposition rate, and the lower flow velocity would reduce the deposit removal rate.

It is important to note that there was no crystal formation in the bulk fluid irrespective of the fact that the solution was supersaturated (Bansal, 1994). The reason for this is that the bulk temperature was not high enough to produce a large reaction rate constant K_R. For the same reason, there was no fouling on the colder (lower) parts of the plate (see Fig. 3).

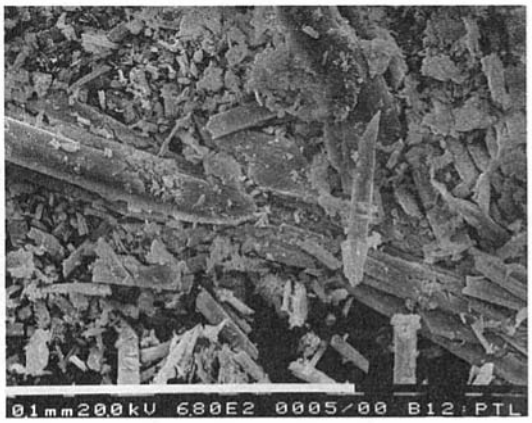

Fig. 4 Scanning electron microscope micrograph of calcium sulphate particles present in the solution before the start of calcium sulphate crystallization

Due to the shear related removal of crystals deposited on the heat transfer surface and the presence of the undissolved matter, some particulate were always present in the bulk solution. The concentration of these particles was determined by filtering a certain amount of the solution through 0.22 μm millipore filter paper. The particulate concentration was found to be 0.010–0.014 kg/m^3. Note that the term "particles" is used for both the undissolved matter as well as the crystals. These particles were investigated using a scanning electron microscope. Figures 4 and 5 illustrate typical scanning electron microscope micrographs of the particles present:

- before the start of the fouling process and
- once the crystalline deposits were formed on the heat transfer surface

Surprisingly, some crystals were present even before the start of the experiment, even though the entire set up was cleaned with acetic acid (Bansal and Müller-Steinhagen, 1993). These crystals were formed probably during the preparation of the calcium sulphate solution. While sodium sulphate and calcium nitrate are highly soluble in water, the possibility of the formation of calcium sulphate crystals in the bulk solution can not be ruled out completely. No visual difference could be detected in the morphology of the particles collected at different times. The particles had a wide size range. Most of them were 10–20

Fig. 5 Scanning electron microscope micrograph of calcium sulphate particles present in the solution once calcium sulphate deposits were formed on the heat transfer surface

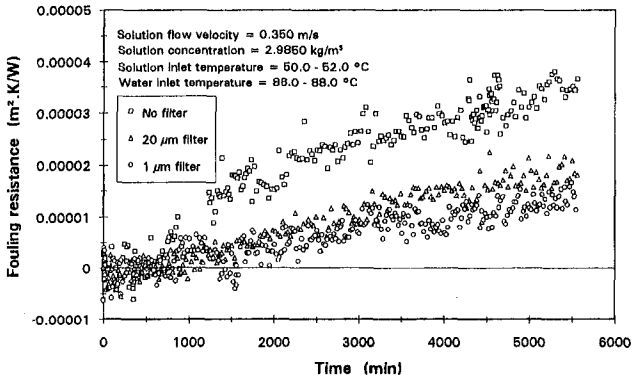

Fig. 6 Effect of filtration on fouling resistance

μm long but some were smaller than 10 μm, and others were several hundred microns long.

These particles can affect the deposition rate in the following ways (Bansal, 1994):

1 They may cause particulate fouling.
2 Depending on their size, some of the particles present in the bulk may cause breakage of the crystals growing on the heat transfer surface by direct collision. Larger particles are more efficient at this type of removal. This would reduce fouling.
3 The crystals formed from particles settling on the heat-transfer surface may be removed easily because these particles attach loosely to the surface. This would result in the formation of more particles and hence, more nucleation sites.
4 The most important effect probably is the generation of extra nucleation sites associated with the settling of these particles on the heat transfer surface (particulate fouling). The resettling of the broken crystals would have little effect on the fouling resistance directly since the total amount of deposit does not alter. However, the availability of the additional nucleation sites would enhance the crystallization rate significantly. It is important to mention that any particles entering the bulk solution may break into smaller fragments when the solution is circulated in the test loop. This may augment the deposition rate since smaller particles have a higher surface-to-volume ratio which enhances their activity as nucleation sites.

Effect of Filtration. To determine the effect of the presence of particulate matter a 20 μm filter was installed in-line before the plate heat exchanger. The "Betapure" filter was supplied by Cuno Inc. (Process Filtration Products, Commercial Intertech Corporation, USA). It was made of polyethylene and polypropylene. The effect of filtration on fouling is illustrated in Fig. 6. The fouling rate changed significantly with filtration in the following ways:

- The roughness delay time increased
- The fouling rate reduced
- The absolute fouling resistance reduced

The overall reduction in the fouling resistance after 5500 minutes was 47 percent. Since some particles were smaller than 20 μm (see Figs. 4 and 5), they were able to reach the heat exchanger plate and affect the crystallization process. Therefore, in order to remove the smaller particles, the 20 μm filter was replaced by a 1 μm filter. The fouling curve obtained in the presence of the 1 μm filter is illustrated in Fig. 6. The fouling resistance reduced by another 14 percent. Note that the reduction was comparatively less this time, but it was still significant. Apart from the presence of the filter, the operating conditions were identical in all three experiments.

The photograph of the plate fouled in the presence of the 1 μm filter is illustrated in Fig. 7. The amount of deposits reduced significantly with filtration compared with when there was no filtration (Fig. 3).

The growth of the deposits was limited to the low velocity zones in the presence of the filter since little assistance was available from particle-generated nucleation sites. The growth pattern near the exit (top right side of the plate) illustrates that irrespective of the higher surface temperature (hot end), the higher level of turbulence in this region (channel width reduced from 10 cm to 4 cm) kept the surface clean. However, when the filter was absent, particles were able to settle even there and cause deposition.

Although it was confirmed that fouling increased significantly in the presence of particles, it could not be determined whether this was due to particles present before the start of the experiment or particles generated by the removal of deposits during the fouling process.

To investigate this, an experiment was performed where the 1 μm filter was installed in-line before the start of the fouling process. The solution was then recirculated in the flow set up for several hours to make sure that there were no particles present before the start of the experiment. The filter was then removed and the experiment was started. The resulting fouling curve is compared with the experiment when no filter was present at all. The results are illustrated in Fig. 8. Both fouling curves are identical, which indicates that the fouling process was not affected significantly by particles present before the start of the experiment. Therefore, it can be concluded that the removal of deposit during the fouling process provided a continuous supply of particles that enhanced the crystallization rate significantly.

These results have also been analyzed in another way. The fouling curve for the experiment, with the 1 μm filter present only before the start of the experiment, is compared with the one when the 1 μm filter was present throughout the fouling process. This means that there were no particles present at the start of both experiments. Therefore, any difference between these two curves should be exclusively due to the particles

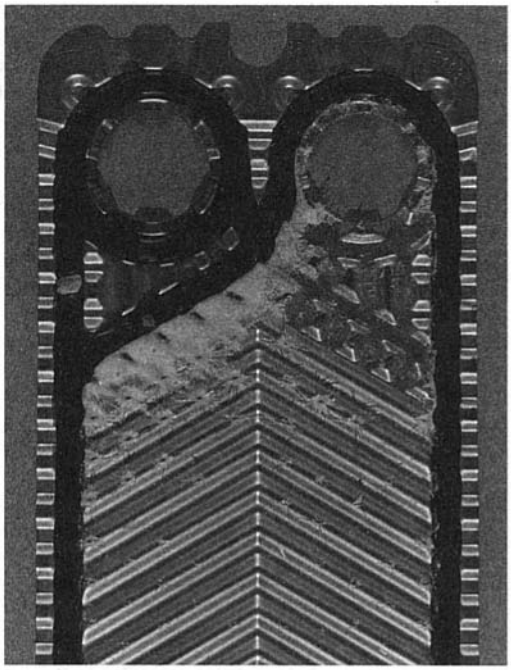

Fig. 7 Photograph of the plate fouled in the presence of 1 μm filter

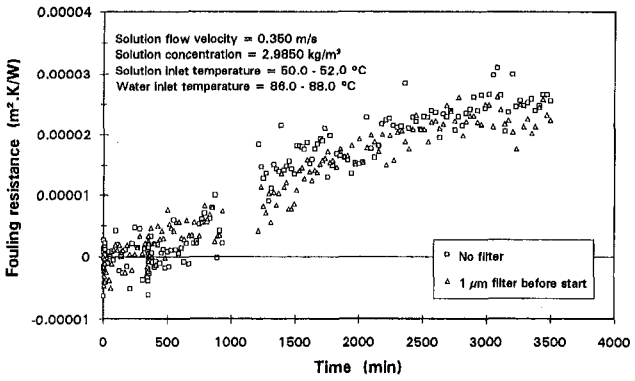

Fig. 8 Effect of 1 μm filter used before the start of the experiment

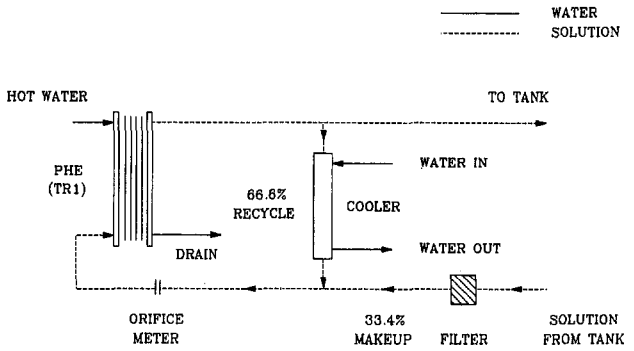

Fig. 10 Experimental set up used to investigate the effect of recycling of the calcium sulphate solution (directly to the plate heat exchanger) on fouling

generated by the removal of the deposits during the fouling process. The resulting fouling curves are illustrated in Fig. 9. Fouling increased significantly when the 1 μm filter was absent during the experiment. This confirms that there was breakage of deposits during the fouling process, and the removed particles enhanced the crystallisation rate significantly.

It is important to note that the possibility of additional nucleation sites created by the particles cannot be ruled out completely, even in the presence of an in-line filter. Some fractured crystals may settle again further downstream rather than leaving with the bulk fluid and then being trapped by the filter. Nothing could be done in the present investigation to avoid this process. It was also not possible to measure the amount of particles entrapped by the crystalline deposits.

At this stage it is important to mention that the filtration was effective because a closed flow loop was used in the present investigation and the broken particles were recirculated to the plate heat exchanger. However, the amount of particles that increased fouling significantly was so low that one might be suspicious of the nature of the crystallization fouling processes in the industry. In fact, while industrial processes are once-through, their impurity levels are generally higher than those of the laboratory experiments in the present study (even in the absence of a filter). Therefore, the filter may be very effective in industrial processes irrespective of open or closed systems.

Effect of Recycling. Direct recycling of the calcium sulphate solution to the plate heat exchanger was another method to investigate the effect of particles on crystallization fouling. A simple experiment was performed where part of the outgoing solution was recycled directly to the plate heat exchanger. The flow loop had to be modified slightly as shown in Fig. 10. Instead of returning the entire solution back to the tank, as in the experiments discussed above, 66.6 percent of it was recycled to the plate heat exchanger. Before that, it was cooled to the inlet temperature of the plate heat exchanger in a double pipe heat exchanger using cooling water. The rest of the solution (33.4 percent) was supplied from the tank. The 1 μm filter was present only in the make-up line and the recycled solution was supplied without any filtration. Any difference in fouling in both cases would be due to the presence of particles (formed by the removal of the deposits in the plate heat exchanger) in the recycled solution.

The effect of recycling on fouling is illustrated in Fig. 11. The roughness delay time reduced, and the fouling rate increased significantly with recycling. This confirmed that the presence of the particles provided extra nucleation sites which increased the crystallization rate.

The effect of recycling was also observed by opening the plate heat exchanger after the experiment and visualizing the deposit formation. The deposition was much more severe with recycling. The deposition extended to areas which were otherwise free from fouling. For example, deposits were formed in the turbulent zone near the exit as well as on the colder (lower) part of the plate. The deposit layer was denser. Analysis of the deposits with the help of the scanning electron microscope revealed the following:

- The number of the crystals formed was higher
- The crystals were smaller in size

The reason for crystals being smaller in size is that more crystals grew at the same time due to the availability of extra nucleation sites provided by the resettled particles due to recycling.

Hasson and Zahavi (1970) also investigated the effect of the presence of particles on calcium sulphate fouling. In their study, the solution was prepared using calcium sulphate reagent directly. The heat exchanger used was a double-pipe heat exchanger. A 25 μm filter was installed in-line before the double-

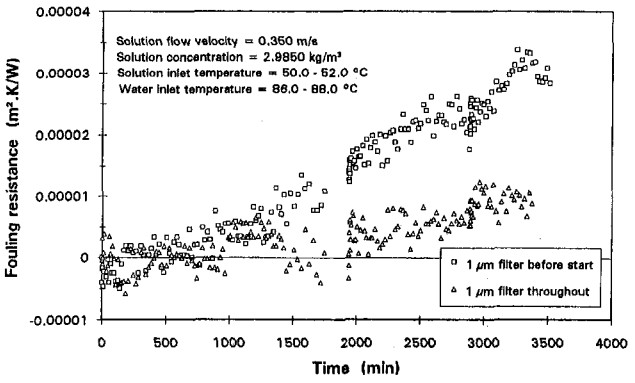

Fig. 9 Effect of calcium sulphate particles generated by the removal of deposit

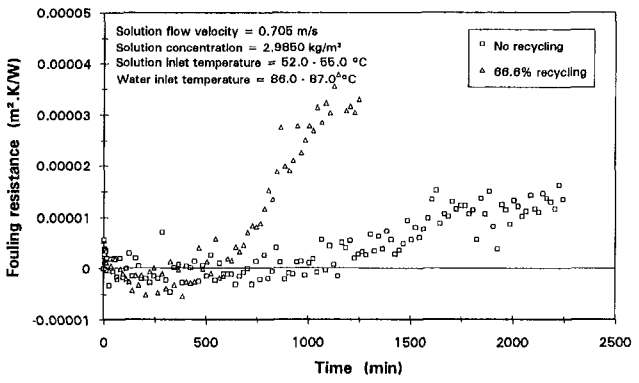

Fig. 11 Effect of solution recycling on calcium sulphate deposition

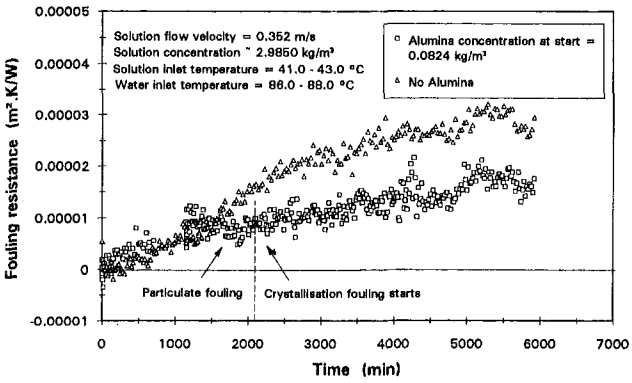

Fig. 12 Effect of the presence of alumina particles on crystallisation fouling of calcium sulphate

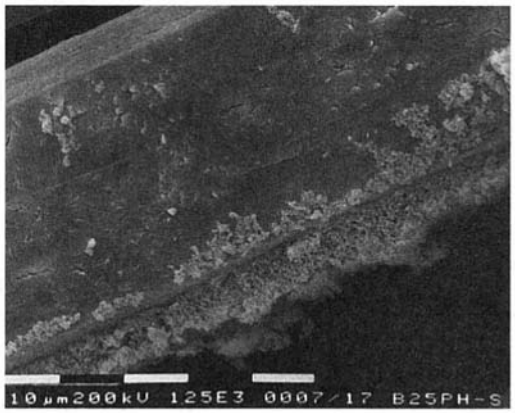

Fig. 13 Scanning electron microscope micrograph of crystals present in the bulk solution

pipe heat exchanger. They found that the filtration of the calcium sulphate solution reduced fouling by a factor of 3–4. In comparison, the recycling of the solution did not have any effect on fouling. Note that the filter was removed when the effect of recycling was investigated. The only possible explanation for this unexpected behavior is that there were already so many particles present in the solution in the absence of the filter that the availability of extra particles by recycling did not noticeably affect the particle concentration. The effect of recycling could have been identified more effectively if the recycling experiment had been performed with a filter, as in the present investigation.

Effect of Inert Particles. Since the presence of calcium sulphate particles had a pronounced effect on the crystallization rate, it would be interesting to investigate the effect of the presence of particles made of noncrystallizing material. 1 μm alumina, Al_2O_3, particles (Microlux-RZ, Alpha Alumina, Optical Polishing Compound, Adolf Meller Company, Providence, RI, USA) were selected for this purpose.

The calcium sulphate solution was prepared as before using calcium nitrate and sodium sulphate. 0.082 kg/m^3 of alumina particles were added just before the start of the experiment. A mechanical stirrer was added to the solution tank to prevent settling of the particles. No filter was used in these experiments to avoid trapping of the alumina particles. Since the plate heat exchanger with corrugated plates may be prone to blockage by suspended particles, the corrugated plates were replaced by flat plates for this set of experiments. The absence of the corrugations resulted in very low heat transfer in the flat plate heat exchanger.

The fouling curve obtained in the presence of alumina particles is illustrated in Fig. 12 and is compared with the one where no alumina particles were present. Note that no filter was present in-line in both experiments.

Contrary to the results obtained with calcium sulphate particles, the overall fouling resistance reduced significantly in the presence of alumina particles. Also, the fouling curve obtained was quite different in nature. The usual long roughness delay time was replaced by almost no roughness delay time. The fouling rate increased immediately after the start of the experiment. The fouling rate was very high initially and settled to an asymptotic value just after 1000 minutes. This is typical for particulate fouling. The calcium sulphate concentration remained almost unchanged for 2100 minutes after the start of the experiment. This suggests that the presence of alumina particles prevented calcium sulphate fouling in the initial stages. Only after the alumina particle concentration dropped calcium sulphate crystals started to form. Therefore, the fouling resistance increased after 2100 minutes.

Based on these observations, possible explanations for the reduction in calcium sulphate fouling in the presence of alumina particles can be suggested:

- At the start of the experiment, alumina particles settle quickly on the heat transfer surface. These particles attach loosely to the surface compared with crystalline deposits which adhere strongly. Therefore, the crystals growing on alumina particles would have week adherence and can be removed easily
- Alumina particles, when settled on the growth faces of the crystals, may act as distorting agent. This slows down further growth of the crystals

The possibility of the reduction in deposition rate through erosion by Al_2O_3 particles has been ruled out. The reason for this is that visual observation of the crystals formed on the heat transfer surface, and those suspended in the bulk solution, indicated no effect of Al_2O_3 particles on the morphology of the crystals.

Since the driving force for heterogeneous nucleation is higher than for homogeneous nucleation, there was a possibility for crystallization of calcium sulphate to occur on alumina particles present in the bulk. To check this, a solution sample from the tank was filtered through a 0.22 μm millipore filter paper. The filtered material was analyzed using the scanning electron microscope. The scanning electron microscope micrograph, illustrating the filtered material, is shown in Fig. 13.

While some alumina particles settled on the calcium sulphate crystals, there was no indication that alumina particles themselves acted as nucleation sites for calcium sulphate crystals. All particles remained clean. Also, no changes were noticed in

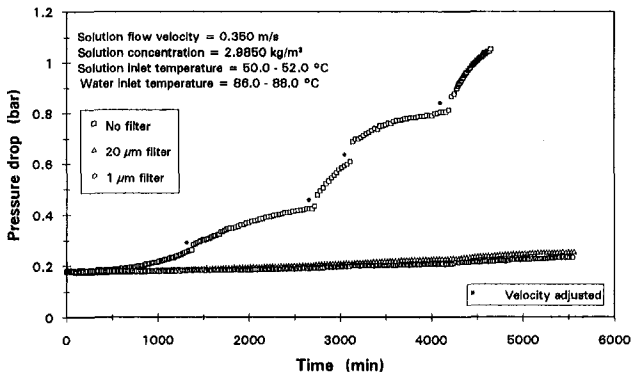

Fig. 14 Effect of the presence of filter on the increase in pressure drop across the plate heat exchanger with deposit formation

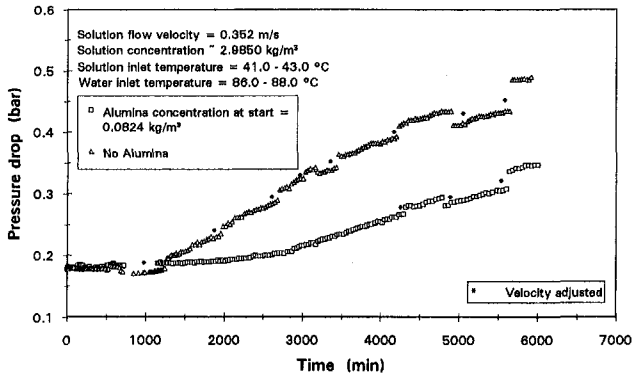

Fig. 15 Effect of the presence of alumina particles on the increase in pressure drop across the plate heat exchanger with deposit formation

the morphology of the crystals. Therefore, the possibility that alumina particles provided nucleation sites in the bulk solution was ruled out.

Pressure Drop. The presence of the filter not only affected the reduction in heat transfer with fouling, it also reduced the increase in pressure drop across the plate heat exchanger with deposit formation. Fig. 14 shows the effect of the presence of the filter on the increase in the pressure drop with deposit formation. The narrow flow channel in the plate heat exchanger blocked significantly in the absence of the filter. The pressure drop across the plate heat exchanger increased from 0.18 bar to 1.04 bar resulting in an increase of more than 475 percent. The presence of the 20 μm filter reduced the increase in pressure drop by a factor of 15 as the pressure drop increased from 0.18 bar to 0.24 bar. The presence of the 1 μm filter limited the increase in the pressure drop to only 0.04 bar. Note that the pressure drop across the filter was insignificant in comparison.

Apart from less reduction in heat transfer due to fouling, the presence of alumina particles also reduced the increase in pressure drop across the plate heat exchanger (see Fig. 15). The pressure drop increased from 0.16 bar to 0.49 bar in the absence of alumina particles. In comparison, the pressure drop increased from 0.16 bar to 0.35 bar in the presence of alumina particles representing a reduction of around 90 percent in the increase in the pressure drop.

Conclusions

The effect of suspended particles on crystallization fouling has been found to depend on the nature of the particles. The presence of calcium sulphate particles significantly increased the crystallisation rate. Most of these particles were generated by the removal of the crystalline deposits growing on the heat-transfer surface during the fouling process. Some particles were also formed during the preparation of calcium sulphate solution. The presence of these particles on the heat-transfer surfaces created extra nucleation sites for crystallization resulting in significant increase in the fouling rate.

The presence of alumina particles reduced the crystallization rate. The settling of alumina particles on the heat-transfer surface reduced the deposit strength resulting in higher deposit removal rates. Also, alumina particles settled on the crystals and acted as distorting agents. This reduced the crystal growth rate.

The results presented above clearly demonstrate that the removal of particles (made of the crystallizing material) from process fluid can be a potential mitigation technique for crystallization fouling. The removal of these particles prevents formation of additional nucleation sites and hence, no extra assistance for crystallization. Therefore, the crystallization rate reduces significantly.

Acknowledgments

The authors wish to acknowledge the support from Alfa-Laval (Sweden, New Zealand) and APV (USA, England, Denmark, New Zealand). The help of Dr. Wolfgang Augustin (Braunschweig, Germany) is greatly appreciated.

References

Amjad, Z., 1988, "Calcium Sulphate Dihydrate (Gypsum) Scale Formation on Heat Exchangers Surfaces: The Influence of Scale Inhibitors," *Journal of Colloid and Interface Science,* Vol. 123, No. 2, pp. 523–536.

Bansal, B., 1994, "Crystallisation Fouling in Plate Heat Exchangers," Ph.D. thesis, Department of Chemical and Materials Engineering, The University of Auckland, New Zealand.

Bansal, B., and Müller-Steinhagen, H., 1993, "Crystallisation Fouling in Plate Heat Exchangers," ASME JOURNAL OF HEAT TRANSFER, Vol. 115, pp. 584–591.

Bansal, B., and Müller-Steinhagen, H., 1996, "Pressure Drop in Plate Heat Exchangers during Crystallisation Fouling," *Proceedings of the Conference of the Institution of Professional Engineers,* Vol. 2, Part 2, Dunedin, New Zealand, pp. 302–307.

Bott, T. R., 1981, *The Fouling of Heat Exchangers,* Department of Scientific and Industrial Research (DSIR), Wellington, New Zealand.

Branch, C. A., Müller-Steinhagen, H., and Seyfried, F., 1991, "Heat Transfer to Kraft Black Liquor in Plate Heat Exchangers," *APPITA Journal,* Vol. 44, No. 4, pp. 270–272.

Cooper, A., Suitor, J. W., and Usher, J. D., 1980, "Cooling Water Fouling in Plate Heat Exchangers," *Heat Transfer Engineering,* Vol. 1, No. 3, pp. 50–55.

Cross, P. H., 1979, "Preventing Fouling in Plate Heat Exchangers," *Chemical Engineering,* pp. 87–90.

Gilmour, C. H., 1965, "No Fooling—No Fouling," *Chemical Engineering Progress,* Vol. 61, No. 7, pp. 49–54.

Harris, A., and Marshall, A., 1981, "The Evaluation of Scale Control Additives," *Proceedings of the Conference on Progress in the Prevention of Fouling in Industrial Plant,* University of Nottingham, UK.

Hasson, D., and Zahavi, J., 1970, "Mechanism of Calcium Sulfate Scale Deposition on Heat Transfer Surfaces," *I & EC Fundamentals,* Vol. 9, No. 1, pp. 1–10.

Klima, W. F., and Nancollas, G. H., 1981, "The Growth of Gypsum," *AIChE Symposium Series: Crystallization and Precipitation Processes,* Vol. 83, No. 253, pp. 23–30.

Krisher, A. S., 1978, "Raw Water Treatment in the CPI," *Chemical Engineering,* pp. 79–98.

Liu, S., and Nancollas, G. H., 1970, "The Kinetics of Crystal Growth of Calcium Sulphate Dihydrate," *Journal of Crystal Growth,* Vol. 6, pp. 281–289.

Müller-Steinhagen, H. M., 1988, "Verschmutzung von Wärmeübertragerflächen," 5th ed., Section OC, *VDI-Wärmeatlas.*

Müller-Steinhagen, H., 1993, "Fouling: The Ultimate Challenge for Heat Exchanger Design," *Proceedings of the Sixth International Symposium on Transport Phenomena in Thermal Engineering,* Seoul, Korea, pp. 811–823.

Nancollas, G. H., and Reddy, M. M., 1974, "The Kinetics of Crystallization of Scale Forming Minerals," *Society of Petroleum Engineers Journal,* pp. 117–126.

Novak, L., 1982, "Comparison of the Rhine River and the Öresund Sea Water Fouling and Its Removal by Chlorination," ASME JOURNAL OF HEAT TRANSFER, Vol. 104, pp. 663–669.

Schlichting, H., 1968, *Boundary Layer Theory,* 6th ed., McGraw-Hill Book Co., Inc., New York, pp. 596–625.

A Maintenance Strategy for Heat Transfer Equipment Subject to Fouling: A Probabilistic Approach

S. M. Zubair
zubair@ccse.kfupm.edu.sa

A. K. Sheikh

M. O. Budair

M. A. Badar

Mechanical Engineering Department,
King Fahd University of Petroleum
and Minerals,
Dhahran 31261,
Saudi Arabia

Fouling of heat transfer surfaces introduces a major uncertainty into the design and operation of heat transfer equipment. After a brief discussion on impact of fouling, we present and discuss a stochastic approach to the analysis of fouling models. In view of the performance indicator (U/U_c) of the heat exchangers, a maintenance strategy for planned maintenance schedules is presented. Various scenarios of reliability based maintenance strategy are introduced. The strategy is explained in terms of the scatter parameter ($\sqrt{\alpha}$) of the time-to-fouling distribution corresponding to a critical level of fouling, and the risk factor (p) representing the probability of tubes being fouled to a critical level after which a cleaning cycle is needed. In addition, the cost implications of the above mentioned strategy are explained and their impact on heat exchanger maintenance is highlighted.

1 Introduction

The term "fouling" is defined as the deposition of unwanted (initially fluid) particles on heat transfer equipment which results in an increase in thermal resistance to heat transfer and subsequent loss of the equipment's thermal efficiency. The growth of these fluid impurities causes the thermal-hydraulic performance of heat transfer equipment to decrease continuously with time. These fluid impurities may result in (Taborek et al., 1972a, 1972b; Suitor et al., 1976; Chenoweth, 1990; Al-Ahmad and Abdelaleem, 1991; Bott, 1995): sedimentation, crystallization, organic or biological growths, corrosion products, or a combination of these. In addition, where the heat flux is relatively high, as in steam generators, fouling can lead to local hot spots and ultimately it may result in mechanical failure of the heat transfer equipment, and hence an unscheduled shutdown of the plant. This may result in economic and human loss, particularly in nuclear power plants. It should be noted that the designers and operators of heat transfer equipment must be able to predict performance variations as the fouling proceeds. The designer needs this information to ensure that the user requirements with regard to preventive maintenance schedules can be met, while the user of heat transfer equipment must be able to formulate rational operating schedules for equipment management purposes.

To meet the requirements of the designers and operators of heat transfer equipment, a project is being carried out at the King Fahd University of Petroleum and Minerals, Dhahran. The overall objective of the project is to provide an appropriate mathematical structure to the heat-exchanger fouling problem and then discuss rational maintenance and/or replacement strategies to reduce the overall maintenance and operating costs of heat exchangers. In this paper, which is an initial outcome of the above mentioned project, we describe a probabilistic approach to the analysis of fouling models and its impact on heat exchangers maintenance.

2 Impact of Fouling on Overall Heat Transfer Coefficient

Fouling forms an essentially solid deposit on the heat transfer surface. If the thickness of the deposits are independent of time, then fouling simply adds another conduction resistance in series with the wall. In general, fouling varies with time. We, therefore, introduce a time dependent fouling resistance in computing the overall heat transfer coefficient of the surface. Since the heat-transfer resistances are in series, we can express the time dependent, overall heat transfer coefficient in terms of the cleanliness factor as (Knudsen, 1990):

$$U(t)/U_C = 1/[1 + U_C R_f(t)]. \quad (1)$$

Equation (1) is plotted in Fig. 1, where the cleanliness factor is shown as a function of fouling resistance R_f, and the overall heat transfer coefficient under clean condition U_C. We note that the larger the heat transfer coefficient U_C, the greater is the effect of fouling on the cleanliness factor U/U_C. For example, where $U_C = 8{,}000\ \mathrm{W/m^2.K}$ and $R_f = 2.0 \times 10^{-4}\ \mathrm{m^2.K/W}$, the U/U_C value decreases by about 60 percent. This decrease in the cleanliness factor is reflected in additional materials, fabrication, installation and energy costs. As energy and materials costs increase, there will be a tendency to design heat transfer equipment with even higher overall heat transfer coefficients. Therefore, the control and assessment of fouling becomes more important, particularly in the case of higher overall heat transfer coefficients for clean conditions.

3 Fouling Models

The most widely accepted fouling model is based on the following general material balance equation first proposed by Kern and Seaton (1959):

$$dR_f/dt = \phi_d - \phi_r. \quad (2)$$

The rate of fouling deposition ϕ_d depends on the type of fouling mechanism (sedimentation, crystallization, organic material growth, etc.), while the rate of fouling removal ϕ_r depends on both the hardness or adhesive force of the deposit and the shear stress due to the flow velocity as well as the system configuration. The rates of deposition and removal have been given many different forms by various investigators (Taborek et al., 1972a, 1972b; Epstein, 1981; Al-Ahmad and Abdelaleem, 1991), the most widely accepted combinations result in the following three fouling growth (or fouling resistance) models (Zubair et al., 1992):

Contributed by the Heat Transfer Division for publication in the JOURNAL OF HEAT TRANSFER. Manuscript received by the Heat Transfer Division October 29, 1996; revision received April 21, 1997; Keywords: Fouling; Heat Exchangers; Modeling & Scaling. Associate Technical Editor: Y. Jaluria.

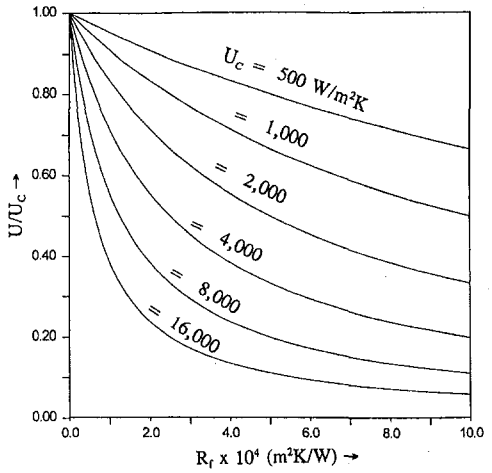

Fig. 1 The impact of fouling on reduced overall heat transfer coefficient, U/U_c

$$R_f(t) = A + Bt, \quad \text{for} \quad t \geq 0 \tag{3}$$

$$R_f(t) = A + B \ln(t), \quad \text{for} \quad t \geq 1 \tag{4}$$

$$R_f(t) = R_f^*(1 - e^{-t/\tau}), \quad \text{for} \quad t \geq 0 \tag{5}$$

where $R_f(0) = A$ (for Eq. (3)), $R_f(0) = 0$ (for Eq. (5)), and $R_f(1) = A$ (for Eq. (4)). If the time is measured in relatively smaller units (compared to the time required to reach a critical fouling level) such as minutes, hours, or days, then $R_f(1) = A \approx R_f(0)$, and the range of Eq. (4) could be treated as $t \geq 0$. In the following discussion, we will assume such time measurements and will consider the range as $t \geq 0$ in the corresponding equations.

3.1 Fouling Models with Induction Time. It is frequently observed that when the heat transfer surface is exposed to the fluid stream for some time, there is no measurable growth of fouling resistance. A delay in time between the start of the fouling growth process and the formation of fouling deposits is often observed. This period is defined as an induction or delay time, t_i. Thus, the fouling growth models discussed earlier can be generalized by introducing the delay time as

$$R_f(t) = A + B(t - t_i), \quad \text{for} \quad t \geq t_i \tag{6}$$

$$R_f(t) = A + B \ln(t - t_i), \quad \text{for} \quad t \geq (t_i + 1) \tag{7}$$

$$R_f(t) = R_f^*[1 - e^{-(t-t_i)/\tau}], \quad \text{for} \quad t \geq t_i \tag{8}$$

3.2 Stochastic Analysis of Fouling Models. Field investigations as well as replicate laboratory experiments (Somerscales and Kassemi, 1987; and Zubair et al., 1997) in the study of fouling growth models suggest that there is a considerable scatter in the values of R_f at any time t and similarly for any fixed value of R_f there will be a corresponding scatter in the values of t. The scatter in R_f can be expressed by its probability distribution $f[R_f(t)]$; and main indicators of this distribution are its mean value $\mu[R_f(t)]$ and standard deviation $\sigma[R_f(t)]$. It is often desirable to discuss the scatter in terms of the nondimensional parameter defined as coefficient of variation,

$$K[R_f(t)] = \sigma[R_f(t)]/\mu[R_f(t)]. \tag{9}$$

The evolution of the $R_f(t)$ distribution with respect to t is represented by the random sample functions of the fouling resistance growth. Each sample function represents a realization of the process. For understanding the concept, consider a heat exchanger which has many tubes. The fouling resistance response of the tubes will show a considerable scatter. This scatter, or randomness, is due to several reasons, some of these reasons are as follows (Zubair et al., 1992):

- Maldistribution of fluid-flow in heat exchanger tubes
- Variations and fluctuations in velocity around the nominal value
- Variations and fluctuations in pressure around the nominal value
- Variations and fluctuations in surface temperature around the average value
- Perturbations in the foulant chemistry
- Fluctuations in environmental factors
- Tube materials variability of metallurgical features
- Variability of surface finish
- Fluctuations in the initial quality characteristics of heat exchanger tubes attributed to manufacturing and assembling process

It is thus apparent that each heat exchanger tube will have its own fouling growth curve. These fouling growth curves will follow some type of fouling kinetic models such as linear, asymptotic, or falling rate. The ensemble of m such realizations for each of these curves are shown in Fig. 2. Mathematically, these functions are the same as those discussed earlier in Eqs. (3) through (8). However, due to a number of randomness sources, as described above, the parameters of the above equa-

Nomenclature

C = total cost rate of operating and maintaining a heat exchanger, dollars/year
CNDF = cumulative normal distribution function
d = performance degradation after heat exchanger cleaning ($0 \leq d \leq 1.0$)
f = probability density function, 1/h
K = coefficient of variation of time to reach critical level of fouling
M = median time to reach critical level of fouling, h
m = constant reflecting severity of financial penalty due to fouling
p = risk level, p
R = heat transfer resistance, $m^2.K/W$
r = reliability ($r = 1 - p$)
t = time, hr
U = overall heat transfer coefficient, $W/m^2.K$

Greek Symbols

σ = standard deviation, h
μ = mean value, h
$\Phi(\ )$ = cumulative normal distribution function
ϕ = rate of deposition or removal, $m^2.K/J$
τ = time constant, hr
$\sqrt{\alpha}$ = scatter parameter
θ = time interval between cleaning, h

Subscripts

c = clean
d = deposition
f = fouled condition or fouling
i = induction
k = kth cleaning cycle
kp = kth preventive cleaning cycle
l = life or limiting
max = maximum
min = minimum
r = removal

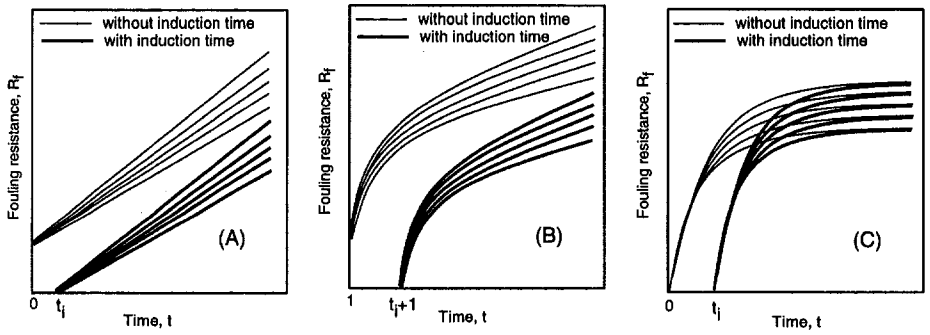

Fig. 2 Typical sample functions of fouling-resistance models with and without induction time, t_i

tions should be treated as random. These random functions represent fouling resistance laws as follows:

$$\mathbf{R}_f(t) = \mathbf{A} + \mathbf{B}t, \quad \text{for} \quad t \geq 0 \tag{10}$$

$$\mathbf{R}_f(t) = \mathbf{A} + \mathbf{B} \ln (t), \quad \text{for} \quad t \geq 1 \tag{11}$$

$$\mathbf{R}_f(t) = \mathbf{R}_f^*(1 - e^{-t/\tau}), \quad \text{for} \quad t \geq 0 \tag{12}$$

$$\mathbf{R}_f(t) = \mathbf{A} + \mathbf{B}(t - t_i), \quad \text{for} \quad t \geq t_i \tag{13}$$

$$\mathbf{R}_f(t) = \mathbf{A} + \mathbf{B} \ln (t - t_i), \quad \text{for} \quad t \geq (t_i + 1) \tag{14}$$

$$\mathbf{R}_f(t) = \mathbf{R}_f^*[1 - e^{-(t-t_i)/\tau})], \quad \text{for} \quad t \geq t_i \tag{15}$$

where bold letters represent random parameters with their appropriate distribution; having mean and variance. Notice that in most cases there is no initial fouling; that is, **A** is negligible. In this regard, we are exploring the above random processes in detail and their influence on the statistical nature of time to system maintenance. However, here we will explain a linear random growth model and its implications, which is an outcome of our initial effort in this direction.

Referring to Eq. (13) and considering $\mathbf{A} = 0$, which means that there is no initial fouling, the random fouling growth law will become $\mathbf{R}_f(t) = \mathbf{B}(t - t_i)$. If **B** is normally distributed with mean $\mu(\mathbf{B})$ and standard deviation $\sigma(\mathbf{B})$ then the coefficient of variation of the time rate of fouling resistance ($d\mathbf{R}_f(t)/dt = \mathbf{B}$) is:

$$K(\mathbf{B}) = \sigma(\mathbf{B})/\mu(\mathbf{B}), \tag{16}$$

where t_i is treated as a constant quantity (i.e., its variance is negligible), and $\mathbf{B}t_i$ also has a negligible variance.

We define $R_{f,\max}$ as a limiting value of the fouling resistance. A preventive maintenance action needs to be taken periodically. In this regard, the time interval between cleaning (θ_k) for the kth preventive maintenance action taken at time t_k can be defined as

$$\theta_k = t_k - t_{k-1} \tag{17}$$

where the time to the kth preventive maintenance action is measured from $t = 0$. The corresponding distribution of the interval between cleaning is expressed as (Zubair et al., 1992):

$$f(\theta_k) = [M_k/(2\pi\alpha)^{1/2}\theta_k^2] \exp[-(1 - M_k/\theta_k)^2/(2\alpha)]. \tag{18}$$

Notice that fifty percent of the tubes will reach $R_{f,\max}$ before the median time M_k. The scatter in time θ_k for the kth preventive-maintenance action $\sqrt{\alpha}$ is approximately linked to the coefficient of variation of the fouling growth rate (Ahmad and Sheikh, 1984): $\sqrt{\alpha} \approx K(\mathbf{B}) = \sigma(\mathbf{B})/\mu(\mathbf{B})$, in addition it is assumed that $\alpha_1 = \alpha_2 = \alpha_3 = \ldots = \alpha$.

4 Maintenance Scheme

Referring to Eq. (1), we note that at time $t = 0$, $U(0)/U_C = U_{\max}/U_C = 1$. When $R_f(t)$ reaches a limiting value such as $R_{f,\max}$ then $U(t)/U_C$ reaches $U_{f,\min}/U_C$. At this stage, one or more of the following maintenance actions are needed:

- Clean all the tubes or tube bundle(s)
- Clean all the tubes or tube bundle(s) and plug the leaking tube(s)
- Replace the tube(s) or tube bundle(s)

In a given replacement (or life) cycle of a set of tubes, there could be several cleaning cycles. Suppose t_k ($k = 0, 1, 2, 3, \ldots j \ldots$) represents the time locations where the kth cleaning is done (for $k = 0$, $t_o = 0$ represents the heat exchanger commissioning time). Therefore, after every successive cleaning cycle, $U_{\max}(t_k)/U_C$ will either restore the heat transfer surface to its original condition or, in some cases when some of the tubes are plugged or if the cleaning is not perfect, it will slightly decrease; viz.,

$$U_{\max}(t_o)/U_C = 1 > U_{\max}(t_1)/U_C > \ldots > U_{\max}(t_j)/U_C > \ldots \tag{19}$$

When $U_{\max}(t_k)/U_C$ approaches $U_{\min}/U_C$, then the time interval θ_k will start to decrease rapidly, resulting in a substantial increase in the operation and maintenance costs. As a result, we must either derate the system by further lowering $U_{f,\min}/U_C$ (which implies that lower heat transfer equipment performance is acceptable) or replace the tube(s) or tube bundle(s) prior to time t_l. In view of the probabilistic nature of $R_f(t)$, the reduced variable $U(t)/U_C$ will exhibit a stochastic pattern, i.e., the random variable "time between cleaning schedules" is; $\theta_{1p} = t_{1p} - t_o$, $\theta_{2p} = t_{2p} - t_{1p}$, $\theta_{3p} = t_{3p} - t_{2p}$, $\ldots$ $\theta_{jp} = t_{jp} - t_{j-1p}$, $\ldots$ all are distributed according to the probability model of Eq. (18). For a risk level p (i.e., $100p$ percent of the tubes have reached $U_{f,\min}/U_C$ or $U_{f,l}/U_C$, whichever is applicable), the time interval θ_{kp} is given by (Zubair et al., 1992):

$$\theta_{kp} = M_k/[1 - \sqrt{\alpha}\,\Phi^{-1}(p)], \tag{20}$$

where $\Phi^{-1}(p)$ is the inverse of Cumulative Normal Distribution Function (CNDF), which can be read from any modern spread sheet programs, or from text books on reliability and quality control (Mitra, 1993). It should be noted that the stochastic nature of the above equation in a life cycle t_l, with $t_{k-1} < t_l < t_k$, is shown in Fig. 3. In addition, the cleaning cycles $\theta_{1p} > \theta_{2p} > \ldots > \theta_{jp} \ldots >$ are also shown in the figure.

5 Reliability Based Maintenance Strategies

In this section we discuss various scenarios of the maintenance strategy in terms of the scatter parameter ($\sqrt{\alpha}$) of the time-to-fouling distribution corresponding to a critical level of fouling, and the risk level (p) representing the probability of tubes being fouled up to a critical level after which a cleaning cycle is needed.

5.1 Maintenance Restores the Exchanger Performance: Case I. Maintenance will fully restore the heat exchanger performance, i.e., a perfect maintenance scheme. In this scheme,

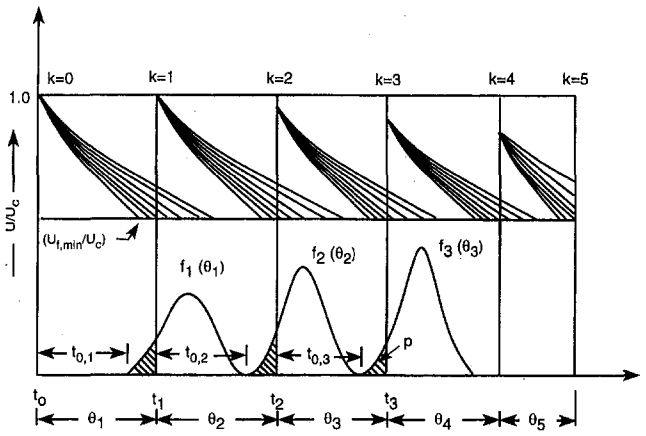

Fig. 3 The performance of a group of heat exchangers working under same thermal-hydraulic conditions

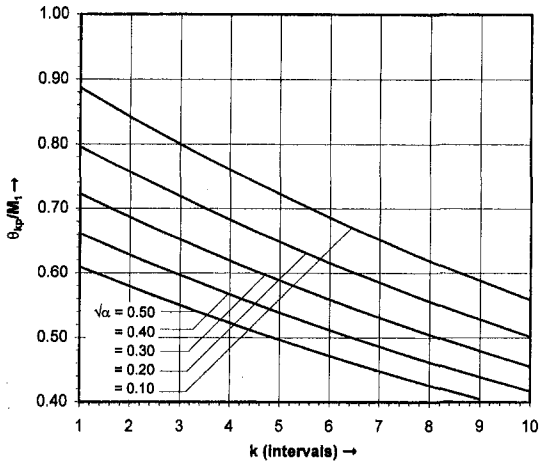

Fig. 5 The reduced time interval between cleaning θ_{kp}/M_1 for the performance degradation $d = 0.05$ and risk level of 0.10

every preventive-maintenance cycle will be a replicate of the previous cycle, repeating at an equal interval. Thus, the interval between cleanings is given by Eq. (20), and the reduced time can be expressed as

$$\theta_p/M = 1/[1 - \sqrt{\alpha}\,\Phi^{-1}(p)], \tag{21}$$

where $M_1 = M_2 = M_3 = \ldots = M$.

Figure 4 shows the plot of reduced time (Eq. (21)) as a function of risk level p and scatter parameter $\sqrt{\alpha}$ of the interval between cleanings θ_k for the kth preventive-maintenance action at time t_k. It can be seen from the figure that the reduced time decreases considerably with the risk level p and scatter parameter $\sqrt{\alpha}$.

5.2 Unequal Maintenance Intervals: Case II. There will be a fixed performance degradation d after each maintenance interval (or a block of equal maintenance intervals), resulting in a gradually decreasing preventive-maintenance intervals. Based on the above assumption, this imperfect maintenance scheme can be characterized by the following geometric sequence, which represents the ratio of two adjacent median times between cleanings:

$$M_2/M_1 = M_3/M_2 = \ldots = M_k/M_{k-1} = (1 - d). \tag{22}$$

Here, $k = 1, 2, 3 \ldots$ may represent the successive blocks of maintenance cycles in which the risk level p is maintained as fixed. In the limiting case, a block may have only one maintenance cycle. Thus, in general

$$M_k = (1 - d)^{k-1} M_1 \tag{23}$$

and the reduced time between the cleanings is

$$\theta_{kp}/M_1 = (1 - d)^{k-1}/[1 - \sqrt{\alpha}\,\Phi^{-1}(p)]. \tag{24}$$

Figure 5 represents the impact of the scatter parameter $\sqrt{\alpha}$ and maintenance intervals on the reduced time between cleanings for a fixed performance degradation after each maintenance interval (or a block of equal maintenance intervals) and a risk level of 0.05 and 0.10, respectively.

5.3 Maintenance at Equal Intervals: Case III. The user of heat transfer equipment will like to schedule maintenance at equal intervals for the case of an imperfect maintenance scheme described above. This will result in a gradual increase in the risk level p. In this situation, the risk level can be expressed as

$$p_k = \Phi\{[1 - ((1 - d)^{k-1})/(\theta_{kp}/M_1)]/\sqrt{\alpha}\}, \tag{25}$$

where $\theta_{k1} = \theta_{k2} = \theta_{k3} = \ldots = \theta_{kp}$.

Figure 6 shows that at a fixed reduced time of $\theta_{kp}/M_1 = 0.80$, the risk level p increases considerably with the scatter parameter $\sqrt{\alpha}$ and maintenance interval k.

Illustrative Example 1. Consider a heat exchanger that has a bundle of tubes. For these tubes, the time to reach a critical level of fouling is α-distributed, with a median time $M = 6$ months and the scatter parameter $\sqrt{\alpha} = 0.20$. The probability

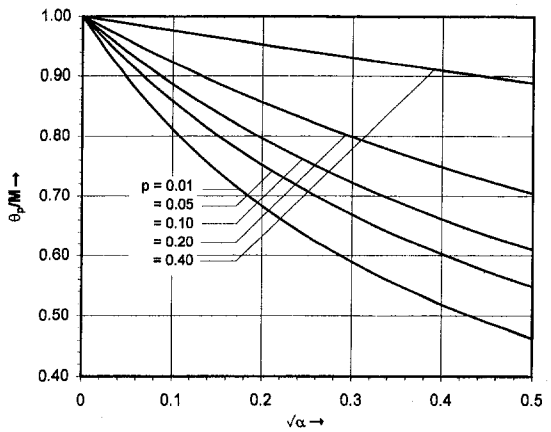

Fig. 4 The reduced time interval between cleaning θ_p/M for a maintenance scheme with no performance degradation after each maintenance interval

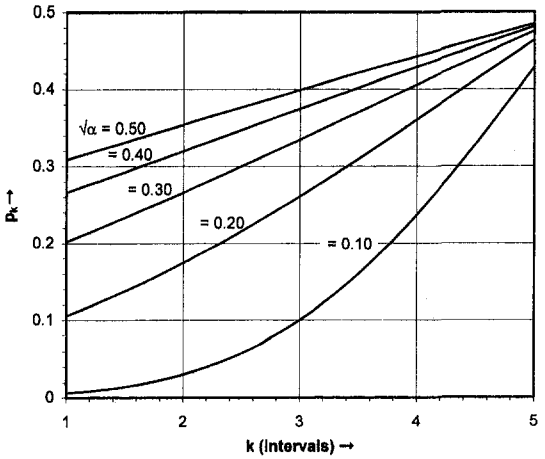

Fig. 6 The risk parameter p_k for $\theta_{kp}/M_1 = 0.80$ and performance degradation $d = 0.05$

Table 1 Maintenance schedules for reliability based scheme: solution to example 1

Maintenance Interval k	Policy			
	Perfect Maintenance (Refer to Fig. 4), or Cleaning of Tubes (Case I)		Imperfect Maintenance or Cleaning of Tubes with $d = 0.05$ (Case II)	
	$\theta_{kp} = \frac{M}{1 - \sqrt{\alpha}\,\Phi^{-1}(p)}$ (months)	t_{kp} (months)	$\theta_{kp} = \frac{M_1(1-d)^{k-1}}{1 - \sqrt{\alpha}\,\Phi^{-1}(p)}$ (months)	t_{kp} (months)
1	4.50	4.50	4.50	4.50
2	4.50	9.00	4.28	8.78
3	4.50	13.50	4.06	12.84
4	4.50	18.00	3.86	16.70
5	4.50	22.50	3.67	20.37
6	4.50	27.00	3.48	23.85

of the overall heat transfer coefficient ($U_{f,\min}$ or $U_{f,l}$) of the exchanger reaching a critical level is desired to be less than 0.05 (i.e., a risk level $p \leq 0.05$). Calculate the maintenance schedule for the next two years for the following cases: (a) after every maintenance interval the performance indicator $U(t)/U_C$ is restored to the original condition; (b) after every maintenance interval the $U(t)/U_C$ is not restored to the original condition and the performance degradation is estimated to be $d = 0.05$; and (c) it is similar to case (b), however, the management has decided to use equal-maintenance intervals with $\theta_{kp}/M_1 = 0.80$: discuss how the risk level p will vary with time.

Solution. The information available about the heat exchanger tubes is $M = 6$ months, $\sqrt{\alpha} = 0.20$, and desired risk level $p = 0.05$. For the given risk level, the solution for (a) and (b) is given in Table 1 by using Eq. (21) or Fig. (4) and Eq. (24) or Fig. 5, respectively. It can be seen from the table that, as expected, the time interval between cleaning (θ_{kp}) is constant for case (a), whereas it decreases continuously for case (b).

We note that the solution for case (c) is based on the fact that $\theta_{kp1} = \theta_{kp2} = \theta_{kp3} = \ldots = \theta_{kp} = 0.80(M)$, or $\theta_{kp} = 0.80(6) = 4.80$ months. The impact of this decision is reflected in a gradual increase in risk level p, which can be determined from Eq. (25) or Fig. (6). On using Eq. (25), we get the risk level p for maintenance intervals $k = 1, 2, 3, 4$ and 5 as $p_k = 0.106$, 0.175, 0.260, 0.348, and 0.464, respectively. It should be emphasized that a gradual increase of the risk level exceeding the critical fouling level is quite severe; therefore, this possibility is not a good choice. However, the risk level can be decreased by using, for example, $\theta_{kp}/M = 0.70$, which may result in an acceptable maintenance policy.

It should be noted that operating a heat exchanger at a critical risk level of a system or component is important in some applications, such as a heat exchanger network in a refinery. In this situation, the maintenance strategy will be primarily governed by an acceptable level of heat exchanger overall heat transfer coefficient. However, in some situations, heat exchangers are not in a network, or in a critical system; here, maintaining the exchanger at a higher-reliability level (or at a lower-risk level p) implies more frequent maintenance intervals, which can often result in an increasing operation and maintenance costs. It is therefore important to note that situations in which the cost of operation and maintenance is an important factor along with the exchanger reliability ($r = 1 - p$), the maintenance decisions can be optimized by developing cost as a function of reliability (or risk level) and then search for a minimum cost-based solution. This cost-optimized solution will also result in an optimal level of a heat exchanger reliability (Sheikh et al., 1996).

6 Cost Based Maintenance Strategies

We consider a specific heat exchanger whose fouling in tubes is characterized by the α-distribution with a median time to reach a critical level of fouling, M, and scatter parameter, $\sqrt{\alpha}$. It is possible to propose a cost-based operating and maintenance model of a heat exchanger subject to fouling that includes costs due to extra energy to overcome the fouling penalty, antifoulant, and cleaning costs. Such a deterministic cost model has been extensively discussed by Casado (1990). By critically examining various cost elements in this model, a simplified version of such a cost model can be expressed in terms of the median life of heat exchanger tubes as

$$C = C_1/(t/M) + C_2(t/M) + C_3(t/M)^m \qquad (26)$$

where C_1, C_2, and C_3 are various cost parameters representing antifoulant, cleaning, and the additional fuel consumption due to fouling, respectively, expressed as dollars/hr; m is a constant reflecting the severity of financial penalty associated with the exchanger performance degradation due to fouling. It is normally greater than one and is a function of the heat exchanger configuration. We note that the total cost function given by Eq. (26) is a convex function in every preventive-maintenance (or cleaning) cycle. This characterization of operating and maintenance costs of a heat exchanger corresponds to the median time to reach a critical level of fouling (M), which represents $p = 0.50$ and any value of, $\sqrt{\alpha}$ or it can also be interpreted as a deterministic case ($\sqrt{\alpha} = 0$). For a more general representation corresponding to any risk level p and scatter parameter $\sqrt{\alpha}$, the above mentioned cost function can be expressed by incorporating the case of perfect cleaning represented by Eq. (21) as follows:

$$\begin{aligned} C(t, \theta_p; \sqrt{\alpha}) &= C_1/(t/\theta_p) + C_2(t/\theta_p) + C_3(t/\theta_p)^m. \\ &= C_1/\{t[1 - \sqrt{\alpha}\,\Phi^{-1}(p)]/M\} \\ &\quad + C_2[1 - \sqrt{\alpha}\,\Phi^{-1}(p)](t/M) \\ &\quad + C_3\{[1 - \sqrt{\alpha}\,\Phi^{-1}(p)](t/M)\}^m. \end{aligned} \qquad (27)$$

The probabilistic cost function discussed above is plotted in Fig. 7 for $\sqrt{\alpha} = 0.20$ and $p = 0.05$, 0.10, 0.20, 0.50, and in Fig. 8 for $p = 0.20$ and $\sqrt{\alpha} = 0.05$, 0.10, 0.20, 0.30. These figures clearly demonstrate the relationship between the total operation and maintenance costs, risk level p, and the scatter parameter $\sqrt{\alpha}$. We note that Eq. (27) reduces to Eq. (26) for the case when $p = 0.50$ and $\theta_p = M$, which indicates a case with no scatter in fouling resistance ($\sqrt{\alpha} = 0$).

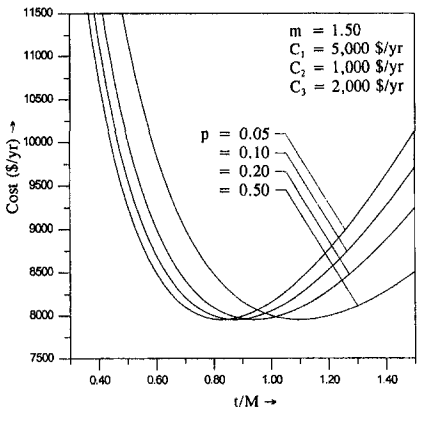

Fig. 7 The total cost for operating and maintaining a heat exchanger subject to fouling; the influence of risk factor p for a fix scatter parameter $\sqrt{\alpha} = 0.2$

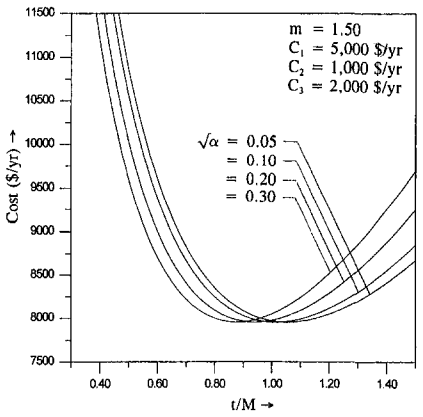

Fig. 8 The total cost for operating and maintaining a heat exchanger subject to fouling; the influence of scatter parameter $\sqrt{\alpha}$ for a fix risk level $p = 0.20$

Illustrative Example 2. The operation and maintenance costs of the heat exchanger discussed in example 1 ($\sqrt{\alpha} = 0.20$ and $M = 6$ months) is estimated to be characterized by Eq. (27), while the constant reflecting severity of financial penalty due to the exchanger performance degradation is given by $m = 1.5$, and the cost coefficients associated with antifoulant, cleaning, and extra fuel consumption are, $C_1 = 5{,}000$ dollars/yr, $C_2 = 1{,}000$ dollars/yr, $C_3 = 2{,}000$ dollars/yr, respectively. Calculate the optimal operation and maintenance costs for a risk level of $p = 0.05$.

Solution. Referring to Fig. 7, we note that for $p = 0.05$, the optimum reduced time $t_{opt}/M = 0.825$, which gives $t_{opt} = 0.825 \times 6 = 4.95$ months, compared to 4.5 months found earlier in Example No. 1. It can be seen from the figure that at an optimum time, the total cost of maintaining the heat exchanger is about \$8,000/yr. In addition, other maintenance strategies that are described earlier with respect to the reliability based model can easily be incorporated into the cost model by expressing the median time M in the model as a function of heat exchanger performance degradation parameter d. The resulting cost equation can then be studied to find an optimum solution.

7 Concluding Remarks

A stochastic approach is discussed to characterize various fouling models and its implications on maintenance of heat exchangers subject to fouling. The concept of a time interval between cleaning ($\theta_k = t_k - t_{k-1}$) for the kth preventive maintenance action is introduced to define the maintenance intervals. For a linear fouling growth model, it is found that the distribution of the time interval is α-distributed with a median time to reach a critical level of fouling as M and scatter parameter $\sqrt{\alpha}$. In this regard, both reliability as well as cost-based maintenance schemes are discussed to operate and maintain the heat exchanger performance at the desired risk level.

The mathematical structure of reliability based maintenance model is discussed in detail, which is illustrated by an example problem to explain three possible scenarios of the model: (i) the performance of the exchanger is restored to the original condition; (ii) the performance of the exchanger is not restored to the original condition and there is some degradation; and (iii) it is desired to operate the exchanger at fixed maintenance intervals.

The cost based maintenance model for operating and maintaining the exchanger is also treated in a probabilistic manner by introducing the risk level p and the scatter parameter $\sqrt{\alpha}$ in the algebraic expression of the total cost equation. The resulting plots of the total cost clearly indicate the influence of these parameters. It is observed from these plots that decreasing the risk level from $p = 0.50$ increases the total costs of operating and maintaining the exchanger, particularly in the non-optimal region of t/M. The greater the departure from the optimal region, the larger the impact of risk level p is observed. However, in the vicinity of optimal region of t/M for different levels of p, the optimal cost essentially remains constant. In addition, it is important to mention that the approach presented in this paper is general and can be applied to any type of heat exchangers whose performance degrades due to fouling and/or corrosion.

Acknowledgments

The authors acknowledge the support provided by the King Fahd University of Petroleum and Minerals through the research project ME/FOULING/176. The constructive comments made by the reviewers are appreciated.

References

Ahmad, M., and Sheikh, A. K., 1984, "Bernstein Reliability Model: Derivation and Estimation of Parameters," *Reliability Engineering*, Vol. 8, No. 6, pp. 131–148.

Al-Ahmad, M. I., Abdelaleem, F. A., 1991, "Scale and Fouling Problems and its Reflection on the Performance of Industrial Thermal Processes," *Proceedings of the 3rd Saudi Engng. Conference*, Riyadh, Saudi Arabia, Vol. 1, pp. 1–11.

Bott, T. R., 1995, *Fouling of Heat Exchangers*, Elsevier Science Publishers Ltd., Amsterdam.

Casado, E., 1990, "Model Optimizes Exchanger Cleaning," *Hydrocarbon Processing*, Vol. 69, No. 8, pp. 71–76.

Chenoweth, J. M., 1990, "Final Report of the HTRI/TEMA Joint Committee to Review the Fouling Section of the TEMA Standards," *Heat Transfer Engineering*, Vol. 11, No. 1, pp. 73–107.

Epstein, N., 1981, "Fouling: Technical Aspects (Afterword to Fouling in Heat Exchangers)," *Fouling of Heat Transfer Equipment*, E. F. C. Somerscales and J. G. Knudsen, eds., pp. 31–53, Hemisphere, Washington, D.C.

Kern, D. Q., and Seaton, R. E., 1959, "A Theoretical Analysis of Thermal Surface Fouling," *British Chemical Engineering*, Vol. 4, No. 5, pp. 258–262.

Knudsen, J. G., 1990, "Fouling in Heat Exchangers," *Hemisphere Handbook of Heat Exchanger Design*, Hemisphere, Washington, D.C.

Mitra, A., 1993, *Fundamentals of Quality Control and Improvement*, MacMillan Publishing Company, New York, NY.

Sheikh, A. K., Zubair, S. M., Haq, M. U., and Budair, M. O., 1996, "Reliability-Based Maintenance Strategies for Heat Exchangers Subject to Fouling," *ASME Journal of Energy Resources Technology*, Vol. 118, No. 4, pp. 306–312.

Somerscales, E. F. C., and Kassemi, M., 1987, "Fouling Due to Corrosion Products Formed on a Heat Transfer Surface," ASME JOURNAL OF HEAT TRANSFER, Vol. 109, pp. 267–271.

Suitor, J. W., Marner, W. J., and Ritter, R. B., 1976, "The History and Status of Research in Fouling of Exchangers in Cooling Water Service," *The Canadian Journal of Chemical Engineering*, Vol. 55, pp. 374–380.

Taborek, J., Aoki, T., Ritter, R. B., Palen, J. W., and Knudsen, J. G., 1972a, "Fouling: The Major Unresolved Problem in Heat Transfer," *Chemical Engineering Progress*, Vol. 68, No. 2, pp. 59–67.

Taborek, J., Aoki, T., Ritter, R. B., Palen, J. W., and Knudsen, J. G., 1972b, "Predictive Methods for Fouling Behavior," *Chemical Engineering Progress*, Vol. 68, No. 7, pp. 69–78.

Zubair, S. M., Sheikh, A. K., and Shaik, M. N., 1992, "A Probabilistic Approach to the Maintenance of Heat Transfer Equipment Subject to Fouling," *ENERGY*, Vol. 17, No. 8, pp. 769–776.

Zubair, S. M., Sheikh, A. K., Budair, M. O., Haq, M. U., Quddus, A., and Ashiru, O. A., 1997, "Statistical Aspects of $CaCO_3$ Fouling in AISI 316 Stainless Steel Tubes," ASME JOURNAL OF HEAT TRANSFER, Vol. 119, No. 3, pp. 581–588.

S. M. Zubair
zubair@ccse.kfupm.edu.sa

A. K. Sheikh

M. O. Budair

M. U. Haq

Mechanical Engineering Department
King Fahd University of
Petroleum and Minerals
Dharan 31261,
Saudi Arabia

A. Quddus

O. A. Ashiru

Research Institute
King Fahd University of
Petroleum and Minerals
Dharan 31261,
Saudi Arabia

Statistical Aspects of $CaCO_3$ Fouling in AISI 316 Stainless-Steel Tubes

Calcium carbonate fouling is typically encountered in a cooling-water circulating system. An experimental program is initiated to study fouling growth law(s) as well as the basic mechanism of calcium carbonate ($CaCO_3$) scaling. After a brief description of the experimental apparatus and procedure for calculating fouling resistance, we present the deposition data in terms of fouling resistance as a function of time taken at different sections of the tube. In addition, the randomness of fouling growth is illustrated by repeating the experiments several times under the same thermal-hydraulic conditions. The results are presented in terms of a set of sample functions and their associated probability density functions at various levels of fouling. In addition, basic mechanism of $CaCO_3$ scale formation is also explained through Scanning Electron Microscopy (SEM) and Energy Dispersive X-Ray Spectroscopy (EDX).

1 Introduction

Cooling water, whether provided on a once-through basis or from an evaporative cooling tower, contains dissolved inorganic salts which can precipitate and crystallize on heat transfer surfaces. Typical salts that are encountered in cooling-water systems are calcium carbonate, calcium sulfate, calcium phosphate, magnesium salts, silica, and iron oxide (Suitor et al., 1976; Coates and Knudsen, 1980; and Bott, 1995). Some of these salts, or their combinations, have inverse solubility properties so that they are less soluble in the hot stream adjacent to the heat transfer surface. This hot layer can become supersaturated causing the salts to precipitate and adhere on the surface. The deposit thus formed is a major cause of reduced efficiency and capacity of heat transfer equipment (Knudsen, 1990). As energy and material costs have increased over the past several years, there has been additional attention devoted to cooling water fouling and its causes, control, and prevention.

It is found through chemical analysis of water that calcium carbonate ($CaCO_3$) concentration is predominant in a cooling-water circulating system (Knudsen, 1990). An experimental program is initiated to study fouling growth law(s) as well as basic mechanism of $CaCO_3$ scaling. In this paper, which is partially based on the above mentioned project, we first discuss the motivation to study fouling in a statistical framework. It is followed by details of experimental procedure and finally, the analysis and interpretation of the fouling data are presented.

2 Motivation to Study Fouling Processes in A Statistical Framework

It is natural to expect that our knowledge of fundamental sciences that include heat transfer, mass transfer, chemical kinetics, and fluid mechanics will provide a means for the development of methods for predicting the performance of heat exchangers subject to fouling and, perhaps more importantly, suggesting ways in which fouling can be minimized. As noted by Somerscales (1988), this expectation is overly optimistic because fouling is a complex phenomenon, even if consideration is restricted to a single category of fouling without the complications arising from interaction between two or more categories of fouling. Although there are limitations of approaching fouling from a fundamental viewpoint, several researchers (Nancollas and Reddy, 1971; Taborek et al., 1972a, b; Coates and Knudsen, 1980; Epstein, 1981; Hasson et al., 1968; Hasson, 1981; Knudsen, 1990; Chan and Ghassemi, 1991; Chamra and Webb, 1994) have somewhat successfully studied deposition and removal processes from the fundamental aspects. It should, however, be noted that the use of conventional (deterministic) models developed by considering fundamentals of fouling have the following limitations (Somerscales, 1988; and Bott, 1995):

1. There is a lack of information on many of the transport and chemical kinetic processes, particularly as the removal processes are concerned. Specifically, there is no precise information on rates of reaction, sticking probability, mass transfer rates, and the properties of foulant deposits such as density ρ, thermal conductivity k, and nutrient diffusivity.
2. The correlations proposed in these models are generally subject to simplifying assumptions (so that the mathematical solutions can be achieved). The errors so introduced could be substantial for practical applications in design, operation and maintenance of heat exchangers.

A list of deposition and removal models, which is well documented by Somerscales (1988) and Bott (1995), have a large number of vital constants and parameters whose exact values, as mentioned above, are rather difficult to determine even in carefully controlled laboratory experiments. A small pertuba-

Contributed by the Heat Transfer Division for publication in the JOURNAL OF HEAT TRANSFER. Manuscript received by the Heat Transfer Division October 29, 1996; revision received April 21, 1997; Keywords: Fouling; Heat Exchangers; Modeling & Scaling. Associate Technical Editor: Y. Jaluria.

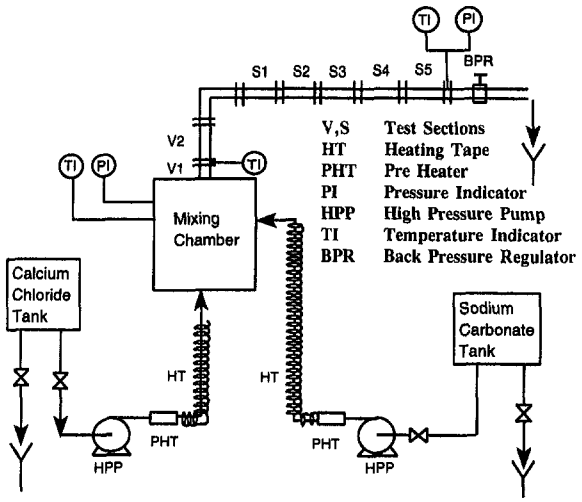

Fig. 1 Schematic of the scale-deposition test equipment

tion, for example, in velocity, temperature, and pH of the solution sometimes results in a significant change in the fouling growth rate. This fact is recognized in the literature as an experimental uncertainty. It should, however, be noted that the experimental uncertainty can best be treated by postulating that the fouling resistance is a time-dependent random process, given by $\mathbf{R}_f = \varphi(\mathbf{A}, \mathbf{B}, t)$, where the cumulative effect of all the uncertainties is embedded in the parameters **A** and **B** of the underlying kinetic models. This postulation of fouling models provides a simplified probabilistic framework to characterize the fouling processes.

3 Experimental Method

3.1 Apparatus. Figure 1 shows a schematic diagram of the scaling-loop test facility. The loop is of once-through type which consists of (two) 40 liter storage tanks, variable-stroke high-pressure metering pumps (HPPs), flow dampeners, pre-heaters, back-pressure regulator (BPR), mixing chamber, and test sections. The flow of the system is controlled by adjusting the stroke length of HPPs. The pressure and temperature are controlled by BPR and temperature controllers. In addition, the apparatus also uses 15 micron filters at the outlet of solution tanks to eliminate any suspended particles.

3.2 Test Solution. Equimolar solutions of $CaCl_2.xH_2O$ and Na_2CO_3 (having concentration of 0.0006 moles/liter each) were prepared from reagent-grade chemicals dissolved in distilled water. The deposits of $CaCO_3$ crystals were generated by mixing equal volume of $CaCl_2$ and Na_2CO_3 solutions from the two tanks at 60°C and 690 kPa in the mixing chamber to produce $CaCO_3$ precipitates according to the following chemical reaction:

$$CaCl_2.xH_2O + Na_2CO_3 \rightarrow CaCO_3 + 2NaCl + xH_2O. \quad (1)$$

The homogenized solution was then passed through the vertical sections, bends, and the horizontal test sections where the $CaCO_3$ deposition took place. It should be noted that the solution samples were taken at both inlet and outlet of the test sections to study chemistry of the solution, the results are given in Table 1. It can be seen from the table that there are negligible amounts of Mg, Fe, Cu, K, Sr, and Ba which can influence kinetics of the process, also pH of the solution varied from 9.63 to 9.34 while flowing through the test sections. This variation in pH is anticipated because of the change in solution alkalinity corresponding to the amount of precipitated $CaCO_3$ in the test apparatus. Furthermore, the flow rate was maintained at a constant value. In this regard, the flow measurements (by using a graduated cylinder and stop watch) were taken intermittently several times at the outlet section during each run.

Table 1 Chemical analysis of the solution samples at inlet and outlet of the test sections*

Parameter	Inlet at 60°C (mg/l)	Outlet at 60°C (mg/l)
Barium	<0.0500	<0.0500
Calcium	22.0000	12.0000
Magnesium	<0.0500	<0.0500
Potassium	<0.2000	<0.2000
Sodium	28.0000	29.0000
Strontium	<0.0500	<0.0500
Chloride	43.5000	42.8300
Sulfate	<0.2000	<0.2000
Bicarbonate	40.0200	30.0200
Carbonate	22.7800	10.7100
TDS	119.0000	103.0000
pH	9.6300	9.3400
Conductivity (in μS)	238.0000	207.0000
Density (in g/ml)	0.9999	0.9997

* Chloride and sulfate were analyzed by ion chromatography, carbonates and bicarbonates by memotitrator, conductivity and TDS by checkmate conductivity/TDS meter, pH by Fisher pH meter, density by pycnometer method and barium, calcium, potassium, magnesium, sodium, and strontium by Inductively Coupled Plasma (ICP).

3.3 Test Specimens. The test sections were made from commercial-grade AISI 316 stainless-steel tubing, with 6.35 mm OD and 4.57 mm ID. The length of each section was set to 76 mm, approximately. Each of the test sections was

Nomenclature

CDF = cumulative distribution function
BPR = back pressure regulator
DF = damage function
EDX = energy dispersive x-ray spectroscopy
F = unreliability function
f = probability density function (PDF), 1/hr
HPP = high pressure pump
K = coefficient of variation of time to reach a critical level of fouling
k = thermal conductivity of the scale, W/m.K
L = length of the test section, m
M = median time to reach a critical level of fouling, hr
ML = maximum likelihood
N = number of observations
P = probability of events
R_f = fouling thermal resistance, m^2.K/W
r_1 = average radius of the scale deposit, m
r_2 = inside radius of the tube, m
$r = 1 - F$ = reliability function
SEM = scanning electron microscopy
t = time, hr
t_i = induction time, hr

Greek Symbols

σ = standard deviation, hr
μ = mean value, hr
ρ = mass density of the scale, kg/m^3
τ = variable of integration.
$\sqrt{\alpha}$ = scatter parameter
φ = function

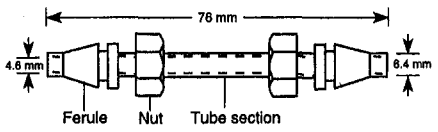

Fig. 2 Schematic of the test section with ferrules and nuts

provided with ferrules and nuts, as shown in Fig. 2. These test specimens were washed carefully with distilled water and acetone to remove dirt and oil contaminations. They were then dried in a temperature-controlled oven. After drying, the test sections were carefully weighed to determine the initial mass on a highly precise electronic balance (±0.1 mg precision). Five test sections were then connected in line with the help of unions and used for a single test run, as shown in Fig. 1.

3.4 Calculation of Fouling Resistance. It should be noted that when the experiment is allowed to run for some specific period of time it results in deposition of $CaCO_3$ scale. This deposition results in an additional resistance to heat transfer, commonly described as fouling resistance, R_f. The procedure for calculating this resistance involves dismantling the test sections at the end of each test run and mildly washing them with distilled water. These were again dried in an oven to yield the true mass gain due to the $CaCO_3$ scale, i.e., vaporizing any of the water contents in and around the test sections. The mass gain due to the scale is then calculated by subtracting the initial mass from the final mass, which is typically used in quantifying scale deposition experiments (Bott, 1995). We can then calculate the fouling resistance due to the mass gain by (Bejan, 1993):

$$R_f = (r_2 - r_1)/k. \tag{2}$$

Here, r_2 is the inside radius of the tube while r_1 is the average radius due to the scale deposit for a particular section. This can be calculated by using the relation

$$r_1 = (r_2^2 - \text{mass gain}/\pi\rho L)^{1/2} \tag{3}$$

where thermal conductivity of the scale (k = 2.25 W/m.K) and mass density (ρ = 2,700 kg/m^3) are used for calculating fouling resistance data (Perry and Green, 1984). It should be noted that the above values are for calcite; however, both thermal conductivity and density depend on the degree of porosity of the deposit, which varied along the length of the test sections.

4 Experimental Results and Analysis

The first set of experiments were performed with an interval of 2 h for recording the mass-gain data. Each time when the experiment was stopped (without disturbing the scale), the procedure for calculating fouling resistance, as described earlier, was repeated. Notice that the test sections were always assembled at their previous locations with the same orientation, i.e., the upstream side of the section remained upstream for every test run. During the experiments, operating parameters of the test apparatus such as temperature, velocity, pressure, as well as the concentrations of $CaCl_2.xH_2O$ and Na_2CO_3, were kept constant at 60°C, 0.17 m/sec, 690 kPa, and 0.0006 moles/liter each, respectively. The experiments were continued till the complete blockage of the tubes due to the $CaCO_3$ scale.

The recorded data and fouling resistance-time curves are shown in Fig. 3. It can be seen from these curves that the characteristic fouling resistance-time curves for $CaCO_3$ scaling are essentially linear in the range investigated. In addition, the figure shows that for about 1.5 h, there is no deposition, i.e., there is an induction time for scaling growth. This may be explained by the fact that a relatively new heat transfer surface was exposed to the solution. In addition, the figure shows that the fouling rate progressively falls as the test section location moves further downstream. This result is expected. As is seen in Table 1, the flow stream becomes increasingly depleted in both Ca^{++} and CO_3^{--} as it moves downstream; furthermore, to the extent that mass transfer controls the deposition process, the developing velocity and concentration boundary layers as one moves downstream give rise to a decreasing mass transfer coefficient. Thus, a declining driving force for mass transfer results in a declining deposition rate. This is exactly what is predicted by the Hasson (1981) deposition rate model, i.e., the farther the test section is along the flow passage, the lower the growth rate. In addition, it is found that the theoretical predictions, by using the Hasson model, are closer to the observed values if we consider higher values of mass transfer coefficient (than that calculated by laminar flow correlations) due to the bend in the inlet passage and the considerable roughness one expects in a deposit formed at very low Reynolds number.

4.1 Replicate Experiments. In view of the general trends of fouling resistance-time curves, the experiments were run in six replicates under nominally identical operating conditions, as described previously. For each replicate, the data were recorded every 2, 6, and 14 hours, or at times in between, whenever necessary. It should be noted that the vertical sections and 90 deg bend were kept in a clean condition from inside as long as possible under the existing operating conditions. This was achieved by washing them with a dilute acid at the end of each run and rinsing with distilled water to neutralize the effect of acidic contents in these sections, if any. The fouling resistance data thus obtained is presented in Figs. 4–6 for test sections 1, 2, and 3, respectively. As can be seen from these figures, the experimental duration in different replicates is not constant. This was due to the experimental limitations, i.e., sometime the experiment had to be stopped due to BPR blockage by $CaCO_3$

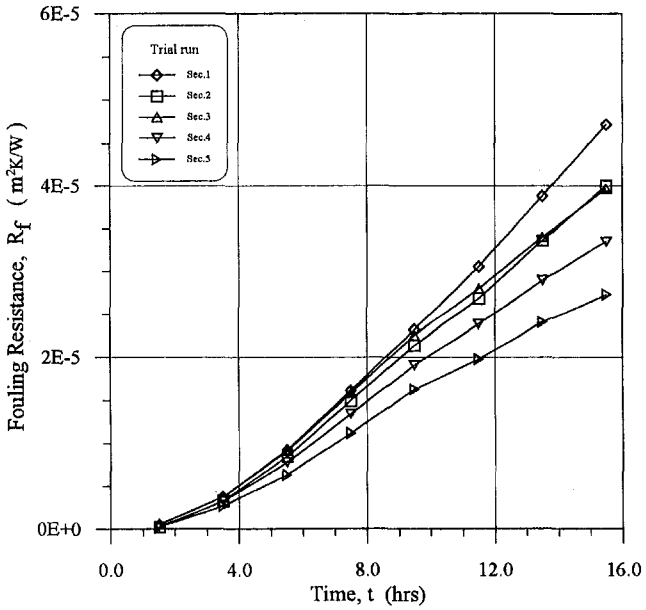

Fig. 3 Fouling resistance versus time for all the test sections: operating temperature, velocity, pressure, and the concentrations of $CaCl_2.xH_2O$ and Na_2CO_3 are maintained at 60°C, 0.17 m/s, 690 kPa, and 0.0006 moles/liter each, respectively

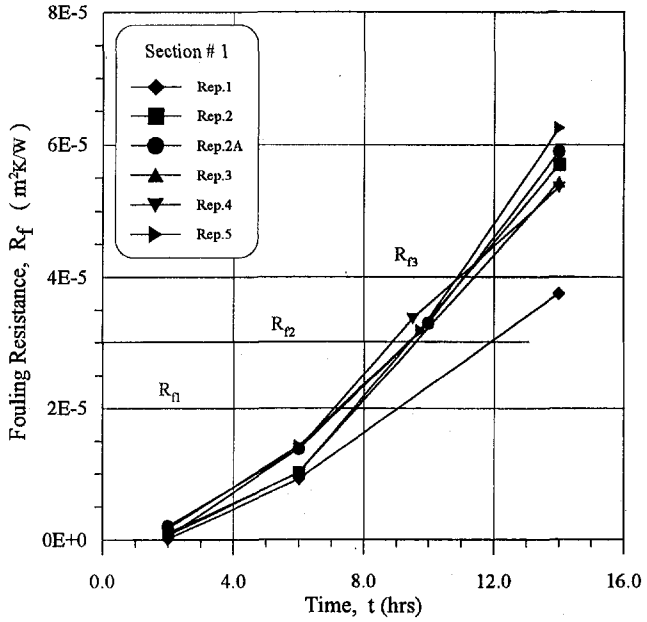

Fig. 4 Replicate data for fouling resistance versus time for test section 1: operating parameters are same as that indicated in Fig. 3

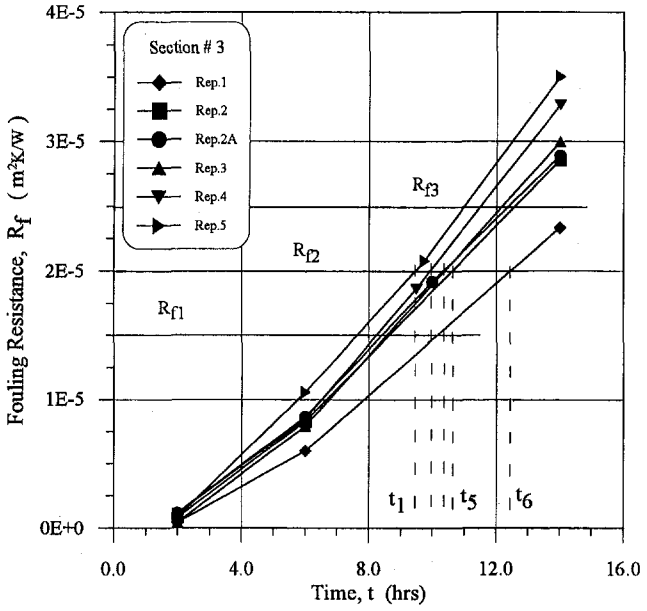

Fig. 6 Replicate data for fouling resistance versus time for test section 3, where $t_1, t_2, \ldots, t_6$ indicate interpolated values: operating parameters are same as that indicated in Fig. 3

deposits. In these operating situations, the readings were obtained by linear interpolation. These figures show that the deposition rate is slow in the beginning with an induction time but gradually increases with time and is relatively smooth until the blockage of the tubes. The characteristic of the fouling resistance-time curves is again found to be linear.

4.2 Statistical Analysis of $CaCO_3$ Scaling. Figure 7 shows linearly fitted curves of the data presented in Fig. 6 by using a linear regression technique. These fitted curves indicate induction time of 2.10 h for section 3. The set of these linear fouling resistance versus time curves for all the test sections (Haq, 1995), suggests that the kinetics of $CaCO_3$ scaling can be characterized by a random linear fouling resistance (damage or degradation) function of the form $\mathbf{R}_f(t) = \mathbf{A} + \mathbf{B}(t - t_i)$, for $t \geq t_i$. Assuming $\mathbf{A} = 0$, and considering $(t - t_i)$ as t, the fouling growth law will become $\mathbf{R}_f(t) = \mathbf{B}t$, for $t \geq 0$, where both $\mathbf{R}_f$ and $\mathbf{B}$ are normally distributed with mean $\mu(\mathbf{B})$ and $\mu(\mathbf{R}_f)$, and standard deviation $\sigma(\mathbf{B})$ and $\sigma(\mathbf{R}_f)$, respectively. It should be noted that these fitted curves in Fig. 7 represent realizations of the random process, where the ith realization is represented by $R_{fi}(t) = B_i t$, $i = 1, 2, \ldots, N$. Notice that such linear random damage functions have been discussed in detail by Ahmad and Sheikh (1984), Sheikh et al. (1986), in a general framework of reliability theory. In addition, Shaik (1990) and Zubair et al. (1992) proposed its utility in modeling the fouling kinetics. They have shown that when both the growth rate of fouling resistance $\mathbf{B}$ and $\mathbf{R}_f(t)$ at any time t are normally distributed, then the distribution of the random variable $\mathbf{t}$ (embedded in $\mathbf{R}_f(t) = \mathbf{B}t$), to reach a critical level of fouling $R_{f,C}$ (indicated in Figs. 4, 5, 6, 8, and 9 as $R_{f,1}$, $R_{f,2}$, and $R_{f,3}$, respectively), is

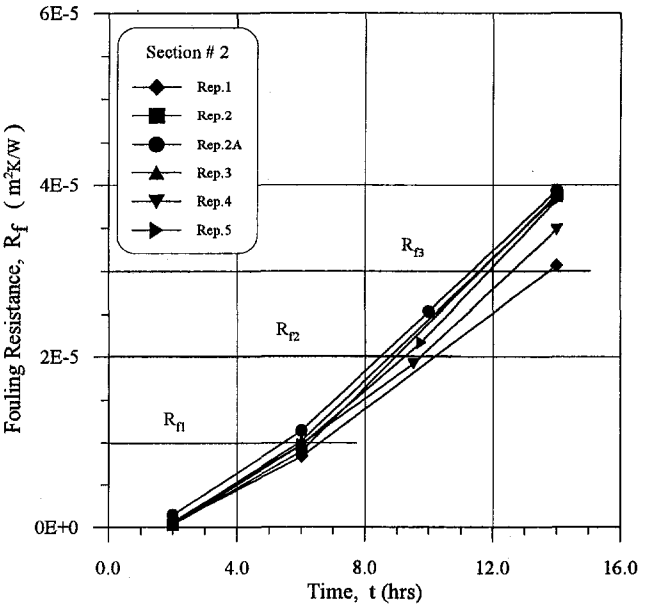

Fig. 5 Replicate data for fouling resistance versus time for test section 2: operating parameters are same as that indicated in Fig. 3

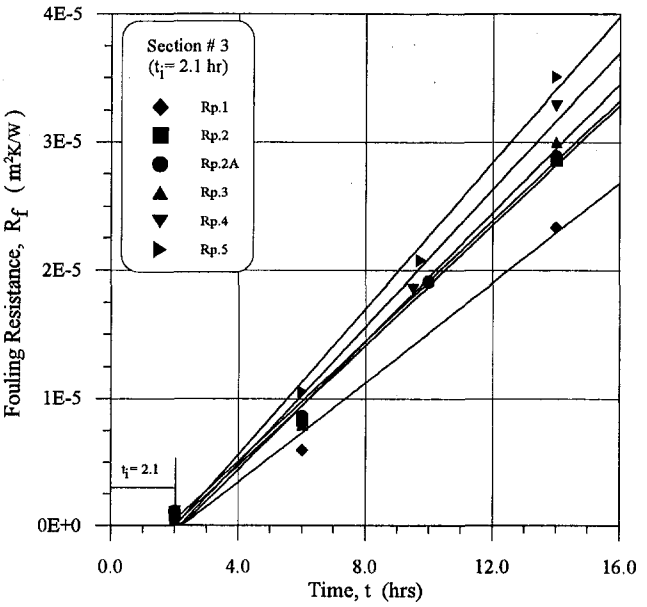

Fig. 7 Linearly fitted curves for the replicate data for test section 3

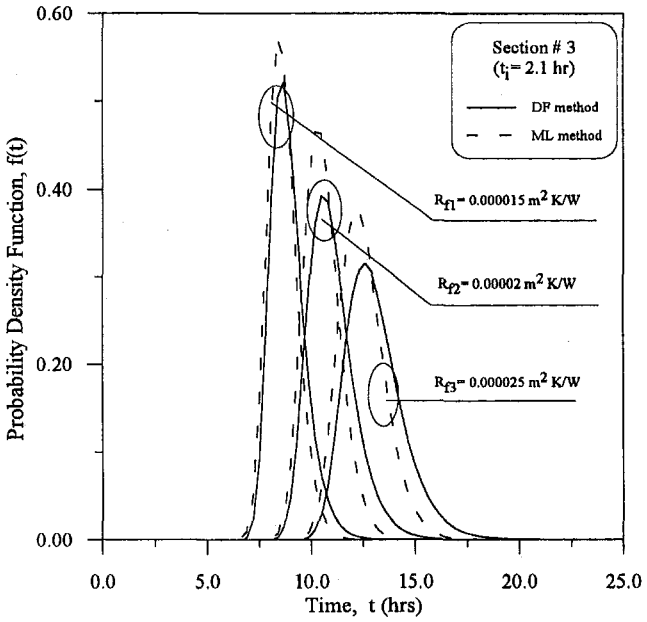

Fig. 8 Probability distribution curves for time to reach a critical level of fouling data for test section 3

α-distributed, also known as a two parameter Bernstein distribution. The derivation of α-distribution in the context of $CaCO_3$ is explained below.

We note that the probability of events $[\mathbf{R}_f(t) < R_{f,C}]$ and $[\mathbf{t} > t]$ is the same and for the α-distribution it is expressed in terms of reliability function $r(t)$ of the fouled surface as

$$r(t) = P[\mathbf{t} > t] = 1 - P[\mathbf{t} \leq t] \tag{4}$$

or

$$r(t; \alpha, M) = 1 - F(t; \alpha, M) = 1 - \Phi\left[\frac{t - M}{\sqrt{\alpha t}}\right] = \Phi\left[\frac{M - t}{\sqrt{\alpha t}}\right], \tag{5}$$

where $\Phi(-z) = 1 - \Phi(z)$, is the well known Gaussian function or standardized normal Cumulative Distribution Function (CDF), given by

$$\Phi(z) = \frac{1}{\sqrt{2\pi}} \int_{-\infty}^{z} e^{-\tau^2/2} d\tau. \tag{6}$$

The parameters M and $\sqrt{\alpha}$ represent median time to reach a critical level of damage, and the spread or scatter in the distribution of $\mathbf{t}$, respectively. Ahmad and Sheikh (1984) have shown that the scatter in time $\mathbf{t}$ to reach the critical damage is approximately linked to the coefficient of variation $[\sqrt{\alpha} \approx K(\mathbf{t}) = \sigma(\mathbf{B})/\mu(\mathbf{B})]$. Note that the probability density function $f(t)$ of the α-distribution is given by Eq. (A.5).

For a specified value of $R_{f,C}$, the distribution parameters M and α can be estimated from a set of linearly fitted curves of a linear random growth process by using the Damage Function (DF) approach (Ahmad and Sheikh, 1984), given by Eqs. (A.6) and (A.7), respectively. In another approach, known as the method of Maximum Likelihood (ML), the direct values of times to reach a critical level of fouling in the form of $\{t_1, t_2, \ldots, t_N\}$ are used to estimate the parameters (given as Eqs. (A.8) and (A.9) in the appendix). Notice that the set of values $\{t_1, t_2, \ldots, t_N\}$ are not always available. In this regard, we have to interpolate the times for a specified value of $R_{f,C}$, as shown in Fig. 6. Since both approaches will give slightly different values of the parameters, the resulting postulated α-distributions will differ correspondingly. Here, we compare these postulated distributions with the empirical (nonparametric) distribution obtained by the method of ranking data as explained in the appendix. The fouling data of the third test section (refer to Fig. 6) are used in conjunction with Fig. 7 to illustrate the validity of α-distribution; analysis of other test sections also show same trends (Haq, 1995). The results are shown in Figures 8–9. In these figures, the empirical distribution is indicated by the data points, while the postulated α-distribution is represented by two continuous curves (by using the estimated parameters M and α according to the two approaches as explained previously). The validity of α-distribution is quite evident in Fig. 9, as reflected by the closeness of the curves with the experimental data. Although special statistical tests for goodness-of-fit are possible, however, here we have relied only on the visual observations of the fitted models.

4.3 Morphology and Characterization of $CaCO_3$ Crystals. For morphological studies of $CaCO_3$ crystals, test coupons (18 × 8 × 1.5 mm) were cut from an AISI 316 stainless-steel sheet to fit into a special Teflon holder. These coupons were then progressively wet polished to 600 grit with a silicon-carbide paper. After polishing, the samples were washed with distilled water and degreased with acetone. The assembly, including the polished samples, was then placed in the mixing chamber of the apparatus where the experiments were run for a specific period of time. After the test, the coupons were retrieved from the chamber, mildly rinsed with distilled water and acetone, and preserved for SEM analysis. For this purpose, a Jeol JSM 840 microscope interfaced with a polaroid camera and a personal computer was used. The samples were energized by a 20 kV AC source to reveal morphology of the deposited crystals on the coupons. In addition, EDX analysis was also used to characterize and confirm the nature of crystals. In the following paragraphs, we present the pertinent results of the SEM analysis, whereas a somewhat more detailed characterization of $CaCO_3$ crystals has been discussed by Haq (1995).

Figure 10 is a typical representation of the $CaCO_3$ crystal growth observed through SEM. This micrograph reveals a variety of crystal structures comprising mainly of rhombic, hexagonal, needle, half moon, and dendritic shapes. It should be emphasized that the statistical characteristics of crystal morphology (i.e., shape and size) at a specified time location, indicate that

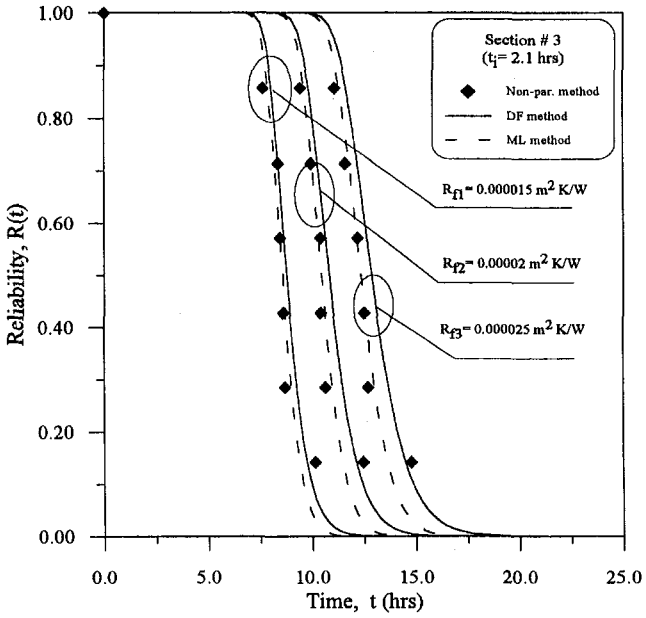

Fig. 9 Reliability curves for time to reach a critical level of fouling data for section 3

Fig. 10 SEM micrograph illustrating morphology of $CaCO_3$ crystals on SS-316 coupon exposed for 2 h to the scale forming solution in the test loop—magnification 200×

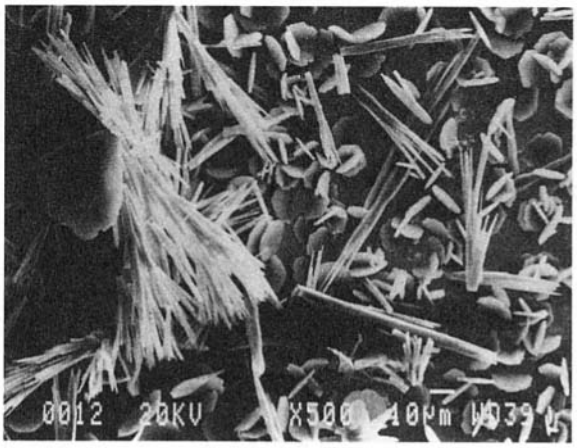

Fig. 11 Magnified (500×) SEM photomicrograph of central portion of Fig. 10, depicting some pertinent features of $CaCO_3$ crystal shapes

the future growth pattern will also be random. The corresponding EDX spectra of the deposited crystals on AISI 316 substrate of the above micrograph showed that the crystals are rich in Ca content and are, in fact, of $CaCO_3$, which is also confirmed through solution sample analysis at the inlet and outlet of the test sections as described earlier. Figure 11 presents a close-up micrograph indicating some of the above mentioned special structural shapes of the crystals obtained in the present study under the fluid-flow conditions.

It can be seen through these micrographs that the growth generally started at preferential nucleating sites consisting of surface heterogeneities such as scratches or polishing marks, and surface roughness. Figure 12 is a SEM photomicrograph depicting the growth mechanism at preferential locations on AISI 316 substrate. These surface imperfections provide the necessary nucleation sites for the inception and subsequent (random) crystal growth. For the crystals to stick at scratches and other surface irregularities, the deposition must occur in the following multistep reaction (Bockris and Reddy, 1970; Nancollas and Reddy, 1971): surface diffusion and transfer from plane sites to step sites, followed by diffusion along the step to a kink site; and finally, surface incorporation. It should also be noted that the time for the apparent crystal growth during these analyses is noticed after about a 1 h exposure of the test coupons in the scale deposition test apparatus. This fact can be related to the induction time shown in the fouling resistance-time curves, as indicated earlier in the presentation of experimental results.

5 Discussion and Concluding Remarks

It has been observed during the experiments that there is a negligible mass gain during the initial experimental runs. We emphasize that any appreciable deposition of crystals and the resulting fouling resistance depends solely on the induction time for a new heat transfer surface and the prevailing process conditions.

The primary deposits are fine, homogeneous, and tightly held to the inside surface of the test sections. However, the subsequent deposits are loose and nonhomogeneous and they grow at a faster rate. We note that the loose scale particles are likely to change their position with time and move along the tube. There is a chance of accumulation of these particles at some point along the tube to cause the flow blockage. Sometimes these accumulated scale particles form small lumps, which are hard to break and can move from one point to another in the test sections, that have every chance of accumulating into bigger lumps at any point, thus causing a line blockage. In addition, these deposits can cause the blockage of the back-pressure regulator. Once the line blockage occurs, it causes the back pressure to increase considerably. To avoid a sudden increase in the back pressure it is necessary to clean the tubes regularly.

It is found through the data analysis that the deposition is slow in the beginning, with an induction time, then gradually rises with time untill the blockage of the flow path. We found that the characteristics of fouling resistance-time curves can be approximated by a linear growth curve. The stochastic nature of these growth curves is reflected in a set of realizations of the process which shows a linear growth of mean level of fouling, and a corresponding time-dependent increase in the standard deviation of deposition process. This random behavior of fouling growth laws is presented in terms of the probability and reliability functions of the α-model. Although stochastic analysis of fouling data in this paper is explained only for $CaCO_3$ fouling, the method of analysis can easily be applied to any random fouling process; for example, fouling in cooling water systems, in petroleum refining, soot deposits in steam boilers, etc. It should be noted that the fouling data in the present problem are characterized by a linear growth model, however, in some applications the growth model may be nonlinear (Zubair et al., 1992), which can also be handled on similar lines. In addition, it is important to emphasize that the stochastic characterization of fouling processes and the resulting distributions are needed in establishing reliability

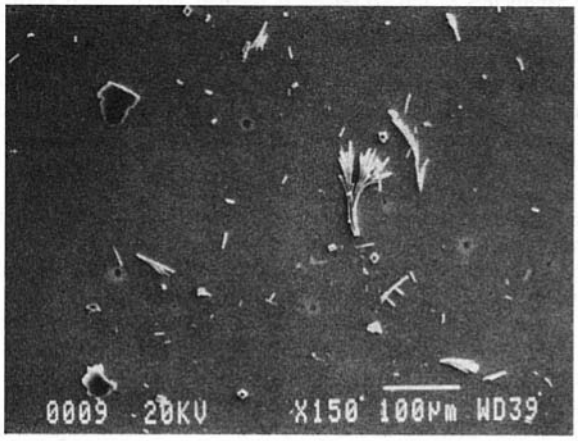

Fig. 12 SEM micrograph indicating nucleation growth of $CaCO_3$ crystals at preferential locations on the SS-316 coupon exposed for $1\frac{1}{4}$ h in the test loop—magnification 150×

based maintenance strategies of heat exchangers subject to fouling (Zubair et al., 1997); for example, in the companion paper the maintenance problem is dealt with analytically in terms of parameters M and α of the α-distribution.

Acknowledgments

The authors acknowledge the support provided by the King Fahd University of Petroleum and Minerals through the research project ME/FOULING/176. The authors also would like to thank the support received from the Research Institute of KFUPM with regard to the experimental program. The constructive comments made by the reviewers are appreciated.

References

Ahmad, M., and Sheikh, A. K., 1984, "Bernstein Reliability Model: Derivation and Estimation of Parameters," *Reliability Engineering,* Vol. 8, No. 6, pp. 131–148.

Bejan, A., 1993, *Heat Transfer,* John Wiley & Sons Inc., New York.

Bockris, J. O. M., and Reddy, A. K. N., 1970, *Modern Electrochemistry,* Vol. 2, Pleum Press, New York.

Bott, T. R., 1995, *Fouling of Heat Exchangers,* Elsevier Science Publishers Ltd., Amsterdam.

Chan, S. H., and Ghassemi, K. F., 1991, "Analytical Modeling of Calcium Carbonate Deposition for Laminar Falling Films and Turbulent Flow in Annuli: Part I—Formulation and Single-Species Model; Part II—Multi-Species Model," ASME JOURNAL OF HEAT TRANSFER, Vol. 113, pp. 735–746.

Chamra, L. M., and Webb, R. L., 1994, "Modeling Liquid-Side Particulate Fouling in Enhanced Tubes," *International Journal of Heat and Mass Transfer,* Vol. 37, No. 4, pp. 571–579.

Coates, K. E., and Knudsen, J. G., 1980, "Calcium Carbonate Scaling Characteristics of Cooling Tower Water," *ASHRAE Transactions,* Vol. 86, Part 2, pp. 68–91.

Epstein, N., 1981, "Fouling in Heat Exchangers," *Fouling of Heat Transfer Equipment,* E. F. C. Somerscales and J. G. Knudsen, eds., Hemisphere, Washington, D.C., pp. 701–743.

Hasson, D., Avriel, M., Resnick, W., Rozenman, T., and Windreich, S., 1968, "Mechanisms of Calcium Carbonate Deposition on Heat Transfer Surfaces," *Industrial and Engineering Chemistry Fundamentals,* Vol. 7, No. 1, pp. 59–65.

Hasson, D., 1981, "Precipitation Fouling," *Fouling of Heat Transfer Equipment,* E. F. C. Somerscales and J. G. Knudsen, eds., Hemisphere, Washington, D.C., pp. 527–568.

Haq, M. U., 1995, Reliability-Based-Maintenance Strategies for Heat-Transfer Equipments Subject to Fouling," M.Sc. Thesis, King Fahd University of Petroleum and Minerals, Dhahran.

Kapur, K. C., and Lamberson, L. R., 1977, *Reliability in Engineering Design,* John Wiley & Sons Inc., New York.

Knudsen, J. G., 1990, "Fouling in Heat Exchangers," *Hemisphere Handbook of Heat Exchanger Design,* Hemisphere, Washington, D.C.

Lewis, E. E., 1995, *Introduction to Reliability Engineering,* John Wiley & Sons Inc., New York.

Mann, N. R., Schafer, R. E., and Singpurwalla, N. D., 1974, *Methods for Statistical Analysis of Reliability and Life Data,* John Wiley & Sons Inc., New York

Nancollas, G. H., and Reddy, M. M., 1971, "The Crystallization of Calcium Carbonate. II. Calcite Growth Mechanism," *Journal of Colloid and Interface Science,* Vol. 37, pp. 824–830.

Perry, R. H., and Green, D. W., 1984, *Perry's Chemical Engineers' Handbook,* McGraw-Hill, New York.

Shaik, M. N., 1990, "Reliable Life-Prediction Models for Various Material Damage Processes," M.Sc. Thesis, King Fahd University of Petroleum and Minerals, Dhahran.

Sheikh, A. K., Younas, M., and Ahmad, M., 1986, "A Comparative Study of Reliability Models in Fatigue Life Prediction," *Res Mechanica, International Journal of Structural and Materials Science,* Vol. 19, pp. 189–218.

Somerscales, E. F. C., 1988, "Fouling," *Two-Phase Flow Heat Exchangers: Thermal-Hydraulic Fundamentals and Design,* S. Kakac, A. E. Bergles, and E. O. Fernandes, eds., Kluwer Academic Publishers, Dordrecht, The Netherlands, pp. 407–460.

Suitor, J. W., Marner, W. J., and Ritter, R. B., 1976, "The History and Status of Research in Fouling of Exchangers in Cooling Water Service," *The Canadian Journal of Chemical Engineering,* Vol. 55, pp. 374–380.

Taborek, J., Aoki, T., Ritter, R. B., Palen, J. W., and Knudsen, J. G., 1972a, "Fouling: The Major Unresolved Problem in Heat Transfer," *Chemical Engineering Progress,* Vol. 68, No. 2, pp. 59–67.

Taborek, J., Aoki, T., Ritter, R. B., Palen, J. W., and Knudsen, J. G., 1972b, "Predictive Methods for Fouling Behavior," *Chemical Engineering Progress,* Vol. 68, No. 7, pp. 69–78.

Zubair, S. M., Sheikh, A. K., and Shaik, M. N., 1992, "A Probabilistic Approach to the Maintenance of Heat-Transfer Equipment Subject to Fouling," *ENERGY,* Vol. 17, No. 8, pp. 769–776.

Zubair, S. M., Sheikh, A. K., Budair, M. O., and Badar, M. A., 1997 "A Maintenance Strategy for Heat Exchangers Subject to Fouling: A Probabilistic Approach," ASME JOURNAL OF HEAT TRANSFER, Vol. 119, No. 3, pp. 575–580.

APPENDIX

Statistical Characterization of Fouling Data. The "N" observations of time (t_1, t_2, t_3, t_4, . . . , t_N) to reach a critical level of fouling represent a set of realizations or an outcome of the random variable $\mathbf{t}$. For example, these values of t can be determined from the set of sample functions (similar to Figs. 4–6). From these figures, at a critical-fouling level, the corresponding values of t_i can be obtained by linear interpolation between the available data points. It should be noted that the main indicators of the random variable $\mathbf{t}$ are the mean time $\mu(\mathbf{t})$ and the standard deviation $\sigma(\mathbf{t})$ expressed as

$$\mu(\mathbf{t}) = \bar{t} = \frac{t_1 + t_2 + \ldots + t_k + \ldots + t_N}{N} = \frac{1}{N}\sum_{j=1}^{N} t_j \quad \text{(A.1)}$$

$$\sigma(\mathbf{t}) = \sqrt{\frac{(t_1 - \bar{t})^2 + (t_2 - \bar{t})^2 + \ldots + (t_N - \bar{t})^2}{(N-1)}} \quad \text{(A.2)}$$

A.1 Empirical Distribution of Random Variable t. The empirical distribution of $\mathbf{t}$ can be determined by a nonparametric approach (Kapur and Lamberson, 1977). In this approach, the data obtained from experiments are treated in an ungrouped form. This data, after ranking in an increasing order, is given by $t_1 > t_2 > t_3 > \ldots > t_j \ldots > t_N$ for N units in a test. In statistical nomenclature, the t_j's are referred to as "the rank statistics" of the test. We may estimate the fraction of the tubes to reach the critical level by time t_j, expressed as (Kapur and Lamberson, 1977)

$$\hat{F}(t_j) = j/(N+1) \quad \text{(A.3)}$$

where the hat symbol ($\hat{}$) indicates the estimated values.

The fraction of the tubes which have not yet reached a critical level of fouling by t_j is defined as the reliability function $r(t_j) = 1 - F(t_j)$, while the PDF is defined by $f(t) = dF(t)/dt = -dr(t)/dt$, given by (Kapur and Lamberson, 1977):

$$\hat{f}(t) = 1/[(t_{j+1} - t_j)(N+1)], \quad t_j < t < t_{j+1}. \quad \text{(A.4)}$$

The above empirical (or nonparametric) distribution is the correct representation of the fouling processes, however, the application of the results to practical heat transfer equipment is more conveniently done using the parametric characterization (Mann et al., 1974; Lewis, 1995). We note that such parametric characterization of the statistical phenomena also help to generalize the knowledge about variability in time to reach a critical level of fouling. For this purpose, it is necessary to fit appropriate probability models to the data. The parameters of these models are related to the spread, $\sigma(\mathbf{t})$ and central tendency, $\mu(\mathbf{t})$ of the random quantity (Kapur and Lamberson, 1977).

A.2 The Postulated Distribution for $CaCO_3$ Fouling. The PDF of the postulated α-model is given by

$$f(t; \hat{\alpha}, \hat{M}) = \frac{dF}{dt} = -\frac{dr}{dt} = \frac{\hat{M}}{\sqrt{2\pi\hat{\alpha}t^2}} \exp\left[-\frac{1}{2}\left(\frac{t-\hat{M}}{\sqrt{\hat{\alpha}t}}\right)^2\right]. \quad \text{(A.5)}$$

A.3 Estimation of Parameters M and α.

From Fouling Growth Curves. The Damage Function (DF)-based parameters in the case of linear fouling model can be estimated from the slopes of the linearly fitted lines such as those shown in Fig. 7. These are

$$\hat{\alpha} = \frac{\sigma^2(B)}{[E(B)]^2} = \frac{\sum_{i=1}^{N}\left(B_k - \frac{1}{N}\sum_{i=1}^{N} B_i\right)^2}{(N-1)\left(\frac{1}{N}\sum_{i=1}^{N} B_i\right)^2} \tag{A.6}$$

and

$$\hat{M} = R_{f,c}/\left(\frac{1}{N}\sum_{i=1}^{N} B_i\right) = R_{f,c}/\bar{B} \tag{A.7}$$

where B_i represents the slope of the ith fitted line; $E(B)$ and $\sigma^2(B)$ are the average and variance of the slope in a given set, respectively.

From the Times to Reach Critical Level of Fouling. The equations for estimating the distribution parameters from N observations of time (t_1, t_2, t_3, t_4, . . . , t_N) to reach the critical level of fouling by Maximum Likelihood (ML) method are

$$\hat{M} = 1/\left(\frac{1}{N}\sum_{j=1}^{N}\frac{1}{t_j}\right), \tag{A.8}$$

$$\hat{\alpha} = \left[\frac{1}{N}\sum_{j=1}^{N}\left(\frac{1}{t_j} - \frac{1}{\hat{M}}\right)^2\right]\hat{M}^2. \tag{A.9}$$

In this method, t_js are either actual values to reach the critical level of fouling or they could be linearly interpolated values between the data points obtained from Figs. 4–6.

In view of the difference between the DF and ML methods used to estimate the parameters α and M, it is important to emphasize that when extrapolation is made to calculate the times to reach the critical level of fouling, then the only option is to use DF-based parameters to derive the distribution. However if the critical times are exactly known or interpolated then the ML estimators should be used, which will give slightly different values then DF-based estimators. Notice that in the DF approach, the estimators are based on the fitted regression curves to each data set of realizations rather than actual data. Therefore, the better the correlation of the fitted curves to the actual data, the less the discrepancy will be between the above mentioned two approaches of estimating the parameters.

T. D. Bennett
Department of Mechanical Engineering,
University of California,
Berkeley, CA 94720

D. J. Krajnovich
IBM Research Division,
Almaden Research Center,
650 Harry Road,
San Jose, CA 95120

C. P. Grigoropoulos
Department of Mechanical Engineering,
University of California,
Berkeley, CA 94720
cgrigoro@euler.berkeley.edu

P. Baumgart

A. C. Tam

IBM Research Division,
Almaden Research Center,
650 Harry Road,
San Jose, CA 95120

Marangoni Mechanism in Pulsed Laser Texturing of Magnetic Disk Substrates

This paper proposes a mechanism for topographical features formed during pulsed laser texturing of Ni-P magnetic disk substrates. A salient feature of the process is the ability to raise a central peak in the irradiated spot, providing a low contact area bearing for the slider-head of a computer hard drive. Formation of topography is believed to involve gradient capillary forces acting at the surface of the molten pool (Marangoni effect). However, the central peak cannot be explained with thermocapillary forces alone. Therefore, it is suggested that a compositional gradient due to the depletion of a surfactant at the molten surface provides the necessary condition to reverse the capillary force in the central region. This perspective is investigated using finite element modeling of the Lagrangian fluid mechanics coupled with heat and mass diffusion.

Introduction

Stiction is an adverse adhesive force between two smooth surfaces. In the computer industry, stiction between the slider-head (performing read-write operations) and the magnetic disk surface has long been a problem. The slider-head flies on an air bearing during normal operation, but comes to rest on the disk surface when the computer is powered-off [1]. One solution to the stiction problem is to texture the entire disk surface. Texture reduces the contact area between the slider-head and the disk surface, thereby reducing the capillary forces arising between the two surfaces. However, new high performance disk drives require a polished surface in the data storage region of the magnetic disk. The polished surface accommodates lower flying slider-heads, which in turn increases data storage densities and read-write speeds. Consequently, a dedicated texture zone needs to be fabricated for landing the slider-head. Traditional methods, such as mechanical or sputter processes, are not well suited for zone-texturing because of inherent difficulties in implementing the processes locally. Furthermore, traditional methods provide limited control over the dimensions of surface asperities, and therefore are less suited for low flying slider-head designs.

A new innovation in zone-texturing of magnetic disk drives has been discussed by Baumgart et al. (1995). Texturing of Ni-(12 wt.%)P disk substrate material is accomplished using a Q-switched Nd:YLF laser ($\tau_p \cong 50$ ns, $\lambda = 1047$ nm). It was shown that single pulse topographic features are sensitively dependent on laser pulse-energy. Of particular interest was the development of two distinct topographic forms, see Fig. 1. The first can be described as a bowl shape, having a rim of material elevated above the disk surface. The second topographic form resembles a Sombrero, having a central peak extending from the bottom of the bowl. The extent of the central peak is variable, ranging from nonexistent (bowl shape), to having a peak elevation above the surrounding rim.

An important aspect of the laser texturing process is that bump features can be produced with only tens of nanometers extent from the disk surface. High-performance disk drives require extremely low fly height of the slider—imposing strict height specifications on the textured landing zone. Baumgart et al. (1995) introduced the Sombrero bump shape which demonstrates a superior reduction in slider-to-disk contact area when the central peak extends above the bowl rim. Stiction, which is an adverse adhesive force between the slider and the disk, can be minimized by reducing the slider-to-disk contact area.

The purpose of this paper is to expand on the work of Baumgart et al. (1995), and to advance a specific mechanism of bump formation involving surface capillary forces. Mechanisms involving etching (i.e., removal of material around topographic features by vaporization) are excluded from consideration because of the reported (Baumgart et al., 1995) conservation of bulk material at the surface. Rather, hydrodynamic redistribution of material will be considered.

Hydrodynamic Mechanisms for Topography Growth

In general, the possible forces giving rise to motion of the melt can be categorized as either body or surface forces. Considering body forces first, the familiar static force of gravity is recognized as insignificant on the nanosecond time scale of this problem. However, a significant dynamic body (inertial) force acting on the melt might arise from an elastic motion of underlying material. Such a force has to be connected with the formation and liberation of micrometer sized droplets from the molten surface of a gold target (Bennett et al., 1995). In that study, the kinetics of the liquid-solid interface, in combination with a decrease in material density going from the solid to liquid state,

Contributed by the Heat Transfer Division for publication in the JOURNAL OF HEAT TRANSFER. Manuscript received by the Heat Transfer Division January 18, 1996; revision received April 1997; Keywords: Laser Processing; Mat'ls. Processing & Manufacturing Process; Thermocapillary Flows. Associate Technical Editor: T. Tong.

[1] For some designs, the slider is parked entirely off the disk surface.

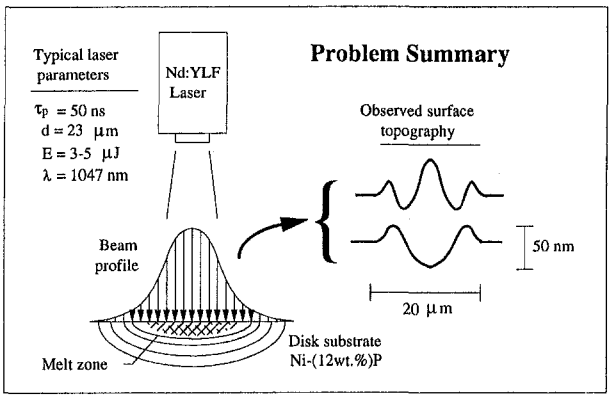

Fig. 1 Summary of the disk texturing problem

produced an inertial force acting on the melt that directed material away from the surface. However, the amorphous Ni-P system experiences no discontinuity in density going from the solid to the liquid state. An inertial force acting on the melt will arise from a nonzero coefficient of thermal expansion. This effect is not modeled in this work because of the inability of inertial forces to provide for nonmonotonic redistribution of surface material as a function of pulse-energy. At low pulse-energy there is a depletion of material from the central region, while at slightly higher pulse-energy there is an accumulation of material in the center (Baumgart et al., 1995). While the magnitude of inertial forces acting on the molten layer changes with pulse-energy, the direction does not. For long time scales, capillary wave motion of the surface might explain the observations. However, in the time scale provided for by the melt duration, full-period capillary wave motion occurs only on a spatial scale much smaller than the main features of the bump.

Surface forces include both normal and shear stress. A significant normal stress may arise in the problem due to the surface recoil pressure of vaporized material. A second normal stress arises from the Young-Laplace pressure discontinuity across a curved interface. The Marangoni effect involves the second category of surface stress, due to shear. This effect refers to motion of liquid due to surface tension gradients[2], and will be categorized here with two distinct components: thermocapillary and chemicapillary. As the names suggest, the first results from the thermal potential of a temperature gradient, and the second results from the chemical potential of a compositional gradient. The thermocapillary force acts to move material toward cooler regions of higher surface tension. For both bowl and Sombrero-shaped bumps, the thermocapillary force is responsible for the formation of the rim. It will be argued that the formation of the central peak of the Sombrero is due to chemicapillary force. The chemicapillary force acts to move material toward regions of higher surface energy corresponding to lower surface surfactant concentration[3].

Baumgart et al. (1995) offer several important experimental clues toward understanding the mechanism of bump formation. The first is the fact that there exists a threshold pulse energy for the formation of a central peak. Below this threshold the bump shape is that of a bowl having only the rim protruding from the disk surface. A second clue is that the central peak does not monotonically grow above this threshold energy. Rather, the height of the central peak first increases and then decreases, and its width broadens as the pulse energy rises from approximately 3.5 to 4.6 μJ. A final clue is that the central peak does not continue to grow when additional laser pulses are delivered to the same spot on the disk. Instead, after the Sombrero shape is formed on the initial laser pulse, the central peak is reduced with subsequent pulses until the bump shape is driven to that of a bowl, after 10–20 pulses. The modeling presented here pursues the premise that Marangoni-driven flow is (predominantly) responsible for the redistribution of surface material (although secondary effects due to surface curvature and vapor recoil pressure are included). Under all conditions, surface temperature gradients will act to redistribute surface material by thermocapillary action. In addition, it will be shown that a surface compositional gradient may arise from the depletion of a more volatile surfactant. If local depletion of the surfactant is sufficient, the resulting chemicapillary action will also contribute to redistribution of material. To pursue this picture, three transient fields are simultaneously modeled establishing distri-

[2] Representative work on this subject can be found in the ASME proceedings, "*Surface-Tension-Driven Flows,*" Neitzel and Smith, 1993.

[3] Balandin et al. (1995) recently published an interesting study of compositional effects on surface-tension-driven flow resulting from nanosecond laser pulses.

Nomenclature

a_γ = surface tension constant
A_μ = coefficient of viscosity
A_D = coefficient of diffusion
b_γ = surface tension constant
d = $1/e^2$ diameter of Gaussian beam profile
D_m = mass diffusivity
$\mathbf{e}_n$ = unit normal surface vector
$\mathbf{e}_t$ = unit tangent surface vector
E = laser pulse energy
F_E = Eulerian property
F_L = Lagrangian property
γ = surface tension
γ_o = surface tension constant
H_D = apparent activation energy of diffusion
H_μ = apparent activation energy of viscous flow
ΔH_v = enthalpy of vaporization of surfactant
I_s = laser surface radiant flux
I_t = temporal profile of laser radiant flux
j_s = vaporized surfactant mass flux
k = thermal conductivity
k_B = Boltzmann constant
k_γ = surface tension constant
m = mass fraction in wt. percent
m_o = initial mass composition distribution
m_s = surface mass composition
m_s^o = initial surface mass composition
M = molecular weight
N_A = Avogadro's number
P = pressure
P_γ = Young-Laplace pressure ($2\gamma/r_c$)
P_r = vapor recoil pressure
r = radial distance
r_c = mean radius of curvature
R = reflectivity
R^o = initial reflectivity of Ni-P
R_{Ni} = reflectivity of Ni
t = time
T = temperature
t_o = initial time
t^o = reference time
$\mathbf{t}_s$ = free surface stress vector
T_c = critical temperature
T_o = initial temperature
$\mathbf{u}$ = velocity vector
$\mathbf{x}$ = spatial vector
$\mathbf{x}_i$ = spatial vector to liquid-solid interface
$\mathbf{x}^o$ = reference spatial vector
α = thermal diffusivity
λ = laser wavelength
μ = dynamic viscosity
ν_j = coefficient of vapor-pressure
ρ = fluid density
τ_p = laser pulse temporal full-width at half-maximum

butions of temperature, surfactant concentration, and ensuing fluid motion.

Governing Equations, Boundary and Initial Conditions

For brevity, the equations governing heat, mass, and momentum transfer, with appropriate boundary and initial conditions, will simply be stated in this section. The governing equations will be written it terms of the more familiar Eulerian variables, deferring the problem of a Lagrangian formulation until the following section.

The equations of motion (continuity and momentum) will assume the form for incompressible flow in the absence of body forces as follows:

$$\text{continuity:} \quad \nabla \cdot \mathbf{u} = 0 \tag{1}$$

$$\text{momentum:} \quad \rho \frac{D}{Dt}(\mathbf{u}) = -\nabla P + \mu \nabla^2 \mathbf{u}. \tag{2}$$

The initial condition is $\mathbf{u}(t = t_o) = 0$. The two boundary conditions are (1) a no-slip condition at liquid-solid interface, $\mathbf{u}(\mathbf{x} = \mathbf{x}_i) = 0$, and (2) transient stress $\mathbf{t}_s$ at the free surface. The shear force at melt surface will be specified by the Marangoni effect. Normal surface forces arise from the Young-Laplace pressure and the recoil vapor pressure. Formally, $\mathbf{t}_s = \nabla\gamma - (P_\gamma + P_r)\mathbf{e}_n$. The liquid-solid interface is assumed to track the glass transition temperature isotherm. Because of the steep temperature gradients, deviations from this isotherm will not correspond to significant changes in the melt domain.

The thermal energy transport equation for an incompressible fluid with constant thermal properties has the form

$$\text{thermal energy:} \quad \frac{DT}{Dt} = \alpha \nabla^2 T. \tag{3}$$

The initial condition is $T(t = t_o) = T_o$. The two boundary conditions are (1) a constant temperature condition at infinity, $T(\mathbf{x} \to \infty) = T_o$, and (2) a transient heat flux condition at the surface ($I_s = -k(\nabla T)_s \cdot \mathbf{e}_n$). The surface heat flux will be specified by the laser pulse. There is no latent heat associated with the transition between solid and liquid states of an amorphous material, nor is there a change in density with this transition. The latent heat of vaporization is negligible compared with conduction transport. The same is true with respect to radiation losses. Heat conduction accounts for roughly three orders of magnitude more energy than the latent heat of vaporization, and six orders of magnitude more than thermal emission. Consequently, in the model the surface is taken as adiabatic, except for the laser energy flux.

Mass diffusion in the solid phase is negligible for this problem. Mass transport in a constant density fluid is governed by the following equation:

$$\text{mass diffusion:} \quad \frac{Dm}{Dt} = D_m \nabla^2 m. \tag{4}$$

The initial condition is $m(t = t_o) = m_o(\mathbf{x})$. The two boundary conditions are (1) a constant concentration condition at infinity, $m(\mathbf{x} \to \infty) = m_o$, and (2) a transient mass flux condition at the surface ($j_s = -\rho D_m (\nabla m)_s \cdot \mathbf{e}_n$). The mass flux boundary condition is specified by a kinetic relation for vaporization of the surface surfactant.

Numerical Modeling

The free-surface flow makes a Lagrangian formulation more attractive than the Eulerian problem as stated. The transformation $F_E(\mathbf{x}, t) \to F_L(\mathbf{x}^o, t^o, t)$ changes the Eulerian problem of determining the fluid property F_E at time t and position $\mathbf{x}$ to a Lagrangian problem of determining F_L at time t for the fluid that was at $\mathbf{x}^o$ when $t = t^o$. In short, the current position of the fluid, $\mathbf{x}(\mathbf{x}^o, t^o, t)$, is a dependent variable in the Lagrangian problem. The simplifying aspect of this transformation is that the rate of change of F_L is simply the substantial derivative of F_E ($\partial F_L/\partial t = DF_E/Dt$). However, spatial derivatives appearing on the right hand side of the governing equations are, for the Lagrangian formulation, in terms of the current fluid position $\mathbf{x}(\mathbf{x}^o, t^o, t)$, which must also be determined.

This work uses an algorithm proposed by Bach and Hassager (1985) that has also been used recently by Zhao et al. (1996). The algorithm determines the unknown coordinates $\mathbf{x}(\mathbf{x}^o, t^o, t)$ and flow field velocities $\mathbf{u}(\mathbf{x}^o, t^o, t)$ through an iterative procedure. The discretized equations of fluid motion are solved to determine $\mathbf{u}(\mathbf{x}^o, t^o, t = t^o + dt)$ using a pure implicit time integration scheme under the assumption that $\mathbf{x}(\mathbf{x}^o, t^o, t = t^o + dt)$ is already known. Recall that the coordinate field $\mathbf{x}(\mathbf{x}^o, t^o, t = t^o + dt)$ is needed to evaluate the spatial derivatives in the governing equations. Since $\mathbf{x}(\mathbf{x}^o, t^o, t = t_o + dt)$ is not known, it is arrived at through iterations of guessing the new coordinate positions, solving for $\mathbf{u}(\mathbf{x}^o, t^o, t = t^o + dt)$ based on that guess, and then evaluating that guess with the constraint results in the following:

$$\mathbf{x}(\mathbf{x}^o, t^o, t = t^o + dt) = \mathbf{x}(\mathbf{x}^o, t^o, t = t^o) + (\tfrac{1}{2})\{\mathbf{u}(\mathbf{x}^o, t^o, t = t^o + dt) + \mathbf{u}(\mathbf{x}^o, t^o, t = t^o)\} \cdot dt. \tag{5}$$

Once $\mathbf{u}(\mathbf{x}^o, t^o, t = t^o + dt)$ and $\mathbf{x}(\mathbf{x}^o, t^o, t = t^o + dt)$ are found, such that both the discretized equations of motion and Eq. (5) are identically satisfied, the reference condition is updated, $t^o \to t^o + dt$.

The system of equations, subject to the specified initial and boundary conditions, is solved numerically for an axisymmetric domain using the finite element method. The procedure for isoparametric discretization of the diffusion equation (i.e., heat and mass transfer) can be found in most elementary texts. The equations of viscous incompressible flow are discretized using the penalty function method as described by Reddy (1979). The penalty finite element model uses the continuity equation as a constraint to the problem of finding the solution $\mathbf{u}$ to the momentum equation. The continuity constraint is satisfied in a least-squares sense. Following Reddy (1979), rectangular nine-node Lagrange elements are used with reduced integration on the penalty terms in the stiffness matrix. The penalty parameter used was 10^8.

The discretized problem uses two meshes, both containing 350 elements (1491 nodes). A common mesh is used for the fluid flow and heat-transfer problems that discretizes a 16 μm radial extent and 6 μm axial depth. The mass diffusion problem is distinguished by a short axial length scale that is incompatible with the main mesh. Consequently, this problem is solved by mapping a second mesh into the 0.3 μm surface region of the main mesh. The diffusion problems use the Crank-Nicolson time integration scheme, while the fluid problem is integrated implicitly. All three problems are advanced in time using 0.5 ns steps. Solutions are checked for independence of mesh and integration step size.

Physical Assumptions

Surface tension is assumed to be a function of both temperature T and surfactant mass concentration m_s, with the form

$$\gamma = a_\gamma (T - T_c)[1 + b_\gamma \ln(1 + k_\gamma m_s)] - \gamma_o. \tag{6}$$

The linear dependence of surface tension on absolute temperature, Eötvös law, is well known for pure liquids. For pure Ni near the melting point, the temperature coefficient of surface tension is about -0.43 ($\times 10^{-3}$)N/mK (Iida and Guthrie, 1993). The Gibbs adsorption energy equation predicts a loga-

rithmic dependence of surface tension on the activity of the solute in the liquid. For dilute solutions the solute's activity can be replaced by concentration in accordance with Henry's law. Controlled nonmetal solute additions to liquid metals have experimentally demonstrated surface tension varying linearly with log (wt.%) over a mass fraction range 0.01–10 wt.% solute. In Fe, the slope of the surface tension with respect to the natural log of composition ranges from −0.02 to −0.2 N/m for various nonmetal solutes (Iida and Guthrie, 1993). Vitol and Orlova (1984) derived an expression of surface tension dependent on both temperature and composition. By making the argument that vacancies can be treated with the same formalism as impurities, temperature effects are introduced (as vacancy concentrations) through the Gibbs adsorption energy isotherm. One success of this model is the ability to account for a surface tension rise with increasing temperature under certain conditions. Specifically, it has been experimentally observed for particular systems that at temperatures not too far from the liquidus, and for sufficiently high surface concentrations, surface tension can initially rise with temperature prior to falling at higher temperatures (Allen, 1972). This behavior is either not inherent to Ni-P, or is a second-order effect since this trend would tend to deplete the rim region of material (where material accumulates for all of the experimental conditions reported by Baumgart et al., 1995). Equation (6) assumes that surface tension decreases monotonically with rising temperature. Equation (6) is simply an empirical combination of the isotherm behavior of surface tension, with respect to composition, and the pure liquid behavior, with respect to temperature.

The solute mass vapor flux is given by the Hertz-Knudsen-Langmuir formula:

$$j_s = m_s(M/2\pi N_A k_B T)^{1/2}\nu_j \exp(-\Delta H_v/k_B T) \qquad (7)$$

The exponential term and coefficient ν_j give the surfactant vapor pressure dependence on temperature. The term under the square-root relates the pressure to an ideal gas mass flux, and the leading surface mass fraction concentration factor m_s enforces the fact that the solute mass vapor flux must go to zero with depletion of surface concentration. Redeposition of vaporized material is neglected.

The absorbed laser energy flux is assumed to be independent of temperature but dependent on mass surface concentration due to changes in surface reflectivity

$$I_s = (1 - R)I_t(8E/\pi d^2)\exp(-8r^2/d^2) \qquad (8)$$

where E is the total incident laser energy per pulse, and d is the diameter of the Gaussian focused laser spot measured at the $1/e^2$ intensity. R is the surface reflectivity, which is assumed to vary linearly with mass concentration, between the initial surface reflectivity R^o and the pure Ni reflectivity R_{Ni}.

$$R = (m_s/m_s^o)(R^o - R_{\mathrm{Ni}}) + R_{\mathrm{Ni}} \qquad (9)$$

where I_t is the laser pulse temporal profile, which is assumed to be a symmeric triangular profile with full-width at half-maximum of τ_p.

$$I_t = \begin{cases} \dfrac{t}{\tau_p^2} & 0 < t < \tau_p \\ \dfrac{(2\tau_p - t)}{\tau_p^2} & \tau_p < t < 2\tau_p \end{cases} \qquad (10)$$

The fluid viscosity is given by

$$\mu = A_\mu \exp(H_\mu/k_B T) \qquad (11)$$

where H_μ is estimated to be 25 kJ/mol, and A_μ is normalized such that Eq. (11) gives 10^{-3} Pa·s at the glass transition temperature. The mass diffusion coefficient is given by

$$D_m = A_D \exp(-H_D/k_B T) \qquad (12)$$

where H_D is estimated to be 10 kJ/mol, and A_D is normalized such that Eq. (12) gives 10^{-9} m^2·s at the glass transition temperature.

Closure Problem

Despite having written the governing field equations, one may have noticed that no mention has been made of what is being modeled in the mass transfer problem—other than the notion that this species acts as a surfactant for the chemicapillary action. Delaying this subject illustrates that the formalism of the problem statement is largely independent of this issue.

The original idea was to model the preferential vaporization of phosphorus from the surface, with the notion that P also acts as a surfactant. Unfortunately, there is little quantitative information available for modeling diffusion and vaporization of P in a Ni matrix, or the effect of P on surface tension of Ni. This forces one to abandon the goal of seeking a solution for the phosphorus picture that is necessarily unique or distinguishable from other possible surface surfactants. The scope of this study should be perceived as somewhere between first and second-order: the role of numerical modeling is to evaluate a general hypothesis rather than to present a refined description of a well-defined thermophysical problem. The challenge to the model is whether a reasonable set of physical parameters can be found that reproduces not only the general bump shape but additionally, all observed experimental trends.

Notwithstanding the technological importance of amorphous Ni-P, very limited thermophysical data is available for this material. Consequently, a mostly constant property formulation is used to describe the system. The values of material properties are ascertained in several manners. Some of the physical properties can be found in the literature. The remaining can be estimated to within an order of accuracy acceptable for this study. Some of the unknown properties are constrained by the experimental outcome. As an example of this, consider the heat transfer problem that involves knowledge of the thermal heat capacity and conductivity[4], the glass transition temperature, surface optical properties, and laser pulse temporal and spatial profiles. The surface optical properties of Ni-P and the laser pulse are specified by Baumgart et al. (1995). The thermal heat capacity can be estimated to within an uncertainty of about 20 percent, leaving the glass transition temperature and thermal conductivity as the two major unknowns. However, the maximum melt diameter is known from the bump formation, and the specification of the glass transition temperature constrains possible choices of thermal conductivity to one value. The outcome is that the absolute value of the temperature field is known only as well as the glass transition temperature can be specified. The surface temperature gradients, which are important to modeling Marangoni flow, are dictated predominantly by the laser pulse spatial distribution and are fairly insensitive to uncertainties in the material thermal properties. From the problem formulation, one might justifiably expect that knowledge of the absolute temperature scale will be important to quantifying transport processes such as the vapor flux boundary condition for mass diffusion, or viscosity for fluid flow. However, generally the values of physical parameters are only known (or estimated) for one liquid temperature, the glass transition temperature. Consequently, temperature dependent transport in the liquid phase is effectively attached to a sliding temperature scale, which is defined (in the absolute sense) only as well as the glass transition temperature itself. Fortunately, the thermophysics of this problem arises from relative thermal conditions, established with respect to either spatial or temporal scales.

[4] A heat flux boundary condition requires specification of both thermal conductivity and diffusivity independently, as can be seen from analytic solutions of one-dimensional problems without phase change.

Table 1 The thermophysical properties used in the simulation

Constant name	Symbol	Value
Ni-P density	ρ	8000 kg/m^3
Ni-P viscosity	μ, H_μ	10^{-3} Pa·s, 25 kJ/mol
Ni-P thermal conductivity	k	14 W/m·K
Ni-P heat capacity	C_p	600 J/kg·K
Ni-P transition temperature	T_g	1200 K
Ni-P mass diffusivity	D_m, H_D	10^{-9} m^2/s, 10 kJ/mol
Surface tension constants	a_γ,	-0.6×10^{-3} N/m·K,
	γ_o, T_c	0.46 N/m, 6000 K
	b_γ, k_γ	−0.12, 600
Vapor activation enthalpy	ΔH_v	350 kJ/mol
Vapor pressure coefficient	ν_j	5×10^{12} Pa
Mass concentration	m_o	12 wt. % P
Laser pulse width	τ_p	50 ns
$1/e^2$ focused spot diameter	d	23 μm
Ni-P and pure Ni reflectivity	R_o, R_{Ni}	0.65, 0.72

Phosphorus as the Surfactant

The initial formulation considers phosphorus as the important surfactant. The only tangible effect of this assumption is that the specified initial concentration distribution is uniform throughout the material. Table 1 summarizes the thermophysical properties used in the simulation. Figure 2 shows the transient surface conditions established by a 4.2 μJ laser pulse. The radial distribution of temperature at the surface reflects the Gaussian spatial profile of the laser pulse (Fig. 2(a, b)). The peak surface temperature occurs approximately 10 ns after the peak in irradiative flux. The axial thermal penetration depth (~2–3 μm) is relatively small compared to the radial distribution of the irradiation flux. Within the time scale of the pulse, most of the conductive heat transfer is axial. Consequently, the surface temperature gradients established by the spatial profile of the laser pulse are not reduced much by radial diffusion. The surface is molten for a total time of about 300 ns. The maximum melting depth is about 0.5 μm.

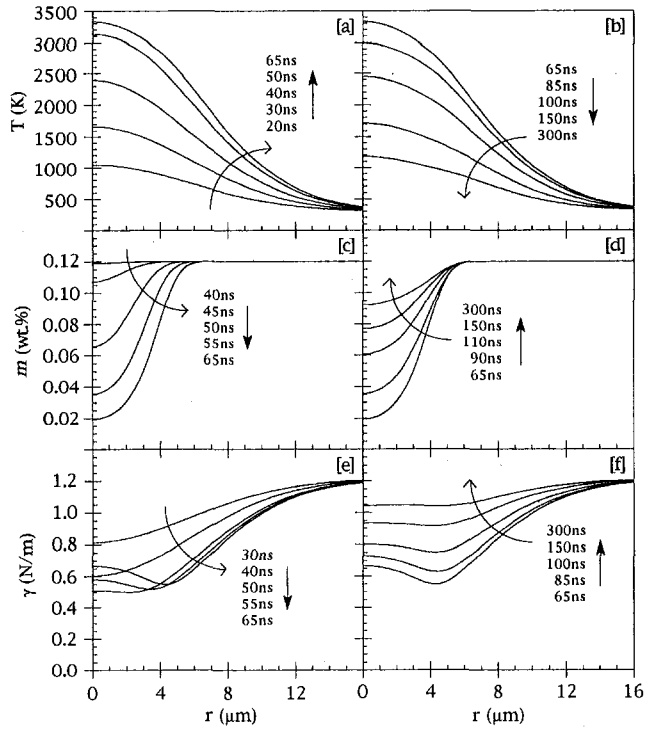

Fig. 2 Transient thermophysical surface conditions: (*a*) heating; (*b*) cooling surface temperature distributions; (*c*) heating; and (*d*) cooling phosphorus surface composition; (*e*) heating; and (*f*) cooling surface tension profiles. Conditions shown are for a laser pulse energy of 4.2 μJ.

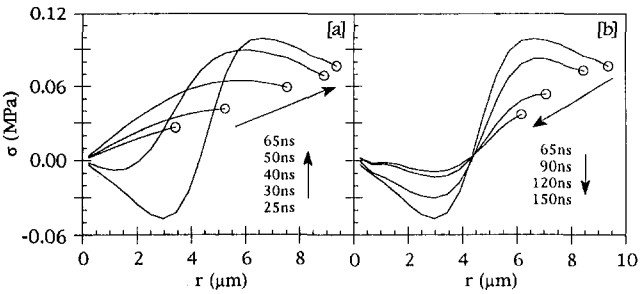

Fig. 3 Transient shear stress imposed on molten surface during (*a*) heating and (*b*) cooling for the same conditions as Fig. 2. Positive values reflect a radially outward force, and negative values reflect a radially inward force. Circles reflect the melt pool boundary.

The transient surface composition is shown in Fig. 2(c–d). The phosphorus vaporization occurs relatively late in the heating cycle after the surface temperature achieves ~70 percent of the peak value. This circumstance is not incidental. Vaporization is thermally activated and the existence of a threshold temperature for this process is an integral part of the explanation for why center bump formation is dependent on incident laser energy. Surface depletion through vaporization is in direct competition with diffusion of phosphorus from the bulk to the surface. Consequently, there is a minimum in the surface concentration occurring some time after the peak in surface temperature. Liquid-phase diffusion restores the surface phosphorus composition to about 75 percent of the original bulk composition. The fact that diffusion so efficiently restores surface composition has a bearing on the multiple-pulse experiment, as will be discussed later.

The combined effect of temperature and composition on surface tension, as given by Eq. (6), is shown in Fig. 2(e–f). The absolute value of surface tension only factors into normal surface stress calculations from the Young-Laplace equation. This force is a restraining force for the redistribution of material that only becomes significant in the last stages of bump growth when surface curvatures become significant. On the other hand, the first order Marangoni shear forces are proportional only to gradients in surface tension. The transient behavior of the net surface shear force is shown in Fig. 3. The radial direction of the shear force is indicated by the sign, positive for radial outward force and negative for radial inward force. As can be anticipated from the temporal depletion of surface phosphorus, capillary forces are entirely thermocapillary for the first 40 ns of the laser pulse. Subsequently, phosphorus vaporization establishes a surface compositional gradient, and the chemicapillary force reverses the shear force in the central region of the irradiated spot. The bidirectional capillary forces acting on the free surface are sustained for about half the melt duration time. After the temperature peak, the thermocapillary forces in the rim region decay as temperature gradients are diminished by thermal diffusion. Simultaneously, in the central region, chemicapillary forces decay as diffusion diminishes surface compositional gradients. For times greater than 200 ns, the weakened thermocapillary and chemicapillary forces approximately cancel.

The state of transient field variables are detailed in Figs. 4, 5, and 6. Notice that the axial depth of each figure has been scaled to resolve the appropriate thermophysical conditions. Contours for the transient temperature field in Fig. 4 are given for +300 K intervals, with the deepest contour corresponding to 400 K for all panels. In Fig. 5, contours for the transient phosphorus composition field are given for −1 wt.%P intervals, with the deepest corresponding to 11 wt.%P for all panels. The

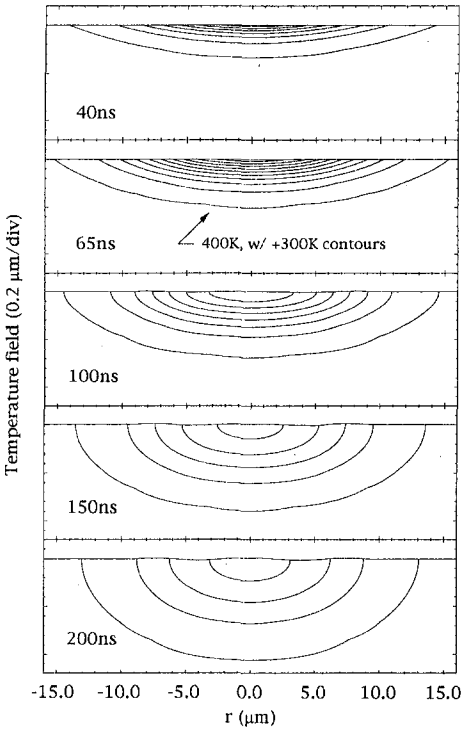

Fig. 4 Transient temperature field for the same conditions as Figs. 2–6. Contours are given for +300 K intervals with the deepest corresponding to 400 K for all panels.

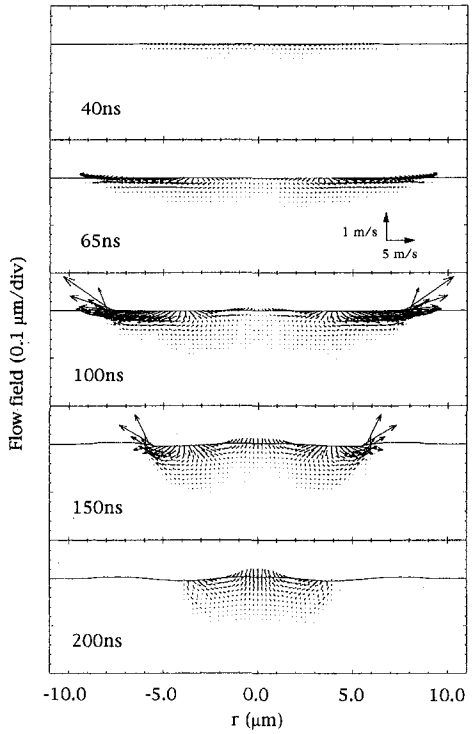

Fig. 6 Transient velocity field for the same conditions as Figs. 2–6. Reference vector scale applies to all panels.

reference vector scale shown in the second panel of the Fig. 6 applies to all panels.

Figure 7 shows the evolution of surface topography for the conditions corresponding to four pulse energies. Figure 7(*c*) illustrates surface topography arising from the thermophysical conditions detailed in Figs. 2–6. The delayed action of chemicapillary forces result in an initial redistribution of material by thermocapillary forces alone. However, the surface temperature eventually surpasses the threshold for phosphorus vaporization. The ensuing chemicapillary action arrests, and subsequently reverses, the outward flow in the central region. Very little redistribution of material occurs on the heating half of the thermal cycle. The strongest capillary forces accelerate surface motion over a 40 ns period following the irradiation peak. However, 60 percent of the material redistribution occurs in the subsequent 200 ns of the melt duration. At the peak surface temperature, the recoil pressure (normal stress) from the phosphorus vapor flux becomes large (~2 atm). The temporally integrated effect of the recoil pressure on the final bump height is about 50 percent; the relatively short duration of intense vapor flux prevents this effect from being larger. As surface curvature develops, Young-Laplace type normal surface stresses grow. Inertia sustains motion, however, until resolidification finally arrests the flow.

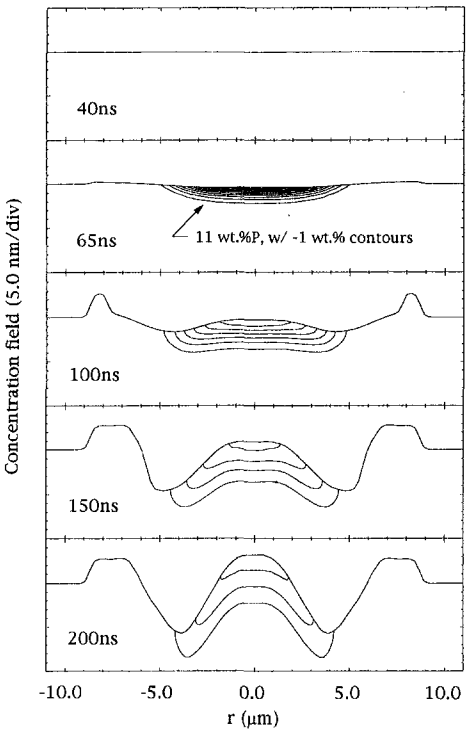

Fig. 5 Transient phosphorus composition field for the same conditions as Figs. 2–6. Contours are given for −1 wt.%P intervals with the deepest corresponding to 11 wt.%P for all panels. Note the expanded vertical scale.

The amount of phosphorus vaporized has a less than 2 percent effect on surface modification through etching, as compared with the hydrodynamic redistribution process. Furthermore, it is clear that surface etching as a principal effect is inconstant with experimental trends. Vaporization is confined to the central (hottest) region of the irradiated area. Consequently, the observed growth of a center peak with increasing pulse energy is inconsistent with surface etching forming this topographic feature. The near-surface depletion of phosphorus also has negligible affect on the hydrodynamic problem. There is a 15 percent difference in density between the Ni-P alloy and pure Ni. However, it should be emphasized that the scales for mass transfer and momentum transfer are quite different. The length scale of mass diffusion is only about 4 percent of the length scale of momentum transfer.

As previously mentioned, an important characteristic of the bump formation process is that center bump formation depends nonmonotonically on laser fluence. The proposed description

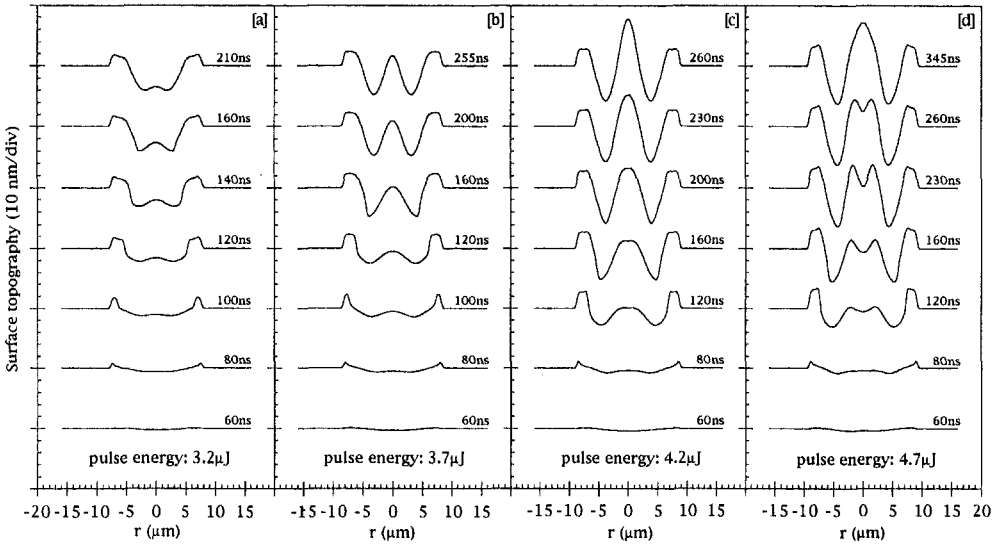

Fig. 7 Summary of transient surface topography for different pulse energies

of the process can nicely account for this experimental fact. The top row of Fig. 7 shows the final surface topography formed for a range of incident laser pulse energies. Slightly below the lowest pulse energy shown, the center bump will not form at all. As the pulse energy increase, the central bump emerges and initially exhibits increasing extent with increasing fluence. However, after exceeding a certain pulse energy, the center bump height stops increasing and actually starts decreasing. Three regimes emerge from the experimental observations and can be classified (within the context of the model).

The First Regime. Corresponding to low pulse energy and bowl-shaped surface topography, it can be identified with surface conditions that are subthreshold to phosphorus vaporization. In the absence of compositional gradients at the surface, material redistribution is left to the thermocapillary forces alone. If, however, the peak surface temperature exceeds the activation energy for significant vaporization, depletion of phosphorus introduces chemicapillary action.

The Second Regime. Compositional gradients are determined by the temperature distribution and the associated vapor pressure, and the center bump height increases monotonically with pulse energy. This trend terminates in the final regime.

The Third Regime. Surface depletion becomes significantly limited by diffusion rates. Surface concentrations in the central region may be driven so low that the respective gradients are no longer significant. The strength of the associated chemicapillary force is consequently diminished, and can succumb to the thermocapillary force in the central region once again. Under such circumstances the transient growth of topography results in broadening and dimpling of the central bump. The final topographic structure may not retain this feature if the Young-Laplace curvature force is sufficient to cause the dimple to "pop-up" during the course of the cooling cycle. For fluences above 4.7 μJ, the dimpling is retained in the final bump structure in the model.

The success of the model is in the ability to explain a wide range of experimental observations. One may wish to consider whether the mostly constant property formulation, for a system undergoing large temperature changes, will effect the conclusions of this study. Setting aside the lack of alternatives, it should be emphasized that the nature of effects advanced in the model have little bearing on the temperature dependence of thermal properties. For example, the model predicts that radial flow reverses with the transition from thermocapillary dominated flow to chemicapillary dominated flow. It is unlikely that this results has an alternative explanation related to the temperature dependence of thermal properties. The model also predicts a threshold pulse-energy for the center peak formation that corresponds to the thermal activation barrier of surfactant vaporization. The value of this threshold pulse-energy will depend on the temperature dependence of properties, but existence and consequence of this threshold on experimental and numerical trends do not.

Alternative Possibilities

The picture presented thus far offers an attractive explanation for many of the experimental observations. The proper redistribution of surface material to yield the Sombrero bump topography is explained by the combined effects of thermocapillary and chemicapillary forces. A physical explanation for the sharp threshold fluence required for center bump formation emerges naturally from the picture of an activation energy for surfactant vaporization. The model accounts for increasing extent of the central bump with pulse energy, observed over the middle range of pulse energies, as well as the end of this trend at higher pulse energies. However, one trend reported by Baumgart et al. does not emerge in the present form of the model, suggesting that the surface chemistry is more complicated than what is presented here.

The final experimental clue offered by Baumgart et al. (1995) is that the central bump is diminished when subsequent laser pulses are delivered to the same disk spot. This result has not been replicated by the numerical model; instead, center bump growth continues with repeated irradiation until surface curvature is sufficient for Young-Laplace normal surface stress to arrest the process. The persistent growth is related to the recovery of the near-surface chemical composition during the cooling half of the thermal cycle. A consequence of this recovery is that the starting condition for each subsequent pulse is reasonably similar to the previous pulse. As a result, the same Marangoni mechanisms are reestablished in subsequent pulses with comparable magnitude and net effect. The rim continues to grow (consistent with the experimental observations), but so does the central bump (the flaw).

The multiple-pulse experiment encourages additional thought concerning one of the initial hypotheses. It was assumed that phosphorus acts as the surfactant species for the chemicapillary role of central bump formation. However, this assumption imposes the condition of a uniform initial concentration over a

semi-infinite domain. This, in turn, provides for recovery of the near-surface chemical composition which is incompatible with the multiple-pulse results. A possible solution is to change the compositional distribution to one where the surfactant species is initially confined to the near-surface region. This alternate initial condition is inconsistent with the view that phosphorus is the surfactant species but could arise if another surfactant were adopted, such as a surface oxide. The potential benefit of this scenario is the limited reservoir of the surfactant chemical to compete with the surface depletion. Under this initial condition the ability of the near-surface chemical condition to recover through diffusion from the bulk is removed, or at least greatly reduced, thereby making the initial pulse unique from subsequent pulses. However, an additional complication to modeling this picture involves accounting for surface chemistry interactions with the ambient gas. In the model presented, no concern was given to adsorption and in-diffusion of the ambient gases during the cooling cycle. The disk texturing process developed by Baumgart et al. (1995) is of course done in air. Adopting the view that surface oxides are important for the bump formation process makes ambient gas interactions important in trying to resolve the multiple-pulse experiment.

References

Allen, B. C., 1972, "The Surface Tension of Liquid Metals," *Liquid Metals: Chemistry and Physics,* S. Z. Beer, ed., Converta, New York, pp. 161–212.

Bach, P., and Hassager, O., 1985, "An Algorithm for the use of the Lagrangian Specification in Newtonian Fluid Mechanics and Applications to Free-Surface Flow," *Journal of Fluid Mechanics,* Vol. 152, pp. 173–190.

Balandin, Yu. V., Otte, D., and Bostanjoglo, O., 1995, "Thermocapillary Flow Excited by Focused Nanosecond Laser Pulses in Contaminated Thin Liquid Iron Films," *Journal of Applied Physics,* Vol. 78, pp. 2037–2044.

Baumgart, P., Krajnovich, D. J., Nguyen, T. A., and Tam, A. C., 1995, "A New Laser Texturing Technique for High Performance Magnetic Disk Drives," *IEEE Transactions on Magnetics,* Vol. 31, pp. 2946–2951.

Bennett, T. D., Grigoropoulos, C. P., and Krajnovich, D. J., 1995, "Near-Threshold Laser Sputtering of Gold," *Journal of Applied Physics,* Vol. 77, pp. 849–864.

Iida, T., and Guthrie, R. I. L., 1993, *The Physical Properties of Liquid Metals,* Clarendon Press, Oxford, England.

Neitzel, G. P., and Smith, M. K., eds., 1993, *Surface-Tension-Driven Flows,* ADM-Vol. 170, ASME Winter Annual Meeting, New Orleans.

Reddy, J. N., 1979, "On the Finite Element Method With Penalty for Incompressible Fluid Flow Problems," *The Mathematics of Finite Elements and Applications III,* J. R. Whiteman, ed., Academic Press, New York.

Vitol, E. N., and Orlova, K. B., 1984, "The Surface Tension of Liquids," *Izvestiya Akademii Nauk SSSR. Metally,* Vol. 4, pp. 37–42.

Zhao, Z., Poulikakos, D., and Fukia, J., 1996, "Heat Transfer and Fluid Mechanics During the Collision of a Liquid Droplet on a Substrate: Part I—Modeling," accepted for publication in the *International Journal of Heat and Mass Transfer.*

Zonal Method to Model Radiative Transport in an Optical Fiber Drawing Furnace

Z. Yin

Y. Jaluria
Fellow, ASME

Department of Mechanical and Aerospace Engineering, Rutgers, The State University of New Jersey, New Brunswick, NJ 08903

Precise modeling of radiative heat exchange between the furnace and the glass preform is a very important part of the modeling of the fiber drawing process in a high temperature furnace. Most earlier studies on this process have used the optically thick approximation, i.e., the radiative heat exchange is assumed to depend only on the preform surface temperature while the transmission, emission, and absorption within the preform are approximated as a diffusion process. The validity of this approximation in the modeling of the fiber drawing process is dubious since the diameter of the preform undergoes a drastic reduction during the drawing process. The objectives of this research are to use a more accurate approach—the zonal method—to replace the optically thick approximation for computing the radiative heat exchange between the furnace and the preform, and to determine if the optically thick approximation is valid for this process. In applying the zonal method, the preform surface is assumed to be diffuse to both transmission and reflection. An enclosure analysis is performed for the radiative exchange between the furnace and the outer surface of the preform and the zonal method is employed to consider the radiative exchange within the glass preform. The emissivity for the glass preform has been calculated based on the diffuse surface assumption and applied to the computation of radiative heat flux with the optically thick approximation for the purpose of comparison with the present work. The results obtained by the zonal method show that the radiative heat flux is strongly influenced by the radial temperature variation within the preform, while those obtained by the optically thick approximation do not show this effect, as expected. Comparisons of the results obtained by these two approaches reveal that the optically thick approximation predicts the radiative heat flux satisfactorily for a range of axial temperature variations, but only when the radial temperature variation within the preform is small. The diameter change in the neck-down region has almost no effect on the validity of the optically thick approximation.

Introduction

The drawing of optical fibers usually requires a cylindrical glass preform to be heated axisymmetrically to a temperature higher than its softening point of about 1900 K. In most cases, this is accomplished by feeding the preform into a cylindrical, electrically heated furnace, as shown in Fig. 1, where the radiation is the dominant mode of heat transport (Myers, 1989). When it is heated beyond its softening point and an axial tension is applied to its lower end, the preform is drawn into a fiber after a drastic diameter reduction which is usually referred to as the neck-down process. The quantity and quality of the fiber produced are strongly affected by the thermal and flow processes within the neck-down region (Hanafusa et al., 1985; Kaminski, 1996). Therefore, a rigorous study of the radiative heat transport in the furnace is imperative.

Paek and Runk (1978) were among the first to deal with the radiative transport in the furnace. They separated the radiative exchange into outgoing energy from the preform and incoming energy from the furnace, which was measured by focusing an infrared spectrometer on to a spherical aluminum probe which was lowered into the furnace, but they did not consider the coupling between the furnace and the preform. Myers (1989) employed a similar approach, with the energy from the furnace being calculated instead of being measured. A more comprehensive analysis was carried out by Lee and Jaluria (1995) who computed the radiative heat flux by performing an enclosure analysis for the enclosure consisting of the furnace, preform, and top and bottom disks.

The earlier investigators (Paek and Runk, 1978; Myers, 1989; Lee and Jaluria, 1995) employed the effective emissivity of the glass preform to calculate the radiative transport. In these analyses, only the preform surface temperature was considered to account for the emissive power of the preform. However, based on the nature of the glass emission and absorption, this approximation applies only when the preform is at a uniform temperature or is optically thick. Although these conditions are not always satisfied for the optical fiber drawing process, this approach is still used widely in the field of glass fiber drawing due to its simplicity in analysis and the lack of accurate property data for glass, but its validity has not been satisfactorily investigated.

Recently, Kaminski (1996) used the banded P_1 approximation to calculate the radiative transport in the furnace by considering the preform as a semitransparent participating medium with the Fresnell boundary condition at the preform-gas interface, but the model was restricted to the upper neck-down region where the diameter is much larger than that in the lower neck-down region and the conditions for an optically thick medium are satisfied.

All the previous researchers have explicitly or implicitly employed the optically thick assumption which is not always applicable, especially in the lower neck-down region. In the present

Contributed by the Heat Transfer Division for publication in the JOURNAL OF HEAT TRANSFER. Manuscript received by the Heat Transfer Division June 10, 1996; revision received March 3, 1997; Keywords: Mat'ls. Processing & Manufacturing Process, Numerical Methods, Radiation. Associate Technical Editor: M. Modest.

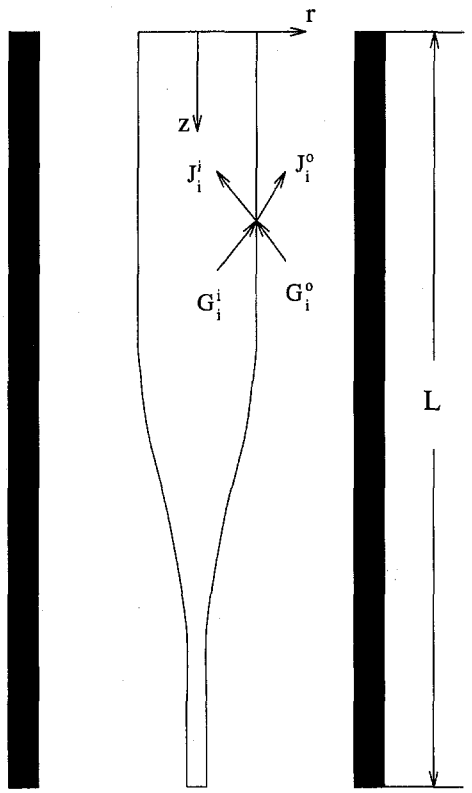

Fig. 1 Schematic diagram of a typical fiber drawing furnace

study, this assumption has not been used and the entire preform is considered as a participating medium within which the transmission, absorption, reflection, and interior emission are all considered, with appropriate simplifications. The zonal method (Hottel and Cohen, 1958; Modest, 1993) is employed to consider the radiative exchange within the glass preform and an enclosure analysis similar to that of Lee and Jaluria (1995) is carried out to compute the radiative exchange between the furnace and the outer surface of preform. The zonal method is a practical and powerful approach, especially when scattering is negligible. The comparisons done by Crosbie and Schrenker (1984) show that this method yields fairly accurate results for a variety of circumstances. In addition, the zonal method is useful for considering the variation in optical properties of the preform in the radial direction. The objective of our current study is to apply the zonal method to the modeling of the radiative heat transfer in the optical fiber drawing furnace. This paper, however, is only concerned with the radiative heat flux which is the main result discussed here. A coupling with the flow and other modes of heat transfer is needed for modeling the entire process. The optically thick approximation is also used in this study, and the conditions for the validity of this approximation are ascertained by comparing the results obtained with those from the zonal method.

Analysis

To simulate the radiative transport in the furnace, two enclosures are introduced. The first is composed of the furnace, the outer surface of preform, and the top and bottom openings, and the second consists of the inner surface and the top and bottom ends of the preform. The furnace is considered to be gray and diffuse with an emissivity of 0.75 (Paek and Runk, 1978). Both the top and bottom openings are approximated as black and are taken at ambient temperature. The preform is considered as a semitransparent participating medium with banded absorption coefficients. The two-band model (Myers, 1989) is used here, which is shown in Fig. 2. The material is considered to be sufficiently homogeneous so that the effect of scattering can be neglected in comparison to absorption (Viskanta and Anderson, 1975).

In order to make this radiative problem tractable, the inner and outer surfaces of the preform are both assumed diffuse, instead of specular, with respect to transmission and reflection, which means that when the irradiation reaches the outer or inner surface of preform it is transmitted and reflected uniformly in all directions. This assumption, which has been adopted by Siegel and Spuckler (1992), Amlin and Korpela (1979) and Tarshis et al. (1969), is reasonable for a preform that has not been polished. The transmissivities and reflectivities of the inner and outer surfaces of the preform can be obtained using the correlations employed by Siegel and Spuckler (1992). The results are $\rho^i = 0.54$, $\rho^o = 0.08$, $\tau^i = 0.46$, and $\tau^o = 0.92$ for $n = 1.42$.

Nomenclature

A = area, m^2
a_λ = absorption coefficient of glass, m^{-1}
D = diameter of preform, m
$e_{\lambda b}$ = spectral black body emissive power, $W/(m^2 \cdot \mu m)$
f = fraction of black body emissive power for an absorbing band
F_{i-j} = view factor between zone i and zone j
G = irradiation, W/m^2
$\overline{G_jS_i}$ = direct exchange area between volume zone j and surface zone i, m^2
J = radiosity, W/m^2
L = length of furnace, m
M = number of absorbing bands
n = index of refraction
N_g = number of discretized volume zones
N_i = number of discretized surface zones for enclosure inside preform
N_o = number of discretized surface zones for enclosure outside preform
q = radiative heat flux, W/m^2
q_{ref} = reference heat flux, 8.505×10^5 W/m^2
r = radial coordinate, m
R = radius of preform, m
S_{i-j} = distance between zone i and zone j, m
$\overline{S_jS_i}$ = direct exchange area between surface zone j and surface zone i, m^2
T = temperature, K
V = volume, m^3
z = axial coordinate, m

Greek Letters

ϵ = emissivity
θ_i = angle between the normal to zone i and the connecting line from zone i to zone j
λ = wavelength, μm
ρ = reflectivity of preform surface
σ = Stefan-Boltzmann constant, 5.67051×10^{-8} $W/(m^2 \cdot K^4)$
τ = transmissivity of preform surface
ψ = ratio of interior temperature to surface temperature for preform, $\psi(r) = [T(r, z)/T(R, z)]$

Superscripts

i = inside preform
o = outside preform

Subscripts

b = black body
i = zone i
j = zone j
l = absorbing band l
s = preform surface
λ = spectral

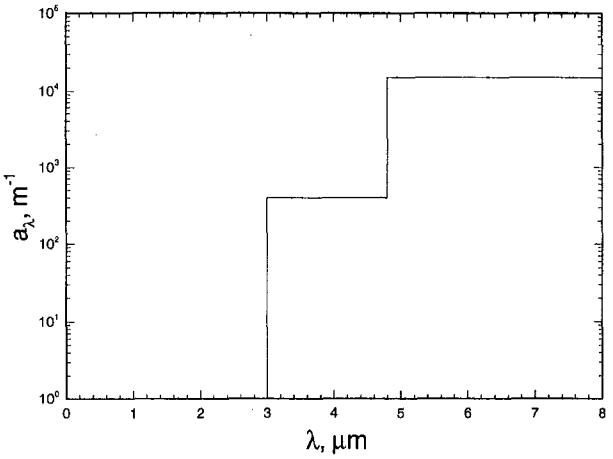

Fig. 2 Two-band spectral absorption coefficient for glass

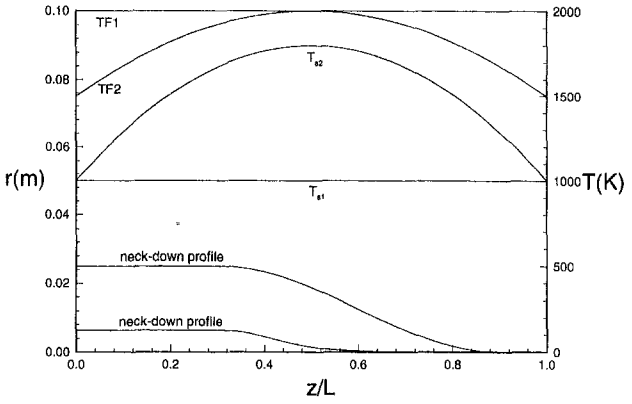

Fig. 4 Neck-down profiles and furnace and preform surface temperature distributions considered in this paper

The radiative energy equations can be formulated in terms of radiosity and irradiation for each absorbing band using the enclosure analysis. For the enclosure outside the preform, the equations are given as

$$G^o_{i,l} = \sum_{j=1}^{N_o} F_{i-j} J^o_{j,l} \tag{1}$$

for all surfaces

$$J^o_{i,l} = \epsilon_i \sigma T_i^4 f_{i,l} + (1 - \epsilon_i) G^o_{i,l} \tag{2}$$

for the furnace and the top and bottom openings, and

$$J^o_{i,l} = \rho^o G^o_{i,l} + \tau^i G^i_{i,l} \tag{3}$$

for the outer surface of the preform. The equations for the enclosure inside the preform, with refractive index n, are given as

$$G^i_{i,l} = \frac{1}{A_i} \left(\sum_{j=1}^{N_i} \overline{S_j S_i} J^i_{j,l} + \sum_{j=1}^{N_g} \overline{G_j S_i} n^2 \sigma T_j^4 f_{j,l} \right) \tag{4}$$

$$J^i_{i,l} = \tau^o G^o_{i,l} + \rho^i G^i_{i,l} \tag{5}$$

where $f_{j,l}$ is the black body fraction, F_{i-j} is the view factor between two discretized surface zones on the enclosure surface outside the preform, $\overline{S_j S_i}$ is the direct exchange area between two discretized surface zones on the enclosure surface inside the preform, and $\overline{G_j S_i}$ is the direct exchange area between a discretized volume zone and a discretized surface zone on the inner surface of the preform. The view factor and the direct exchange areas are defined as (Modest, 1993)

$$F_{i-j} = \frac{1}{A_i} \int_{A_i} \int_{A_j} \frac{\cos\theta_i \cos\theta_j}{\pi S_{i-j}^2} \, dA_i \, dA_j \tag{6}$$

$$\overline{S_j S_i} = \int_{A_i} \int_{A_j} \exp(-a_\lambda S_{i-j}) \frac{\cos\theta_i \cos\theta_j}{\pi S_{i-j}^2} \, dA_i \, dA_j \tag{7}$$

$$\overline{G_j S_i} = \int_{A_i} \int_{V_j} a_\lambda \exp(-a_\lambda S_{i-j}) \frac{\cos\theta_i}{\pi S_{i-j}^2} \, dA_i \, dV_j. \tag{8}$$

The view factors are computed using the approach formulated by Lee and Jaluria (1995), and the direct exchange areas are calculated using Gaussian quadrature. The view factors and direct exchange areas should satisfy the following relations (which can be used to check the accuracy of the results):

$$\sum_{j=1}^{N_o} F_{i-j} = 1 \tag{9}$$

$$\frac{1}{A_i} \left(\sum_{j=1}^{N_i} \overline{S_j S_i} + \sum_{j=1}^{N_g} \overline{G_j S_i} \right) = 1. \tag{10}$$

Once the radiosity and irradiation are determined from Eqs. (1)–(5), the net radiative heat flux at the surface of the preform can be obtained as

$$q_i = \sum_{l=1}^{M} (J^o_{i,l} - G^o_{i,l}). \tag{11}$$

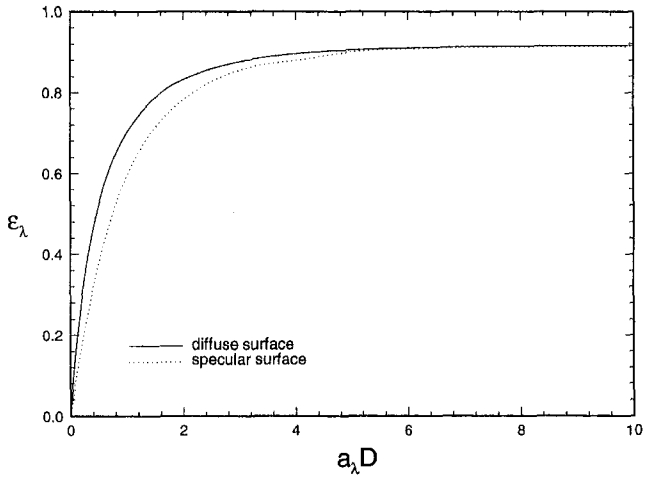

Fig. 3 Hemispherical spectral emissivity for a glass cylinder

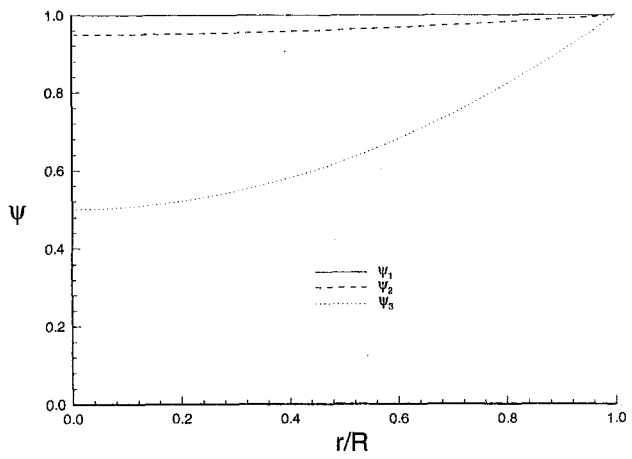

Fig. 5 Radial temperature variations in the preform considered in the calculations

Results and Discussion

Before the realistic drawing situations are considered, a very simple problem is studied. An infinitely long glass cylinder at uniform temperature is considered and the hemispherical spectral emissivity is calculated using the method just formulated above. At the outer surface the irradiation is zero and the radiosity is a constant to be determined. At the inner surface, both the radiosity and irradiation are constant. After replacing $\sigma T_j^4 f_{j,l}$ with the spectral black body emissive power $e_{\lambda b}$ in Eq. (4) and carrying out some manipulations of Eqs. (4) and (5), the spectral emissive power of the glass cylinder is obtained as

$$J^o_{i,\lambda} = \tau^o e_{\lambda b} \frac{1}{A_i} \sum_{j=1}^{\infty} \overline{G_j S_i} \Big/ \left(1 - \rho^i \frac{1}{A_i} \sum_{j=1}^{\infty} \overline{S_j S_i}\right). \quad (12)$$

Therefore, the hemispherical spectral emissivity is given as

$$\epsilon_\lambda = \frac{J^o_{i,\lambda}}{e_{\lambda b}} = \tau^o \frac{1}{A_i} \sum_{j=1}^{\infty} \overline{G_j S_i} \Big/ \left(1 - \rho^i \frac{1}{A_i} \sum_{j=1}^{\infty} \overline{S_j S_i}\right) \quad (13)$$

where the sum of direct exchange areas can be derived from Eqs. (7) and (8) as

$$\frac{1}{A_i} \sum_{j=1}^{\infty} \overline{S_j S_i} = \int_{A_j} \exp(-a_\lambda S_{i-j}) \frac{\cos\theta_i \cos\theta_j}{\pi S_{i-j}^2} dA_j \quad (14)$$

$$\frac{1}{A_i} \sum_{j=1}^{\infty} \overline{G_j S_i} = \int_{V_j} a_\lambda \exp(-a_\lambda S_{i-j}) \frac{\cos\theta_i}{\pi S_{i-j}^2} dV_j \quad (15)$$

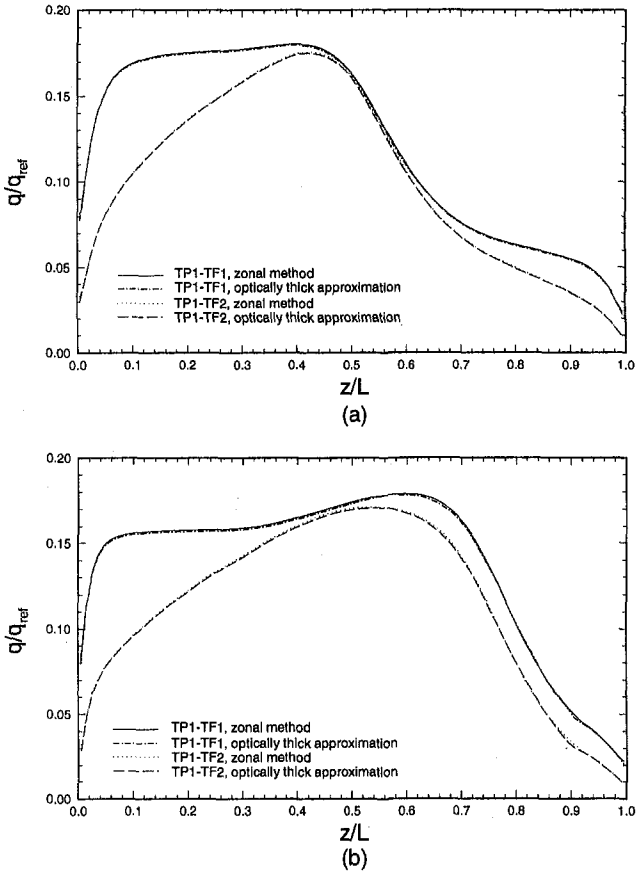

Fig. 6 Net radiative heat flux for the case of uniform temperature within preform: (*a*) preform of diameter 1.2576 cm; and (*b*) preform of diameter 5 cm

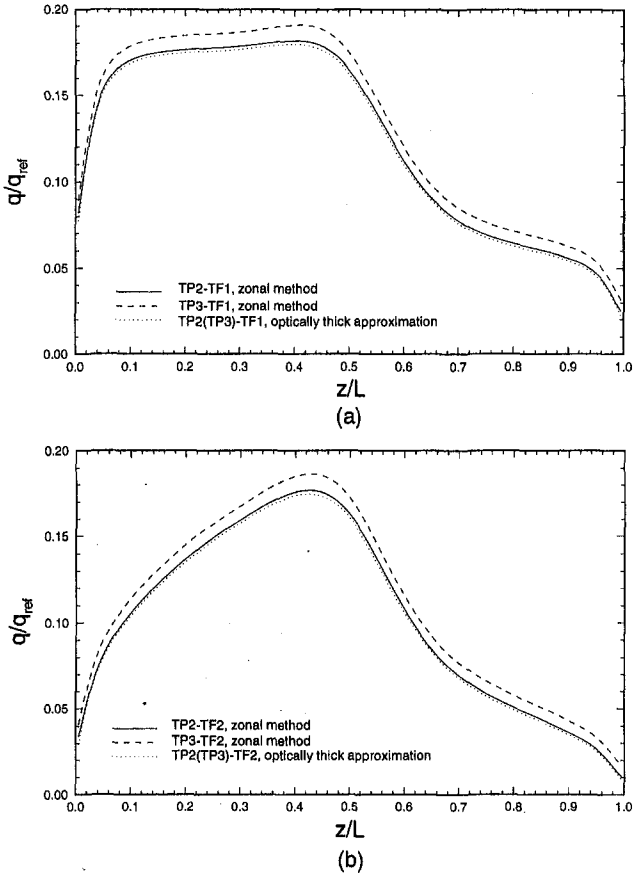

Fig. 7 Net radiative heat flux for the case of preform temperature varying only radially when preform diameter is 1.2576 cm

Here, i is an arbitrary point at the inner surface, A_j the whole inner surface, and V_j the whole volume within the cylinder. These integrals are calculated using Gaussian quadrature. The emissivity is shown in Fig. 3 with that based on the specular surface assumption (Sayles and Caswell, 1981). It is found that the former is higher in the region of medium to small optical thickness. The emissivity just obtained above will be used in the computation of heat flux with the optically thick approximation.

In the following computation, two different diameter preforms will be considered. The first one is 1.2576 cm in diameter and the second is 5 cm in diameter. Both of these are drawn into a 118 μm diameter fiber. The neck-down process is assumed to begin at 0.3 and finish at 0.9 of the whole length L of the furnace. These numbers are based on actual measurements and results in the literature. The neck-down profile for the small diameter preform is taken from the results obtained by Paek and Runk (1978), which can be represented approximately by an eighth-order polynomial as (Lee, 1993)

$$\begin{aligned}\log_{10} R = {} & -6.66531 \times 10^5 (z - 0.07)^8 \\ & + 1.5152 \times 10^6 (z - 0.07)^7 \\ & - 6.20906 \times 10^5 (z - 0.07)^6 \\ & + 1.56512 \times 10^4 (z - 0.07)^5 \\ & + 3.0826 \times 10^4 (z - 0.07)^4 \\ & - 4.71803 \times 10^3 (z - 0.07)^3 \\ & + 78.84 (z - 0.07)^2 \\ & + 1.57224 (z - 0.07) - 2.231642. \quad (16)\end{aligned}$$

For the large diameter preform, the neck-down profile is assumed to be a cosinusoidal function given by

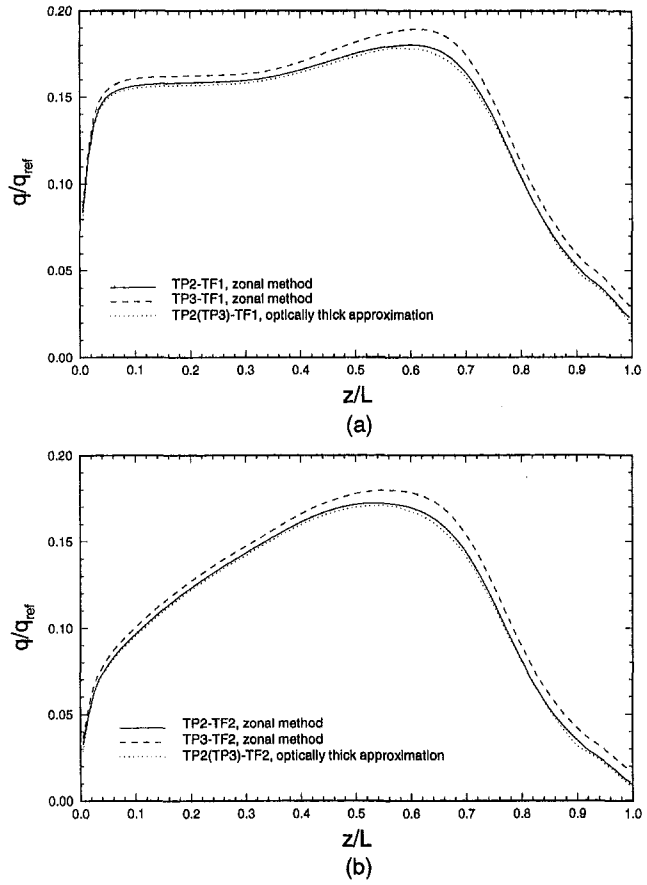

Fig. 8 Net radiative heat flux for the case of preform temperature varying only radially when preform diameter is 5 cm

$$R = 0.0125295 + 0.0124705 \cos\left(\pi \frac{z - 0.09}{0.18}\right). \quad (17)$$

The length of the furnace is 30 cm and the diameter of the furnace is taken to be 3.8 cm and 6.35 cm, respectively for two different preforms. Again, these values are based on typical furnace dimensions. The profiles of the preform are shown in Fig. 4. The view factors and direct exchange areas are calculated using the approaches described above and the results satisfy Eqs. (9) and (10) with an error of less than 2 percent.

For the above situations, the optical thickness will undergo a drastic reduction in the axial direction. Based on the two-band absorption model, the optical thickness for the small preform decreases from 188.64 to 1.77 for the high absorption band and from 5.0304 to 0.0472 for the low absorption band. For the large preform it decreases from 750 to 1.77 and from 20 to 0.0472, respectively, for the two absorption bands.

In order to study the effect of temperature on the radiative heat flux, two different furnace and six different preform temperature profiles are studied. For the furnace, two different surface temperature distributions are specified by the following equations

$$TF1: \quad T = 2000 \quad (18)$$

$$TF2: \quad T = 2000 - 2000\left(\frac{z}{L} - 0.5\right)^2. \quad (19)$$

These are plotted in Fig. 4. For the preform, two different surface temperature distributions are considered, which are also plotted in Fig. 4 and given as follows:

$$T_{s1} = 1000 \quad (20)$$

$$T_{s2} = 1800 - 3200\left(\frac{z}{L} - 0.5\right)^2. \quad (21)$$

At the same time, three different radial temperature variations within the preform are considered for each surface temperature distribution. These radial variations are plotted in Fig. 5 and are specified as follows:

$$\psi_1 = 1 \quad (22)$$

$$\psi_2 = 0.95 + 0.05\left(\frac{r}{R}\right)^2 \quad (23)$$

$$\psi_3 = 0.5 + 0.5\left(\frac{r}{R}\right)^2. \quad (24)$$

Therefore, six different temperature distributions for the preform can be given as follows

$$TP1: \quad T = T_{s1} \times \psi_1 \quad (25)$$

$$TP2: \quad T = T_{s1} \times \psi_2 \quad (26)$$

$$TP3: \quad T = T_{s1} \times \psi_3 \quad (27)$$

$$TP4: \quad T = T_{s2} \times \psi_1 \quad (28)$$

$$TP5: \quad T = T_{s2} \times \psi_2 \quad (29)$$

$$TP6: \quad T = T_{s2} \times \psi_3. \quad (30)$$

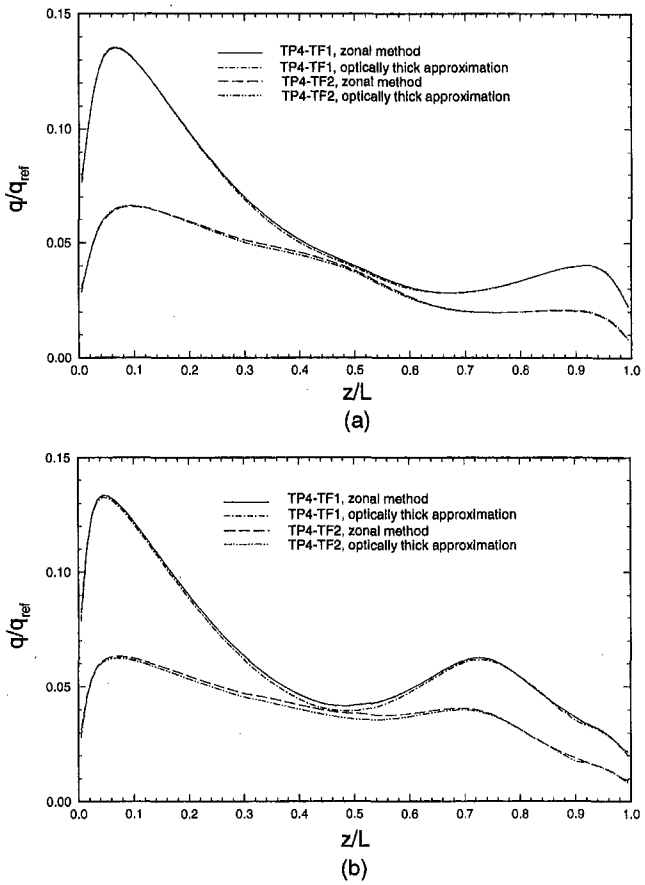

Fig. 9 Net radiative heat flux for the case of preform temperature varying only axially: (*a*) preform of diameter 1.2576 cm; and (*b*) preform of diameter 5 cm

All these distributions represent typical conditions encountered in the process. However, the simulation of the complete drawing process is much more involved and requires coupling the glass flow and convective transport with the radiation heat transfer considered here.

Two different grid sizes (6×31 and 11×51) have been tried, but no significant difference has been found in the results. Therefore, the size 6×31 has been adopted.

For the case of uniform preform temperature (*TP*1), the results are plotted in Fig. 6. In this, and all the other heat flux plots, a reference heat flux, q_{ref}, is used, which is defined as the heat flux when the furnace and the preform are both assumed to be black, infinitely long, and at uniform temperatures of 2000 K and 1000 K, respectively. In this case, the optically thick approximation is expected to give an accurate prediction due to the uniformity of preform temperature. This is evident in Fig. 6 in that the results predicted by the optically thick approximation agree closely with those predicted by the zonal method. No analytical results are available for similar comparisons to be made.

When a radial temperature variation within the preform exists, the radiative heat flux is expected to be different from that for the case of uniform temperature. This is indicated in Figs. 7 and 8, where 5 percent (*TP*2) and 50 percent (*TP*3) variations have been assumed. When the radial variation is 5 percent, the heat fluxes predicted by the optically thick approximation and the zonal method are very close, but when the radial variation is increased to 50 percent, the heat flux predicted by the zonal method is notably higher than that predicted by the optically thick approximation. This arises because the substantial decrease in the interior emission is considered by the zonal method but not by the optically thick approximation. Therefore, only

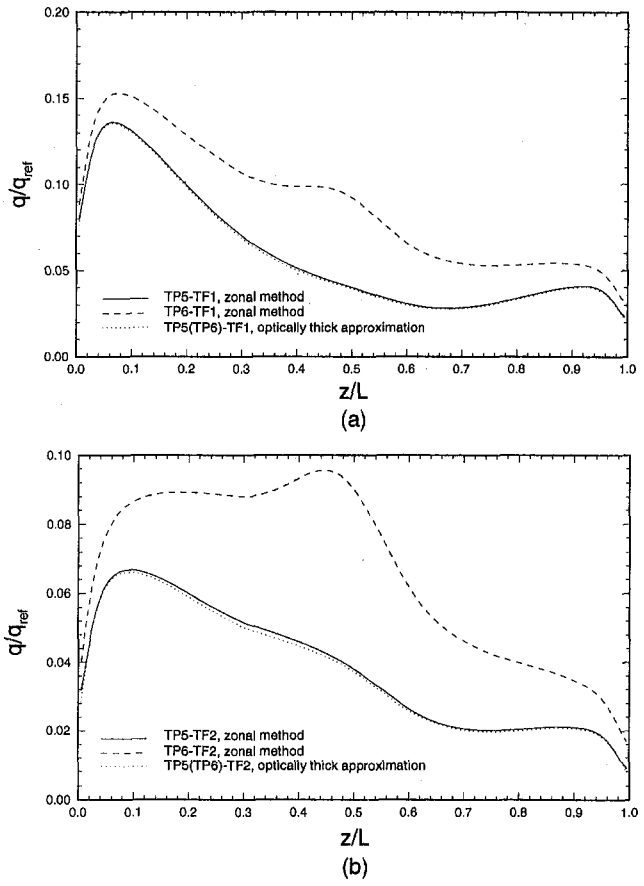

Fig. 10 Net radiative heat flux for the case of preform temperature varying both radially and axially when preform diameter is 1.2576 cm

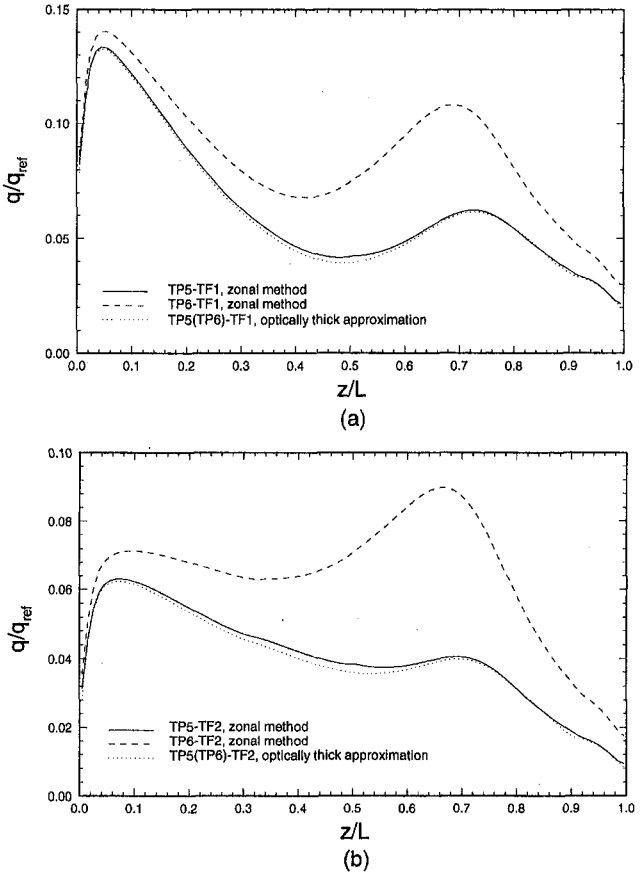

Fig. 11 Net radiative heat flux for the case of preform temperature varying both radially and axially when preform diameter is 5 cm

when the radial temperature variation is small, which is the case for relatively small diameter preforms, can the optically thick approximation give satisfactory results.

Figure 9 shows the results when the preform temperature only varies in the axial direction. The heat fluxes predicted by the two methods agree with each other closely. This means that although the radial temperature variation within the preform affects the accuracy of prediction by the optically thick approximation significantly, particularly when the variation is substantial, the axial temperature variation has little effect. This is very important for optical fiber drawing processes using relatively small diameters of the preform since the temperature in the preform then changes mainly in the axial direction. Therefore, the optically thick approximation can be employed to calculate the radiative heat flux for the fiber drawing process with high accuracy, but this does not mean that it will ensure accurate prediction of the temperature field in the preform, particularly for large diameters, which are of growing interest in industry today.

When the temperature within the preform varies both radially and axially, the results are plotted in Figs. 10 and 11. The peak in the plot is due to the temperature profiles chosen for the furnace and the preform. It is still true that the optically thick approximation gives fairly accurate results as long as the radial temperature variation is small. The results obtained by the zonal method indicate that the radiative heat flux changes significantly if the radial temperature variation within the preform is substantial.

In all the heat flux plots, when the radial temperature variation is 5 percent the results of the optically thick approximation and the zonal method are very close at every axial location. This means that the diameter change in the neck-down region has

almost no effect on the validity of the optically thick approximation.

Conclusions

The zonal method and the optically thick approximation have been used to compute the net radiative heat flux input to the preform used in the drawing of optical fibers. The assumption of diffuse preform surface was employed for simplicity. Different furnace and preform temperature distributions have been considered. The results show that the zonal method can predict the radiative heat flux quite well no matter what temperature distribution is within the preform, but the optically thick approximation can predict the flux satisfactorily only when the radial temperature variation within the preform is small. In addition, for the same axial temperature variation the results of the two approaches are almost the same, which means that the optically thick approximation is valid for a wide range of axial temperature variation. Due to the fact that the temperature within the preform changes mainly in the axial direction for relatively small diameter preforms during the optical fiber drawing process, the optically thick approximation is valid in terms of the surface radiative heat flux for such cases. Large temperature variations can arise in the radial direction for large diameter preforms making it imperative to use the zonal method instead of the optically thick approximation. Finally, the variation in the diameter in the neck-down region has almost no effect on the validity of the optically thick approximation.

Acknowledgments

The support of the National Science Foundation under grant No. DDM92-13458 is gratefully acknowledged. This work was made possible by the supercomputer time allocated by Pittsburgh Supercomputing Center under grant No. CBT920017P. The discussions with Professor C. E. Polymeropoulos are also gratefully acknowledged.

References

Amlin, D. W., and Korpela, S. A., 1979, "Influence of Thermal Radiation on the Temperature Distribution in a Semitransparent Solid," ASME JOURNAL OF HEAT TRANSFER, Vol. 101, No. 1, pp. 76–80.

Crosbie, A. L., and Schrenker, R. G., 1984, "Radiative Transfer in a Two-Dimensional Rectangular Medium Exposed to Diffuse Radiation," *J. Quant. Spectrosc. Radiat. Transfer,* Vol. 31, No. 4, pp. 339–372.

Hanafusa, H., Hibino, Y., and Yamamoto, F., 1985, "Formation Mechanism of Drawing Induced E′ Centers in Silica Optical Fibers," *J. Appl. Physics,* Vol. 58, pp. 1356–1361.

Hottel, H. C., and Cohen, E. S., 1958, "Radiant Heat Exchange in a Gas-Filled Enclosure: Allowance for Nonuniformity of Gas Temperature," *AIChE Journal,* Vol. 4, No. 1, pp. 3–14.

Kaminski, D. A., 1996, "Thermal Transport in Optical Fiber Manufacturing," *Proceedings of the International Symposium on Radiative Heat Transfer,* P. M. Mengue, ed., Kusadasi, Turkey, Begell House Pub., NY.

Lee, S. H.-K., 1993, "Numerical Investigation on the Neck-down Region of a Furnace-Drawn Optical Fiber," Ph.D. dissertation, Rutgers, The State University of New Jersey, New Brunswick, NJ.

Lee, S. H.-K., and Jaluria, Y., 1995, "The Effects of Geometry and Temperature Variations on the Radiative Transport during Optical Fiber Drawing," *Journal of Materials Processing & Manufacturing Science,* Vol. 3, pp. 317–331.

Modest, M. F., 1993, *Radiative Heat transfer,* McGraw-Hill, NY.

Myers, M. R., 1989, "A Model for Unsteady Analysis of Preform Drawing," *AIChE Journal,* Vol. 35, No. 4, pp. 592–602.

Paek, U. C., and Runk, R. B., 1978, "Physical Behavior of the Neck-Down Region during Furnace Drawing of Silica Fibers," *Journal of Applied Physics,* Vol. 49, pp. 4417–4422.

Sayles, R., and Caswell, B., 1981, "A Finite Element Analysis of the Upper Jet Region of a Fiber Drawing Flow Field," National Science Foundation, NSF-18421/1.

Siegel, R., and Spuckler, C. M., 1992, "Effect of Index of Refraction on Radiation Characteristics in a Heated Absorbing, Emitting, and Scattering Layer," ASME JOURNAL OF HEAT TRANSFER, Vol. 114, pp. 781–784.

Tarshis, L. A., O'Hara, S., and Viskanta, R., 1969, "Heat Transfer by Simultaneous Conduction and Radiation for Two Absorbing Media in Intimate Contact," *International Journal of Heat and Mass Transfer,* Vol. 12, pp. 333–347.

Viskanta, R., and Anderson, E. E., 1975, "Heat Transfer in Semitransparent Solids," *Advances in Heat Transfer,* Vol. 11, pp. 317–441.

Theoretical and Experimental Study of Electrohydrodynamic Heat Transfer Enhancement Through Wire-Plate Corona Discharge

B. L. Owsenek
Mantech Services Corporation,
339 Busch's Frontage Road,
Annapolis, MD 21401

J. Seyed-Yagoobi
Department of Mechanical Engineering,
Texas A&M University,
College Station, TX 77843-3123
jyagoobi@mengr.tamu

Heat and mass transfer between a surface and the surrounding gas can be enhanced by the application of electric body forces that induce jet or plume-like fluid motion. Such enhancement causes no noise or vibration, can be applied in complex, isolated geometries, and allows simple control of surface temperatures. This paper examines the potentially useful case of multiple fine-wire electrodes suspended in the open air above a grounded and heated horizontal surface. An infrared camera system was used to obtain a complete and accurate distribution of local heat transfer coefficients on the impingement surface. A numerical code was developed and verified by comparison with experimental data. This code was then used to investigate and compare the heat transfer generated by novel electrode geometries.

1 Background

Heat and mass transfer between a surface and the surrounding air can be significantly enhanced through the application of a high electric field. When a high voltage is applied to a small diameter electrode, such as a fine wire or sharp needle, air in the vicinity of the electrode becomes ionized. The free ions are forced away from the electrode along the electric field lines and are drawn towards the nearest electrical ground. Collisions between the ions and the air transfer momentum to the fluid and create a plume-like gas flow. The resulting transport enhancement requires little power, causes virtually no sound or vibration, and can be controlled by simply changing the applied voltage.

Although this phenomenon was first described as an "electric wind" by Hauksbee in 1719, application to heat transfer enhancement was not considered until Marco and Velkoff's seminal 1963 paper. Using an apparatus in which a wire-generated corona wind impinged on a vertical plate, they were able to increase average heat transfer coefficients to approximately five times the free convection values. Local heat transfer coefficients showed even greater enhancement in the vicinity of the impingement point. They also showed that the average heat transfer coefficient could be related to the $\frac{1}{4}$ power of the applied current, and successfully modeled this with a momentum-integral analysis.

A significant advancement in the analysis of corona discharge flow was presented by Yabe et al. in their 1978a paper. They constructed an experimental apparatus consisting of a horizontal downward-facing plate fixed over a platinum 40 μm wire electrode and enclosed in a Plexiglas chamber. Mostly using dried nitrogen, they measured the pressure and current density on the plate. In addition, they mapped the electrostatic field with a Langmuir probe and were thus able to compute the space charge distribution. Experimentally generated surface pressure data were compared to results from a two-dimensional stream function numerical simulation. Through the use of appropriate simplifications, an ingenious coordinate transformation, and the measured current distribution, the authors were able to successfully model the recirculating flow inside the chamber and achieve fairly good agreement between their experimental and numerical pressure and potential figures. Yabe et al. (1978b) extended their work to include both numerical and experimental heat transfer results for a horizontal downward-facing plate in an enclosed chamber. Neglecting Joule heating and assuming a constant temperature plate, they were able to obtain quite accurate local heat transfer coefficients in the stagnation region. However, the analysis failed to match experimental data at radial distances greater than the wire-plate separation distance, and they did generalize the solution or extend the work to the case of multiple wire electrodes.

An investigation by Takimoto et al. (1988) examined the corona wind heat transfer enhancement in a channel flow. The heat transfer enhancement from high potential wire electrodes along the center line of a channel was examined both experimentally and numerically. Flow streamlines revealed an induced secondary flow that significantly enhanced the surface heat transfer coefficients. In many cases, the calculated coefficients were in good agreement with the experimental data. In addition, the calculated current flux distribution was in excellent agreement with measured values.

Ohadi et al. (1991) experimentally investigated heat transfer enhancement of laminar and turbulent pipe flow via corona discharge. The working fluid in all experiments was air. It was found that heat transfer enhancements were significant only in the laminar and transitional flow regimes with a single electrode wire mounted in the center along the tube. With two-electrode wires mounted inside and along the tube, the enhancements extended to the turbulent flow regime as well.

Recently, Owsenek et al. (1995) experimentally investigated the corona wind heat transfer enhancement with the single needle-plate geometry in air. Local enhancements of more than 25:1 over natural convection were measured. The enhancement extended over a significant area, often reaching beyond the 30 cm measurement radius. At high power levels, Joule heating significantly reduced the effective impingement point heat transfer coefficient.

Contributed by the Heat Transfer Division for publication in the JOURNAL OF HEAT TRANSFER. Manuscript received by the Heat Transfer Division May 7, 1996; revision received April 7, 1997; Keywords: Augmentation & Enhancement; Natural Convection. Associate Technical Editor: S. Ramadhyani.

A number of papers have appeared over the years that involve experimental investigation of corona discharge-induced flow phenomenon and transfer enhancement (see Kulacki, 1982; Owsenek, 1993). However, a detailed description of flow structure is difficult to obtain experimentally due to the low flow velocities and high voltages. Furthermore, because of difficult boundary conditions, numerical simulation is somewhat problematic and has not been explored to its full potential.

This paper presents a numerical means of handling the relevant equations and open boundaries, verifies it through comparison with experimental work, and uses the procedure to examine the important single wire-plate and multiple wire-plate geometries in the atmospheric air. Novel electrode geometries, which focus the electric fields and force densities, are explored and evaluated in order to develop a more effective electrode geometry.

2 Theory

The wire-plate corona discharge system is governed by the fundamental differential equations of electrostatics, fluid flow, and heat transfer. Since the electrical phenomena drives both the fluid flow and the heat transfer, it must be calculated first. Given suitable boundary conditions and a known or assumed space charge distribution, the potential field can be calculated from the Poisson equation

$$\nabla^2\Phi = -\frac{\rho_e}{\epsilon}. \tag{1}$$

The steady-state unipolar space charge distribution is governed by the electric field and the conservation of charge carriers, where electric field is defined as the negative gradient of potential,

$$\nabla\cdot(\sigma\mathbf{E} + \rho_e b\mathbf{E} + \rho_e\mathbf{u}) = 0. \tag{2}$$

The conduction term (first term in the above equation) is generally very small in gasses and is neglected in this analysis. In addition, charge convection (last term in the above equation) due to fluid flow can also be neglected when it has a characteristic velocity u that is much less than the charge mobility velocity bE. This is not generally a good assumption in liquids, where charge mobility is quite low. However, in corona-driven air and other gasses, the charge mobility is high and u/bE is almost always on the order of 0.1 or less. This simplifies Eq. 2 considerably by allowing the electrostatic equations to be decoupled from the fluid-flow solution.

The electrostatic quantities of charge density and electric field enter the momentum equations through the electrostatic force, $f = \rho_e E$, and act as a distributed body force in the laminar, steady-state momentum equations,

$$\nabla\cdot(\rho\mathbf{u}\mathbf{u}) = \nabla\cdot\mu\nabla\mathbf{u} - \nabla P + \rho\mathbf{g} + \rho_e\mathbf{E}. \tag{3}$$

The momentum equations can be decoupled from the energy equation when viscous dissipation and buoyancy forces can be neglected. Viscous heating is very small at corona wind velocities and may be eliminated in all cases considered here. Buoyancy forces, however, can only be neglected when the surface heat flux, and thus temperature gradient, is small or when corona forces can be shown to be dominant. An electric Grashoff number was defined in prior work (Owsenek et al., 1995) which shows that, in the cases examined here, the ratio of electric force to buoyancy force is very high. This justifies the approximation of decoupling the momentum, electric, and energy equations.

Although the solution of the flow and temperature fields is significantly simplified when the equations can be decoupled, the energy equation includes another complexity. The passage of current through the air releases energy which warms the air. Joule heating can have a significant effect at high corona power dissipation level. The energy equation should therefore include a source term to account for the volumetric rate of heat generation. Expressing enthalpy as c_pT and neglecting viscous heating, the energy equation can be expressed as

$$\nabla\cdot(\rho\mathbf{u}c_pT) = \nabla\cdot(k\nabla T) + b\rho_e\mathbf{E}^2. \tag{4}$$

3 Numerical Solution

Simultaneous solution of the discretized Poisson and current conservation equations in Cartesian coordinates yields the current density and electric field. The grid spacing was reduced to the wire diameter in the vicinity of the wire electrode to allow for proper solution of the Poisson equation. The Poisson equation was discretized in a central difference fashion, while the current conservation equation was discretized in an upwind manner. An "upwind" or "donor-cell" assumption based on the electric field direction at the control volume interfaces is used to determine the charge density at grid interfaces. This discretization form eliminates problems associated with the solution of first-order equations and requires only a single charge density boundary condition, located on the corona wire surface. Unfortunately, available means of calculating the charge density on the emitter surface generally do not lead to accurate solutions, so experimental relationships between the total current and applied voltage were used to determine this boundary condition.

In each iteration, the relaxed Poisson equation was solved based on a previously obtained charge density. The electric field was then calculated, and the current conservation equation solved, to yield new charge density values. The total current was then calculated and compared with the experimental figure. Assuming that the coronation took place uniformly all around the wire electrode, the charge density boundary condition at the wire surface was adjusted accordingly and the procedure repeated until convergence was obtained. The convergence was assumed to be achieved when the change in the total current

Nomenclature

A = area/unit length wire, m
b = ion mobility, m^2/Vs
c_p = air specific heat, J/kgK
E = electric field, V/m
g = gravity acceleration, m/s^2
H = height of horizontal computational boundary, m
h_{loc} = local convection coefficient, W/m^2K
$h_{loc,0kV}$ = local convection coefficient at 0 kV applied voltage, (i.e. free convection heat transfer coefficient) W/m^2K
f_e = body force on elemental volume, N/m^3
I = current, A/m
J = surface current flux, A/m^2
k = air thermal conductivity, W/mK
l = horizontal distance from wire to vertical computational boundary, m
P = pressure, Pa
q = conductive heat flux, W/m^2
r_w = wire radius, m
T = air temperature, K
T_o = ambient air temperature, K
u = air velocity in x-direction, m/s
v = air velocity in y-direction, m/s
W = wire electrode height above surface, m
x = distance along surface, m
y = height above surface, m
ϵ = air electric permittivity, F/m
Φ = electric potential, V
ρ_e = free electric charge density, C/m^3
ρ = air density, kg/m^3
σ = air electric conductivity, S/m
μ = dynamic viscosity, Ns/m^2

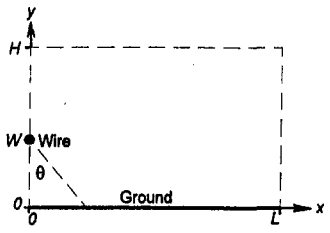

Fig. 1 Single wire-plate coordinate system with symmetry plane at $x = 0$

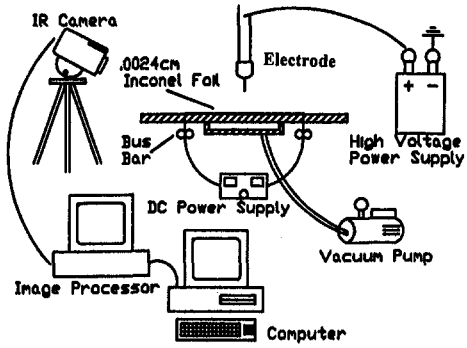

Fig. 2 Heat transfer jet impingement facility

was less than 1×10^{-5} μA/m and the change in the sum of the absolute values of the voltage at all grid points was less than 1×10^{-5} V.

The predicted charge density and electric field appear as a distributed body force in the momentum equations. The SIMPLEC modification (Van Doormal and Raithby, 1984) of Patankar's (1980) SIMPLE procedure was used to solve the flow field for the single wire-plate geometry shown in Fig. 1. Numerically, the problem was straight forward and it did not require any special techniques. Convergence was obtained by imposing a zero fluid velocity at $y = H$ of Fig. 1 and by forcing outflow along the boundary $x = L$. The H and L were selected such that further increase in their values resulted in less than one percent change in the numerical heat transfer results. The energy equation was also solved along lines suggested by Patankar (1980), with the addition of a source term to account for electrostatic Joule heating.

The wire-plane geometry in an open atmosphere presents special difficulties for the specification of the electrostatic equation boundary conditions, since boundaries at infinity are considered. In contrast to the hyperbolic current continuity equation, the elliptic Poisson equation requires specification of the boundary condition along all four sides shown in Fig. 1. The boundary at $x = 0$ can be specified with the symmetry Neumann condition, the ground plane can be specified with the Dirichlet condition of $\Phi = 0$, and the imposed voltage can be specified at the wire electrode. The unbounded domain in the x and y-directions, however, requires special treatment.

The imposition of the natural Dirichlet or Neumann conditions may be acceptable along the unbounded domains when a large enough computational region is considered because both of these boundary conditions lead to similar solutions in the important region near the corona source (Owsenek, 1993). However, it is also possible to specify an analytical approximation for the potential field at these boundaries which assumes negligible space charge effects. This analytical approximation is applied in terms of the Neumann condition and thus represents the assumption that the space charge does not distort the shape of the potential field. While not exact, the analytical Neumann boundary condition is superior to other methods of approximating a boundary at infinity. Boundary conditions are given in Table 1.

For the multiple wire-plate geometry, identical numerical procedure to single wire-plate geometry was followed and the electric field, flow field, and the heat transfer results for the regions between the wire electrodes were determined. An array of wire electrodes was modeled by imposing similar symmetric boundary conditions at $x = L$ to those at $x = 0$ for Poisson, momentum, and energy equations. The boundary conditions for multiple wire electrodes at $y = 0$ and $y = H$ were identical to those of a single wire electrode. Other boundary conditions for Poisson equation at $y = H$ were considered, however, it was concluded that the boundary conditions at $y = H$ had very little influence on the numerical solutions, especially within the vicinity of electrodes.

4 Experimental Apparatus

Heat transfer measurements were conducted using the heat transfer jet impingement facility shown in Fig. 2. The details of the apparatus are given in Page et al. (1992). This apparatus was developed to obtain highly accurate local heat transfer coefficients with conventional and innovative impinging jet flows. The facility consists of a thin resistance-heated flat inconel sheet mounted on an insulating vacuum chamber, a Mikron infrared camera, an image processor, and a computer.

The inconel foil serves as the heat transfer surface and is electrically heated by a DC power supply. The foil is situated on an insulating vacuum chamber and held flat by the distributed vacuum pressure of 900 small holes in the top surface of the Plexiglas chamber. A vacuum pump provides a 98.5 kPa vacuum, sufficient to hold the foil in place and nearly eliminate convection and gaseous conduction losses inside the chamber. The foil is connected to the power supply on each side by a pair of copper bus bars. In addition, to enhance the accuracy of the infrared camera, the top surface of the foil was painted black to eliminate reflections and increase emmissivity to nearly unity.

Foil surface temperatures were measured with a Mikron thermal vision system. This camera is capable of temperature reso-

Table 1 Numerical boundary conditions for single wire-plate geometry

	x=0	y=0	x=L	y=H
Poisson	$\partial\Phi/\partial x=0$	$\Phi=0$	$\frac{\partial\Phi}{\partial x} = \frac{V_0}{\ln\frac{2W}{r_w}}\left(\frac{L}{L^2+(y+W)^2} - \frac{L}{L^2+(y-W)^2}\right)$	$\frac{\partial\Phi}{\partial y} = \frac{V_0}{\ln\frac{2W}{r_w}}\left(\frac{H+W}{x^2+(H+W)^2} - \frac{H-W}{x^2+(H-W)^2}\right)$
Momentum u-component	u=0	u=0	$\partial u/\partial x=0$	u=0
Momentum-v-component	$\partial v/\partial x=0$	v=0	v=0	$\partial v/\partial y=0$
Energy (influx)	$\partial T/\partial x=0$	$\partial T/\partial y=$ -q/k	$T=T_o$ for inflow	$T=T_o$ for inflow
Energy (efflux)	$\partial T/\partial x=0$	$\partial T/\partial y=$ -q/k	$\partial T/\partial x=0$ for outflow	$\partial T/\partial y=0$ for outflow

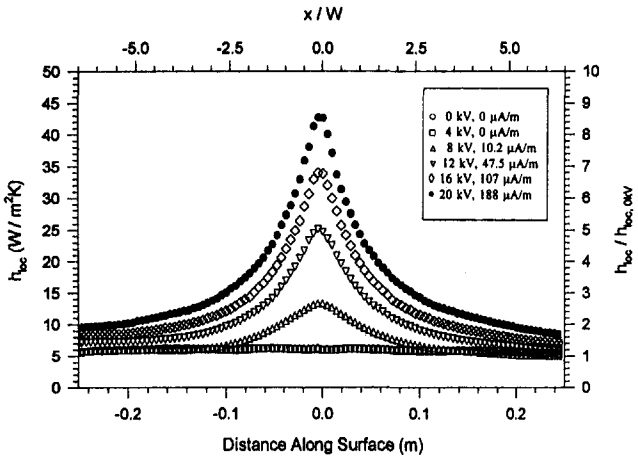

Fig. 3 Single wire-plate heat transfer at 4 cm height and various voltages

lution of ±.025°C and spatial resolution of 0.475 mm/pixel. In order to examine the temperature and spatial ranges of interest, the temperature sensitivity was decreased to ±.06°C and the pixel size increased to 2.375 mm. The surface temperatures were averaged over a sufficient time with the thermal vision system during each measurement in order to eliminate the effect of unsteady nature of the corona flow. Local heat transfer coefficients were calculated using the local measured temperatures and taking into account the calculated radiative and conductive heat losses (see Owsenek et al., 1995).

The inconel foil surface was cooled by the imposition of corona discharge flow. The corona discharge was generated by an adjustable high voltage power supply which could supply up to 50 kV at 5 mA. This power source was connected to a single or multiple 79 μm stainless steel wire electrodes suspended above the inconel foil. High voltage connecting wires carried current from the power supply, through a microammeter, to the electrodes. The current then bridged the air gap in the form of a corona discharge, traveled through the grounded foil, and completed the circuit back to the high voltage power supply. The supplied voltage was measured with a voltage-divider circuit and multimeter, and current loss was checked by measuring the current leaving the foil.

Error Analysis. The method of Kline and McClintock (1953) was used to determine the uncertainties. The maximum and minimum uncertainties of the local heat transfer coefficients were 16.2 percent and 3.2 percent, respectively. The maximum uncertainty of the local heat transfer coefficients occurred at the outer edge of the heat transfer enhancement region where the local heat transfer coefficients were the smallest. The maximum and minimum uncertainties of the applied current were 7.5 percent and 1.8 percent, respectively. The experimental data proved highly repeatable. For instance, in a series of 10 measurements taken with an electrode 3 cm above the impingement surface at 10 and 15 kV, a standard error (standard deviation divided by local heat transfer) of just one percent was measured at the impingement point. Standard error varied with radial distance as a result of flow unsteadiness, but was at all points less than 9 percent.

5 Experimental Results

Local heat transfer coefficients on the heated surface below the charged wire electrode exhibit qualitative characteristics similar to impinging slot-jet flow. Typical heat transfer coefficients achieved with a single wire electrode suspended 4 cm above the heated surface are presented in Fig. 3. Note the single, high heat transfer peak and the rapid reduction in heat transfer with distance from the wire electrode. At 20 kV, an enhancement by a factor of 8.5 in the local peak heat transfer coefficient has been achieved. This enhancement is significant but it is less than those achieved with the needle-plate geometry at the same applied voltage (Owsenek et al., 1995).

Since the flow generated by a corona discharge in a wire-plate geometry has some similarity to a jet flow from a slot nozzle impinging on a flat surface, comparison of their performance is of interest. The area averaged heat transfer coefficient for the single wire electrode at 20 kV and 188 μA/m, located at 4 cm above the surface, as shown in Fig. 3, is approximately equal to 17 W/m^{2}K. The area considered is based on a wire electrode unit length for a distance along the surface of 0.0 to 0.25 m (see Fig. 3). To achieve the same average heat transfer coefficient as above over the same area, an air exit velocity of 2 m/s is required for a slot nozzle of a unit length with a slot width of 1.25 cm, also located at 4 cm above the plate (Martin, 1977). The corresponding air exit Reynolds number, defined based on the slot nozzle exit hydraulic diameter, becomes 3300. It is important to realize that the wire-plate corona discharge flow field is not quite similar to a slot-nozzle jet flow field, due to, for example, the upward flow that exists with the corona discharge flow. In general, the flow is spread more with the corona discharge, and the unstable nature of corona discharge flow also contributes to these differences. For a precise comparison it will be necessary to measure the flow fields for the wire-plate corona discharge flow and a slot jet nozzle flow.

Figure 4 illustrates heat transfer coefficients induced by multiple wire electrodes suspended over the transfer surface. Data are presented for two and three-wire electrodes 2 cm above the surface, with 10 kV applied voltage. A symmetry plane at x = 0 illustrates the 20 cm spacing of the two-wire case and the 10 cm spacing of the three-wire case. In a group of three-wire electrodes, the heat transfer coefficients below the center wire electrode were smaller than those below the exterior wire electrodes. This may be attributed both to the fact that interior wire electrodes have a more limited access to the ambient fluid reservoir and to the fact that the exterior wire electrodes can produce significantly more current than the interior wire electrode due to the electric field distribution.

The heat transfer coefficients below the outer wire electrodes were distorted and deflected outwards. This is a result of asymmetry in both the flow field and the driving electrostatic forces, both of which deflect away from the symmetry plane. Note that the maximum local heat transfer coefficients observed with 10 cm and 20 cm wire spacing were nearly identical, indicating that maximum heat transfer from the external wire electrodes of a wire array is only weakly affected by the wire spacing.

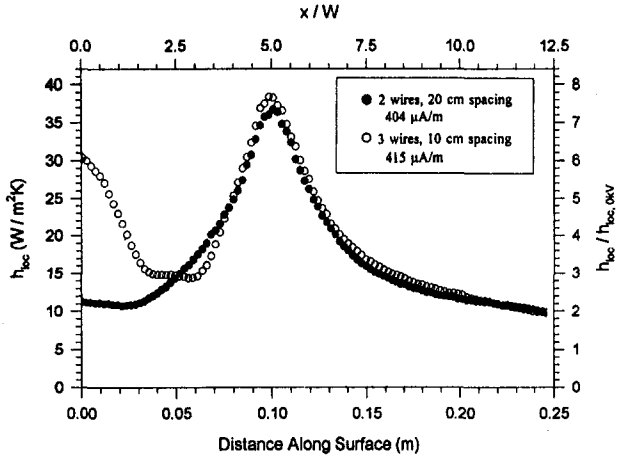

Fig. 4 Heat transfer coefficients for two and three-wire electrodes at 2 cm above the surface with 10 kV applied voltage. Symmetry plane at x = 0

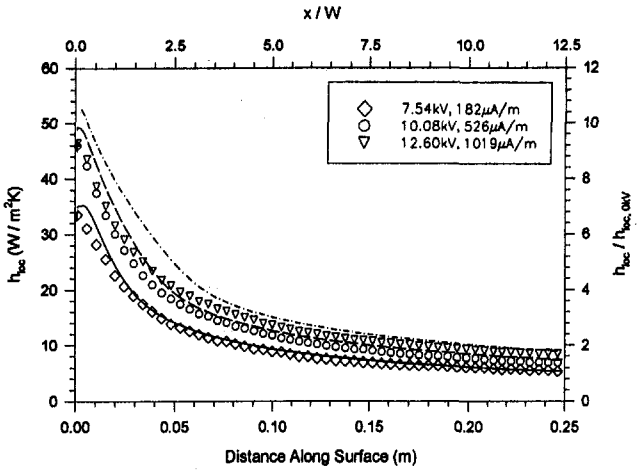

Fig. 5 Comparison of numerical and experimental heat transfer coefficients with single wire electrode situated 2 cm above impingement surface

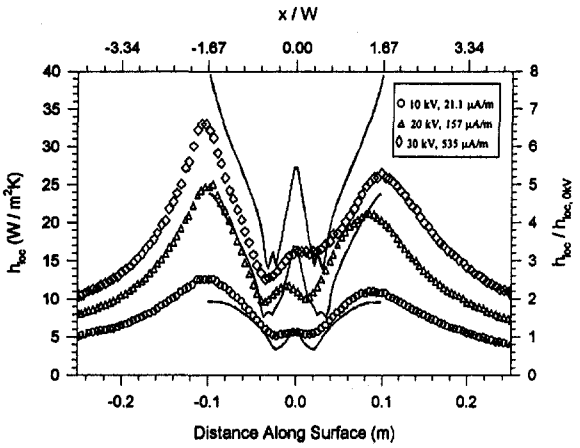

Fig. 6 Numerical and experimental local heat transfer with wire electrodes 6 cm above impingement surface, 20 cm apart, and with 10 kV, 20 kV, and 30 kV imposed voltage

According to Fig. 3, the maximum electric power required to corona discharge a single wire electrode was 3.76 W/m at 20 kV applied voltage. The electric power increased further with two or three-wire electrodes (see Fig. 4). Such required electric power levels are generally quite high considering the enhancements achieved in heat transfer. However, the power requirement can be reduced by selecting a smaller diameter wire electrode. The main advantages of a wire corona discharge to enhance heat transfer are the absence of noise or vibration, applicability to complex and isolated geometries, and its simplicity in design and operation.

6 Numerical Results

6.1 Single Wire. Experimental and numerical local heat transfer coefficients generated by a single, corona wire electrode suspended 2 cm above an infinite plate, at a voltage of 10 kV and an applied current of 526 μA/m (526 microamps/unit length of wire) are illustrated by Fig. 5. Both experimental and numerical heat transfer coefficients were calculated using the ambient temperature of 20°C and a uniform heat flux of 187 W/m^2 at the impingement surface.

Good agreement is shown between numerical and experimental results, providing verification of the accuracy and reliability of the numerical prediction. The accuracy of the numerical prediction appears to decrease with increasing voltage. This may be a result of increasingly unsteady behavior in regions with strong electric fields and high space charge. Nevertheless, the relatively close agreement between the experimental and predicted heat transfer coefficients suggests that additional heat transfer enhancement mechanisms, such as turbulence enhancement and polarization forces, do not play a significant role, since these effects were not included in the numerical model.

6.2 Wire Array. In practice, some sort of wire array would be employed to enhance heat or mass transfer over a large area. Such an array generally takes the form of a number of parallel wires mounted at equal distance from the ground and at a constant spacing. The fields of adjacent wire electrodes interact, reducing the current per unit length of wire. In addition, the induced airflow must both enter and exit from above the array, changing the character of the flow field and reducing the heat transfer effectiveness.

Figure 6 presents experimental and numerical results for a case where wire electrodes were suspended 6 cm above the impingement surface. Symbols represent experimental results, while solid lines denote the results of numerical solution. Only two wire electrodes, located at $x = -0.1$ m and $x = +0.1$ m, were used in the experimental work, so symmetry exists only in the region between the wire electrodes. Numerical results, calculated under the assumption of strict symmetry for wire arrays, are therefore shown only between the two neighboring wire electrodes. Note that experimentally, in the case presented here, the wire electrode on the left was presumably coronating more effectively than the wire electrode on the right, accounting for the difference in heat transfer. Experimental results, mirrored by numerical predictions, illustrate that local heat transfer maxima are found at the centerline between adjacent wire electrodes. These maxima are the result of the intersection of the two opposing wall-jet flows.

Figure 7 presents the computed flow field streamlines for a case in which the wire electrodes are 20 cm apart, located at $x = -0.2$ m, $x = 0$ m, $x = +0.2$ m, etc., and are all 2 cm above the surface. Of particular interest is the recirculation zone near the right symmetry plane at $x = 0.1$ m. The reverse jet flow leads to an increase in heat transfer at the right symmetry plane. As expected, however, the recirculation zone leads to increased temperatures and reduced heat transfer. Numerical simulation of various wire electrode spacings, illustrated in Fig. 8, predict the breakdown of this recirculatory behavior when the ratio of wire spacing to wire height approaches approximately 2–3. At lower ratios of wire spacing to wire height, no local maxima are observed between wire electrodes.

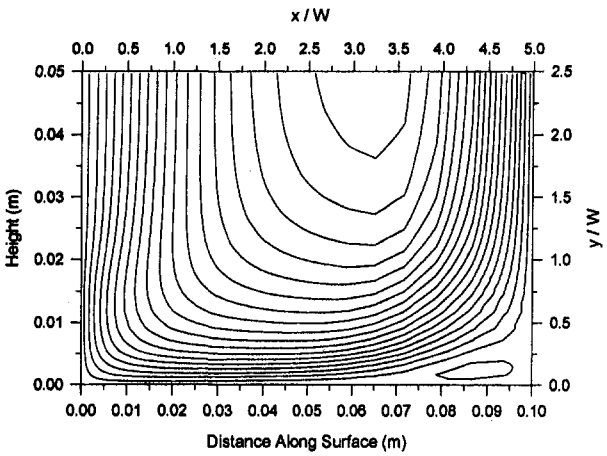

Fig. 7 Flow streamlines in a symmetric array with wire electrodes at 2 cm height, 20 cm separation, and an imposed voltage of 10 kV and current of 388 μA/m

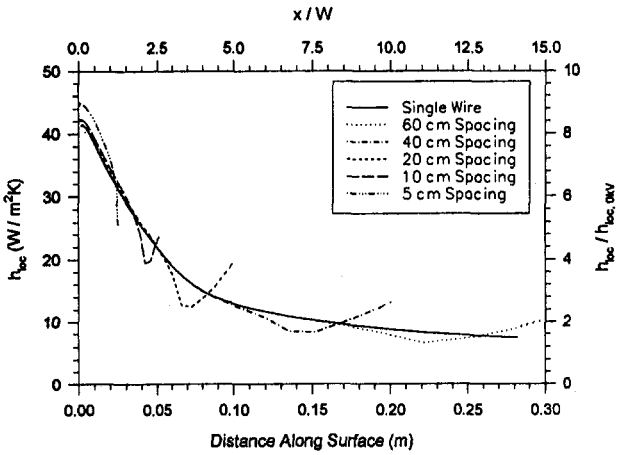

Fig. 8 Numerical local heat transfer coefficients with wire electrodes at 2 cm height with increasing wire spacing; 20 kV and 500 μA/m imposed. Curves terminate at respective symmetry planes in between the two neighboring wire electrodes

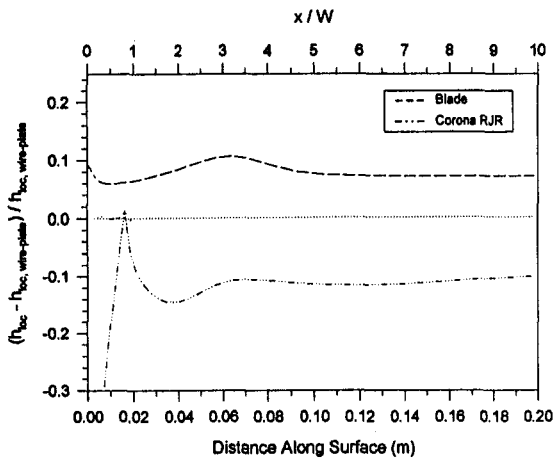

Fig. 10 Local heat transfer relative to simple wire-plate geometry for two of novel electrode configurations at 2 cm height

These results are based upon 500 μA/m assumed current per wire electrode, which may not be appropriate when the wire spacing becomes small, as total current per wire electrode tends to drop when the wire electric fields begin to interact. Experiments revealed little decrease in current per wire electrode until the ratio of spacing to wire height reached approximately 3. Since the number of wires, and therefore total power drawn, increases with decreasing wire spacing, wire spacing for maximum power consumption and heat transfer are likely to exist, but with a wire spacings that draw large amounts of power.

6.3 Novel Electrode Configurations. The body force imposed by corona discharge can be directed, focused, and deflected by an externally imposed electric field, changing the flow field and potentially increasing heat transfer. In particular, it is possible to focus or deflect the corona wind through the use of a "director" electrode, an electrode with a large enough radius of curvature that no corona discharge takes place on surface. A variety of electrode configurations are possible; two cases are presented here to demonstrate the possibilities inherent in electric flow field control (see Fig. 9).

An inherent drawback of the wire-plate electrode configuration is the generation of an upward-directed body force above the wire electrode which is caused by the coronation all around the wire. This force, while much smaller than the force between the wire electrode and the plate, can be expected to reduce the degree of heat transfer enhancement. However, the electric field produced by a "razor-blade" electrode, a thin metal plate normal to the heat transfer surface that coronates only at the sharp bottom surface, imposes no such upward force.

The predicted local heat transfer for the razor-blade geometry, relative to the predicted heat transfer coefficients for the simple wire-plate geometry, are given in Fig. 10. The resultant "razor-blade" heat transfer is up to 10 percent greater for identical power consumption. The upward force above a wire electrode may therefore explain, at least partially, the fact that greater heat transfer enhancement is achieved with needle than with wire electrodes.

A novel geometry was considered that uses two director wire electrodes which modify the force density field. The noncoronating director wire electrodes of larger diameter than the corona wire electrode were energized to the same voltage (10 kV) and were imposed 1 cm below and 2 cm above the corona wire electrode. This arrangement forces ions, and therefore the electric body force, away form the corona wire electrode in a horizontal direction.

As predicted by Fig. 10, the resultant heat transfer was somewhat smaller than that for the standard wire-plate arrangement. However, a recirculatory flow field is produced (Fig. 11) which closely resembles the flow structure obtained with radial jet reattachment (RJR) nozzles (Page et al., 1989). Like standard

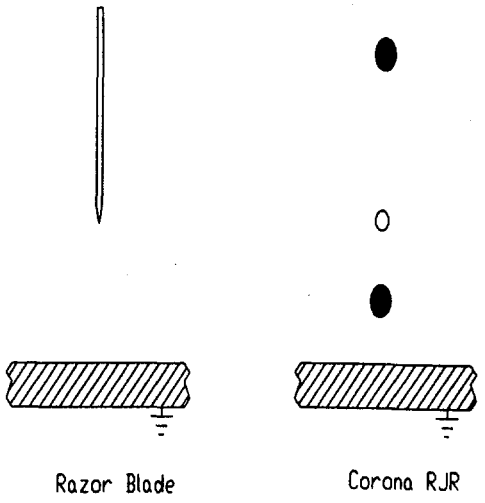

Fig. 9 Novel electrode geometries at 2 cm height; solid circles are large diameter wires and do not coronate

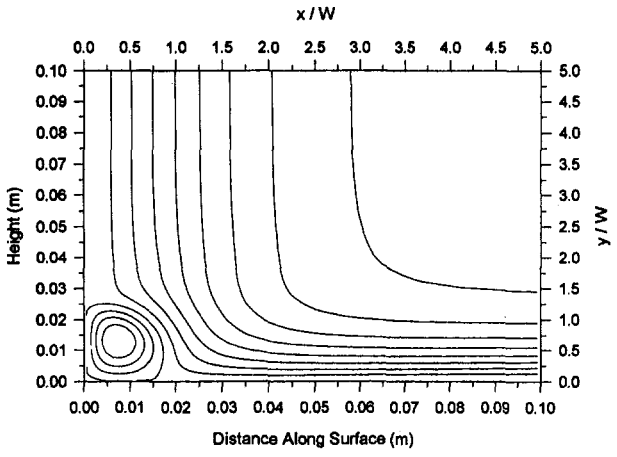

Fig. 11 Corona RJR flow streamlines, coronating electrode at 2 cm height

RJR, corona RJR yields high heat transfer coefficients at the impingement regions and relatively weak heat transfer in the recirculation zones. RJR technology has found applications in drying processes because it creates high heat transfer coefficients while imposing a net force on the drying surface that can be positive, negative, or zero (Page and Seyed-Yagoobi, 1990). Similar control of surface pressure is possible with corona RJR through simple adjustments of the voltages applied to the director wire electrodes.

7 Conclusions

Electrohydrodynamic heat transfer enhancement with wire electrodes suspended above a transfer surface is shown to induce significant heat transfer coefficients on the grounded impingement surface. In the case of a single wire electrode, an impinging jet flow is created. Multiple wire electrodes yield less heat transfer enhancement per wire electrode for a given applied power, and may form, under some conditions, dual recirculation zones at the centerline between wire electrodes. Heat transfer enhancement caused by internal wire electrodes in the array is smaller than that caused by the external wire electrodes due to reduced current flow and access to the fluid reservoir.

Numerical simulations of novel electrode geometries suggest that a primary reason for the superiority of needle electrodes is the upward force created above a wire electrode. This inefficiency may be eliminated through the use of a razor-blade geometry. Director wires may be used, as in the case of 'Corona RJR' to create unusual and potentially useful flow structures.

8 Acknowledgments

This work was supported in part by the Texas A&M University Drying Research Center.

References

Hauksbee, F., 1719, *Physico-Mechanical Experiments on Various Subjects,* 1st ed., London, pp. 46–47.

Kline, S. J., and McClintock, F. A., 1953, "Describing Uncertainties in Single Sample Experiments," *Mechanical Engineering,* Vol. 75, pp. 3–8.

Kulacki, F. A., 1982, "Electrohydrodynamical Enhancement of Convective Heat Transfer," *Advances in Transport Processes,* Vol. II, A. S. Mujumdar and R. A. Mashelkar, eds., Halstead Press, New York.

Marco, S. M., and Velkoff, H. R., 1963, "Effect of Electrostatic Fields on Free Convection Heat Transfer From Flat Plates," ASME Paper No. 63-HT-9.

Martin, H., 1977, "Heat and Mass Transfer Between Impinging Gas Jets and Solid Surfaces," *Advances in Heat Transfer,* J. P. Harnett and T. F. Irvine, Jr., eds., Vol. 13, Academic Press, New York, New York.

Ohadi, M. M., Nelson, D. A., and Zia, S., 1991, "Heat Transfer Enhancement of Laminar and Turbulent Pipe Flow via Corona Discharge," *International Journal of Heat and Mass Transfer,* Vol. 34, pp. 1175–1187.

Owsenek, B. L., 1993, "An Experimental, Theoretical and Numerical Investigation of Corona Wind Heat Transfer Enhancement," M. S. thesis, Texas A&M University, College Station, TX.

Owsenek, B. L., Seyed-Yagoobi, J., and Page, R. H., 1995, "Experimental Investigation of Corona Wind Heat Transfer Enhancement With a Heated Horizontal Flat Plate," ASME JOURNAL OF HEAT TRANSFER, Vol. 117, pp. 309–315.

Page, R. H., and Seyed-Yagoobi, J., 1990, "A New Concept for Air or Vapor Impingement Drying," *TAPPI Journal,* Vol. 73, pp. 229–234.

Page, R. H., Hadden, L. L., and Ostowari, C., 1989, "Theory for Radial Jet Reattachment Flow," *AIAA Journal,* Vol. 27, pp. 1500–1505.

Page, R. H., Ostowari, C., and Seyed-Yagoobi, J., 1992, "Infrared Images of Jet Impingement," *Proceedings of 20th International Congress on High Speed Photography and Photonics,* Vol. 1801, pp. 703–709.

Patankar, S. V., 1980, *Numerical Heat Transfer and Fluid Flow,* Hemisphere Publishing Corporation, New York.

Takimoto, A., Tada, Y., Hayashi, Y., and Yamada, K., 1988, "Convective Heat Transfer Enhancement by a Corona Discharge," *Transactions of JSME,* Vol. 54 (B), pp. 695–703.

Van Doormal, J. P., and Raithby, G. D., 1984, "Enhancements of the SIMPLE Method for Predicting Incompressible Fluid Flows," *Numerical Heat Transfer,* Vol. 7, pp. 147–163.

Yabe, A., Mori, Y., and Hijitata, K., 1978a, "EHD Study of the Corona Wind Between Wire and Plate Electrodes," *AIAA Journal,* Vol. 16, pp. 340–345.

Yabe, A., Mori, Y., and Hijitata, K., 1978b, "Heat Transfer Augmentation Around a Downward-Facing Flat Plate by Nonuniform Electric Fields," *Proceedings of 5th International Heat Transfer Conference,* National Research Council of Canada, Vol. 3, pp. 171–176.

Heat Transfer in an Electromagnetic Bearing

G. F. Jones
Associate Professor,
jones@merlin.engr.vill.edu

C. Nataraj
Associate Professor.

Department of Mechanical Engineering,
Villanova University,
800 Lancaster Avenue,
Villanova, PA 19085-1681

An exact solution for two-dimensional, full transient, and steady periodic heat conduction in an electromagnetic bearing is obtained. Classical methods are used to obtain an analytical expression for the temperature distribution that arises from power dissipated in the pole windings. Among the key findings is the need for cooling in the immediate neighborhood of the bearing support due to the relatively large thermal resistance of the supporting structure. The results presented prove the existence of large temperature gradients in the bearing in both the radial and circumferential directions. This demands the need for a fine mesh when performing the commonly used nodal-network thermal analysis. Conditions are described under which the temperature distribution is independent of the frequency of the time-dependent current supplied to the poles. For these cases the problem reduces to steady state, and the solution is given. A peak circumferential temperature difference of about 55°C in the bearing is possible under certain conditions that are discussed. Attention to proper thermal design is critical to reduce the dimensional distortion of the bearing caused by thermal expansion. The effects of thermal expansion can range from catastrophic, should the shaft come in contact with the bearing, to an undesirable change in the force and dynamic control characteristics caused by a variation in the critical shaft-to-bearing clearance, which is of the order of a fraction of a millimeter.

1 Background and Approach

The suspension of a rotating shaft assembly in a magnetic field, thereby avoiding mechanical contact and lubrication, is an idea that is very attractive and has been the subject of some research in recent years (Schweitzer et al., 1994; Allaire, 1994). Apart from the obvious advantage of reducing wear, the magnetic bearings are unique in that the bearing characteristics can be changed in an active control loop just by changing the controller parameters. This makes it possible not only to reduce rotor vibration in general, but also to control the rotor in case of instabilities and other such potentially catastrophic situations.

There has been some interest in estimating the temperature rise in magnetic bearings (Saari and Lindgren, 1994) that arises from power dissipated in the pole windings[1]. As indicated by Saari and Lindgren, the proper thermal design of electrical machinery is critical since their lifetime is reduced by about half for a 10°C increase in the continuous operating temperature. Predictive models for thermal performance typically employ a nodal-network, the accuracy of which may be in question due to large temperature gradients within a coarse-network grid and the lack of accurate thermal resistance data at the outset. The current paper establishes an analytical basis for such thermal analyses by obtaining an exact solution for the two-dimensional, full transient, and steady periodic temperature distribution in the bearing. The rotor is assumed to be in a steady circular periodic orbit due to a rotating unbalance.

2 Analysis

2.1 Geometry and Assumptions. An overview of the configuration and the geometry of the magnetic bearing are shown in Fig. 1 and 2, respectively. The poles are attached to the stator ring of inside radius r_i and outside radius r_o. The angles θ_k are the orientations of the centerlines for each pole and $\Delta\phi$ is the angle spanned by a pole at $r = r_i$. θ_k are written as

$$\theta_k = \frac{\pi}{n_p}[1 + 2(k - 1)], \tag{1}$$

where $k = 1, 2, 3 \ldots n_p$ is the pole index and n_p is the number of poles. The outside radius of the bearing contacts a structural support which, in turn, is thermally linked to a constant sink temperature. The sink temperature is assumed to be equal to the initial temperature of the bearing. The electrical power dissipated in the windings on each pole provides a periodic source of heating that is conducted radially into the stator ring and onward to the thermal sink. The poles themselves are nearly isothermal as a result of the uniform heating around them. Thermophysical properties are assumed to be constant in this work since the variation of temperature in the stator ring is not expected to be extreme.

2.2 Equation Development. The heat conduction equation is written in dimensionless form as

$$\frac{\partial\psi}{\partial\tau} = \frac{1}{\eta}\frac{\partial}{\partial\eta}\left(\eta\frac{\partial\psi}{\partial\eta}\right) + \frac{\partial^2\psi}{\eta^2\partial\theta^2}, \tag{2}$$

where

$$\psi(\eta, \theta, \tau) = \frac{T(r, \theta, t) - T^i}{q_r r_o/k}, \quad \eta = \frac{r}{r_o},$$

$$\tau = \frac{\kappa t}{r_o^2}, \quad \alpha = \frac{r_i}{r_o}. \tag{3}$$

In Eq. (3), T^i is the uniform initial temperature, q_r is the characteristic heat flux yet to be defined, κ is the thermal diffusivity, and k is the thermal conductivity. We note that the dimensionless temperature used in this study is a dimensionless temperature rise measured from the uniform initial temperature of the bearing.

Contributed by the Heat Transfer Division for publication in the JOURNAL OF HEAT TRANSFER. Manuscript received by the Heat Transfer Division February 6, 1996; revision received February 14, 1997; Keywords: Conduction, Modeling & Scaling, Transient & Unsteady Heat Transfer. Associate Technical Editor: T. Tong.

[1] This is the dominant source of heating. Power losses from windage and eddy currents (Mizuno and Higuchi, 1994) are smaller by a factor of about four and may be neglected for this study.

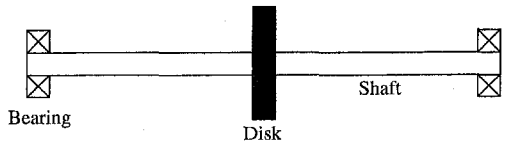

Fig. 1 Overview of rotor configuration

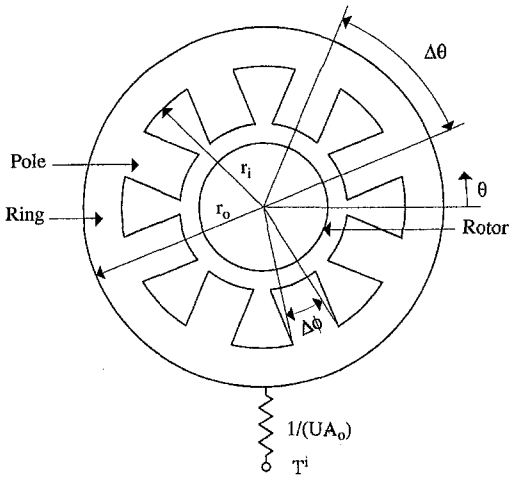

Fig. 2 Geometry

The boundary and initial conditions are written in dimensionless form as

$$-\left.\frac{\partial\psi}{\partial\eta}\right|_{\eta=\alpha} = q(\theta, \tau)/q_r,$$

$$-\left.\frac{\partial\psi}{\partial\eta}\right|_{\eta=1} = \mathrm{Bi}\,\psi(1, \theta, \tau), \quad \psi(\eta, \theta, 0) = 0, \tag{4}$$

together with the usual periodicity of 2π in the temperature, ψ, and temperature gradient in the circumferential direction, $\partial\psi/\partial\theta$. The function $q(\theta, \tau)$ is from

$$q(\theta, \tau) = \begin{cases} q_k(\tau), \ \theta_k - \Delta\phi/2 \le \theta \le \theta_k + \Delta\phi/2, \\ k = 1, 2, 3 \ldots n_p \\ 0, \quad \text{all other } \theta, \text{ where } 0 \le \theta \le 2\pi. \end{cases} \tag{5}$$

In eq. (5), $q_k(\tau)$ are the prescribed time-dependent heat fluxes at the inside radius of the stator ring. These are addressed below. The parameter Bi in eq. (4) is the Biot number, Ur_o/k. The overall heat transfer coefficient, U, depends on the conductance of the path between the outside surface of the stator ring and the sink temperature and whether or not forced convection is present at the inside surfaces of the bearing (Kreith, 1968). Contributing to U is the conductance of the bearing structural support, the contact conductance, and the convective conductance where the support is cooled by a fluid. If we assume the presence of good metallic conductors along a short path, then the principal contribution to U will be the contact conductance at the ring/mount interface, and that due to convective cooling. These issues will be discussed in more detail below.

2.3 Solution. The solution for Eqs. (2)–(5) is obtained by replacing the time-dependent boundary condition $q_k(\tau)/q_r$ with unity. This is referred to as the fundamental solution and is given the symbol $\psi_f(\eta, \theta, \tau)$. The time-dependent boundary condition is then accounted for by using the Duhammel superposition integral (Arpaci, 1966). We have

$$\psi(\eta, \theta, \tau) = \int_0^\tau \sum_{k=1}^{n_p} \frac{q_k(\beta)}{q_r} \frac{\partial\psi_f(\eta, \theta, \tau - \beta)}{\partial\tau}\, d\beta, \tag{6}$$

where β is a dummy variable of integration.

The heat flux, $q_k(\tau)$, is proportional to the electrical power dissipated per pole. Thus,

$$q_k(\tau) = \frac{i_k^2(\tau)R_k}{A_i}, \tag{7}$$

where R_k is the electrical resistance of the winding per pole and A_i, the surface area for heat flow between a pole and the stator ring, is

$$A_i = \alpha r_o W \Delta\phi. \tag{8}$$

The time-dependent current in Eq. (7), $i_k(\tau)$, is obtained by

Nomenclature

a = bias current, A
A = area, m^2
B_n, $C_{m,n}$ = coefficients
Bi = Biot number, Ur_o/k
c, d = ratio of amplitude of control current to bias current
F = function (Eqs. (16), (20), and (23))
h_c = contact conductance, W m^{-2} K^{-1}
i = current, A
k = thermal conductivity, W m^{-1} K^{-1}
L = conductive path length in bearing support structure, m
n_p = number of poles
p = function (Eq. (14))
q = heat flux, W m^{-2}
r = radial coordinate, m
R = electrical resistance, Ω
s = constant assigned to c_k and d_k (Table 1)
t = time, s
T = temperature, K
T^i = initial temperature, K
U = overall heat transfer coefficient, W m^{-2} K^{-1}
$u_0 \ldots u_4$ = coefficients (Eq. (17))
V = function (Eq. (13))
v_1, v_2 = coefficients (Eq. (17))
W = width of bearing, m
w = dummy variable
x_p = thermal penetration depth, $\sqrt{2\kappa/\omega}$, m
α = r_i/r_o
β = dummy variable of integration
$\Delta\phi$ = angle spanned by a pole at $r = r_i$
η = dimensionless radial coordinate, r/r_o
θ = circumferential coordinate
θ_k = pole angle
$\theta_{1,k}$ = $\theta_k - \Delta\phi/2$
$\theta_{2,k}$ = $\theta_k + \Delta\phi/2$
κ = thermal diffusivity, m^2 s^{-1}
$\lambda_{m,n}$ = roots of Eq. (15)
ω = frequency, s^{-1}
ω^* = dimensionless frequency, $\omega r_o^2/\kappa$
τ = dimensionless time, $\kappa t/r_o^2$
τ^* = dimensionless time for steady, periodic regime
ψ = dimensionless temperature

Subscripts

f = fundamental problem
i = inside radius
k = pole index
m, n = indices
o = outside radius
r = reference

Table 1 Values for the control-current amplitude ratios, c_k and d_k, in Eq. (9). s, the ratio of the amplitude of the control current to the bias current, is a prescribed constant.

Pole, k	c_k	d_k
1	$-s$	0
2	$-s$	0
3	0	$-s$
4	0	$-s$
5	s	0
6	s	0
7	0	s
8	0	s

establishing a simple control strategy for the bearing. The rotor is assumed to perform a steady, synchronous, centered circular orbit. Such an orbit would result from gravity-free and isotropic conditions with rotating unbalance. It is also assumed that the magnetic bearing control circuit results in a simple proportional gain. A more complicated (and realistic) control circuit would not substantially change the heat transfer results but would only bring in more parameters that would detract from the essential theme of this investigation.

With the above assumptions and with a differential mode of operation (Schweitzer et al., 1994), the currents to the poles would be as follows,

$$i_k(\tau) = a_k[1 + c_k \sin(\omega^*\tau) + d_k \cos(\omega^*\tau)], \quad (9)$$

where the coefficients a_k and the products $a_k c_k$ and $a_k d_k$ are bias currents and amplitudes of the control current per pole, respectively, and ω^* is a dimensionless frequency, $\omega r_o^2/\kappa$. It may be noted that the bias current is likely to be the same for all the poles but, for generality, it will remain as a variable here. The values for the ratio of the control current amplitude to the bias current per pole, c_k and d_k, are given in Table 1 where, for simplicity, each is assumed to be a constant magnitude s.

Note that the nature of this control algorithm is such that, if perfectly implemented, the rotor would experience zero vibration since the unbalance force would be exactly canceled by the magnetic bearing forces.

2.3.1 Full Transient Solution. The fundamental solution of Eqs. (2)–(5), $\psi_f(\eta, \theta, \tau)$, is obtained using classical methods. Taking the derivative of $\psi_f(\eta, \theta, \tau)$ as indicated in Eq. (6), substituting Eqs. (7) and (9) and integrating, the solution for the time-dependent problem is obtained as follows:

$$\psi(\eta, \theta, \tau) = \sum_{n=1}^{\infty} B_n V_{o,n}(\eta) \sum_{k=1}^{n_p} F_k(\lambda_{0,n}, \omega^*/\lambda_{0,n}^2, \tau)\Delta\phi + \sum_{n=1}^{\infty}\sum_{m=1}^{\infty} C_{m,n} V_{m,n}(\eta) \sum_{k=1}^{n_p} F_k(\lambda_{m,n}, \omega^*/\lambda_{m,n}^2, \tau) \times \{\sin(m\theta)[\cos(m\theta_{2,k}) - \cos(m\theta_{1,k})] + \cos(m\theta)[\sin(m\theta_{1,k}) - \sin(m\theta_{2,k})]\}, \quad (10)$$

where $\theta_{1,k} = \theta_k - \Delta\phi/2$ and $\theta_{2,k} = \theta_k + \Delta\phi/2$, and the coefficients and related functions are

$$C_{m,n} = \frac{-2\int_\alpha^1 p_m(\eta) V_{m,n}(\eta)\eta d\eta}{[(\mathrm{Bi}^2 - m^2)/\lambda_{m,n}^2 + 1]V_{m,n}^2(1) + (4/\pi^2)[(m/\alpha\lambda_{m,n})^2 - 1]}, \quad (11)$$

$$B_n = \frac{-(\alpha/\pi)\int_\alpha^1 [1/\mathrm{Bi} - \ln(\eta)] V_{0,n}(\eta)\eta d\eta}{(\mathrm{Bi}^2/\lambda_{0,n}^2 + 1)V_{0,n}^2(1) - 4/\pi^2}, \quad (12)$$

$$V_{m,n}(\eta) = J_m'(\lambda_{m,n}\alpha)Y_m(\lambda_{m,n}\eta) - Y_m'(\lambda_{m,n}\alpha)J_m(\lambda_{m,n}\eta), \quad (13)$$

$$p_m(\eta) = \frac{\eta^{-m} + (m/\mathrm{Bi} - 1)\eta^m/(m/\mathrm{Bi} + 1)}{m^2\pi[\alpha^{m-1}(m/\mathrm{Bi} - 1)/(m/\mathrm{Bi} + 1) - \alpha^{-m-1}]}. \quad (14)$$

The eigenvalues, $\lambda_{m,n}$, are obtained from the characteristic equation

$$J_m'(\lambda_{m,n}\alpha)[Y_m'(\lambda_{m,n}) + \mathrm{Bi}\, Y_m(\lambda_{m,n})] - Y_m'(\lambda_{m,n}\alpha)[J_m'(\lambda_{m,n}) + \mathrm{Bi} J_m(\lambda_{m,n})] = 0. \quad (15)$$

In Eqs. (13) and (15), the prime indicates a derivative with respect to η.

The terms J_m and Y_m in the above equations are mth order Bessel functions of the first and second kinds (Abramowitz and Stegun, 1965). The function, F_k, in Eq. (10) is

$$F_k(\lambda_{m,n}, w, \tau) = [(1 + w^2)(1 + 4w^2)]^{-1}[R_k a_k^2/(R_1 a_1^2)] \times \{u_{0,k}(w) - u_{1,k}(w)\sin(\omega^*\tau) + u_{2,k}(w)\cos(\omega^*\tau) - u_{3,k}(w)\sin(2\omega^*\tau) - u_{4,k}(w)\cos(2\omega^*\tau) + [v_{1,k}(w) + v_{2,k}(w)]e^{-\lambda_{m,n}^2\tau}\}, \quad (16)$$

where

$$\begin{aligned} u_{0,k}(w) &= -(1 + w^2)(1 + 4w^2)(2 + c_k^2 + d_k^2)/2, \\ u_{1,k}(w) &= 2(1 + 4w^2)(c_k + wd_k), \\ u_{2,k}(w) &= 2(1 + 4w^2)(wc_k - d_k), \\ u_{3,k}(w) &= (1 + w^2)[c_k d_k + w(d_k^2 - c_k^2)], \\ u_{4,k}(w) &= (1 + w^2)(d_k^2 - c_k^2 - 4wc_k d_k)/2, \\ v_{1,k}(w) &= (1 + w^2)[2w^2 c_k^2 - 2wc_k d_k + (1 + 2w^2)d_k^2], \\ v_{2,k}(w) &= (1 + 4w^2)[2(d_k - wc_k) + 1 + w^2], \end{aligned} \quad (17)$$

and w is a dummy variable.

The reference heat flux, q_r, is arbitrarily taken to be that for pole 1. Thus,

$$q_r = a_1^2 R_1/A_i, \quad (18)$$

where a_1 is the bias current and R_1 is the electrical resistance for pole 1. With Eq. (18), the dimensional temperature rise is written as

$$T(\eta, \theta, \tau) - T^i = \psi(\eta, \theta, \tau)a_1^2 R_1 r_o/(A_i k). \quad (19)$$

2.3.2 Steady Periodic Solution. The steady periodic solution follows from the above solution with two changes. First, the exponential term in F_k (Eq. (16)) becomes zero in the large-time limit. Secondly, the characteristic time for the problem changes from the diffusion time scale, r_o^2/κ, to the frequency time scale, ω^{-1}. Defining ωt as τ^*, where $0 \le \tau^* \le 2\pi$, $F_k(\lambda_{m,n}, w, \tau)$ in Eq. (16) becomes

$$F_k(w, \tau^*) = [R_k a_k^2/(R_1 a_1^2)][u_{0,k}(w) - u_{1,k}(w)\sin(\tau^*) + u_{2,k}(w)\cos(\tau^*) - u_{3,k}(w)\sin(2\tau^*) - u_{4,k}(w)\cos(2\tau^*)]/[(1 + w^2)(1 + 4w^2)]. \quad (20)$$

The coefficients $u_{0,k}(w)$ through $u_{4,k}(w)$ are as defined in Eq. (17).

3 Results

3.1 The Parameters and Cases Studied. Inspection of Eqs. (10)–(16) reveals that the solution for the temperature rise depends on seven parameters: θ_k, $\Delta\phi$, $R_k a_k^2/R_1 a_1^2$, α, s, Bi, and ω^*, as well as the independent variables η, θ, and τ. Although electromagnetic bearing technology is in its infancy, at

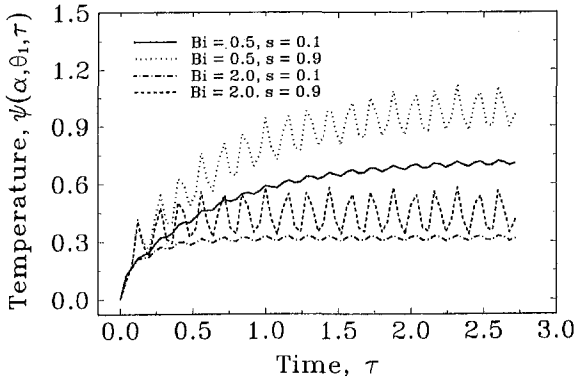

Fig. 3 Transient temperature history

this time it appears that eight-pole bearings are most commonly used (Schweitzer et al., 1994). Hence, for the results that follow, attention is focused on an eight-pole bearing having $\Delta\phi$ of 20 deg (Fig. 2). The resulting values for θ_k are 22.5, 67.5, 112.5, 157.5, 202.5, 247.5, 292.5, and 337.5 deg. For simplicity, the bias current and pole electrical resistance are assumed to be constant so that $R_k a_k^2/R_1 a_1^2$ is unity.

Realistic values for α can range from 0.6 to 0.9. Reducing α reduces temperature variations in the θ direction. For a bulk of this study, α was chosen as 0.6. We note, however, that the circumferential temperature variations obtained in this work are less than would be obtained for larger values of α. The results for α of 0.9 are discussed in the conclusions. Since s ranges from zero to one, the effects of two extremes for s are investigated; 0.1 and 0.9.

Values for the Biot number, Bi, are obtained by considering the thermal resistances in a heat flow path from the outer surface of the ring to a thermal sink at temperature T^i. If the effect of forced convection at the edges of the bearing is neglected for the moment, Bi is written as

$$\mathrm{Bi} = \frac{r_o/k}{1/h_c + L/k}, \tag{21}$$

where $1/h_c$ is the contact resistance, L is the path length, and L/k is the conductive resistance through the bearing structural support.

For an air gap between the bearing and support in the range of 0.1 to 0.05 mm, and a contact-area ratio of 0.1 to 0.7, the contact resistance is approximately 10^{-4} m^2 K/W (Henry and Fenech, 1964). If the bearing support structure is of carbon steel and the path length ranges from about 3 to 10 cm, which appears to be realistic, the conductive resistance is several times greater than the contact resistance. This result points to the need for cooling in the *immediate* neighborhood of the bearing support if a reasonably small temperature rise in the bearing is to be realized.

In any event, for r_o in the range of 5 cm, Eq. (21) predicts values for Bi from about 0.5 to nearly 2. Biot numbers smaller than 0.5 will result from conductive path lengths longer than 10 cm, and larger than 2 for lengths shorter than 3 cm. If the edges of the bearing are exposed to forced convective cooling, Bi larger than 2 can also be achieved. Moreover, edge cooling produces the desirable effect of reducing the bearing temperature at all radial locations equally. This is contrasted with cooling at only the outer radius of the bearing, which tends to reduce the temperatures nearest r_o more so than at other radial points.

The effect of the frequency, ω, on the temperature distribution arises through the term $\omega^* = \omega r_o^2/\kappa$. It is more insightful to cast this variable in terms of the ratio of the thermal penetration depth, x_p, to r_o. Thus

$$\frac{x_p}{r_o} = \sqrt{\frac{2\kappa}{\omega r_o^2}} = \sqrt{\frac{2}{\omega^*}}, \tag{22}$$

where x_p is the dimensional depth to which the effect of the periodicity of the heat flux penetrates. x_p is determined from an independent analysis of conduction in a semi-infinite slab subject to a steady, periodic heat flux (Carslaw and Jaeger, 1959). In this study, values for x_p/r_o range from unity, for which the effect of the periodicity is large, to 0.01 for which it is nearly imperceptible. An intermediate value of x_p/r_o is chosen to be 0.1.

The value for the bias current, a, is chosen as 5 A for this study (Nataraj and Trotter, 1997). The temperature scale in Eq. (19), $a_1^2 R_1 r_o/(A_i k)$, is estimated to be 31°C for a bearing having r_o and W of 5 cm and 1.25 cm, respectively, and an electrical resistance of 0.2 Ω per pole. This temperature will be used below to produce order-of-magnitude estimates for the dimensional temperature rise in the bearing.

Twenty terms were evaluated for each infinite series in Eq. (10). The solution was carried out in Mathcad 6.0+ (Mathsoft, Inc., Cambridge, Massachusetts) (an unsupported copy of the code developed in this work is available by contacting the lead author). For most of the parameters considered in this study, additional terms in a summation produced less than a 3 percent change in the temperature.

3.2 Temperature Distributions.

3.2.1 Full Transient Regime. The temperature history $\psi(\alpha, \theta_1, \tau)$ is presented in Fig. 3 for x_p/r_o of 0.1 and two values for each of Bi and s. The full transient and steady periodic regimes are clearly visible. For the larger Bi, steady periodic conditions are achieved after an elapsed time, τ, of about 0.5. For Bi of 0.5, the elapsed time increases to about 2.5 as a greater span of time is needed to produce the elevated temperatures associated with this value of Bi. We note that τ of one corresponds to a dimensional time of about 150 s for r_o of 5 cm. Also evident from inspection of Fig. 3 is that s has no influence on the approach to steady periodic conditions. The only effect of s is to change the mean value and amplitude of the temperature wave.

3.2.2 Steady Periodic Regime. The influence of x_p/r_o, and the temperature variation with radius is investigated in Figs. 4 and 5 for Bi of 0.5 and 2, respectively, and for τ^* equal to $\pi/2$. s is 0.9 for both figures. For τ^* equal to $\pi/2$, poles 5 and 6 (see Table 1 and Eq. (9)) experience the largest heating whereas poles 1 through 4 have current flows that are less than the bias current and poles 7 and 8 have experienced their maximum heating at τ^* of zero. Evidence of this is clearly seen in both Figs. 4 and 5 where we note lower temperatures at $\eta = \alpha$ for the first four poles, larger temperatures for poles 5 and

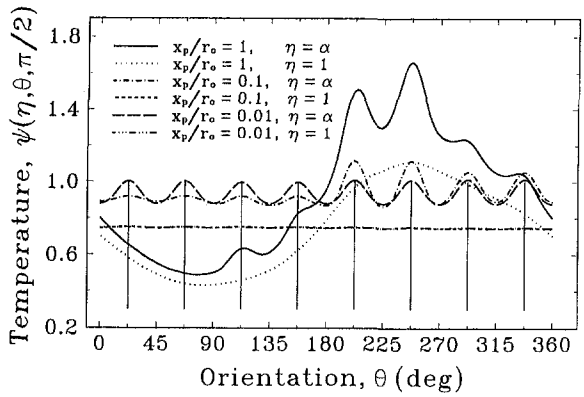

Fig. 4 Steady periodic temperature distribution for Bi = 0.5 and s = 0.9; $\tau^* = \pi/2$

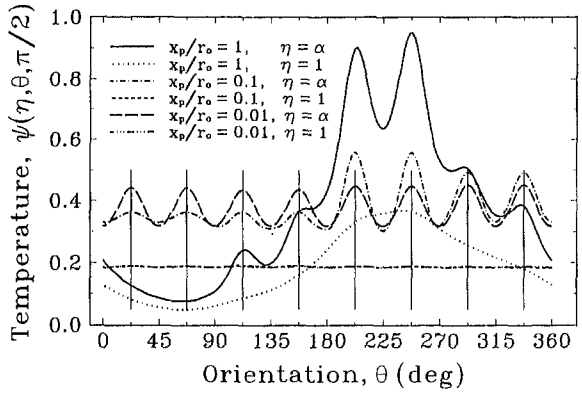

Fig. 5 Steady periodic temperature distribution for Bi = 2 and s = 0.9; $\tau^* = \pi/2$

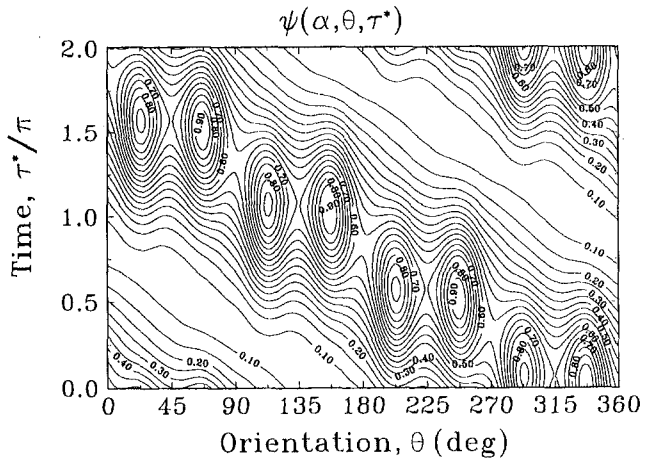

Fig. 6 Steady periodic temperature history at $\eta = \alpha$, for Bi = 2, s = 0.9, and x_p/r_o = 1

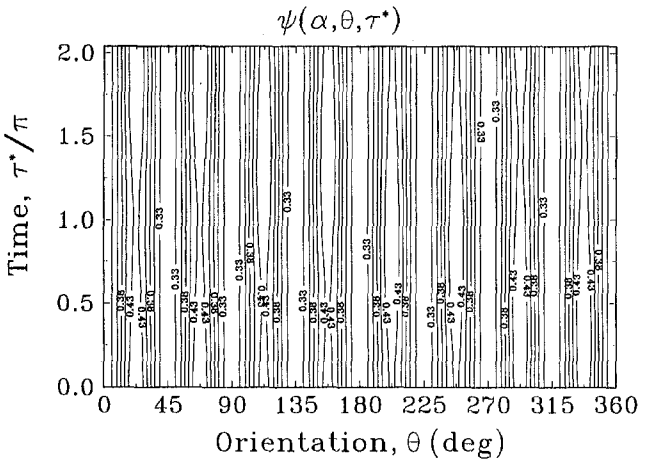

Fig. 7 Steady periodic temperature history at $\eta = \alpha$, for Bi = 2, s = 0.9, and x_p/r_o = 0.01

6, and intermediate values for poles 7 and 8. This trend is most obvious for x_p/r_o of unity where the effect of the heat flux on the periodicity of temperature is the largest. For x_p/r_o of 0.1 and 0.01, the effect of τ^* is weakened to the extent that for $x_p/r_o \leq 0.01$, the temperature distribution for all η is nearly independent of the periodic nature of the heating. For this condition the problem becomes steady state where the solution is given by Eqs. (10) – (15) and (17) – (19). Instead of Eq. (20), the time-averaged $F_k(w, \tau^*)$ becomes

$$F_k = -[R_k a_k^2/(R_1 a_1^2)](2 + c_k^2 + d_k^2)/2. \qquad (23)$$

For $\eta = 1$ (Figs. 4 and 5), we note that the temperature is circumferentially uniform for $x_p/r_o \leq 0.1$ but tends to follow that at $\eta = \alpha$ for larger x_p/r_o.

The mean temperature of the stator ring and, to a lesser extent, the maximum temperature difference across the ring in the radial direction are dependent upon Bi. We see this by comparing Figs. 4 and 5. The temperature difference between the inner and outer radii on average for Bi of 0.5 is from ψ of 0.75 to about 0.9 (23°C to 27°C), but for Bi of 2 decreases to between ψ of 0.2 and 0.4 (6°C to 12°C). These trends are reasonable since it is understood that the bearing temperature increases with thermal resistance between it and the sink temperature. To put the foregoing temperature results in perspective, recall that the dimensional temperature presented above is actually the temperature rise above the initial temperature of the bearing (see eq. (19)).

The extent of temperature rise is nominal for the cases considered here. However, we note that a peak temperature rise of ψ equal to 1.6 (50°C) (Fig. 4) and larger is likely for x_p/r_o of unity, Bi of 0.5 and smaller, bias currents larger than 5 A, and values of A_i smaller than that encountered here.

The extent of the variation of temperature in the circumferential direction is seen from inspection of Figs. 4 and 5 to be of the same order or less than that in the radial direction. This variation will increase substantially with increasing α, as discussed above, and decrease with decreasing s.

Contour maps of $\phi(\alpha, \theta, \tau^*)$ for s of 0.9, Bi of 2, and two values of x_p/r_o are shown in Figs. 6 and 7. In Fig. 6, x_p/r_o is equal to unity, and in Fig. 7, 0.01. Focusing on Fig. 6, localized regions of high temperature stand out, occurring first for poles 7 and 8, and proceeding to lower numbered pole pairs as time progresses. This pattern is dictated by the control strategy established by Eq. (9) and Table 1. The extremes in ψ range from 0.9 to about 0.1 as also reflected in the first two curves in Fig. 5. Contrasted with Fig. 6, the results from Fig. 7 indicate freedom from the control strategy, as the temperature history is nearly independent of τ^*. These conclusions would be identical for s and Bi other than those considered here. The sensitivity of the time dependence of temperature to the input heat flux for $\eta > \alpha$ will be even weaker than for $\eta = \alpha$ as the temperature wave attenuates with the diffusion of heat into the stator ring.

4 Conclusions

An exact solution for two-dimensional, full transient, and steady periodic heat conduction in an electromagnetic bearing was obtained. The key parameters are: the ratio of the inside radius to the outside radius of the stator ring (α), the dimensionless heat transfer coefficient (Bi), the angular positions of the poles (θ_k), the pole angle ($\Delta\phi$), the ratio of the control current amplitude to the bias current (s), and control current frequency (as characterized by the parameter x_p/r_o), the ratio of the bias current per pole to that for pole 1, and the characteristic temperature scale, $a_1^2 R_1 r_o/(A_i k)$.

The principal conclusions are as follows:

1 The contact thermal resistance dominates the value for Bi only if the conductive path between the bearing and the sink temperature is less than about 3 cm. Otherwise, Bi becomes strongly dependent on the conductive resistance in this path. Since 3 cm is a relatively short path length, this conclusion points to the need for cooling in the *immediate* neighborhood of the bearing support.

2 For Bi of 2, steady periodic conditions are achieved after an elapsed time, τ, of about 0.5. τ of one corresponds to a dimensional time of about 150 s for r_o of 5 cm.

3 For $2\kappa/(\omega r_o^2) < 10^{-4}$, the temperature distribution is independent of the control strategy, i.e., the frequency of the time-dependent current supplied to the poles. The problem is reduced to steady state, the solution for which is given by Eqs. (10)–(15), (17)–(19), and (23).

4 The largest radial and circumferential temperature differences from this study range from about 20 to 30°C. Because of the relatively large temperature gradients present in the bearing in both the radial and circumferential directions, a fine mesh is necessary when performing a nodal-network thermal analysis for an electromagnetic bearing.

5 The control current amplitude, s, affects only the mean temperature, and in cases of $2\kappa/(\omega r_o^2) < 10^{-4}$, the amplitude of the temperature in the bearing. s plays no role in the approach to steady periodic conditions.

6 A larger temperature rise in the bearing than indicated above is possible. The characteristic temperature scale, $a_1^2 R_1/(\alpha W \Delta \phi k)$, imposes a first-order effect on the dimensional temperature rise. Thus, the temperature will increase with the pole electrical resistance and the square of the bias current, and decrease with bearing width, W. An increase in α (a thinner stator ring) decreases the characteristic temperature but increases the circumferential temperature gradient by reducing the the area for conduction in this direction. For example, for $\alpha = 0.9$, a circumferential temperature variation of more than 55°C (with a peak temperature rise of about 60°C) is obtained. However, an increase in the number of poles (say, to 16 from 8) with $\Delta\phi$ fixed will produce smaller circumferential temperature gradients by increasing the heat transfer surface area at $r = r_i$. Increasing the value of Bi from 0.5 to 2 decreases the local bearing temperature by about 60 percent.

7 Because of the potentially large temperature and temperature gradients in the electromagnetic bearing, attention to proper thermal design is critical to ensure adequate bearing performance and lifetime. The principal concern regarding the temperature gradients is the dimensional distortion of the bearing caused by thermal expansion. The effects of thermal expansion may range from catastrophic, should the shaft come in contact with the bearing, to an undesirable change in the force and dynamic control characteristics. The latter effect comes about because the shaft-to-bearing clearance, which is of the order of a fraction of a millimeter, is a very critical electromagnetic bearing design variable. The topic of dimensional distortion in response to the temperature distribution is part of ongoing work by the authors.

References

Abramowitz, M., and Stegun, I. A., 1965, *Handbook of Mathematical Functions,* Dover Publications, Inc., New York.

Allaire, P. E., 1994, "Magnetic Bearings," *CRC Handbook of Lubrication and Tribology,* Vol. III, E. R. Booser, ed., Boca Raton, FL.

Arpaci, V. S., 1966, *Conduction Heat Transfer,* Addison-Wesley Publishing Company, Reading, MA.

Carslaw, H. S., and Jaeger, J. C., 1959, *Conduction of Heat in Solids,* Oxford University Press, London, England.

Henry, J. J., and Fenech, H., 1964, "The Use of Analog Computers for Determining Surface Parameters for Prediction of Thermal Contact Conductance," ASME JOURNAL OF HEAT TRANSFER, Vol. 86, pp. 543–551.

Kreith, F., 1968, "Convection Heat Transfer in Rotating Systems," *Advances in Heat Transfer,* Academic Press Inc, New York, pp. 129–251.

Mizuno, T., and Higuchi, T., 1994, "Experimental Measurement of Rotational Losses in Magnetic Bearings," *Proceedings of the Fourth International Symposium on Magnetic Bearings,* ETH Zürich, Switzerland.

Nataraj, C., and Trotter, A. V., 1997, "Design of Magnetic Bearings for a Laboratory Setup." Internal Report, Department of Mechanical Engineering, Villanova University, Villanova, PA.

Saari, J., and Lindgren, O., 1994, "Estimation of the Temperature Rise in High-Speed Electrical Machines With Magnetic Bearings," *Proceedings of the Fourth International Symposium on Magnetic Bearings,* ETH Zürich, Switzerland.

Schweitzer, G., Traxler, A., and Bleuler, H., 1994, *Active Magnetic Bearings,* Verlag der Fachvereine, ETH-Zürich, Switzerland.

A Modified Analysis of Counter Flow Wet Cooling Towers

H. T. A. El-Dessouky
eldessouky@kuc01.kuniv.edu.kw

A. Al-Haddad

F. Al-Juwayhel

College of Engineering & Petroleum,
Kuwait University,
P.O. Box 5969,
13060 Safat, Kuwait

The paper describes a theoretical investigation for the steady-state counter flow wet cooling tower with modified definitions for both the number of transfer units and the tower thermal effectiveness. The modified number of transfer units is dependent on both air and water heat capacity. The effectiveness is defined by the tower cooling range and the approach to equilibrium. A new expression relating the tower effectiveness to the modified number of transfer units and the capacity rate ratio has been developed. The model considered the resistance to heat transfer in the water film, the nonunity of the Lewis number, and the curvature of the saturated air enthalpy curve. A procedure for implementing the model in designing or rating cooling towers has been outlined and demonstrated through illustrative examples. The model compares very satisfactorily with other methods such as Logarithmic Mean Enthalpy Difference (LMED) and conventional effectiveness—NTU. Within the ranges used, the obtained results showed that substantial errors varied from +4.289 to −2.536 percent can occur in calculating the cooled water outlet temperature, and errors from +42.847 to −16.667 percent can occur in estimating the tower thermal characteristics.

Introduction

Cooling towers are used extensively wherever water is used as a cooling medium or process fluid. In many industrial locations, cold fresh water is too scarce to permit its unlimited use as a cooling medium. Thereupon, the continuous recooling and reuse of the limited fresh water is common and economical. The process of cooling water is accomplished by bringing the hot water into intimate contact with unsaturated air under such conditions that the air is humidified and the water brought approximately to the wet-bulb temperature of ambient air. This method is applicable only in those situations where the wet-bulb temperature of the air is less than the desired temperature of the cooled water. The most efficient apparatus in which this cooling process may be realized is the cooling tower. Another strong motivation for the increased use of cooling towers is the environmental protection secured/provided through the reduction of water withdrawals and the minimizing of thermal discharge. The problems associated with the disposal of large amounts of waste heat to the local atmosphere have caused growing concern.

Cooling towers are among the largest mass and heat transfer devices in common use. They are widely used in most industrial power generation units, space conditioning processes, and chemical, petrochemical, and petroleum industries to reject the escape of excess heat to the environment. In particular, steam power plants reject heat at approximately twice the rate at which electricity is generated. The advantages of cooling towers include the absence of heat transfer surfaces which can become foul or corroded, potentially higher rates of heat and mass transfer per unit volume combined with a relatively low pressure drop per unit heat transfer rate, and lower initial and operating costs. A wet cooling tower needs only about one-fifth the amount of contact surface for the given water-cooling effect that is needed by an exchanger (a dry tower) in which mass transfer is prevented by the use of an indirect-contact design.

Water cooling towers are sized and selected based on economic considerations and constraints imposed by system components. However, careful and accurate analysis of cooling towers must be available to ensure a precise cooling water temperature. This temperature constitutes a major consideration, having direct impact on the economics of the design. This is especially true today for the chemical and power industries. Chemical plants establish their cooling water temperature on the operating pressures of the condenser of distillation and evaporation operations and consequently, on equipment preceding them. In the power generation plants, the temperature of cooling water fixes the ultimate recovery of heat from the turbine and the discharge pressure of the heat engines. For these vital reasons, the accurate analysis of cooling towers and the temperature of the water made available by it, is of great importance.

The purpose of cooling tower analysis (also called rating) is to predict the temperature of water cooled in the tower for given values of design and operating variables. Cooling tower design has a somewhat different emphasis, namely, to specify the design parameters that will result in a desired change of water temperature for known operating conditions. The theoretical analysis of wet cooling towers has a long history, which has led to an excessively large number of publications. A complete review of the origin and early history of technical papers dealing with cooling tower theories is surveyed by Baker (1984). The main objective of early investigators of cooling tower theory grappled with the problem presented by the dualistic transfer of heat and mass. Baker (1984) reevaluated different suggestions of coupling both the heat and mass transfer in a single driving force. He reported that Coffey and Horne (1914) proposed and proved that cooling performance depends on the wet-bulb temperature of the ambient air, which is the lower limit of cooling. They obtained a single driving force based on vapor pressure at the wet-bulb temperature. On the other hand, Walker et al. (1937) used the air humidity as the sole driving force for the cooling process in cooling towers. London et al. (1940) used the enthalpy of the humid air-water vapor mixture as the actual driving force without explaining the derivation. They also recognized, for the first time, that a true heat balance must take water evaporation into account.

The most widely and universally adopted means used for cooling tower calculation is based on the theory developed in principle over 70 years ago by Merkel (1925). In this theory, the sensible heat transfer because of temperature difference and the latent heat flow due to evaporation, are lumped together and

Contributed by the Heat Transfer Division for publication in the JOURNAL OF HEAT TRANSFER. Manuscript received by the Heat Transfer Division June 18, 1996; revision received December 11, 1996; Keywords: Direct-Contact Heat Transfer, Heat Exchangers, Modeling & Scaling. Associate Technical Editor: T. J. Rabas.

a single driving force for total heat transfer and a unique transfer coefficient are used. The driving force is the difference between the enthalpy of the saturated air at the interface and the enthalpy of the humid air stream. The formulation and implementation of Merkel's theory in cooling tower design and rating is presented and discussed in detail throughout most unit operations and process heat transfer textbooks. Examples are Foust et al. (1980), Coulson and Richardson (1990), Treybal (1980), Kern (1950), and Hewitt et al. (1994). Extensive sets of curves for cooling tower design, based on Merkel's theory, have been prepared by the American Society of Heating, Refrigerating and Air Conditioning Engineers, ASHRAE, (1975). However, Merkel's theory is relatively simple and based on many assumptions. The basic postulations and approximations that are inherent in Merkel's equation are (1) the resistance for heat transfer in the liquid film is negligible, (2) the mass flow rate of water per unit of cross sectional area of the tower is constant (there is no water loss due to evaporation), (3) the specific heat of the air-stream mixture at constant pressure is the same as that of the dry air, and (4) the Lewis number for humid air is unity. It is necessary to emphasis that better analysis will lead to a better tower design and result in overall cost savings for the tower as well as trouble-free operation. Therefore, there have been many endeavors to improve upon Merkel's theory for the prediction of a cooling tower's performance. The obvious source of error considered by investigators is the common practice of ignoring the effects of water evaporation. Sutherland (1983) developed a computer program to compare the accurate analysis of mechanical draught counter flow cooling towers, including water loss by evaporation, with the approximate Merkel method. The results showed that a substantial underestimate of a tower volume, from 5 to 15 percent with the average value being as good as 8 percent, is obtained. Nahavandi et al. (1975) showed that ignoring the evaporation losses introduces an error in the Merkel results which is not conservative, and may reach 12 percent depending on design conditions. On the other hand, Baker (1984) cited that the effect of water evaporation is relatively small and varies with the operating conditions and gives a value for number of transfer units (NTU) that is 1.34 percent too low. The effect of water evaporation on the cooling tower performance has also been studied by Threlkeld (1970), Webb (1984), and Yadigaroglie and Pastor (1974).

Nonetheless, contemplation of the effects of different Merkel approximations preclude the analytical solutions. In this case, the best alternative is often one that uses numerical techniques. The most common way of performing the numerical solution is subdividing the tower into a number of small regions and writing the mass, heat, and rate equations for each node. The numerical accuracy of calculations depends strongly on the number of designated nodel points. The large number of points make the use of a digital computer inevitable.

Another source of errors which has been examined is the resistance to heat transfer in the water film and the nonunity values of the Lewis number. Raghavan (1991), Stevens et al. (1989), and Jefferson (1972) introduced an adjustment coefficient to account for the effect of the actual value of the Lewis number. Sadasivam and Balakrishnan (1995) initiated a new definition of air enthalpy, thereby obviating the need to invoke the Lewis relation. Yadigaroglue and Pastor (1974) proved that the approximations inherent in the Merkel equation contribute to the overall error. Fortunately, these errors tend to cancel each other. Webb (1988) stated that none of the available analysis

Nomenclature

a = effective surface area for heat and mass transfer per unit volume of tower, m^2/m^3
a_h = effective surface area for heat transfer per unit volume of tower, m^2/m^3
a_m = effective surface area for mass transfer per unit volume of tower, m^2/m^3
A = cooling tower approach ($T_{w2} - T_{wb2}$), K
Cp_a = specific heat of dry air at constant pressure, J/(kgK)
Cp_m = specific heat of moist air at constant pressure, J/(kgK)
Cp_w = specific heat of water at constant pressure, J/(kgK)
Cp_v = specific heat of water vapor at constant pressure, J/(kgK)
C_r = capacity rate ratio (fM_a/CpM_w), dimensionless
E = slope of tie line ($-h/K_y$), J/(kgK)
F = correction factor (ϵ'/ϵ) defined in Eq. (43), dimensionless
F_1 = correction factor defined in Eq. (15), dimensionless
F_2 = correction factor defined in Eq. (19), dimensionless
f = slope of saturated air enthalpy curve versus temperature at the average water temperature of the tower range, J/(kgK)
$\bar{f}$ = slope of saturated air enthalpy curve versus temperature at the average water temperature of the tower range approach, J/(kgK)
h = convective heat transfer coefficient, $W/(m^2K)$
H_a = specific enthalpy of moist air, J/kg of dry air
H_d = specific enthalpy of dry air, J/kg
H_i^* = specific enthalpy of saturated air at the interface temperature, J/kg
H_v = specific enthalpy of vapor phase, J/kg
$\bar{H}_i$ = specific enthalpy of water vapor at air saturation temperature T_i, J/kg
K_y = mass transfer coefficient, $kg/(m^2S)$
Le = convective Lewis number for moist air ($h/Ky\ Cpm$), dimensionless
M = modified number of transfer units, dimensionless as defined by Eq. (36)
M_a = mass flow rate of humid air, kg/S
M_d = mass flow rate of dry air, kg/S
$M_{\min}$ = minimum mass flow rate, kg/S
M_w = mass flow rate of water, kg/S
NTU = conventional number of transfer units, dimensionless
q = rate of heat transfer, W
q_s = rate of sensible heat transfer, W
q_l = rate of latent heat transfer, W
q_{act} = actual rate of heat exchanged between air and water, W
q_{max} = maximum possible amount of heat which can be transferred between air and water, W
Pr = Prandtl number, dimensionless
R = temperature range ($T_{w1} - T_{w2}$), K
Sc = Schmidt number, dimensionless
T = temperature, K
V = volume of cooling tower, m^3
Z = height of packing in the cooling tower, m

Subscripts

1 = top of tower
2 = bottom of tower
a = dry air
i = interface
o = reference state
w = water
wb = wet-bulb

Greek Symbols

λ = latent heat of evaporation, J/kg
ϵ = true tower effectiveness, defined by Eq. (38), dimensionless
$\bar{\epsilon}$ = apparent tower effectiveness defined by Eq. (42), dimensionless
η = tower thermal performance ($A/(A + R)$), dimensionless
ω = moisture content of humid air (kg of water vapor/kg of dry air), dimensionless

is totally satisfactory in (1) calculating the error of the Merkel analysis, and/or (2) defining the operating conditions within which the greatest errors exist. Accordingly, he presented a more precise method to assess the errors associated with the approximate Merkel method. He found that the approximations of unity of the Lewis number and the specific heat of the air-water vapor mixture are the same as that of the dry air, affecting the driving potential by a very small amount (−1.5 to 0.2 percent), and the neglecting of water film resistance probably results in a greater error. He pointed out that a more complete, systematic analysis for a range of practical interest would be of value.

A simple compution method is the effectiveness-number of transfer units (ϵ-NTU) approach. The ϵ-NTU method offers many advantages for the analysis of design cases in which a comparison between various types of packings must be made for the purpose of selecting the fillings best suited to accomplish a particular objective. One of the great virtues of this method is that you can develop a feel for the cooling tower performance, owing to the thermodynamic importance of the dimensionless groups appearing in the analysis. The number of transfer units concept had been proposed earlier by Sherwood (1937) in connection with the chemical engineering problems of absorption and extraction. London et al. (1940) introduced definitions of ϵ and NTU to use in plotting cooling tower test data. Moffatt (1966) is apparently the first to derive the ϵ-NTU equation for a counter-current cooling tower. Jaber and Webb (1989) mentioned that the Moffatt method applies only if the water is the minimum capacity rate fluid, but fails if it is not; and the rash of NTU definitions reported in research literature has contributed little, but a myriad of conflicting definitions. Consequently, they redefined the NTU to be based only on the minimum flow capacity fluid and asserted that their definition is the only correct and consistent one. The proposed definitions for both ϵ and NTU are in precise agreement with those widely used for heat exchanger design. However, the definition of tower effectiveness may cause some confusion, as it will be shown later. Additionally, it is necessary to keep track of the minimum flow capacity fluid (C_{min}). This is not always precisely settled because (1) cooling towers are specified to operate over a wide range of water rates, air quantities, air ambient conditions and heat loads, (2) the true characteristics can only be deduced from actual tests, and (3) types and/or nature of packings can be varied for a given cooling tower during its operating lifetime (El-Dessouky, 1996).

The main objectives of this study are as follows:

1 To develop a new relationship for designing or analyzing the counter-current wet cooling towers by applying the ϵ-NTU method. Two new definitions for both the number of transfer units and the cooling tower effectiveness have been proposed. The modified number of transfer units is dependent on both the air and the water heat capacity. The effectiveness is defined by the tower cooling range and the approach to equilibrium.

2 To determine the magnitude of errors associated with the possible approximations inherent in the Merkel equation when the modified ϵ-NTU approach is applied for cooling tower analysis. As far as the author is aware, however, no detailed study has been made to contemplate these errors in the ϵ-NTU method. The problems coupled with the curvature of the saturated air-water vapor mixture enthalpy are also treated.

Mathematical Formulation

The analysis presented here employs the following principle assumptions:

- the cooling tower is of wet counter-current type and operates under steady-state conditions

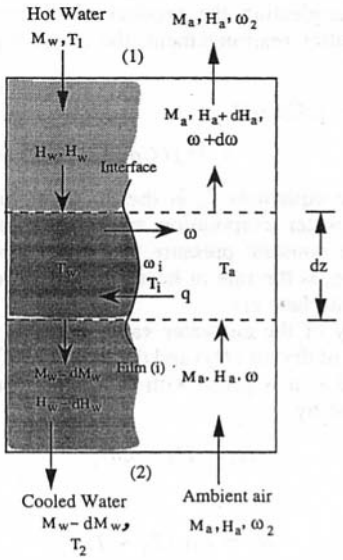

Fig. 1 A schematic diagram of a wet counter flow cooling tower

- miscellaneous thermal loads such as make-up water additions, pump heat gain, and the net heat exchange with the ambient surroundings are negligible
- uniform air and water flow rates over the tower cross sectional area
- the thermodynamic properties of the upward air flow and downward water flow vary vertically, but are constant across any cross section inside the tower
- the specific heats at constant pressure of the two fluids are constant throughout the cooling tower
- the heat and mass transfer coefficients are invariable inside the fill region

A schematic diagram of a wet counter-current cooling tower is shown in Fig. 1. Here, Points 1 and 2 refer to the top and the bottom of the tower, respectively. Consider a differential segment, dV, with a vertical height of dZ. Postulating that all the water evaporated flows to the air-water vapor mixture (no water entrainment with air stream), a mass balance of the water element over the control volume and practicing the third assumption in the preceding section, gives

$$dM_w = -M_d d\omega = -M_a d\omega \tag{1}$$

where M_w, M_d and M_a are the mass flow rate of water, and dry and humid air respectively, and ω is the moisture content of humid air.

A heat balance on the same control volume produces

$$q_w = M_w Cp_w (T_w - T_o) - (M_w - dM_w) Cp_w (T_w - dT_w - T_o) \tag{2}$$

with T_w as the water temperature and q_w as the rate of heat flow from the water stream to the air-water interface (i), and T_o as the reference temperature. Nevertheless, the product of the differential quantities ($dM_w dT_w$) is small compared with the other terms in the above equation. Neglecting this term yields

$$q_w = M_w Cp_w dT_w + Cp_w (T_w - T_o) dM_w. \tag{3}$$

On the other hand, the heat balance of the air stream can be presented by the following equation:

$$q_a = M_a Cp_a (T_a - T_o) + M_d \omega Cp_v (T_a - T_o) + M_a \omega \lambda_i - M_a Cp_a (T_a + dT_a - T_o) - M_a (\omega + d\omega) \times Cp_v (T_a + dT_a - T_o) - M_a (\omega + d\omega) \lambda_i. \tag{4}$$

As before, neglecting the product of differential amounts ($dT_a d\omega$) and after rearrangement, the above equation can be expressed as

$$q_a = M_a(Cp_a + \omega Cp_v)dT_a + M_a[(Cp_v(T_a - T_o) + \lambda_i]d\omega. \quad (5)$$

In the above equations T_a is the air temperature, λ_i is the latent heat of water evaporation at T_i, Cp_v, and Cp_a are the specific heat at constant pressure for water vapor and dry air severally, and q_a is the rate of heat flow from the air stream to the air-water interface (i).

The enthalpy of the air-water vapor mixture H_a is the sum of the enthalpy of dry air (H_d) and the enthalpy of the associated water vapor (H_v). It is given with sufficient accuracy over the range of interest by

$$H_a = H_d + \omega H_v \quad (6)$$

with,

$$H_d = Cp_a(T_a - T_o) \quad (7)$$

and

$$H_v = Cp_v(T_a - T_o) + \lambda_i. \quad (8)$$

Substituting Eq. 8 in Eq. 5, we obtain

$$q_a = M_a dH_a. \quad (9)$$

Equating Eqs. 3 and 9 provides

$$M_a dH_a = M_w Cp_w dT_w + Cp_w(T_w - T_o)dM_w. \quad (10)$$

This equation establishes the relationship between the rate of change in the humid air enthalpy with both the variation in the water temperature and the rate of water evaporation.

Heat is transferred from water to air by two different mechanisms according to the nature of the available driving force. The first one is the sensible heat transfer q_s, which is due to the temperature difference and can be expressed as

$$q_s = h(T_i - T_a)a_h S dZ \quad (11)$$

where h is the heat transfer coefficient from the liquid film/air film interface to the air stream, a_h is the effective surface area for heat transfer per unit volume of tower and S is the cross sectional area of the air flow.

The second mechanism for thermal energy transfer is the latent heat transfer because of water evaporation q_l. Webb (1990) reported that the driving force for mass transfer can be presented by six different ways. These are: partial pressure, mole fraction, mass fraction, molar density, mass density, and specific humidity of air. Accordingly, there are six different definitions for the mass transfer coefficients. The six potentials are typically used by different researchers in analyzing the cooling towers. This causes substantial confusion. In this work, we adopted the nomenclature system proposed by Webb (1990). The key advantage of this system is that the driving potential associated with the mass transfer coefficient is clearly indicated by the definition of the mass transfer coefficient itself. Thus, the rate of heat transfer due to water evaporation q_l is presented as follows:

$$q_l = M_a \bar{H}_i d\omega = K_y a_m S(\omega_i - \omega_a)\bar{H}_i dZ \quad (12)$$

where K_y is the mass transfer coefficient based on mass fraction, a_m is the specific surface area available for the mass transfer per unit volume, and $\bar{H}_i$ is the enthalpy of water vapor at air saturation temperature T_i. The above equation has been developed by many investigators (Sutherland, 1983; Maclaine-Cross and Banks, 1981). However, some of them used faulty λ_i instead of $\bar{H}_i$.

Equation (12) can be rearranged to the following form:

$$\int_2^1 \frac{d\omega}{\omega_i - \omega_a} = \frac{K_y a_m SZ}{M_a}. \quad (13)$$

However, the left-hand side term in this equation cannot be integrated directly since the conditions at the interface (i) are not necessarily constant; nor can they be expressed directly in terms of the corresponding property in the gas or liquid streams (Coulson and Richardson, 1990).

Adding Eqs. (11) to (12) and substituting the value of q_a from Eq. (9) gives

$$M_a dH_a = ha_h S(T_i - T_a)dZ + K_y a_m S(\omega_i - \omega_a)\bar{H}_i dZ. \quad (14)$$

The sensible heat transfer between the water and the air-vapor mixture is mainly due to temperature difference. However, there is also a concentration gradient between the two phases. This will effect the heat transfer rate because of (i) it is a direct occasion of molecular motion, (ii) it may cause bulk motion of the fluid, and (iii) it influences the equilibrium conditions at the liquid-vapor interface. To account for the effect of mass transfer on the rate of heat transfer Webb (1984) multiplied the first term in the right-hand side term of Eq. (14) by a correction factor F_1. This coefficient is defined by Collier (1981) as follows:

$$F_1 = \frac{a}{1 - e^{-a}} \quad (15)$$

where

$$a = \frac{Cp_m K_y(\omega_i - \omega_a)}{h} \quad (16)$$

and

$$Cp_m = Cp_a + \omega Cp_v \quad (17)$$

where Cp_m is the specific heat at constant pressure for the air-water vapor mixture.

It should be stressed, that the use of this correction factor is valid only if the idea of the analogy between the heat and mass transfer is not employed in the rest of the analysis. This is because the analogy concept fails if there are additional mechanisms of transfer present in one process but not associated with the other process. Also, the heat flow due to molecular diffusion is usually of very small contribution if fluxes by other mechanisms are present (Bordkey and Hershey, 1988), the numerical value of F_1 for normal conditions of a cooling tower is nearly unity, and most of the references used in their analysis $F_1 = 1$. Thus, we have neglected this effect in our analysis.

Assuming that the available interfacial area for heat transfer a_h is the same as that of mass transfer a_m, this will be true only at such high water flow rates that the tower packing is thoroughly irrigated. Now, Eq. (14) can be rearranged to produce

$$\frac{M_a dH_a}{K_y a S dZ} = \frac{h}{K_y Cp_m} Cp_m(T_i - T_a) + \bar{H}_i(\omega_i - \omega_a). \quad (18)$$

Threlkeld (1970) produced the following relationship from the analogy between heat and mass transfer:

$$\frac{h}{K_y Cp_m} = \left(\frac{\mathrm{Sc}}{\mathrm{Pr}}\right)^{2/3} = (\mathrm{Le})^{2/3} = F_2 \quad (19)$$

where Sc, Pr and, Le are Schmidt, Prandtl, and Lewis dimensionless numbers respectively, and F_2 is constant. The exponent, $\frac{2}{3}$, is based on experimental evidence. In this study we adopted the definition of the Lewis number as the ratio between the Schmidt and Prandtl numbers. This definition was proposed by Webb (1984). The Lewis relationship is necessary to combine the transfer of mass and sensible heat into an overall coefficient based on the enthalpy difference as the driving force.

Equation (19) can be used to calculate the heat transfer coefficient h given the mass transfer coefficient K_y, or vice versa.

Equation (18) can be written as

$$\frac{dH_a}{dZ}\frac{M_a}{K_y aS} = F_2 Cp_m(T_i - T_a) + \bar{H}_i(\omega_i - \omega_a). \quad (20)$$

Assuming Cp_a and Cp_v are constant, and inserting the value of Cp_m from Eq. (17) and $\bar{H}_i = \lambda_i + Cp_v(T_a - T_i)$ from Eq. (20), and reorganizing, it can be shown that

$$\frac{dH_a}{dZ}\frac{M_a}{k_y aS} = [F_2 Cp_a T_i + F_2\omega_i Cp_v T_i + F_2\omega_i\lambda_i]$$
$$- [F_2 Cp_a T_a + F_2\omega_a Cp_v T_a + \omega_a\lambda_i]$$
$$+ (1 - F_2)(\omega_i - \omega_a)\lambda_i + Cp_v(T_a - T_i)(\omega_i - \omega_a). \quad (21)$$

The integration of the above equation between the inlet and outlet points of the cooling tower will give the exact solution for the cooling towers. This equation must be numerically integrated. However, it is worth noting that the exact solution is not always used in practice because of the following points:

1 The water film/air film interface heat transfer coefficient h used in evaluating the F_2 factor is typically unknown.
2 The numerical integration suffers from the following:

(*i*) The finite-difference techniques employed require a very large number of segments through the column to obtain reasonably acceptable results. Thus, analysis cannot be handled with hand-held calculators.
(*ii*) Being iterative procedures, the use of a computer is mandatory.
(*iii*) There is some scatter in the numerical results, mainly due to the relatively loose convergence criterion used for the numerical calculations, and to the approximate nature of the finite-difference method of solution.

The following approximations are usually implemented to facilitate the analytical calculation:

1 Neglect the superheating of steam associated with the humid air or simply omit the last part on the right-hand side of Eq. 21. Also ignore the term $(1 - F_2)(\omega_i - \omega_a)\lambda_i$. Actually, the numerical value of these terms is very small compared to the amounts of the other two preceding terms.
2 The constant water flow rate, or the water evaporated into the air stream, and that lost by entrainment, are negligible. Baker and Shryock (1960) showed that the error associated with ignoring the effects of evaporation appears to be quite small. Cheremisinoff (1986) reported that for normal operations, evaporation losses are generally less than 2 percent of the circulating water; therefore, a good estimate can be made by assuming constant water flow rate.

The employment of approximation number 2 ($dM_w = 0$) in Eq. (10) becomes

$$M_a dH_a = M_w Cp_w dT_w \quad (22)$$

or

$$\frac{dH_a}{dT_w} = \frac{M_w Cp_w}{M_a}. \quad (23)$$

Equation (23) is the slope of the straight cooling tower operating line shown in Fig. 2. The operating line passes through the points representing the terminal conditions for the two fluids.

Implementing the first approximation in Eq. (21) and replacing the value of H_a from Eq. (6), Eq. (21) can be written in the following form:

$$\frac{M_a}{k_y aS}\frac{dH_a}{dZ} = (H_i^* - H_a)F_2 \quad (24)$$

where H_i^* is the enthalpy of the saturated air-water vapor mixture at the interface temperature Ti.

Webb (1984) reported that the use of $F_2 = 0.87$ is satisfactory for practical ranges of interest. Sutherland (1983), Threlkeld (1970), and ASHRAE (1975) set F_2 at a value of 0.9, while Stevens et al. (1989) used F_2 with a value of 1.129. Rearranging Eq. (24) produces

$$\text{NTU} = \frac{F_2 k_y aSZ}{M_a} = \int_2^1 \frac{dH_a}{H_i^* - H_a} \quad (25)$$

where NTU is called, conventionally, the number of transfer units and sometimes referred to as the packing function. The right-hand side of the above equation is often referred to as the Merkel integral. The magnitude of NTU is a measure of the difficulty or ease of the cooling process and is determined only by the process conditions imposed upon the tower and not the performance of the tower itself. The above equation is often integrated numerically by Tchebycheff's method (Bagnoli et al. 1984) or by the British standard quadrature method (BS 4485) (Hewitt et al., 1994). Both methods assume that $(H_i^* - H_a)$ is constant.

Equation 25 is not self-sufficient and is not subject to direct mathematical solution (Anon, 1983; Webb, 1984). Two additional equations are required to evaluate the local value of $H_i^* - H_a$ along the air flow path. The first one is an energy balance that defines the local humid air enthalpy H_a as a function of the specified water temperature T_w. The second equation relates the enthalpy of saturated air H_i^* at a given water temperature. The first required relationship can be developed by integrating Eq. (23) between the bottom and the top of the tower (points 2 and 1 in Fig. 1). Thus

$$H_a = H_{a_2} + \frac{M_w Cp}{M_a}(T_w - T_{w_2}) \quad (26)$$

where H_{a_2} is the enthalpy of unsaturated air flowing to the tower and H_a is the enthalpy of air at any point inside the tower.

The second required relationship is the equilibrium curve presented in the following equation:

$$H_i^* = 35.72 - 1.084T_i + 0.10765T_i^2. \quad (27)$$

Equation (27) was obtained by fitting the tabulated thermodynamic properties of the saturated air-water vapor mixture. In the above equation H^* in kJ/kg and T_i are in °C. The equation is valid only for the temperature range 10–50°C.

A widely used approximation is the use of local water temperature T_w instead of the interface water temperature T_i in estimating H_i^*. This will overpredict the value of H_i^* and consequently the driving force $H_i^* - H_a$, because T_w is always higher than T_i. Webb (1984) reported that T_w is nearly equal to $T_i + 0.5$.

Figure 3 shows both the enthalpy of the saturated air-water vapor mixture and the tower operating line as functions of the water temperature. Considering that the short distance between H_w^* and H_i^* on the saturation curve is a straight line, the following simple relationships can be easily deduced:

$$H_w^* - H_a = (H_w^* - H_i^*) + E(T_w - T_i) \quad (28)$$

where H_w^* and H_i^* are the enthalpy of the saturated humid air at water and film temperatures (T_w and T_i), respectively, H_a is the enthalpy of the unsaturated air-water vapor mixture at water temperature T_w, and E is the slope of the tie line and it is constant for a given cooling tower. This slope is defined as

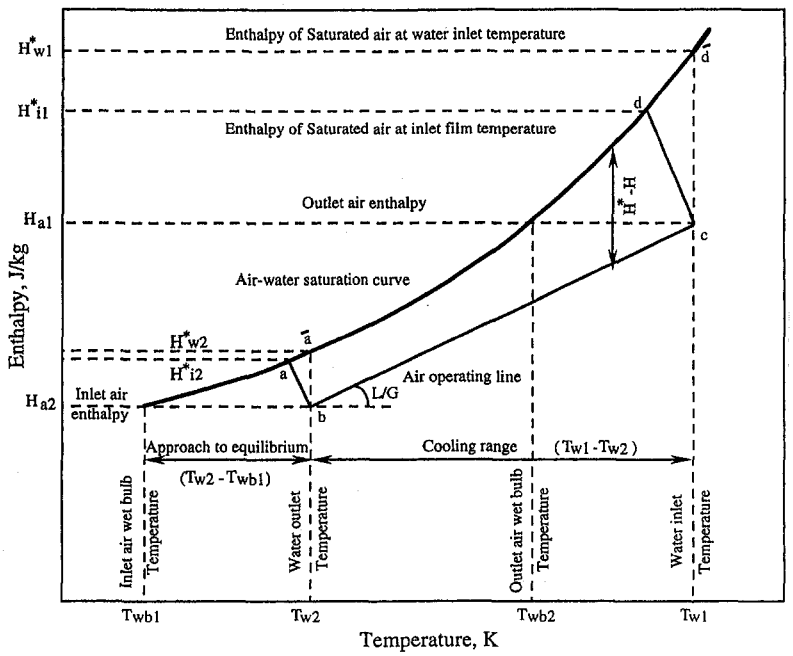

Fig. 2 Definition of the parameters used in presenting the thermal performance of wet cooling towers

$$E = -\frac{h}{K_y}. \tag{29}$$

Substituting the values of H_w^* and H_i^* from Eq. (27), neglecting the small term $(0.10765(T_w - T_i))$, and rearranging gives

$$T_i = \frac{(H_w^* - H_a) - T_w(E - 1.084)}{1.084 - E}. \tag{30}$$

Equation (30) relates the film temperature T_i to the water temperature T_w, the difference between $(H_w^* - H_a)$ and the slope of the tie line at any point inside the cooling tower. The standard value of E as supported by Webb (1988) is 15. However, he used $E = 45$ in his analysis. On the other hand, Baker and Shryock (1961) found that $E = 11.1$ yields the best results.

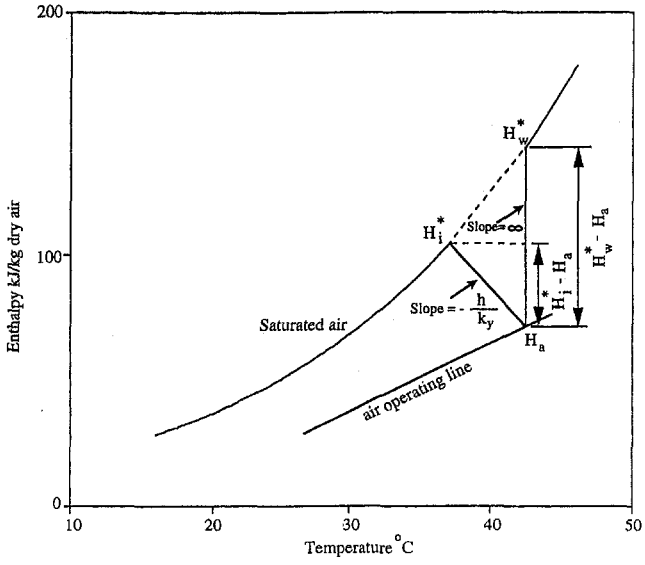

Fig. 3 General operating diagram for cooling tower showing the true and apparent enthalpies of saturated air-water vapor mixture

Differentiating Eq. (27) and using the previous assumption of a straight line relationship in the short distance between H_w^* and H_i^* or $dT_w = dT_i$, we have

$$\frac{dH_i^*}{dT_i} = \frac{dH_i^*}{dT_w} = 0.2153T_i - 1.084 = f. \tag{31}$$

The right-hand side of the above Eq. (f) is the slope of the H_w^* versus the T_w curve. Substituting the value of dT_w from Eq. (22) in Eq. (31) gives

$$dH_i^* = q(f/M_w Cp_w). \tag{32}$$

From Eq. (9) we have

$$dH_a = q/M_a. \tag{33}$$

Using $dH_i^* - dH_a = d(H_i^* - H_a)$ and substituting the values of dH_i^* and dH_a from Eqs. (32) and (33) produces

$$d(H_i^* - H_a) = q\left(\frac{f}{M_w Cp_w} - \frac{1}{M_a}\right). \tag{34}$$

Substituting the value of $q = M_a dH_a$ from Eq. (24) in the above equation and rearranging gives

$$\frac{d(H_i^* - H_a)}{H_i^* - H_a} = F_2 K_y aS\left(\frac{f}{M_w Cp_w} - \frac{1}{M_a}\right) dZ. \tag{35}$$

Upon integration of the above equation over the entire length of the packing in the cooling tower from the bottom to the top, we have

$$\ln \frac{(H_i^* - H_a)_1}{(H_i^* - H_a)_2} = F_2 K_y aSZ\left[\frac{f}{M_w Cp_w} - \frac{1}{M_a}\right]$$

$$= F_2 \frac{K_y aSZ}{M_a}[C_r - 1] = M \tag{36}$$

where M is the proposed modified number of transfer units

and $C_r = fM_a/M_wCp_w$ is the capacity rate ratio. It is worth emphasizing the following points:

1 The modified number of transfer units (M) depends on both M_a and M_w and not on either M_a or M_w alone. Thus, there is no need to keep track of the maximum or the minimum flow rate.
2 The numerical value of M may be either positive or negative depending on the capacity rate ratio C_r. When C_r is a fraction, the value of M is negative, while it is positive when C_r is higher than 1. The value of C_r is determined according to the required degree of cooling and the selected depth and type of packing. This ratio usually ranges from 0.5 to 2.5 in industrial cooling towers.
3 The capacity rate ratio depends on both the air and water mass flow rates, and also on the cooling tower range. This is because the rate of change of the enthalpy of saturated humid air with respect to temperature (f) is not constant but depends on T_i. In Eq. (31) the value of $f = dH_i^*/dT_i$ is 8.6045 at $T_i = 45$°C, while it is 2.1455 at $T_i = 15$ or f at 45°C, is about four times its magnitude at 15°C.
4 The area bounded by (a, b, c, d) in Fig. 2 is proportional to the reciprocal of the value of the modified number of transfer units (M).
5 There are three cases of interest: (i) when C_r is infinite or M_a is too large with respect to M_w, thus, there is no increase in air enthalpy or when the operating line is horizontal (Eq. 26), M will be minimum; (ii) when C_r is zero or M_a is very small compared to M_w, the driving force is zero and M becomes infinite; and (iii) when $C_r = 1$, it follows from Eq. (36) that $M = 0$, and the previous analysis produces an indeterminate result.

Another important dimensionless group in the analysis of a cooling tower is the tower effectiveness (ϵ) which is defined as

$$\epsilon = \frac{q_{\text{act}}}{q_{\max}}. \tag{38}$$

where q_{act} and $q_{\max}$ are the actual and the maximum possible (theoretical) amount of heat which can be exchanged between the air and the water, respectively. In most research literature the maximum rate of heat transfer is defined as the difference between the enthalpy of saturated air-water vapor mixture leaving the tower, H_{i1}^*, and the enthalpy of air flowing to the bottom of the tower, H_{a_2}, times the minimum fluid flow rate ($q_{\max} = M_{\min}(H_{i_1}^* - H_{a_2})$). In a situation where air flow rate (M_a) is the minimum mass flow rate, the dry and wet-bulb temperatures of the humid air are equal at the top of the tower. This condition is satisfied when the tower operating line intersects the humid air saturation curve at the top of the tower. In this status, the driving force for mass and heat transfer is zero. Nonetheless, the point of zero driving force may occur at any intermediate point in the tower and not necessarily at the top of the tower. The point at which the tower operating line crosscuts the saturation enthalpy curve of the humid air depends on the air inlet conditions and the water to air mass flow ratio (the slope of the operations line). Theoretically, the operating line can cut the saturation curve at more than one single point because of the curvature of the saturation curve. Furthermore, a common misconception is that cooling towers cannot function when the air becomes saturated at any interpose point inside the tower. Nevertheless, saturated air can aquire sensible heat from the hot water in the top section of the tower, thereby increasing its dry-bulb temperature so that it is no longer saturated. Consequently, extra water will evaporate continuously into the air phase. Thus, the tower operating line will not remain a straight line.

The previous discussion shows clearly that the use of $M_a(H_{i_1}^* - H_{a_2})$ as the maximum possible heat flow is not always accurate and may lead in same cases to serious errors and confusion. In order to avoid these possible errors and confusion, it is preferably to define the maximum heat exchange between the two streams occurring when the cooling tower approach becomes zero. The approach in a cooling tower is the difference between the water-exit temperature and the wet-bulb temperature of the air entering the tower. Basically, it is an index or gauge of how difficult the cooling operation is. This is a strong function of ambient air conditions and is independent from the air to water mass flow ratio, thus,

$$q_{\text{act}} = M_w(H_{w_1} - H_{w_2}) \tag{39}$$

$$q_{\max} = M_w(H_{w_1} - H_{a_2}) \tag{40}$$

and

$$\epsilon = \frac{H_{w_1} - H_{w_2}}{H_{w_1} - H_{a_2}} = \frac{fR}{\bar{f}(R + A)} = \frac{f(T_{w_1} - T_{w_2})}{\bar{f}(T_{w_1} - T_{wb_1})} \tag{41}$$

where f is the slope of the saturated air enthalpy curve at the average temperature of the tower range ($T = 0.5\,(T_{w1} + T_{w2})$), while $\bar{f}$ is the slope of the saturated air enthalpy curve at the average temperature of the tower range plus the approach ($T = 0.5(T_{w1} + T_{wb1})$). On the other hand, A and R are the cooling tower approach ($T_{w2} - T_{wb1}$) and range ($T_{w1} - T_{w2}$), respectively.

It is worth noting that according to the above equations, the cooling effectiveness can be defined by both the tower cooling range and the approach. The two terms are widely used in expressing the cooling tower performance. Majumdar et al. (1983) defined the thermal effectiveness, ($\eta = A/(A + R)$). The cooling tower effectiveness (ϵ), prescribed in Eq. (41), is the true effectiveness and differs from apparent effectiveness $\bar{\epsilon}$ defined as

$$\bar{\epsilon} = \frac{H_{i_1} - H_{i_2}}{H_{i_1} - H_{a_2}}. \tag{42}$$

The true and the apparent tower effectiveness can be related to each other by the following correction factor, F:

$$F = \left(\frac{H_{i_1} - H_{i_2}}{H_{i_1} - H_{a_1}}\right) \Big/ \left(\frac{H_{w_1} - H_{w_2}}{H_{w_1} - H_{a_2}}\right). \tag{43}$$

It is worth noting that the correction coefficient (F) is a measure of the resistance for heat transfer in the liquid film and its value is not constant, but depends on the slope of the tie line (E). When $F = 1$, it automatically implies that the liquid film does not offer any resistance to heat transfer and $\epsilon = \bar{\epsilon}$.

Using the definitions of the tower effectiveness as defined in Eqs. (41, 42, and 43), and the modified number of transfer units in Eq. (36), the following expression can be developed:

$$F\epsilon = \bar{\epsilon} = \frac{C_r[1 - \text{Exp}(-M)]}{C_r - \text{Exp}(-M)}. \tag{44}$$

Equation (44) relates three important dimensionless groups widely used in defining the cooling tower performance and have a thermodynamic significance. The tower effectiveness ϵ is an efficiency factor and its value is limited, even with infinite tower size. It is the ratio between the tower cooling range and the range plus the wet-bulb temperature approach. The cooling tower range depends on process characteristics and requirements, as well as the type of cooling tower under consideration. The zero wet-bulb temperature approach represents the limit to which the discharge water temperature can fall in a cooling tower where adiabatic equilibrium exits between the water and inlet air. Commercial manufacturers and users of cooling towers often specify the tower thermal performance by giving the maximum number of degrees Kelvin that the exit water stream should

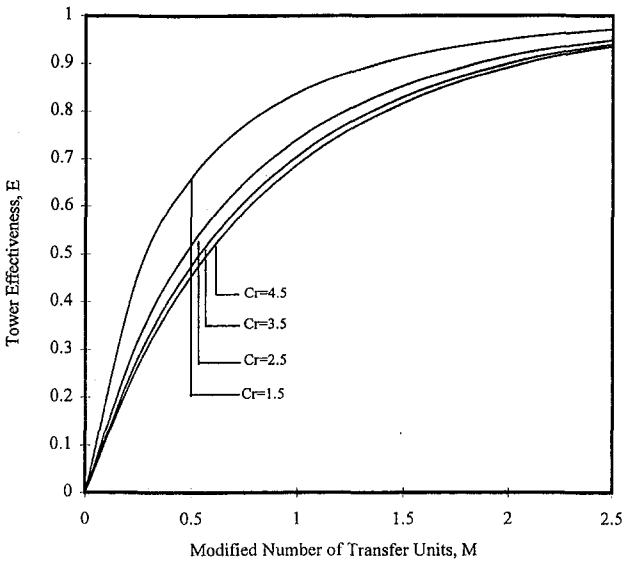

Fig. 4 Cooling tower effectiveness as a function of positive values of modified number of transfer units (M) and various values of capacity rate ratio (C_r)

exceed the wet-bulb temperature of the air that is available in a particular locality. Also, the tower range and wet-bulb approach are established by the hot water inlet temperature T_{w_1}, the cooled water outlet temperature T_{w_2}, and the incoming air wet-bulb temperature T_{wb_1}. These are the only three temperatures used to stipulate the forced draft cooling towers. The capacity rate ratio C_r is simply a ratio of air thermal capacity to water thermal capacity. It is necessary to observe that Eq. (44) is not similar to the equation developed by Webb (1989) for cooling tower design or by Sadasivan and Balakrishnan (1992), and Stevens et al. (1989) for designing packed bed liquid desiccant dehumidifiers, and also differs from those used for heat exchanger design (Shouman and El-Dessouky, 1991). Figures (4) and (5) show the relationships between ϵ and M for different values of C_r.

Calculation Procedure

The effectiveness-modified number of transfer units (ϵ-M) relationship developed in Eq. (44) can be used to either design or rate counter-current wet cooling towers. A classical problem of designing a cooling tower is the calculation of the required tower height Z, given the type of packing, the wet bulb temperature of the air entering the tower T_{wb_2}, the cooling range ($R = T_{w_1} - T_{w_2}$), the approach to wet-bulb temperature ($A = T_{w_2} - T_{wb_2}$), and the dry air to water specific mass flow rate ratio (M_a/M_w). The procedure for utilizing this method is outlined as follows:

1 Find the values of mass and heat transfer coefficients (k_y and h) from the available literature for the specified type of packing and the prevailing operating conditions. Then, calculate the slope of the tie line $E = -(h/k_y)$ (Eq. 29). Also determine the magnitude of F_2.
2 Determine the enthalpies of air flowing through the tower H_{a_2}, and of saturated air-water vapor mixtures at the top and the bottom of the tower ($H^*_{w_1}$ and $H^*_{w_2}$) using Eq. 27 with T_i equal to, severally, the wet-bulb temperature of air entering the tower T_{wb_2}, the temperature of hot water flowing to the tower top T_{w_1}, and that of the cooled water flowing out from the tower T_{w_2}.
3 Find the enthalpy of humid air flowing out of the tower H_{a_1} (Eq. 26).
4 Figure the corresponding saturated film temperatures T_{i_1} and T_{i_2} (Eq. 30).
5 Calculate the slope of the saturation curve for both the range f and the range plus the wet-bulb approach ($\bar{f}$) (Eq. 31).
6 Find the effectiveness correction factor (F) (Eq. 43).
7 Compute the cooling tower effectiveness ϵ (Eq. 41).
8 Figure the capacity rate ratio (Eq. 37).
9 Calculate (Eq. 44) or read from either Fig. 4 or Fig. 5 the modified number of transfer units M, based on the values of ϵ and C_r.
10 Determine the required height from the following relationship:

$$Z = \frac{MM_a}{k_y aS(C_r - 1)F_2}. \tag{45}$$

On the other hand, in a typical rating problem giving the tower height Z, type of packing, hot water inlet temperature T_{w_1}, wet-bulb temperature of air entering the tower T_{wb_2}, and capacity rate ratio (M_a/M_w), it is required to determine the exit cooled water temperature T_{w_2}. The rating problems are solved through iterative calculation. The steps are:

1 Assume a value for the cooled water outlet temperature T_{w_2}.
2 Follow exactly the procedure outlined above in the design problem and calculate the tower height.
3 If the estimated tower height is not essentially equal to the specified height, reassume the cooled water outlet temperature and repeat item 2 until the calculated height becomes equal to the given height.

Illustrative Example

The purpose of this example is to present the implementation of the model developed in the preceding sections and compare the results obtained with the data available in the literature. Therefore, we will consider the same conditions given by Jaber and Webb (1989). Hot water enters at a temperature of 35°C (T_{w_1}) and is cooled to 30°C (T_{w_2}). The wet-bulb temperature of air entering is 25°C (T_{wb_1}). The mass flow rate ratio $M_a/M_w = 1.0$.

The calculated tower characteristics (T.C. = $k_y aV/M_a$) and the combined errors for different values of E and F_2 are depicted in Table 1. As can be seen in the Table, the results are very

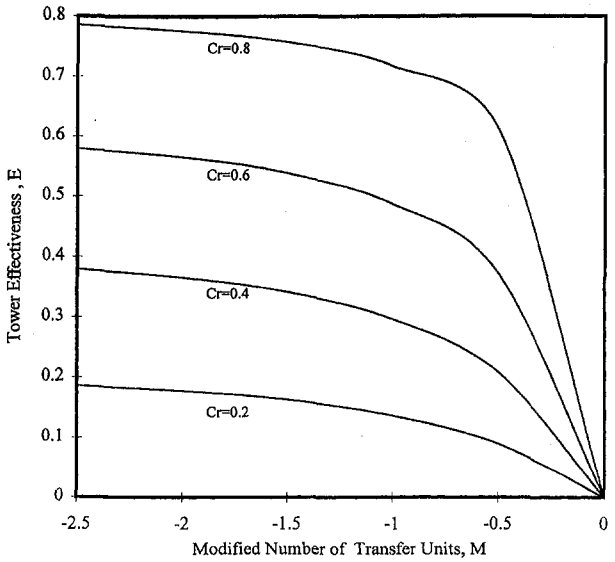

Fig. 5 Cooling tower effectiveness as a function of negative values of modified number of transfer units (M) and various values of capacity rate ratio (C_r)

Table 1 The calculated tower characteristics and combined percentage errors for different values of E and F_2

E	15		30		45		60		∞	
F_2	T.C.	% Err.	T.C.	% Err.	T.C.	% Err.	T.C.	% Err.	T.C.	% Err.
0.87	1.0575	42.847	0.9299	25.611	0.8997	21.532	0.886	19.68	0.8509	14.94
0.9	1.0223	38.093	0.8989	21.423	0.8697	17.48	0.8566	15.71	0.8225	11.104
1	0.92	24.273	0.809	9.28	0.7827	5.727	0.771	4.147	0.7403	-
1.1	0.8364	12.98	0.7355	-0.648	0.7116	-3.877	0.7009	-5.32	0.6729	-9.1
1.2	0.7667	3.566	0.6742	-8.93	0.6523	-11.887	0.6425	-13.21	0.6169	-16.669

Table 2 The calculated water outlet temperature and the associated percentage errors for different values of F_2 and E

E	15		30		45		60		∞	
F_2	Tw_2	%Er	Tw_2	%Er	Tw_2	%Er	Tw_2	%Er	Tw_2	%Er
0.87	25.774	4.289	25.448	2.97	25.361	2.618	25.343	2.545	25.212	2.015
0.9	25.646	3.771	25.323	2.4642	25.237	2.116	25.197	1.954	25.089	1.517
1	25.250	2.169	24.939	0.9104	24.856	0.575	24.818	0.421	24.714	0
1.1	24.9	0.7526	24.6	-0.46	24.52	-0.785	24.484	-0.93	24.383	-1.339
1.2	24.587	-0.514	24.299	-1.679	24.222	-1.99	24.187	-2.133	24.0897	-2.536

sensitive to the values of E and F_2. For example, T.C. at E = 15 and F_2 = 0.87 is about 171 percent of T.C. at $E = \infty$ and F_2 = 1.2. Jaber and Webb (1989) used F_2 = 1 and $E = \infty$ in their analysis. The T.C. calculated by the Logarithmic Mean Enthalpy Difference (LMED) method was 0.76 and by the ϵ-NTU method was 0.74, which agreed completely with our calculations.

For the rating case, assume that the given is T.C. = 1.87 and M_w/M_a = 1, the air and water inlet conditions are T_{w_1} = 35°C and T_{wb_2} = 20, respectively. The outlet water temperature Tw_2, and the associated percentage error for different values of F_2 and E are shown in Table 2. As can be seen in the table, the errors can be varied from +25.774 to −2.536 depending on the values of F_2 and E. Jaber and Webb (1989) give T_{wb_2} = 25, which agreed very well with our results (T_{w2} = 24.714). The small difference in the numerical values obtained is due to round-off errors.

In Table 1 and 2 the percentage errors are defined as % Err = $(X_1 - X_2/X_2)$*100 where X_1 and X_2 refer to the calculated variable and the value of the parameters when F_2 = 1 and $E = \infty$. A very promising way for using the developed relationships for designing or rating cooling towers is the use of one of the available general computer packages capable of solving a set of simultaneous equations.

Conclusions

The paper presents a solution for the steady-state counterflow wet cooling tower with new definitions of tower effectiveness and number of transfer units. In this model, we have considered the resistance of the heat transfer in the water film, nonunity of the Lewis number, and the curvature of the saturated air enthalpy versus the temperature. A new expression relating the tower effectiveness, the fluid capacity ratio, and the modified number of transfer units has been developed. The data obtained from the application of the model showed that a substantial error can be obtained when the resistance to heat transfer in water film is neglected and the Lewis number is considered to be unity. However, the amount of error depends very strongly on the ratio between the heat and mass transfer coefficients used in the calculations.

References

Anon, 1983, "Cooling Towers," chap. 21, in *ASHRAE—Handbook, 1983 Equipment, Am. Soc. of Heating, Refrigerating and Air Conditioning Engineers,* Atlanta, GA, USA.

ASHRAE, 1975, *ASHRAE Handbook and Product Directory—Equipment,* chap. 21, American Society of Heating, Refrigerating and Air Conditioning Engineers, Atlanta, GA, USA.

Bagnoli, E., Norris, R. W., Flynn, T. M., and Timmerhaus, K. D., 1984, "Psychrometry, Evaporative Cooling, Refrigeration, and Cryogenic Processes," chap. 12, in *Perry's Chemical Engineers Handbook,* 6th ed., Perry, R. H., and Green, D., eds., McGraw-Hill, New York.

Baker, D., 1984, *Cooling Tower Performance,* Chemical Publishing Co., Inc., New York, pp. 79–106.

Baker, D. R., and Shryock, H. A., 1961, "A Comprehensive Approach to the Analysis of Cooling Tower Performance," *ASME Trans.,* Vol. 83, pp. 339–349.

Brodkey, R. S., and Hershey, H. C., 1988, *Transport Phenomena: A Unified Approach,* McGraw-Hill, New York, pp. 228.

Cheremisinoff, N. P., 1986, "Cooling Towers Operations," chap. 34, in Editors Handbook of Heat and Mass Transfer, Volume 1: Heat Transfer Operations, chapter 34, Gulf Publishing Company, Houston, TX. USA.

Cheremisinoff, N. P., and Cheremisinoff, P. N., 1981, *Cooling Towers: Selection, Design and Practice,* Ann Arbor Science Publishers, Ann Arbor, MI.

Coffey, B. H., and Horne, G. A., 1914, *A Theory of Cooling Towers* Compared with Results, *Am. Soc. of Refrig. Engrs.,*

Collier, J. G., 1972, *Convective Boiling and Condensation,* McGraw-Hill, New York, NY.

Collier, J. G., 1981, "Convective Boiling and Condensation," 2nd ed., McGraw-Hill, New York, pp. 325.

Coulson, J. M., and Richardson, J. F., 1990, *Chemical Engineering,* Vol. 1, 4th ed., Pergamon Press, Oxford, pp. 594–598.

CTI, "Cooling Tower Performance Testing: An Overview and Update of Cooling Tower Institute Services and Activities," *J. of the Cooling Tower Institute,* Vol. 9, No. 2, pp. 16–23.

El-Dessouky, H., 1983, "Thermo-Hydraulic Characteristics of a Packed Bed Cooling Tower," ASME-HTD, 37, pp. 53–55.

El-Dessouky, H. T., 1993, "Thermal and Hydraulic Performance of a Three-Phase Fluidified Bed Cooling Tower," *Experimental Thermal and Fluid Science,* Vol. 6, No. 4, pp. 417–426.

El-Dessouky, H. T., 1996, "Enhancement of the Thermal Performance of a Wet Cooling Tower," *Canadian J. of Chemical Engineering,* Vol. 71, pp. 1–8.

Foust, A. S., Wenzel, L. A., Clump, C. W., Maus, L., and Anderson, L. B., 1980, "Principles of Unit Operations," 2nd ed., John Wiley & Sons, Inc., New York, pp. 436–444.

Hewitt, G. F., Shires, G. L., and Bott, T. R., 1994, *Process Heat Transfer,* CRC Press, Inc., Ann Arbor, pp. 762–772.

Jaber, H., and Webb, R. L., 1989, "Design of Cooling Towers by the Effectiveness—NTU method," ASME JOURNAL OF HEAT TRANSFER, Vol. 111, pp. 837–843.

Jeffreson, C. P., 1972, "Prediction of Breakthrough Curves in Packed Beds," *AIChE Journal,* Vol. 18, No. 2, pp. 409.

Kern, D. Q., 1950, *Process Heat Transfer,* McGraw-Hill, New York, pp. 583–593.

London, A. L., Mason, W. E., and Boelter, L. K., 1940, "Performance Characteristics of a Mechanically Induced Draft, Counterflow, Packed Cooling Tower," *Trans. ASME,* 62, pp. 41–50.

Maclaine-Cross, I. L., and Banks, P. J., 1981, "A General Theory of Wet Surface Heat Exchanger and its Application to Regenerative Evaporative Cooling," ASME JOURNAL OF HEAT TRANSFER, Vol. 103, No. 3, pp. 579–585.

Majumdar, A. K., Singhal, A. K., Reilly, H. E., and Batz, J. A., 1983, "Numerical Modeling of Wet Cooling Towers—Part 1: Mathematical and Physical Models," ASME JOURNAL OF HEAT TRANSFER, Vol. 105, pp. 728–735.

Maulbetch, J. S., and Bartz, J. A., 1985, "Cooling Towers and Cooling Ponds," chap. 10, in *Handbook of Heat Transfer Applications,* Rohsenow, W. M., Hartnett, J. P., and Ganic, E. N., eds., 2nd ed., pp. 1–48, McGraw-Hill, New York.

Merkel, F., 1925, "Verdunstungshuhlung," *Zeitschrift des Vereines Deutscher Ingenieure (V.D.I.),* Vol. 70, pp. 123–128.

Moffatt, R. J., 1966, "The Periodic Flow Cooling Tower: A Design Analysis," Technical Report No. 62, Dept. of Mech. Eng., Stanford University, Ca.

Nahavandi, A. N., Kershah, R. M., and Serico, B. J., 1975, "The Effect of Evaporation Losses in the Analysis of Counterflow Cooling Towers," *J. of Nuclear Engineering and Design,* Vol. 32, pp. 29–36.

Raghavan, R., 1991 "Cooling Tower Analysis Consideration of Environmental Factors," *Practical Aspects and Performance of Heat Exchanger Components and Materials,* PWR-Vol. 14, ASME, pp. 33–39.

Sadasivam, M., and Balakrishnan, A. R., 1992, "Effectiveness—NTU Method for Design of Packed Bed Liquid Desiccant Dehumidifiers," *Transactions of Institution of Chemical Engineers,* Vol. 70, Part A, pp. 572–577.

Sadasivam, M., and Balakrishnan, A. R., 1995, "On the Effective Driving Force for Transport in Cooling Towers," ASME JOURNAL OF HEAT TRANSFER, Vol. 117, pp. 512–515.

Sherwood, T. K., 1937, *Absorption and Extraction,* 1st ed., Mcgraw-Hill, New York.

Stevens, D. I., Braun, J. E., and Klein, S. A., 1989, "An Effectiveness Model of Liquid-Desiccant System Heat/Mass Exchangers," *Solar Energy Journal,* Vol. 42, No. 6, pp. 449–455.

Sutherland, J. W., 1983, "Analysis of Mechanical-Draught Counterflow Air/Water Cooling Towers," ASME JOURNAL OF HEAT TRANSFER, Vol. 105, pp. 576–583.

Shouman, A. R., and El-Dessouky, H. T., 1991, "A Modified Approach of Heat Exchanger Analysis," *Kerntechnik,* Vol. 56, No. 5, pp. 307–311.

Threlkeld, J. L., 1970, *Thermal Environmental Engineering,* Prentice-Hall, Englewood Cliffs, N.J., pp. 191–193.

Treybal, R. E., 1969, "Adiabatic Gas Absorption and Stripping in Packed Towers," *Industrial and Engineering Chemistry,* Vol. 61, No. 7, pp. 36–41.

Treybal, R. E., 1980, *Mass Transfer Operations,* 3rd ed., Mcgraw-Hill, New York, pp. 242–252.

Walker, W. H., Lewis, W. K., McAdams, W. H., and Gilliland, E. R., 1937, *Principles of Chemical Engineering,* McGraw-Hill, New York.

Webb, R. L., 1984, "A Unified Theoretical Treatment for Thermal Analysis of Cooling Towers, Evaporative Condensers, and Fluid Coolers," *ASHRAE Tran.,* Vol. 90, Part 2, pp. 398–415.

Webb, R. L., 1988, *A Critical Evaluation of Cooling Tower Design Methodology, in Heat Transfer Equipment Design,* Shah, R. K., Subba Rao, E. C., and Mashelkar, R. A., eds., Hemisphere Publishing Co., Washington, pp. 547–558.

Webb, R. L., 1990, "Standard Nomenclature for Mass Transfer Process," *ASHRAE Trans.,* Vol. 97, Part 2, pp. 114–117.

Yadigaroglu, G., and Pastor, E. J., 1974, "An Investigation of the Accuracy of the Merkel Equation for Evaporative Cooling Tower Calculations," ASME Paper No. 74-HT-59, Proceedings of the AIAA/ASME Thermophysics and Heat Transfer Conference, Boston, MA, pp. 1–8.

Zafar, M., and MaClaine-Cross, I. L., 1985, "A General Theory of Wet Surface Heat Exchangers Modified for the Effects of Lewis Number," *Proc. of Third Australian Conf. on Heat and Mass Transfer,* University of Melbourne, Australia, pp. 513–520.

Journal of Heat Transfer

Technical Notes

This section contains shorter technical papers. These shorter papers will be subjected to the same review process as that for full papers.

Enhancement of Thermal Conductivity by Using Polymer-Zeolite in Solid Adsorption Heat Pumps

E. J. Hu[1], D.-S. Zhu[2], X.-Y. Sang[3], L. Wang[4], and Y.-K. Tan[5]

A thermal conductivity augmentation technology for zeolite beds has been studied in this paper. To enhance the effective thermal conductivity of zeolite, the zeolite particle was coated with a thermal polymer material in a new synthesis process. It was found that the effective thermal conductivity of the polymer-zeolite was increased two to three times, while its adsorptive ability remains the same. The results of the experiment show that the polymer synthesis technique could be used as a heat transfer enhancement method to improve thermal conductivity among zeolite particles.

1 Introduction

The Solid Sorption Heat Pump (SSHP) is a type of heat pump driven by heat and it has recently received increasing attention for space conditioning (heating or cooling) purposes. This is a result of the increasing worldwide effort to reduce the electrical energy consumption and the impact of air-conditioning equipment on the environment (Meunier, 1992). The typical refrigerants used in solid sorption systems are environmentally benign. This is one of the important advantages of SSHP because CFCs and HCFCs refrigerants are to be phased out in the near future.

[1] Gippsland School of Engineering, Monash University, Churchill, Victoria 3842, Australia
[2] Research Institute of Chemical Engineering, South China University of Technology, Guangzhou 510641, China
[3] Research Institute of Chemical Engineering, South China University of Technology, Guangzhou 510641, China
[4] Research Institute of Chemical Engineering, South China University of Technology, Guangzhou 510641, China
[5] Research Institute of Chemical Engineering, South China University of Technology, Guangzhou 510641, China

Contributed by the Heat Transfer Division of THE AMERICAN SOCIETY OF MECHANICAL ENGINEERS. Manuscript received by the Heat Transfer Division May, 20, 1996; revision received January 17, 1997; Keywords: Conduction, Packed & Fluidized Beds, Porous Media. Associate Technical Editor: K. Vafai.

2 Mechanism of the Heat Transfer Enhancement

An intermittent adsorption heat pump consists of the evaporator, condenser, and adsorber. The work of "compression" is done in the adsorber (it is also called an adsorbent bed or fixed bed) through the adsorption and desorption processes. It can be seen that the solid bed plays an important role in the SSHP to release, absorb heat, and adjust system pressure at various stages. The function of the adsorbent bed is similar to an electrical vapor compressor in a compression cooling unit. It is also similar to the absorber or regenerator of liquid absorption heat pump. The effective thermal conductivity of the granular media (zeolite) in the solid bed is a key property which can significantly influence the design and performance of a system which must dissipate heat to or extract heat from these materials (Jackson and Black, 1983).

Consider a system consisting of two parallel plates at different temperatures; the zeolite particles are placed between the plates. The heat has to cross the particles and interparticle gaps to transfer from one plate to another. The thermal resistance for this heat transfer is largely due to the consecutive nature of the transfer path and the small conductivity of the particle itself. The speed of the adsorption and desorption cycle is actually controlled by the heat transfer process in the bed (Zhu and Tan, 1993). The low value of the effective thermal conductivity of a granular fixed bed is mainly due to the fact that both the particles and the vapor which surrounds the grains have a low thermal conductivity. There were some attempts to improve the effective thermal conductivity of the solid bed such as using a thermal binder (Jackson and Black, 1983) and establishing a better heat transfer path between the temperature gap by mixing (zeolite) grains with a metallic foam or a polymer thermal material which have better thermal conductivity (Guilleminot et al., 1993). However, if a thermal binder was to be used on the microporous particles, the micropores' surface would be covered by the binder so that the capacity of adsorption of the particles would be reduced if not lost totally.

The heat transfer augmentation technology we developed is based on the idea that if every individual particle was coated on the surface with high thermal conductivity materials in the form of matrix in a material synthesis process, these thermal polymer matrix coatings on individual particles would contact each other. This in turn would form a continuous phase conductor when the coated particles were packed to form a solid bed. The heat could then be easily transferred across the solid bed without a significant impact on its adsorption properties.

Polyaniline was traditionally recognized to be the only air-stable conducting polymer and was considered to be an intractable material. But, during the last few years it was found that both the doped and undoped forms of Polyaniline can be dissolved in various solvents if the proper technology is used (Armes, 1991).

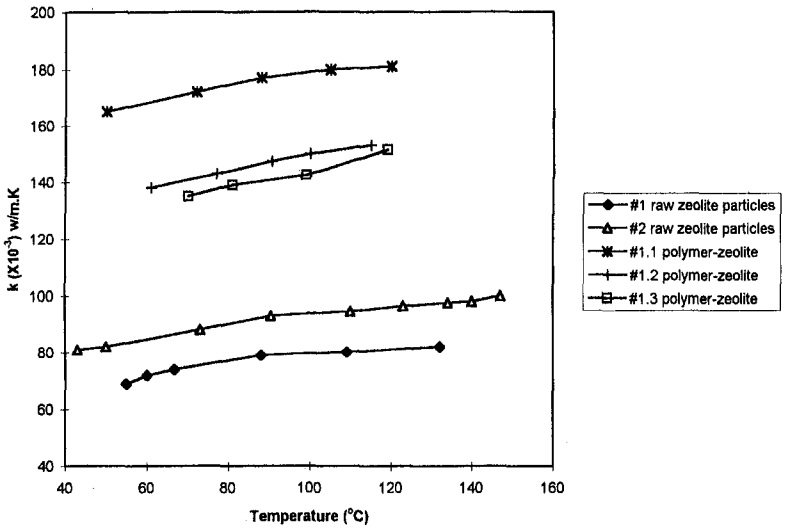

Fig. 1 Effective thermal conductivity (k) of dry raw zeolite and polymer-zeolite particles at different temperatures

It is now well known that both organic and inorganic zeolite with a wide range of particle sizes and morphologies can be coated with Polyaniline. In our study we used Polyaniline as thermal conductive material for preparing a polymer-zeolite composite which would improve the thermal conductivity of zeolite particles, while retaining its adsorptive capacity.

3 Experimental Results and Discussion

Sample Preparation. The polymer zeolite composites were prepared by a modified chemical synthesis technology (Kang, 1996). During the synthetic preparation, polymer is grown as a thin conducting matrix layer on each zeolite particle. As a fine net this layer would not block the openings of the micropores of the zeolite particles. When the zeolite particles are packed, the net-Polyaniline coat on the particles contacting each other would form a thermal conducting polymer bridge across the solid bed.

Thermal Conductivity Measurements With Steady Static Method. The methods of measuring thermal conductivity can be divided into two categories: (1) static and (2) dynamic. These two categories are determined by whether the temperature distribution within the sample is time dependent or not (Bjurstrom et al., 1984). In our study we focused on the improvement of effective thermal conductivity of zeolite. That is, the difference of thermal conductivity between raw zeolite and polymer-zeolite was measured to evaluate the effect of heat transfer enhancement of the polymer-zeolite; therefore, the static method was applied for the study. Static measurements of thermal conductivity involves the use of the Fourier Law of Conduction and it is necessary to determine the rate of heat flow (q) and the temperature gradient (dT/dx) along the normal to the isothermal surface. It is assumed that the heat loss from the sample periphery and along the thermometers are negligible.

The effective thermal conductivity measurements were carried out in a specially designed apparatus which was built up according to the steady state flat thermal conductivity measurement principle, in the laboratory of South China University of Technology. A detailed description of the thermal conductivity measurement system was given by Kang (1996).

After the system reached its steady operation state, and the temperatures of the central points of the ends of the sample column were taken, the mean conductivity (k_{eff}) of the sample is then to be determined by

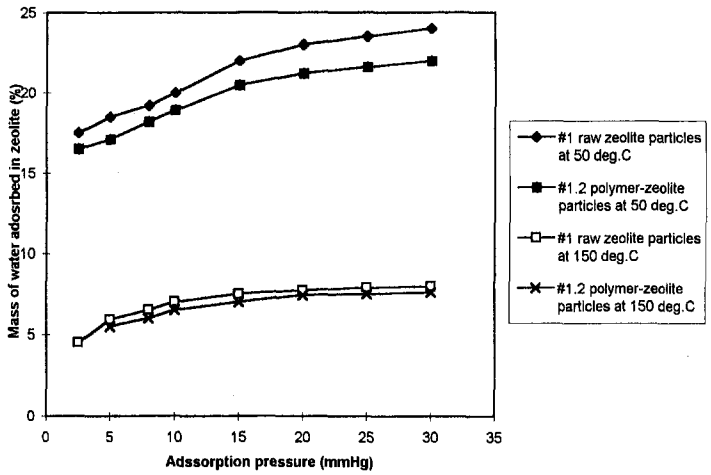

Fig. 2 The mass of water adsorbed in zeolite versus the pressure (P mmHg) in isotherm

$$k_{\text{eff}} = -\frac{q}{A}\cdot\frac{\Delta L}{\Delta T} = \frac{q}{A}\cdot\frac{L}{(T_1 - T_2)}. \quad (1)$$

The heat flow rate q/A across the packed sample particles was measured by a Surface Heat Flux instrument (Shotherm HIT made in Japan). The temperature difference $(T_1 - T_2)$ along the sample column was measured by thermocouples which had been calibrated by a standard quartz thermometer (Hp2086 made in USA). The data was taken only after the system had achieved its steady state. The steady static method gives a high degree of precision of measurement for packed materials. However, achieving steady state of the system is a time consuming process (it took at least several hours) and makes the method only suitable for low temperatures. Therefore, we selected the temperature range for measurement to be 50 ~ 120°C and every sample was tested three times to obtain the result. A standard sample, with a known effective thermal conductivity, was used to calibrate our setup before actual samples were tested. It was found that the difference between the value of k_{eff} measured from our plant and the standard value we had known for the standard sample was less than 7 percent after repeated tests. Therefore, the test apparatus was thought to be suitable for use as a conductivity measurement with the average uncertainty less than 7 percent.

Characterization of Thermal Conductivity. The effective thermal conductivity of a solid bed is primarily dependent on the thermal conductivities of the composite phase, the liquid phase of water, the vapor, and the structure of the particles (Sarwar and Majumdar, 1995). Generally, the contact area between particles depends on the sample preparation conditions, the amount of impurities, additives or inert materials, as well as on particle shape and size distribution. In our study, Polyaniline which has the better conductivity was coated as a net to form the conduct felts over the surface of each particle in a synthetic process. It is thought that the coated polymer formed a continuous system allowing the heat flow to cross the polymer net with less resistance.

The effective thermal conductivity of the solid bed packed with dry raw zeolite particles #1 and #2 and polymer-zeolite particles (which are raw zeolite #1 particles with polymer coatings) were measured, respectively. The difference between #1 and #2 is their size. The size of particles #2 is smaller than that of #1. The #1.1, #1.2, and #1.3 are the polymer zeolites from raw zeolite #1 prepared by different synthesis processes. The test results are shown in Fig. 1. From this figure it can be seen that the thermal conductivity of #2 raw zeolite particles is higher than that of #1. This means that the small size particles have higher pack density; the higher the density, the higher the conductivity. It can also be seen that the conductivity has been significantly increased for the zeolite #1 by 80 percent to 250 percent after being coated with Polyaniline. In addition, the conductivity of two kinds of raw kaolin (which is a raw material popularly used in the ceramic industry) particle beds, with and without polymer coating, was measured. By using this technology, the effective thermal conductivity of polymer-kaolin particle beds was found to be increased by two to three times that of the effective thermal conductivity of the raw particle beds.

We also found that different synthesis processes gave different degrees of thermal conductivity improvement. Further research is still necessary for optimizing the preparation process to produce the most appropriate polymer-zeolite particles for the solid bed (adsorber) in the SSHP.

Characterization of Adsorption and Desorption. For the utilization in SSHP, the zeolite is expected to have not only a good conductivity but also a good adsorptive character with the corresponding adsorbate. A similar apparatus to the one described by Hu and Exell (1993) has been built to test the isotherms of the polymer-zeolite. Figure 2 shows the experimental results. It can be noticed that the difference between zeolite and polymer-zeolite in terms of adsorptive capacity is very small, and the adsorptive ability remains stable after multi-adsorption and desorption. It means that the polymer-zeolite has better thermal conductivity than raw zeolite and also has mass transfer ability as effective as raw zeolite. Because the total amount of polymer used to coat the zeolite particles is comparatively small (less than 8 percent of the zeolite mass), its impact on the adsorption/desorption heat of the solid bed is negligible. From the results of these experiments we can say it is possible to make use of polymer-zeolite instead of raw zeolite in SSHP to improve the thermal performance of the solid bed.

Further Work. We are attempting to physically compress polymer-zeolite particles into a brick for use in the SSHP. It is expected that the behavior of the heat and mass transfer of a polymer-zeolite block will be even better than that of the particles.

4 Conclusions

The polymer-zeolite is the zeolite coated with Polyaniline in a special Polyaniline synthetic preparation process. The thermal conductivity of the solid bed packed with raw zeolite and polymer-zeolite particles has been measured and compared. The effective thermal conductivity of the bed packed with polymer-zeolite was increased two to three times by the Polyaniline coating than that with normal zeolite. At the same time, the adsorptive ability of polymer-zeolite remains the same as the normal zeolite.

This technology may lead to the production of high performance polymer-zeolite for use in the SSHP system. It is anticipated that if a polymer-zeolite brick would be used, the performance of SSHP could be improved further.

5 Acknowledgments

The project and the writing of the paper were supported by National Nature Science Fund of China, Natural Science Fund of Guangdong Province China, and TILS of DEETY Australia.

6 References

Armes, S. P, 1991, "Conducting Polymer-Colloidal Silica Composites," *Polymer,* Vol. 32, No. 13, pp. 2325–2330.

Bjurstrom, H., Kasrawacki, E., and Carlsson, M., 1984 "Thermal Conductivity of a Microporous Particulate Medium: Moist Silica Gel," *Int. J. Heat Mass Transfer,* Vol. 27, pp. 2025–36.

Guilleminot, A., Choisier, J. B., Chalfen, S., Reymoney, J. L., 1993, "Heat Transfer Intensification in Fixed Bed Adsorbers," *Heat Recovery Systems & CHP,* Vol. 13, No. 4, pp. 297–300.

Hu, J., and Exell, R. H. B., 1993, "Adsorptive Properties of Activated Charcoal/Methanol Combinations," *Renewable Energy,* Vol. 3, No. 6/7, pp. 567–575.

Jackson, K. W., Black, W. Z., 1983, "A Unit Cell Model for Predicting the Thermal Conductivity of a Granular Medium Containing an Adhesive Binder," *Int. J. Heat Mass Transfer,* Vol. 26, No. 1, pp. 87–99.

Kang, X. Y., 1996, "Study of Heat Transfer Enhancement of Adsorbent in Sorption Heat Pump," Master thesis, South China University of Technology.

Meunier, F., 1992, "Solid Sorption: An Alternative to CFC's," *Solid Sorption Refrigeration Sym.,* Paris, France, pp. 44–52.

Sarwar, M. K., and Majumdar, P., 1995, "Thermal Conductivity of Wet Composite Porous," *Heat Recovery System & CHP,* Vol. 15, No. 4, pp. 369–381.

Zhu, D. S., and Tan, Y. K., 1993, "Investigation of Heat and Mass Transfer in Heat Pump Adsorbed," *J. Chem. Industry & Engineering,* (Chinese), Vol. 44, No. 2, pp. 212–217.

Flow Field Effects on Heat Transfer in Confined Jet Impingement

J. A. Fitzgerald[1] and S. V. Garimella[2]

Introduction

Due to their effective transport capabilities, impinging jets are used in a wide variety of applications, from turbine-blade cooling to electronics packaging. The heat transfer trends observed in jet impingement are related to the velocities and turbulence levels in the jet flow field. Experimental and analytical studies of the flow field in free and submerged (unconfined) jets have provided valuable information regarding their heat transfer characteristics. In real applications, however, the outflow of the jet is often confined (between parallel plates) resulting in a more complicated flow structure. The confined flow field is less readily analyzed and little information is available in the literature for this configuration. In the present study, laser-Doppler velocimetry was used to map the flow field in a confined and submerged liquid jet, and the results were used to interpret heat transfer measurements obtained previously for the same configuration.

Experiments

The experiments were conducted using FC-77 (a perfluorinated dielectric liquid) in a closed-loop facility as described in Garimella and Rice (1995). The jet issues from a flow-conditioning plenum into a reservoir of stagnant fluid, impinging normally onto a heat source centered on the target plate. Heat transfer and flow field measurements were obtained for jets with sharp-edged nozzles that were 3.18 mm and 6.35 mm in diameter (d). The aspect ratio (nozzle-length to diameter) of both nozzles was unity. The diameter of the confining nozzle plate was 22 and 11 nozzle diameters, respectively, for the two nozzles. Results are presented for nozzle-to-target plate spacings (H) of 2, 3, and 4 nozzle diameters at turbulent-flow Reynolds numbers ($\mathrm{Re}_d = Ud/\nu$) of 8500, 13000, and 23000.

The electrically heated foil heater was square and 10 mm on the side. Details of its construction are available in Garimella and Rice (1995). Local surface temperatures were measured in fine increments using a 36 gage T-type thermocouple attached to the underside of the foil heat source.

The local mean velocity and turbulence measurements were obtained with a TSI laser-Doppler velocimeter. The measurements were obtained using the green line (514.5 nm) of the laser with receiving optics in backscatter mode. Frequency shifting was used to accurately determine negative velocities in the flow. The flow was seeded with corn starch particles (diameter $\approx 5\ \mu$m). The local mean and fluctuating components of velocity were obtained at each position as an average of 7000 data points. The axial velocity and turbulence levels were obtained in fine increments in a region around the jet axis, extending over a radius of 1.75 nozzle diameters and to within 4.5 mm of the nozzle and target plates. Radial measurements spanned a nonuniform grid over one side of the axisymmetric confinement region; this mesh was most dense along the impingement surface and near stagnation where flow characteristics are of most interest. The experimental set up and flow field measurement locations are shown in Fig. 1. Additional details of the experiments, as well as a more complete set of LDV measurements, are available in Fitzgerald and Garimella (1996).

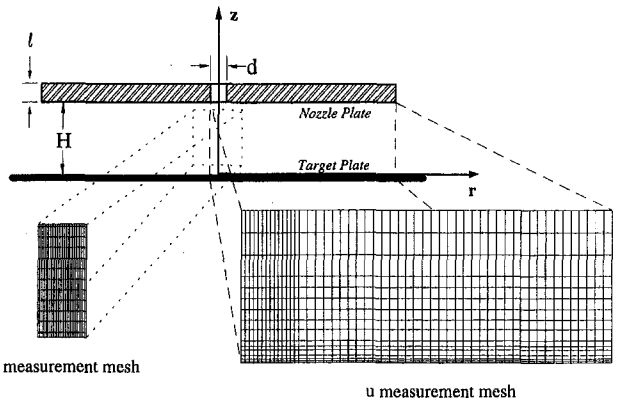

Fig. 1 Schematic diagram of the experimental set up and measurement locations for the axial (v) and radial (u) velocity and turbulence measurements

Uncertainties in local heat transfer coefficient were estimated to be 5 percent, based on a standard uncertainty analysis (Garimella and Rice, 1995). Uncertainty in setting the jet flow rate was always less than 4 percent. The uncertainty in the local velocity measurements was estimated to be 2 percent.

Results and Discussion

The heat transfer to an impinging jet has been found to be dependent upon the velocity of the jet (Re_d), the spacing between the jet and the impingement surface (H/d), the diameter of the jet (d), and the Prandtl number of the fluid (Pr). Gardon and Akfirat (1965), den Ouden and Hoogendoorn (1974), Hoogendoorn (1977), and Obot et al. (1982) have all contributed to the discussion of the significance of turbulence on the heat-transfer characteristics of impinging jets. With all other parameters held constant, greater turbulence levels in the jet were found to result in higher heat transfer at stagnation. Along the lines of stagnation heat transfer correlations for cylinders, Hoogendoorn (1977) incorporated turbulence levels of the jet into correlations for stagnation heat transfer on a flat surface. Gardon and Akfirat (1965) effectively correlated data for fully developed jets without a separate parameter to characterize turbulence levels, stating that, "The intensity of turbulence in the jets is uniquely determined by the jet Reynolds number and the dimensionless jet length." They also stated, however, that the correlation was not adequate in cases where velocity and turbulence are not uniquely related, as is the case of a turbulent but not fully developed jet.

A study of the potential core in confined and unconfined jets by Ashforth-Frost and Jambunathan (1996) suggested that nozzle geometry as well as turbulence levels affected stagnation heat transfer. Two nozzles were studied, one with a uniform exit velocity profile and another with a fully developed profile. The nozzle with a uniform profile at the jet exit showed a greater decay in jet velocity, and thus a shorter potential core, than that for a fully developed profile due to higher shear at the edge of the former. Although initial turbulence levels were higher in the fully developed profile, turbulence intensities increased more rapidly in the uniform jet resulting in higher levels of centerline turbulence over a region of 1 to 8 diameters from the nozzle. Despite this fact, stagnation heat transfer measurements obtained at an optimum nozzle-to-target plate spacing were higher for the nozzle with the fully developed profile due to its higher centerline velocity.

[1] Graduate Student, Department of Mechanical Engineering, University of Wisconsin—Milwaukee, PO Box 784, Milwaukee, WI 53201

[2] Cray-Research Associate Professor, Department of Mechanical Engineering, University of Wisconsin—Milwaukee, PO Box 784, Milwaukee, WI 53201: sureshg@csd.uwm.edu

Contributed by the Heat Transfer Division of THE AMERICAN SOCIETY OF MECHANICAL ENGINEERS. Manuscript received by the Heat Transfer Division August 8, 1996; revision received April 28, 1997; Keywords: Electronic Equipment; Forced Convection; Jets. Associate Technical Editor: B. W. Webb.

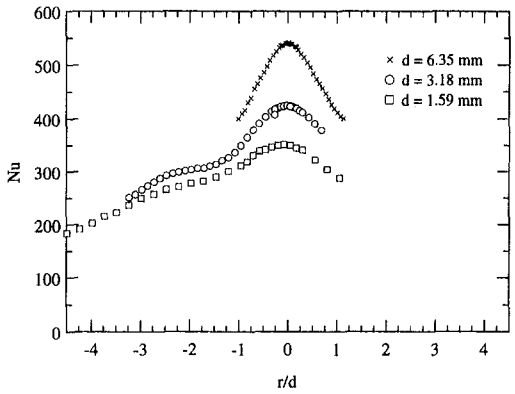

Fig. 2 Variation in local Nusselt numbers for Re = 13000, H/d = 4, and d = 1.59, 3.18, and 6.35 mm

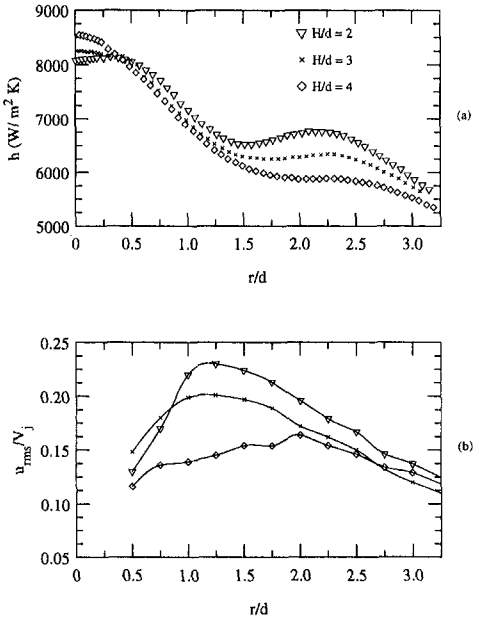

Fig. 4 Variation with H/d in (a) local convective heat-transfer coefficients, and (b) local turbulence levels in the wall jet (z/d = 0.04), for Re = 13000 and d = 3.18 mm

The effect of nozzle geometry on heat transfer in confined and submerged liquid jets was studied by Garimella and Nenaydykh (1996). Short (knife-edged, $l/d < 1$) nozzles yielded significantly higher heat-transfer coefficients than longer nozzles. The heat-transfer coefficients in the stagnation region decreased as the length of the nozzle increased to an l/d of 4, and thereafter gradually increased. These trends in heat transfer were attributed to the change in the velocity profile and turbulence levels as the aspect ratio was modified. Moreover, when nozzle aspect ratio was held constant, they reported an increase in Nusselt number (hd/k) due to an increase in nozzle diameter alone; this effect was most pronounced in the stagnation region ($r/d < 1$). Obot et al. (1982) also observed this dependence on nozzle diameter in confined air jets for sharp-edged nozzles with $l/d = 1$; they also noted reports in the literature of reductions of 15 to 20 percent in average heat transfer coefficients over the stagnation region due to a 50 percent reduction in nozzle diameter.

Figure 2 shows the nozzle-diameter effect on heat transfer at $H/d = 4$ and Re = 13000, for nozzles with $l/d = 1$. It is evident that the larger nozzle diameter results in significantly higher Nusselt numbers in the stagnation region. The effect is strongest at the stagnation point, and becomes less pronounced with distance from the jet axis. The development of normalized velocity (v/V_j) and turbulence (v_{rms}/V_j) profiles for these jets (d = 3.18 and 6.35 mm) at the same Re and H/d are shown in Fig. 3. The mean jet exit velocity is denoted V_j and the location $z/d = 0$ corresponds to the target plate. Throughout the development of the jets, the larger diameter not only maintains higher levels of turbulence, but also exhibits higher centerline normalized velocities. Both conditions would contribute to the higher stagnation-region heat transfer observed in Fig. 2 for the larger-diameter jet. Outside the stagnation region ($r/d > 1$), the differences in velocities and turbulence levels are seen to greatly diminish, explaining the lack of differences in the corresponding heat-transfer distributions in this region.

At small nozzle-to-target plate spacings, secondary peaks in the heat-transfer distributions were reported by Garimella and Rice (1995), den Ouden and Hoogendoorn (1974), Gardon and Akfirat (1965), and Obot et al. (1982). Figure 4(a) illustrates the effect of H/d on the secondary peaks in heat-transfer coefficient for Re = 13000 with a 3.18 mm nozzle. The peaks are more pronounced at small H/d, decreasing in prominence and moving radially away from the jet axis as H/d increases. These peaks are generally understood to result from a transition to turbulence in the wall-jet boundary layer.

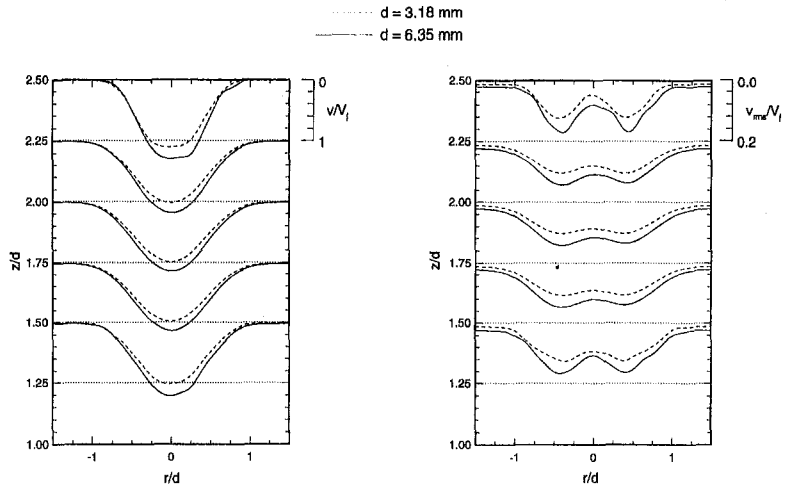

Fig. 3 Developing axial velocity and turbulence profiles for Re = 13000, H/d = 4, and d = 3.18, and 6.35 mm

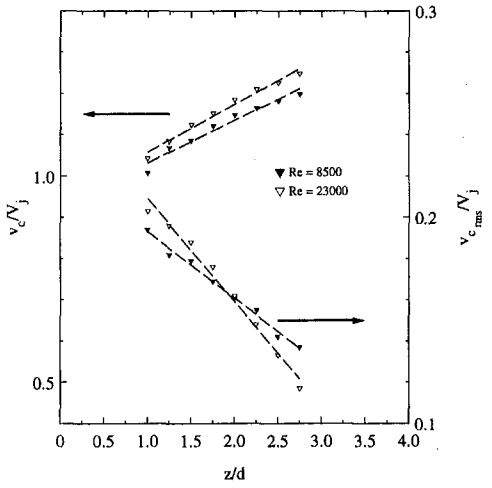

Fig. 5 Centerline velocity and turbulence levels in the developing jet for d = 6.35 mm, Re = 8500 and 23000, and H/d = 4

Local turbulence levels in the wall-jet region near the impingement surface ($z/d = 0.04$) are shown in Fig. 4(b) for the same cases as the heat-transfer measurements of Fig. 4(a). The turbulence level in the wall-jet region increases with r/d, reaching a maximum at the position of transition to turbulence. The peak levels of turbulence near the impingement surface are highest at narrow spacings, and decrease as H/d is increased. The radial location of the onset of transition, based on peak turbulence levels, is seen to move radially outward as H/d is increased. These trends in magnitude and shift in location of the peak radial turbulence levels match the trends seen in the secondary peaks in heat-transfer measurements. However, turbulence measurements show the onset of transition occurring nearer the jet axis than the location of the secondary peaks in heat transfer. In unconfined air jets, Hoogendoorn (1974) also reported measurements indicating that transition to turbulence significantly precedes (occurs closer to the jet axis) the secondary peaks in heat transfer. In the case shown, onset of transition is seen at $1.25 < r/d < 2$, while the secondary peaks occur at $2.25 < r/d < 2.75$. It is likely that the secondary peaks in heat transfer are seen at the position where the boundary layer has become fully turbulent rather than at the onset of transition.

It is also seen in Fig. 4(a) that at low nozzle-to-target spacings (within the length of the potential core of the jet), the stagnation heat-transfer coefficient increases slightly as H/d increases. Since the centerline velocity is slightly decreasing within the potential core, this increase in heat-transfer measurements must be attributed to increase in turbulence level as the jet develops (Fig. 3).

The increase in stagnation heat-transfer coefficients (h_0) as H/d increases is more pronounced at higher Reynolds numbers (Garimella and Rice, 1995). Heat-transfer measurements for the 6.35 mm jet showed an increase in h_0 of 10.3 percent as H/d is increased from 2 to 4 at Re = 8500, while the same increase in spacing yielded an increase in h_0 of 18.4 percent at Re = 23,000. Centerline velocity and turbulence intensities for Re = 8500 and 23,000 at H/d = 4 are shown for the 6.35 mm nozzle in Fig. 5. It can be seen that the reduction in centerline velocity as the target plate is approached is comparable (in slope) for both cases. However, a marked increase is seen in the centerline turbulence intensity at Re = 23,000 over that for Re = 8500 as the jet develops. Over a distance of 1.75 diameters (from z/d = 2.75 to z/d = 1), the centerline turbulence levels increase by 41.6 percent for Re = 8500, while an increase of 73.5 percent is seen in the Re = 23,000 case. The larger increases in turbulence levels with jet development seen at the higher Reynolds numbers (resulting from the greater shear-induced turbulence at the higher jet velocity) explain the corresponding effect on heat transfer.

Conclusions

Velocity and turbulence measurements in the flow field of a confined and submerged impinging liquid jet were used to interpret the observed trends in heat transfer. Measurements showed that in jets with developing profiles, an increase in the nozzle diameter alone caused an increase in the turbulence levels, with all other parameters (Re, H/d, l/d) held constant. This explains the increase in stagnation-region Nusselt number with increase in nozzle diameter, again with all other parameters held constant. Increasing the nozzle-to-target plate spacing (H/d) resulted in decreased peak turbulence levels and a delay in the onset of transition. Likewise, secondary peaks in heat transfer were less pronounced and moved radially away from the jet axis at the larger H/d. An increase in H/d results in higher stagnation heat transfer, corresponding to an increase in measured turbulence levels. This increase is more pronounced at the higher Reynolds numbers as the increased jet velocities promote higher levels of turbulence in the jet.

Acknowledgments

Partial funding for this work through a grant from Cray Research of Chippewa Falls, Wisconsin, is gratefully acknowledged. This material is based upon work supported under a National Science Foundation Graduate Research Fellowship to JAF.

References

Ashforth-Frost, S., and Jambunathan, K., 1996, "Effect of Nozzle Geometry and Semi-Confinement on the Potential Core of a Turbulent Axisymmetric Free Jet," *Int. Comm. Heat Mass Transfer,* Vol. 23, pp. 152–162.

den Ouden, C., and Hoogendoorn, C. J., 1974, "Local Convective Heat Transfer Coefficient for Jets Impinging on a Plate: Experiments Using a Liquid Crystal Technique," *Procs. 5th Int. Heat Transfer Conf.,* Tokyo, Japan, Vol. 5, pp. 293–297.

Fitzgerald, J. A., and Garimella, S. V., 1996, "Flow Field Measurements in Confined and Submerged Jet Impingement," *Procs. ASME IMECE,* Atlanta, Georgia, HTD-Vol. 333 (2), pp. 121–129.

Gardon, R., and Akfirat, J. C., 1965, "The Role of Turbulence in Determining the Heat-Transfer Characteristics of Impinging Jets," *Int. J. Heat Mass Transfer,* Vol. 8, pp. 1261–1272.

Garimella, S. V., and Nenaydykh, B., 1996, "Nozzle-Geometry Effects in Liquid Jet Impingement Heat Transfer," *Int. J. Heat Mass Transfer,* Vol. 39, No. 14, pp. 2915–2923.

Garimella, S. V., and Rice, R. A., 1995, "Confined and Submerged Liquid Jet Impingement Heat Transfer," ASME JOURNAL OF HEAT TRANSFER, Vol. 117, pp. 871–877.

Hoogendoorn, C. J., 1977, "The Effect of Turbulence on Heat Transfer at a Stagnation Point," *Int. J. Heat Mass Transfer,* Vol. 20, pp. 1333–1338.

Obot, N. T., Douglas, W. J. M., and Mujumdar, A. S., 1982, "Effect of Semi-Confinement on Impingement Heat Transfer," *Procs. 7th Int. Heat Transfer Conf.,* Vol. 3, pp. 395–400.

Heat Transfer From a Pair of Radial Jet Reattachment Flames

J. W. Mohr,[1] J. Seyed-Yagoobi,[1,2] and R. H. Page[1]

Nomenclature

A = impingement surface area = 0.836 m^2
b = RJR nozzle exit gap width = 3.68 mm
D_f = fuel supply pipe diameter = 5.1 mm
D_h = air exit hydraulic diameter = $2b$
ILJ = in-line jet
h_f = fuel heating value = 53,326 kJ/kg
$\dot{m}_f$ = fuel mass flow rate = 0.0223 kg/min
q = heat transfer rate to impingement surface, kW
q_f = fuel heating capability = $(\dot{m}_f h_f)$, kW
q'' = local heat flux, kW/m^2
q^* = nondimensional heat flux = $q''/(q_f/A)$
R_o = air supply pipe inside radius = 12.7 mm
RJR = radial jet reattachment
RJRC = radial jet reattachment combustion
S = center-to-center nozzle spacing parallel to y-coordinate, mm
X_p = nozzle-to-plate spacing, mm
y = coordinate direction parallel to impingement surface and parallel to S
z = coordinate direction parallel to impingement surface and perpendicular to S
Φ = fuel equivalence ratio, $(\text{fuel/air ratio})_{\text{actual}}/(\text{fuel/air ratio})_{\text{stoichiometric}}$

Background

In order to provide a more uniform and stable flame heating of an impingement surface, a new design for an impingement burner has been investigated. This new flame impingement nozzle utilizes the concept of Radial Jet Reattachment (RJR) nozzles (Page et al., 1989), which has use in nonreacting jet impingement heat transfer and drying processes (Thiele et al., 1995). The aerodynamics of the RJR nozzle differs greatly from a standard ILJ nozzle, and this RJR flow pattern has been utilized to design a Radial Jet Reattachment Combustion (RJRC) nozzle (Mohr et al., 1996; 1997). A typical air flow pattern for a pair of reacting RJRC nozzles is depicted in Fig. 1. As shown in Fig. 1, a RJRC nozzle is created from a typical RJR nozzle by introducing gaseous fuel radially into the recirculation region, ensuring that the fuel does not directly impinge upon the surface. Since the fuel and airflows can be independently controlled, the RJRC nozzle effectively becomes a partially premixed combustor. The net force exerted on the impingement surface by a RJRC nozzle can be negative, null, or positive, depending on the air exit angle of the nozzle. Since the exit angle used in this study was +10 deg, the nozzle exerted a slight, positive force upon the impingement surface in the reattachment ring.

Mohr et al.'s (1997) work reported the heat transfer characteristics of a single RJRC nozzle. Local heat flux, temperature, and pressure measurements at the impingement surface were combined with the flame temperature and the gas analyses data to identify the size of the RJRC combustion zone. This paper examines the heat transfer characteristics of two practical RJRC nozzles operating in an array configuration. Local heat flux distributions in two perpendicular directions along the impingement surface are reported as a function of the between-nozzle spacing (S/R_o).

Experimental Apparatus and Procedure

The details of the experimental apparatus and procedure can be found in Mohr et al. (1997) and Mohr (1996). The RJRC nozzle pair geometry and 0.836 m^2 water-cooled copper flame impingement surface are schematically shown in Fig. 1. Utility natural gas with a heating value of 53,326 kJ/kg was used in this study. All measurements in this study were obtained under steady state.

The impingement surface heat flux was measured with a single Vatell Corporation factory calibrated HFM-2 heat flux sensor mounted flush with the front side of the impingement surface. The HFM-2 utilizes 120 thermocouple pairs of platinum/platinum-rhodium wires. This 0.2 mm wide line sensor is sputter-deposited onto a 25.4 mm OD, 6.35 mm thick aluminum nitride substrate and secured within a specially designed copper block. The copper block is threaded into a hole near the center of the copper impingement surface. The depth of the HFM-2 sensing pattern is 2 μm, making it nearly invisible to any boundary layer flow across the sensor. Openings machined into the copper mounting block, allow the HFM-2 sensor to be cooled from the backside in an identical manner as the remainder of the flame impingement surface. Local heat flux values, q'', were normalized by the maximum possible average heat flux over the entire impingement surface. This maximum average heat flux was obtained by dividing the heating capability of the natural gas, q_f, by the impingement surface area, A. The resulting nondimensional heat flux is designated by q^*. This normalization procedure allows the data obtained in this study to be compared to other data obtained using different fuels and impingement surface sizes.

Error Analysis. Using the method of Kline and McClintock (1953), the minimum and maximum uncertainties for all of the reported heat flux values were 1.16 and 12.00 percent, respectively. The uncertainty in the equivalence ratio (based on metered air and fuel-flow rates) was 4.00 percent. Several runs at a between-nozzle spacing of S/R_o = 8.0 were conducted and averaged. This spacing was chosen because it provided the highest local heat flux to the impingement surface. The minimum and maximum standard deviations in local heat flux values were 0.49 and 12.93 percent of the mean heat flux values, respectively.

Results

Detailed experimental results such as impingement surface heat flux and temperature profiles, flame temperatures, and flame structure and appearance can be found in Mohr (1996). From previous results (Mohr et al., 1997), the ideal operating conditions for a single practical RJRC nozzle were identified. These conditions corresponded to a relatively high percent of heat transfer to the impingement surface, with a relatively low level of NO_x pollution formation. These were as follows: $\dot{m}_f$ = 0.0223 kg/min; Φ = 1.0, X_p/R_o = 1.18; and b = 3.68 mm. Based on D_f, the corresponding fuel Reynolds number was 8855, while the Reynolds number for the air flow at the nozzle exit, based on D_h, was 6700. For the nozzle pair data reported here, each nozzle was also operating under these same conditions. For all between-nozzle spacings considered in this work, the combined flames from the two nozzles were stable and blue in color, and very little soot deposition on the impingement surface was observed. The heat transfer to the impingement

[1]Drying Research Center, Department of Mechanical Engineering, Texas A&M University, College Station, Texas 77843-3123.
[2]jyagoobi@mengr.tamu
Contributed by the Heat Transfer Division of THE AMERICAN SOCIETY OF MECHANICAL ENGINEERS. Manuscript received by the Heat Transfer Division August 21, 1996; revision received March 3, 1997; Keywords: Combustion, Fire/Flames, Furnaces & Combustors. Associate Technical Editor: B. W. Webb.

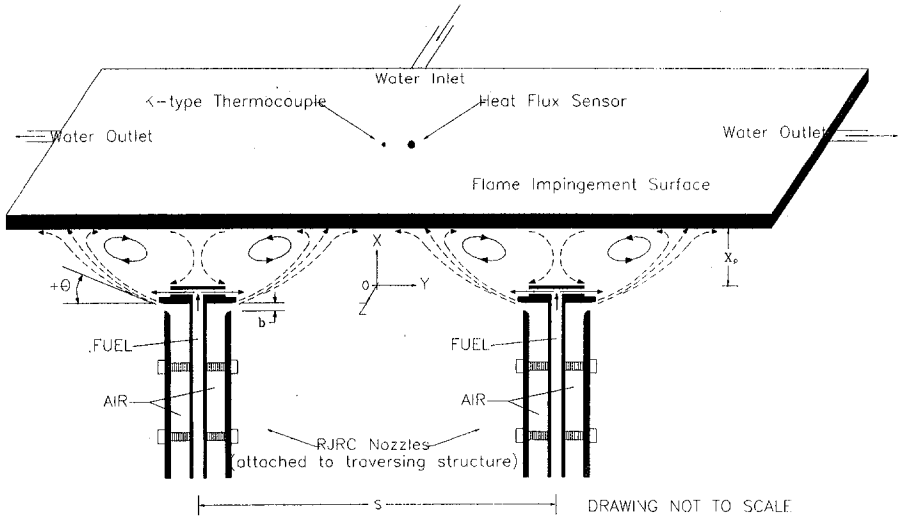

Fig. 1 RJRC nozzle pair geometry and flame impingement surface

surface by radiation was negligible since it was only a few percent of the total heat transfer (Mohr, 1996).

The measured local heat flux distributions along the impingement surface in the $\pm y$-directions are shown in Fig. 2. Note that the horizontal coordinate is such that $y/S = 0$ corresponds to the midpoint between the two nozzles. Also note that the nondimensional local heat flux values, q^*, were mostly greater than unity within the region of interest because the local heat flux, q'', was normalized by the maximum possible average heat flux over the entire impingement surface. Heat flux profiles at seven different between-nozzle spacings were obtained over the range of $5.0 < S/R_o < 11.0$. At the smallest spacing ($S/R_o = 5.0$), the heat flux profile is fairly uniform, but the measured heat fluxes are much lower than the values obtained at larger spacings. These lower heat fluxes are attributed to a change in aerodynamic structure, wherein the two flames combined to form an elliptic flame. The elliptic structure of the two combined flames at $S/R_o = 5.0$ is such that direct impingement of the flame on the surface is inhibited, providing a fairly low and uniform nondimensional surface heat flux, q^*, of 0.8–1.0 ($q'' = 30$–50 kW/m^2) between the nozzles. As the spacing was increased to $S/R_o = 5.5$, partial impingement of the flames upon the surface occurred, indicated by the higher peak heat flux at the midpoint between the nozzles.

An increase in the spacing to $S/R_o = 6.0$ shows a tremendous increase, both in the magnitude of the heat flux and in the nondimensional width of the high heat flux region between the nozzles. Therefore, a yet higher uniform heat flux around $y/S = 0$ is obtained by increasing the between-nozzle spacing from $S/R_o = 5.5$ to $S/R_o = 6.0$. Such a small change in between-nozzle spacing demonstrates the much greater sensitivity of reacting jets to between-nozzle spacing than is observed with nonreacting jets (Viskanta, 1993). By increasing the spacing between the nozzles, a greater volume is created wherein the combustion reactions can occur. Also, at these higher spacings, each individual jet is able to impinge upon the impingement surface prior to interaction with the other jet. This impingement interaction causes the slope of the heat flux profiles for $S/R_o = 6.0$, 7.0, and 8.0 to be flat near the measured peak heat flux for each profile. The large, peak heat flux values for $S/R_o = 6.0$, 7.0, and 8.0 are almost 50 percent higher than the measured local heat flux from a single nozzle operating under identical conditions as each of the nozzles used in this study (Mohr et al., 1997). This increase is attributed to the greater (twice) fuel input for the two nozzle system compared with the single nozzle. Whereas the total heat transfer to the impingement surface, q, was 6.4 kW with a single RJRC nozzle (Mohr et al., 1997), the total heat transfer was 11.0 kW with the RJRC nozzle pair. Therefore, doubling the fuel input with two nozzles did not correspond exactly with a doubling of the total heat transfer to the impingement surface. This effect is attributed to the fixed size of the impingement surface and the relative sizes of a small single RJRC flame and the larger combined flame of the RJRC nozzle pair. The high local heat flux for the moderately interacting RJRC flames ($6.0 < S/R_o < 9.0$), relative to the single RJRC nozzle is also attributed to the turbulent flow field between the moderately interacting jets. Turbulence has the effect of increasing the convection coefficient to the impingement surface as well as enhancing the mixing of the fuel with air.

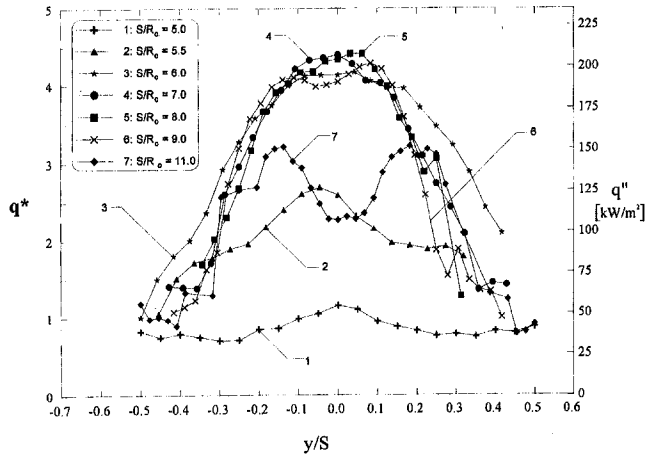

Fig. 2 Impingement surface heat flux distribution in the *y*-direction

A slight decrease in the nondimensional width of the high heat flux region is observed as the spacing is increased to $S/R_o = 9.0$. This profile differs from the previously discussed profiles in that two maxima are present in the profile. These maxima correspond to the point of impingement for each individual RJRC jet, and the peak local heat flux is lower than the peak of the $S/R_o = 7.0$ and 8.0 profiles. The slight "dip" in the heat flux profile still allows for a very uniform surface heating over a distance of $y/S \approx \pm 0.15$. The "dip" in the heat flux profile is much more pronounced at the wider spacing of $S/R_o = 11$, which also shows two narrower high heat flux regions and a much lower q^* value of 3.2 ($q'' = 150$ kW/m^2). While still showing weak interaction at $y/S = 0$, the two RJRC jets are

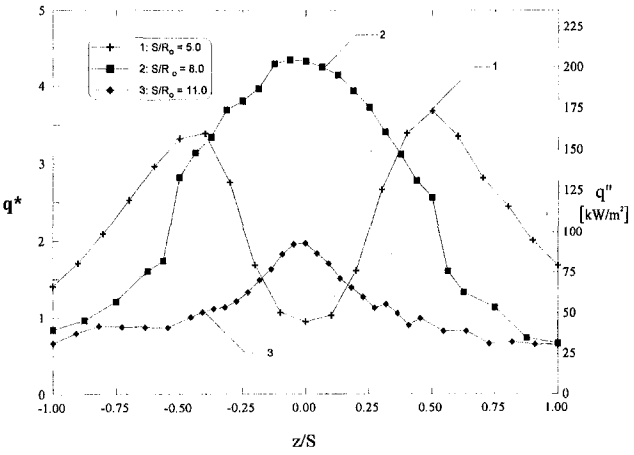

Fig. 3 Impingement surface heat flux distribution in the z-direction

operating, for the most part, independently of each other at $S/R_o = 11.0$. Previous data for a single RJRC nozzle showed the maximum local heat flux to be about $q'' = 140$ kW/m^2 (Mohr et al., 1997). These data show a similarity between the single nozzle data and the peak heat flux measured for the weakly interacting nozzle pair case of $S/R_o = 11.0$.

In order to give a more complete understanding of the interaction of the two flames, profiles of impingement surface heat flux were also obtained in the z-direction for highly, moderately, and weakly interacting flames. Figure 3 shows the nondimensional and actual local heat flux values as functions of between-nozzle spacing, S/R_o, and location along the impingement surface, z/S. In Fig. 3, for $S/R_o = 5.0$, the local heat flux is low at $z/S = 0.0$. At large values (positive and negative) of z, the heat flux increases nonlinearly to the measured maximum at $z/S = \pm 0.5$. The maximum heat flux values at $z/S = \pm 0.5$ mark the location of both sides of the elliptical flame created by the highly interacting flames at $S/R_o = 5.0$. This unique surface heat flux profile in the z-direction for $S/R_o = 5.0$ is attributed to the fact that the flames did not properly impinge on the surface.

Whereas a minimum in the heat flux profile of Fig. 3 was observed at $z/S = 0.0$ for the highly interacting flames ($S/R_o = 5.0$), maximums in the profiles for moderately interacting ($S/R_o = 8.0$) and weakly interacting ($S/R_o = 11.0$) flames are observed at $z/S = 0.0$. At these two, larger between-nozzle spacings, each RJRC flame jet impinges on the surface, interacts with the other jet, and then exits the zone of interaction in the z-direction. Because of this flow structure, the maximum heat flux in the z-direction for these two cases ($S/R_o = 8.0$ and $S/R_o = 11.0$) is measured at the midpoint between the two nozzles, corresponding to $z/S = 0.0$. As was the case in the y-direction, the maximum local heat flux in the z-direction along the impingement surface occurred when the nozzles were moderately interacting ($S/R_o = 8.0$).

Comparison of the heat flux profiles in the y and z-directions provides some additional insight into the capability of the RJRC nozzle pair to heat a surface. In the z-direction, very high heat fluxes were possible for both highly and moderately interacting flames, while relatively low heat fluxes were measured for weakly interacting flames. This result is in contrast to the y-direction profiles that showed high heat fluxes for moderately and weakly interacting flames, and low heat fluxes for the highly interacting case. Therefore, high heat fluxes in both the y and z-directions were achieved only when the flames were moderately interacting.

Based on the data from Figs. 2 and 3, it is possible to determine the desired between-nozzle spacing for the RJRC nozzle pair. Two different criteria must be considered in determining the desired spacing. First, uniformity of the heat flux profile along the impingement surface is an important consideration. In the y-direction, the most uniform profile occurred when the RJRC flames were highly interacting at $S/R_o = 5.0$, while the most uniform profile in the z-direction was measured for weakly interacting flames at $S/R_o = 11.0$. A second criteria used to determine the optimal spacing is the actual level of heat flux required for a particular process. Generally, a flame impingement process is used to provide very high heat flux to a surface. For the RJRC nozzle pair, the highest heat fluxes in both directions were achieved for the moderately interacting flames at a between-nozzle spacing of $S/R_o = 8.0$. In an industrial process with more than one row of RJRC nozzles, the surface to be heated will likely move along the z-direction. By properly staggering neighboring arrays (more than two consecutive arrays may be necessary) of RJRC nozzles in the z-direction, with each array operating at a between-nozzle spacing of $S/R_o = 8.0$, one would be able to provide high heat flux while improving the uniformity of surface heat flux profiles in the y and z-directions.

Flame temperatures measured in the y-direction for $S/R_o = 8.0$ showed a relatively uniform high temperature reaction zone near the impingement surface. The flame temperatures also showed the existence of a secondary flame jet formed by the gasses exiting the zone of interaction between the two nozzles. In the z-direction for $S/R_o = 8.0$, the flame temperatures remained high near the interaction zone of the two nozzles and then declined away from the nozzles. Among the flame temperature measurements, the highest flame temperatures recorded were approximately equal to 1,825°C, occurring primarily at 10 mm away from the impingement surface with $z/S = 0.0$ and $y/S = \pm 0.37$.

Acknowledgment

This research was partially supported by the Texas Hazardous Waste Research Center through the Gulf Coast Hazardous Substances Research Center and the Texas A&M University Drying Research Center.

References

Kline, S. J., and McClintock, F. A., 1953, "Describing Uncertainties in Single Sample Experiments," *Mechanical Engineering,* Vol. 75, pp. 3–8.

Mohr, J. W., 1996, "Studies of Single and Multiple Impinging Radial Jet Reattachment Flames," Ph.D. thesis, Texas A&M University, College Station, TX.

Mohr, J. W., Seyed-Yagoobi, J., and Page, R. H., 1996, "Combustion Measurements From an Impinging Radial Jet Reattachment Flame," *Combustion and Flame,* Vol. 106, No. 1–2, pp. 69–80.

Mohr, J. W., Seyed-Yagoobi, J., and Page, R. H., 1997, "Heat Transfer Characteristics of a Radial Jet Reattachment Flame," ASME JOURNAL OF HEAT TRANSFER, in press.

Page, R. H., Hadden, L. L., and Ostowari, C., 1989, "Theory for Radial Jet Reattachment Flow," *AIAA Journal,* Vol. 27, No. 11, pp. 1500–1505.

Thiele, E. W., Seyed-Yagoobi, J., Page, R. H., and Castillo-Garcia, H., 1995, "Enhancement of Drying Rate, Moisture Profiling, and Sheet Stability on an Existing Paper Machine with RJR Blow Boxes," *Proceedings of the TAPPI Papermakers Conference,* Chicago, IL, pp. 223–228.

Viskanta, R., 1993, "Heat Transfer to Impinging Isothermal Gas and Flame Jets," *Experimental Thermal and Fluid Science,* Vol. 6, pp. 111–134.

A Simple Analysis of Free Convection Film Boiling Around a Horizontal Elliptical Tube With Surface Tension

S.-A. Yang[1] and C.-H. Hsu[2]

Nomenclature

Bo = Bond number, $(\rho_l - \rho_v)ga^2/\sigma$
Cp_v = specific heat of vapor at constant pressure
e = eccentricity of ellipse, $\sqrt{1 - (b/a)^2}$
g = acceleration due to gravity
h_c = local convective heat transfer coefficient
h_{fg} = latent heat of vaporization
k_v = thermal conductivity of vapor
Nu, $\overline{\text{Nu}}$ = local and mean Nusselt number
Pr_v = Prandtl number of vapor, $Cp_v\mu_v/k_v$
l = length of vertical plate
y = boundary layer coordinate normal to the elliptical surface
δ_v = local thickness of vapor film
ΔT = $T_w - T_{\text{sat}}$ difference between wall temperature and saturated temperature
μ_l, μ_v = absolute viscosity of liquid, vapor
ρ_l, ρ_v = density of liquid, vapor
σ = surface tension coefficient
ϕ = the angle between the tangent to tube surface and the normal to direction of gravity

1 Introduction

Considerable analytical and experimental works have been performed in stable film boiling on external bodies. These include vertical plates (Bromley, 1950; Breen and Westwater, 1962), horizontal tubes (Bromley, 1950; Baumeister and Hamill, 1967; Sakurai et al., 1990) and other curved surfaces (Nakayama and Koyama, 1986). Although Nakayama and Koyama (1986) studied the film boiling from elliptical cylinders, however, they did not present the mean heat transfer result and excluded the surface tension effect.

In fact, a horizontal elliptical tube with its major axis aligned in a gravitational direction can serve to thin the boiling vapor film not only through surface tension (manifested by the curvature of the surface) but also through an increased effect of gravity as a result of placing a larger proportion of the boiling surface in line with the vertical. Owing to the reduction of vapor film thickness, the film boiling heat transfer is enhanced. Basically, the present note extends Bromley's analysis to the film boiling over an elliptical body by employing an eccentricity "e" of ellipse to unify the various geometrical configurations, such as a vertical plate ($e = 1$) and a circular tube ($e = 0$).

2 Analysis

Consider a horizontal elliptical tube, which is at its saturation temperature T_{sat}, with its major axis, $2a$, in the direction of gravity and minor axis, $2b$, situated in a quiescent liquid. The wall temperature T_w is uniform and above the saturation temperature. Thus, one may consider that film boiling occurs on the wall and a continuous film of the vapor runs upward over the tube by a gravitational buoyancy force.

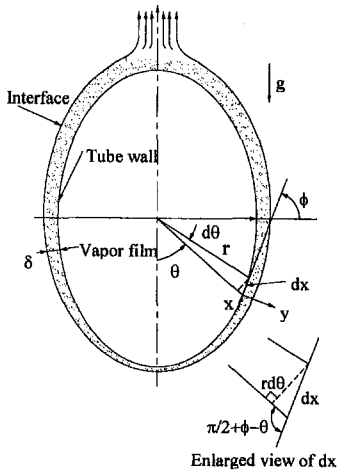

Fig. 1 Physical model and coordinate system

Fig. 1 shows the physical model and coordinate system under consideration. With the standard (Bromley, 1950) film boiling boundary layer assumptions, this leads to the following governing equations for the momentum and energy balance in the vapor film:

$$\mu_v \frac{\partial^2 u_v}{\partial^2 y_v} + g(\rho_l - \rho_v)[\sin\phi + \text{Bo}(\phi)] = 0 \qquad (1)$$

and

$$-k_v \frac{\partial T_v}{\partial y_v} = k_v \frac{\Delta T}{\delta_v} = \frac{2h'_{fg}\rho_v}{I_f(\phi)D_e}\frac{d}{d\phi}\left(\int_0^{\delta_v} u_v dy_v\right) \qquad (2)$$

where, $h'_{fg} = h_{fg} + 0.34\ Cp_v\Delta T$ is an effective latent heat corrected for the superheating effect in the vapor film. As derived in Yang and Chen (1993), $\text{Bo}(\phi)$ is the surface tension effect as follows:

$$\text{Bo}(\phi) = \frac{3e^2}{2\text{Bo}}\left(\frac{1 - e^2\sin^2\phi}{1 - e^2}\right)^2 \sin 2\phi. \qquad (3)$$

D_e is an equivalent diameter based on the same boiling surface area as follows:

$$D_e = \frac{2a}{\pi}\int_0^{\pi} [(1 - e^2)(1 - e^2\sin^2\phi)^{-3/2}]d\phi \qquad (4)$$

and

$$I_f(\phi) = \pi(1 - e^2\sin^2\phi)^{-3/2} \Big/ \int_0^{\pi} (1 - e^2\sin^2\phi)^{-3/2}d\phi. \qquad (5)$$

One-phase boundary layer analysis can be accomplished by two extreme boundary conditions, viz.: (i) no slip at the wall ($u_v = 0$, at $y_v = 0$), and (ii) zero interfacial shear ($\mu_v(\partial u_v/\partial y_v) = 0$ at $y_v = \delta_v$ if $\mu_l = 0$) or (ii) zero interfacial velocity ($u_v = 0$ at $y_v = \delta_v$ if $\mu_l = \infty$).

Now, using the following dimensionless variables:

$$y \equiv y_v\left(\frac{g\rho_v^2}{\mu_v^2 D_e}\right)^{1/4}; \quad \delta \equiv \delta_v\left(\frac{g\rho_v^2}{\mu_v^2 D_e}\right)^{1/4}$$

$$u \equiv u_v/\sqrt{gD_e} \quad \text{and} \quad \rho_r \equiv (\rho_l - \rho_v)/\rho_v$$

and the superheating parameter

[1] Department of Mold and Die Engineering, National Kaohsiung Institute of Technology, Kaohsiung 807, Taiwan: sayang@diemaking.nkit.edu.tw
[2] Department of Mold and Die Engineering, National Kaohsiung Institute of Technology, Kaohsiung 807, Taiwan.

Contributed by the Heat Transfer Division of THE AMERICAN SOCIETY OF MECHANICAL ENGINEERS. Manuscript received by the Heat Transfer Division January 6, 1997; revision received April 16, 1997; Keywords: Boiling; Natural Convection; Numerical Methods; Phase-Change Phenomena. Associate Technical Editor: M. Kaviany.

$$Sp \equiv \frac{Cp_v \Delta T}{h'_{fg} \mathrm{Pr}_v} \tag{6}$$

the governing equations may then become

$$\frac{\partial^2 u}{\partial^2 y} + \rho_r [\sin \phi + \mathrm{Bo}(\phi)] = 0 \tag{7}$$

and

$$\frac{2\delta}{I_f(\phi)} \frac{d}{d\phi} \left(\int_0^\delta u dy \right) = Sp \tag{8}$$

with the following boundary conditions:

$$\text{(i) } u = 0 \quad \text{at} \quad y = 0 \tag{9}$$

$$\text{(ii) } u = 0 \quad \text{at} \quad y = \delta \tag{10}$$

or

$$\frac{\partial u}{\partial y} = 0 \quad \text{at} \quad y = \delta. \tag{11}$$

In general, $0 < \mu_l < \infty$, i.e., the interfacial velocity and interfacial shear are different from zero. To reduce the two-phase boundary layer problem to one-phase boundary layer problem, we propose a simple model to deal with the interfacial condition and to include two extreme cases of interfacial conditions, i.e., boundary condition (ii) as follows:

$$(1 - \lambda) \frac{\partial u}{\partial y} + \lambda u = 0 \quad \text{at} \quad y = \delta \tag{12}$$

where λ is an index of liquid viscosity, e.g., $\lambda = 0$ indicates $\mu_l = 0$; $\lambda = 1.0$ indicates $\mu_l = \infty$. Note that for usual cases ($0 < \mu_l < \infty$), $0. < \lambda < 1.0$.

The solution for Eq. (7), to satisfy the above boundary conditions given by Eqs. (9) and (12), is

$$u = \rho_r [\sin \phi + \mathrm{Bo}(\phi)] \left[\left(\frac{1 - \lambda + 0.5\,\lambda\delta}{1 - \lambda + \lambda\delta} \right) y\delta - \frac{y^2}{2} \right]. \tag{13}$$

By substituting Eq. (13) into Eq. (8) and introducing

$$\delta^* \equiv \delta (\rho_r / Sp)^{1/4} \tag{14}$$

one obtains the resulting differential equation for the vapor film thickness:

$$\frac{\delta^*}{I_f(\phi)} \frac{d}{d\phi} \left\{ \delta^{*3} [\sin \phi + \mathrm{Bo}(\phi)] \times \left[\frac{1 - \lambda + \frac{\lambda}{2} \delta^* (Sp/\rho_r)^{1/4}}{1 - \lambda + \lambda\delta^* (Sp/\rho_r)^{1/4}} - \frac{1}{3} \right] \right\} = 1 \tag{15}$$

with the boundary condition

$$d\delta^*/d\phi = 0 \quad \text{at} \quad \phi = 0. \tag{16}$$

Further, the condition for the occurrence of the vapor film transforming into a thick vapor wake (separation point) is given by

$$\left(\frac{\partial u}{\partial y} \right)_{y=0} \leq 0 \quad \text{or} \quad \sin \phi_s + \mathrm{Bo}(\phi_S) = 0 \tag{17}$$

where ϕ_S is the angle of the separation point measured from the bottom of the elliptical tube.

The local heat transfer coefficient for the free-convection film boiling can be shown to be:

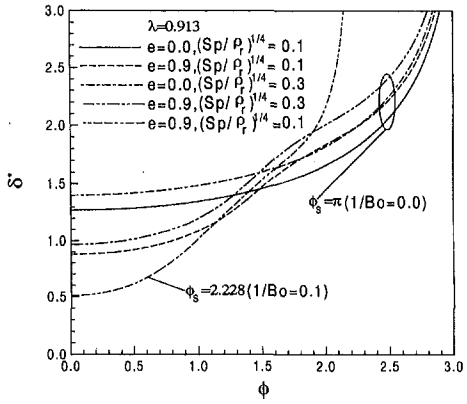

Fig. 2 Dimensionless local film thickness around periphery of ellipse

$$\mathrm{Nu} = \frac{h_c D_e}{k_v} = (\mathrm{Gr}/Sp)^{1/4}/\delta^* \tag{18}$$

where Gr is the Grashof number; $\mathrm{Gr} = D_e^3 g(\rho_l - \rho_v)\rho_v/\mu_v^2$.

The mean convective heat-transfer coefficient, given in the dimensionless form, can be determined from

$$\overline{\mathrm{Nu}}(\mathrm{Gr}/Sp)^{-1/4} = \int_0^{\phi_S} \frac{I_f(\phi)}{\delta^*} d\phi \Big/ \int_0^{\pi} I_f(\phi) d\phi. \tag{19}$$

It is noted that surface temperatures are usually high in film boiling and heat may be transferred by radiation too. Similar to Bromley (1950), one may propose the following approximation for combining the effects of convection and radiation:

$$h = h_c + 0.75\, h_r. \tag{20}$$

Here, h_r is the radiation coefficient and is calculated by assuming radiation between two infinite parallel plates with the liquid acting as a perfect black body as follows:

$$h_r = \sigma_s \epsilon \left[\frac{T_w^4 - T_{\mathrm{sat}}^4}{T_w - T_{\mathrm{sat}}} \right] \tag{21}$$

where σ_S is the Stefan-Boltzman constant and ϵ is the emissivity of the heating surface. Besides, Sakurai et al. (1990) also presented a general correlation for pool boiling heat transfer from a horizontal cylinder including radiation contributions.

3 Results and Discussion

3.1 Film Thickness Distribution. Characteristics of film flow of boiling vapor can be seen in Fig. 2, which is obtained from Eq. (15) by employing a fourth-order Runge-Kutta integration that uses a step size of $\Delta\phi = 0.05$ deg. As e is ap-

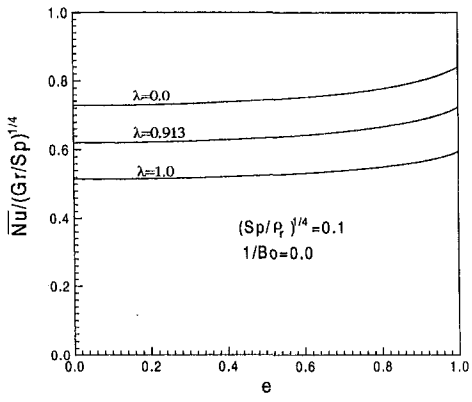

Fig. 3 Effect of liquid viscosity index λ on dimensionless mean heat transfer coefficient for various eccentricities of ellipse

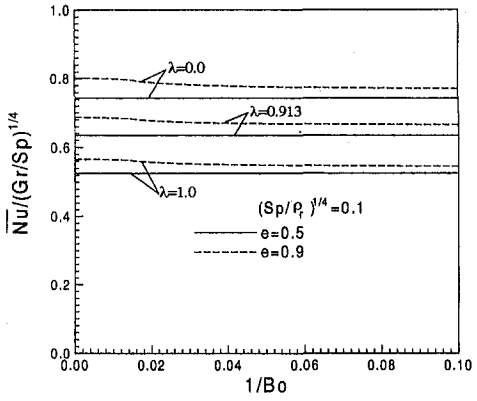

Fig. 4 Effect of surface tension on dimensionless mean heat transfer coefficient

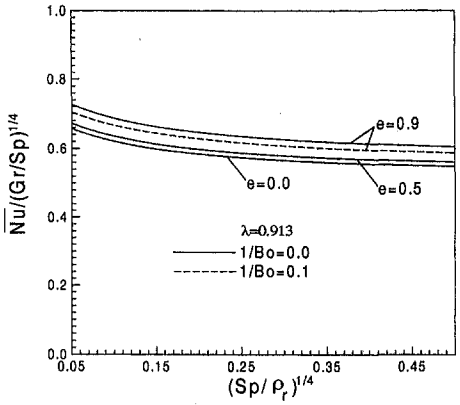

Fig. 5 Effect of superheating on dimensionless mean heat transfer coefficient

proaching unity, δ^* is becoming thinner in the lower half of the tube due to the favorable surface tension effect (pressure gradient), while δ^* is becoming thicker in the rear half of the tube due to the adverse surface tension effect. Meanwhile, owing to the surface tension effect, the vapor film will separate at smaller ϕ_s in the rear half of the elliptical tube. For example, the separation angle ϕ_S for $e = 0.9$ and $1/\mathrm{Bo} = 0.1$ is 2.228 rad. Comparing various cases of $(Sp/\rho_r)^{1/4}$, one may see that, for a larger degree of superheating, the film of boiling vapor becomes thicker in the rear half of the tube.

3.2 Mean Nusselt Number: Effect of λ and *e*. Fig. 3 shows that for the case of $(Sp/\rho_r)^{1/4} = 0.1$ and $1/\mathrm{Bo} = 0$, the mean Nusselt number is varying with λ and is increasing with e. It is found that when $\lambda = 0.913$ and $e = 0$ (circular tube), $\overline{\mathrm{Nu}}(\mathrm{Gr}/Sp)^{-1/4} = 0.62$, which is the same mean value of Bromley's (1950) experimental data. Compared with circular tube at the same condition, the mean heat transfer of elliptical tube is enhanced by about a 16.65 percent increase as e is approaching unity. It is to be noted that when $e = 1$ (vertical plate), one should use $D_e = 2l/\pi$ in Gr and obtain 0.943 for $\lambda = 0$ (zero interfacial shear); $\overline{\mathrm{Nu}}(\mathrm{Gr}/Sp)^{-1/4} = 0.665$ for $\lambda = 1.0$ (zero interfacial velocity) almost coincides with those obtained from Bromley (1950).

3.3 Mean Nusselt Number: Effect of Surface Tension. Fig. 4 indicates the effect of surface tension on the dimensionless mean heat transfer coefficient. For small values of e, it is obvious that the surface tension effect is almost negligible. For large values of e (about 0.9), the influence of surface tension on the mean Nusselt number is more significant but is still small. When $e = 0.9$ the mean Nusselt number is reduced by about 2.94 percent as $1/\mathrm{Bo}$ increases from 0 to 0.1.

3.4 Mean Nusselt Number: Effect of Vapor Superheating. As seen in Fig. 5, the larger the degree of superheating, the more the mean heat transfer reduces. The cause for this is that the thickness of vapor film is increased with the increase of superheating degree. Such a decrease in mean heat transfer is similar to that obtained from Nishikawa and Ito (1966) by employing a two-phase boundary layer analysis.

4 Concluding Remarks

1 The present solutions are accurate for elliptical tubes with intermediate diameters. However, for very large or small tubes, the result should be modified by adopting the Breen and Westwater (1962) model.

2 The present note is quite straightforward and is easily applied to a first approximation for film boiling on an inclined tube since a vertical plane passing through a circular tube yields an ellipse.

3 In the present analysis, the surface tension effect has been given first to the film boiling heat transfer from elliptical tubes.

References

Baumeister, K. J., and Hamill, T. D., 1967, "Film Boiling From a Thin Wire as an Optimal Boundary-Value Process," ASME Paper No. 67-HT-62.

Breen, B. P., and Westwater, J. W., 1962, "Effect of Diameter of Horizontal Tubes on Film Boiling Heat Transfer," *Chemical Engineering Progress,* Vol. 58, pp. 67–72.

Bromley, L. A., 1950, "Heat Transfer in Stable Film Boiling," *Chemical Engineering Progress,* Vol. 46, pp. 221–227.

Nakayama, A., and Koyama, H., 1986, "An Integral Method in Laminar Film Pool Boiling From Curved Surfaces," ASME JOURNAL OF HEAT TRANSFER, Vol. 108, pp. 490–493.

Nishikawa, K., and Ito, T., 1966, "Two-Phase Boundary-Layer Treatment of Free-Convective Film Boiling," *International Journal Heat and Mass Transfer,* Vol. 9, pp. 103–115.

Sakurai, A., Shiotsu, M., and Hata, K., 1990, "A General Correlation for Pool Film Boiling Heat Transfer From a Horizontal Cylinder to Subcooled Liquid: Part 1-A—Theoretical Pool Film Boiling Heat Transfer Model Including Radiation Contributions and Its Analytical Solution," ASME JOURNAL OF HEAT TRANSFER, Vol. 112, pp. 430–440.

Yang, S. A., and Chen, C. K., 1993, "Role of Surface Tension and Ellipticity in Laminar Film Condensation on A Horizontal Elliptical Tube," *International Journal Heat and Mass Transfer,* Vol. 36, No. 12, pp. 3135–3141.

A Note on Unsteady Hydromagnetic Free Convection From a Vertical Fluid Saturated Porous Medium Channel

A. J. Chamkha[1]

Nomenclature

B_0 = magnetic induction
C = inertia coefficient for porous medium
C_f = skin friction coefficient at heated wall

[1] Department of Mechanical and Industrial Engineering, Kuwait University, PO Box 5969, Safat 13060, Kuwait: chamkha@kuc01.kuniv.edu.kw

Contributed by the Heat Transfer Division of THE AMERICAN SOCIETY OF MECHANICAL ENGINEERS. Manuscript received by the Heat Transfer Division February 6, 1996; revision received April 14, 1997; Keywords: Natural Convection; Porous Media; Transient & Unsteady Heat Transfer. Associate Technical Editor: K. Vafai.

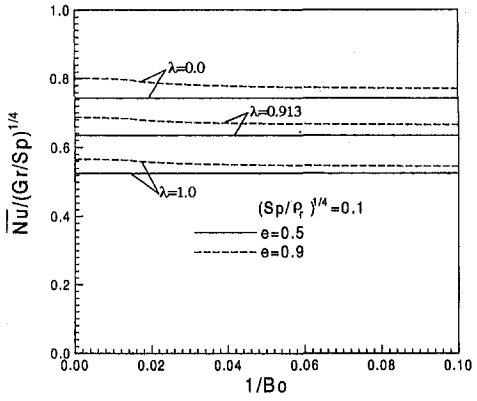

Fig. 4 Effect of surface tension on dimensionless mean heat transfer coefficient

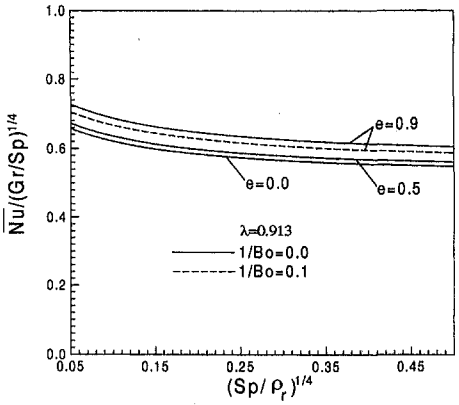

Fig. 5 Effect of superheating on dimensionless mean heat transfer coefficient

proaching unity, δ^* is becoming thinner in the lower half of the tube due to the favorable surface tension effect (pressure gradient), while δ^* is becoming thicker in the rear half of the tube due to the adverse surface tension effect. Meanwhile, owing to the surface tension effect, the vapor film will separate at smaller ϕ_s in the rear half of the elliptical tube. For example, the separation angle ϕ_S for $e = 0.9$ and $1/\mathrm{Bo} = 0.1$ is 2.228 rad. Comparing various cases of $(Sp/\rho_r)^{1/4}$, one may see that, for a larger degree of superheating, the film of boiling vapor becomes thicker in the rear half of the tube.

3.2 Mean Nusselt Number: Effect of λ and *e*. Fig. 3 shows that for the case of $(Sp/\rho_r)^{1/4} = 0.1$ and $1/\mathrm{Bo} = 0$, the mean Nusselt number is varying with λ and is increasing with e. It is found that when $\lambda = 0.913$ and $e = 0$ (circular tube), $\overline{\mathrm{Nu}}(\mathrm{Gr}/Sp)^{-1/4} = 0.62$, which is the same mean value of Bromley's (1950) experimental data. Compared with circular tube at the same condition, the mean heat transfer of elliptical tube is enhanced by about a 16.65 percent increase as e is approaching unity. It is to be noted that when $e = 1$ (vertical plate), one should use $D_e = 2l/\pi$ in Gr and obtain 0.943 for $\lambda = 0$ (zero interfacial shear); $\overline{\mathrm{Nu}}(\mathrm{Gr}/Sp)^{-1/4} = 0.665$ for $\lambda = 1.0$ (zero interfacial velocity) almost coincides with those obtained from Bromley (1950).

3.3 Mean Nusselt Number: Effect of Surface Tension. Fig. 4 indicates the effect of surface tension on the dimensionless mean heat transfer coefficient. For small values of e, it is obvious that the surface tension effect is almost negligible. For large values of e (about 0.9), the influence of surface tension on the mean Nusselt number is more significant but is still small. When $e = 0.9$ the mean Nusselt number is reduced by about 2.94 percent as $1/\mathrm{Bo}$ increases from 0 to 0.1.

3.4 Mean Nusselt Number: Effect of Vapor Superheating. As seen in Fig. 5, the larger the degree of superheating, the more the mean heat transfer reduces. The cause for this is that the thickness of vapor film is increased with the increase of superheating degree. Such a decrease in mean heat transfer is similar to that obtained from Nishikawa and Ito (1966) by employing a two-phase boundary layer analysis.

4 Concluding Remarks

1 The present solutions are accurate for elliptical tubes with intermediate diameters. However, for very large or small tubes, the result should be modified by adopting the Breen and Westwater (1962) model.

2 The present note is quite straightforward and is easily applied to a first approximation for film boiling on an inclined tube since a vertical plane passing through a circular tube yields an ellipse.

3 In the present analysis, the surface tension effect has been given first to the film boiling heat transfer from elliptical tubes.

References

Baumeister, K. J., and Hamill, T. D., 1967, "Film Boiling From a Thin Wire as an Optimal Boundary-Value Process," ASME Paper No. 67-HT-62.

Breen, B. P., and Westwater, J. W., 1962, "Effect of Diameter of Horizontal Tubes on Film Boiling Heat Transfer," *Chemical Engineering Progress,* Vol. 58, pp. 67–72.

Bromley, L. A., 1950, "Heat Transfer in Stable Film Boiling," *Chemical Engineering Progress,* Vol. 46, pp. 221–227.

Nakayama, A., and Koyama, H., 1986, "An Integral Method in Laminar Film Pool Boiling From Curved Surfaces," ASME JOURNAL OF HEAT TRANSFER, Vol. 108, pp. 490–493.

Nishikawa, K., and Ito, T., 1966, "Two-Phase Boundary-Layer Treatment of Free-Convective Film Boiling," *International Journal Heat and Mass Transfer,* Vol. 9, pp. 103–115.

Sakurai, A., Shiotsu, M., and Hata, K., 1990, "A General Correlation for Pool Film Boiling Heat Transfer From a Horizontal Cylinder to Subcooled Liquid: Part 1-A—Theoretical Pool Film Boiling Heat Transfer Model Including Radiation Contributions and Its Analytical Solution," ASME JOURNAL OF HEAT TRANSFER, Vol. 112, pp. 430–440.

Yang, S. A., and Chen, C. K., 1993, "Role of Surface Tension and Ellipticity in Laminar Film Condensation on A Horizontal Elliptical Tube," *International Journal Heat and Mass Transfer,* Vol. 36, No. 12, pp. 3135–3141.

A Note on Unsteady Hydromagnetic Free Convection From a Vertical Fluid Saturated Porous Medium Channel

A. J. Chamkha[1]

Nomenclature

B_0 = magnetic induction
C = inertia coefficient for porous medium
C_f = skin friction coefficient at heated wall

[1] Department of Mechanical and Industrial Engineering, Kuwait University, PO Box 5969, Safat 13060, Kuwait: chamkha@kuc01.kuniv.edu.kw

Contributed by the Heat Transfer Division of THE AMERICAN SOCIETY OF MECHANICAL ENGINEERS. Manuscript received by the Heat Transfer Division February 6, 1996; revision received April 14, 1997; Keywords: Natural Convection; Porous Media; Transient & Unsteady Heat Transfer. Associate Technical Editor: K. Vafai.

Da = Darcy number, $K/(\epsilon H^2)$
F = dimensionless fluid vertical velocity
g = gravitational acceleration
Gr = Grashof number, $CK^{3/2}\rho^2 g\beta\Delta T/\mu^2$
H = channel width
K = permeability of porous medium
M = Hartmann number, $B_0 H(\epsilon\sigma/\mu)^{1/2}$
Nu = Nusselt number
Pr = Prandtl number, $\mu/(\rho\alpha_e)$
r_v = dimensionless suction or injection velocity, $\mu V_w/(\epsilon\rho g\beta H^2\Delta T)$
R_w = wall Reynold's number, $\rho V_w H/(\epsilon\mu)$
t = time
T = dimensional fluid temperature
T_0 = unheated wall temperature
u = dimensional vertical velocity
v = dimensional horizontal velocity
V_w = suction or injection velocity
x, y = Cartesian coordinates as shown on Fig. 1

Greek symbols

α_e = effective thermal diffusivity
β = coefficient of thermal expansion
ΔT = temperature increase
ϵ = porosity of porous medium
η = dimensionless horizontal distance
μ = fluid dynamic viscosity
ρ = fluid density
σ = fluid electrical conductivity
τ = dimensionless time
θ = dimensionless fluid temperature

Introduction

Increasingly in the past decade there has been considerable interest in investigating free convection flows in porous media (see, for instance, Nakayama et al., 1990; Chen and Lin, 1995). This interest stems from various industrial applications such as thermal insulation systems, enhanced oil recovery, regenerative heat exchangers, petroleum reservoirs, geothermal reservoirs, and filtration. Also, there has been a renewed interest in studying the magnetohydrodynamic effects on free convection of electrically conducting fluids from surfaces embedded in porous and nonporous media (see, for instance, Pop and Watanabe, 1994; Aldoss et al., 1995).

The transient phenomena of such flows has also been the subject of many investigators. For example, Ingham and Brown (1986) reported series expansion solutions for the problem of transient free convection on a suddenly heated vertical plate in a porous medium, respectively. Recently, Chen et al. (1989) and Nakayama et al. (1990) considered similar flat plate problems with non-Darcy porous medium inertial effects. More recently, the most fundamental problem of transient non-Darcy free convection between vertical impermeable plates in a fluid saturated porous medium with suddenly heated and suddenly cooled walls was treated by Nakayama et al. (1993). They reported closed-form approximate solutions for small and large times as well as numerical solutions for the intermediate times.

It is of interest in this paper to consider the problem discussed by Nakayama et al. (1993) (with only one of the walls subjected to sudden change in temperature) to study the effects of suction and injection at the walls as well as the influence of the presence of a magnetic field force normal to the direction of motion on the flow and heat transfer characteristics of the problem. It is assumed that the fluid is incompressible and electrically conducting. In addition, the magnetic Reynolds number is assumed small so that the induced magnetic field is neglected.

Problem Formulation

Consider transient hydromagnetic buoyancy induced flow and heat transfer through a vertical fluid saturated porous medium channel of infinite extent and having a width of H. Initially, both the channel walls as well as the porous medium are kept at the same temperature T_0. One of the channel walls is then suddenly heated by a temperature increase ΔT while the temperature of the other wall is kept unchanged. Uniform fluid suction and injection are imposed at the left side and right-side channel walls, respectively. Due to the sudden heating of the left-side channel surface, a fluid vertical motion is induced due to density gradients causing a buoyancy force. As the flow is induced, a magnetic field of uniform strength B_0 is applied normal to the flow direction. Let the x-axis be directed upwards along the channel walls and the y-axis be normal to it. The porous medium is assumed to have uniform porosity and permeability. The dimensionless governing equations and initial and boundary conditions can be written as (see, Vafai and Tien, 1981; Nakayama et al., 1993; Chen and Lin, 1995)

$$\frac{\partial F}{\partial \tau} - \Pr\frac{\partial^2 F}{\partial \eta^2} - \Pr R_w\frac{\partial F}{\partial \eta} + \Pr\left(M^2 + \frac{1}{\mathrm{Da}}\right)F + \frac{\mathrm{Gr}}{\mathrm{Da}^2}\Pr F\sqrt{F^2 + r_v^2} - \Pr\theta = 0 \quad (1)$$

$$\frac{\partial \theta}{\partial \tau} - \frac{\partial^2 \theta}{\partial \eta^2} - \Pr R_w\frac{\partial \theta}{\partial \eta} = 0 \quad (2)$$

$$F(0, \eta) = 0, \quad \theta(0, \eta) = 0, \quad F(\tau, 0) = 0,$$
$$\theta(\tau, 0) = 1, \quad F(\tau, 1) = 0, \quad \theta(\tau, 1) = 0 \quad (3a\text{–}f)$$

where

$$\tau = \alpha_e t/H^2, \quad \eta = Y/H, \quad F = \mu u/(\epsilon\rho g\beta H^2\Delta T),$$
$$\theta = (T - T_0)/\Delta T, \quad \Pr = \mu/(\rho\alpha_e),$$
$$R_w = \rho V_w H/(\epsilon\mu), \quad \mathrm{Da} = K/(\epsilon H^2),$$
$$\mathrm{Gr} = CK^{3/2}\rho^2 g\beta\Delta T/\mu^2, \quad M^2 = \epsilon\sigma B_0^2 H^2/\mu, \quad \text{and}$$
$$r_v = \mu V_w/(\epsilon\rho g\beta H^2\Delta T)$$

are the dimensionless time, vertical distance, fluid velocity and temperature, the Prandtl number, wall Reynold's number, Darcy's number, Grashof number, square of the Hartmann number, and dimensionless suction velocity, respectively.

Important physical parameters for this type of flow are the skin-friction coefficient and the wall heat transfer at the heated wall (herein called the Nusselt number). These are defined in dimensionless form as

$$C_f = \frac{\partial F}{\partial \eta}(\tau, 0), \quad \mathrm{Nu} = -\frac{\partial \theta}{\partial \eta}(\tau, 0). \quad (4a, b)$$

Steady-State Solutions. For sufficiently large time, the dependent variables of the problem will no longer change with time, and the flow is assumed to have reached steady-state conditions. In the absence of inertial porous medium effects (sometimes called Forchheimer effects), that is for slow flow, a closed form solution of the governing equations is possible. The neglect of the porous medium inertial effects ($C = 0$) causes the Grashof number to vanish. It should be noted that setting $\mathrm{Gr} = 0$ does not only mean slow flow ($C = 0$) but it can also mean that the flow is not dominated by natural convection since $\Delta T = 0$ in this case. Therefore, the steady-state Darcian flow and heat transfer problem becomes

$$F'' + R_w F' - \left(M^2 + \frac{1}{\mathrm{Da}}\right)F - \theta = 0 \quad (5)$$

$$\theta'' + \Pr R_w\theta' = 0 \quad (6)$$

$$F(0) = 0, \quad F(1) = 0, \quad \theta(0) = 1, \quad \theta(1) = 0 \quad (7a\text{–}d)$$

where a prime denotes ordinary differentiation with respect to η.

Without going into detail, it can be shown that Eqs. (5) and (6), subject to Eqs. (7), have the following solutions:

$$\theta = C_1 + C_2 \exp(-\mathrm{Pr}R_w\eta) \tag{8}$$

$$F = A + B\exp(-\mathrm{Pr}R_w\eta) + C_3\exp(\lambda_1\eta) + C_4\exp(\lambda_2\eta) \tag{9}$$

where

$$\lambda_1 = \frac{-R_w + \left(R_w^2 + 4\left(M^2 + \frac{1}{\mathrm{Da}}\right)\right)^{1/2}}{2},$$

$$\lambda_2 = \frac{-R_w - \left(R_w^2 + 4\left(M^2 + \frac{1}{\mathrm{Da}}\right)\right)^{1/2}}{2} \tag{10a, b}$$

$$C_1 = \frac{-\exp(-\mathrm{Pr}R_w)}{1 - \exp(-\mathrm{Pr}R_w)}, \quad C_2 = \frac{1}{1 - \exp(-\mathrm{Pr}R_w)},$$

$$A = \frac{C_1}{M^2 + \frac{1}{\mathrm{Da}}}$$

$$B = \frac{C_2}{\mathrm{Pr}R_w(1 - \mathrm{Pr}) + M^2 + \frac{1}{\mathrm{Da}}},$$

$$C_3 = \frac{A(\exp(\lambda_2) - 1) + B(\exp(\lambda_2) - \exp(-\mathrm{Pr}R_w))}{\exp(\lambda_1) - \exp(\lambda_2)}$$

$$C_4 = \frac{A(\exp(\lambda_1) - 1) + B(\exp(\lambda_1) - \exp(-\mathrm{Pr}R_w))}{\exp(\lambda_2) - \exp(\lambda_1)}. \tag{11a–f}$$

Some special limiting cases can now be obtained. For the case of impermeable walls ($R_w = 0$), the steady-state solutions become

$$\theta = 1 - \eta \tag{12}$$

$$F = \frac{1}{m^2}\left(1 - \eta - \frac{\sinh(m(1 - \eta))}{\sinh(m)}\right),$$

$$m = \left(M^2 + \frac{1}{\mathrm{Da}}\right)^{-1/2} \tag{13a, b}$$

$$C_f = \frac{1}{m^2}(m\coth(m) - 1), \quad \mathrm{Nu} = 1 \tag{14a, b}$$

where these solutions reduce exactly to those reported by Nakayama et al. (1993) in the absence of the magnetic field ($M = 0$). In addition, the closed-form solutions reported in this section were compared favorably with some of the analytical solutions given by Vafai and Kim (1989) and some of those reported later by Nield et al. (1996) for forced convection in porous medium channel with various thermal boundary conditions. It should be mentioned that the form of the analytical solutions reported herein does not compare directly with those of Nield et al. (1996) because the free convection effect (θ in Eq. (5)) must be dropped out.

Time-Dependent Solutions. It is possible to obtain a closed-form solution for the dimensionless energy equation (2) subject to the corresponding initial and boundary conditions (3*b*, *d*, *f*) by the separation of variables method. This can be shown to be

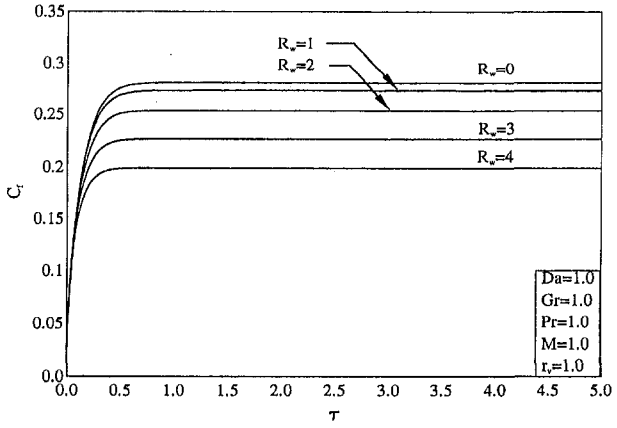

Fig. 1 Effects of R_w on temporal development of skin friction

$$\theta(\tau, \eta) = \frac{\exp(-\mathrm{Pr}R_w(\eta - 1)) - 1}{\exp(\mathrm{Pr}R_w) - 1} - 2\sum_{n=1}^{\infty}\frac{n\pi}{\lambda_n^2}\exp\left(\frac{-\mathrm{Pr}R_w}{2}\eta - \lambda_n^2\tau\right)\sin(n\pi\eta) \tag{15}$$

where $\lambda_n^2 = n^2\pi^2 + (\mathrm{Pr}R_w/2)^2$ are the square Eigenvalues for this problem. As the wall Reynolds number R_w approaches zero, the solution for $\theta(\tau, \eta)$ given by Nakayama et al. (1993) for impermeable walls is recovered.

Equation (15) leads to the following transient development solution of the Nusselt number:

$$\mathrm{Nu}(\tau) = \frac{\mathrm{Pr}R_w\exp(\mathrm{Pr}R_w)}{\exp(\mathrm{Pr}R_w) - 1} + 2\sum_{n=1}^{\infty}\frac{n^2\pi^2}{\lambda_n^2}\exp(-\lambda_n^2\tau) \tag{16}$$

which is also consistent with that given by Nakayama et al. (1993) for $R_w = 0$.

Equation (1) governing the flow or the velocity development in the porous medium channel is nonlinear and must be solved numerically. The standard, implicit, iterative, tridiagonal finite-difference method discussed by Blottner (1970) is employed herein for the solution of the whole initial-value problem. The exact solutions reported earlier served as a vehicle for calibration of the numerical solutions. The computational domain was divided up into 201 nodes in the η direction and 301 nodes in the τ direction. Constant η step sizes ($\Delta\eta = 0.005$) and variable τ step sizes ($\Delta\tau_1 = 0.01$ with a growth factor of 1.01) were employed in the present work. These step sizes were chosen after many numerical experimentations to assess grid independence.

Figures 1 and 2 present transient skin friction and Nusselt number profiles for various values of the wall Reynold's number R_w, respectively. As the wall Reynold's number increases, that is increasing the injection at the right-side wall and the suction at the left-side wall, a distinctive peak in the velocity profile similar to that reported by Chamkha (1994), starts to form close to the left-side wall and the volumetric flow rate up the channel decreases. This is obvious since as the fluid is injected into the channel; a force normal to the flow direction is created which tends to push the fluid particles towards the left-side wall causing the fluid to slow down and the boundary friction to reduce. This is clearly shown in Fig. 1. For the case of $R_w = 0$ (impermeable walls), the temperature profile is linear, as shown by the closed-form solution reported earlier (Eq. (12)). However, as the suction (or injection) is increased, a faster decay in temperature from the left-side hot wall to the right-side wall is observed. This fast decay in temperature causes the slope of the temperature profile at the hot wall to increase, which results

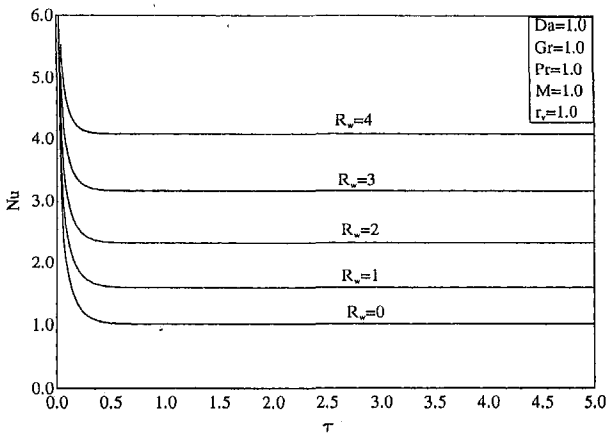

Fig. 2 Effects of R_w on temporal development of skin friction

in an increase in the Nusselt number, as clearly evident from Fig. 2. It should be mentioned that in obtaining the results associated with $R_w = 0$, r_v is set to zero since both of the parameters R_w and r_v are related to V_w. Thus, when $V_w = 0$, then both R_w and r_v must be zero.

Conclusion

The problem of unsteady hydromagnetic non-Darcy free convection from a fluid saturated porous medium supported by two infinitely long porous vertical plates is considered. One of the plates is suddenly heated while the other is maintained at the initial temperature. Fluid suction and injection are imposed at the hot and other wall, respectively. The mathematical model accounts for non-Darcy inertial effects of the porous medium and for the Hartmann effects of Magnetohydrodynamics. Several closed form and limiting solutions were obtained under steady-state conditions. In addition, the energy equation, which is independent of the flow equations, was solved analytically by the separation of variables method. The full initial-value problem was solved numerically by an implicit, tridiagonal, finite-difference methodology. Few of the obtained results were illustrated graphically to show special features of the solutions.

References

Aldoss, T., Al-Nimr, M., Jarrah, M., and Al-Sha'er, B., 1995, "Magnetohydrodynamic Mixed Convection From a Vertical Plate Embedded in a Porous Medium," *Numerical Heat Transfer,* Part A, Vol. 28, pp. 635–645.

Blottner, F., 1970, "Finite Difference Methods of Solutions of the Boundary-Layer Equations," *AIAA J.,* Vol. 8, pp. 193–205.

Chamkha, A., 1994, "Transient Power-Law Fluid Flow in a Porous Medium Channel," *Fluid/Particle Separation Journal,* Vol. 7, pp. 4–7.

Chen, C., and Lin, C., 1995, "Natural Convection From an Isothermal Vertical Surface Embedded in a Thermally Stratified High-Porosity Medium," *Int. J. Engng. Sci.,* Vol. 33, pp. 131–138.

Chen, C.-K., Hung, C.-I., and Horng, H.-C., 1989, "Transient Natural Convection on a Vertical Flat Plate Embedded in a High-Porosity Medium," ASME JOURNAL OF HEAT TRANSFER, Vol. 109, pp. 112–118.

Ingham, D. B., and Brown, S. N., 1986, "Flow Past a Suddenly Heated Vertical Plate in a Porous Medium," *Proc. R. Soc. Lond.,* Vol. A403, pp. 51–80.

Nakayama, A., Kokudai, T., and Koyama, H., 1990, "Non-Darcy Boundary Layer Flow and Forced Convective Heat Transfer Over a Flat Plate in a Fluid-Saturated Porous Medium," ASME JOURNAL OF HEAT TRANSFER, Vol. 112, pp. 157–162.

Nakayama, A., Kuwahara, F., and Koyama, H., 1993, "Transient Non-Darcy Free Convection Between Parallel Vertical Plates in a Fluid Saturated Porous Medium," *Appl. Sci. Res.,* Vol. 50, pp. 29–42.

Nield, D. A., Junqueira, S. L. M., and Lage, J. L., 1996, "Forced Convection in a Fluid-Saturated Porous-Medium Channel With Isothermal or Isoflux Boundaries," *J. Fluid Mech.,* Vol. 322, pp. 201–214.

Pop, I., and Watanabe, T., 1994, "Hall Effects on Magnetohydrodynamic Free Convection About a Semi-Infinite Vertical Flat Plate," *Int. J. Engng Sci.,* Vol. 32, pp. 1903–1911.

Vafai, K., and Tien, C. L., 1981, "Boundary and Inertia Effects on Flow and Heat Transfer in Porous Media," *Int. J. Heat Mass Transfer,* Vol. 24, pp. 195–203.

Vafai, K., and Kim, S. J., 1989, "Forced Convection in a Channel Filled With a Porous Medium: An Exact Solution," ASME JOURNAL OF HEAT TRANSFER, Vol. 111, pp. 1103–1106.

Interaction of Surface Radiation and Free Convection in an Enclosure With a Vertical Partition

K. Sri Jayaram[1], C. Balaji[2], and S. P. Venkateshan[3]

Nomenclature

A = aspect ratio, H/d
d = total width of the enclosure, m
F_{ij} = diffuse view factor between area elements i and j
g = acceleration due to gravity, m/s^2
H = height of the enclosure, m
J = radiosity of wall element, W/m^2
k = thermal conductivity of the fluid, $W/m \cdot K$
N_{RC} = radiation conduction interaction parameter, $\sigma T_H^4 d/[k(T_H - T_C)]$
Nu = local Nusselt number based on d (bar indicates the mean value, appropriate subscript indicates convective or radiative as the case may be), $qd/[k(T_H - T_C)]$
Pr = Prandtl number of the fluid, ν/α
q = heat flux, W/m^2
Ra = Rayleigh number based on d, $g\beta(T_H - T_C)d^3/(\nu\alpha)$
T = temperature, K
T_R = temperature ratio, T_C/T_H
x = vertical coordinate, m
X = dimensionless vertical coordinate, x/d
y = horizontal coordinate, m
Y = dimensionless horizontal coordinate, y/d
W = vorticity, s

Greek Symbols

α = thermal diffusivity of the fluid, m^2/s
β = coefficient of expansion, $1/K$
ϵ = total hemispherical emissivity
ν = kinematic viscosity of the fluid, m^2/s
ϕ = dimensionless temperature, $(T - T_C)/(T_H - T_C)$
ψ' = stream function, m^2/s
ψ = nondimensional stream function, ψ'/α

[1] Research Scholar, Heat Transfer and Thermal Power Laboratory, Department of Mechanical Engineering, Indian Institute of Technology, Madras 600 036, India.

[2] Senior Project Manager, National Institute of Ocean Technology, Indian Institute of Technology, Madras 600 036.

[3] Professor, Heat Transfer and Thermal Power Laboratory, Department of Mechanical Engineering, Indian Institute of Technology, Madras 600 036, India: mech3@iitm.ernet.in

Contributed by the Heat Transfer Division of THE AMERICAN SOCIETY OF MECHANICAL ENGINEERS. Manuscript received by the Heat Transfer Division January 19, 1996; revision received February 14, 1997; Keywords: Enclosure Flows, Natural Convection, Radiation Interactions. Associate Technical Editor: T. Tong.

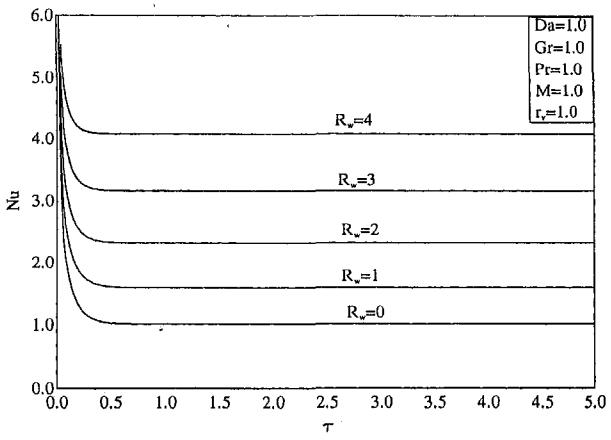

Fig. 2 Effects of R_w on temporal development of skin friction

in an increase in the Nusselt number, as clearly evident from Fig. 2. It should be mentioned that in obtaining the results associated with $R_w = 0$, r_v is set to zero since both of the parameters R_w and r_v are related to V_w. Thus, when $V_w = 0$, then both R_w and r_v must be zero.

Conclusion

The problem of unsteady hydromagnetic non-Darcy free convection from a fluid saturated porous medium supported by two infinitely long porous vertical plates is considered. One of the plates is suddenly heated while the other is maintained at the initial temperature. Fluid suction and injection are imposed at the hot and other wall, respectively. The mathematical model accounts for non-Darcy inertial effects of the porous medium and for the Hartmann effects of Magnetohydrodynamics. Several closed form and limiting solutions were obtained under steady-state conditions. In addition, the energy equation, which is independent of the flow equations, was solved analytically by the separation of variables method. The full initial-value problem was solved numerically by an implicit, tridiagonal, finite-difference methodology. Few of the obtained results were illustrated graphically to show special features of the solutions.

References

Aldoss, T., Al-Nimr, M., Jarrah, M., and Al-Sha'er, B., 1995, "Magnetohydrodynamic Mixed Convection From a Vertical Plate Embedded in a Porous Medium," *Numerical Heat Transfer,* Part A, Vol. 28, pp. 635–645.

Blottner, F., 1970, "Finite Difference Methods of Solutions of the Boundary-Layer Equations," *AIAA J.,* Vol. 8, pp. 193–205.

Chamkha, A., 1994, "Transient Power-Law Fluid Flow in a Porous Medium Channel," *Fluid/Particle Separation Journal,* Vol. 7, pp. 4–7.

Chen, C., and Lin, C., 1995, "Natural Convection From an Isothermal Vertical Surface Embedded in a Thermally Stratified High-Porosity Medium," *Int. J. Engng. Sci.,* Vol. 33, pp. 131–138.

Chen, C.-K., Hung, C.-I., and Horng, H.-C., 1989, "Transient Natural Convection on a Vertical Flat Plate Embedded in a High-Porosity Medium," ASME JOURNAL OF HEAT TRANSFER, Vol. 109, pp. 112–118.

Ingham, D. B., and Brown, S. N., 1986, "Flow Past a Suddenly Heated Vertical Plate in a Porous Medium," *Proc. R. Soc. Lond.,* Vol. A403, pp. 51–80.

Nakayama, A., Kokudai, T., and Koyama, H., 1990, "Non-Darcy Boundary Layer Flow and Forced Convective Heat Transfer Over a Flat Plate in a Fluid-Saturated Porous Medium," ASME JOURNAL OF HEAT TRANSFER, Vol. 112, pp. 157–162.

Nakayama, A., Kuwahara, F., and Koyama, H., 1993, "Transient Non-Darcy Free Convection Between Parallel Vertical Plates in a Fluid Saturated Porous Medium," *Appl. Sci. Res.,* Vol. 50, pp. 29–42.

Nield, D. A., Junqueira, S. L. M., and Lage, J. L., 1996, "Forced Convection in a Fluid-Saturated Porous-Medium Channel With Isothermal or Isoflux Boundaries," *J. Fluid Mech.,* Vol. 322, pp. 201–214.

Pop, I., and Watanabe, T., 1994, "Hall Effects on Magnetohydrodynamic Free Convection About a Semi-Infinite Vertical Flat Plate," *Int. J. Engng Sci.,* Vol. 32, pp. 1903–1911.

Vafai, K., and Tien, C. L., 1981, "Boundary and Inertia Effects on Flow and Heat Transfer in Porous Media," *Int. J. Heat Mass Transfer,* Vol. 24, pp. 195–203.

Vafai, K., and Kim, S. J., 1989, "Forced Convection in a Channel Filled With a Porous Medium: An Exact Solution," ASME JOURNAL OF HEAT TRANSFER, Vol. 111, pp. 1103–1106.

Interaction of Surface Radiation and Free Convection in an Enclosure With a Vertical Partition

K. Sri Jayaram[1], C. Balaji[2], and S. P. Venkateshan[3]

Nomenclature

A = aspect ratio, H/d
d = total width of the enclosure, m
F_{ij} = diffuse view factor between area elements i and j
g = acceleration due to gravity, m/s^2
H = height of the enclosure, m
J = radiosity of wall element, W/m^2
k = thermal conductivity of the fluid, $W/m \cdot K$
N_{RC} = radiation conduction interaction parameter, $\sigma T_H^4 d/[k(T_H - T_C)]$
Nu = local Nusselt number based on d (bar indicates the mean value, appropriate subscript indicates convective or radiative as the case may be), $qd/[k(T_H - T_C)]$
Pr = Prandtl number of the fluid, ν/α
q = heat flux, W/m^2
Ra = Rayleigh number based on d, $g\beta(T_H - T_C)d^3/(\nu\alpha)$
T = temperature, K
T_R = temperature ratio, T_C/T_H
x = vertical coordinate, m
X = dimensionless vertical coordinate, x/d
y = horizontal coordinate, m
Y = dimensionless horizontal coordinate, y/d
W = vorticity, s

Greek Symbols

α = thermal diffusivity of the fluid, m^2/s
β = coefficient of expansion, $1/K$
ϵ = total hemispherical emissivity
ν = kinematic viscosity of the fluid, m^2/s
ϕ = dimensionless temperature, $(T - T_C)/(T_H - T_C)$
ψ' = stream function, m^2/s
ψ = nondimensional stream function, ψ'/α

[1] Research Scholar, Heat Transfer and Thermal Power Laboratory, Department of Mechanical Engineering, Indian Institute of Technology, Madras 600 036, India.

[2] Senior Project Manager, National Institute of Ocean Technology, Indian Institute of Technology, Madras 600 036.

[3] Professor, Heat Transfer and Thermal Power Laboratory, Department of Mechanical Engineering, Indian Institute of Technology, Madras 600 036, India: mech3@iitm.ernet.in

Contributed by the Heat Transfer Division of THE AMERICAN SOCIETY OF MECHANICAL ENGINEERS. Manuscript received by the Heat Transfer Division January 19, 1996; revision received February 14, 1997; Keywords: Enclosure Flows, Natural Convection, Radiation Interactions. Associate Technical Editor: T. Tong.

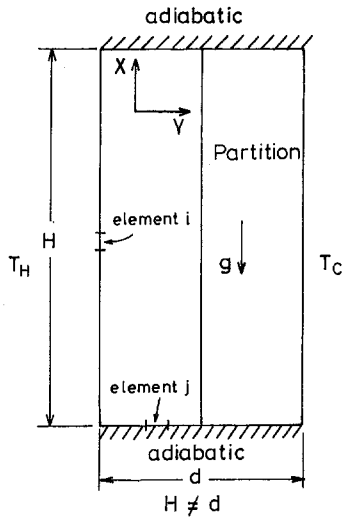

Fig. 1 Schematic of the geometry of the enclosure

σ = Stefan-Boltzmann constant, 5.67×10^{-8} $W/m^2 \cdot K^4$
ω = dimensionless vorticity, $W\, d^2/\nu$

Subscripts

B, C, H, P, T = pertaining respectively to the bottom wall, cold wall, hot wall, the partition and the top wall
c = convective component
i, j = wall-element indices
r = radiative component

1 Introduction

Free convection heat transfer is the best method of cooling stand-alone systems as it does not require any external high grade energy in the form of pump work. In view of this, natural convection assumes importance in heat transfer, though the maximum heat loss possible by natural convection is limited in magnitude. On the other hand, in case of insulating systems, there is a need to reduce natural convection heat transfer. For example, natural convection suppression is accomplished in such cases by the use of partitions introduced inside enclosures (Asako and Nakamura 1982; Nishimura et al., 1988). Further, the cooling of nuclear reactors may sometimes be modeled as free convective heat transfer in partitioned enclosures.

Natural convection in multiple vertical partitioned enclosures was studied by Nishimura et al. (1988). They have shown that natural convection heat transfer will be reduced by a factor ($N + 1$), where N is the number of partitions present, when compared to an enclosure with no partitions. Surface radiation was not taken into account in their study. The study of Jayaram (1996), has, however, shown that surface radiation plays a significant role in a square enclosure with a single vertical partition placed at the middle. This is because of the fact that surface radiation suppresses free convection and increases the total heat transfer.

In most practical situations, rectangular tall enclosures are employed. Moreover, the studies of Balaji and Venkateshan (1993, 1994) have shown that the mechanism of heat transfer becomes more complex in tall enclosures when both surface radiation and free convection are present. The present two-dimensional study allows for both surface radiation and free convection and attempts to throw more light on the effect of aspect ratio as well as the emissivities of the various surfaces on the interaction of these two modes of heat transfer in partitioned rectangular enclosures. Figure 1 shows the geometry considered in the present study. It is an enclosure with top and bottom walls insulated, right and left walls kept isothermal at T_H and $T_C (T_H > T_C)$, respectively, and a perfectly conducting thin partition placed at the middle of the enclosure. The surfaces are all assumed to be gray and diffuse. With regard to free convection, the Boussinesq approximation is assumed to be valid, and the medium inside the enclosure is air, which is assumed transparent to radiation.

2 Mathematical Formulation

The mathematical formulation for the present problem considered is similar to that of Balaji and Venkateshan (1993, 1994). The governing equations with the boundary conditions are given below.

Governing Equations. Flow equations are written down in the stream function vorticity formulation.

$$\mathrm{Pr}\omega = -\left[\frac{\partial^2\psi}{\partial X^2} + \frac{\partial^2\psi}{\partial Y^2}\right] \tag{1}$$

$$\frac{\partial\psi}{\partial Y}\frac{\partial\omega}{\partial X} - \frac{\partial\psi}{\partial X}\frac{\partial\omega}{\partial Y} = \mathrm{Pr}\left[\frac{\partial^2\omega}{\partial X^2} + \frac{\partial^2\omega}{\partial Y^2}\right] - \mathrm{Ra}\frac{\partial\phi}{\partial Y} \tag{2}$$

$$\frac{\partial\psi}{\partial Y}\frac{\partial\phi}{\partial X} - \frac{\partial\psi}{\partial X}\frac{\partial\phi}{\partial Y} = \frac{\partial^2\phi}{\partial X^2} + \frac{\partial^2\phi}{\partial Y^2} \tag{3}$$

Radiosity equation:

$$J_i = \epsilon_i\sigma T_i^4 + (1 - \epsilon_i)\sum_j F_{ij}J_j. \tag{4}$$

In the above, the summation over j is to be taken for all the elements of the boundary with which the element i can interact radiatively. The view factors F_{ij} are determined by the well known Hottel's crossed string method. The radiant heat flux q_r is then calculated by the formula

$$q_r = \epsilon_i[\sigma T_i^4 - \sum_j F_{ij}J_j]. \tag{5}$$

The Boundary Conditions. As far as the flow variables are concerned the stream function and its derivatives vanish on all the boundaries under the no slip condition. For vorticity, as suggested by Balaji and Venkateshan (1993), only the derivatives of the stream function normal to the boundaries are important and hence, the vorticity on all the boundaries are calculated as $\omega = -(1/\mathrm{Pr})(\partial^2\psi/\partial n^2)$, where n stands for distance measured normal to the boundary. The temperature and heat flux boundary conditions are specified as under.

Left wall:

$$Y = 0, \quad 0 \le X \le A, \quad \phi = 1 \tag{6a}$$

Right wall:

$$Y = 1, \quad 0 \le X \le A, \quad \phi = 0 \tag{6b}$$

Bottom wall:

$$X = 0, \quad 0 \le Y \le 1, \quad \frac{\partial\phi}{\partial X} + N_{RC}\frac{q_r}{\sigma T_H^4} = 0 \tag{6c}$$

Top wall:

$$X = A, \quad 0 \le Y \le 1, \quad \frac{\partial\phi}{\partial X} + N_{RC}\frac{q_r}{\sigma T_H^4} = 0 \tag{6d}$$

Partition:

(a) Temperature Continuity:

$$Y = 0.5, \quad 0 \le X \le A, \quad \phi|_{0.5^-} = \phi|_{0.5^+} \tag{6e}$$

Table 1 Range of parameters used in the present study

Parameter	Range
Ra	4.54×10^4–1.2×10^6
A	2–35
$\epsilon_C = \epsilon_H$, ϵ_P	0.05–0.95
$\epsilon_B = \epsilon_T$	0.85 (fixed)
T_R	0.72–0.94
N_{RC}	7.14–26.85

(b) Heat flux Continuity:

$$Y = 0.5, \quad 0 \le X \le A,$$

$$\left[\frac{\partial \phi}{\partial Y} + N_{RC}\frac{q_r}{\sigma T_H^4}\right]\Bigg|_{0.5^-} = \left[\frac{\partial \phi}{\partial Y} + N_{RC}\frac{q_r}{\sigma T_H^4}\right]\Bigg|_{0.5^+} \quad (6f)$$

3 Method of Solution

The finite volume method based on Gosman et al. (1969) is used to solve the governing equations. The advection terms in the governing equations are handled by using a second order upwinding procedure. This enables one to obtain stable and convergent solutions. An under relaxation technique (relaxation parameter 0.8 in most of the cases) is employed in solving the resulting algebraic equations. A nonuniform cosine grid of 40 × 40 has been used for the analysis selected on the basis of a convergent study as reported in Balaji (1994). The nonuniform grids ensure very fine grid spacing near all the walls where the gradients are large.

Once the temperature distribution for the problem geometry is obtained, the local Nusselt number values are evaluated using the first derivatives of the temperature at the walls. The mean Nusselt number is then estimated by integrating over the entire height using an extended trapezoidal rule for nonuniform step sizes. The velocity distributions are obtained by calculating the derivatives of the stream function at the walls.

The calculations have been performed for a range of parameters presented in Table 1.

4 Results and Discussion

Comparison for the Pure Free Convection Case. The results for the pure free convection case are obtained by taking all the wall emissivities equal to zero. This provides validation of the present code since such a solution is available in the literature (Nishimura et al., 1988). Figure 2 shows the results

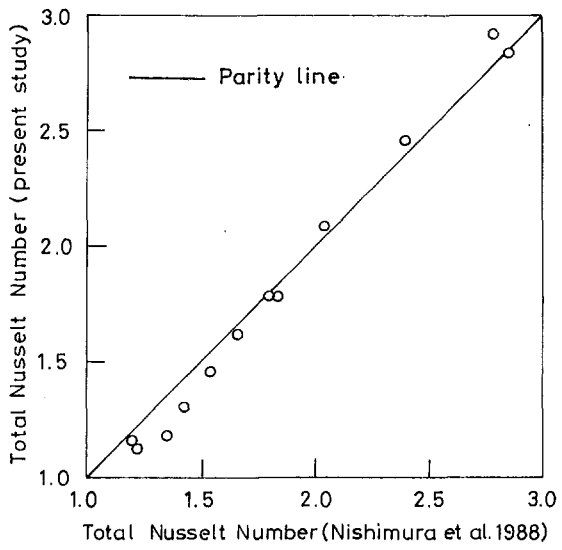

Fig. 2 Comparison of results for the pure free convection case

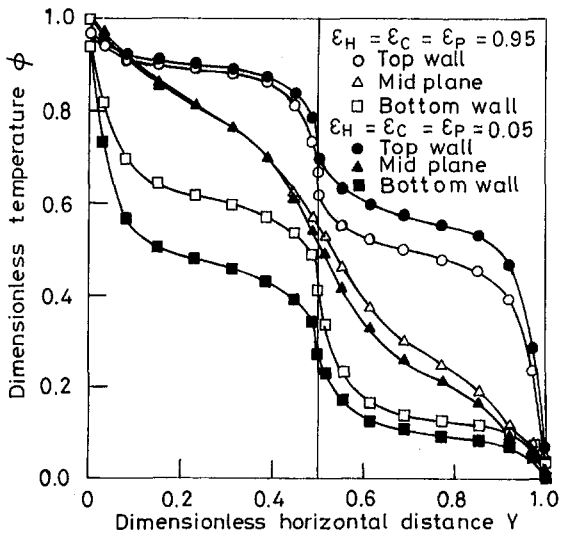

Fig. 3 Variation of temperature along horizontal planes across the enclosure (Ra = 2.72×10^5, $A = 10$, $\epsilon_T = \epsilon_B = 0.85$)

of the two cases—the present study and the study of Nishimura et al. (1988)—in the form of a parity plot. The close agreement between the two validates the present code.

Effect of Surface Radiation on Temperature Distribution. A typical case with Ra = 2.72×10^5, $A = 10$, $\epsilon_T = \epsilon_B = 0.85$ (held fixed in all the cases presented here), Pr = 0.71 has been considered to study the effect of emissivity of the left wall, right wall, and the partition on the heat transfer charcterstics of the problem. Further, two cases corresponding to low and high emissivities are presented here. Figure 3 shows the temperature profiles along the horizontal planes, as indicated. In general, the top wall is at a higher mean temperature compared to the bottom wall. All the temperatures tend to move closer to each other as the emissivity increases. This is consistent with the fact that the presence of surface radiation tends to reduce the temperature variation inside any enclosure.

Effect of Surface Radiation on Convection Heat Transfer. For the case of an enclosure without partitions, it has been observed that surface radiation reduces the convective heat transfer and increases the overall heat transfer across the enclosure by direct radiation (see, for example, Asako and Nakamura, 1982; Balaji and Venkateshan 1994). In the case of partitioned enclosures, the same is observed to be true, as can be seen from Fig. 4 which exhibits the variation of the local Nusselt number along the left wall for both the high and low emissivity cases. The suppression of convection heat transfer is significant with high emissivity. But, the radiation heat transfer increases with emissivity, thus increasing the total heat transfer across the enclosure. This is because with increase in emissivity, the fluid temperatures inside the enclosure increase considerably, thereby decreasing the gradients at the wall (see Fig. 3). An interesting aspect of the problem is that when the Rayleigh number is decreased, and the conduction limit is approached, the convective Nusselt number reduces to a value less than unity when all heat transfer quantities are based on the left wall. This is due to the interaction between the two modes of heat transfer which manifests in an average partition temperature greater than 0.5.

Correlations. Based on a large scale parametric study, correlations for calculation of radiation and convection Nusselt number were determined. In these correlations, the cases that lead to the conduction limit have been avoided.

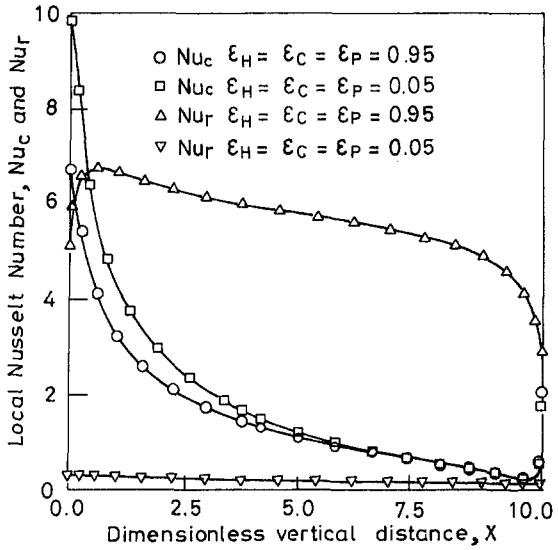

Fig. 4 Variation of convective and radiative Nusselt number along the left wall of the partitioned enclosure (Ra = 2.72 × 10^5, A = 10, $\epsilon_T = \epsilon_B$ = 0.85)

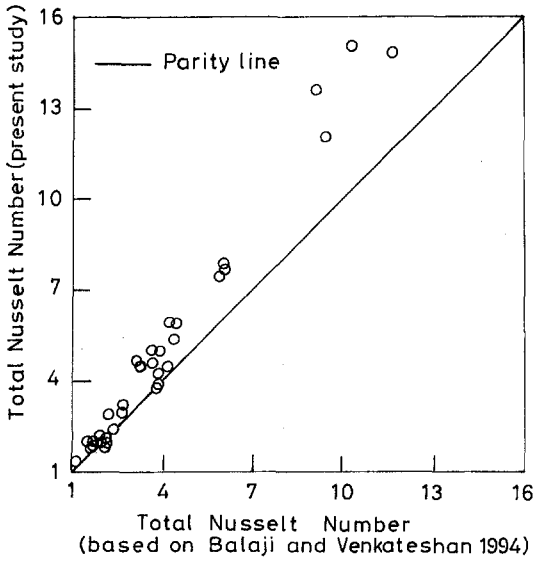

Fig. 5 Parity plot comparing the results of Balaji and Venkateshan (1994) with the present results

$$\overline{\mathrm{Nu}_c} = 0.190\ \mathrm{Ra}^{0.234}(1+\epsilon_H)^{-0.294}(1+\epsilon_C)^{-0.0269} \times A^{-0.250}\left[\frac{N_{RC}}{N_{RC}+1}\right]^{0.994} \quad (7)$$

$$\overline{\mathrm{Nu}_r} = 0.662\ \mathrm{Ra}^{0.0029}\left[\frac{A}{A+1}\right]^{0.088} \times \left[\frac{1}{\epsilon_H}+\frac{1}{\epsilon_P}-1\right]^{-0.962}[1-T_R^4]^{1.106}N_{RC}^{0.929} \quad (8)$$

The form of the correlations, the coefficients, and the exponents of various parameters provide an insight into the mechanism of heat transfer. The negative exponents for the two emissivity terms in the convection correlation indicate that surface radiation tends to reduce the free convection component. The partition emissivity has a weak influence on the hot left wall convection heat transfer. The significance of the interaction can be seen through the appearance of the radiation conduction interaction parameter in the correlation for convection. As the aspect ratio increases, the convection Nusselt number decreases, and this effect is similar to what is observed in the case of a enclosure without partition (Balaji, 1994). This shows that the suppression of convection by radiation is a strong function of emissivities.

The radiation Nusselt number correlation was chosen in the above form so that, in the limiting case, it reduces to the parallel plate formula, as pointed out by Balaji and Venkateshan (1994). In the current study, the Rayleigh number has a very weak influence on the radiative heat transfer. The aspect ratio influences radiation heat transfer to a small extent. The parameter involving the emissivities in Eq. (8) has an exponent of −0.962. This is because the parallel plate formula does not account for the top and bottom walls, aside from the fact that radiation has been solved more accurately in the present study.

As mentioned earlier, Nishimura et al. (1988) observed that convective heat transfer in a partitioned enclosure is reduced by a factor of $(N + 1)$ when N partitions are used. Since the mechanism of heat transfer is complex when surface radiation is also present, it is unlikely that the same will be true for the partitioned case in the presence of surface radiation. In order to bring out this fact, a parity plot has been presented in Fig. 5. In this figure, the total Nusselt number in an enclosure without a partition, but with radiation and divided by 2 (i.e., $N + 1$, here N, the number of partitions is 1), is plotted along the horizontal axis, the result being based on the work of Balaji and Venkateshan (1994). Along the vertical axis, the total Nusselt number from the present calculations is plotted. The figure clearly indicates that there is a bias with the data points of the present study always above the values obtained from Balaji and Venkateshan (1994). Hence, the total heat transfer in a partitioned enclosure with N partitions is not equal to the total heat transfer in an unpartitioned enclosure divided by the factor $(N + 1)$. The bias is strongly influenced by the emissivity and weakly by the other parameters. As an example, for Ra = 4.54 × 10^4, A = 35, T_R = 0.94, N_{RC} = 7.14 the discrepancy increases from 1 percent to 34 percent when emissivity changes from 0.05 to 0.95. Thus, in the limit $\epsilon \to 0$, the results tend towards parity in agreement with the findings of Nishimura et al. (1988).

5 Conclusions

The following conclusions can be drawn from the present analysis:

1 Surface radiation suppresses the free convection and in total, augments the total heat transfer. This is consistent with observations of earlier studies by Balaji and Venkateshan (1993, 1994) which considered enclosures without partitions.
2 The partition emissivity has a weak influence on natural convection and a strong influence on surface radiation, as seen from the correlations.
3 In the case of a partitioned enclosure, under the influence of both surface radiation and free convection, the total heat transfer cannot be predicted using the results for enclosures without partition. This in essence brings out the highly nonlinear effect of radiation.

6 References

Asako, Y., and Nakamura, H., 1982, "Heat Transfer Across a Parallelogram Shaped Enclosure," *Bulletin J.S.M.E.*, Vol. 25, pp. 1412–1424.

Balaji, C., 1994, "Laminar Free Convection With Conduction and Surface Radiation in Open and Closed Cavities," Ph.D. thesis, Indian Institute of Technology, Madras, India.

Balaji, C., and Venkateshan, S. P., 1993, "Interaction of Surface Radiation With Free Convection in a Square Cavity," *Int. J. Heat and Fluid Flow*, Vol. 14, No. 3, pp. 260–267.

Balaji, C., and Venkateshan, S. P., 1994, "Combined Surface Radiation and Free Convection in Cavities," *AIAA Journal of Thermo Physics and Heat Transfer*, Vol. 8, pp. 373–376.

Gosman, A. D., Pun, W. M., Runchal, A. K., Spalding, D. B., and Wolfshtein, M., 1969, *Heat and Mass Transfer in Recirculating Flows*, Academic Press, London.

Nishimura, T., Shiraishi, M., Nagasawa, F., and Kawamura, Y., 1988 "Natural Convection Heat Transfer in Enclosures With Multiple Vertical Partitions," *Int. J. Heat Mass Transfer*, Vol. 31, No. 8, pp. 1679–1686.

Sri Jayaram, K., 1996, "Interaction of Surface Radiation and Free Convection in Partitioned Enclosures," M.S. thesis, Indian Institute of Technology, Madras, India.

Reexamination of the Transmittance Formulae of a Lamina

Z. M. Zhang[1]

Expressions for the optical properties of laminated layers have drawn much attention from researchers in recent years because of emerging optoelectronic applications (Chen and Tien, 1992; Cunsolo et al., 1992; Zhang and Flik, 1993, Engelbrecht, 1994; Grossman and McDonald, 1995; Anderson and Bayazitoglu, 1996). Different equations must be applied in particular situations (Chen and Tien, 1992; Zhang, 1994). After carefully examining the transmittance formulae of a lamina, this work shows that the geometric-optics formula may result in a significant error for a highly absorbing medium even in the incoherent limit (when interference effects are negligible).

Introduction

Consider the transmission of electromagnetic radiation through a lamina with smooth and parallel surfaces. In the incoherent limit when radiation coherence length is much smaller than the thickness of the lamina, the transmittance (or reflectance) may be obtained either by tracing the multiply reflected radiant power fluxes (ray-tracing method) or by separating the power flux at each interface into an outgoing component and an incoming component (net-radiation method), viz. (Siegel and Howell, 1992)

$$T = \frac{(1-\rho)^2\tau}{1-\rho^2\tau^2} \tag{1}$$

where ρ is the reflectance at the interface and τ is the internal transmittance. This formula is also called the geometric-optics formula since it is obtained without considering interference effects. For a plane wave, ρ equals the square of the absolute value of the complex Fresnel reflection coefficient (i.e., the ratio of the reflected electric field to the incident electric field at the interface). The Fresnel reflection coefficient is (Heavens, 1965)

$$r_{12} = \begin{cases} \dfrac{N_1\cos\theta_2 - N_2\cos\theta_1}{N_1\cos\theta_2 + N_2\cos\theta_1}, & \text{for } p-\text{polarization} \\ \dfrac{N_1\cos\theta_1 - N_2\cos\theta_2}{N_1\cos\theta_1 + N_2\cos\theta_2}, & \text{for } s-\text{polarization} \end{cases} \tag{2}$$

where θ_1 is the angle of incidence, $N_1 = 1$ is the refractive index of air or vacuum, $N_2 = n + i\kappa$ is the complex refractive index of the lamina material, and θ_2 is the (complex) angle of refraction, which is related to θ_1 by Snell's law: $N_1 \sin\theta_1 = N_2 \sin\theta_2$. Since $r_{21} = -r_{12}$, the reflectance at both interfaces is equal to $\rho = r_{12}r_{12}^*$, where * denotes the complex conjugate. The internal transmittance τ is related to the (complex) phase change δ by $\tau = \exp[-2\,\mathrm{Im}(\delta)]$, where Im denotes the imaginary part. The phase change inside the lamina is

$$\delta = \frac{2\pi d}{\lambda} N_2\cos\theta_2 \tag{3}$$

where d is the lamina thickness and λ is the wavelength in vacuum.

In the coherent limit, the transmittance of a lamina may be obtained from thin-film optics (i.e., wave optics) either by tracing the reflected and transmitted waves (Airy's method) or by separating the electric fields into a forward-propagating component (forward wave) and a backward-propagating component (backward wave), viz. (Heavens, 1965; Born and Wolf, 1980; Yeh, 1988)

$$T = \frac{[1+\rho^2 - 2\,\mathrm{Re}(r_{12}^2)]\tau}{1+\rho^2\tau^2 - 2\tau\,\mathrm{Re}(r_{12}^2 e^{i2\phi})} \tag{4}$$

where $\phi = \mathrm{Re}(\delta)$ is the real part of the phase change. The resulting spectral transmittance oscillates because of interference effects.

As pointed out by Cunsolo et al. (1992), integrating Eq. (4) over a period of oscillation yields

$$T = \frac{[1+\rho^2 - 2\,\mathrm{Re}(r_{12}^2)]\tau}{1-\rho^2\tau^2} = \frac{(1-\rho)^2\tau}{1-\rho^2\tau^2} + \frac{4[\mathrm{Im}(r_{12})]^2\tau}{1-\rho^2\tau^2}. \tag{5}$$

Although the second term at the right is often very small, the above equation is different from Eq. (1). It is worthwhile to investigate the physical origin of this discrepancy and to discuss practical situations where Eq. (5) should be used instead of Eq. (1).

Analysis and Discussion

The power transmittance at the interface between the air (or vacuum) and the medium (lamina) is (Yeh, 1988)

$$T_{12} = \frac{\mathrm{Re}(N_2\cos\theta_2)}{\mathrm{Re}(N_1\cos\theta_1)}(1+r_{12})(1+r_{12}^*) \tag{6}$$

where $(1 + r_{12})$ is the Fresnel transmission coefficient. The power transmittance at the second interface between the medium and the air can be obtained by exchanging the subscripts 1 and 2 in Eq. (6). At normal incidence, $r_{12} = (1 - n - i\kappa)/(1 + n + i\kappa)$ and $\rho = [(n-1)^2 + \kappa^2]/[(n+1)^2 + \kappa^2]$. Therefore, $T_{12} = 4n/[(n+1)^2 + \kappa^2] = 1 - \rho$ and,

$$T_{21} = \frac{1}{n}\frac{4(n^2+\kappa^2)}{(n+1)^2+\kappa^2} = 1 - \rho + \frac{2\kappa\,\mathrm{Im}[r_{21}]}{n}. \tag{7}$$

If both κ and $\mathrm{Im}(r_{21})$ are nonzero, $T_{21} \neq 1 - \rho$. As discussed by Salzberg (1948) and Knittl (1976), this inequality is caused by the interference effect between the reflected wave and the incident wave at the interface for radiation incident from an absorbing medium. No incident power flux and reflected power flux can be defined in an absorbing medium because of the coupling between the incident and the reflected waves, although it is always possible to separate the electric field into forward and backward components. In addition to the assumption that the interference effects are negligible, geometric optics implies that the power flux in the medium equals the sum of the power fluxes of the forward wave and the backward wave, i.e., the coupling term is negligible.

[1] Department of Mechanical Engineering, University of Florida, PO Box 116300, Gainesville, FL 32611-6300

Contributed by the Heat Transfer Division of THE AMERICAN SOCIETY OF MECHANICAL ENGINEERS. Manuscript received by the Heat Transfer Division May 6, 1996; revision received March 2, 1997; Keywords: Radiation, Thermophysical Properties. Associate Technical Editor: T. Tong.

Balaji, C., and Venkateshan, S. P., 1994, "Combined Surface Radiation and Free Convection in Cavities," *AIAA Journal of Thermo Physics and Heat Transfer*, Vol. 8, pp. 373–376.

Gosman, A. D., Pun, W. M., Runchal, A. K., Spalding, D. B., and Wolfshtein, M., 1969, *Heat and Mass Transfer in Recirculating Flows*, Academic Press, London.

Nishimura, T., Shiraishi, M., Nagasawa, F., and Kawamura, Y., 1988 "Natural Convection Heat Transfer in Enclosures With Multiple Vertical Partitions," *Int. J. Heat Mass Transfer*, Vol. 31, No. 8, pp. 1679–1686.

Sri Jayaram, K., 1996, "Interaction of Surface Radiation and Free Convection in Partitioned Enclosures," M.S. thesis, Indian Institute of Technology, Madras, India.

Reexamination of the Transmittance Formulae of a Lamina

Z. M. Zhang[1]

Expressions for the optical properties of laminated layers have drawn much attention from researchers in recent years because of emerging optoelectronic applications (Chen and Tien, 1992; Cunsolo et al., 1992; Zhang and Flik, 1993, Engelbrecht, 1994; Grossman and McDonald, 1995; Anderson and Bayazitoglu, 1996). Different equations must be applied in particular situations (Chen and Tien, 1992; Zhang, 1994). After carefully examining the transmittance formulae of a lamina, this work shows that the geometric-optics formula may result in a significant error for a highly absorbing medium even in the incoherent limit (when interference effects are negligible).

Introduction

Consider the transmission of electromagnetic radiation through a lamina with smooth and parallel surfaces. In the incoherent limit when radiation coherence length is much smaller than the thickness of the lamina, the transmittance (or reflectance) may be obtained either by tracing the multiply reflected radiant power fluxes (ray-tracing method) or by separating the power flux at each interface into an outgoing component and an incoming component (net-radiation method), viz. (Siegel and Howell, 1992)

$$T = \frac{(1-\rho)^2\tau}{1-\rho^2\tau^2} \tag{1}$$

where ρ is the reflectance at the interface and τ is the internal transmittance. This formula is also called the geometric-optics formula since it is obtained without considering interference effects. For a plane wave, ρ equals the square of the absolute value of the complex Fresnel reflection coefficient (i.e., the ratio of the reflected electric field to the incident electric field at the interface). The Fresnel reflection coefficient is (Heavens, 1965)

$$r_{12} = \begin{cases} \dfrac{N_1\cos\theta_2 - N_2\cos\theta_1}{N_1\cos\theta_2 + N_2\cos\theta_1}, & \text{for } p-\text{polarization} \\ \dfrac{N_1\cos\theta_1 - N_2\cos\theta_2}{N_1\cos\theta_1 + N_2\cos\theta_2}, & \text{for } s-\text{polarization} \end{cases} \tag{2}$$

where θ_1 is the angle of incidence, $N_1 = 1$ is the refractive index of air or vacuum, $N_2 = n + i\kappa$ is the complex refractive index of the lamina material, and θ_2 is the (complex) angle of refraction, which is related to θ_1 by Snell's law: $N_1 \sin\theta_1 = N_2 \sin\theta_2$. Since $r_{21} = -r_{12}$, the reflectance at both interfaces is equal to $\rho = r_{12}r_{12}^*$, where * denotes the complex conjugate. The internal transmittance τ is related to the (complex) phase change δ by $\tau = \exp[-2\,\mathrm{Im}(\delta)]$, where Im denotes the imaginary part. The phase change inside the lamina is

$$\delta = \frac{2\pi d}{\lambda} N_2\cos\theta_2 \tag{3}$$

where d is the lamina thickness and λ is the wavelength in vacuum.

In the coherent limit, the transmittance of a lamina may be obtained from thin-film optics (i.e., wave optics) either by tracing the reflected and transmitted waves (Airy's method) or by separating the electric fields into a forward-propagating component (forward wave) and a backward-propagating component (backward wave), viz. (Heavens, 1965; Born and Wolf, 1980; Yeh, 1988)

$$T = \frac{[1+\rho^2 - 2\,\mathrm{Re}(r_{12}^2)]\tau}{1+\rho^2\tau^2 - 2\tau\,\mathrm{Re}(r_{12}^2 e^{i2\phi})} \tag{4}$$

where $\phi = \mathrm{Re}(\delta)$ is the real part of the phase change. The resulting spectral transmittance oscillates because of interference effects.

As pointed out by Cunsolo et al. (1992), integrating Eq. (4) over a period of oscillation yields

$$T = \frac{[1+\rho^2 - 2\,\mathrm{Re}(r_{12}^2)]\tau}{1-\rho^2\tau^2} = \frac{(1-\rho)^2\tau}{1-\rho^2\tau^2} + \frac{4[\mathrm{Im}(r_{12})]^2\tau}{1-\rho^2\tau^2}. \tag{5}$$

Although the second term at the right is often very small, the above equation is different from Eq. (1). It is worthwhile to investigate the physical origin of this discrepancy and to discuss practical situations where Eq. (5) should be used instead of Eq. (1).

Analysis and Discussion

The power transmittance at the interface between the air (or vacuum) and the medium (lamina) is (Yeh, 1988)

$$T_{12} = \frac{\mathrm{Re}(N_2\cos\theta_2)}{\mathrm{Re}(N_1\cos\theta_1)}(1+r_{12})(1+r_{12}^*) \tag{6}$$

where $(1 + r_{12})$ is the Fresnel transmission coefficient. The power transmittance at the second interface between the medium and the air can be obtained by exchanging the subscripts 1 and 2 in Eq. (6). At normal incidence, $r_{12} = (1 - n - i\kappa)/(1 + n + i\kappa)$ and $\rho = [(n-1)^2 + \kappa^2]/[(n+1)^2 + \kappa^2]$. Therefore, $T_{12} = 4n/[(n+1)^2 + \kappa^2] = 1 - \rho$ and,

$$T_{21} = \frac{1}{n}\frac{4(n^2+\kappa^2)}{(n+1)^2+\kappa^2} = 1 - \rho + \frac{2\kappa\,\mathrm{Im}[r_{21}]}{n}. \tag{7}$$

If both κ and $\mathrm{Im}(r_{21})$ are nonzero, $T_{21} \neq 1 - \rho$. As discussed by Salzberg (1948) and Knittl (1976), this inequality is caused by the interference effect between the reflected wave and the incident wave at the interface for radiation incident from an absorbing medium. No incident power flux and reflected power flux can be defined in an absorbing medium because of the coupling between the incident and the reflected waves, although it is always possible to separate the electric field into forward and backward components. In addition to the assumption that the interference effects are negligible, geometric optics implies that the power flux in the medium equals the sum of the power fluxes of the forward wave and the backward wave, i.e., the coupling term is negligible.

[1] Department of Mechanical Engineering, University of Florida, PO Box 116300, Gainesville, FL 32611-6300

Contributed by the Heat Transfer Division of THE AMERICAN SOCIETY OF MECHANICAL ENGINEERS. Manuscript received by the Heat Transfer Division May 6, 1996; revision received March 2, 1997; Keywords: Radiation, Thermophysical Properties. Associate Technical Editor: T. Tong.

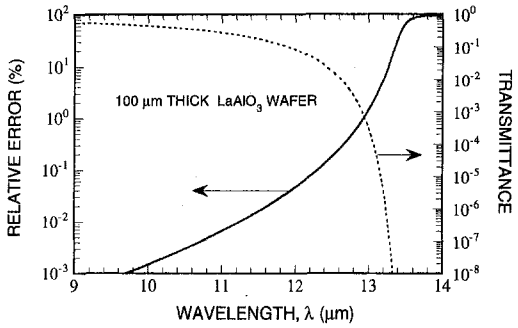

Fig. 1 Relative error of Eq. (1) and the transmittance of a $LaAlO_3$ lamina calculated using Eq. (8) at normal incidence

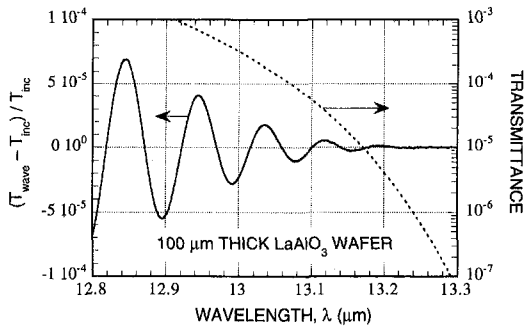

Fig. 2 Comparison between the wave-optics formula, Eq. (4) for T_{wave}, and the incoherence formula, Eq. (8) for T_{inc}. The transmittance value is also calculated from Eq. (8)

Zhang (1994) derived an equation for the transmittance in the incoherent limit using partial-coherence theory:

$$T = \frac{T_{12}T_{21}\tau}{1 - \rho^2\tau^2}. \tag{8}$$

The above equation is identical to Eq. (5). However, it is not a simple replacement of $(1 - \rho)^2$ in Eq. (1) with $T_{12}T_{21}$, because the ray-tracing method and the net-radiation method inherently assume that $T_{12} = T_{21} = 1 - \rho$ in order to satisfy the first law of thermodynamics. For an absorbing medium, T_{21} cannot be interpreted as the power transmittance at the interface because no incident power flux can be defined in the medium. In fact, T_{21} could be greater than 1. Hence, Eq. (8) is distinct from the geometric-optics formulation. All the above equations, except Eq. (7), are applicable to both normal and oblique incidence. The partial-coherence formulation was verified by Anderson and Bayazitoglu (1996) for arbitrary angles of incidence and polarization states. Taking Eq. (5) or (8) as the exact expression for the incoherent limit, the relative error of Eq. (1) can be evaluated. At normal incidence, the relative error equals $\kappa^2/(n^2 + \kappa^2)$. Since the internal transmittance is $\tau = \exp(-4\pi\kappa d/\lambda)$, the requirements of $\lambda < d$ and transparency of the lamina often exclude large values of κ.

As an example, suppose the lamina is a $LaAlO_3$ wafer of thickness $d = 100$ μm. The optical constants are calculated from the Lorentian dielectric function determined by Zhang et al. (1994). At 1 μm $< \lambda <$ 11 μm, $\kappa < 0.01$ and $n > 1$. The relative error is less than 0.01 percent, which is smaller than the uncertainty of most experiments. The relative error of Eq. (1) and the transmittance for a $LaAlO_3$ lamina at wavelengths from 9 to 14 μm at normal incidence are shown in Fig. 1. As the wavelength increases, the relative error increases, but the transmittance decreases because of a decreasing n and an increasing κ. The relative error of Eq. (1) is less than 1 percent for $\lambda <$ 13 μm, where the transmittance is greater than 0.001. The error of Eq. (1) becomes substantial for very low transmittance.

The difference between the wave-optics formula and the incoherent formula is shown in Fig. 2, where T_{wave} and T_{inc} are calculated using Eqs. (4) and (8), respectively. Because of an increasing κ, the strength of oscillation decreases as the wavelength increases. Notice that $N_2 = (0.8 + i\ 0.06)$ at 12.8 μm and $(0.44 + i\ 0.17)$ at 13.3 μm for $LaAlO_3$. The agreement between the incoherent formula and the wave-optics formula in the case with strong absorption further confirms the applicability of Eq. (5) or (8). Similar trends can be shown for other dielectric materials and/or in different spectral regions.

For a highly absorbing lamina (i.e., $\tau \ll 1$), multiple reflections may be neglected. The transmittance obtained from Eq. (1), when multiple reflections are negligible, is $(1 - \rho)^2\tau$. The transmittance calculated from Eq. (8) for $\tau \ll 1$ is

$$T = T_{12}T_{21}\tau = \frac{16(n^2 + \kappa^2)\tau}{[(n + 1)^2 + \kappa^2]^2} \tag{9}$$

where the last expression is for normal incidence only. Eq. (9) agrees with the wave-optics equation for $\tau \ll 1$ (Born and Wolf, 1980). The error of using $(1 - \rho)^2\tau$, instead of Eq. (9), can be substantial for a metallic film since κ is on the same order of n. Take a 50 nm thick free-standing gold film at 2 μm as an example. Using $n = 0.47$ and $\kappa = 12.5$, from Siegel and Howell (1992), the normal transmittance calculated from Eq. (9) is $\approx 2 \times 10^{-3}$, whereas $(1 - \rho)^2\tau \approx 2.8 \times 10^{-6}$. The nearly three orders of magnitude discrepancy is caused by the difference between $T_{21} = 8.4$ and $1 - \rho = 0.012$.

Concluding Remarks

By inspecting the energy balance at the second interface, this work reveals an implicit assumption associated with Eq. (1), that is, the power flux equals the sum of the power fluxes of the forward wave and the backward wave. Using the expressions given by Eqs. (5) and (8), the relative error of Eq. (1) is evaluated. Corrections are rarely needed since $\kappa \ll n$ for most engineering applications when interference effects may be neglected. For a highly absorbing lamina however, the power transmittance and reflectance at the second interface cannot be defined. Hence, for applications that involve very low transmittance laminae, Eq. (1) is inappropriate even though interference effects are negligible.

Certain important applications require the determination of transmittance below 10^{-4}. Examples are in the characterization of attenuation filters, bandpass filters, and materials with strong absorption bands (Frenkel and Zhang, 1994; Zhang et al., 1995a, b). Infrared transmittance as low as 10^{-10} can be measured using modern spectrometric and laser techniques as reviewed by Gentile et al. (1995).

Acknowledgments

This work has been supported by the University of Florida through a start-up fund and an Interdisciplinary Research Initiative award.

References

Anderson, C. F., and Bayazitoglu, Y., 1996, "Radiative Properties of Films Using Partial Coherence Theory," *Journal of Thermophysics and Heat Transfer*, Vol. 10, pp. 26–32.

Born, M., and Wolf, E., 1980, *Principles of Optics*, 6th ed., Pergamon Press, Oxford, UK, chap. 1, pp. 36–66, and chap. 13, pp. 627–633.

Chen, G., and Tien, C. L., 1992, "Partial Coherence Theory of Thin Film Radiative Properties," ASME JOURNAL OF HEAT TRANSFER, Vol. 114, pp. 636–643.

Cunsolo, S., Dore, S., and Varsamis, C. P., 1992, "Refractive Index of Crystals from Transmission and Reflection Measurements: MgO in the Far-Infrared Region," *Applied Optics*, Vol. 31, pp. 4554–4558.

Engelbrecht, J. A. A., 1994, "Modelling of the Reflectance of Silicon," *Infrared Physics and Technology,* Vol. 35, pp. 701–708.

Frenkel, A., and Zhang, Z. M., 1994, "Broadband High Optical Density Filters in the Infrared," *Optics Letters,* Vol. 19, pp. 1495–1497.

Gentile, T. R., Frenkel, A., Migdall, A. L., and Zhang, Z. M., 1995, "Neutral Density Filter Measurements at the National Institute of Standards and Technology," Spectrophotometry, Luminescence and Colour; Science and Compliance, C. Burgess and D. G. Jones, eds., Elsevier, Amsterdam, The Netherlands, pp. 129–139.

Grossman, E. N., and McDonald, D. G., 1995, "Partially Coherent Transmittance of Dielectric Lamellae," *Optical Engineering,* Vol. 34, pp. 1289–1295.

Heavens, O. S., 1965, *Optical Properties of Thin Solid Films,* Dover Publications, Inc., New York, chap. 4, pp. 46–95.

Knittl, Z., 1976, *Optical of Thin Films,* John Wiley & Sons, Inc., NY, pp. 203–204.

Salzberg, B., 1948, "A Note on the Significance of Power Reflection," *American Journal of Physics,* Vol. 16, pp. 444–446.

Siegel, R., and Howell, J. R., 1992, *Thermal Radiation Heat Transfer,* 3rd ed., Hemisphere Publishing Corp., Washington D.C., chap. 4, p. 120, and chap. 18, pp. 928–930.

Yeh, P., 1988, *Optical Waves in Layered Media,* John Wiley & Sons, Inc., New York, chap. 4, pp. 83–101.

Zhang, Z. M., 1994, "Optical Properties of Layered Structures for Partially Coherent Radiation," *Heat Transfer 1994—Proceedings of the Tenth International Heat Transfer Conference,* Vol. 2, G. F. Hewitt, ed., Institution of Chemical Engineers, Rugby, UK, pp. 177–182.

Zhang, Z. M., and Flik, M. I., 1993, "Predicted Absorptance of $YBa_2Cu_3O_7$/YSZ/Si Multilayer Structures for Infrared Detectors," *IEEE Transactions on Applied Superconductivity,* Vol. 3, pp. 1604–1607.

Zhang, Z. M., Choi, B. I., Flik, M. I., and Anderson, A. C., 1994, "Infrared Refractive Indices of $LaAlO_3$, $LaGaO_3$, and $NdGaO_3$," *Journal of the Optical Society of America B,* Vol. 11, pp. 2252–2257.

Zhang, Z. M., Datla, R. U., and Hanssen, L. M., 1995a, "Development of Neutral-Density Infrared Filters Using Metallic Thin Films," *MRS Symp. Proc.,* Vol. 374, pp. 117–122.

Zhang, Z. M., Hanssen, L. M., and Datla, R. U., 1995b, "High-Optical-Density Out-of-Band Spectral Transmittance Measurements of Bandpass Filters," *Optics Letters,* Vol. 20, pp. 1077–1079.

Thermal Convection in an Infinite Porous Medium Induced by a Heated Sphere

R. Ganapathy [1]

This paper investigates the transient behavior of the free convection motion and heat transfer induced by a heated sphere with prescribed wall temperature embedded instantaneously in an infinite porous medium. Solutions for the velocity and temperature fields have been obtained in the form of series expansions in Rayleigh number which is based on the medium permeability and the temperature of the sphere. All discussions are based on the assumption that the flow is governed by Darcy's law and the thermal Rayleigh number is small.

Nomenclature

a = radius of the sphere (L)
c_p = specific heat of fluid at constant pressure ($L^2T^2\Theta^{-1}$)
f = function of η (Eq. 13)
G = function of η (Eq. 18)
g = gravitational acceleration (LT^{-2})
K = medium permeability (L^2)
L = length
Q = prescribed wall temperature on the sphere (θ)
R = nondimensional radial coordinate
R_o = nondimensional radius of the sphere ($a/\sqrt{K}$)
Ra = thermal Rayleigh number, $(\beta g K\sqrt{K}/\alpha\nu)Q$
Re = Reynolds number, (UL/ν)
r = radial coordinate (L)
T = temperature (θ)
t = time (T)
U = nondimensional radial velocity
u = radial velocity (LT^{-1})
V = nondimensional transverse velocity
v = transverse velocity (LT^{-1})

Greek Symbols

α = effective thermal diffusivity of the porous medium [L^2T^{-1}]
β = coefficient of thermal expansion [θ^{-1}]
Θ = azimuthal angle
ϕ = meridian angle
η = similarity variable, $R/2\sqrt{t}$
η_o = similarity variable $R_o/2\sqrt{t}$
ν = kinematic viscosity (L^2T^{-1})
σ = heat capacity ratio (eq. 2)
ψ = stream function [L^3T^{-1}]

Subscripts

0 = zeroth-order solution
1 = first-order solution
∞ = reference state

1 Introduction

Since the work of Yamamoto (1974), there has been a spate of research papers on thermal convection due to the presence of heated spheres in saturated porous media. Most of them, with the possible exception of the work of Ganapathy and Purushothaman (1990), were primarily concerned with steady-state solutions only. However, as the analysis of such flows is essential for the solution of many engineering problems such as the hydrodynamics of weak thermal explosions, cooling of the components of electrical and electronic equipment, and the management of nuclear waste, a knowledge of the transient behavior of the flow and heat transfer becomes necessary, especially when the heated sphere is buried instantaneously. It is towards this end that we propose to present a solution to this problem of transient convection due to the presence of a heated sphere embedded instantaneously in an unbounded porous medium and investigate the ensuing flow field and heat transfer in the context of thermal flows in porous media.

2 Mathematical Formulation

We consider the natural convection around a heated sphere of radius a and of constant temperature Q (in excess of the reference temperature), buried instantaneously in an unbounded fluid-saturated porous medium of low permeability. The medium is assumed to be rigid, homogeneous, and isotropic, and the fluid saturating the medium is assumed to be Boussinesq incompressible.

A spherical-polar coordinate system (r, ϕ, Θ) is chosen (Fig. 1), with the origin of the system at the centre of the sphere and the axis $\phi = 0$ vertically upwards. Taking advantage of the continuity equation, we define a stream function ψ such that

$$u = (r^2 \sin\phi)^{-1}\partial\psi/\partial\phi, \quad v = (r\sin\phi)^{-1}\partial\psi/\partial r \qquad (1)$$

where u and v are the radial and transverse components of velocity and introduce the nondimensional quantities (see nomenclature)

[1] Department of Mathematics, National College, Tiruchirapalli 620 001, India.

Contributed by the Heat Transfer Division of THE AMERICAN SOCIETY OF MECHANICAL ENGINEERS. Manuscript received by the Heat Transfer Division July 1, 1996; revision received March 3, 1997; Keywords: Natural Convection; Porous Media; Transient & Unsteady Heat Transfer. Associate Technical Editor: K. Vafai.

Engelbrecht, J. A. A., 1994, "Modelling of the Reflectance of Silicon," *Infrared Physics and Technology,* Vol. 35, pp. 701–708.

Frenkel, A., and Zhang, Z. M., 1994, "Broadband High Optical Density Filters in the Infrared," *Optics Letters,* Vol. 19, pp. 1495–1497.

Gentile, T. R., Frenkel, A., Migdall, A. L., and Zhang, Z. M., 1995, "Neutral Density Filter Measurements at the National Institute of Standards and Technology," Spectrophotometry, Luminescence and Colour; Science and Compliance, C. Burgess and D. G. Jones, eds., Elsevier, Amsterdam, The Netherlands, pp. 129–139.

Grossman, E. N., and McDonald, D. G., 1995, "Partially Coherent Transmittance of Dielectric Lamellae," *Optical Engineering,* Vol. 34, pp. 1289–1295.

Heavens, O. S., 1965, *Optical Properties of Thin Solid Films,* Dover Publications, Inc., New York, chap. 4, pp. 46–95.

Knittl, Z., 1976, *Optical of Thin Films,* John Wiley & Sons, Inc., NY, pp. 203–204.

Salzberg, B., 1948, "A Note on the Significance of Power Reflection," *American Journal of Physics,* Vol. 16, pp. 444–446.

Siegel, R., and Howell, J. R., 1992, *Thermal Radiation Heat Transfer,* 3rd ed., Hemisphere Publishing Corp., Washington D.C., chap. 4, p. 120, and chap. 18, pp. 928–930.

Yeh, P., 1988, *Optical Waves in Layered Media,* John Wiley & Sons, Inc., New York, chap. 4, pp. 83–101.

Zhang, Z. M., 1994, "Optical Properties of Layered Structures for Partially Coherent Radiation," *Heat Transfer 1994—Proceedings of the Tenth International Heat Transfer Conference,* Vol. 2, G. F. Hewitt, ed., Institution of Chemical Engineers, Rugby, UK, pp. 177–182.

Zhang, Z. M., and Flik, M. I., 1993, "Predicted Absorptance of $YBa_2Cu_3O_7$/YSZ/Si Multilayer Structures for Infrared Detectors," *IEEE Transactions on Applied Superconductivity,* Vol. 3, pp. 1604–1607.

Zhang, Z. M., Choi, B. I., Flik, M. I., and Anderson, A. C., 1994, "Infrared Refractive Indices of $LaAlO_3$, $LaGaO_3$, and $NdGaO_3$," *Journal of the Optical Society of America B,* Vol. 11, pp. 2252–2257.

Zhang, Z. M., Datla, R. U., and Hanssen, L. M., 1995a, "Development of Neutral-Density Infrared Filters Using Metallic Thin Films," *MRS Symp. Proc.,* Vol. 374, pp. 117–122.

Zhang, Z. M., Hanssen, L. M., and Datla, R. U., 1995b, "High-Optical-Density Out-of-Band Spectral Transmittance Measurements of Bandpass Filters," *Optics Letters,* Vol. 20, pp. 1077–1079.

Thermal Convection in an Infinite Porous Medium Induced by a Heated Sphere

R. Ganapathy [1]

This paper investigates the transient behavior of the free convection motion and heat transfer induced by a heated sphere with prescribed wall temperature embedded instantaneously in an infinite porous medium. Solutions for the velocity and temperature fields have been obtained in the form of series expansions in Rayleigh number which is based on the medium permeability and the temperature of the sphere. All discussions are based on the assumption that the flow is governed by Darcy's law and the thermal Rayleigh number is small.

Nomenclature

a = radius of the sphere (L)
c_p = specific heat of fluid at constant pressure ($L^2T^2\Theta^{-1}$)
f = function of η (Eq. 13)
G = function of η (Eq. 18)
g = gravitational acceleration (LT^{-2})
K = medium permeability (L^2)
L = length
Q = prescribed wall temperature on the sphere (θ)
R = nondimensional radial coordinate
R_o = nondimensional radius of the sphere ($a/\sqrt{K}$)
Ra = thermal Rayleigh number, $(\beta g K\sqrt{K}/\alpha\nu)Q$
Re = Reynolds number, (UL/ν)
r = radial coordinate (L)
T = temperature (θ)
t = time (T)
U = nondimensional radial velocity
u = radial velocity (LT^{-1})
V = nondimensional transverse velocity
v = transverse velocity (LT^{-1})

Greek Symbols

α = effective thermal diffusivity of the porous medium [L^2T^{-1}]
β = coefficient of thermal expansion [θ^{-1}]
Θ = azimuthal angle
ϕ = meridian angle
η = similarity variable, $R/2\sqrt{t}$
η_o = similarity variable $R_o/2\sqrt{t}$
ν = kinematic viscosity (L^2T^{-1})
σ = heat capacity ratio (eq. 2)
ψ = stream function [L^3T^{-1}]

Subscripts

0 = zeroth-order solution
1 = first-order solution
∞ = reference state

1 Introduction

Since the work of Yamamoto (1974), there has been a spate of research papers on thermal convection due to the presence of heated spheres in saturated porous media. Most of them, with the possible exception of the work of Ganapathy and Purushothaman (1990), were primarily concerned with steady-state solutions only. However, as the analysis of such flows is essential for the solution of many engineering problems such as the hydrodynamics of weak thermal explosions, cooling of the components of electrical and electronic equipment, and the management of nuclear waste, a knowledge of the transient behavior of the flow and heat transfer becomes necessary, especially when the heated sphere is buried instantaneously. It is towards this end that we propose to present a solution to this problem of transient convection due to the presence of a heated sphere embedded instantaneously in an unbounded porous medium and investigate the ensuing flow field and heat transfer in the context of thermal flows in porous media.

2 Mathematical Formulation

We consider the natural convection around a heated sphere of radius a and of constant temperature Q (in excess of the reference temperature), buried instantaneously in an unbounded fluid-saturated porous medium of low permeability. The medium is assumed to be rigid, homogeneous, and isotropic, and the fluid saturating the medium is assumed to be Boussinesq incompressible.

A spherical-polar coordinate system (r, ϕ, Θ) is chosen (Fig. 1), with the origin of the system at the centre of the sphere and the axis $\phi = 0$ vertically upwards. Taking advantage of the continuity equation, we define a stream function ψ such that

$$u = (r^2 \sin\phi)^{-1}\partial\psi/\partial\phi, \quad v = (r\sin\phi)^{-1}\partial\psi/\partial r \qquad (1)$$

where u and v are the radial and transverse components of velocity and introduce the nondimensional quantities (see nomenclature)

[1] Department of Mathematics, National College, Tiruchirapalli 620 001, India.

Contributed by the Heat Transfer Division of THE AMERICAN SOCIETY OF MECHANICAL ENGINEERS. Manuscript received by the Heat Transfer Division July 1, 1996; revision received March 3, 1997; Keywords: Natural Convection; Porous Media; Transient & Unsteady Heat Transfer. Associate Technical Editor: K. Vafai.

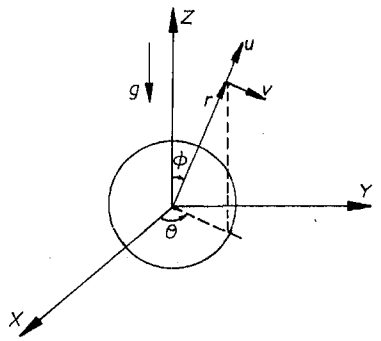

Fig. 1 Configuration of interest. Spherical-polar coordinate system (r, ϕ, Θ) with the origin of the system at the center of the sphere and the $\phi = 0$ axis parallel to the gravity vector

$$R = r/\sqrt{K}, \quad t_* = \alpha t/K\sigma,$$

$$\psi_* = \psi/\alpha\sqrt{K}, \quad T_* = (T - T_\infty)/Q \tag{2}$$

to obtain, finally, for the conservation of mementum and energy in the nondimensional form (after dropping the asterisk) (Ganapathy and Purushothaman, 1990):

$$\frac{1}{R^2}\frac{\partial}{\partial\phi}\left(\frac{1}{\sin\phi}\frac{\partial\psi}{\partial\phi}\right) + \frac{1}{\sin\phi}\frac{\partial^2\psi}{\partial R^2} = \mathrm{Ra}\left(\cos\phi\ \frac{\partial T}{\partial\phi} + R\sin\phi\ \frac{\partial T}{\partial R}\right) \tag{3}$$

$$\frac{\partial T}{\partial t} + \frac{1}{R^2\sin\phi}\frac{\partial(\psi, T)}{\partial(\phi, R)} = \frac{1}{R^2}\left[\frac{\partial}{\partial R}\left(R^2\frac{\partial T}{\partial R}\right) + \frac{1}{\sin\phi}\frac{\partial}{\partial\phi}\left(\sin\phi\ \frac{\partial T}{\partial\phi}\right)\right] \tag{4}$$

where

$$\frac{\partial(\psi, T)}{\partial(\phi, R)} = \frac{\partial\psi}{\partial\phi}\frac{\partial T}{\partial R} - \frac{\partial\psi}{\partial R}\frac{\partial T}{\partial\phi} \tag{5}$$

and

$$\mathrm{Ra} = (\beta g K\sqrt{K}/\alpha\nu)Q \tag{6}$$

is the thermal Rayleigh number, based on the medium permeability and the temperature prescribed on the sphere. The nondimensional form of the velocity components are given by

$$(U, V) = (\sqrt{K}/\alpha)(u, v). \tag{7}$$

Accordingly, in this nondimensional form the initial and boundary conditions reduce to

$$U = V = T = 0 \text{ at } t = 0,$$

$$U, V, T \to 0 \text{ and } R \to \infty,$$

$$(R^2\sin\phi)^{-1}\partial\psi/\partial\phi = 0; \quad T = 1 \text{ on } R = R_o,$$

$$\partial U/\partial\phi = V = \partial T/\partial\phi = 0 \text{ when } \phi = 0, \pi \tag{8}$$

where R_o $(=a/\sqrt{K})$ is the nondimensional radius of the sphere.

3 Results and Discussion

Consistent with the hypothesis that the thermal Rayleigh number is small, we seek a perturbation solution by assuming power series expansions for ψ and T in the form

$$(\psi, T) = \sum_0^\infty \mathrm{Ra}^n(\psi_n, T_n) \tag{9}$$

with similar expressions for U and V to satisfy the conditions (8). As ψ_o corresponds to a state of pure conduction, there will be no fluid motion, and hence we take $\psi_o = 0$. The function T_o is then found from the solution of the equation

$$\frac{\partial T_o}{\partial t} = \frac{1}{R^2}\left[\frac{\partial}{\partial R}\left(R^2\cdot\frac{\partial T_o}{\partial R}\right) + \frac{1}{\sin\phi}\frac{\partial}{\partial\phi}\left(\sin\phi\ \frac{\partial T_o}{\partial\phi}\right)\right]. \tag{10}$$

From Landau and Lifshitz (1963), we have

$$T_o = (R_o/R)\ erfc\ [(R - R_o)/2\sqrt{t}]. \tag{11}$$

The first convective correction to the velocity field is now found from the solution of the equation

$$\frac{1}{R^2}\frac{\partial}{\partial\phi}\left(\frac{1}{\sin\phi}\frac{\partial\psi_1}{\partial\phi}\right) + \frac{1}{\sin\phi}\frac{\partial^2\psi_1}{\partial R^2} = \cos\phi\ \frac{\partial T_o}{\partial\phi} + R\sin\phi\ \frac{\partial T_o}{\partial R} \tag{12}$$

in which the variables are separated by setting

$$\psi_1 = 2\sqrt{t}\cdot R_o\cdot\sin^2\phi f(\eta) \tag{13}$$

where $\eta = R/2\sqrt{t}$. This then leads to an ordinary differential equation of the second-order for f:

$$\eta^2 f''(\eta) - 2f(\eta) = -\eta\ erfc\ (\eta - \eta_o) - 2\eta^2\exp[-(\eta - \eta_0)^2]/\sqrt{\pi} \tag{14}$$

where $\eta_0 = R_o/2\sqrt{t}$ and the primes denote differentiation with respect to η. The general solution of this equation is found to be

$$f(\eta) = C_1/\eta + C_2\eta^2 + (\eta^2 - \eta_0^2)[erfc\ (\eta - \eta_0)]/2\eta - [erfc\ (\eta - \eta_0)]/4\eta - [(\eta + \eta_0)/2\eta\sqrt{\pi}]\exp[-(\eta - \eta_0)^2] \tag{15}$$

where $C_2 = 0$, by virtue of the boundary condition at infinity, and $C_1 = (4\eta_0 + \sqrt{\pi})/4\sqrt{\pi}$, by virtue of the boundary condition at $R = R_o$. Thus we finally obtain

$$\psi_1 = \sqrt{t}\cdot\sin^2\phi\cdot\frac{R_o}{\eta}\left[\frac{2}{\sqrt{\pi}}\eta_0 + (\eta^2 - \eta_0^2)\ erfc\ (\eta - \eta_0) + \frac{1}{2}erf(\eta - \eta_0) - \frac{1}{\sqrt{\pi}}(\eta + \eta_0)\exp[-(\eta - \eta_0)^2]\right]. \tag{16}$$

The map of the streamlines $\psi_1/(R_o\sqrt{t}) = \text{const.}$ is presented in Fig. 2, from which it is deducible that in the initial stages closed loops appear in the flow whose geometry considerably changes at higher values of t, although the symmertry about the plane $\phi = \pi/2$ is preserved at all times. Further, during the initial stages of the flow development there is a concentration of the velocity field around the sphere, and as time increases, the flow pattern present near the sphere spreads outwards filling the entire space. These streamlines enclose the stagnation points (points of maximum ψ) whose distance from the center of the sphere increases with time and finally recedes to infinity in the ultimate state as $t \to \infty$. There is no accumulation of heat into the flow field and the flow in and around the streamlines remains laminar, the entire process being dominated by viscosity cou-

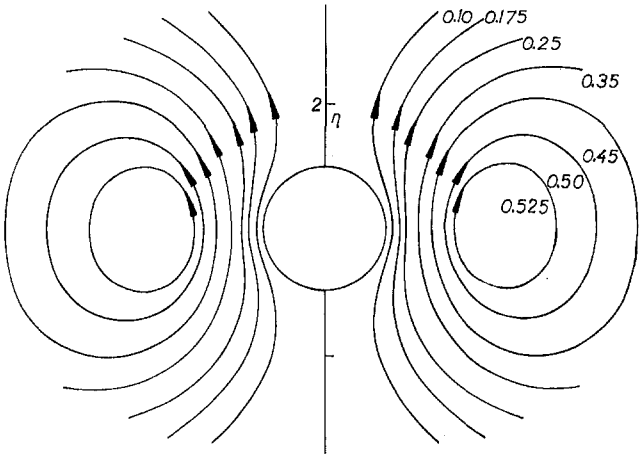

Fig. 2 Transient flow pattern. Curves represent the streamlines $(\psi_1/R_o)t^{-1/2}$ = const. with $\eta_o = 1$

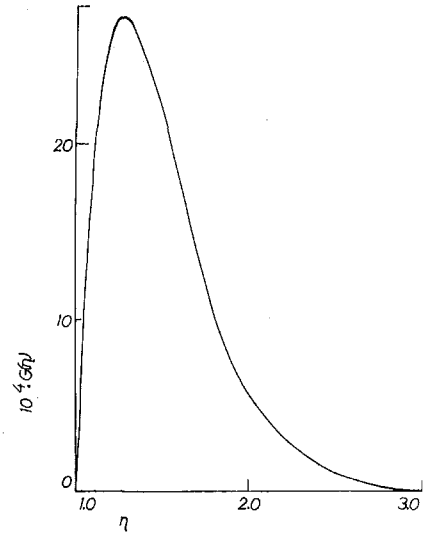

Fig. 3 Map of the function $G(\eta)$

pled with thermal diffusion. Further, the smaller the radius of the sphere, the lesser the concavity of the streamlines in its vicinity will be. It may be noted here that as the solution is uniformly valid, we do not require an Oseen-type approximation to determine the velocity distribution farther away from the sphere.

The first convective correction to the thermal field is now found from the solution of the equation

$$\frac{\partial T_1}{\partial t} + \frac{1}{R^2 \sin\phi}\left[\frac{\partial(\psi_o, T_1)}{\partial(\phi, R)} + \frac{\partial(\psi_1, T_o)}{\partial(\phi, R)}\right] = \frac{1}{R^2}\left[\frac{\partial}{\partial R}\left(R^2\frac{\partial T_1}{\partial R}\right) + \frac{1}{\sin\phi}\frac{\partial}{\partial\phi}\left(\sin\phi\ \frac{\partial T_1}{\partial\phi}\right)\right] \quad (17)$$

in which the separation of variables can be achieved by setting

$$T_1 = \cos\phi \cdot G(\eta)/\sqrt{t}. \quad (18)$$

This then leads to a second order differential equation for G:

$$\eta^2 G''(\eta) + 2\eta(\eta^2+1)G'(\eta) + 2(\eta^2-1)G(\eta) = -(R_o/\eta)^2 f(\eta)\left[erfc\,(\eta-\eta_0) + \frac{1}{2\sqrt{\pi}}\eta\exp[-(\eta-\eta_0)^2]\right] \quad (19)$$

with the boundary conditions $G(\eta_0) = G(\infty) = 0$. As an exact solution is found to be not possible, we solve Eq. (19) numerically using a finite difference scheme (Jain, 1984) choosing $\eta_o = 1$. We plot the graph of $G(\eta)$ in Fig. 3 from which it is deducible that $G(\eta)$ increases from zero on the surface of the sphere to a certain value and then starts decreasing at an ever decreasing rate to zero at positions farther away from the sphere. Albeit tacitly, this then implies that there is an increase in temperature for points in the upper half-space ($0 \le \phi \le \pi/2$) accompanied by an equal decrease in temperature in the lower half-space; consequently, the fluid particles in the upper half-space will be warmer than those in the lower half-space.

Owing to prohibitive algebraic complexities, higher-order corrections to the velocity and temperature fields were not obtained. However, the error due to the noninclusion of these higher-order terms is of the order of Ra^2 which is marginal in view of the fact that $Ra < 1$. Moreover, as the thermal field is relatively unaffected by convection when $Ra < 1$ (Hickox and Watts, 1980), higher-order corrections are not of great significance.

In the limiting case as $t \to \infty$, we recover the results of Yamamoto (1974), of course with a different nondimensionalization scheme. As an adequate description of the evolution of the flow field and heat transfer has already been given in that paper, we omit a discussion on the steady state for the sake of brevity.

4 Conclusion

We have presented a thoretical study of natural convection from a heated sphere buried instantaneously in an unbounded porous medium and obtained the transient solution for the velocity and temperature fields using a perturbation analysis in the limit of small Rayleigh number. The results are valid in the diffusion-dominated regime only. As the thermal Rayleigh number is assumed to be small, the magnitude of the prescribed wall temperature, namely Q, cannot exceed $\alpha\nu/\beta g K\sqrt{K}$. The solution we have obtained for the stream function is expected to give a reasonably good picture of the free convection motion, and in the absence of instability effects, the behavior of the flow is unlikely to change radically for moderate values of Ra also. As the thermal Rayleigh number depends only on the prescribed surface temperature, the permeability of the medium and the fluid properties, the evolution of the flow pattern is expected to be the same irrespective of the nature of the material embedded. Lastly, we note that as our solution is uniformly valid, neither do we require an Oseen type approximation to determine the velocity distribution farther away from the sphere, nor do we require the condition $R \ll \mathrm{Re}^{-1}$ for the validity of the time-independent solution where Re is the Reynolds number associated with the fluid motion.

Acknowledgment

The author is thankful to the referees for their many useful suggestions which led to a definite improvement of the paper.

References

Cheng, P., 1978, "Heat Transfer in Geothermal Systems," *Advances in Heat Transfer*, Vol. 14, Academic Press, pp. 1–105.

Ganapathy, R., and Purushothaman, R., 1990, "Free Convection in an Infinite Porous Medium Induced by a Heated Sphere," *International Journal of Engineering Science*, Vol. 28, No. 8, pp. 751–759.

Hockox, C. E., and Watts, H. A., 1980, "Steady Thermal Convection From a Concentrated Source in a Porous Medium," ASME JOURNAL OF HEAT TRANSFER, Vol. 102, No. 2, p. 248.

Jain, M. K., 1984, *Numerical Solution of Differential Equations,* Wiley Eastern Limited, p. 193.
Landau, L. D., and Lifshitz, E. M., 1963, *Fluid Mechanics,* Pergamon Press, p. 201.
Yamamoto, K., 1974, "Natural Convection About a Heated Sphere in a Porous Medium," *Journal of Physical Society of Japan,* Vol. 37, No. 4, pp. 1164–1166.

Cross-Stream Thermal Dispersion in a Staggered Tube Bundle With Crossflow

J. M. Ashcroft[1] and D. A. Kaminski[2]

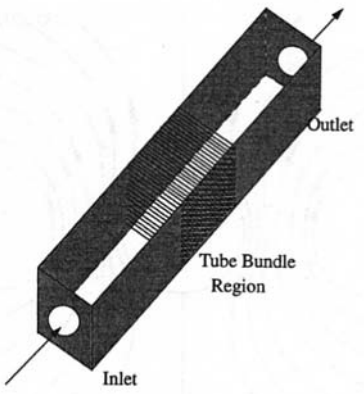

Fig. 1 The air flow test sections. Each test section has twelve rows of tubes with eleven full tubes and one half tube in each row, all located within a rectangular duct. The side walls are steel and the top and bottom walls are glass.

Introduction

Heat transfer and pressure drop in tube bundles with crossflow has been studied for years. Until recently, however, numerical models of tube bundle flows have been limited to unheated flows. Diaper and Haseler (1990) studied the detailed flow distribution around unheated tubes in a staggered rectangular tube bundle using the FLOW3D code. Their pressure drop results showed good agreement to correlations. Numerical modeling of heated crossflow was performed by Ashcroft and Kaminski (1996) showed good agreement with correlations by Zukaukas (1989) for both pressure drop and heat transfer coefficient (less than 10 percent deviation).

One difficulty associated with numerical modeling of heated tube bundle flows is in the selection of the turbulent Prandtl number applicable for this flow field. Kays' review paper (1994) suggests a turbulent Prandtl number of 0.85 for boundary layer flows. Antonia and Browne (1987) suggested lower values of the turbulent Prandtl number are appropriate for wake flows. Thermal dispersion in a tube bundle is dependent on both boundary layer and wake heat transfer, making selection of the appropriate turbulent Prandtl number unclear.

Procedures for using a porous body approximation to simulate flow and heat transfer in heat exchangers are well developed, as demonstrated by Zhang (1994) and Roetzel (1996). However, effective thermal conductivity models for the fluid are not well developed. Yagi and Wakao (1960), Cheng and Vortmeyer (1988) and Adnani et al. (1995) each developed effective thermal conductivity models for packed beds. Similar effective thermal conductivity models are needed to simulate cross-stream dispersion in tube bundles with the porous media approximation. An effective thermal conductivity model was developed by Ashcroft and Kaminski (1996) assuming a turbulent Prandtl number of 0.9. That work was modified by using the turbulent Prandtl number inferred from subsequent experiments, as described in this paper.

Thermal Mixing Experiments and Results

Thermal mixing experiments were conducted in order to measure the rate of cross-stream dispersion in a tube bundle with crossflow. The tests studied equilateral staggered tube bundles, each with 12 streamwise rows with 11 full tubes and 1 half tube per row, with pitch to diameter ratios (p/d) of 1.20, 1.33, 1.50, and 1.75, as shown in Fig. 1. In all cases, 9.5 mm diameter internally insulated, thin walled stainless steel tubes were used. In each test, a single cartridge heater, positioned in the center of the fourth tube row, was used to heat the uniform inlet flow of air. The temperature distribution in the wake of the heater was measured using wall mounted thermocouples on tubes on the wake centerline and off-centerline locations. The air flow rate was controlled in order to provide Reynolds numbers, based on the tube diameter and the maximum velocity, of between 1200 and 20,000. Further details on the apparatus are given in Ashcroft (1996). Ashcroft (1996) also provides a detailed error assessment for the experiments run. The combined effect of thermocouple errors, flow measurement errors, uncertainties in heat input and in flow distribution all contribute to a total uncertainty of 8 percent of the measured temperature rise.

The results of the experiments show that the temperature distribution remains nearly constant with changes in Reynolds number. The temperature rise from the inlet to each of the thermocouples on the wake centerline downstream of the heater is shown in Fig. 2 for the 1.50 p/d case. The temperature rise is nondimensionalized by dividing by the average temperature rise through the bundle, calculated from an energy balance, and by the number of tubes in each row of the test section:

$$T^* = (T - T_{in})/(\Delta T_{ave} N). \quad (1)$$

This method of nondimensionalizing provides an approximation of the fraction of energy added to the flow by the heater which remains in the centerline path. Lower values of remaining energy represent a greater rate of turbulent diffusion of energy to off-centerline flow paths.

Figure 3 shows the effect of tube bundle spacing on the rate of turbulent diffusion. Here the average temperature rise for all Reynolds numbers for each of the four tube bundles is shown. The tighter tube bundle spacings have a lower centerline temperature rise, and therefore a greater fraction of energy diffusion from the centerline path to adjacent paths. This trend is also seen at the off-centerline instrumented tube locations.

Numerical Simulations and Results

Seven detailed numerical grids were made for comparison with the experimental results (p/d = 1.10, 1.20, 1.25, 1.33, 1.50, 1.75, and 2.00). The seven numerical grids represented a three-tube by ten-tube section of staggered tube bundles deep within the tube bundle, away from the effects of inlet conditions. Each grid has 15 control volumes between adjacent tubes for a total of 22,050 control volumes. A single tube surface on the right symmetry plane is provided with a constant heat flux. The temperature distribution downstream of the heater was calcu-

[1] Lockheed Martin Corporation, Schenectady, NY 12301
[2] Mechanical Engineering, Aeronautical Engineering and Mechanics, Rensselaer Polytechnic Institute, Troy, NY 12180-3590
Contributed by the Heat Transfer Division of THE AMERICAN SOCIETY OF MECHANICAL ENGINEERS. Manuscript received by the Heat Transfer Division August 6, 1996; revision received December 23, 1996; Keywords: Numerical Methods, Porous Media, Turbulence. Associate Technical Editor: T. J. Rabas.

Jain, M. K., 1984, *Numerical Solution of Differential Equations,* Wiley Eastern Limited, p. 193.
Landau, L. D., and Lifshitz, E. M., 1963, *Fluid Mechanics,* Pergamon Press, p. 201.
Yamamoto, K., 1974, "Natural Convection About a Heated Sphere in a Porous Medium," *Journal of Physical Society of Japan,* Vol. 37, No. 4, pp. 1164–1166.

Cross-Stream Thermal Dispersion in a Staggered Tube Bundle With Crossflow

J. M. Ashcroft[1] and D. A. Kaminski[2]

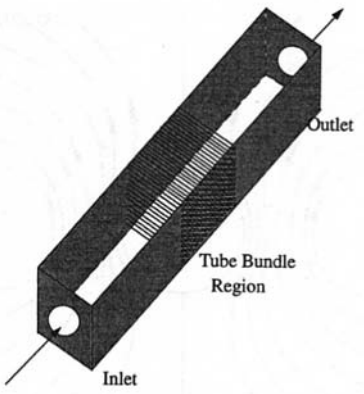

Fig. 1 The air flow test sections. Each test section has twelve rows of tubes with eleven full tubes and one half tube in each row, all located within a rectangular duct. The side walls are steel and the top and bottom walls are glass.

Introduction

Heat transfer and pressure drop in tube bundles with crossflow has been studied for years. Until recently, however, numerical models of tube bundle flows have been limited to unheated flows. Diaper and Haseler (1990) studied the detailed flow distribution around unheated tubes in a staggered rectangular tube bundle using the FLOW3D code. Their pressure drop results showed good agreement to correlations. Numerical modeling of heated crossflow was performed by Ashcroft and Kaminski (1996) showed good agreement with correlations by Zukaukas (1989) for both pressure drop and heat transfer coefficient (less than 10 percent deviation).

One difficulty associated with numerical modeling of heated tube bundle flows is in the selection of the turbulent Prandtl number applicable for this flow field. Kays' review paper (1994) suggests a turbulent Prandtl number of 0.85 for boundary layer flows. Antonia and Browne (1987) suggested lower values of the turbulent Prandtl number are appropriate for wake flows. Thermal dispersion in a tube bundle is dependent on both boundary layer and wake heat transfer, making selection of the appropriate turbulent Prandtl number unclear.

Procedures for using a porous body approximation to simulate flow and heat transfer in heat exchangers are well developed, as demonstrated by Zhang (1994) and Roetzel (1996). However, effective thermal conductivity models for the fluid are not well developed. Yagi and Wakao (1960), Cheng and Vortmeyer (1988) and Adnani et al. (1995) each developed effective thermal conductivity models for packed beds. Similar effective thermal conductivity models are needed to simulate cross-stream dispersion in tube bundles with the porous media approximation. An effective thermal conductivity model was developed by Ashcroft and Kaminski (1996) assuming a turbulent Prandtl number of 0.9. That work was modified by using the turbulent Prandtl number inferred from subsequent experiments, as described in this paper.

Thermal Mixing Experiments and Results

Thermal mixing experiments were conducted in order to measure the rate of cross-stream dispersion in a tube bundle with crossflow. The tests studied equilateral staggered tube bundles, each with 12 streamwise rows with 11 full tubes and 1 half tube per row, with pitch to diameter ratios (p/d) of 1.20, 1.33, 1.50, and 1.75, as shown in Fig. 1. In all cases, 9.5 mm diameter internally insulated, thin walled stainless steel tubes were used. In each test, a single cartridge heater, positioned in the center of the fourth tube row, was used to heat the uniform inlet flow of air. The temperature distribution in the wake of the heater was measured using wall mounted thermocouples on tubes on the wake centerline and off-centerline locations. The air flow rate was controlled in order to provide Reynolds numbers, based on the tube diameter and the maximum velocity, of between 1200 and 20,000. Further details on the apparatus are given in Ashcroft (1996). Ashcroft (1996) also provides a detailed error assessment for the experiments run. The combined effect of thermocouple errors, flow measurement errors, uncertainties in heat input and in flow distribution all contribute to a total uncertainty of 8 percent of the measured temperature rise.

The results of the experiments show that the temperature distribution remains nearly constant with changes in Reynolds number. The temperature rise from the inlet to each of the thermocouples on the wake centerline downstream of the heater is shown in Fig. 2 for the 1.50 p/d case. The temperature rise is nondimensionalized by dividing by the average temperature rise through the bundle, calculated from an energy balance, and by the number of tubes in each row of the test section:

$$T^* = (T - T_{in})/(\Delta T_{ave} N). \quad (1)$$

This method of nondimensionalizing provides an approximation of the fraction of energy added to the flow by the heater which remains in the centerline path. Lower values of remaining energy represent a greater rate of turbulent diffusion of energy to off-centerline flow paths.

Figure 3 shows the effect of tube bundle spacing on the rate of turbulent diffusion. Here the average temperature rise for all Reynolds numbers for each of the four tube bundles is shown. The tighter tube bundle spacings have a lower centerline temperature rise, and therefore a greater fraction of energy diffusion from the centerline path to adjacent paths. This trend is also seen at the off-centerline instrumented tube locations.

Numerical Simulations and Results

Seven detailed numerical grids were made for comparison with the experimental results (p/d = 1.10, 1.20, 1.25, 1.33, 1.50, 1.75, and 2.00). The seven numerical grids represented a three-tube by ten-tube section of staggered tube bundles deep within the tube bundle, away from the effects of inlet conditions. Each grid has 15 control volumes between adjacent tubes for a total of 22,050 control volumes. A single tube surface on the right symmetry plane is provided with a constant heat flux. The temperature distribution downstream of the heater was calcu-

[1] Lockheed Martin Corporation, Schenectady, NY 12301
[2] Mechanical Engineering, Aeronautical Engineering and Mechanics, Rensselaer Polytechnic Institute, Troy, NY 12180-3590
Contributed by the Heat Transfer Division of THE AMERICAN SOCIETY OF MECHANICAL ENGINEERS. Manuscript received by the Heat Transfer Division August 6, 1996; revision received December 23, 1996; Keywords: Numerical Methods, Porous Media, Turbulence. Associate Technical Editor: T. J. Rabas.

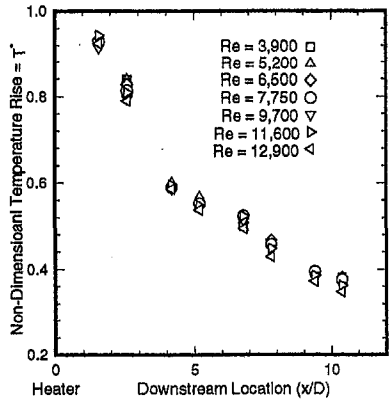

Fig. 2 Centerline temperature rise distribution downstream of the heated tube in the 1.50 p/d test section. The abscissa represents the distance downstream of the rear of the heated tube, given in tube diameters. Note that the nondimensional temperature rise measured is nearly independent of Reynolds number.

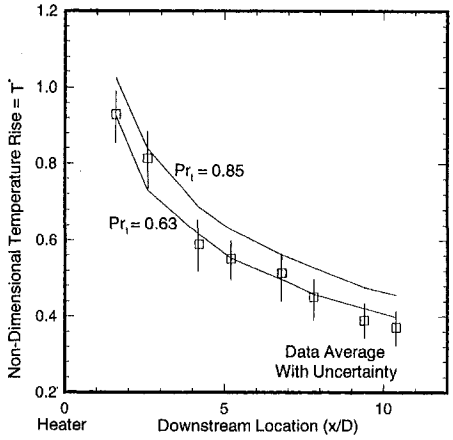

Fig. 4 Comparison of the experimental and numerical results for the 1.50 p/d case. The numerical results show that a turbulent Prandtl number of 0.63 provides better agreement to data than the case with a turbulent Prandtl number of 0.85. This trend is true for all geometries studied.

lated. The flow and temperature field for the numerical models was determined by the FLOW3D computational fluid dynamics program. This program solved the standard continuity, momentum and energy equations for each control volume for steady, incompressible flow with constant properties. The effective viscosity in the momentum equation and the effective thermal conductivity in the energy equation are the sum of the molecular (μ, k) and turbulent (μ_t, k_t) components. The standard k-ϵ turbulence model was used to determine the turbulent viscosity in the momentum equation. The turbulent thermal conductivity is assumed to be proportional to the turbulent viscosity, the specific heat and the turbulent Prandtl number:

$$k_t = \mu_t c_p / \mathrm{Pr}_t. \tag{2}$$

The numerical models developed were shown to be grid insensitive. The current model, with 15 control volumes between adjacent tubes was compared to models with 10 and 30 control volumes between tubes. The computed temperature distributions differed by less than 1 percent at all locations. Pressure drops and tube surface heat transfer coefficients were in good agreement with correlations, as described in Ashcroft (1996).

The numerical simulations were run with the same conditions as were tested in the experiments in order to compare the results. The numerical models showed the same relative insensitivity to flow rate as was seen in the experiments. Figure 4 shows the comparison for the 1.50 pitch to diameter ratio tube bundle. The numerical simulation run using the turbulent Prandtl number recommended for boundary layer flows, $\mathrm{Pr}_t = 0.85$, underestimates the rate of cross-stream dispersion and therefore overestimates the temperature rise contour of the centerline path. Based on comparisons of all four test sections, a turbulent Prandtl number of 0.63 was determined to minimize the difference in centerline and off-centerline temperature rise between the simulations and the data.

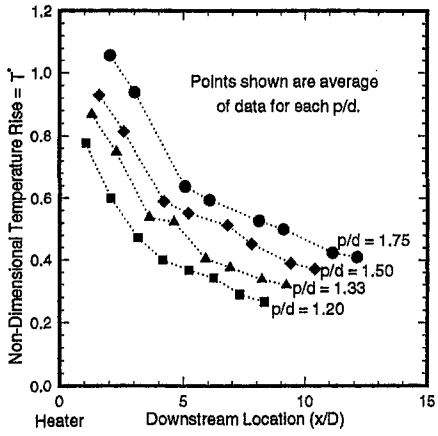

Fig. 3 Comparison of centerline temperature rise for different tube bundle spacing. The tighter tube bundles have a greater rate of cross-stream diffusion and therefore a lower centerline nondimensional temperature rise.

Porous Body Simulations of Tube Bundles

A porous body model of a tube bundle offers the advantage of limited resolution of a large tube bundle with a comparatively low number of grid nodes required. The two-dimensional porous simulations of the 3 × 10 tube bundles considered here have just 120 control volumes. Porous models, however, require input values for the hydraulic resistance and for the porous region effective thermal conductivity. The porous body effective thermal conductivity used in the steady-state incompressible energy equation for a porous medium with constant properties is:

$$\rho c_p \nabla \cdot (UT) - \nabla(k_{\mathrm{por}} \Delta T) = 0. \tag{3}$$

The porous body effective thermal conductivity (k_{por}) is the sum of the molecular and turbulent thermal conductivities of the fluid. The cross-stream effective thermal conductivity is assumed to be equal to the streamwise component. It is also assumed that the tube walls are insulating.

The development of an effective thermal conductivity model starts with the observation that for any given pitch to diameter ratio, and at higher Reynolds numbers (above Re = 5000), the temperature distribution downstream of the heated tube in the numerical simulations does not change with the Reynolds number. In this case, the turbulent diffusion is proportional to the heat added, which is in turn proportional to the flow rate:

$$k_{\mathrm{turb}} \Delta T_1 \sim Q \sim \dot{m} c_p \Delta T_2. \tag{4}$$

The temperature distributions in the cross-stream and streamwise directions, ΔT_1 and ΔT_2, are constant. The mass flow rate, $\dot{m}$, and the specific heat, c_p, can be given in terms of the Reynolds number, the Prandtl number, and the bundle geometry:

$$k_{\mathrm{turb}} \sim m c_p = k \,\mathrm{Re}\,\mathrm{Pr}(p/d - 1). \tag{5}$$

The thermal conductivity used in the porous body model accounts for the average cross-stream distance of energy transport, given in terms of the tube bundle porosity (γ):

$$k_{por} = (k + k_{turb})/\gamma = k[1/\gamma + C\ \mathrm{Re}\ \mathrm{Pr}]. \quad (6)$$

A value of the mixing constant (C) of 0.043 for all of the tube bundles tested provided agreement between the two simulation techniques with no greater than 3 percent error at any location within the flow.

Discussion

The effective thermal conductivity model developed for tube bundles has the same form as that developed previously for packed beds. For packed beds, Adnani et al. (1995) developed an effective thermal conductivity of:

$$k_{por}/k = k_0/k + D\ \mathrm{Re}\ \mathrm{Pr} \quad (7)$$

where the mixing constant $D = 0.14$. The Reynolds number for this model however used the average velocity instead of the maximum velocity. When compared on an equal basis, the mixing constant for tube bundles is about 60 percent of that for packed beds. A reduced rate of mixing for a tube bundle as compared to a packed bed seems logical in light to the fixed spacing and the two-dimensional flow field in a tube bundle.

The effective thermal conductivity model has been used to study cases with multiple heated tubes and tubes with different heating rates. In all cases, the temperature distribution of the porous simulation matches that of the detailed numerical simulation. Therefore, the model developed appears valid for large nonuniformly heated tube bundles where the effects of inlet conditions and side walls can be safely ignored. Cases with multiple heated tubes are discussed by Ashcroft (1996).

Conclusions

The investigation of thermal dispersion in tube bundles has shown two things. First, numerical simulations with the k-ϵ turbulence model can accurately represent the molecular and turbulent thermal dispersion in a tube bundle when a turbulent Prandtl number of 0.63 is used. Second, porous body simulations can accurately represent the effects of cross-stream diffusion when an effective thermal conductivity model is used. The effective conductivity is linearly dependent on Reynolds number and Prandtl number, and nearly independent of tube spacing. A mixing constant of 0.043 provided good agreement to the numerical results in the range of conditions tested. The effective thermal conductivity model has been used to analyze tube bundle flows with multiple heated tubes.

References

Adnani, P., Catton, I., and Abdou, M. A., 1995, "Non-Darcian Forced Convection in Porous Media with Anisotropic Dispersion," ASME JOURNAL OF HEAT TRANSFER, Vol. 117, pp. 447–451.

Antonia, R. A., and Browne, L. W. B., 1987, "Conventional and Conditional Prandtl Number in A Turbulent Plane Wake," *Int. Journal of Heat and Mass Transfer,* Vol. 30, pp. 2023–2030.

Ashcroft, J. M., 1996, "Cross-Stream Thermal Diffusion in Staggered Tube Bundles with Cross Flow," Ph.D. thesis, Rensselaer Polytechnic Institute, Troy, NY.

Ashcroft, J. M., and Kaminski, D. A., 1996, "A Thermal Mixing Model of Crossflow in Tube Bundles for use With the Porous Body Approximation," *Proceedings of the International Conference on Porous Media and its Applications,* Kambiz Vafai, ed., Kona, HI.

Cheng, P., and Vortmeyer, D., 1988, "Transverse Thermal Dispersion and Wall Channeling in Packed Beds With Forced Convective Flow," *Chem. Eng. Sciences,* Vol. 43, pp. 2523–2532.

Diaper, A. D., and Haseler, L. E., 1990, "Crossflow Pressure Drop and Flow Distribution Within a Tube Bundle Using Computational Fluid Dynamics," *Heat Transfer 1990: Proceedings of the 9th International Heat Transfer Conf.,* Vol. 3, Hemisphere Publishing Corp., G. Hetsroni, ed., Jerusalem, Israel.

Kays, W. M., 1994, "Turbulent Prandtl Number, Where Are We?," ASME JOURNAL OF HEAT TRANSFER, Vol. 116, pp. 284–294.

Roetzel, W., 1996, "Transient Analysis in Heat Exchangers," *New Developments in Heat Exchangers,* Gordon & Breach, Science Publishers Inc., NY.

Yagi, S., and Wakao, N., 1960, "Heat and Mass Transfer From Wall to Fluid in Packed Beds," *AIChE Journal,* Vol. 5, pp. 79–85.

Zhang, C., 1994, "Numerical Modeling Using a Quasi-Three-Dimensional Procedure for Large Power Plant Condensers," ASME JOURNAL OF HEAT TRANSFER, Vol. 116, pp. 180–188.

Zukauskas, A., 1989, *High Performance Single Phase Heat Exchangers,* Hemisphere Publishing Corp., Bristol, PA.

Laws for Fiber Temperature Prediction During Drawing

P. G. Simpkins[1] and P. A. Blythe[2]

Nomenclature

- A = the fiber cross sectional area
- a = amplitude, see Eq. (6)
- Bi = the Biot number, $(=h_\infty R_f'/k_{f_\infty})$
- c_p = specific heat
- E = defined by Eq. (5)
- H = defined by Eq. (5)
- h = heat transfer coefficient
- k = thermal conductivity of silica
- M = defined by Eq. (7)
- P = the fiber perimeter
- Pe = Peclet number, $(=WR_f'/\alpha_\infty)$
- r', z' = cylindrical co-ordinates
- R_f' = the fiber radius
- Re = Reynolds number, $(=WR_f'/\nu_\infty)$
- t_c' = characteristic cooling time, see §2
- T = temperature
- U = dimensionless draw speed, $(=WR_f'^2/k_{f_\infty}z')$
- V = cross flow speed
- W = draw speed
- z_c' = characteristic cooling length, see Eq. (1)
- Z = dimensionless axial scale, see Eq. (9)

Greek Symbols

- α = thermal diffusivity
- ϵ = emissivity
- η = dimensionless axial distance
- ρ' = fiber density
- σ = Stefan-Boltzmann constant
- ν = kinematic viscosity

Superscripts

- Primes($'$) = where appropriate, primes denote dimensional quantities

Subscripts

- c = convective scale
- f = fiber
- s = softening point
- o = effective origin for lumped parameter solution
- ∞ = ambient conditions

1 Introduction

Optical fibers are manufactured by drawing material from the end of a heated solid silica preform rod. Prior to applying a

[1] Bell Laboratories, Lucent Technologies, Murray Hill, NJ 07974: pgs@bell-labs.com

[2] Lehigh University, Bethelehem, PA 18015: pab0@lehigh.edu

Contributed by the Heat Transfer Division of THE AMERICAN SOCIETY OF MECHANICAL ENGINEERS. Manuscript received by the Heat Transfer Division July 29, 1996; revision received February 19, 1997; Keywords: Forced Convection, Mat'ls Processing & Manufacturing Process, Modeling & Scaling. Associate Technical Editor: Y. Jaluria.

$$k_{por} = (k + k_{turb})/\gamma = k[1/\gamma + C\ \mathrm{Re}\ \mathrm{Pr}]. \quad (6)$$

A value of the mixing constant (C) of 0.043 for all of the tube bundles tested provided agreement between the two simulation techniques with no greater than 3 percent error at any location within the flow.

Discussion

The effective thermal conductivity model developed for tube bundles has the same form as that developed previously for packed beds. For packed beds, Adnani et al. (1995) developed an effective thermal conductivity of:

$$k_{por}/k = k_0/k + D\ \mathrm{Re}\ \mathrm{Pr} \quad (7)$$

where the mixing constant $D = 0.14$. The Reynolds number for this model however used the average velocity instead of the maximum velocity. When compared on an equal basis, the mixing constant for tube bundles is about 60 percent of that for packed beds. A reduced rate of mixing for a tube bundle as compared to a packed bed seems logical in light to the fixed spacing and the two-dimensional flow field in a tube bundle.

The effective thermal conductivity model has been used to study cases with multiple heated tubes and tubes with different heating rates. In all cases, the temperature distribution of the porous simulation matches that of the detailed numerical simulation. Therefore, the model developed appears valid for large nonuniformly heated tube bundles where the effects of inlet conditions and side walls can be safely ignored. Cases with multiple heated tubes are discussed by Ashcroft (1996).

Conclusions

The investigation of thermal dispersion in tube bundles has shown two things. First, numerical simulations with the k-ϵ turbulence model can accurately represent the molecular and turbulent thermal dispersion in a tube bundle when a turbulent Prandtl number of 0.63 is used. Second, porous body simulations can accurately represent the effects of cross-stream diffusion when an effective thermal conductivity model is used. The effective conductivity is linearly dependent on Reynolds number and Prandtl number, and nearly independent of tube spacing. A mixing constant of 0.043 provided good agreement to the numerical results in the range of conditions tested. The effective thermal conductivity model has been used to analyze tube bundle flows with multiple heated tubes.

References

Adnani, P., Catton, I., and Abdou, M. A., 1995, "Non-Darcian Forced Convection in Porous Media with Anisotropic Dispersion," ASME JOURNAL OF HEAT TRANSFER, Vol. 117, pp. 447–451.

Antonia, R. A., and Browne, L. W. B., 1987, "Conventional and Conditional Prandtl Number in A Turbulent Plane Wake," *Int. Journal of Heat and Mass Transfer,* Vol. 30, pp. 2023–2030.

Ashcroft, J. M., 1996, "Cross-Stream Thermal Diffusion in Staggered Tube Bundles with Cross Flow," Ph.D. thesis, Rensselaer Polytechnic Institute, Troy, NY.

Ashcroft, J. M., and Kaminski, D. A., 1996, "A Thermal Mixing Model of Crossflow in Tube Bundles for use With the Porous Body Approximation," *Proceedings of the International Conference on Porous Media and its Applications,* Kambiz Vafai, ed., Kona, HI.

Cheng, P., and Vortmeyer, D., 1988, "Transverse Thermal Dispersion and Wall Channeling in Packed Beds With Forced Convective Flow," *Chem. Eng. Sciences,* Vol. 43, pp. 2523–2532.

Diaper, A. D., and Haseler, L. E., 1990, "Crossflow Pressure Drop and Flow Distribution Within a Tube Bundle Using Computational Fluid Dynamics," *Heat Transfer 1990: Proceedings of the 9th International Heat Transfer Conf.,* Vol. 3, Hemisphere Publishing Corp., G. Hetsroni, ed., Jerusalem, Israel.

Kays, W. M., 1994, "Turbulent Prandtl Number, Where Are We?," ASME JOURNAL OF HEAT TRANSFER, Vol. 116, pp. 284–294.

Roetzel, W., 1996, "Transient Analysis in Heat Exchangers," *New Developments in Heat Exchangers,* Gordon & Breach, Science Publishers Inc., NY.

Yagi, S., and Wakao, N., 1960, "Heat and Mass Transfer From Wall to Fluid in Packed Beds," *AIChE Journal,* Vol. 5, pp. 79–85.

Zhang, C., 1994, "Numerical Modeling Using a Quasi-Three-Dimensional Procedure for Large Power Plant Condensers," ASME JOURNAL OF HEAT TRANSFER, Vol. 116, pp. 180–188.

Zukauskas, A., 1989, *High Performance Single Phase Heat Exchangers,* Hemisphere Publishing Corp., Bristol, PA.

Laws for Fiber Temperature Prediction During Drawing

P. G. Simpkins[1] and P. A. Blythe[2]

Nomenclature

A = the fiber cross sectional area
a = amplitude, see Eq. (6)
Bi = the Biot number, $(=h_\infty R_f'/k_{f_\infty})$
c_p = specific heat
E = defined by Eq. (5)
H = defined by Eq. (5)
h = heat transfer coefficient
k = thermal conductivity of silica
M = defined by Eq. (7)
P = the fiber perimeter
Pe = Peclet number, $(=WR_f'/\alpha_\infty)$
r', z' = cylindrical co-ordinates
R_f' = the fiber radius
Re = Reynolds number, $(=WR_f'/\nu_\infty)$
t_c' = characteristic cooling time, see §2
T = temperature
U = dimensionless draw speed, $(=WR_f'^2/k_{f_\infty}z')$
V = cross flow speed
W = draw speed
z_c' = characteristic cooling length, see Eq. (1)
Z = dimensionless axial scale, see Eq. (9)

Greek Symbols

α = thermal diffusivity
ϵ = emissivity
η = dimensionless axial distance
ρ' = fiber density
σ = Stefan-Boltzmann constant
ν = kinematic viscosity

Superscripts

Primes($'$) = where appropriate, primes denote dimensional quantities

Subscripts

c = convective scale
f = fiber
s = softening point
o = effective origin for lumped parameter solution
∞ = ambient conditions

1 Introduction

Optical fibers are manufactured by drawing material from the end of a heated solid silica preform rod. Prior to applying a

[1] Bell Laboratories, Lucent Technologies, Murray Hill, NJ 07974: pgs@bell-labs.com

[2] Lehigh University, Bethelehem, PA 18015: pab0@lehigh.edu

Contributed by the Heat Transfer Division of THE AMERICAN SOCIETY OF MECHANICAL ENGINEERS. Manuscript received by the Heat Transfer Division July 29, 1996; revision received February 19, 1997; Keywords: Forced Convection, Mat'ls Processing & Manufacturing Process, Modeling & Scaling. Associate Technical Editor: Y. Jaluria.

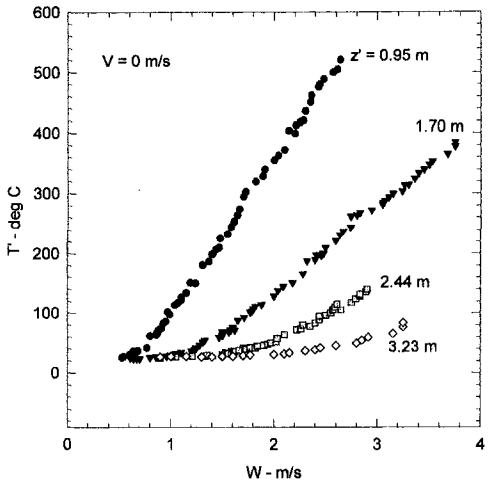

Fig. 1 Dimensional temperature measurements as a function of location and draw speed (from Blyler et al. 1986)

protective coating to the fiber, it is necessary to reduce its temperature by a suitable cooling process, see Blyler and DiMarcello (1987). Early studies of the fiber temperature variation can be found in Anderson (1958) and in Arridge and Prior (1964). The required temperature drop places an important practical limitation on the minimum height of production draw towers. Filtered cross-flows are often used to augment the cooling process (Choudhary et al., 1994). Such flows also help to prevent the deposition of particulates onto the pristine fiber, thereby minimizing the introduction of flaw sites. In this paper a discussion is given of the temperature decay, including cross-flow effects. These results lead to scaling laws that can be applied directly to draw tower design.

In addition to material properties and atmospheric conditions, the cooling rate in a particular draw tower is governed by the distance z' from the preform rod, the draw speed W, and the cross-flow speed V. Dimensional reasoning shows that the fiber temperature distribution depends on the draw speed Reynolds number Re, the speed ratio V/W, and a suitable scaled vertical coordinate, see Section 2. Since the typical Biot number is small, a standard lumped-parameter approach can be used to predict the fiber temperature distribution, see Section 3. Radiative effects are included in the general analysis but are found not to play a significant role in the final stages of the cooling process. When cross-flow effects are absent, the asymptotic temperature decay is shown to be dependent only on the scaled vertical coordinate. Inclusion of crossflows leads to an additional dependence on the crossflow Reynolds number, see Section 4. The temperature variations predicted by these laws correlate well with measurements taken in a standard draw tower.

2 Observations and Dimensional Analysis

Fiber temperatures, at a distance z' below the furnace, have been recorded as a function of the draw speed by Blyler et al. (1986). These measurements were taken on a cryogenically stabilized infrared pyrometer with an indium antimonide detector and calcium fluoride optics. The instrument was sensitive to radiation in the 4 μm wavelength range and it was calibrated by focussing onto a 127 μm aperture in a temperature controlled blackbody. Measurement errors are believed to be within ± 1 K. Figure (1) shows typical temperature data. For fixed ambient conditions and fiber material (i.e., silica with radius $R_f' = 62.5$ μm), the cooling process depends on the characteristic time scale z'/W associated with the passage of a fiber element from the furnace exit to the measuring point. The heat loss from the fiber to the surroundings can be characterized by the time scale

$$t_c' = \left(\frac{\rho' c_p}{h}\right)_\infty R_f' \tag{1}$$

where the suffix ∞ denotes evaluation at the ambient air temperature T_∞'. Consequently, a length scale over which convective cooling is important can be defined by

$$z_c' = Wt_c' = (\mathrm{Bi}^{-1}\,\mathrm{Pe})R_f'. \tag{2}$$

Here Bi is the Biot number and Pe is the fiber Peclet number.

Typical experimental results indicate that $\mathrm{Bi} \ll 1$, see Section 3. For practical draw speeds (0.5 m/s $< W <$ 12 m/s), $\mathrm{Pe} \gg 1$ ($\sim 50 - 500$). Consequently, from (2), $R_f' \ll z_c'$ (i.e., $\mathrm{Bi}\,\mathrm{Pe}^{-1} \ll 1$), and the influence of axial diffusion over the cooling length scale z_c' is negligible compared with radial diffusion. In fact, since $\mathrm{Bi} \ll 1$, the time scale for radial diffusion is much less than the cooling time scale t_c'. It is therefore appropriate to view the fiber temperature as being independent of r' in the region $z' = O(z_c')$. Similarly, since $(\mathrm{Pe}z_c'/R_f') \gg 1$, it also follows that axial diffusion is negligible compared with the advective term on the scale z_c'. These remarks do not apply in the draw-down region near the furnace where axial and radial diffusion will be comparable over a length scale defined by the preform diameter.

3 Theoretical Considerations

A combined convection-radiation analysis for the heat transfer between the fiber and the surrounding air is relatively complex. As noted above, for characteristic fiber radii, the effective Biot number is expected to be small. Consequently, a standard lumped parameter approximation can be made in which the spatial temperature distribution $T' = T'(r', z')$ is replaced by $T' = T'(z')$ and axial conduction is neglected. An energy balance for a fiber element, allowing for convective and radiative losses, leads to the equation

$$\rho' c_p A W \frac{dT'}{dz'} = -hP(T' - T_\infty') - \epsilon\sigma P(T'^4 - T_\infty'^4). \tag{3}$$

Related results, based on similar but not identical approximations, can be found, for example, in Bejan (1993) and Incropera and DeWitt (1990).

Defining $T = T'/T_s'$, $\eta = z'/z_c'$, where T_s' is the silica softening temperature ($\approx$1880 K), gives from (3)

$$\eta - \eta_o = \frac{1}{2}\int_T^{T_0} \frac{du}{H(u - T_\infty) + E(u^4 - T_\infty^4)}, \tag{4}$$

with

$$H = \frac{h}{h_\infty}, \quad E = \frac{\epsilon\sigma T_s'^3}{h_\infty}. \tag{5}$$

E is a dimensionless measure of the relative magnitude of the radiative and convective heat transfer coefficients. In general $H = H(T)$, $E = E(T)$, and the integral (4) must be evaluated numerically. If H and E are constants, (4) can be expressed in terms of elementary functions. Note that the solution (4) will not be valid sufficiently close to the furnace where the lumped parameter approach is inappropriate. The constant η_o, with $T(\eta_o) = T_o$, defines a location beyond which the lumped approximation holds.

Irrespective of the overall behavior of $H(T)$ and $E(T)$, and the location of η_o, it follows from (4) that the final stages of the cooling process ($T \to T_\infty$ as $\eta \to \infty$) are governed by

$$(T - T_\infty) \sim a \exp(-M\eta), \tag{6}$$

where

$$M = 2(1 + 4E_\infty T_\infty^3), \tag{7}$$

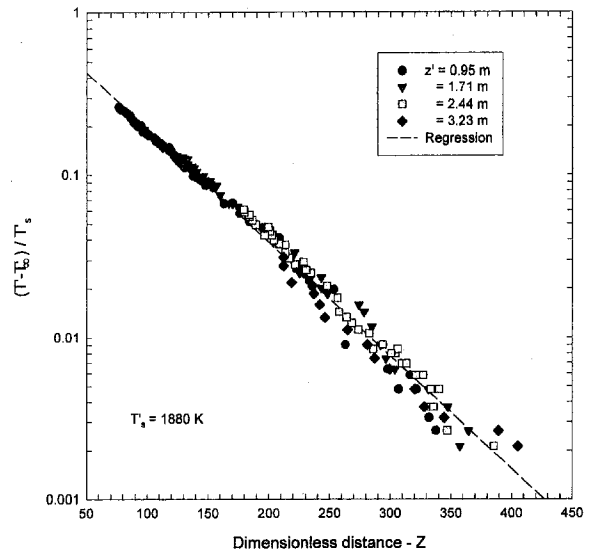

Fig. 2 Exponential decay law for fiber cooling with regression fit through the data

and $E_\infty = E(T_\infty)$. Although not given here, an explicit expression for the constant a, which is dependent on η_o, can be written down. It is, however, important to emphasize that (6) is not applicable for all η, so that the amplitude $a \neq 1 - T_\infty$. Paek and Schroeder (1981) also used a lumped parameter approach to deduce an exponential decay law of the form (6). They employed, however, averaged values for the material properties and assumed that the law was valid for $z' \geq 0$ so that $a \equiv (1 - T_\infty)$.

Estimates of the relative radiative contribution to the final decay (defined by $4E_\infty T_\infty^3$) suggest that

$$M \simeq 2 \tag{8}$$

with an error of less than 4 percent even for an emissivity $\epsilon \simeq 1$. This calculation is based on the value of Bi determined below, see (11). Radiative effects will, however, be significant for $\eta = O(1)$.

The result (6) with $M = 2$ indicates that for a fixed T_∞, $T = T(\eta)$, $\eta \gg 1$. Since the definition of η includes the unknown heat transfer coefficient h_∞, it is convenient to introduce

$$Z = \frac{z'}{R_f' \,\mathrm{Pe}} \text{ so that } \eta = \mathrm{Bi}\, Z. \tag{9}$$

Equation (6), using (8) and (9), is now rewritten

$$T - T_\infty = a \exp\{-2\ \mathrm{Bi}\ Z\}. \tag{10}$$

Figure (2) shows that the experimental data contained in Fig. (1) do correspond to an exponential decay of this type, with

$$\mathrm{Bi} \simeq 0.0081 \text{ and } a \simeq 0.98. \tag{11}$$

As can be seen, $\mathrm{Bi} \ll 1$ is consistent with the assumption made earlier. Note that the result holds for silica in air with an ambient temperature of approximately 298 K. At this temperature, $(1 - T_\infty) \simeq 0.84 \neq a$. The increased spread in the data as $(T - T_\infty)$ decreases is associated with small errors in the temperature measurements recorded close to the ambient temperature T_∞', as well as with uncertainties in T_∞' itself. A change of 2 K in T' encompasses most of the temperature excursions for $|T - T_\infty| < 4 \times 10^{-3}$. All data points with $|T - T_\infty| < 2 \times 10^{-3}$ have been excluded from the regression fit represented by (11).

Practical values of the Reynolds number, $\mathrm{Re} = WR_f'/\nu_\infty$, are relatively small, i.e., < 50. Consequently, there is an effectively thick gas layer surrounding the fiber that moves at the fiber speed. Since heat loss from the fiber occurs primarily by conduction through this layer, it can be expected that Bi will be independent of Re, i.e., it will not depend on the draw speed W. This postulate is confirmed by (11). Hence, the heat transfer coefficient h is independent of Re, and from (4), (8), (9), and (11) it is evident that

$$T = F(U), \tag{12}$$

where $U = Z^{-1} = WR_f'^2/k_{f_\infty} z'$ can be viewed, for a given z', as a dimensionless draw speed. If the original data from Fig. (1) are recast in this way, a single curve consistent with the parameter free law (12) is obtained; see Fig. (3). Similarly, Z can be interpreted as a dimensionless distance from the furnace or, equivalently, as a dimensionless particle travel time.

4 Crossflow Effects

Forced convective flows, normal to the fiber axis, are often used to augment the cooling process. If V is the cross-flow speed, dimensional reasoning now implies that, for a given material and fixed ambient conditions,

$$T'/T_s' \equiv T = G(Z;\ V/W,\ \mathrm{Re}), \tag{13}$$

where again, since h_∞ is unknown, it is convenient to use Z rather than η; see (9). The general law (13) can also be written as

$$T = \hat{G}(Z;\ \mathrm{Re}_V,\ \mathrm{Re}), \text{ where } \mathrm{Re}_V = \frac{VR_f'}{\nu_\infty} = \frac{V}{W}\,\mathrm{Re}. \tag{14}$$

Because of control instrumentation, a typical production draw tower does not permit uniform cross-flows to be applied over the length of the fiber. In particular, for the experiments reported here, the data at any fixed measuring station has a different nonuniform cross-flow history when compared with another measuring station. An average cross-flow speed $\bar{V}$ can, however, be used to define an effective cross-flow Reynolds number

$$\overline{\mathrm{Re}_V} = \frac{\bar{V}}{W}\,\mathrm{Re}. \tag{15}$$

Inclusion of the cross-flow history suggests that, with Re small, (13) can be replaced by

$$T = \bar{G}(Z;\ \overline{\mathrm{Re}_V}). \tag{16}$$

Experimental data for two different average cross-flow speeds

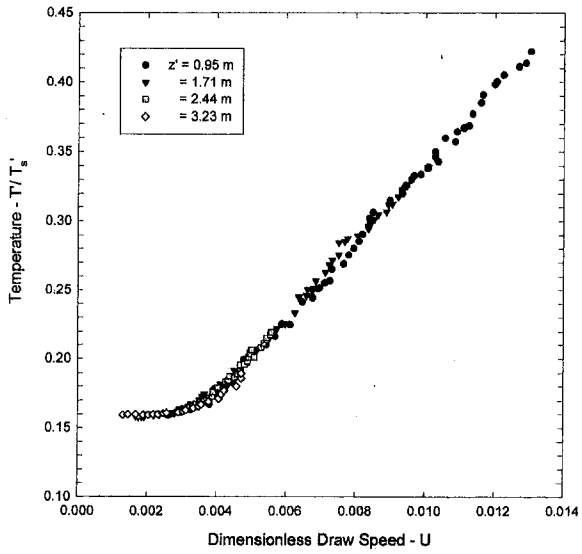

Fig. 3 Reduced curve for the fiber temperature

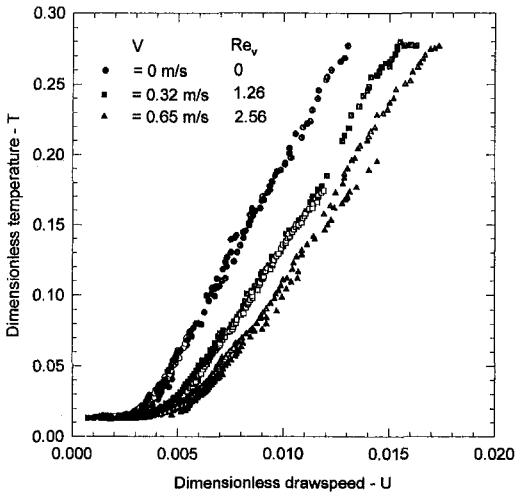

Fig. 4 Crossflow correlations

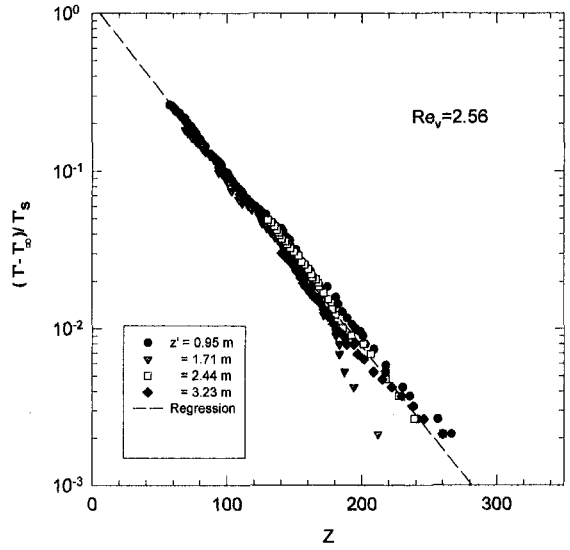

Fig. 5 Exponential law with crossflow

Table 1 Biot number and amplitude dependence on effective crossflow Reynolds number

$\overline{\text{Re}}_v$	0	1.26	2.56
Bi	0.0081	0.011	0.013
a	0.98	1.13	1.16

were obtained by Blyler et al. (1986). Corresponding dimensionless plots are given in Fig. 4 together with the data for $V = 0$. Again, these results effectively collapse onto a single curve for each $\overline{\text{Re}}_V$. Some sensitivity to the cross-flow history is evident when data from different locations is compared directly. (See results for $\overline{\text{Re}}_V = 2.56$ in Fig. 4 where differences between data at $z' = 1.71$ m and $z' = 3.23$ m are clearly visible.)

As discussed in Section 3, the final stages of the cooling process will be governed by (9) and (10), but now Bi = Bi ($\overline{\text{Re}}_V$), etc. Tests of the exponential law (10), including cross-flow, are shown in Fig. 5 for $\overline{\text{Re}}_V = 2.56$. Linear regression fits to the data lead to the results given in Table 1.

5 Closing Remarks

Without crossflows, temperature data for the cooling of silica fibers have been shown to collapse onto a single curve of the form (12). A particular model for the cooling process leads to the specific result (4) giving the asymptotic decay law (10) which provides a good correlation of the experimental observations. The results demonstrate that the heat transfer coefficient h_∞ is independent of the Reynolds number Re.

Cross-flow data reported here are associated with a particular draw tower configuration in which there is a nonuniform blowing profile, and consequently a variable cooling history that depends on location within the draw tower. Use of an averaged cross-flow Reynolds number still leads to the cooling law (10), but now the Biot number is dependent on $\overline{\text{Re}}_v$. It is believed that this type of law will apply to any draw tower of a similar type, but the results for Bi ($\overline{\text{Re}}_v$) will be tower specific and must be determined as part of its performance characteristics. Even with cross-flow, however, the data show that Bi (or h_∞) does not depend on the draw speed W.

Acknowledgment

We thank L. L. Blyler for making available the temperature measurements used in this note and for providing details of the instrumentation. Useful comments by the referees are also acknowledged.

References

Blyler, L. L., and DiMarcello, F. V., 1987, "Optical Fibers, Drawing and Coating," *Encyc. Phys. Sci. & Technol.*, Vol. 9, pp. 647–657, Academic Press, New York.

Anderson, O. L., 1958 "Cooling Time for Strong Glass Fibers," *J. Appl. Phys.*, Vol. 29, p. 9.

Arridge, R. G. C., and Prior, K., 1964 "Cooling Time for Silica Fibres," *Nature*, Vol. 203, p. 386.

Choudhary, S. R., Jaluria, Y., Vaskopoulos, T., and Polymeropoulos, C. E., 1994 "Forced Convective Cooling of Optical Fiber During Drawing Process," ASME JOURNAL OF HEAT TRANSFER, Vol. 116, p. 790.

Blyler, L. L., Cogan, K. A., DiMarcello, F. W., Ferrara, J. A., Hart, A. C., and Progelhof, R. C., 1986, unpublished data, Bell Laboratories, Murray Hill, NJ.

Bejan, A., 1993 *Heat Transfer*, John Wiley & Sons, New York.

Incropera, F. P., and DeWitt, D. P., 1990 "Fundamentals of Heat and Mass Transfer," 3rd ed., John Wiley & Sons, New York.

Paek, U. C., and Schroeder, C. M., 1981, "High Speed Coating of Optical Fibers With UV Curable Materials at a Rate of Greater than 5m/sec," *Appl. Optics*, Vol. 20, pp. 4028–4034.

Inverse Method To Predict Temperature and Heat Flux Distribution in a Cutting Tool

W. Xu[1], J. Genin[2], and Q. Dong[3]

Introduction

Although machining, as we know it today, got its start before the industrial revolution, it was not until the 1940s that the basic mechanisms associated with the machining process were put on

[1] Assistant Professor, Department of Mechanical Engineering, New Mexico State University, Box 30001, Department 3450, Las Cruces, NM 88003-8001.

[2] Professor, Department of Mechanical Engineering, New Mexico State University, Box 30001, Department 3450, Las Cruces, NM 88003-8001. E-mail: jgenin @nmsu.edu

[3] Graduate Student, Department of Mechanical Engineering, New Mexico State University, Box 30001, Department 3450, Las Cruces, NM 88003-8001.

Contributed by the Heat Transfer Division of THE AMERICAN SOCIETY OF MECHANICAL ENGINEERS. Manuscript received by the Heat Transfer Division December 5, 1995; revision received April 3, 1997; Keywords: Direct-Contact Heat Transfer; Mat'ls. Processing & Manufacturing Process; Modeling & Scaling. Associate Technical Editor: A. S. Lavine.

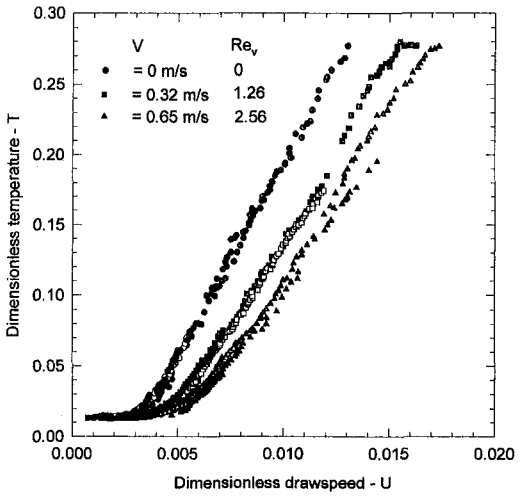

Fig. 4 Crossflow correlations

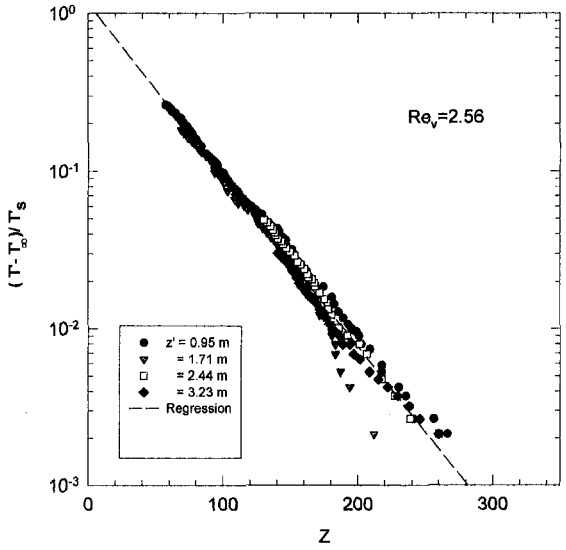

Fig. 5 Exponential law with crossflow

Table 1 Biot number and amplitude dependence on effective crossflow Reynolds number

$\overline{Re_v}$	0	1.26	2.56
Bi	0.0081	0.011	0.013
a	0.98	1.13	1.16

were obtained by Blyler et al. (1986). Corresponding dimensionless plots are given in Fig. 4 together with the data for $V = 0$. Again, these results effectively collapse onto a single curve for each $\overline{Re}_V$. Some sensitivity to the cross-flow history is evident when data from different locations is compared directly. (See results for $\overline{Re}_V = 2.56$ in Fig. 4 where differences between data at $z' = 1.71$ m and $z' = 3.23$ m are clearly visible.)

As discussed in Section 3, the final stages of the cooling process will be governed by (9) and (10), but now Bi = Bi ($\overline{Re}_V$), etc. Tests of the exponential law (10), including cross-flow, are shown in Fig. 5 for $\overline{Re}_V = 2.56$. Linear regression fits to the data lead to the results given in Table 1.

5 Closing Remarks

Without crossflows, temperature data for the cooling of silica fibers have been shown to collapse onto a single curve of the form (12). A particular model for the cooling process leads to the specific result (4) giving the asymptotic decay law (10) which provides a good correlation of the experimental observations. The results demonstrate that the heat transfer coefficient h_∞ is independent of the Reynolds number Re.

Cross-flow data reported here are associated with a particular draw tower configuration in which there is a nonuniform blowing profile, and consequently a variable cooling history that depends on location within the draw tower. Use of an averaged cross-flow Reynolds number still leads to the cooling law (10), but now the Biot number is dependent on $\overline{Re}_v$. It is believed that this type of law will apply to any draw tower of a similar type, but the results for Bi ($\overline{Re}_v$) will be tower specific and must be determined as part of its performance characteristics. Even with cross-flow, however, the data show that Bi (or h_∞) does not depend on the draw speed W.

Acknowledgment

We thank L. L. Blyler for making available the temperature measurements used in this note and for providing details of the instrumentation. Useful comments by the referees are also acknowledged.

References

Blyler, L. L., and DiMarcello, F. V., 1987, "Optical Fibers, Drawing and Coating," *Encyc. Phys. Sci. & Technol.*, Vol. 9, pp. 647–657, Academic Press, New York.

Anderson, O. L., 1958 "Cooling Time for Strong Glass Fibers," *J. Appl. Phys.*, Vol. 29, p. 9.

Arridge, R. G. C., and Prior, K., 1964 "Cooling Time for Silica Fibres," *Nature*, Vol. 203, p. 386.

Choudhary, S. R., Jaluria, Y., Vaskopoulos, T., and Polymeropoulos, C. E., 1994 "Forced Convective Cooling of Optical Fiber During Drawing Process," ASME JOURNAL OF HEAT TRANSFER, Vol. 116, p. 790.

Blyler, L. L., Cogan, K. A., DiMarcello, F. W., Ferrara, J. A., Hart, A. C., and Progelhof, R. C., 1986, unpublished data, Bell Laboratories, Murray Hill, NJ.

Bejan, A., 1993 *Heat Transfer*, John Wiley & Sons, New York.

Incropera, F. P., and DeWitt, D. P., 1990 "Fundamentals of Heat and Mass Transfer," 3rd ed., John Wiley & Sons, New York.

Paek, U. C., and Schroeder, C. M., 1981, "High Speed Coating of Optical Fibers With UV Curable Materials at a Rate of Greater than 5m/sec," *Appl. Optics*, Vol. 20, pp. 4028–4034.

Inverse Method To Predict Temperature and Heat Flux Distribution in a Cutting Tool

W. Xu[1], J. Genin[2], and Q. Dong[3]

Introduction

Although machining, as we know it today, got its start before the industrial revolution, it was not until the 1940s that the basic mechanisms associated with the machining process were put on

[1] Assistant Professor, Department of Mechanical Engineering, New Mexico State University, Box 30001, Department 3450, Las Cruces, NM 88003-8001.

[2] Professor, Department of Mechanical Engineering, New Mexico State University, Box 30001, Department 3450, Las Cruces, NM 88003-8001. E-mail: jgenin @nmsu.edu

[3] Graduate Student, Department of Mechanical Engineering, New Mexico State University, Box 30001, Department 3450, Las Cruces, NM 88003-8001.

Contributed by the Heat Transfer Division of THE AMERICAN SOCIETY OF MECHANICAL ENGINEERS. Manuscript received by the Heat Transfer Division December 5, 1995; revision received April 3, 1997; Keywords: Direct-Contact Heat Transfer; Mat'ls. Processing & Manufacturing Process; Modeling & Scaling. Associate Technical Editor: A. S. Lavine.

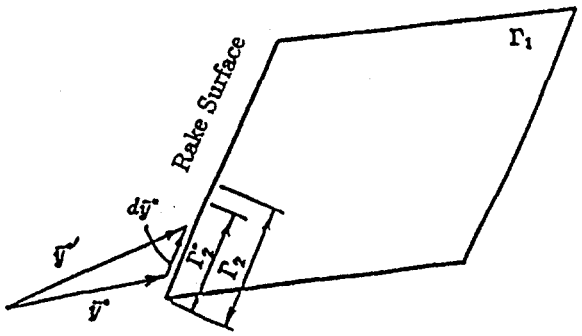

Fig. 1 Two-dimensional domain of cutting tool

a firm mathematical basis; see Ernst and Merchant (1941), and Merchant (1945). Since then, machining research has progressed rapidly. Researchers have shown an interest in the thermal elastic-plastic stress-strain and temperature distributions in the workpiece and on the tool surface. These characterize the accuracy of the machining model and affect the properties of manufactured parts, as well as tool life.

In order to model the machining process, the condition of the tool-workpiece interface in the field of metal cutting has to be understood. Merchant's model assumes the normal and frictional stresses on the tool face over the workpiece and chip contact areas to be uniform. This is not the case in metal cutting. The normal and shear stresses along the chip-tool interface vary in the cutting process. Zorev (1963) characterized the interface as being divided into two regions called the sticking and sliding regions. Further, the coefficient of friction is found to decrease with increased normal stress, Hosford and Caddell (1983). When studying the problem the temperature and heat-flux distribution must first be determined for the tool-workpiece system. Then one can establish the total contact length (area) and the location of the point which distinguishes the sticking and sliding regions of the cutting tool-chip interface.

In this work we develop an inverse problem for the thermoelastic model to solve the contact problem in orthogonal cutting. Our goal is to determine the chip contact length, the thermal gradient in the tool, and the contact stresses on the tool-workpiece interface. To our knowledge this is the first use of inverse theory to solve the orthogonal cutting contact problem. An excellent reference on thermal inverse problems is Beck et al. (1985).

Problem Definition

Consider a two-dimensional domain Ω, shown in Fig. 1, bounded by the boundary Γ which may be written as $\Gamma = \Gamma_1 + \Gamma_2^*$. Here the boundary condition of Γ_1 is prescribed, the geometry of which depends on the geometry of Γ_2^*. Γ_2^* is the unknown contact length with unknown boundary conditions.

The temperature distribution for the steady-state condition is described by

$$\nabla^2\phi(\vec{x}) = 0, \quad \vec{x} \in \Omega; \quad \phi(\vec{x}) = \phi^0,$$

$$\vec{x} \in \Gamma_{1\phi}; \quad \frac{\partial\phi}{\partial\vec{n}}(\vec{x}) = q^0, \quad \vec{x} \in \Gamma_{1q} \tag{1}$$

where $\vec{x}$ is the position vector, $\Gamma_{1\phi}$ and Γ_{1q} are the portions of Γ_1 with specified values of temperature, ϕ, and thermal gradient, q. Two inverse problems can then be formulated as shown in Figs. 1 and 2.

I Identification Problem. Here the contact length Γ_2^* is unknown. The set of experimental measurements that can be made available are

$$\phi(x_m, \Gamma_2^*) = \phi_e^0(x_m, \Gamma_2^*), \quad x_m \in \Gamma_1$$

$$q(x_n, \Gamma_2^*) = q_e^0(x_n, \Gamma_2^*), \quad x_n \in \Gamma_1 \tag{2}$$

where $m = 1, 2, \ldots, M$; $n = 1, 2, \ldots, N$. The subscript e represents the experimental measurements and the second variable Γ_2^* refers to these values as functions of the contact length. The identification problem consists of determining the contact length Γ_2^* based on these given experimental values.

II Reconstruction Problem. Here the length of contact is known and the total boundary can be described as

$$\Gamma_\phi = \Gamma_{1\phi^0} + \Gamma_{2\bar{\phi}}^*, \quad \Gamma_q = \Gamma_{1q^0} + \Gamma_{2\bar{q}}^* \tag{3}$$

where the superscript ^{0} denotes specified boundary conditions, and the superscript $\bar{}$ denotes the unknown boundary conditions. The reconstruction problem consists of determining these unknown boundary conditions based on the prescribed boundary conditions given in Eq. (2). In the reconstruction problem, temperature measurements at interior locations of the tool may also be used. These measurements are expressed as

$$\phi(\vec{x}_p, \Gamma_2^*) = \phi_e^0(\vec{x}_p, \Gamma_2^*); \quad \vec{x}_p \in \Omega; \quad p = 1, 2, \ldots, P. \tag{4}$$

It is noted that the identification and reconstruction problems posed here must be solved simultaneously.

Theoretical Formulation

The boundary integral relationship, presented by Banerjee and Butterfield (1981), for temperature in a solid corresponding to the actual contact area Γ_2^* is given as

$$\phi(\vec{x}, \Gamma_2^*) = \int_{\Gamma-\Gamma_2^*} \left[\frac{\partial G(\vec{x}, \vec{y})}{\partial n(\vec{y})} \phi(\vec{y}, \Gamma_2^*) - G(\vec{x}, \vec{y}) \frac{\partial\phi(\vec{y}, \Gamma_2^*)}{\partial n(\vec{y})} \right] d[\Gamma(\vec{y}) - \Gamma_2^*(\vec{y}^*)]$$

$$+ \int_{\Gamma_2^*} \left[\frac{\partial G(\vec{x}, \vec{y}^*)}{\partial n(\vec{y}^*)} \phi(\vec{y}^*, \Gamma_2^*) - G(\vec{x}, \vec{y}^*) \frac{\partial\phi(\vec{y}^*, \Gamma_2^*)}{\partial n(\vec{y}^*)} \right] d\Gamma_2^*(\vec{y}^*) \tag{5}$$

where G is a Green's function determined from

$$\nabla^2 G(\vec{x}, \vec{y}) = \delta(\vec{x} - \vec{y}).$$

$\delta(\vec{x})$ is a Dirac delta function, $\vec{y}$ represents the coordinates of points which locate the boundary, and the superscript * denotes quantities associated with the unknown contact area. To initiate the solution of the inverse problem, a contact area Γ_2 is assumed.

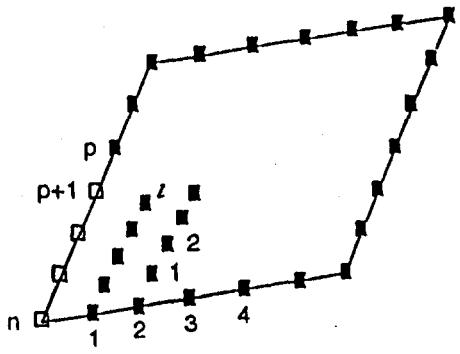

Fig. 2 Two-dimensional domain of boundary element method

Similar to Eq. (5), the temperature distribution for the assumed area Γ_2 can be written as

$$\phi(\vec{x}, \Gamma_2) = \int_{\Gamma_1} \left[\frac{\partial G(\vec{x}, \vec{y})}{\partial n(\vec{y})} \phi(\vec{y}, \Gamma_2) - G(\vec{x}, \vec{y}) \frac{\partial \phi(\vec{y}, \Gamma_2)}{\partial n(\vec{y})} \right] d\Gamma_1(\vec{y}) + \int_{\Gamma_2} \left[\frac{\partial G(\vec{x}, \vec{y})}{\partial n(\vec{y})} \phi(\vec{y}, \Gamma_2) - G(\vec{x}, \vec{y}) \frac{\partial \phi(\vec{y}, \Gamma_2)}{\partial n(\vec{y})} \right] d\Gamma_2(\vec{y}). \quad (6)$$

The variation of the temperature in the domain with an assumed contact length at the field location $\vec{x}$ with respect to the actual temperature is defined as

$$\delta\phi(\vec{x}, \Gamma_2) = \phi(\vec{x}, \Gamma_2^*) - \phi(\vec{x}, \Gamma_2). \quad (7)$$

The temperature $\phi(\vec{x}, \Gamma_2^*)$ is obtained from experimental measurements at location $\vec{x}$. Since the assumed contact area Γ_2 is known, $\phi(\vec{x}, \Gamma_2)$ may be calculated using the usual boundary element procedure. Thus, $\delta\phi(\vec{x}, \Gamma_2)$ can be determined at the location $\vec{x}$. The right-hand side of Eq. (7) can be expressed by the integrals of Eqs. (5) and (6). Evaluation of the integral in (5) requires using the contact length Γ_2^*, which is not known. We may express this integral in terms of the assumed contact length Γ_2 by using a Taylor expansion, see Xu and Genin (1995). On neglecting higher order terms, this yields

$$\delta\phi(\vec{x}, \Gamma_2) = \int_{\Gamma_1} \left\{ \left[G(\vec{x}, \vec{y}_1)\delta q(\vec{y}_1, \Gamma_2) - \frac{\partial G(\vec{x}, \vec{y}_1)}{\partial n(\vec{y}_1)} \delta\phi(\vec{y}_1, \Gamma_2) - \phi(\vec{y}_1, \Gamma_2) \frac{d}{d\vec{y}_1} \left[\frac{\partial G(\vec{x}, \vec{y}_1)}{\partial n(\vec{y}_1)} \right] \cdot \delta\vec{y}_1 \right.$$

$$+ G(\vec{x}, \vec{y}_1) \frac{dq(\vec{y}_1, \Gamma_2)}{d\vec{y}_1} \cdot \delta\vec{y}_1 - \frac{\partial G(\vec{x}, \vec{y}_1)}{\partial n(\vec{y}_1)} \frac{d\phi(\vec{y}_1, \Gamma_2)}{d\vec{y}_1} \cdot \delta\vec{y}_1$$

$$\left. + q(\vec{y}_1, \Gamma_2) \frac{dG(\vec{x}, \vec{y}_1)}{d\vec{y}_1} \cdot \delta\vec{y}_1 \right]$$

$$+ [J(\vec{y}_1) - 1] \left[G(\vec{x}, \vec{y}_1) q(\vec{y}_1, \Gamma_2) - \frac{\partial G(\vec{x}, \vec{y}_1)}{\partial n(\vec{y}_1)} \phi(\vec{y}_1, \Gamma_2) \right] \Bigg\} d\Gamma_1(\vec{y}_1)$$

$$+ \int_{\Gamma_2} \left\{ \left[G(\vec{x}, \vec{y}_2)\delta q(\vec{y}_2, \Gamma_2) - \frac{\partial G(\vec{x}, \vec{y}_2)}{\partial n(\vec{y}_2)} \delta\phi(\vec{y}_2, \Gamma_2) \right.\right.$$

$$- \phi(\vec{y}_2, \Gamma_2) \frac{d}{d\vec{y}_2} \left[\frac{\partial G(\vec{x}, \vec{y}_2)}{\partial n(\vec{y}_2)} \right] \cdot \delta\vec{y}_2$$

$$+ G(\vec{x}, \vec{y}_2) \frac{dq(\vec{y}_2, \Gamma_2)}{d\vec{y}_2} \cdot \delta\vec{y}_2 - \frac{\partial G(\vec{x}, \vec{y}_2)}{\partial n(\vec{y}_2)} \frac{d\phi(\vec{y}_2, \Gamma_2)}{d\vec{y}_2} \cdot \delta\vec{y}_2$$

$$\left. + q(\vec{y}_2, \Gamma_2) \frac{dG(\vec{x}, \vec{y}_2)}{d\vec{y}_2} \cdot \delta\vec{y}_2 \right]$$

$$+ [J(\vec{y}_2) - 1] \left[G(\vec{x}, \vec{y}_2) q(\vec{y}_2, \Gamma_2) - \frac{\partial G(\vec{x}, \vec{y}_2)}{\partial n(\vec{y}_2)} \phi(\vec{y}_2, \Gamma_2) \right] \Bigg\} d\Gamma_2(\vec{y}_2). \quad (8)$$

Now we shall consider the boundary conditions and rewrite Eq. (8) in a matrix form using numerical discretization.

In order to solve the problem, we shall first determine the unknown boundary conditions on assumed boundary Γ_2 from Eq. (6), which is a reconstruction problem. Then we shall solve Eq. (8), which is an identification problem.

Discretization of Reconstruction Problem. Our domain is shown in Fig. 2. The temperatures at the dot nodes are measured data which include nodes, 1, 2, . . . , p, on Γ_1 and some interior points 1, 2, . . . , l. The circular nodes, $p + 1$, $p + 2$, . . . , n, are on the assumed boundary Γ_2 with unknown temperature. The boundary of the domain is divided into n elements. Now Eq. (6) may be written as

$$\phi_k(\vec{x}_k, \Gamma_2) = \sum_{i=1}^{p} \int_{\Gamma_i} \left[G(\vec{x}, \vec{y}_1) q(\vec{y}_1, \Gamma_2) - \phi(\vec{y}_1, \Gamma_2) \frac{\partial G(\vec{x}, \vec{y}_1)}{\partial n(\vec{y}_1)} \right] d\Gamma_i + \sum_{j=p+1}^{n} \int_{\Gamma_j} \left[G(\vec{x}, \vec{y}_2) q(\vec{y}_2, \Gamma_2) - \phi(\vec{y}_2, \Gamma_2) \frac{\partial G(\vec{x}, \vec{y}_2)}{\partial n(\vec{y}_2)} \right] d\Gamma_j. \quad (9)$$

For each element, the temperature distribution can be expressed by nodal temperatures using shape functions. Eq. (9) may be written as

$$\phi_k(\vec{x}_k, \Gamma_2) = \{a\}_{1\times n}\{\phi_B\}_{n\times 1} + \{b\}_{1\times n}\{q_B\}_{n\times 1} \quad (10)$$

where the elements of vector $\{a\}$ and $\{b\}$ are

$$a_i = \int_{s_i} -\frac{\partial G}{\partial n} N_1 ds_i + \int_{s_{i-1}} -\frac{\partial G}{\partial n} N_2 ds_{i-1}$$

$$b_i = \int_{s_i} G N_1 ds_i + \int_{s_{i-1}} G N_2 ds_{i-1}$$

where N_1, N_2 are shape functions.

In the foregoing, $\{\phi_B\}$ is a temperature vector containing all boundary nodes for which ϕ_{B_1} to ϕ_{B_p} are known and $\phi_{B_{p+1}}$ to ϕ_{B_n} are unknown. $\{q_B\}$ is a temperature gradient vector containing all boundary nodes for which q_{B_1} to q_{B_p} are known and $q_{B_{p+1}}$ to q_{B_n} are unknown. From Eq. (10), any boundary temperature can be written as

$$\alpha\phi_B(\vec{x}_B, \Gamma_2) = \{a\}_{1\times n}\{\phi_B\}_{n\times 1} + \{b\}_{1\times n}\{q_B\}_{n\times 1} \quad (11)$$

where α is a coefficient for a singular point caused by the boundary element method Brebbia, et al. (1984). Therefore, using Eq. (11) all the boundary temperatures can be expressed in matrix form as

$$[H]_{n\times n}\{\phi_B\}_{n\times 1} = [G]_{n\times n}\{q_B\}_{n\times 1}. \quad (12)$$

Using Eqs. (10), all the interior measured temperatures can be expressed in matrix form as

$$\{\phi_k(\vec{x}_k)\}_{l\times 1} = [A]_{l\times n}\{\phi_B\}_{n\times 1} \quad (13)$$

where

$$[A] = [G]_{l\times n}[G]^{-1}_{n\times n}[H]_{n\times n} - [H]_{l\times n}.$$

In Eq. (13), if the number l is greater than $n - p$, the problem is called over-determined. If the number l is less than $n - p$, the problem is termed under-determined. Here we consider the simplest case, called a uniquely-determined problem, in which $l = n - p$. Eq. (13) can also be written as

$$[A_2]\{\phi_{B_{\Gamma_2}}\} = \{F\} \tag{14}$$

where

$$F_i = \phi_k(\vec{x}_k) - A_{i1}\phi_{B_1} - A_{i2}\phi_{B_2} - \ldots - A_{ip}\phi_{B_p}.$$

From Eqs. (14) and (11), the unknown boundary conditions for Γ_2, $\phi_{B_{\Gamma_2}}$ and $q_{B_{\Gamma_2}}$, can be obtained.

Discretization of Identification Problem. Returning to the general equation, Eq. (8), we rewrite it in the form

$$\delta\phi(\vec{x}) = \sum_{i=1}^{p} \int_{\Gamma_i} [A(\vec{x}, \vec{y}_1) + \vec{B}(\vec{x}, \vec{y}_1)\cdot\delta\vec{y}_1 + C(\vec{x}, \vec{y}_1)]d\Gamma_i + \sum_{j=p+1}^{n} \int_{\Gamma_j} [A(\vec{x}, \vec{y}_2) + \vec{B}(\vec{x}, \vec{y}_2)\cdot\delta\vec{y}_2 + C(\vec{x}, \vec{y}_2)]d\Gamma_j \tag{15}$$

where $i = 1, 2$ correspond to the integrals on Γ_1 and Γ_2, respectively, and

$$A(\vec{x}, \vec{y}_i) = G(\vec{x}, \vec{y}_i)\delta q(\vec{y}_i) - \frac{\partial G(\vec{x}, \vec{y}_i)}{\partial n(\vec{y}_i)}\delta\phi(\vec{y}_i)$$

$$\vec{B}(\vec{x}, \vec{y}_i) = G(\vec{x}, \vec{y}_i)\frac{dq(\vec{y}_i)}{d\vec{y}_i} - \phi(\vec{y}_i)\frac{d}{d\vec{y}_i}\left[\frac{\partial G(\vec{x}, \vec{y}_i)}{\partial n(\vec{y}_i)}\right] - \frac{\partial G(\vec{x}, \vec{y}_i)}{\partial n(\vec{y}_i)}\frac{d\phi(\vec{y}_i)}{d\vec{y}_i} + q(\vec{y}_i)\frac{dG(\vec{x}, \vec{y}_i)}{d\vec{y}_i}$$

$$C(\vec{x}, \vec{y}_i) = [J(\vec{y}_i) - 1]\left[G(\vec{x}, \vec{y}_i)q(\vec{y}_i) - \frac{\partial G(\vec{x}, \vec{y}_i)}{\partial n(\vec{y}_i)}\phi(\vec{y}_i)\right].$$

Hence, Eq. (15) may now be written as

$$\delta\phi(\vec{x}_k) = \{f_1\}_{1\times m}\{\delta\phi\}_{m\times 1} + \{f_2\}_{1\times n}\{\delta q\}_{n\times 1} + \{f_3 \quad f_4\}_{1\times 2(m-1)}\{\delta y_1 \quad \delta y_2\}^T_{2(m-1)\times 1} \tag{16}$$

where $m = n - p$, and $\{f_{1-4}\}$ are combinations of the coefficient matrices $[A]$, $[B]$, and $[C]$. We can also write Eq. (16) in matrix form as

$$\delta\phi(\vec{x}) = [H(\vec{x})]\{W\} \tag{17}$$

where

$$\{W\} = [\delta\phi_{p+1} \ldots \delta\phi_n\, \delta q_1 \ldots \delta q_n\, \delta y_{(p+2)1}\, \delta y_{(p+2)2} \ldots \delta y_{n1}\, \delta y_{n2}]^T$$

(a) Let $\vec{x} \to \xi$, where $\xi \in \Gamma_2$, Eq. (17) can be written as

$$([C] - [H_1])\{W\} = 0. \tag{18}$$

(b) Let $\vec{x} \to \xi$, where $\xi \in \Gamma_1$, we obtain

$$[H_2]\{W\} = [C]\{\phi^* - \phi\} = \{0\}. \tag{19}$$

(c) Let $\vec{x} \to \xi$, where $\xi \in \Omega^*$; Eq. (17) reduces to

$$[H_3]\{W\} = \{\phi^* - \phi\}. \tag{20}$$

Combining Eqs. (18), (19), and (20), we obtain the final boundary element equation in matrix form as

$$\begin{pmatrix} [C_1] - [H_1] \\ \cdots \\ [H_2] \\ \cdots \\ [H_3] \end{pmatrix}\{W\} = \begin{Bmatrix} \{0\} \\ \cdots \\ \{0\} \\ \cdots \\ \{\phi^* - \phi\} \end{Bmatrix}. \tag{21}$$

The solution to Eq. (21) yields the unknown quantities $\{W\}$. From these, the $\{\delta\vec{y}\}$ are obtained and used to update the coordinates of the boundary Γ_2. This iteration procedure is continued until a designated convergence criterion is satisfied.

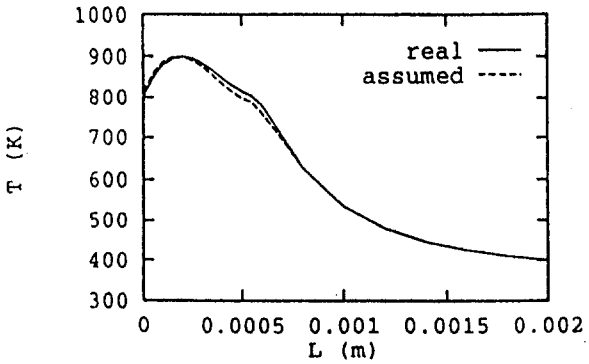

Fig. 3 Temperature distribution on rake surface

Numerical Results of Example Problem

We applied the computational approach to the two-dimensional cutting model shown in Fig. 2. Experimentally, the temperature of seven internal points were measured. The workpiece is T6061-T6 aluminum, the rake angle of the cutting tool is 20 deg, the depth of cut is 0.6325 mm, and the cutting speed is 5 m/s; see Laake and Anderson (1991). In our computation the unknown contact length was initially assumed to be 1.2 mm with unknown boundary conditions. On the other surfaces (free surfaces) the heat flux is assumed as constant. After a number of iterations, determined by our convergence criterion, the real contact length of the chip-tool interface was found to be 0.8 mm. The corresponding temperature and thermal gradient are shown in Figs. 3 and 4. In the Figs., L represents part of the rake surface. The temperature and heat-flux distributions remained reasonably stable beyond the distances L. Zero length represents the cutting tool tip.

Discussion

In the example, we assumed the number of measured internal temperature points to be the same as the number of nodes on the assumed contact length. We used a LUD (Lower and Upper triangular Decomposition) approach to solve the uniquely determined problem. If the measurements are limited by the experimental environment, the number of measured temperature points can be less than that of the number of nodes on the assumed contact length, producing an under-determined problem. In this case, one can use a SVD (Singular Value Decomposition) approach to obtain an approximate solution. If the measured data are more than the number of nodes on the assumed contact length, an over-determined problem, one can use a general linear least squares approach to obtain an accurate solution.

With respect to criteria for ending the iteration process, one can choose from among the following parameters: variation of contact length, temperature, and thermal gradient. In our exam-

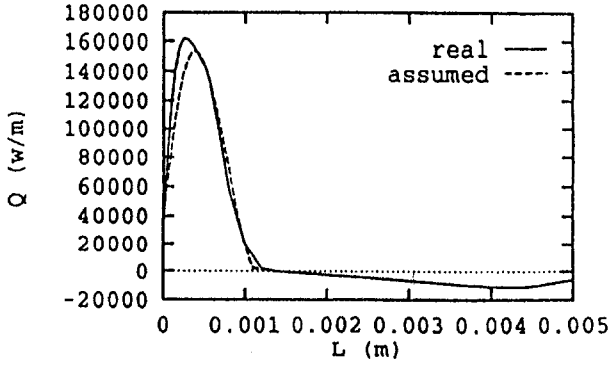

Fig. 4 Heat-flux distribution on rake surface

ple problem the variation of contact length was too small (10^{-6}–10^{-7} m), and the variation of the thermal gradient was too big (10^{3}–10^{4} W/m^2). Therefore, the criterion of variation of temperature (10^{-1} K), computational and measured internal temperature, was used.

Mathematically, the inverse problem is an ill-posed boundary value problem, and its sensitivity matrix dominates the accuracy of the solution. An important feature of our approach is that one does not require the computation of the sensitivity. The foregoing approach is also applicable to the problem of contact stresses between the cutting tool and workpiece.

Acknowledgment

This research project was supported by the U.S. Army Research Office, Research Triangle Park, N.C.

References

Banerjee, P. K., and Butterfield, R., 1981, "Boundary Element Methods in Engineering Science," McGraw-Hill Book Co. Inc., U.K.

Beck, J. V., Blackwell, B., and St. Clair, C. R., 1985, "Inverse Heat Conduction: Ill-posed Problems," Wiley Interscience, New York.

Brebbia, C. A., Telles, J. C. F., and Wrobel, L. C., 1984, "Boundary Element Techniques," Springer-Verlag Berlin, Heidelberg.

Ernst, H., and Merchant, M. E., 1941, "Chip Formation, Friction and Finish, in Surface Treatment of Metals," *Amer. Soc. for Metal,* Metals Park OH.

Hosford, W. H., and Caddell, R. M., 1983, *Metal Forming,* Prentice Hall, Englewood Cliffs NJ, pp. 122–128.

Laake, B. A., and Anderson, C. A., 1991, "Finite Element Modeling of Orthogonal Machining Using an Elastic-Viscoplastic Material Model," LA12151-MS, Los Alamos National Laboratory.

Merchant, M. E., 1945, "Mechanics of the Cutting Process," *J. Appl. Phys.,* Vol. 216, pp. 267, 318.

Xu, W., and Genin, J., 1995, "Inverse Technique for Analyzing the Orthogonal Cutting Process," *Proceedings, The American Society of Precision Engineering 10th Annual Meeting,* D. A. Lucca, ed., Austin, Texas.

Zorev, N. N., 1963, "Interrelationship Between Shear Processes Occurring Along Tool Face and Shear Plane in Metal Cutting," *International Research in Production Engineering,* ASME, NY, p. 42.